

Excitation Force and Frequency Effects in Wave-Based Techniques for the
Characterization of Geomaterials at Different Scales

by

Fredy A. Díaz-Durán

A thesis

presented to the University of Waterloo

in fulfillment of the

thesis requirement for the degree of

Doctor of Philosophy

in

Civil Engineering

Waterloo, Ontario, Canada, 2020

© Fredy A. Díaz-Durán 2020

Examining committee membership

The following served on the Examining Committee for this thesis. The decision of the Examining Committee is by majority vote.

External examiner

Dr. Glenn J. Rix
Senior Principal – Geosyntec Consultants, Inc.
Former Professor in Geosystems Engineering
Georgia Institute of Technology

Co-Supervisor

Dr. Giovanni Cascante
Professor
Department of Civil and Environmental Engineering
University of Waterloo

Co-supervisor

Dr. Mahesh Pandey
Professor, Industrial Research Chair
Department of Civil and Environmental Engineering
University of Waterloo

Internal member

Dr. Maria Anna Polak
Professor
Department of Civil and Environmental Engineering
University of Waterloo

Internal member

Dr. Dipanjan Basu
Professor
Department of Civil and Environmental Engineering
University of Waterloo

Internal-external member

Dr. Maurice Dusseault
Professor, Engineering Geology
Earth and Environmental Sciences Department
University of Waterloo

Author's Declaration

This thesis consists of material all of which I authored or co-authored: see Statement of Contributions included in the thesis. This is a true copy of the thesis, including any required final revisions, as accepted by my examiners.

I understand that my thesis may be made electronically available to the public.

Statement of Contributions

This thesis contains materials that have been submitted for publications in conference proceedings (Chapters 5 and 7), and in an indexed journal (Chapter 9). It also includes some laboratory results for bender element (BE) tests obtained by Dr. Cristiana Ferreira (University of Porto, Portugal). In addition, the help of Dr. Muhammad Irfan (University of Waterloo, Canada) was fundamental to simultaneously obtain the data from bender elements (BE) and resonant column (RC) tests on reconstituted samples of transparent soil. All those laboratory results are included, used for comparison purposes, and properly referenced in Chapter 9 of this thesis.

Except for the data obtained in laboratory tests by the aforementioned researchers, the rest of the thesis is the sole contribution of the author. Furthermore, for Chapter 9, the whole analysis of the data, the calibration of the bender element (BE) using the laser vibrometer, and the conclusions of the chapter are solely contributions of the author of the thesis.

Abstract

All around the world, building codes require the characterization of geomaterials as a fundamental step in the foundation design process. Specifically, in seismic design, the evaluation of dynamic properties is a key requirement for the dynamic site characterization. Soil dynamic properties can be obtained in-situ and in the laboratory. However, there are limitations to either approach. The effect of the acoustic impedance ratio for the top materials in a layered media can have a major influence on in-situ measurements. On the other hand, the effect of the frequency content of the excitation source on the dynamic properties obtained from either field or laboratory measurements is not well understood. In addition, the scale or dimensions of the volume of material being tested represents also a challenge in the interpretation of field and laboratory measurements. Hence, the combination of impedance ratio, frequency content, and scale effects may lead to significant errors in the seismic design of civil infrastructure.

The acoustic impedance ratio between top materials in a layered media is currently not considered when performing seismic testing in the field. However, this ratio plays a key role in the evaluation of the potential success of seismic tests such as MASW and sCPTU for the quantification of dynamic properties in different soil profiles. The lack of understanding of impedance ratio effects can lead practitioners to the incorrect interpretation of field test results. Likewise, the lack of characterization of the seismic source used in the field (i.e. applied force amplitude, pulse duration, and frequency content) prevents practitioners and researchers from improving the reliability of seismic tests. Furthermore, the incorrect characterization of the seismic source prevents the accurate representation of field conditions in numerical models; which are needed to advance the interpretation and understanding of complex field conditions.

On the other hand, seismic source characterization is also needed to enhance laboratory testing techniques. For instance, the unknown characteristics of the excitation in typical bender elements test are preventing practitioners and researchers from the correct interpretation of lab results and the understanding of the bender element – soil specimen interaction. Overcoming this challenge is needed to make reliable standards

for bender element testing, which has become a frequent practice because of their simple and economical implementation in different geotechnical instruments (e.g. triaxial, odometer, and direct simple shear devices).

The main objective of this thesis is to address these three issues to improve the dynamic characterization of geomaterials at low strain levels at different scales using mechanical waves. Hence, field, laboratory, and numerical tests are used to study the effects of acoustic impedance ratio in layered media, the frequency content of the source in seismic (i.e. sCPTU and MASW tests), and the bender element testing.

The problem of soil dynamic characterization is addressed by considering different spatial distributions of materials (i.e. homogeneous media, layered media, and spatially variable media), different frequency contents in the input source of seismic tests, and different scales (i.e. field scale, physical laboratory models, and soil sample-scale in bender element testing). Thus, the main contributions of this research are given in these three main areas. First, the excitation frequency and impedance ratios between the top layers are studied using calibrated numerical models. The results show that there is an important limitation for the applicability of the MASW test in soft soils. Soil profiles with impedance ratios between 0.4 and 0.5 showed a reduction of up to 20% in the estimated value of the average shear wave velocity for the shallower 30 meters (v_{s-30}).

Second, a new methodology for the characterization of the excitation source in near-surface seismic testing using laboratory, field, and numerical simulation results is presented. The results show that when the frequency content of the excitation source is limited in the generation of high-frequencies (e.g. wavelengths three times smaller than the layered thickness) the dynamic properties obtained in sCPTU could overestimate or underestimate shear wave velocities up to 9%. A novel technique using the transfer function approach is used to characterize the source in a seismic test. Once the input source is known, the study of the effect of changes in the frequency content of the source is possible for multiple soil profiles.

Finally, the characterization of the transmitter bender element using a modern laser vibrometer and a resonant column device is presented. The results demonstrate

there is significant participation of P-waves in the response of typical bender element tests. The transmitter bender element not only vibrates in the horizontal direction, as commonly assumed but also in the vertical direction. More importantly, the participation of vertical vibration modes increases with the excitation frequency and the confinement level. This discovery improves not only the interpretation of bender element tests but also allows the use of typical bender elements to simultaneously measure P-waves and S-waves by using different excitation frequencies.

Acknowledgements

In the first place, I want to thank my supervisor Dr. Giovanni Cascante for allowing me to be part of and work in the NDT research group at the University of Waterloo. Also to my co-supervisor Dr. Mahesh Pandey for your motivation to take this process to a good end. Their guidance and support have been fundamental in this journey, which for sure will put me on the right path to pursue a career in academics and scientific research.

I would like to express my thankful to the committee members of my thesis, Dr. Maria Ana Polak, Dr. Dipanjan Basu, and Dr. Maurice Dusseault, for taking the time to review my thesis and for providing valuable comments, suggestions and feedback. I am also very thankful to Dr. Glenn J. Rix, the external examiner member of the committee, who kindly agreed in reviewing the document and attending my thesis defense.

I would also like to thank Dr. Cristiana Ferreira, and Dr. Antonio Vianna da Fonseca at the University of Porto (Portugal), and Dr. Muhammad Irfan at the University of Waterloo, for sharing with me parts of the data I used in Chapter 9 of this thesis.

Moreover, my gratitude goes to the Ministry of Transportation of Ontario (MTO), the Natural Sciences and Engineering Research Council of Canada (NSERC), the Department of Civil and Environmental Engineering at the University of Waterloo, and also to the company Pagani Geotechnical Equipment for helping me in carrying out the sCPT tests and getting part of the data used in this research.

Of course, I am greatly grateful to all my friends in the NDT and Geotechnical Engineering groups at University of Waterloo for their support, challenging and motivation: Dr. Hassan Ali, Dr. María José Rodríguez, Dr. Muhammad Irfan, Dr. Sabah Fartosy, Dr. Bijan Mahbaz, Dr. Kamelia Atefi, Dr. Wei Zhang, Dr. Bipin Gupta, Dr. Ammar Shakir, Piotr Wiciak, Cristóbal Lara, Taher Ameen, and Mina Lee, among many other valuable members of the University of Waterloo.

I would also like to express my sincere appreciation for the collaboration received from the administrative staff in the Civil and Environmental Engineering Department at the University of Waterloo, especially Victoria Tolton, Ellie Clark, Nicole Schmidt, and

Shirley Springall. Also my appreciation to Paul Thompson, the IT expert who offered his support every time it was needed.

Thanks to all the students whom I have TA'd and that have shown their appreciation for my efforts to show clarity when teaching geotechnical engineering concepts. Teaching at UW has been one of the most comforting experiences in my life. That experience also helped me in understanding how important the academy will be in my future.

Last but not least, thanks to everyone who I missed above and who helped me in any way during my stay at UW in Canada.

Dedication

I dedicate this work to all the medical practitioners and health workers fighting against the COVID-19 virus at this very moment, please do not give up... we need you all. This is the greatest contemporary challenge that mankind is facing and that will change our perspective about the world we are living at.

God bless you all...!!!

Haud Immemor. Reminiscences of Legal and Social Life in Edinburgh and London, 1850-1900

...Buckle said, in his dogmatic way: "Men and women range themselves into three classes or orders of intelligence; you can tell the lowest class by their habit of always talking about persons; the next by the fact that their habit is always to converse about things; the highest by their preference for the discussion of ideas."

-- Charles Stewart --

"Great minds discuss ideas; average minds discuss events; small minds discuss people."

-- Anna Eleanor Roosevelt --

Table of Contents

Examining committee membership	ii
Author's Declaration	iii
Statement of Contributions	iv
Abstract	v
Acknowledgements	viii
Dedication	x
List of Figures	xviii
List of Tables	xxix
List of abbreviations	xxxi
List of symbols.....	xxxii
1 Introduction	1
1.1 Problem statement	3
1.2 Research objectives	5
1.3 Scope of the work	5
1.4 Thesis organization	7
2 Theoretical background.....	11
2.1 Wave propagation theory	11
2.1.1 Wave propagation in one-dimension	11
2.1.2 Wave propagation in a three-dimensional infinite medium	12
2.1.3 Seismic waves	14
2.1.4 Acoustic impedance	18
2.2 Factors affecting seismic waves propagation in geomaterials	18
2.3 Stress-strain behaviour of geomaterials.....	19
2.3.1 Dynamic soil properties	19
2.3.2 Attenuation	23
2.3.3 Laboratory tests to determine dynamic soil properties	24
2.3.4 Field tests to determine dynamic soil properties	27

2.4	Near-surface geophysical techniques	28
2.4.1	Seismic techniques based on reflection and refraction	29
2.4.2	Seismic techniques based on geophysical well-logging	32
2.4.3	Seismic techniques based on surface waves dispersion analysis	33
2.4.4	Emerging techniques applied to the near-surface	36
2.5	Data analysis: signal processing	37
2.5.1	The Fourier transform	37
2.5.2	The wavelet transform (on-stationary data processing)	38
2.5.3	The synchrosqueezed wavelet transform	38
2.6	Numerical simulation of waves propagation.....	39
2.6.1	Initial and boundary conditions	39
2.6.2	The finite differences method	40
2.6.3	Probabilistic approach of spatial variability: random fields	43
3	Research background – literature review.....	51
3.1	Geotechnical and dynamic properties of geomaterials	52
3.1.1	Very soft soils	55
3.1.2	Dynamic properties of very soft soils	56
3.1.3	Application of seismic techniques to study very soft soils	59
3.2	Wave-propagation based techniques at different scales	61
3.3	Geophysical techniques to study geomaterials – void detection.....	62
3.3.1	Seismic reflection techniques	62
3.3.2	Surface waves dispersion techniques	65
3.3.3	Guideline recommendations on selection of geophysical techniques	67
4	Research Methodology	68
4.1	Main research activities.....	68
4.2	Flowchart of the research methodology	68
4.3	Parametric studies for the average shear wave velocity ($v_s = 30$).....	70
4.3.1	Effect of impedance ratio between top materials and frequency content in the input source.....	70

4.3.2	Effect of considering different approaches to spatially distribute the stiffness in the medium.....	71
4.4	Characterization of geomaterials at large scales	72
4.4.1	sCPTU field test and numerical simulations to study the frequency effects on v_s results	72
4.5	Characterization of geomaterials at intermediate scales	73
4.5.1	MASW laboratory tests and numerical simulations to approach the input source inversion	73
4.6	Characterization of geomaterials at small scales.....	76
4.6.1	Results of RC and BE tests on laboratory samples.....	76
5	Characterization of geomaterials at large scales: layered medium approach – numerical study of the impedance ratio effect and the interface shape effect	78
5.1	Detailed procedure	78
5.2	Numerical model calibration	79
5.2.1	Model geometry definition	79
5.2.2	Boundary and initial conditions	80
5.2.3	Mesh size and time step definition	80
5.2.4	Input force used for calibration	82
5.2.5	Calibration for surface wave propagation: damping selection	84
5.3	Numerical study of waves propagation in a horizontally layered medium.....	86
5.3.1	Model definition	86
5.3.2	Accuracy of the results for shear wave velocity inversion	90
5.3.3	Evaluation of the results for $v_s - 30$	94
5.4	Numerical study of wave propagation in a non-horizontally layered medium ...	99
5.4.1	Geometry definition for the numerical simulation	99
5.4.2	Effect of changes in impedance ratio for models with dipping interfaces .	100
5.4.3	Effect of changes in the shape of interfaces.....	101
5.4.4	Effect of changes in Poisson’s ratio.....	102
5.4.5	Effect of changes in frequency content	103
5.4.6	Damping effect on the FK spectrum	104
5.5	Conclusions.....	105

6	Characterization of geomaterials at large scales: layered medium approach – field tests and numerical simulations	107
6.1	Detailed procedure	107
6.2	sCPTU and MASW field tests	107
6.2.1	Location for the field testing.....	108
6.2.2	sCPTU tests.....	109
6.2.3	MASW tests	115
6.2.4	Travel-time plots and dispersion curves	119
6.3	Numerical simulation to replicate field conditions	121
6.3.1	Numerical model definition	122
6.3.2	Approaches to represent the properties distribution inside a medium.....	125
6.3.3	Comparison of wave-field generated for different approaches for materials distribution	130
6.3.4	Effect of considering different approaches for the medium characterization	140
6.4	Conclusions.....	152
7	Characterization of geomaterials at large scales: layered medium approach – analysis of frequency effects	153
7.1	Detailed procedure	153
7.2	Step 1: interpretation and processing of sCPTU field test results.....	155
7.2.1	Data acquisition in the field.....	155
7.2.2	Near field analysis	161
7.2.3	Data interpretation according to ASTM standard	166
7.3	Step 2: numerical simulations to approach the characterization of the excitation force	169
7.3.1	Numerical model definition	169
7.3.2	Numerical simulation results for different frequencies in the input force ..	171
7.4	Step 3: frequency response analysis of the system (sCPTU field test)	174
7.4.1	Excitation force inversion when the horizontal acceleration is used as the output for the assimilated linear invariant system	178

7.4.2	Excitation force inversion when the horizontal displacement is used as the output for the assimilated linear invariant system	189
7.5	Step 4: analysis of the effect of changes in the frequency of the input in the sCPTU field test.....	197
7.6	Analysis for a spatially variable medium	209
7.7	Conclusions.....	214
8	Characterization of geomaterials at intermediate scales: homogeneous approach vs. lack of spatial continuity approach (void detection).....	216
8.1	Detailed procedure	216
8.2	Step 1: MASW laboratory tests in the sandbox.....	218
8.2.1	Ultrasonic pulse velocity (UPV)	219
8.2.2	Multi-channel analysis of surface waves (MASW) tests	220
8.2.3	Near field and far field identification	227
8.2.4	Transducer characterization using a laser vibrometer.....	228
8.3	Step 2: numerical simulation of waves propagation in the sandbox	233
8.3.1	Material properties	233
8.3.2	Geometry of the model	234
8.3.3	Boundary and initial conditions	235
8.3.4	Mesh size and time step definition	235
8.3.5	Calibration of the numerical model	236
8.4	Step 3: frequency response analysis	243
8.4.1	Inversion process with initial force obtained from transducer's response	246
8.4.2	Inversion process with initial force obtained from vertical displacements in the sandbox: alignment with void	251
8.4.3	Inversion process with initial force obtained from vertical displacements in the sandbox: alignment without void	257
8.5	Step 4: analysis for a medium with lack of continuity	260
8.6	Conclusions.....	262
9	Characterization of geomaterials at small scales: bender element tests for ν_s estimation in homogeneous laboratory samples	264
9.1	Detailed procedure	264

9.2	Bender element (BE) test.....	265
9.3	Background	268
9.3.1	Shear wave velocity.....	268
9.3.2	Estimation of shear wave velocity in BE tests	269
9.3.3	Bender element vibration.....	271
9.3.4	Input signal selection for BE test	272
9.4	Experimental procedure	274
9.4.1	Experimental setup and testing: Stage 1	274
9.4.2	Experimental setup and testing: Stage 2	276
9.4.3	Experimental setup and testing: Stage 3	278
9.5	Testing results	280
9.5.1	Testing results: Stage 1	280
9.5.2	Testing results: Stage 2	283
9.5.3	Testing results: Stage 3	296
9.6	Transfer function calculations	304
9.6.1	Transfer function for the whole BE system H_{soil}	305
9.6.2	Transfer function for the BE transmitter HT_x	307
9.6.3	Transfer function for the BE receiver HR_x	311
9.7	Conclusions.....	318
10	Conclusions.....	320
10.1	Effects of impedance ratio among layers on wave propagation results	321
10.2	Effects of frequency and medium approach on wave propagation results.....	321
10.3	Characterization of the excitation source for field and laboratory seismic testing	322
10.4	Study of participation of P-waves in the results from BE testing	324
10.5	Main contributions and their implications in the construction industry	325
10.5.1	MASW test: impedance ratio effect for the determination of $v_S - 30$	326
10.5.2	sCPTU test: source characterization	327
10.5.3	BE test: source characterization	328
10.6	Future research	329

References	330
Appendices.....	344
Appendix A: Result of Numerical Simulations for Random Field Models	344
Appendix B: Computation of Fast Fourier Transform (FFT)	355
Appendix C: Linear time-invariant (LTI) system.....	358
Appendix D: Guideline for the selection of the near-surface techniques intended to be used in soft grounds	361

List of Figures

Fig. 1-1: Engineering design process (after UCB, 2015).....	6
Fig. 2-1: Stresses and displacements at ends of an element of length dx and cross sectional area A . (Kramer, 1996)	11
Fig. 2-2: Stress notation for an element of dimensions dx , dy , and dz . (Kramer, 1996) 13	
Fig. 2-3: Radiation pattern of Rayleigh surface waves generated by a vertical point source. (Foti et al., 2014)	17
Fig. 2-4: Typical seismic waves' events separation (Tomic, 2017)	18
Fig. 2-5: Shear strain range for laboratory tests (blue boxes) and field tests (red boxes), (after Arango, 1980)	22
Fig. 2-6: Reflected and refracted waves (Van Der Hilst and Burdick, Scott, 2010).....	31
Fig. 2-7: Theoretical travel time curves for a 2-layers model with horizontal interface...32	
Fig. 2-8: Calculation cycle in FLAC TM . (Hart and Han, 2006)	41
Fig. 3-1: Fundamental period of an elastic surface layer. (Finn and Wightman, 2003)..54	
Fig. 3-2: In-situ seismic test using the MudFork (Oh et al., 2008).....	59
Fig. 3-3: Surface wave survey set-up for marine investigation. (Paoletti et al., 2010) ...	60
Fig. 3-4: Summary of shear wave velocity data, location BH4. (Paoletti et al., 2010)....	61
Fig. 4-1. Flowchart for the research methodology.....	69
Fig. 5-1: Definition of geometry and boundaries for the numerical model.....	79
Fig. 5-2: Pulses used as input force in the model.	83
Fig. 5-3: Vertical and horizontal displacements at 40 meters from source, obtained with the analytical solution	85
Fig. 5-4: Normalized wave velocity vs. Poisson's ratio.....	87
Fig. 5-5: Initial model for the numerical simulations of wave propagation in a hypothetical layered medium (after Díaz-Durán et al., 2018a)	88
Fig. 5-6: Modified model for the numerical simulations (after Díaz-Durán et al., 2018a)89	
Fig. 5-7: Example of identification of seismic waves by using a travel-time plot for a model with impedance ratio $I_Z = 0.10$	91
Fig. 5-8: F-K spectrum for a model with impedance ratio $I_Z = 0.10$	92
Fig. 5-9: Contours of shear wave velocity ($v_S - 30$ in m/s) following "Method 1"	96
Fig. 5-10: Contours of shear wave velocity ($v_S - 30$ in m/s) following "Method 2"	96
Fig. 5-11. Contours of normalized $v_S - 30$ (m/s) for different central frequencies in the input force and different impedance ratios for the first two layers. ("Method 1")	98

Fig. 5-12. Contours of normalized $v_s - 30$ (m/s) for different central frequencies in the input force and different impedance ratios for the first two layers. (“Method 2”)	98
Fig. 5-13. Models with a 5° dipping interface: effect of reduction in the impedance ratio.	101
Fig. 5-14. Models with soil class II in top layer: effect of changes in the interface shape.	101
Fig. 5-15. Model with horizontal interface, soil in top layer was type F, class II: effect of Poisson’s ratio in the F-K spectrum.....	102
Fig. 5-16. Model with horizontal interface, soil in top layer was type F, class II: effect of Poisson’s ratio in the dispersion curves.	102
Fig. 5-17. Model with horizontal interface, soil in top layer was type F, class II: effect of frequency content in the F-K spectrum.	103
Fig. 5-18. Model with horizontal interface, soil in top layer was type F, class II: effect of frequency content in the dispersion curves.	104
Fig. 5-19. Model with horizontal interface, soil in top layer was type F, class II: effect of damping increment in the F-K spectrum.	104
Fig. 6-1: Field testing location	108
Fig. 6-2: Field setup for sCPTU and MASW tests	109
Fig. 6-3: Schematic of seismic CPT (SCPT) test procedure (Robertson, 2015)	110
Fig. 6-4: Terminology for cone penetrometers (Robertson, 2015)	111
Fig. 6-5: Equipment used for the seismic cone penetration test (sCPTU)	112
Fig. 6-6: Raw data from the seismic cone penetration test (sCPT-1).....	114
Fig. 6-7: Different arrays for the MASW test. (Nasseri-Moghaddam, 2006).....	116
Fig. 6-8: Tapered cosine window for different cosine fractions (r).....	117
Fig. 6-9: Time domain signals before (left) and after (right) signal processing.	118
Fig. 6-10: Frequency domain signals before (left) and after (right) signal processing.	119
Fig. 6-11: Travel time plot (left) and dispersion curve (right) for MASW field test with source offset distance of 6m.	120
Fig. 6-12: Travel time plot (left) and dispersion curve (right) for MASW field test with source offset distance of 9m.	120
Fig. 6-13: Travel time plot (left) and dispersion curve (right) for MASW field test with source offset distance of 12m.	121
Fig. 6-14: Definition of geometry and boundary conditions for the numerical model. ..	122
Fig. 6-15: Ricker wavelet used to define the shape of the force for the initial numerical models: (a) time domain, and (b) frequency domain (Sheriff, 2002)	124

Fig. 6-16: Ricker wavelet force pulses with different mean frequencies	124
Fig. 6-17: Geometry for the numerical model considering a homogeneous medium... 126	
Fig. 6-18: Geometry for the numerical model using the horizontally layered medium. 127	
Fig. 6-19: Geometry for the numerical model using the spatially variable medium. 128	
Fig. 6-20: Random fields for shear modulus G generated using LU decomposition technique with normalized correlation length $(L_c / H) = 0.125$ 129	
Fig. 6-21: Random fields for shear modulus G generated using LU decomposition technique with normalized correlation length $(L_c / H) = 0.25$ 129	
Fig. 6-22: Random fields for shear modulus G generated using LU decomposition technique with normalized correlation length $(L_c / H) = 0.50$ 129	
Fig. 6-23: Random fields for shear modulus G generated using LU decomposition technique with normalized correlation length $(L_c / H) = 0.75$ 130	
Fig. 6-24: Random fields for shear modulus G generated using LU decomposition technique with normalized correlation length $(L_c / H) = 1.25$ 130	
Fig. 6-25: Screenshot: numerical simulation of wave propagation in a 2-layers medium	131
Fig. 6-26: Screenshot: numerical simulation of wave propagation in a 17-layers medium	131
Fig. 6-27: Screenshot at 0.10s: numerical simulation of wave propagation in a spatially variable medium overlaying a homogeneous medium. The random field simulate the spatial variability of shear modulus – G (normalized correlation length is 0.125).....	132
Fig. 6-28: Screenshot at 0.05s: numerical simulation of wave propagation in a spatially variable medium overlaying a homogeneous medium. The random field simulate the spatial variability of shear modulus – G (normalized correlation length is 0.125).....	132
Fig. 6-29: Screenshot at 0.10s: numerical simulation of wave propagation in a spatially variable medium overlaying a homogeneous medium. The random field simulate the spatial variability of shear modulus – G (normalized correlation length is 1.25).....	133
Fig. 6-30: Screenshot at 0.05s: numerical simulation of wave propagation in a spatially variable medium overlaying a homogeneous medium. The random field simulate the spatial variability of shear modulus – G (normalized correlation length is 1.25).....	133
Fig. 6-31: Surface displacement at 10m from excitation force in time domain (up) and frequency domain (down). Response for different frequency contents in the input force in a 2-layers' medium.	136
Fig. 6-32: Surface displacement at 10m from excitation force in time domain (up) and frequency domain (down). Response for different frequency contents in the input force in a 17-layers' medium.	137

Fig. 6-33: Surface displacement at 10m from excitation force in time domain (up) and frequency domain (down). Response for different frequency contents in the input force in a spatially variable medium. Random field with normalized correlation length 0.125. . 138

Fig. 6-34: Surface displacement at 10m from excitation force in time domain (up) and frequency domain (down). Response for different frequency contents in the input force in a spatially variable medium. Random field with normalized correlation length 1.25. ... 139

Fig. 6-35: Theoretical travel time curves for a 17-layers' model with horizontal interfaces 140

Fig. 6-36: Example of travel time plot obtained from a numerical simulation of wave propagation in a 17-layers model with horizontal interfaces 141

Fig. 6-37: Theoretical dispersion curve obtained from a numerical simulation of wave propagation in the 17-layers model with horizontal interfaces 142

Fig. 6-38: Example of dispersion curve obtained from a numerical simulation of wave propagation in the 17-layers model with horizontal interfaces 143

Fig. 6-39: Travel time curves for a 2-layers' model and applied force (Ricker wavelet pulse) with five different mean frequencies. Horizontal axis is the distance from the source (x), vertical axis is the time (t). 144

Fig. 6-40: Dispersion curves for the 2-layers' model and applied force (Ricker wavelet pulse) with five different mean frequencies. Horizontal axis is the distance from the source (x), vertical axis is the time (t). 145

Fig. 6-41: Travel time curves for a 17-layers' model and applied force (Ricker wavelet pulse) with five different mean frequencies. Horizontal axis is the distance from the source (x), vertical axis is the time (t). 146

Fig. 6-42: Dispersion curves for a 17-layers' model and applied force (Ricker wavelet pulse) with five different mean frequencies. Horizontal axis is the distance from the source (x), vertical axis is the time (t). 147

Fig. 6-43: Travel time curves for a spatially variable model and applied force (Ricker wavelet pulse) with five different mean frequencies. Horizontal axis is the distance from the source (x), vertical axis is the time (t). The random field simulates shear modulus distribution with normalized spatial correlation length of 0.125 148

Fig. 6-44: Dispersion curves for a spatially variable model and applied force (Ricker wavelet pulse) with five different mean frequencies. Horizontal axis is the distance from the source (x), vertical axis is the time (t). The random field simulates shear modulus distribution with normalized spatial correlation length of 0.125 149

Fig. 6-45: Travel time curves for a spatially variable model and applied force (Ricker wavelet pulse) with five different mean frequencies. Horizontal axis is the distance from the source (x), vertical axis is the time (t). The random field simulates shear modulus distribution with normalized spatial correlation length of 1.25 150

Fig. 6-46: Dispersion curves for a spatially variable model and applied force (Ricker wavelet pulse) with five different mean frequencies. Horizontal axis is the distance from the source (x), vertical axis is the time (t). The random field simulates shear modulus distribution with normalized spatial correlation length of 1.25 151

Fig. 7-1: Flow-chart of the procedure to characterize geomaterials at large scales 154

Fig. 7-2: Seismic cone penetration test (sCPTU) setup showing dimensions for the probe located at 1-meter depth and then when it was moved up to 2 meters' depth. 156

Fig. 7-3: Typical responses obtained from the sCPTU field test (for both, left and right side strikes): time domain (normalized) and frequency domain for horizontal acceleration at 4 meters' depth..... 158

Fig. 7-4: Typical signals obtained from numerical integration of acceleration data from the sCPTU field test (left-side test at 4 meters' depth): time domain (left side plots) and frequency domain (right side plots). Plots (a) and (b) correspond to the horizontal acceleration data obtained in the field test. Plots (c) and (d) correspond to the horizontal velocity data obtained from numerical integration of horizontal acceleration data. Plots (e) and (f) correspond to the horizontal displacement data obtained from numerical integration of horizontal velocity data (i.e. double integration of acceleration data).... 160

Fig. 7-5: Theoretical amplitude decay of body waves with respect to depth for different values of near field depth (elastic radius). 163

Fig. 7-6: Fitting of amplitude decay for horizontal accelerations data with respect to depth when a near field depth (elastic radius) of 3 meters is considered. 164

Fig. 7-7: Variation of RMSE with depth of the near field (elastic radius). 165

Fig. 7-8: Impulse seismic source produces P and S waves trains (ASTM D7400, 2017) 167

Fig. 7-9: Typical downhole shear wave arrival traces (signals with reversed polarity) (ASTM D7400, 2017) 167

Fig. 7-10: Shear wave velocity (v_s) profile interpretation of the field test sCPTU #1 in accordance with (ASTM D7400, 2017) 168

Fig. 7-11: Comparison between data of horizontal acceleration at 4 meters' depth obtained from the field sCPTU test (red) and from the numerical simulations (blue) when different peak frequencies are used in the input force (Ricker pulse): a) 50Hz, b) 54Hz, c) 58Hz, d) 68Hz 171

Fig. 7-12: Responses at 4 meters' depth obtained from the field test (red) and from the numerical simulation (blue) when the input pulse has mean frequency of 58Hz. For the field test response, the data recorded in the field was acceleration, while velocity and displacement were obtained by numerical integration. 173

Fig. 7-13: sCPTU field test system and definition of input and output signals to be involved in the transfer function calculation. 175

Fig. 7-14: Input pulse (Ricker wavelet) with mean frequency of 58Hz. 178

Fig. 7-15: Inversion process to obtain the input force when acceleration is used as the system's output (first iteration) 182

Fig. 7-16: Comparison of results of horizontal acceleration from sCPTU field test and from numerical model when the input force was approached by a Ricker wavelet with mean frequency of 58Hz. 183

Fig. 7-17: Inversion process to obtain the input force when acceleration is used as the system's output (second iteration)..... 184

Fig. 7-18: Comparison of results of horizontal acceleration from sCPTU field test and from numerical model, the input force corresponds to the result obtained from the first iteration of the excitation force inversion process. 185

Fig. 7-19: Inversion process to obtain the input force when acceleration is used as the system's output (third iteration) 186

Fig. 7-20: Comparison of results of horizontal acceleration from sCPTU field test and from numerical model, the input force corresponds to the result obtained from the second iteration of the excitation force inversion process. 187

Fig. 7-21: Comparison of input forces used for the numerical simulations through IFFT inversion when acceleration is used as output of the system. The result shown in plot (d) corresponds to the force after three iterations in the inversion process. At each iteration, the dashed red lines correspond to the input force in the previous iteration and it is plotted to facilitate the comparison of results between successive iterations. 188

Fig. 7-22: Inversion process to obtain the input force when displacement is used as the system's output (first iteration) 190

Fig. 7-23: Comparison of results of horizontal displacement from sCPTU field test and from numerical model, the input force corresponds to a Ricker wavelet with mean frequency of 58Hz. 191

Fig. 7-24: Inversion process to obtain the input force when displacement is used as the system's output (second iteration)..... 192

Fig. 7-25: Comparison of results of horizontal displacement from sCPTU field test and from numerical model, the input force corresponds to the result obtained from the first iteration of the excitation force inversion process. 193

Fig. 7-26: Inversion process to obtain the input force when displacement is used as the system's output (third iteration) 194

Fig. 7-27: Comparison of results of horizontal displacement from sCPTU field test and from numerical model, the input force corresponds to the result obtained from the second iteration of the excitation force inversion process. 195

Fig. 7-28: Comparison of input forces used for the numerical simulations through IFFT inversion when the horizontal displacement is used as the output of the system. The result shown in plot (d) corresponds to the force after three iterations in the inversion process. At each iteration, the dashed red lines correspond to the input force in the previous

iteration and it is plotted to facilitate the comparison of results between successive iterations.....	196
Fig. 7-29: Modified input forces for the analysis of the effect of frequency on sCPTU field test results	198
Fig. 7-30: Shear wave velocity (v_s) profile interpretation following ASTM D7400 (2017). Numerical model of sCPTU test: force input with frequency peak = 31.0Hz.....	199
Fig. 7-31: Shear wave velocity (v_s) profile interpretation following ASTM D7400 (2017). Numerical model of sCPTU test: force input with frequency peak = 41.3Hz.....	200
Fig. 7-32: Shear wave velocity (v_s) profile interpretation following ASTM D7400 (2017). Numerical model of sCPTU test: force input with frequency peak = 51.7Hz.....	201
Fig. 7-33: Shear wave velocity (v_s) profile interpretation following ASTM D7400 (2017). Numerical model of sCPTU test: force input with frequency peak = 62.0Hz.....	202
Fig. 7-34: Shear wave velocity (v_s) profile interpretation following ASTM D7400 (2017). Numerical model of sCPTU test: force input with frequency peak = 72.9Hz.....	203
Fig. 7-35: Shear wave velocity (v_s) profile interpretation following ASTM D7400 (2017). Numerical model of sCPTU test: force input with frequency peak = 82.7Hz.....	204
Fig. 7-36: Shear wave velocity (v_s) profile interpretation following ASTM D7400 (2017). Numerical model of sCPTU test: force input with frequency peak = 95.4Hz.....	205
Fig. 7-37: Shear wave velocity profile: sCPTU field test and numerical simulations with different frequency content in the input force	207
Fig. 7-38: Error in v_s estimation for each layer identified in the sCPTU interpretation.	208
Fig. 7-39: Conditioned random field for the simulation of the sCPTU test. The normalized correlation length was 1.25.	211
Fig. 7-40: Response at a 4 meters' depth for numerical model with random fields.....	212
Fig. 7-41: Response at a 4 meters' depth for numerical model including a conditioned random fields	213
Fig. 8-1: Flowchart of the procedure to characterize geomaterials at intermediate scales	217
Fig. 8-2: Sketch of the sandbox used in the laboratory	218
Fig. 8-3: Laboratory setup for laser reading of vertical displacements	221
Fig. 8-4: Transducer placement and reflective tape	222
Fig. 8-5: Comparison of sine pulses in-phase and out-of-phase	223
Fig. 8-6: Example of raw seismogram for the seismic test in the sandbox for the alignment with no void (Input Frequency was 250kHz)	225
Fig. 8-7: Variation of v_p with the input frequency	226
Fig. 8-8: Variation of v_s and v_R with the input frequency	226

Fig. 8-9: Maximum and minimum amplitudes for all the locations tested in the sand box.	227
Fig. 8-10: Grid definition for the reading point in the transducers' face.....	228
Fig. 8-11: Distribution of the maximum displacements for the 54kHz.....	229
Fig. 8-12: Input pulse (red) and average response (blue) in the time domain (a), the frequency domain (b), and transfer function (c) for the characteristic zone of the transducer with resonant frequency of 54 kHz.	230
Fig. 8-13: Input pulse (red) and average response (blue) in the time domain (a), the frequency domain (b), and transfer function (c) for the characteristic zone of the transducer with resonant frequency of 20 kHz.	231
Fig. 8-14: Input pulse (red) and average response (blue) in the time domain (a), the frequency domain (b), and transfer function (c) for the characteristic zone of the transducer with resonant frequency of 150 kHz.	232
Fig. 8-15: Geometry for the numerical models built to replicate the wave propagation phenomena in the sandbox, for a homogeneous medium (left) and for a medium with a lack of continuity represented by a void (right).....	234
Fig. 8-16: Input force used to calibrate the numerical model seeking to replicate the wave propagation in the sandbox.....	237
Fig. 8-17: Vertical and horizontal displacements from the theoretical solution at 0.5 meters from the excitation source.	238
Fig. 8-18: Vertical displacements on surface (U_y) at 0.5 meters from the excitation source for different Rayleigh central frequencies: (a) 46kHz, (b) 50kHz, (c) 54kHz, (d) 58kHz, and (e) 62kHz.....	239
Fig. 8-19: Vertical displacements on surface (U_y) at 0.5 meters from the excitation source for different Rayleigh damping ratios: (a) 0%, (b) 1%, (c) 2%, (d) 3%, (e) 4%, and (f) 5%. (general view).....	240
Fig. 8-20: Vertical displacements on surface (U_y) at 0.5 meters from the excitation source for different Rayleigh damping ratios: (a) 0%, (b) 1%, (c) 2%, (d) 3%, (e) 4%, and (f) 5%. (zoomed view).....	241
Fig. 8-21: Raw seismogram of vertical displacements from the numerical model to identify the near field zone, the far field zone, and the P-wave and S-wave.	242
Fig. 8-22: MASW laboratory test system and definition of input and output signals to be involved in the transfer function calculation.....	243
Fig. 8-23: Time domain and frequency domain for the input (transducer's response) and for the output (vertical displacement) at 0.15m for the excitation source. The transfer function is also presented.....	248
Fig. 8-24: Inversion of the excitation source in the sandbox MASW test (First iteration). The initial input was the transducer's response signal.	249

Fig. 8-25: Inversion of the excitation source in the sandbox MASW test (second iteration). The initial input was the transducer's response signal.	250
Fig. 8-26: Sketch of the sandbox with a lack of continuity (void) in the upper layer	252
Fig. 8-26: Inversion of the excitation source in the sandbox MASW test (First iteration). The initial input was the vertical displacement in the sandbox (with void) at 0.04m away from the excitation source.	253
Fig. 8-27: Inversion of the excitation source in the sandbox MASW test (second iteration). The initial input was the vertical displacement in the sandbox (with void) at 0.04m away from the excitation source.	254
Fig. 8-28: Comparison of outputs from the sandbox (with void) in the laboratory and from the numerical models at 0.04 meters away from the source. The input force was obtained after two iterations in the inversion process.	255
Fig. 8-29: Comparison of outputs from the sandbox (with void) in the laboratory and from the numerical models at 0.15 meters away from the source. The input force was obtained after two iterations in the inversion process	256
Fig. 8-32: Comparison of outputs from the sandbox (without void) in the laboratory and from the numerical models at 0.04 meters away from the source. The input force was obtained after two iterations in the inversion process.	258
Fig. 8-33: Comparison of outputs from the sandbox (without void) in the laboratory and from the numerical models at 0.15 meters away from the source. The input force was obtained after two iterations in the inversion process.	259
Fig. 8-33: Cross-correlation sandbox alignment with void.....	261
Fig. 9-1: Flowchart of the detailed procedure followed to characterize geomaterials at small scales	265
Fig. 9-2: Schematic of the wiring connection in a BE (Ferreira et al., 2020)	266
Fig. 9-3: Shear wave arrival times and transfer functions at different stages in a conventional BE test setup (after Irfan, 2019)	270
Fig. 9-4: Schematic of the experimental setup for laser measurements in air and water	276
Fig. 9-5: Alignment of reading patterns at BE edges for vertically and horizontally oriented laser beams	278
Fig. 9-6: Schematic of resonant column and bender element tests (after Irfan, 2019)	279
Fig. 9-7: v_s and v_p evolution with isotropic confinement (after Ferreira et al., 2020)...	280
Fig. 9-8: BE results for P-waves in dry (thick lines) and saturated (thin lines) conditions, using different input frequencies for effective confining isotropic stresses of 100 kPa.	281
Fig. 9-9: BE results for S-waves in dry (thick lines) and saturated (thin lines) conditions, using different input frequencies for effective confining isotropic stresses of 100 kPa.	281

Fig. 9-10: Frequency spectra for BE signals for 50kHz (a) and 75kHz (b) input frequencies, for dry and saturated conditions, at 100 kPa confining stress282

Fig. 9-11: Power spectrum for the input signal (4 to 100 kHz Sine sweep) used to measure horizontal displacements of BE tested on air (red) and on water (blue).....284

Fig. 9-12: Frequency spectrum for horizontal displacements of BE tested under a 4 to 100 kHz Sine sweep.....284

Fig. 9-13: Power spectrum for the input signal (4 to 100 kHz Sine sweep) used to measure vertical displacements of BE tested on air (red) and on water (blue).....285

Fig. 9-14: Frequency spectrum for vertical displacements of BE tested under a 4 to 100 kHz Sine sweep.....286

Fig. 9-15: Example of signals obtained from the laser readings. In this case horizontal displacements were read at 13 different locations on top edge of the BE for an input frequency of 12kHz: a) Input signal in the time domain, b) Output signal in the time domain c) Input signal in the frequency domain, and d) Output signal in the frequency domain.288

Fig. 9-16: Fourier transform of the raw time signals for bender element (BE) displacement measured with the laser in different orientations and for different frequencies in the input signals.289

Fig. 9-17: Fourier transform of the filtered time signals for bender element (BE) displacement measured with the laser in different orientations and for different frequencies in the input signals. The signals were filtered to isolate vibration modes. 290

Fig. 9-18: Vibration modes separation using continuous wavelet transform (c) and wavelet synchro-squeezed transform for vertical displacements in the middle point on top edge of the BE. The input frequency was 46kHz.291

Fig. 9-19: First and third vibration modes for horizontal displacements on top of the BE, along its length while it was in contact with air292

Fig. 9-20: First and third vibration modes for vertical displacements on top of the BE, along its length while it was in contact with air293

Fig. 9-21: Pattern of points used to read 3D displacements in the BE.....294

Fig. 9-22: Setup for laser readings under different orientations: (a) detailed view of BE, (b) Top readings, (c) lateral readings, (d) horizontal readings.294

Fig. 9-23: First and third vibration modes for horizontal displacements.296

Fig. 9-24: (a) BE-Rx responses to sine pulse (10 kHz) at different confinements (b) frequency spectrum of the time signals in (a).....297

Fig. 9-25: (a) BE-Rx responses to sine pulse (10 kHz) at different strain levels for dry condition (b) frequency spectrum of the time signals in (a).....299

Fig. 9-26: Shear wave velocity (BE and RC) and compressional wave velocity of fused quartz at different confinements300

Fig. 9-27: Shear wave velocity (BE and RC) of fused quartz at different confinements	301
Fig. 9-28: BE-Rx response at different strain levels (RC system turned on). In the lower plot the amplitude was amplified by a factor of 10. In the middle plot the amplitude was amplified by a factor of 4. In the upper plot the amplitudes were not amplified at all. ...	303
Fig. 9-29: Normalized shear wave velocities at different strain levels using BE and RC tests (sine pulse input frequencies: 10 and 50 kHz).....	304
Fig. 9-30: Transfer function H_{soil}	306
Fig. 9-31: Sine 12 kHz: Input signal to measure horizontal and vertical displacements	307
Fig. 9-32: Average vertical displacement on top edge of the BE, the input was a sine pulse at 12 kHz.	307
Fig. 9-33: Average signals of horizontal displacement at different heights from the base of the BE (input was a sine pulse at 12 kHz), measurements on air.....	308
Fig. 9-34: Transfer function HT_x (output was the horizontal displacements signal).....	309
Fig. 9-35: Transfer function HT_x (output was the vertical displacements signal).....	310
Fig. 9-36: Damping ratios calculation for BE horizontal and vertical displacements (input was a sine pulse at 12 kHz), measurements of air.....	312
Fig. 9-37: Screenshot at 0.200ms: numerical simulation of BE test (fused quartz reconstituted sample).	313
Fig. 9-38: Screenshot at 0.465ms: numerical simulation of BE test (fused quartz reconstituted sample).	313
Fig. 9-39: Numerical simulation: Horizontal displacements on top of the BE receiver.	314
Fig. 9-40: Numerical simulation: Vertical displacements on top of the BE receiver.	314
Fig. 9-41: Transfer function HR_x (output was the horizontal displacements signal).....	315
Fig. 9-42: Transfer function HR_x (output was the vertical displacements signal).....	316

List of Tables

Table 2-1. Near-surface geophysical emerging techniques	36
Table 2-2. Matrix decomposition technique to generate random fields (Kim, 2005)	47
Table 3-1. Clay’s classification based on consistency (Terzaghi et al., 1996)	53
Table 3-2. Seismic site classification proposed by NEHRP (1994) and adapted by the National Building Code of Canada (after Finn and Wightman, 2003).	53
Table 3-3. Geotechnical characterization of very soft soils	56
Table 3-4. Dynamic properties of very soft soils	57
Table 3-5. Equations to calculate the shear modulus of very soft soils.....	58
Table 5-1. Maximum mesh sizes for soils with different shear wave velocities and considering different frequencies to use in the numerical model	81
Table 5-2. Minimum time steps to use in the numerical model	82
Table 5-3. Maximum time steps to use in the numerical models	82
Table 5-4. Analytical solution for surface displacements due to a Lamb source point load (after Nasser-Moghaddam, 2006)	84
Table 5-5. Properties of materials in the initial numerical model.....	87
Table 5-6. Properties of soft to very soft soils in layer 1 of the numerical models	90
Table 5-7. RMSE of dispersion curve for MASW models simulated with different spacing between channels (transducers). Input force was a sine pulse ($f_M=20\text{Hz}$).....	93
Table 5-8. RMSE of dispersion curve for MASW models simulated with different frequencies in the input force (sine pulse). Spacing between channels was $dx=1.0\text{m}$. .	93
Table 5-9. Average shear wave velocity for the shallower 30 meters (v_{s-30} in m/s) following “Method 1”. Spacing between channels was $dx=1.0\text{m}$	95
Table 5-10. Average shear wave velocity for the shallower 30 meters (v_{s-30} in m/s) following “Method 2”. Spacing between channels was $dx=1.0\text{m}$	95
Table 5-11. Theoretical values of shear wave velocity (v_{s-30}) for the ten models simulated with different impedance ratio between the two top layers.....	97
Table 5-12. Schematic geometries of the models to study the effect of the shape in the interface between the first two layers.	99
Table 6-1. Material properties obtained from correlations with the cone resistance	115
Table 6-2. Material properties for a homogeneous medium.....	125
Table 7-1. Root mean square error for amplitude decay of maximum and minimum horizontal acceleration in the field test sCPTU #1 (left side and right side tests).....	165

Table 7-2. Mean frequency and characteristic period for different Ricker pulses used to define the excitation force in the numerical models.	170
Table 7-3. Material properties from the seismic records of the sCPTU field test	170
Table 7-4. RMSE values obtained from comparison of frequency spectrums of field data and numerical simulation data with different mean frequencies in the input pulse.	172
Table 7-5. Modified input forces for the analysis of the effect of frequency.	197
Table 7-6. Results for the sCPTU field test and for the numerical simulations	206
Table 7-7. Shear wave velocity obtained from the sCPTU field test and from the numerical simulations	206
Table 7-8. Wavelength for materials in different layers and different frequencies	209
Table 7-9. Materials properties for the conditioned random field generation.	210
Table 8-1. Wave velocities for cemented sand: interpretation from the raw seismograms of the test performed in the line with no void	224
Table 9-1. Typical BE electrical input excitations (after Ferreira, 2009)	273
Table 9-2. Mechanical properties of the soil sample (after Ferreira et al., 2020)	275
Table 9-3. Links to access the videos of displacements measured using a laser vibrometer while the BE was in contact with air.	295
Table 9-4. Identification of input and output for all the transfer functions in a BE test .	305
Table 9-5. Properties of reconstituted sample of fused quartz	311

List of abbreviations

ASHTOO	American Association of State Highway Transportation Officials
ASTM	American Society for Testing and Materials
BE	Bender Element
BLUE	Best Linear Unbiased Estimate
CPT	Cone Penetration Test
FS	Factor of Safety
GPR	Ground Penetrating Radar
MASW	Multichannel Analysis of Surface Waves
NEHRP	National Earthquake Hazards Reduction Program
OCR	Over-Consolidation Ratio
PDE	Partial Differential Equation
RC	Resonant Column
RMSE	Root Mean Square Error
SASW	Spectral Analysis of Surface Waves
sCPT	Seismic Cone Penetration Test
sCPTU	Seismic Cone Penetration Test with Pore Pressure Measurement
SPT	Standard Penetration Test
UPV	Ultrasonic Pulse Velocity

List of symbols

A	area
A_i	amplitude
E	elastic modulus
c	cohesion
c_i	wave velocity
C	damping coefficient
C_{cr}	critical damping coefficient
C_u	undrained shear strength
$[C]$	covariance matrix
\emptyset	diameter
F	external force
FFT	fast Fourier transform
$f(t)$	force function
f_0	fundamental frequency
f_M	mean frequency
f_p, f_{peak}	peak frequency
f_i	frequency
G	shear modulus
G_{max}, G_0	maximum shear modulus
H	layer thickness
$H(\omega)$	transfer function
i_c	critical incident angle
I_Z	acoustic impedance ratio
$IFFT$	inverse fast Fourier transform
K	bulk modulus
L	length
L_c	correlation length
M	constrained modulus
n	porosity
PI	plasticity index
r_e	elastic radius
SWT_x	synchrosqueezing transform
T_i	period
T_0	fundamental period
T_D	dominant period
u, v, w	particle displacement in different directions

$\dot{u}, \dot{v}, \dot{w}$	particle velocity in different orthogonal directions
$\ddot{u}, \ddot{v}, \ddot{w}$	particle acceleration in different orthogonal directions
Uy	vertical displacement on surface
v_s	compressional wave velocity
v_{s-30}	shear wave velocity for the shallower 30m
v_p	shear wave velocity
v_R	Rayleigh wave velocity
w	water content
W_x	wavelet transform
x_c	critical distance
x_d	crossover distance
$x(t)$	system's input in time domain
$X(\omega)$	Fourier transform of the system's input
$y(t)$	system's output in time domain
$Y(\omega)$	Fourier transform of the system's output
Z	acoustic impedance
γ	shear strain
γ_t	total unit weight
Δt	time step
Δx	distance step
λ	wavelength
$\lambda_{Lamé}$	Lame's first parameter
$\mu_{Lamé}$	Lame's second parameter. In elastic theory ($\mu_{Lamé} = G$)
ν	Poisson's ratio
ξ	damping ratio
ρ	mass density
σ_{ij}	stress in the i direction acting on the j plane
ϕ	internal friction angle
φ_i	phase
ω_n	angular resonance frequency
∇^2	Laplacian operator

1 Introduction

The study or analysis of any problem involving vibrations of geomaterials or structures founded over them (e.g. machines vibrations, mining blasting, dynamic impact loads, seismic events, etc.), requires the measurement or quantification of dynamic properties to classify the construction site. The dynamic response of the ground materials can be characterized by the typical dynamic parameters, i.e. shear modulus (G) and damping ratio (ξ) (Kramer, 1996). While shear modulus is a measure of the shear stiffness, damping ratio corresponds to a measure of the dissipation of seismic energy into the media. From shear modulus and material mass density (ρ), it is possible to obtain the shear wave velocity (v_s).

The parameter required by construction codes in North America to classify a construction site is the average shear wave velocity of the top 30 m of the subsoil (v_{s-30}). According to that parameter the materials are designated into a specific class and the seismic design requirements are defined accordingly.

There are two ways to obtain the dynamic properties values when characterizing a geomaterial, they are field tests and laboratory tests. For the field tests there are two main kinds: first, the geophysical methods like the analysis of energy dispersion in surface waves (e.g. MASW test), and second, the direct seismic methods in which a probe is introduced into the soil to measure a true value of shear wave velocity at different depths (e.g. downhole test and sCPT test). In the case of laboratory tests, among the many available methods, there are two widely used and accepted options: the bender element (BE) test, and the resonant column (RC) test.

All these testing techniques are widely used and accepted in the industry, however, they exhibit their own difficulties and drawbacks. For instance, the lack of understanding of the effects of having materials with highly different values of acoustic impedance in the top materials of layered media could lead to erroneous site classifications. Also, the lack of knowledge about the characteristics of the excitation source is still preventing practitioners and researchers from improving the interpretation of the seismic testing results.

Some attempts to overcome specific issues related to the field and laboratory tests are reported in the literature. However, none of them have considered or proposed a solution for the aforementioned issues.

For the MASW test, which is a very well-known and accepted test to obtain the parameter (v_{s-30}) for the dynamic characterization of geomaterials at large scales, a massive amount of papers has been published in the last two decades. However, when looking for papers reporting the progress in the characterization of the excitation force, none of them has approached the problem from that angle. The study of how using different kinds of excitation force influence the results of the test has been reported by multiple researchers (Rix, 1990; Park et al., 2002; Park et al., 2007; Shtivelman et al., 2005; Strobbia, 2003; Xia et al., 2007; Wood and Cox, 2012; Taipodia et al., 2019). Nonetheless, in those studies the excitation force itself was not characterized, they just considered the effect of using different kinds of excitation sources in the field test.

Some progress on the study of near field effects on the MASW test was presented by Roy and Jakka (2017). Also, the application of the transfer function method was reported to be beneficial for the calculation of dispersion curves (Lai and Rix, 1998; Rix et al., 2001; Lai, 2005; and Foti, 2004). Furthermore, interesting progress about the study of the effect of the impedance contrast effect on MASW results was reported by Boaga et al. (2013), and Boaga et al. (2014); however, they were focused on how the presence of high contrast materials affect the proper identification of the vibration modes, which is a critical intermediate result to calculate the dispersion curve. Comina et al. (2011) presented an evaluation of the reliability of (v_{s-30}) values obtained from the MASW test, focusing on the non-uniqueness characteristic of the solution obtained in the inverse problem. Therefore, the combined analysis of impedance effects on the reliability of the results of (v_{s-30}), as it is presented in this thesis, has not been studied before.

For the sCPTU tests, which is one of the most reliable field tests used to characterize geomaterials at large scales, all the efforts in research have been focused on the improvement of signals recording, the reliability of the test, and the quality of the (v_s) profiles (Mayne, 2007; McGillivray, 2007; Robertson, 2009; Robertson, 2016).

Surprisingly, no report was found of any progress in the characterization of the excitation source used in the sCPTU test. As it is presented in this thesis, the characterization of the source in sCPTU tests allows, among others, the study of the effects of input frequency content on the results obtained.

In the case of the BE test, all around the world researchers are trying to progress in improving the interpretation of the results. A consistent research effort has been done by a group of researchers at the University of Porto and the University of Waterloo, which ended in some important contributions done in the past about the study of effects of input frequency on V_s determination using the BE test (Ferreira et al., 2014; Ali, 2015; Camacho-Tauta et al., 2015; Irfan, 2019). This thesis involves a chapter in which the same research line was followed and new discoveries are reported about the generation and detection of P-waves in typical BE tests.

Based on this preliminary review, it is clear that the aforementioned research efforts have been focused on issues other than the ones covered in this thesis, so the results presented here will offer important contributions for researchers and field practitioners dealing with the characterization of geomaterials.

1.1 Problem statement

To meet the requirements of construction codes related to seismic designs, the quantification of the dynamic properties of geomaterials is a fundamental task that can be addressed both with field tests and with laboratory tests. However, there are still practical and theoretical gaps in the understanding of the effect of impedance ratio between materials, the characterization of the excitation source and its frequency content, and the testing scale on laboratory and field testing results.

There is a current lack of understanding of the effect of the impedance ratio between adjacent materials on the results of wave-based propagation tests obtained in a layered medium. When materials are too different in stiffness, the energy used in the test for some specific frequencies could get trapped inside a given material layer, leading to a misinterpretation of the results. This is critical because the results of seismic tests are

used to calculate the (v_{s-30}) parameter, which ends defining a seismic design class for the construction site. If the (v_{s-30}) is not properly representing the subsoil profile, the designed infrastructure will not behave properly when facing a real seismic event.

On the other hand, the characterization of geomaterials using wave-based techniques is governed by the ratio between the wavelength used in the test and the anomaly size (i.e. the geometrical characteristic of interest, for instance, layer thicknesses, depth to some specific material, spatial discontinuities or voids, etc.). Because the anomaly size is usually not known a priori, the use of different frequencies in the input or excitation source should be mandatory for wave-based propagation techniques. However, that is not what happens in the traditional laboratory or field testing, resulting in a not proper characterization of geomaterials because of the lack of understanding of the input source characteristics and its frequency effects.

A critical example of the lack of understanding of the excitation source is the bender element (BE) testing. In the BE test it is assumed that the electrical input pulse sent to the BE transmitter is the excitation source for the soil sample, which is not true as the BE transmitter itself is another subsystem that modifies the input voltage and responds with a displacement inside the soil.

Finally, the testing scale (i.e. the dimension of the materials being tested) also plays a fundamental role in the dynamic site characterization. The dynamic properties obtained for a singular sample in the lab may not properly represent the material deposit or layer in the field because they usually exhibit heterogeneities, high spatial variability in the distribution of their stiffness properties, or even localized discontinuities. All these factors affect the wave propagation process and the results obtained from the tests.

In this research, all these gaps are addressed and new methodologies are proposed to overcome them in real practice both in the field and in the laboratory.

1.2 Research objectives

The main objective of this thesis is to overcome the issues associated with the lack of understanding of the effects of impedance ratio between materials, input frequency content, and testing scale on the results of dynamic characterization of geomaterials at low strain levels by using methods based on the propagation of mechanical waves.

A list of sub-objectives and their associated tasks are presented below:

1. To study, through numerical simulations and laboratory measurements, the wave propagation phenomena in geomaterials.
2. To study, through numerical simulations, the effect of impedance ratio between the top two materials on the results of shear wave velocity of a layered media.
3. To assess the effect of the spatial distribution of elastic properties inside the medium on the results of surface waves testing (i.e. by comparing homogeneous medium, layered medium, and spatially variable medium).
4. To characterize the input excitation force used in seismic tests performed in the field and in the laboratory (i.e. sCPTU test in the field and MASW test in the lab).
5. To study the effect of the changes in the input frequency content on the results of a seismic test performed in the field (i.e. sCPTU test).
6. To study the effect of input frequency and confinement level in bender element (BE) test results, via laboratory tests, and numerical simulations.

1.3 Scope of the work

This research addresses the issues associated with the effect of impedance ratio, input frequency content, and testing scale on the results obtained from seismic wave propagation tests. By doing so, a better understanding of the seismic testing results will be achieved, which will be beneficial for field and laboratory practitioners.

In order to study the aforementioned issues affecting the results obtained in seismic tests, this thesis used field data, laboratory data, and numerical models. The first issue, related to the effect of impedance ratio on the results of shear wave velocity, is

tackled by using extensive numerical simulations in which a number of soft to very-soft soils are considered as top materials in a hypothetical layered media. The second and third issues, related to the effects of input frequency content in seismic tests and the effect of the scale of analysis, were tackled by using field and laboratory testing data, as well as numerical simulations.

The main strategy in this research is the conjunct use of reliable field testing data, laboratory testing data using cutting edge technology (e.g. state-of-the-art laser vibrometer), and numerical simulations results of the wave propagation phenomena under a variety of conditions. First, for the study of wave propagation at large scale, a field site of about 30m long was characterized using near-surface seismic techniques; second, for the intermediate scale, a physical model of about 1m long (i.e. a sandbox) was tested in the laboratory using calibrated ultrasonic transducers and a high-frequency laser vibrometer; third, for the small scale, a reconstituted sample of about 0.14m long was tested in the laboratory using bender element (BE) and resonant column (RC) tests.

The general research method followed in this thesis was based on the engineering design process approach (see Fig. 1-1).

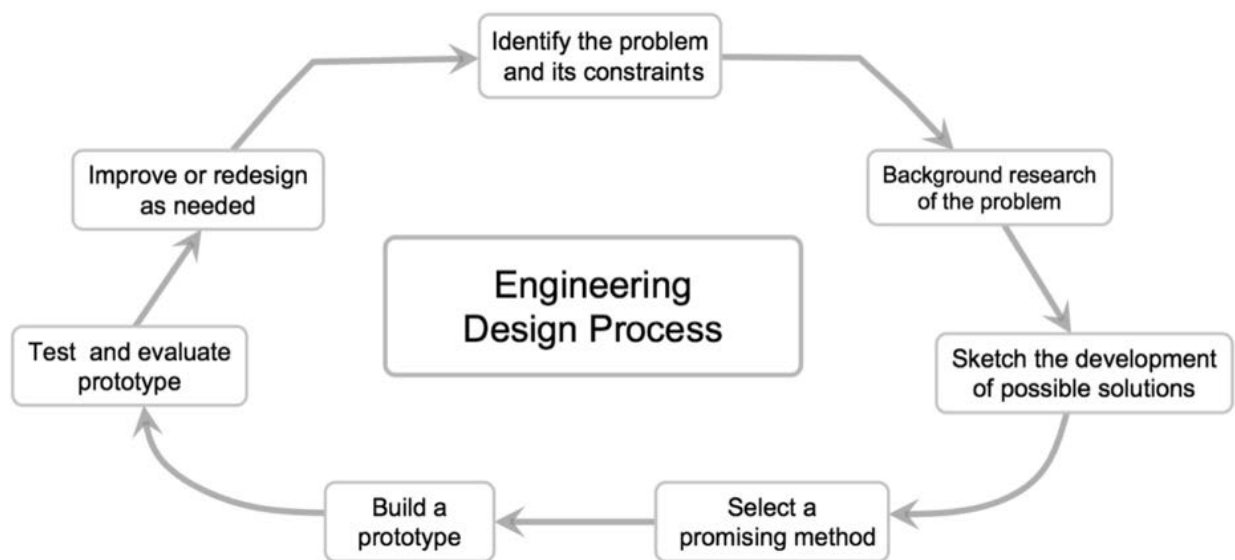


Fig. 1-1: Engineering design process (after UCB, 2015)

According to Lindberg (2011), scientists are “in the business of exploring the unknown and their domain is the natural world,” while the domain of engineers is the “designed world”. This research is intended to contribute to overcoming three specific issues of geomaterials characterization, that is a necessary step for the seismic design of any infrastructure which is part of the “designed world”.

1.4 Thesis organization

This thesis is divided into ten chapters, some of them are actually the core for research papers either already submitted or pending submission to be published in indexed journals.

Chapter 1 introduces the concept of what is known as a geomaterial, identify the problem to be addressed in the research, and discusses the motivation, research objectives, scope of the work, and thesis organization.

Chapter 2 presents the theoretical background for the concepts necessary to understand this research, such as the basics of wave propagation theory, the identification of factors affecting the wave propagation process, the stress-strain behaviour and the dynamic characterization of geomaterials, the near-surface geophysical techniques, the standard concepts and procedures for signal processing, and the basics of numerical simulation for wave propagation, among other topics.

Chapter 3 presents a literature review of geomaterials characterization for engineering purposes. First, the classification of geomaterials based on their stiffness and the factors affecting their dynamic properties are discussed. Second, the geophysical techniques used to characterize geomaterials are presented. Then, the effect of frequency on the results obtained for dynamic properties at different scales is discussed. Finally, the background of the different approaches to characterize geomaterials, and the effects that the assumptions made in each approach have on the results obtained, are discussed.

Chapter 4 presents the methodology followed in this research, along with a breakdown of necessary research activities, steps, tasks, and operations followed to characterize geomaterials at different scales, using different frequencies, and considering three different ways to consider the distribution of materials' properties inside the medium (i.e. homogeneous medium, layered medium, and heterogeneous medium). Detailed flowcharts are also presented in order to ease the reader's understanding of the process followed, as well as the partial and final results obtained.

Chapter 5 presents a numerical parametric study for the characterization of geomaterials at large scales and assuming the underground was a horizontally layered medium. That assumption corresponds to the most widely used and accepted approach in the industry practice when describing the distribution of geomaterials in a subsoil profile. In this chapter, first, the geometry, density, and stiffness properties of geomaterials in a hypothetical layered medium were defined. Then, an extensive set of numerical simulations seeking to study the effect of different parameters on wave propagation was run. Among the parameters considered in this study are the acoustic impedance ratio between subsequent layers, the frequency content in the input excitation force, and the shape of the interface between layers.

Chapter 6 presents a numerical study of wave propagation in geomaterials at large scales and considering three different approaches to characterize the spatial distribution of materials' properties inside the medium. The subsoil profile was characterized according to the results of a CPTU test performed in a testing field site. The results of the field test allowed a clear delineation of the properties up to a depth of 16 meters. Then, the results of three sets of numerical models are presented: for the first set, the subsoil was treated as a single-layer homogeneous medium overlaying a firm bottom layer; for the second set, the subsoil was approached as a multilayered medium; finally, for the third set, the subsoil was approached as a spatially variable medium in which the material properties were distributed using an unconditioned random field in two dimensions.

Chapter 7 presents the characterization of geomaterials at large scales using a horizontally layered medium approach to distribute the properties of materials inside the

medium. In this case the numerical models used the same geometry and same boundary conditions defined for the model in the previous chapter. The material properties were distributed in 16 layers each of one-meter thickness and according to the results of the shear wave velocity values obtained from the seismic cone penetration test (sCPTU) in the field. By applying a novel method of input-source inversion when the medium is assumed to behave as a linear invariant system, the numerical models allowed the characterization of the input source of energy, which is considered the input of the linear system. Then, a further study of the effects of frequency on the sCPTU test results was developed. Finally, a preliminary study of conditioned random fields calibrated to reproduce the field results is presented; in this case the input source used corresponds to the one inverted from the analysis of the layered medium.

Chapter 8 presents the characterization of geomaterials at intermediate scales, in this case for a physical model in the laboratory. The model was a sandbox with two layers, a top layer of cemented sand overlaying a layer of loose sand. The sandbox also had a void in one side of the upper layer, so that a homogeneous medium could be tested at one side of the sandbox, and a medium with a lack of spatial continuity (i.e. a heterogeneous medium) could be tested on the other side. Then, numerical simulations were carried out to replicate the wave propagation process under the laboratory conditions for both a homogeneous and a heterogeneous medium. Finally, the method proposed in Chapter 7 to obtain the characterization of the source of energy when the medium is assumed to be a linear invariant system is also applied to the sandbox results. As the laboratory testing conditions are more controlled than the ones in the field, and the surface displacements were measured using a laser vibrometer, the laboratory results allowed to validate the proposed method not just at different scales, but also for different materials.

Chapter 9 presents the characterization of geomaterials at small scales, in this case using the bender element (BE) test and the resonant column (RC) test on a reconstituted sample. Those are well-known tests to characterize geomaterials' samples in the laboratory. First, the characterization of the BE itself was performed to identify the vibration modes in three dimensions. Then, the effect of frequency in the determination

of shear wave velocity using the BE test was studied. The results obtained at this stage of the research were fundamental to understand how the BE test results are affected by the input frequency used in the laboratory test. The BE test is the cheapest, easiest, and fastest laboratory test to measure the dynamic properties of geomaterials, it is widely used to corroborate the results obtained in the field at large scales. Nonetheless, the main disadvantage is the lack of an ASTM standard for its procedure. So, the results in this chapter may contribute to a better understanding of the test and possibly to standardize the BE test in the future.

Chapter 10 presents the conclusions and recommendations for future research work in this area of geomaterials characterization. The main contributions of this research, related to the improvement of wave-propagation based techniques to characterize materials are also summarized.

2 Theoretical background

2.1 Wave propagation theory

2.1.1 Wave propagation in one-dimension

Following the theory presented by Kramer (1996), the propagation of stress waves is most easily understood by first considering an unbounded, or infinite, medium. The one-dimensional analysis considers the equilibrium of forces and the compatibility of displacements, and the strain-displacement and the stress-strain relationships for an infinitely long rod.

The dynamic equilibrium of one small element of the rod is shown in Fig. 2-1. The formulation yields to:

$$\left(\sigma_{x_0} + \frac{\partial \sigma_x}{\partial x} dx \right) A - \sigma_{x_0} A = \rho A dx \frac{\partial^2 u}{\partial t^2} \quad (2-1)$$

This expression states that any external force acting on the ends of the element must equal the inertial force. Simplifying the expression, it is possible to get the one-dimensional equation of motion:

$$\frac{\partial \sigma_x}{\partial x} = \rho \frac{\partial^2 u}{\partial t^2} \quad (2-2)$$

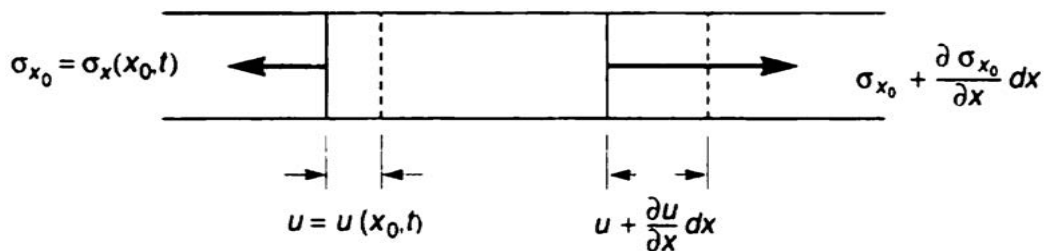


Fig. 2-1: Stresses and displacements at ends of an element of length dx and cross sectional area A . (Kramer, 1996)

Considering the stress-strain relationship, the constrained modulus (M), which relates the elastic modulus and the Poisson's ratio (ν), and the strain-displacement relationship, the form of the one-dimensional longitudinal wave equation for a constrained rod is obtained as:

$$\frac{\partial^2 u}{\partial t^2} = \frac{M}{\rho} \frac{\partial^2 u}{\partial x^2} \quad (2-3)$$

An alternative way to present this equation is:

$$\frac{\partial^2 u}{\partial t^2} = (v_p)^2 \frac{\partial^2 u}{\partial x^2} \quad (2-4)$$

Where v_p is the wave propagation velocity. It is important to clarify that v_p is the velocity at which a stress wave travels along the rod. "It is not the same as the particle velocity, which is the velocity at which a single point within the rod would move as the wave passes through it". (Kramer, 1996)

The particle velocity (\dot{u}) can be obtained by relating strain-displacement and stress-strain relationships.

$$\dot{u} = \frac{\partial u}{\partial t} = \frac{\varepsilon_x \partial x}{\partial t} = \frac{\sigma_x}{M} v_p = \frac{\sigma_x}{\rho (v_p)^2} v_p = \frac{\sigma_x}{\rho v_p} \quad (2-5)$$

The particle velocity (\dot{u}), as described by Kramer (1996), is proportional to the axial stress in the rod. The coefficient of proportionality is called the specific impedance of the material, which is another important property that influences the behaviour of waves at boundaries.

2.1.2 Wave propagation in a three-dimensional infinite medium

"The three-dimensional equations of motion for an elastic solid are obtained from equilibrium requirements in much the same way as for the one-dimensional rod, except that equilibrium must be ensured in three perpendicular directions." (Kramer, 1996)

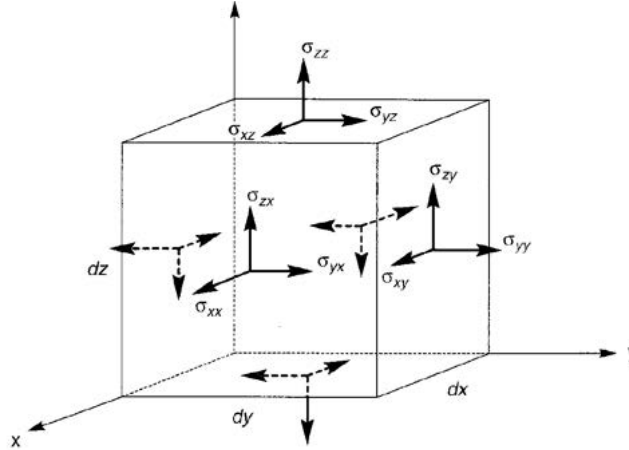


Fig. 2-2: Stress notation for an element of dimensions dx , dy , and dz . (Kramer, 1996)

$$\begin{aligned} \rho \, dx \, dy \, dz \, \frac{\partial^2 u}{\partial t^2} &= \left(\sigma_{xx} + \frac{\partial \sigma_{xx}}{\partial x} dx \right) dy \, dz - \sigma_{xx} \, dy \, dz \\ &+ \left(\sigma_{xy} + \frac{\partial \sigma_{xy}}{\partial y} dy \right) dx \, dz - \sigma_{xy} \, dx \, dz \\ &+ \left(\sigma_{xz} + \frac{\partial \sigma_{xz}}{\partial z} dz \right) dx \, dy - \sigma_{xz} \, dx \, dy \end{aligned}$$

(2-6)

Simplifying and repeating operations in the y and z directions:

$$\begin{aligned} \rho \frac{\partial^2 u}{\partial t^2} &= \frac{\partial \sigma_{xx}}{\partial x} + \frac{\partial \sigma_{xy}}{\partial y} + \frac{\partial \sigma_{xz}}{\partial z} \\ \rho \frac{\partial^2 v}{\partial t^2} &= \frac{\partial \sigma_{yx}}{\partial x} + \frac{\partial \sigma_{yy}}{\partial y} + \frac{\partial \sigma_{yz}}{\partial z} \\ \rho \frac{\partial^2 w}{\partial t^2} &= \frac{\partial \sigma_{zx}}{\partial x} + \frac{\partial \sigma_{zy}}{\partial y} + \frac{\partial \sigma_{zz}}{\partial z} \end{aligned}$$

(2-7)

Kramer (1996) presents these equations of motion in terms of displacements, by using a stress-strain relationship (Hooke's law) and strain-displacement relationships.

$$\rho \frac{\partial^2 u}{\partial t^2} = (\lambda_{Lamé} + \mu_{Lamé}) \frac{\partial \bar{\epsilon}}{\partial x} + \mu_{Lamé} \nabla^2 u$$

$$\rho \frac{\partial^2 v}{\partial t^2} = (\lambda_{Lamé} + \mu_{Lamé}) \frac{\partial \bar{\epsilon}}{\partial y} + \mu_{Lamé} \nabla^2 v$$

$$\rho \frac{\partial^2 w}{\partial t^2} = (\lambda_{Lamé} + \mu_{Lamé}) \frac{\partial \bar{\epsilon}}{\partial z} + \mu_{Lamé} \nabla^2 w$$

(2-8)

Where (∇^2) is the Laplacian operator, and $(\lambda_{Lamé})$ and $(\mu_{Lamé})$ are Lamé's first and second parameters, respectively.

2.1.3 Seismic waves

Lowrie (2007) describes the seismic wave propagation process as the transmission of a disturbance by "periodic elastic displacements of the particles of a material" and the progress of that process "is determined by the advancement of the wavefront". For the analysis of the seismic wave propagation process, is fundamental the understanding of how the wave behaves at the interface between adjacent materials.

In an infinite medium, two kinds of body seismic waves can exist, they are the compressional (P-waves), and the shear waves (S-waves). If a semi-infinite medium is considered, other kinds of waves like the surface waves (R-waves and L-waves) can be generated. Other kinds of waves can propagate in some specific conditions, for example, the "Scholte" waves are generated in the interface between a fluid and a semi-infinite solid medium, and the "Stoneley" waves are generated on a plane interface between different solid media. (Scholte, 1942; Stoneley, 1924)

Out of six kinds of waves mentioned above, this research will be focused on just three of them: P-waves, S-waves, and R-waves.

2.1.3.1 Compressional waves (P-waves)

The solution for the first type of wave, in a three-dimensional medium, indicates that a dilatational wave will propagate through the body at a velocity known as compressional or P-wave velocity:

$$v_p = \sqrt{\frac{\lambda_{Lam\acute{e}} + 2\mu_{Lam\acute{e}}}{\rho}} = \sqrt{\frac{G(2-2\nu)}{\rho(1-2\nu)}} \quad (2-9)$$

Compressional waves or primary waves (P-waves) are body waves traveling back and forth, shaking the ground in the same direction of wave propagation.

2.1.3.2 Shear waves (S-waves)

In a very similar way, the solution for the second type of wave, in a three-dimensional medium, indicates that a distortional wave will propagate through the solid at a velocity known as shear or S-wave velocity:

$$v_s = \sqrt{\frac{\mu_{Lam\acute{e}}}{\rho}} = \sqrt{\frac{G}{\rho}} \quad (2-10)$$

In the shear wave the particle's motion is constrained to planes perpendicular to the direction of wave propagation. S-waves may propagate in a vertical direction with horizontal particle motion (VH-waves), in a horizontal direction with vertical particle motion (HV-waves), or in a horizontal direction with horizontal particle motion (HH-waves). (Knutsen, 2014)

2.1.3.3 Surface waves (R-waves)

The two aforementioned solutions for the equation of motion are for an infinite elastic medium. The earth is obviously not an infinite body, in fact, for near-surface engineering problems the earth is idealized as a semi-infinite body with a planar free surface, called a semi-infinite half-space. In this case a third solution of equation of motion is obtained, which corresponds to a wave confined to the near free surface.

Surface waves are generated due to the interaction of body waves with the free surface. For these waves their maximum amplitude is very close to the surface, and after that an exponential decay of amplitude is observed with depth. There are two main types of surface waves; they are Rayleigh and Love waves. An important property of surface waves is dispersion, i.e., different frequencies travel at different velocities.

Rayleigh Waves: These waves propagate outwards from a source in a cylindrical wave front with a central axis passing through the source location and oriented perpendicular to the surface. Groves (2010), following the previous work done by Lai and Wilmański (2005), stated that “the effective depth of penetration is commonly taken as one wavelength (λ); with most of the energy concentrated between the surface and a depth of $1/3 \lambda$. R-waves are dispersive in layered media. High frequencies (short λ) have limited penetration and propagate at the velocity of upper layers, whereas lower frequencies (larger λ) penetrate deeper and propagate at velocities determined by the characteristics of subsequently deeper soil layers”.

Body waves propagate inside a medium and their energy spreads in horizontal and vertical directions. On the other hand, surface waves originate from stresses dissipating at a free boundary of a medium, and their radiation pattern is essentially two-dimensional (Fig. 2-3), and characterized by a rate of geometric attenuation lower than the one of body waves. (Foti et al., 2014)

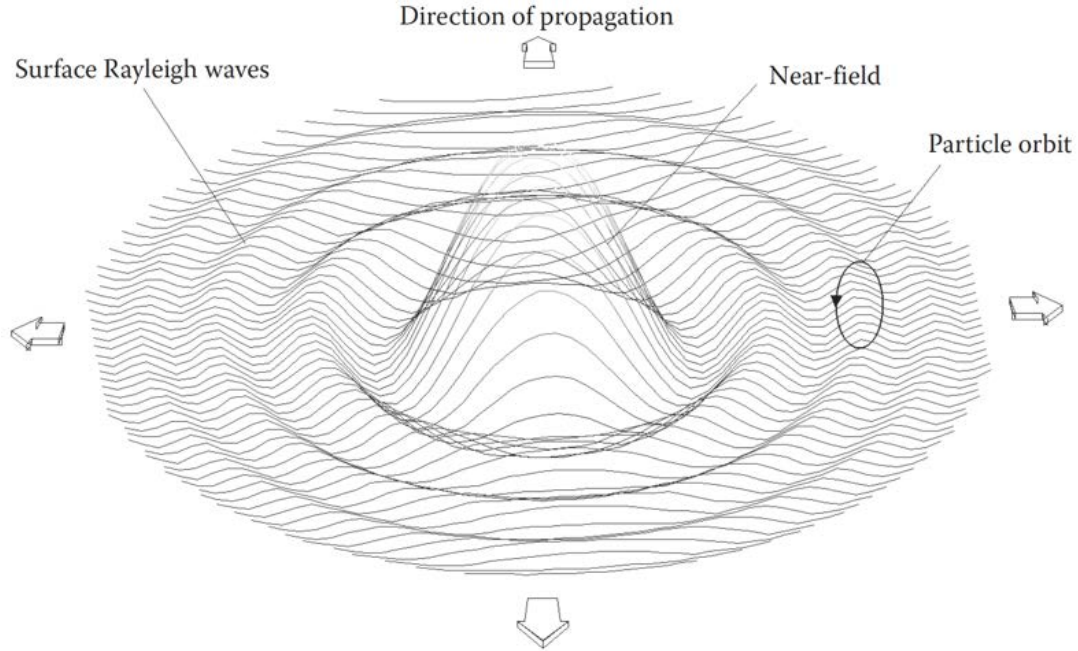


Fig. 2-3: Radiation pattern of Rayleigh surface waves generated by a vertical point source. (Foti et al., 2014)

Foti et al. (2014) presents the equation for the speed of propagation of a wave moving along the free surface of the half-space (Eq. 2-11). As can be seen, v_R depends on v_p and v_s , which are intrinsic, frequency-independent properties of the medium. Now, if the v_p and v_s are known values, it is possible to use the equation to calculate the Rayleigh wave velocity.

$$\left(\frac{v_R}{v_s}\right)^6 - 8\left(\frac{v_R}{v_s}\right)^4 + 8\left(\frac{v_R}{v_s}\right)^2 \left[1 + 2\left(1 - \left(\frac{v_s}{v_p}\right)^2\right)\right] - 16\left(1 - \left(\frac{v_s}{v_p}\right)^2\right) = 0 \quad (2-11)$$

The seismic waves behavior dictates that body waves arrive before the surface waves do, and also that the amplitude of P-waves is much smaller than the amplitude of S-waves. So, in theory it would be easy to differentiate one type of waves from the other. However, that assumption is not always correct and differentiation of some specific kind of waves could be a very challenging task. Fig. 2-4 shows a generic example of a

seismogram where time delay and relative amplitudes between P, S, and surface waves are presented; this figure also allows to see the typical seismic waves' events separation.

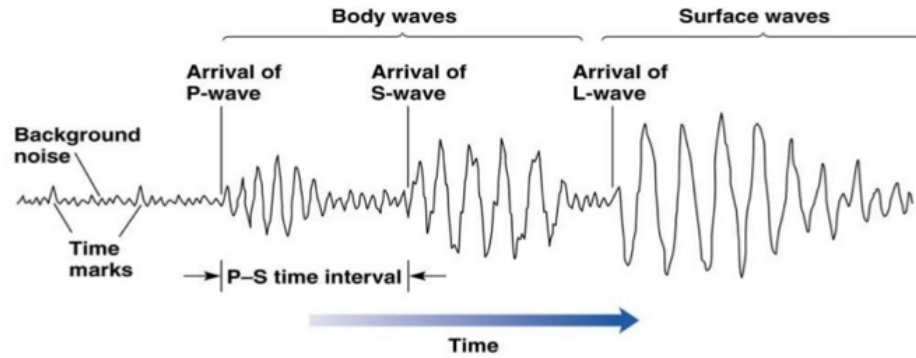


Fig. 2-4: Typical seismic waves' events separation (Tomic, 2017)

2.1.4 Acoustic impedance

When dealing with body waves propagating through different materials, transmission and reflection of energy at the interfaces are well understood. However, the transmission of energy carried by surface waves is not very well understood when they reach interfaces. Transmission and reflection of energy in body waves is calculated by using the acoustic impedance (I_z) of the materials, which depends on mass density (ρ) and shear wave velocity (v_s).

$$I_z = \rho * v_s \quad (2-12)$$

Also, the impedance ratio between adjacent layers could be a good indicator of the effectiveness in the energy transmission process.

2.2 Factors affecting seismic waves propagation in geomaterials

Factors affecting the propagation of seismic waves can be categorized depending if they are internal or external. The former means if they are related to the conditions and properties inside the medium, while the latter refers to the conditions of the load application process.

The internal conditions are those related to either the spatial distribution of materials' properties (i.e. homogeneity, isotropy, linearity and elasticity of the materials), or the geometry of the medium where the waves are propagating (i.e. spatial continuity, layer's distribution, shape of interfaces, boundary conditions, etc.).

On the other hand, the external factors refer to the load application process, not just the maximum amplitude, but also the shape of the force function, and its correspondent frequency content.

2.3 Stress-strain behaviour of geomaterials

2.3.1 Dynamic soil properties

Dynamic soil properties can be measured both with laboratory and field tests. Those techniques have been quickly evolving in the last 40 years. Late in the '70s, the technology was not advanced enough to allow the measurement of soil properties at very low strain ($< 0.001\%$); nowadays, that problem is practically overcome. However, new challenges have arisen like the understanding of the effect of frequency on the dynamic soil properties.

Woods (1994) presented a state of the art of laboratory testing for dynamic soil properties, however, he mentioned that "we should no longer distinguish between "dynamic" and "static" properties as they are indeed a continuum, and we should, rather, distinguish properties on the basis of strain level". Despite that suggestion, in this research, the term "dynamic" for the soil properties is still used because it is widely accepted in geotechnical engineering research.

Kumar et al. (2013) presented a more recent literature review of dynamic soil properties and their influencing parameters, highlighting the importance of each influencing parameter on soil dynamic properties determination. According to them, the dynamic soil properties are affected by many factors, like: method of sample preparation in the laboratory (whether intact and reconstituted samples), relative density, confining

pressure, methods of loading, overconsolidation ratio, loading frequency, soil plasticity, percentage of fines and soil type.

Shear Wave Velocity (v_s): This is the most widely used parameter for dynamic soil characterization. It is used to calculate the other parameters in the elastic range of soil behaviour, like the shear modulus. Luna and Jadi (2000) stated that “the importance in its utility is that the particle of motion travels perpendicular to the direction of wave propagation being able to measure the shear properties of the soil skeleton and not the fluids that cannot take shear” (sic).

Shear Modulus (G): This is a calculated parameter based on the v_s using a simple elastic relationship with mass density. The mass density is a parameter easy to obtain, either by taking a sample to the lab for a unit mass test or by using correlations proposed in the technical literature for similar materials. Various correlations have been proposed to estimate the shear modulus based on the results of standard penetration test (SPT), the plasticity index, the Atterberg limits, and the grain size distributions (e.g. Vucetic and Dobry (1991); Idriss et al., 1978).

Maximum Shear Modulus (G_{max}): it is the shear modulus at very small strains, which determines the dynamic response of soils (Ku and Mayne, 2013). G_{max} is a scaling parameter used to normalize the relationships between shear modulus (G) and shear strain (γ). Seed et al. (1986), proposed a relationship to relate the shear modulus of a cohesionless soil to the effective mean principal stress, and a modulus stiffness coefficient that can be estimated from SPT results. Sun et al. (1988) presented a relationship for normalized dynamic shear moduli and damping factors for cohesive soils, according to them, “the form of this relationship is not significantly affected by consolidation stress history, duration of confinement, frequency of loading (for earthquake frequencies) and sample disturbance up to moderate strain levels”.

As pointed by Luna and Jadi (2000) “these normalized relationships allow the engineer to use well-established degradation curves and scale them to the measured in-situ value of G_{max} ”. The use of correlations is a widely extended practice in geotechnical

engineering, mainly because of the economic constraints to perform extensive soil testing in the field and in the laboratory.

Damping Ratio: denoted by (ξ), it is a dimensionless parameter used in dynamic analysis to describe how the oscillatory movement attenuates after the excitation force is applied to the system. Since damping ratio is also shear strain dependent, it is required to define some relationship with strain. “Dynamic analysis results are also influenced by the damping ratio for single and multi-degree modal systems. The effects of soil-structure interaction also influence the damping of the system making it an area where recent research has focused. The utility of this parameter is based on the ability of the system to absorb dynamic energy and how this will affect the duration and modes of vibration”. (Luna and Jadi, 2000)

Stewart (1992) extended the traditional use of shear wave velocity obtained from seismic cone penetration test (SCPT) in the field to estimate values of damping from actual earthquake records.

Poisson's Ratio: denoted by (ν), this is an elastic parameter difficult to measure in real geomaterials like soils, so it is usually estimated considering that if the material gets pressured in the vertical direction, the Poisson's ratio is defined as the ratio of horizontal to vertical strain. Typical values of Poisson's ratio for soils are above 0.2, however smaller values may be found in some very-soft soils. The Poisson's ratio can also be calculated as a relationship between Elastic (E) and Shear (G) modulus, based on laboratory tests at low strains. (Luna and Jadi, 2000)

Similarly, the Poisson's ratio (ν) can be calculated as a function of the ratio between (v_p) and (v_s), as it follows:

$$\nu = \frac{\alpha^2 - 2}{2(\alpha^2 - 1)} \quad (2-13)$$

where:

$$\alpha = \frac{v_p}{v_s} = \sqrt{\frac{2(1-\nu)}{1-2\nu}} \quad (2-14)$$

Stress-strain behaviour of soil under static loading is complex and it is even more complex under dynamic loading conditions. Nonlinear behaviour of soils leads to the attenuating behaviour of shear modulus (G) with the increase of shear strain (γ) amplitude. Presenting dynamic soil behaviour in simple models is a constant challenge in geotechnical engineering. Rational models have to balance the conflicting requirements of simplicity and accuracy in a good way. (Kramer, 1996)

In Fig. 2-5 it is possible to visualize the shear strain range in which each test works, as well as the variation of the shear modulus ratio.

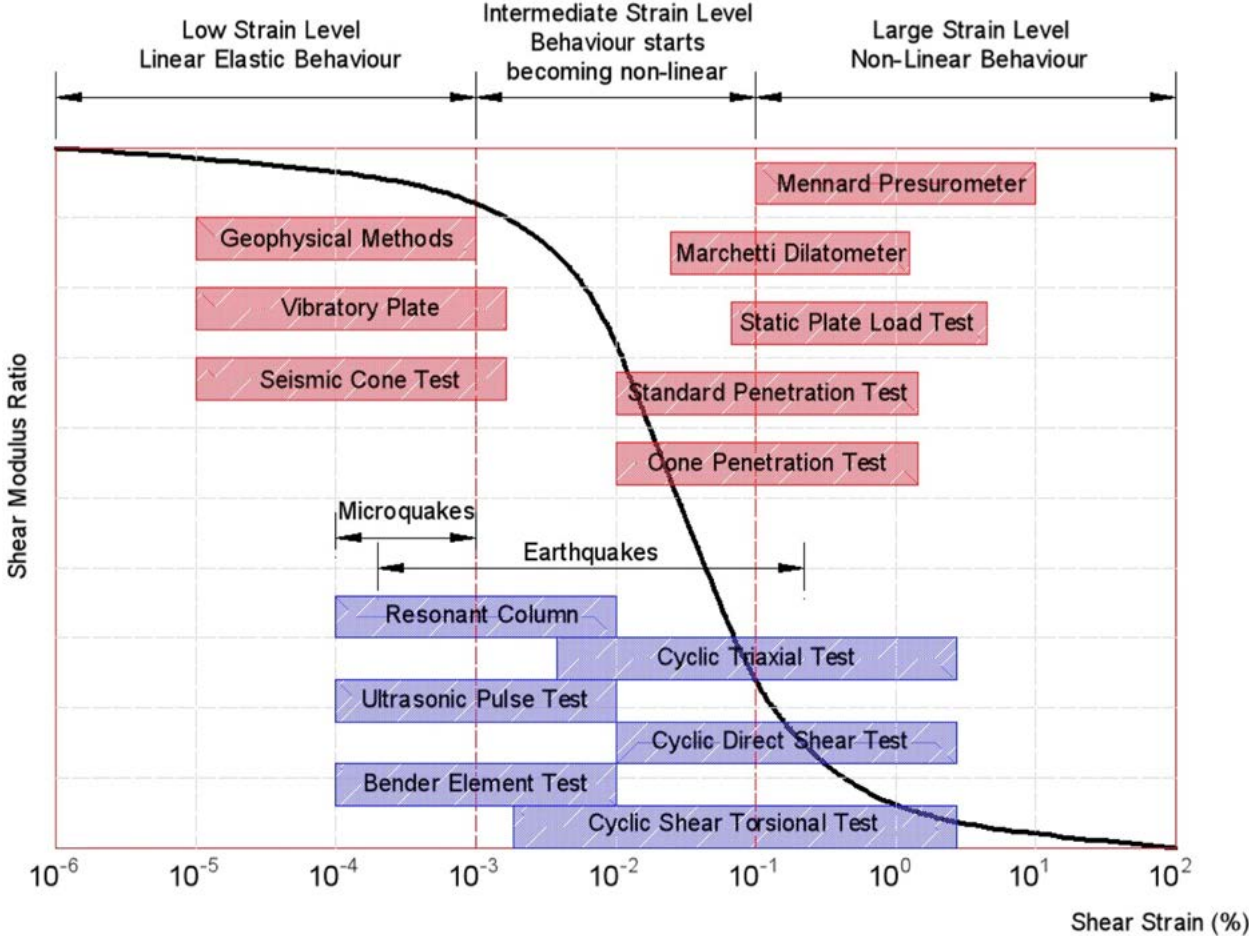


Fig. 2-5: Shear strain range for laboratory tests (blue boxes) and field tests (red boxes), (after Arango, 1980)

2.3.2 Attenuation

Attenuation of waves is the decrease in amplitude of the waves with the increasing distance. Winkler et al. (1979) studied the frictional attenuation of seismic energy in rocks, they were interested only in “processes that convert seismic energy into heat”. Nonetheless, they listed other causes of attenuation are geometrical spreading and partial reflections. All of these causes are represented by parameters defining attenuation. The focus in this research will be on the parameters of attenuation which represent material losses. Following are the definitions of these parameters:

2.3.2.1 Damping ratio

Damping ratio is defined as the ratio between system damping and critical damping. For a single degree of freedom system, the equation of damping ratio is given by:

$$\xi = \frac{C}{C_{cr}} = \frac{C}{2\sqrt{k m}} \quad (2-15)$$

Where C_{cr} is the critical damping coefficient, C is the system damping coefficient, k and m are the stiffness and mass of the system, respectively. The C_{cr} value is also the boundary between oscillatory and non-oscillatory motion. For underdamped systems $C < C_{cr}$, for critically damped systems, $C = C_{cr}$, and for over-damped systems, $C > C_{cr}$.

2.3.2.2 Logarithmic decrement

This parameter is defined as the natural logarithm of the difference between two successive amplitudes of the free vibration response of the system. Its value is given by the following expression:

$$\delta = \frac{1}{n} \ln \left(\frac{u_i}{u_{i+n}} \right) \quad (2-16)$$

where u_i represents the maximum amplitude of i^{th} cycle and n is the number of cycles between the two chosen amplitudes.

2.3.2.3 Complex modulus and quality factor

For a linear viscoelastic medium, attenuation can be quantified using the complex modulus

$$G^* = G_R + iG_I \quad (2-17)$$

where G_R is the storage modulus (real or elastic component) and G_I is the loss modulus (imaginary or viscous component). The ratio between G_R and G_I , is also useful to determine the Quality factor (Q) which is understood as the ratio of the total energy to the damping capacity and can be estimated with the half-power bandwidth method. (Peters, 2002)

Lo Presti (1997) mentioned that both shear modulus and damping ratio are affected by several factors, such as the “frequency or strain rate (f , $\dot{\gamma}$), the drainage conditions, the number of loading cycles (N), the cyclic prestraining at larger strains and so on”. They also mentioned the damping ratio is more sensitive than shear stiffness to the aforementioned factors.

The damping ratio and logarithmic decrement are parameters typically used to determine the material damping in conventional resonant column (RC) testing. The shear modulus is determined independently even though soil behaves as a viscoelastic medium even at very low strains. (Irfan, 2019)

2.3.3 Laboratory tests to determine dynamic soil properties

Resonant Column Test: In this test the soil sample is consolidated in a cell fixed at the bottom and free at the top. During the test a sample is subjected to torsional or axial loading on its top, normally harmonic with a controlled frequency and amplitude. The cyclic loading is initially set at a low frequency, which is increased until a maximum response occurs. The lowest frequency, at which maximum strain amplitude is reached, is the first-mode resonance frequency of the sample (Knutsen, 2014, after Kramer, 1996).

In RC test, the soil specimen is assumed as a continuous, linear elastic, isotropic and homogenous cantilever solid cylinder; therefore, the wave equation is still applied.

The driving and motion monitoring instruments are attached at the free end of the soil specimen. Theoretically, the effects of these instruments are combined into a lumped mass; this lumped mass changes the boundary condition at the free end.

Considering those modifications for the boundary conditions, a torque (T) is applied at the free end for inducing the torsional vibrations. This torque is equal to the rotational inertia of the lumped mass and is calculated as:

$$T = \frac{\partial \theta}{\partial x} GJ = -I_0 \frac{\partial^2 \theta}{\partial t^2} \quad (2-18)$$

where I_0 is the polar moment of inertia of the lumped mass and J is the polar moment of inertia of the rod. Then, knowing that $I = J\rho H$ for a uniform rod, it can be reduced to:

$$\frac{I}{I_0} = \frac{\omega_n H}{v_s} \tan\left(\frac{\omega_n H}{v_s}\right) \quad (2-19)$$

where I is the mass polar moment of inertia of the rod.

The above procedure shows how the 1D wave propagation equation can be used with resonant column (RC) test boundary conditions to estimate v_s of the soil by knowing the resonance frequency (ω_n) of the specimen. Finally, in RC tests, the damping ratio (ξ) is determined independently using the phenomenon of attenuation of waves. (Irfan, 2019)

Bender Element Test: One bender element consists of two thin plates of piezoelectric material, which are bonded together, with two conductive outer layers and a metal shim at the center. For the test, two bender elements are placed opposite one another in the soil sample, one acting as a transmitter and the other as a receiver element. A voltage pulse is applied to the transmitter element, causing one of the plates to contract while the other expands so that the element bends and produces a S-wave, which travels through the sample. When the S-wave reaches the receiver element, this element will distort and cause another voltage pulse.

The wave propagation theory in BE test is relatively simple; travel time of the elastic shear waves along the length of the rod is used to estimate G . If a torsional wave takes the time (t) to travel along the rod of length (H), then G can be estimated as

$$G = \rho \frac{H^2}{t^2} \quad (2-20)$$

where $v_s = (H/t)$ can be substituted in the equation and (ρ) is the mass density of the material. The bender element (BE) tests are not typically used for estimating the damping ratio (ξ) of the soil.

Cyclic Triaxial Test: according to the standard ASTM D5311 (2013), “this test method determines the cyclic strength (liquefaction potential) of saturated soils in either intact or reconstituted states by the load-controlled cyclic triaxial technique. The test is conducted under undrained conditions to simulate essentially undrained field conditions during earthquake or another cyclic loading. This is a destructive test. Failure may be defined on the basis of the number of stress cycles required to reach a limiting strain or 100 % pore pressure ratio”.

Cyclic Direct Simple Shear Test: This test is capable of reproducing earthquake stress condition. The soil specimen is restrained against lateral expansion and after that, it is subjected to K_0 -consolidation stress in steps. By applying cyclic horizontal shear stresses to the top or bottom of the specimen, the soil is deformed in much the same way as an element of soil subjected to vertically propagating S-waves.

Torsional Shear Test: In this test the sample, which is a hollow cylinder of soil, is placed in a cell and consolidated to the desired isotropic or anisotropic stress state. A torque is applied for continuous shearing of the sample (Knutson, 2014, after Pradhan et al., 1988). The simple shear situation requires parallel movement of all parallel planes in the direction of shear, without any change in original shapes. All horizontal normal strains are kept zero during the test.

2.3.4 Field tests to determine dynamic soil properties

Vane Shear Test – VST: according to the standard ASTM D2573 (2018), this test is designed for determination of undrained shear strength in saturated clay and silt soils. “It is not applicable for sandy soils that may allow drainage during the test. This test method addresses testing on land and for testing in drill holes or by self-drilling or continuous push methods from the ground surface. It is often used in conjunction with fluid rotary drilling (ASTM D5783, 2018) or hollow-stem augers (ASTM D6151, 2015)”.

Standard Penetration Test – SPT (following ASTM D1586, 2011): This method drives a split-barrel sampler to obtain a representative disturbed soil sample for identification purposes, and measure the resistance of the soil to penetration of the sampler. The way to get dynamic properties from the results of SPT test is by using correlations previously generated for similar material, where the shear wave velocity (v_s) is plotted versus the SPT corrected “N” value (N_{60}).

Cone Penetration Test – CPT (following ASTM D3441, 2016): Also called Dutch Cone Test or Cone Penetration Test (CPT), it can be done in soils and soft rocks. The principal goal of the test is to measure end bearing (q_c) and side friction (f_s) during the steady slow penetration of a pointed rod into the soil. The interpretation of CPT test results requires some knowledge of materials penetrated, thus, because this test does not permit to obtain soil samples, it is necessary to carry out some parallel borings to get samples and characterization of materials in the laboratory.

Campanella and Stewart (1992) discussed some practical issues related to equipment and procedure to consider when performing CPT tests in field. The main point of their discussion is the fact that the results of the test could be misinterpreted depending on the setup used in the field and the method of analysis used in the office.

Similar to the SPT test, in the CPT test the relative and absolute magnitudes of penetration resistances can be correlated to other soil properties. Thus, the CPT test results have been also used to define correlations with other geotechnical parameters. Some examples of those correlations are reported by Robertson et al. (1983) and Kulhawy et al. (1990), among others.

Seismic Cone Penetration Test – SCPT: Kramer (1996) mentioned the SCPT test is very similar to the down-hole test (ASTM D7400, 2017), except that no previous borehole is required. In the SCPT test, the shear wave velocity of the soil being investigated is measured. Together with the knowledge of the soil saturated unit weight, the shear wave velocity allows an assessment of the small strain shear modulus (G_{max}) and the constrained modulus (M). As it has been mentioned before, the small strain shear modulus is an essential input for different dynamic analyses.

Dilatometer – DMT: according to the standard ASTM D6635 (2015), “the test is initiated by forcing the steel, flat plate, dilatometer blade, with its sharp cutting edge, into a soil. Each test consists of an increment of penetration, generally vertical, followed by the expansion of a flat, circular, metallic membrane into the surrounding soil”. The pressure at which the membrane moves by 0.05 mm (P_0) and the pressure at which its center moves 1.10 mm (P_1), are recorded, corrected and used with the hydrostatic pressure, U_0 , and the overburden pressure, σ_{v_0}' , to compute various indices to which soil properties can be correlated.

Pressuremeter – PMT (following ASTM D4719, 2020): Kramer (1996) considers this as the only in-situ test capable of measuring stress-strain, as well as strength behaviour. A pressuremeter test is performed on the wall of a borehole using a cylindrical probe that is expanded radially. Deformation of the soil can be measured by the volume of fluid injected into the flexible membrane or by feeler arms for pressuremeters that use compressed gas. Then, by using the cavity expansion theory, the stress-strain behaviour of the soil could be defined.

2.4 Near-surface geophysical techniques

The testing methods used for the characterization of geomaterials are either field tests or laboratory tests. In both cases, the dynamic properties obtained from the analysis of the data collected during the test, which could be displacements, velocities, or even acceleration of waves propagating through the soil.

The working principle of most common geophysical methods for soil profiling is to allow the acquisition of wave-field data generated by a specific energy source. Then, that data can be processed in order to quantify the dynamic properties of geomaterials. What is important to point out about the geophysical methods, is that all of them try to derive the profile of the soil by solving an inverse problem.

In the application of seismic geophysical methods, the central idea is to use the propagation of mechanical waves to evaluate some specific characteristics of the subsurface materials. This evaluation is possible by analyzing the dynamic response of the media under the wave-field generated by the excitation source. Seismic wave-propagation based methods are not just useful to determine the dynamic properties of geomaterials, but they also allow the estimation of some geometrical characteristics and the relative differentiation of materials depending on the dynamic response. In addition, near-surface geophysical methods are also useful in subsurface exploration to minimize the number of boreholes needed in geotechnical engineering studies.

Seismic techniques (reflection and refraction) and surface waves techniques use the acoustic wave propagation properties, ground radar uses electromagnetic wave propagation properties, whereas electrical resistivity uses both the electrical and electromagnetic wave propagation properties. In this section, these methods are briefly introduced.

2.4.1 Seismic techniques based on reflection and refraction

Seismic Reflection Test: Kramer (1996) mentions this test allows the wave propagation velocity and thickness of surficial layers to be determined from the ground surface or in offshore environments.

According to the standard ASTM D7128 (2018), “common applications of the method include mapping the top of bedrock, delineating bed or layer geometries, identifying changes in subsurface material properties, detecting voids or fracture zones, mapping faults, defining the top of the water table, mapping confining layers, and the estimation of elastic-wave velocity in subsurface materials. The test is performed by

producing an impulse at the source, (S), and measuring the arrival time at the receiver, (R)”.

Seismic Refraction Test (following ASTM D5777, 2018): This technique provides for the determination of elastic wave velocities and the thickness of each layer in a layered soil profile. Haeni (1988) mentioned three conditions for a medium to be ideally suited for the application of the seismic refraction technique; first, “each successively deeper layer has a higher seismic velocity”; second, “no thin layers are present”; and third, “a significant seismic-velocity change occurs at each interface”. The test aims to accurately measure the arrival-times of the seismic body waves produced by a near-surface seismic source. (Luna and Jadi, 2000)

The excitation force introduces energy into the ground at the source point; that energy creates a mechanical wave propagating away from the application point. The vibration corresponding to the wavefield at the free surface is then recorded in a linear array of transducers. As P-wave velocity is higher, their arrivals are detected before the ones for the S-waves. That is why the detection of P-waves used in seismic refraction tests is recognized to be highly effective in resolving thicknesses in a layered medium.

The measurement of the shear wave velocities, by using a rich source of shearing energy that is able to propagate over long distances, is an advantage for geotechnical earthquake engineering problems. Woods (1978) found that the P-wave velocity in soil depends on its degree of saturation, while the S-wave velocities are inexistent because of the inability of water to carry any shear stress. In the end, for this tests as for all the seismic tests, the calculated wave velocity is directly related to the elastic properties of the material. Thus, the characterization of the particulate materials inside the medium is very important to properly understand the results coming from a seismic refraction test.

When a seismic ray path is considered in a horizontally layered medium (see Fig. 2-6), the critical incident angle is given by:

$$i_c = \sin^{-1} \left(\frac{c_1}{c_2} \right) \quad (2-21)$$

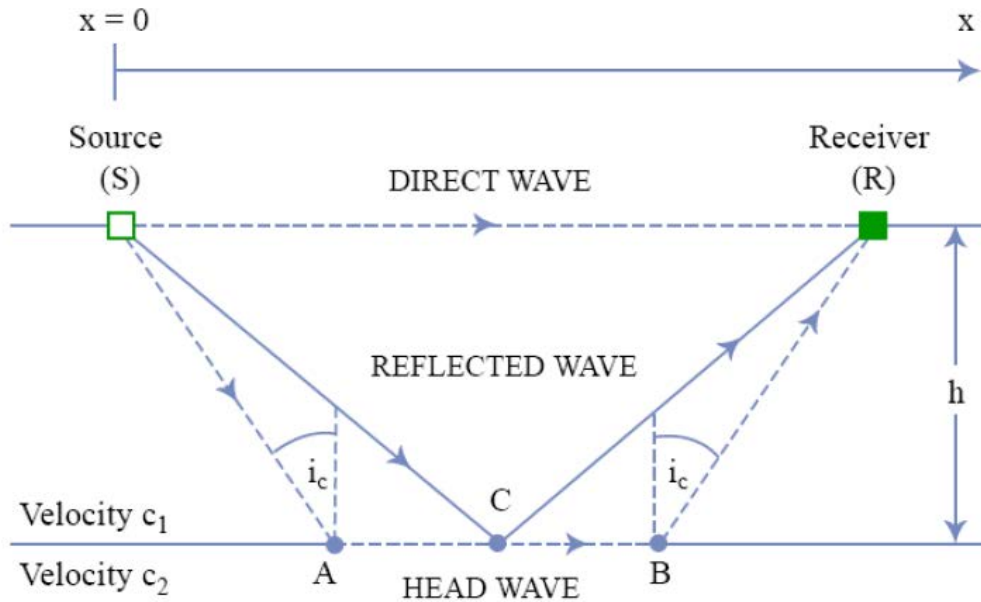


Fig. 2-6: Reflected and refracted waves (Van Der Hilst and Burdick, Scott, 2010)

The proper way to identify the arrival times of each kind of seismic wave is the “Travel-Time curve”. In that plot, direct arrivals and critically refracted arrivals (head waves) are represented as straight lines, while reflected arrivals are represented as hyperbolic curves. Equations of those arrivals are presented below:

$$t_{direct} = \frac{x}{c_1} \quad (2-22)$$

$$t_{head} = \frac{x}{c_2} + \frac{2h}{c_1} \sqrt{1 - \left(\frac{c_1}{c_2}\right)^2} \quad (2-23)$$

$$t_{reflected} = \frac{SC}{c_1} + \frac{CR}{c_1} = \sqrt{\left(\frac{1}{2}x\right)^2 + h^2} \left(\frac{2}{c_1}\right) \quad (2-24)$$

Two important points to identify in the Travel – Time curve are presented below.

critical distance $x_c = 2h \tan i_c$ (2-25)

crossover distance $x_d = 2h \sqrt{\frac{c_2+c_1}{c_2-c_1}}$ (2-26)

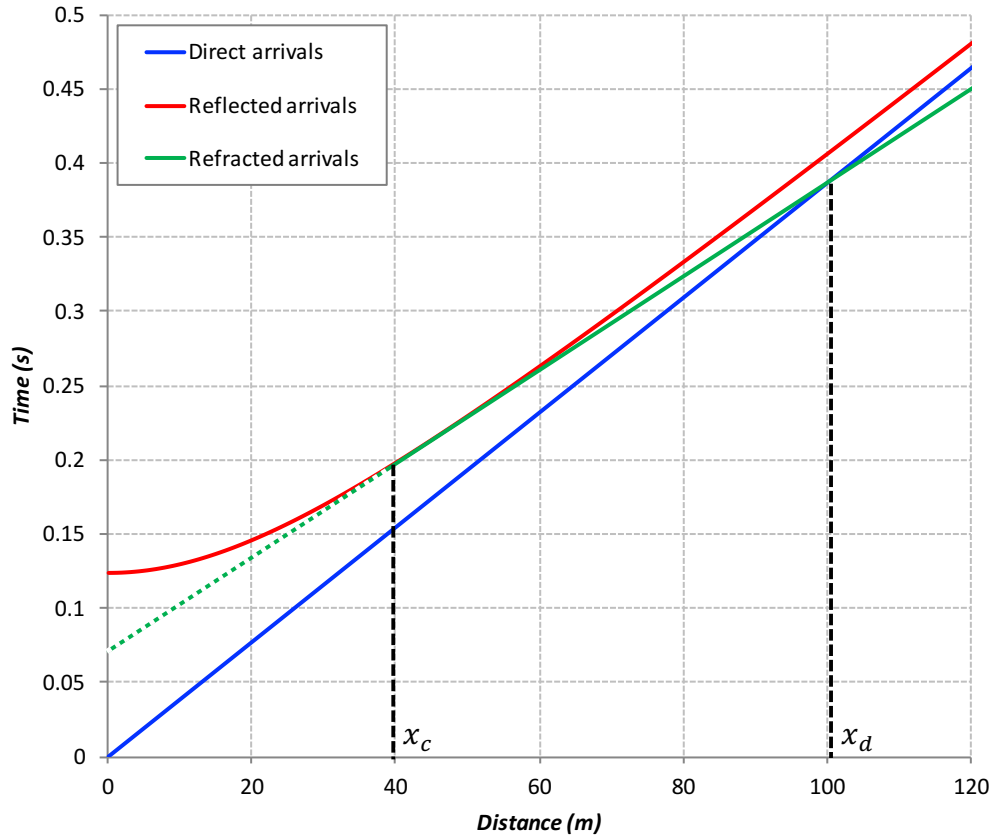


Fig. 2-7: Theoretical travel time curves for a 2-layers model with horizontal interface

2.4.2 Seismic techniques based on geophysical well-logging

Seismic Cross-Hole: this technique is identified by Luna and Jadi (2000) as one of the best methods used for determining the variation of shear wave velocity with depth. They describe the test procedure as it follows: “In this test, a source of seismic energy (mainly S-waves) is generated in or at the bottom of one borehole and the time for that energy to travel to another borehole through the soil layer is measured. From the borehole spacing and travel time, the velocity of the seismic wave is computed”. For this test, two boreholes

are needed, one for the placing of the input source and one more for the recording of the body waves in the wavefield response. The result obtained for the shear wave velocity is then used to calculate the shear modulus using this equation:

$$G = \rho(v_s)^2 \quad (2-27)$$

Seismic Down-Hole (Up-Hole): This technique is very similar to the Cross-hole test, with the difference that in this case the test requires only one drill hole. Luna and Jadi (2000) mentioned that “In the seismic down-hole test, low velocity layers can be detected even if they are between high velocity layers if geophone spacing is sufficiently close. Sources of S-wave used in seismic refraction can be used for the seismic up- and down-hole testing. Depending on the depth of the soil layers investigated, the source of seismic waves will vary from hand generated sources to the use of large mechanical equipment”.

The test results can be very challenging, especially in the picking of the arrivals of the shear waves, which could be sometimes obscured by the compressional waves. The solution to this problem is to reverse the polarity of the wavefield by changing the orientation of the application for the excitation source.

Luna and Jadi (2000) stated that “Reversing the direction of the energy blow, allows for the shear wave pattern to be recorded in the reverse direction while the compression wave pattern is essentially unchanged. In this manner, the shear wave patterns are distinguished from compression wave patterns. However, in the up-hole test, it is more difficult to generate selected shear waves. P-waves tend to be predominant within the source generated”.

2.4.3 Seismic techniques based on surface waves dispersion analysis

Steady State Vibration: This particular technique does not require boreholes because it focuses in the analysis of surface waves to obtain the shear wave velocity and the shear modulus (G) of the soil profile. In this test, a controlled vibrator is used as the excitation source to generate surface waves, mostly Rayleigh waves, which travel at a velocity very close to the one for the shear waves. “The shear wave velocity is computed from the

Rayleigh wave-length measured with receivers placed along the ground surface, and the frequency of vibration at the source”. (Luna and Jadi, 2000)

Luna and Jadi (2000) also stated that “the effective depth of the R-wave has been empirically related to the soil layer at a depth equal to one-half the wave-length, λ_R ”. In this test, it is possible to change the wavelength (λ_R) by changing the frequency of the input energy source, so that the variation of v_s with depth could be analyzed. However, it must be considered that in order to get a deeper penetration a low frequency is needed, so the equipment or device generating the input energy has to be powerful and reliable about the frequency being generated.

Spectral Analysis of Surface Waves (SASW): Luna and Jadi (2000) described that “this method uses a series of successively longer source-receiver arrays to measure the propagation of Rayleigh waves over a wide range in wavelengths. A vertical impact is applied at the ground surface generating transient Rayleigh R-waves. Two or more receivers placed at the surface, at known distances apart monitor the passage of these waves”.

In this case the calculations of phase velocity v_R and wavelength λ_R , which at the end leads to the wave number, are performed for each frequency in the test and the results are then presented in the form of a dispersion curve. Luna and Jadi (2000) also described the dispersion curve as the “signature of a site”. The dispersion curve is then the input of a mathematical inversion process, in which the shear wave velocity profile of the site is determined.

Zerwer et al. (2002) reported the measurement of spectral analysis of surface waves to develop subsurface soil profiles looking for the delineation of abandoned crown pillar structures. This research used an extensive analysis of numerical simulations to investigate two issues: first, the mesh dispersion effects and the appearing of “parasitic modes of vibration”; and second, the definition of the bandwidth for which the mass and stiffness damping parameters are valid in a numerical simulation of surface waves propagation.

Multi-Channel Analysis of Surface Waves (MASW): This technique is an advanced SASW test in which many locations are recorded at the same time. Basically, the test could use the same kind of excitation source in order to generate surface waves of low frequency. The effective depth of investigation in this test is related to the wavelength generated by the excitation source, and typically goes from a few meters to a few tens of meters. Because of this, the result is dependent of the wavelength generated, and directly dependant of the frequency.

In early 90's the first attempts to numerically simulate the propagation of surface waves were reported by Hirai (1992) and Rodríguez-Ordoñez (1994). After that, the interest in surface wave methods was increasing because of the easiness to generate surface waves and the cost-effectiveness when characterizing geomaterials without the need for sampling them. (Foti, 2002)

Park et al. (1999) presented an effective method to generate the dispersion curve obtained from the signals of a multichannel shot gather. They took advantage of the frequency-dependent properties of surface waves to characterize the shallow subsurface. They empathized that “Most surface-wave analysis relies on the accurate calculation of phase velocities for the horizontally traveling fundamental-mode Rayleigh wave acquired by stepping out a pair of receivers at intervals based on calculated ground roll wavelengths”.

Park et al. (2007), highlighted that “The sampling depth of a particular frequency component of surface waves is in direct proportion to its wavelength, and this property makes the surface wave velocity frequency dependent, i.e., dispersive. The multichannel analysis of surface waves (MASW) method tries to utilize this dispersion property of surface waves for the purpose of (v_s) profiling in 1D or 2D (depth and surface location) format”.

Ivanov et al. (2009) used MASW test results to evaluate the impact of “the assumed compressional-velocity and density parameters on the inverted shear-wave velocity results”. They concluded that optimal density parameter selection may result in a considerable improvement of the reliability and quality of the inverted v_s profile.

An important limitation of surface wave methods is that they are based on the hypothesis that the response of soil is due to a multi-degree of freedom system (MDOF), in which each degree of freedom represents a layer in the soil profile. If multiple surface modes contribute to the response, which is actually very common, the dispersion curve could be contaminated by higher modes and the interpretation of the results may not be realistic.

2.4.4 Emerging techniques applied to the near-surface

The techniques listed below are named as emerging techniques, meaning that their application in near-surface geophysics is gaining attention. Some of those techniques are very old, but they had not been used before in near-surface applications. Because these techniques are not considered as an option to solve the problem stated in this research, they are listed just to recognize their existence and to keep in mind their possible applicability in near subsurface investigations.

Table 2-1. Near-surface geophysical emerging techniques

Seismic Techniques	Refraction Microtremor (ReMi)	
	Horizontal to Vertical Spectral Ratio (HVSr)	
	Seismoelectric Coupling	
	Analysis of Love Waves	
	Analysis of Scholte Waves	
	Passive Seismic Interferometry	
Electrical Resistivity Methods	Induce Polarization (IP)	
	Self Potential (SP)	
Electromagnetic Induction Methods	Airborne Electromagnetic (EM)	
	Terrain Conductivity Method	
	Time-Domain Electromagnetic (TDEM) / Transient Electromagnetic (TEM)	
	Finite-Source Excitation of Layered Earth	
	Plane Wave Excitation Methods	Very Low Frequency (VLF)
		Radiomagnetotelluric (RMT)
Controlled-Source Magnetotelluric (CSMT)		
Magnetic–Gravimetric Techniques	Magnetic gradiometry	
	Total field anomaly	
	Time-Lapse Microgravity	

2.5 Data analysis: signal processing

The original signal depends on time, and it is addressed as the time-domain representation of the function. Its transform depends on frequency and is the frequency-domain representation of the function. In theory, the transform is perfectly invertible, and no information is lost in transforming.

2.5.1 The Fourier transform

The Fourier transform derives from the Fourier series, which is the decomposition of an arbitrary periodic signal into a sum of harmonics. It can be shown that an infinite, periodic signal of period T can be decomposed into the sum of an infinite number of harmonic (sine or cosine) functions with frequency $f_n = n/T$, with an amplitude A_n and a phase φ_n . Foti et al. (2014)

The Fourier transform can be written as:

$$G(f) = \int_{-\infty}^{\infty} g(t)e^{-j2\pi ft} dt \quad (2-28)$$

The inverse Fourier transform can be written as:

$$g(t) = \int_{-\infty}^{\infty} G(f)e^{j2\pi ft} df \quad (2-29)$$

Fourier spectral analysis provides a general method for extracting information from the frequency response of a system. It has dominated the data analysis efforts since soon after its introduction, and has been applied to all kinds of data. Xie et al. (2008) highlighted that Fourier transform has some limitations and it is applicable under extremely general conditions, and also points out that “there are some crucial restrictions of the Fourier spectral analysis: the system must be linear; and the data must be strictly periodic or stationary”. If those conditions are not observed when using the Fourier Transform, the resulting spectrum will have no sense, even though its calculation is perfectly possible.

2.5.2 The wavelet transform (on-stationary data processing)

According to Kumar and Foufoula-Georgiou (1997) the wavelet transform could be used in two ways when studying geophysical nonstationary processes: “(1) as an integration kernel for analysis to extract information about the process and (2) as a basis for representation or characterization of the process”. In this context, the wavelet transform can be useful for studying multiscale features, detecting singularities, analyzing transient phenomena, and also for signal compression.

Huang et al. (1998) and Li et al. (2001) describe the wavelet approach as an adjustable window Fourier spectral analysis with the following general definition:

$$W(a, b; X, \psi) = |a|^{-1/2} \int_{-\infty}^{\infty} X(t) \psi^* \left(\frac{t-b}{a} \right) dt \quad (2-30)$$

where $\psi^*(\cdot)$ is the basic wavelet function satisfying some very general conditions, (a) is a dilation factor and (b) is the translation of the origin.

2.5.3 The synchrosqueezed wavelet transform

Daubechies et al. (2011), described synchrosqueezing as a reallocation method, which is used to “sharpen” a time-frequency representation $\mathcal{R}(t, \omega)$ by “allocating” its value to a different point (t', ω') in the time–frequency plane, determined by the local behavior of $\mathcal{R}(t, \omega)$ around (t, ω) . In the case of synchrosqueezing, it starts from the continuous wavelet transform $W_x(a, b)$, where a is the scale, and b is the time offset, so for each of those points the instantaneous frequency is given by:

$$\omega_x(a, b) = -i(W_x(a, b))^{-1} \frac{\partial}{\partial b} W_x(a, b) \quad (2-31)$$

Then the synchrosqueezing transform $SWT_x(\omega_l, b)$ is given by

$$SWT_x(\omega_l, b) = (\Delta\omega)^{-1} \sum_{a_k} W_x(a_k, b) a_k^{-3/2} (\Delta a)_k \quad (2-32)$$

where $a_k = |\omega(a_k, b) - \omega_l| \leq \Delta\omega/2$, $(\Delta a)_k = a_k - a_{k-1}$, frequencies ω_l are centres of the bins $[\omega_l - \frac{1}{2}\Delta\omega, \omega_l + \frac{1}{2}\Delta\omega]$ and $\Delta\omega = \omega_l - \omega_{l-1}$.

2.6 Numerical simulation of waves propagation

The wave equation is a linear second-order partial differential equation (PDE) with two independent variables on a domain Ω in the form:

$$\frac{\partial^2}{\partial t^2} u(x_i, t_n) - c^2 \frac{\partial^2}{\partial x^2} u(x_i, t_n) = 0 \quad (2-33)$$

where u is the displacement in x coordinate direction, and c is the wave velocity.

2.6.1 Initial and boundary conditions

Typical initial conditions are:

- *First Initial Condition:* Function evaluating displacements $u(x)$ at the initial time (t_0) for different nodes. The displacement for every node at the initial time is assumed as zero.
- *Second Initial Condition:* Function evaluating velocity (du/dt) at initial time (t_0) for different nodes. The velocity for every node at the initial time is assumed as zero.

Typical boundary conditions are:

- *First Boundary Condition (Essential):* Function evaluating displacements $u(t)$ at the fixed boundaries, for example the bottom boundary of the model (y_0) for different times.
- *Second Boundary Condition (Natural):* The external force times (EA) at certain nodes (n) is a given value.

$$EA \frac{\partial u}{\partial x} = Q \quad (2-34)$$

2.6.2 The finite differences method

In the finite difference method, each derivative in the previous equations is replaced by an algebraic expression relating variables at specific locations in the grid.

$$\frac{\partial^2}{\partial t^2} u(x_i, t_n) \approx \frac{u_i^{n+1} - 2u_i^n + u_i^{n-1}}{\Delta t^2} \quad (2-35)$$

$$\frac{\partial^2}{\partial x^2} u(x_i, t_n) \approx \frac{u_{i+1}^n - 2u_i^n + u_{i-1}^n}{\Delta x^2} \quad (2-36)$$

Thus, if the second order derivatives in the partial differential equation are replaced by their central differences approximations, then the algebraic form of the PDE would be:

$$\left[\frac{u_i^{n+1} - 2u_i^n + u_i^{n-1}}{\Delta t^2} \right] = c^2 \left[\frac{u_{i+1}^n - 2u_i^n + u_{i-1}^n}{\Delta x^2} \right] \quad (2-37)$$

2.6.2.1 Software FLACTM

FLACTM is a software package that uses an explicit finite differences numerical scheme to perform a Lagrangian analysis (Itasca, 2000). The general governing equations used in that software are the equilibrium of forces and constitutive laws. As the strains are calculated from displacements the compatibility condition is implicitly satisfied through every calculation cycle. The algebraic expressions are fully explicit, meaning all quantities on the right hand side of the expressions are known. The basis of the calculation cycle is presented in Fig. 2-8.

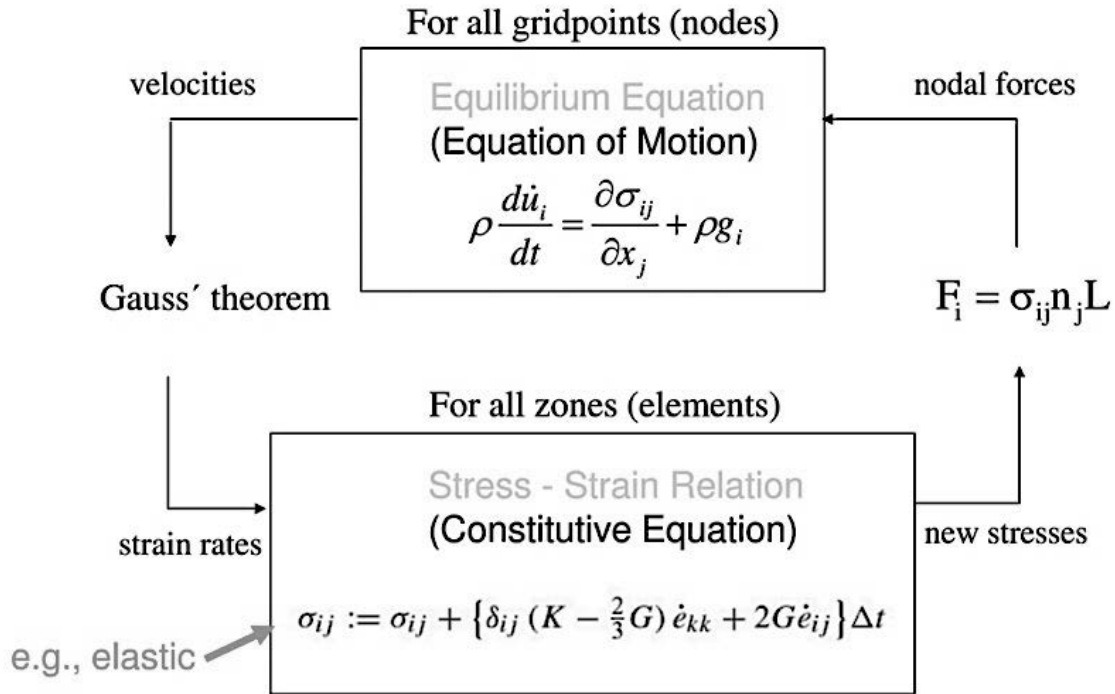


Fig. 2-8: Calculation cycle in FLACTM. (Hart and Han, 2006)

2.6.2.2 Stability criterion

Grigoryan (2012), mentioned that the value of (s) has a crucial effect on the stability of the numerical scheme. He found that when ($s > 1$) the scheme leads to unexpected large values, and hence is unstable. The stability condition is then defined by:

$$s = c_i^2 \frac{(\Delta t)^2}{(\Delta x)^2} \leq 1 \quad (2-38)$$

If the speed of the numerical scheme is defined as $(\Delta x / \Delta t)$, then the stability condition implies that the speed of the scheme must be at least as large as the speed of the exact equation (wave velocity c_i). A different way of understanding stability is by comparing the domains of dependence of the exact equation and the numerical scheme.

This analysis can be done for all the kinds of waves considered in the problem (i.e. compressional, shear, Rayleigh, etc.), thus, the value of c_i will correspond to the wave velocity considered (i.e. v_p , v_s , v_R , etc.).

2.6.2.3 Spatial discretization

Kuhlemeyer and Lysmer (1973) showed that the ratio between the wavelength (λ) and the mesh size determines the accuracy for wave propagation problems. They found that “the value of λ relates to the element length in the direction of propagation (Δx) by a factor of one-tenth to one-eighth”. The technical notes for the software FLACTM recommends a one-tenth factor (Itasca, 2000).

$$\Delta x \leq \frac{\lambda}{10} \quad (2-39)$$

Zerwer et al. (2002) studied the effect of mesh size in numerical models used to simulate wave propagation in an elastic medium. The mesh size can be associated to the removal of short-wavelength (high-frequency) energy. This effect is known as Gibb’s phenomenon, and it can be assimilated to a low-pass filter which can produce spurious oscillations, as well as velocity dispersion. To minimize the effects of mesh filtering, the maximum mesh size is calibrated to the wavelength of the slowest propagating wave. In the temporal domain, improper discretization can cause instability and frequency aliasing for propagating waveforms. (Valliappan and Murti, 1984)

2.6.2.4 Time discretization

The built-in scheme in FLACTM is not unconditionally stable. A time step must be small enough so that the speed of the calculation front is greater than the speed of the fastest existent wave. Thus, a critical time step is defined as:

$$\Delta t_{crit} = \min \left(\frac{A}{c_i \Delta x_{max}} \right) \quad (2-40)$$

where Δx_{max} is the maximum zone dimension defined in the discretization, which corresponds to a diagonal distance, and (A) is the area of the corresponding triangle. The

$\min()$ function is taken over all zones (Itasca, 2000). For a right angle triangle with two equal sides ($\Delta s = \Delta x$) the area would be equal to $\frac{1}{2}\Delta x^2$ and the maximum dimension would be equal to $\Delta x\sqrt{2}$. Hence the following stability condition is obtained for a factor of safety FS = 2.0:

$$\frac{\Delta t}{\Delta x} \leq \frac{1}{4c_i\sqrt{2}} \quad (2-41)$$

This equation requires smaller time increments than the ones introduced in previous sections. However, numerical dispersion should still be considered. Also, this equation is set for a homogeneous medium with no damping, hence it should be used cautiously. The software FLACTM warns the user when the time step could lead to numerical instability and suggests a minimum time step to avoid it, so that warning must be always considered in the time step definition.

2.6.3 Probabilistic approach of spatial variability: random fields

One of the most interesting ideas, when soil behaviour parameters' modeling is required, is to consider randomness in its properties in order to approach design using the stochastic modeling theory. Nowadays, some progress has been reached in static analysis of soil behaviour by considering randomness; however, the progress in soil dynamic analysis considering randomness is still limited.

Manolis (2002) presented a literature review in soil dynamics considering stochastic modeling, which is a comprehensive paper in this topic. The author identified three different approaches considering randomness in soil dynamics modeling, i.e. random loading, random material properties, and random boundaries. In addition, two different analysis techniques are widely used in soils' stochastic modeling, they are the Monte-Carlo simulations, and the numerical methods (i.e. finite elements, finite differences, etc.).

2.6.3.1 Effects of spatial variability of soil properties

Seismic waves are filtered as they pass through soil layers, from bedrock to surface, the change in frequencies and amplitudes happens, and these modifications result in different ground motion characteristics on the surface. That is why it is important to consider the site effect in the evaluation of earthquake ground motion for the design of structures.

Depending on the scale of analysis the characterization of material involves different uncertainties. At large scale the spatial variation of soil properties plays an important role in an heterogeneous layered soil. At small scale, when a sample is taken to the laboratory, most of the times it could be considered homogeneous, however, another set of uncertainties arise, such as measurement error, irregular coupling between material and transducers, etc.

In this research, for the sCPTU and for the MASW tests, which characterize materials at large scales, the inherent variability of shear modulus is described and modeled using both, deterministic parameters (i.e. constant values) and stochastic parameters (i.e. randomly distributed).

2.6.3.2 Stochastic modelling

Stochastic heterogeneity has significant effects on dynamic properties of soils. The major contribution in this topic is to investigate the effect of uncertainty and spatial variability in soil stiffness on the wave propagation phenomena. In order to investigate this, random fields were included in the numerical simulations. A random field is an stochastic process indexed in space (2D), but not necessarily in time; thus, some common concepts to characterize stochastic processes indexed in space must be reviewed:

- Variability at a point: at any specific point in space the variable considered (in this case the shear modulus), has a random value, which is governed by a probability density function (pdf). Thus, any single point in space will have a different pdf, or in other words, the pdf evolves with the spatial position.

- Spatial dependence: in order to be closer to reality, the simulated soil properties must keep some dependence with respect to properties at some points in space.

Fenton and Griffiths (2008) identified the following assumptions which are commonly made in order to simplify the characterization problem when generating a random field:

- The process is Gaussian: this assumption is made only for simplicity because in this way any multivariate normal distribution can be specified by just the mean vector and the covariance matrix.
- The process is stationary: meaning its mean, variance, and autocorrelation structure do not change with position. As we are going to consider a random field, which is a process indexed in space rather than in time, the theory of spatial stationarity in space must be considered when the random fields are to be generated.
- Isotropy: it implies that in two dimensional random fields the joint pdf is invariant under rotation, meaning that the correlation between two points only depends on the distance between the two points, not on their orientation relative to one another. Fenton and Griffiths (2008) properly highlighted the fact that isotropy implies stationarity, although stationarity does not imply isotropy.

Another condition to include in the assumptions is that the process must be ergodic, which means that any realization of the process is a representation of the average statistical properties. In other words, the mean and variance of one realization are the same that mean and variance for the complete process.

Under the assumption that the random field of shear modulus is Gaussian and stationary, the following three parameters must be known in order to generate it:

- 1) The field mean of the shear strength modulus
- 2) The field variance of the shear strength modulus
- 3) How rapidly the shear strength modulus varies in space

Fenton and Griffiths (2008) stated that the last parameter is actually characterized by the second moment of the field's joint distribution, which is captured equivalently by the covariance function, the spectral density function, or the variance function.

2.6.3.3 Non-conditioned random fields

Kim (2005) reported the use of different techniques for the generation of random fields to simulate soil properties, specifically shear stiffness when simulating wave propagation in spatially variable geomaterials. Among the methods studied by Kim (2005), he recommended the use of the covariance matrix decomposition technique because it can model the statistically homogeneous correlated random field with very clear relationship with the preselected correlation length.

In chapter 5 of this research, that technique was used to generate the random fields to spatially distribute the shear modulus and the bulk modulus, which are the parameters controlling the body wave velocities inside an elastic medium. Once the random field was generated, the values were properly indexed and mapped to allow the finite differences software (i.e. FLACTM) the reading and inclusion into the dynamic calculations for the simulation of wave propagation. The algorithm for the covariance matrix-decomposition technique is presented Table 2-2.

Nonetheless, an important consideration to make here is that the technique recommended by Kim (2005) and replicated in Table 2-2 generates non-conditioned random fields, meaning the values are freely generated inside the medium under analysis, which is not useful when the property spatially distributed has been measured at some specific points in the field.

Table 2-2. Matrix decomposition technique to generate random fields (Kim, 2005)

Name	Matrix Decomposition Technique
Reference	El-Kadi A.I. and Williams, S.A., (2000)
Description	The method generates a multidimensional array that satisfies the exponentially decaying covariance function with distance between points.
Procedure	<p>1) Assign an index to each location of the target geometry.</p> <p>2) Generate matrix \underline{d} where d_{ij} is the distance between point i and point j.</p> <p>3) Compute the covariance matrix \underline{A} from matrix \underline{d}</p> $A_{ij} = \sigma^2 e^{-\frac{1}{L} d_{ij} }$ <p>σ = target standard deviation d_{ij} = distance between point i and point j L = correlation length</p> <p>4) Decompose matrix \underline{A} into matrix \underline{C} so that</p> $\underline{A} = \underline{C}\underline{C}^T$ $C_{mm}C_{im} = A_{im} - \sum_{k=1}^{m-1} C_{ik}C_{mk} \text{ (Choleski decomposition; Nash, 1979)}$ <p>5) Generate the uncorrelated Gaussian random field $\underline{\varepsilon}$</p> <p>6) Calculate the correlated Gaussian random field \underline{G}</p> $\underline{G} = \underline{C} \cdot \underline{\varepsilon} + \underline{T}$ <p>T_i = trend value in the random field at point i $\underline{\varepsilon}$ = vector of random numbers with Gaussian distribution, $N[0, 1]$</p>

2.6.3.4 Conditioned random fields

At some point in this research, the need for the generation of conditioned random fields arose. In chapter 7, when the results from the sCPTU test are used to characterize the medium in which the wave propagation is studied, there were some values of shear modulus obtained from the shear wave velocity values measured at specific depth locations. Thus, in order to properly use the random field theory to spatially distribute the shear modulus, it has to be by considering a conditional simulation in which the random field generation technique actually respects the values measured.

The mathematical apparatus needed to generate conditional random fields is presented by Fenton and Griffiths (2008) and summarized next.

The conditional random field is formed from:

$$Z_c(x) = Z_u(x) + [Z_k(x) - Z_s(x)] \quad (2-42)$$

where $Z_c(x)$ is the desired conditional simulation for the property Z at (x) location, $Z_u(x)$ is the unconditional simulation, $Z_k(x)$ is the best linear unbiased estimate (BLUE) of the random field based on known (measured) values at locations (x_η) , $Z_s(x)$ is the best linear unbiased estimate (BLUE) of the random field simulation, and $Z_c(x)$ is the BLUE of the random field based on unconditional simulation values at locations (x_α) . As stated by Fenton and Griffiths (2008), the best estimate at the measurement points (x_α) is equal to the measured value at those points:

$$Z_k(x_\alpha) = z(x_\alpha) \quad (2-43)$$

$$Z_s(x_\alpha) = Z_u(x_\alpha) \quad (2-44)$$

and finally, this leads to the desired condition:

$$Z_c(x_\alpha) = Z_u(x_\alpha) + [Z_k(x_\alpha) - Z_s(x_\alpha)] \quad (2-45)$$

$$Z_c(x_\alpha) = Z_u(x_\alpha) + [z(x_\alpha) - Z_u(x_\alpha)] = z(x_\alpha) \quad (2-46)$$

$$Z_c(x_\alpha) = z(x_\alpha) \quad (2-47)$$

Now, the conditional simulation of the random field followed these steps suggested by Fenton and Griffiths (2008):

- (a) Partition the field into the known (x_α) and unknown (x_η) points.
- (b) Form the covariance matrix $[C]$ between the known points

$$C_{ij} = Cov[Z_u(x_i), Z_u(x_j)] \quad (2-48)$$

then the matrix $[C]$ is inverted to get $[C]^{-1}$, this will more likely be an LU decomposition rather than a full inversion.

- (c) Simulate the unconditional random field $Z_u(x)$ at all points in the field using the matrix decomposition technique.
- (d) For each unknown point ($\eta = 1, 2, \dots, N - n_k$)

- a. Form the vector (b) of covariances between the target points (x_η) and each of the known points.

$$b_\alpha = Cov[Z_u(x_\eta), Z_u(x_\alpha)] \quad (2-49)$$

for ($\alpha = 1, 2, \dots, n_k$).

- b. Calculate the weighting coefficients

$$\beta = [C]^{-1}\{b\} \quad (2-50)$$

- c. Determine the BLUE field based on the measured values

$$Z_k(x_\eta) = \mu_n + \sum_{\alpha=1}^{n_k} \beta_\alpha [z(x_\alpha) - \mu_\alpha] \quad (2-51)$$

- d. Determine the BLUE field of the simulation

$$Z_s(x_\eta) = \mu_n + \sum_{\alpha=1}^{n_k} \beta_\alpha [Z_u(x_\alpha) - \mu_\alpha] \quad (2-52)$$

- e. Compute the difference

$$Z_k(x_\eta) - Z_s(x_\eta) = \sum_{\alpha=1}^{n_k} \beta_\alpha [z(x_\alpha) - Z_u(x_\alpha)] \quad (2-53)$$

f. Form the conditioned random field

$$Z_c(x_\eta) = Z_u(x_\eta) + [Z_k(x_\eta) - Z_s(x_\eta)] \quad (2-54)$$

This procedure could be easily programmed to generate the conditioned random field, which ensures the values obtained from sCPTU field test will be effectively respected in the simulation.

3 Research background – literature review

Every infrastructure project on Earth is founded on geomaterials originated by geological processes taking long periods of time, sometimes even the 4.5 billion years long history of the Earth (Deng et al., 2019). Geotechnical engineers are always looking for good-performance geomaterials to build infrastructure in a safe way. Thus, the ground materials on the construction site must be studied in order to make sure they are suitable to carry on the load to be applied.

A necessary input for the design process is the description of the disposition of the geomaterials in the field along with their properties characterization, which is done by simplifying the reality using a geological geotechnical model (G-G model). The initial approach when creating a GG-model for designing purposes is to assume the geomaterials (rock or soil masses) are continuous, homogeneous, isotropic, linear and elastic materials (CHILE-materials) (Seedsman et al., 2009).

The spatial variability of geomaterials' properties is another issue to be considered in their characterization. In many cases, geomaterials may not be strictly considered as homogeneous, but they could be considered to be distributed in a layered medium. This simplification is widely adopted when using the GG-models in geotechnical engineering. Although, it is very clear that the reality of how geomaterials' are naturally created or deposited in the field leads to a more complex scenario, which is far from the aforementioned suppositions of the ideal CHILE-materials. From a practical point of view, the layered medium simplification can be accepted as long as the material inside each one of the layers can be characterized as a CHILE-material.

For the purposes of this research, out of five necessary conditions to consider a geomaterial as a CHILE-material, two of them are considered to be critical: continuity and homogeneity. Describing a medium as continuous or homogeneous when it is not will lead to a considerable lack of understanding of the geomaterials' behavior inside that medium. Under such assumptions, no design could be considered to be right in solving a problem related to the design of civil infrastructure foundations.

Failing in detecting the lack of continuity or inhomogeneities in the geomaterials is critical, since it could lead to civil infrastructure projects built or founded on top of a void, for example. The detection of underground anomalies is important for geomaterials characterization, as this information is critical for the static design of foundations, embankments, tunnels, etc., and also for seismic design.

Among the various methods available for site characterization, the use of indirect non-invasive methods is gaining the attention of practitioners and field engineers responsible for the task of subsurface exploration. For geotechnical engineering purposes, those methods are known as near-surface geophysical techniques (NSG-techniques) and their use is a valuable tool in any geotechnical engineering design process. Some of the most common NSG-techniques used to characterize geomaterials for geotechnical engineering purposes are the seismic-waves' propagation-based techniques like seismic reflection and multichannel analysis of surface waves (MASW). Seismic reflection can be used to locate underground cavities in the presence of horizontal soil layers above and below the void (Ali, et al., 2011).

As the spatial variability of properties and the lack of continuity in the material were named as critical conditions when geomaterials are assumed to be CHILE-materials in a GG-model, a better understanding of seismic waves propagation under those conditions is necessary to understand the real performance or capacity of foundations designed to work inside those materials.

3.1 Geotechnical and dynamic properties of geomaterials

Geomaterials can be characterized following different criteria, for instance Table 3-1 shows a proposal presented by (Terzaghi et al., 1996) to classify clay soils according to their consistency and unconfined compressive strength. According to Terzaghi and Peck (1948), a clay soil is considered very soft if the number of blows (N) in the SPT test is less than 2 and if unconfined compression strength (q_u) is less than 25 kPa; in the same way a clay soil is soft if N ranges between 2 and 4, while q_u ranges between 25 – 50 KPa. On the other hand, a sand soil is considered very loose if relative density (D_r) is less than

20% and the number of blows (N) in a SPT test is less than 4; while it is considered loose if D_r ranges between 20 – 40% and N between 4 and 10.

Table 3-1. Clay's classification based on consistency (Terzaghi et al., 1996)

Consistency	Unconfined Compressive Strength, q_u (kPa)
Very soft	Less than 25
Soft	25–50
Medium	50–100
Stiff	100–200
Very stiff	200–400
Hard	Over 400

Another criterion for the characterization of geomaterials is the weighted average of shear wave velocity in the soil profile. Several building and construction codes, all around the world, have adopted the average properties for the top 30 meters as criteria for seismic site classification. In Table 3-2 the criteria established in the National Building Code of Canada are presented.

Table 3-2. Seismic site classification proposed by NEHRP (1994) and adapted by the National Building Code of Canada (after Finn and Wightman, 2003).

Site class	Site class name and generic description	Site class definition
A	Hard rock	$\bar{V}_{30} > 1500$ m/s
B	Rock	$760 < \bar{V}_{30} \leq 1500$ m/s
C	Very dense soil and soft rock	$360 < \bar{V}_{30} \leq 760$ m/s, $\bar{N} > 50$, or $\bar{S}_u > 100$ kPa
D	Stiff soil	$180 < \bar{V}_{30} \leq 360$ m/s, $15 \leq \bar{N} \leq 50$, or $50 \leq \bar{S}_u \leq 100$ kPa
E	Soil profile with soft clay	$\bar{V}_{30} < 180$ m/s; plasticity index $PI > 20$, water content $w > 40\%$, and $\bar{S}_u < 25$ kPa
F	Site-specific geotechnical investigations and dynamic site response analyses: (i) soils vulnerable to potential failure or collapse under seismic loading (liquefiable soils, quick and highly sensitive clays, collapsible weakly cemented soils, etc.); (ii) peats and (or) highly organic clays ($H > 3$ m of peat and (or) highly organic clay, where H is thickness of soil); (iii) very high plasticity clays ($H > 8$ m with $PI > 75$); (iv) very thick "soft – medium-stiff clays" ($H > 36$ m)	

Park (2020) stated that the calculation of the average v_s for a certain depth range (for example, top 30 m) can be accomplished in two different ways. Each method leads to significantly different results for the same v_s profile. Nonetheless, it must be said that v_{s-30} as defined in the national building codes in North America, is calculated using the second method.

The first method is based on relative thickness-contribution of each layer, and the calculation of the shear wave velocity is given by:

$$v_{s-30} = \sum v_{s_i} \left(\frac{d_i}{30} \right) \quad (3-1)$$

The second method is based on the definition of velocity – total thickness divided by total travel time, which is given by:

$$v_{s-30} = \frac{\sum d_i}{\sum t_i} = \frac{\sum d_i}{\sum \left(\frac{d_i}{v_{s_i}} \right)} \quad (3-2)$$

Another important concept when dealing with the dynamic characterization of geomaterials is the fundamental period of an elastic layer with the conditions sketched in Fig. 3-1, which can be calculated by:

$$T_0 = \frac{4H}{v_s} \quad (3-3)$$

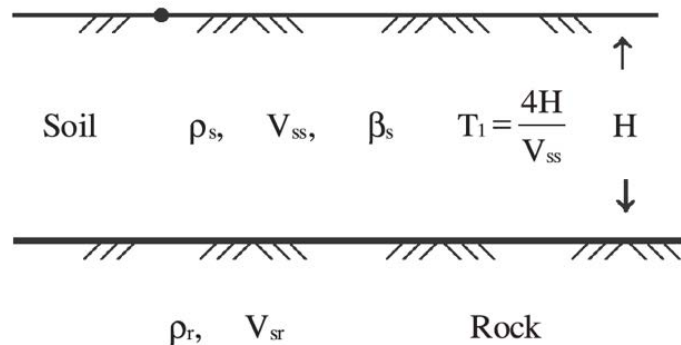


Fig. 3-1: Fundamental period of an elastic surface layer. (Finn and Wightman, 2003)

3.1.1 Very soft soils

In this research, for the analysis of the effect of impedance ratio on the seismic tests results, we are considering the top materials are soft and very soft grounds, which correspond with the soils found in wetlands. According to Fang and Daniels (2006), scientists recognize five major wetland systems: marine, estuarine, lacustrine, riverine, and palustrine. Marine and estuarine include coastal wetlands. The other three categories represent freshwater systems. Inside fresh water systems, the most common identified types of wetlands are:

- Marshes: areas characterized by soft-stemmed herbaceous plants.
- Swamps: areas dominated by woody plants namely trees and shrubs
- Bogs: are peat lands, usually lacking and overlying layer of mineral soils.

Mitsch and Gosselink (1993) define wetlands as those “areas that are inundated or saturated by surface water or groundwater at a frequency and duration sufficient to support, and that under normal circumstances do support, a prevalence of vegetation typically adapted for life in saturated soil conditions”.

Fang and Daniels (2006) highlighted the following geotechnical engineering aspects as characteristic of wetland materials: (a) high water content, (b) low bearing capacity, (c) low hydraulic conductivity, (d) low shear strength, and (e) large settlements. All of these characteristics make the material not just inefficient for load-carrying, but also undesirable for any geotechnical engineering purpose.

In specialized literature, there are not too many studies reporting geotechnical characterization of very-soft soils, which are the materials in wetlands. In Table 3-3, the most relevant results reported are summarized.

Table 3-3. Geotechnical characterization of very soft soils

Authors	Research topic	Geotechnical Characterization									
		Description	γ (KN/m ³)	w (%)	PI (%)	ϕ (°)	c (KN/m ²)	Cu (KN/m ²)	Mv (m ² /MN)	Cv (m ² /year)	OCR
Youdeowei and Nwankwoala (2013)	Evaluation of the subsurface lithologies and examination of soils properties at an area located within the fresh water swamp terrain in the Niger Delta, Nigeria.	silty clay	--	20.6 - 26.5	12 - 18	3	58	---	1.24	3.38	---
Nwankwoala et al. (2014)	Sub-soil profiling to ascertain the geotechnical characteristics of the underlying soils in back-swamps of Akenfa Yenagoa, Bayelsa State, Nigeria	sand, clay and silts	18.76	18.0 - 39.0	13 - 22	---	---	48	0.33 - 0.44	3.66 - 5.12	---
Avwenagha et al. (2014)	Use of surface electrical resistivity survey, borehole drilling and insitu testing by CPT to determine engineering properties of soils at Warri, Western Niger Delta, Nigeria	soft to firm dark, grey organic clay	17.6	---	25 - 150	2 - 3	14 - 18	---	---	---	---
Salami, et al. (2012)	Geophysical and geotechnical investigations for a bridge site within a creek and swamp environment in parts of Agbowa, South East Lagos, Nigeria	fibrous peat	12.2	---	---	---	---	8	---	---	---
		organic clay	15.5	---	---	3	38	---	---	---	---
		silty clay	18.9	---	---	9	93	---	---	1.11	---
Almeida, et al. (2010)	Piezocene (CPTU) tests carried out on very soft soil deposits of Barra da Tijuca and Recreio in the city of Rio de Janeiro	soft to very soft clay	9.8 - 15.7	61 - 600	42 - 300	---	---	2 - 23	---	0.02 - 25.23	---
Baroni, M. and Almeida, M. (2013)	Additional results of laboratory and field tests carried out on very soft soil deposits of Barra da Tijuca in Rio de Janeiro, Brazil	peat	10.4	---	---	---	---	2 - 4	---	---	---
		clay	11.7 - 12.8	---	---	---	---	---	---	---	---
Jung, et al. (2010)	The engineering properties of surface layer on very soft clay of the south coast in Korea	very soft clay, silty clay	15.2 - 16.3	20.0 - 37.5	16 - 24	---	---	< 65	---	---	---
Massad, F. (2009)	Marine soils of Santos lowlands.	sedimented clays	13.5 - 16.3	---	20 - 90	---	---	10 - 60	---	0.09 - 3.15	1.5 - 2.5
Takaki, et al. (2013)	Geotechnical properties of soft to very soft clays of the left bank of the Port of Santos, Brazil.	sedimented clays	14.6-15.4	---	20 - 100	---	---	17.6+1.16z	---	0.63 - 10.09	1.3 - 2.0

Minimum 9.8 18 12 2 14 2 0.33 0.02 1.3
Maximum 18.9 600 300 9 93 60 1.24 10.09 2.5

3.1.2 Dynamic properties of very soft soils

AASHTO (2007) presents the guidelines for seismic design of highway bridges, which includes a classification of soils depending on the shear wave velocity; classes are from A (hard rock, $v_s > 600$ m/s) to F (very-soft soil, $v_s < 180$ m/s). The National Building Code of

Canada (NRC, 2005) follows the same classification of (AASHTO, 2007), where very-soft soils fall in site class F.

A summary of studies reporting dynamic properties of very-soft soils from laboratory or fields test is presented in Table 3-4.

Table 3-4. Dynamic properties of very soft soils

<i>Authors</i>	<i>Research topic</i>	<i>Dynamic Properties</i>			
		<i>Location</i>	<i>Description</i>	<i>Vs (m/s)</i>	<i>Other Parameters</i>
Borcherdt et al. (1994)	The Loma Prieta, California, Earthquake of October 17, 1989 – Strong Ground Motion.	Bay mud, near surface	very soft clay to silty clay	80	---
		Bay mud, at depth	very soft clay to silty clay	108	---
		Alluvium	Loose sand	173	---
Campanella et al. (1994)	Low Strain Dynamic Characteristics of Soils with the Downhole Seismic Piezocone Penetrometer	Burnaby, British Columbia	organic swamp, peat	25	$\zeta = 2, Su < 20$
			organic silty clay	25	$\zeta = 5, Su < 15$
			NC clay to silty clay	46.3	$\zeta = 1$
Likitlersuang et al. (2013)	Small strain stiffness and stiffness degradation curve of Bangkok Clays.	between 0 and 10m depth	silty clay	---	$G_{max} = 5 - 15$
Hunter and Motezedian (2006)	Shear Wave Velocity Measurements for Soft Soil Earthquake Response Evaluation in the Eastern Ottawa Region, Ontario, Canada	0 - 3 m depth	soft soil	145	---
		3 - 23 m depth	soft sediments	110	---
Prasad et al. (2004)	Laboratory Measurements of Velocity and Attenuation in Sediments UCRL-JRNL-205155	0 - 5 m depth (0.0-0.1 MPa)	sand and clay mixtures	90	$\nu = 0.18 - 0.46$

Other studies do not report a specific value for dynamic properties but a relationship between parameters from field tests and shear modulus. Selected examples of these relationships are presented in Table 3-5.

Table 3-5. Equations to calculate the shear modulus of very soft soils

Authors	Research topic	Shear Modulus Equations	
		Comment	G_{max} (MN/m ²)
Hardin and Black (1969)	Vibration modulus of normally consolidated clay. ASCE 95 (SM6), 1531-1537."	clean sand	$G = 3270 \frac{(2.97 - e)^2}{1 + e} p'^{0.5}$
Shibata and Soelarno (1978)	Stress-strain characteristics of clays under cyclic loading. JSCE 276, 101-110.	no for very low consolidation pressures	$G = 41,600 \left(0.67 - \frac{e}{1 + e}\right) \sigma'_v 0.5$
Shibuya and Tanaka (1996)	Estimate of elastic shear modulus in Holocene soil deposits. Soils and Foundations 36 (4), 45-55.	no for very low consolidation pressures	$G = 5000 e^{-1.5} \sigma'_v 0.5$
Kawaguchi and Tanaka (2008)	Formulation of Gmax from reconstituted clayey soils and its application to Gmax measured in the field. Soils and Foundations 48 (6), 821-831.	applicable for reconstituted and in-situ soils	$G = 20,000 w_L^{-0.8} \left(\frac{2}{3} OCR\right)^{0.2} \left(\frac{1 + OCR^{0.5}}{3}\right)^{0.6} \sigma'_v 0.8$

Kalteziotis et al. (1990) presented correlations of pressuremeter tests with values of shear wave velocity and dynamic shear moduli obtained by the cross-hole test in clayey soils. The authors remarked that correlations between G_0 and SPT or CPT tests results are highly unreliable for very-soft or very stiff clays. The paper presents new correlations for a wide range of clay soils in Greece. Especially, there is one correlation for very-soft soil, which relates CPT predictions from q_c (cone resistance) with shear modulus. The correlations presented in the papers are listed below.

From pressuremeter results:

$$G_0 = 138 * P_1^{1.42} \quad (r = 0.97, G_0 \text{ and } P_1 \text{ in MPa}) \quad (3-4)$$

$$v_s = 265 * P_1^{0.67} \quad (r = 0.97, V_s \text{ in m/s, } P_1 \text{ in MPa}) \quad (3-5)$$

$$q_c = 3.0 * P_1 \quad (3-6)$$

From CPT test results:

$$G_0 = 28 * q_c^{1.4} \quad (3-7)$$

(Oh et al., 2008) presented the use of a new in-situ seismic probe developed by Jung et al. (2008). Shear wave measurements and a set of cone penetration tests were performed, along with triaxial compression tests, at a clayey silt site near Incheon, Korea. A linear relationship between undrained shear strength (C_u , in kPa) and shear wave velocity (v_s , m/s) was obtained for normally consolidated clayey silt.

$$C_u = 0.38v_s - 6.65 \quad (3-8)$$

$$G_{max} = 1230 * OCR^k * \frac{(2.973-e)^2}{1+e} * \sqrt{\sigma_0} \quad (3-9)$$

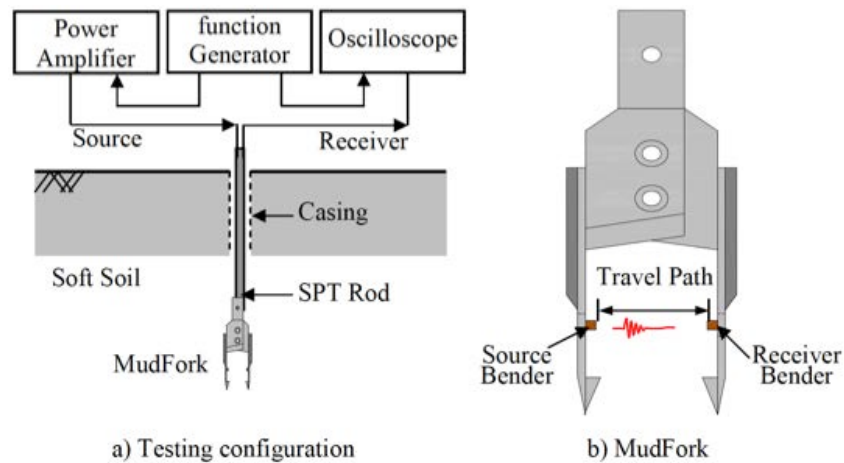


Fig. 3-2: In-situ seismic test using the MudFork (Oh et al., 2008)

3.1.3 Application of seismic techniques to study very soft soils

(Thurber Eng. Ltd., 2013) reported the evaluation of three geophysical techniques (ERI, MASW and Seismic Refraction) for site characterization in a swamp area. The geophysical trials were conducted by the University of Waterloo and the borehole drilling and CPT tests were conducted by Thurber Engineering Ltd. under the Ministry of Transportation Ontario (MTO) requirements. The main conclusions of that report were:

- The electrical resistivity method provided the depth estimate to the underlying dense glacial till with an average error of about 5%. This method is expected to clearly identify the profile of hard bottom in a typical swamp.
- The seismic refraction method, once corrected for the effect of inverse layering, provided the depth estimate to the underlying dense glacial till with an average error of -10% (that is it underestimates depth). The depth estimates of the overlying layers were not accurate due to the limitation of this method in detecting soft soil layers underlying hard soil layers. However, this method would provide reasonably accurate estimate of hard bottom in a typical swamp where there is no inversion of soil layering.
- The MASW method indicated the depth of dense material (glacial till) with an average error of -22%. However, this method provided the advantage of clearly showing the presence of all layers on the site although the thicknesses of layers and depth to dense till were underestimated. The results of the MASW technique can be significantly improved by changing the source for generating waves of larger wavelength and the MASW method shows potential for characterization of the properties of individual layers.

Paoletti et al. (2010) presented a marine investigation carried out offshore Croatia. During the investigation, direct v_s measurements were taken with three methods including seismic Cone Penetration Testing (CPT), Multichannel Analysis of Surface Waves and Downhole method.

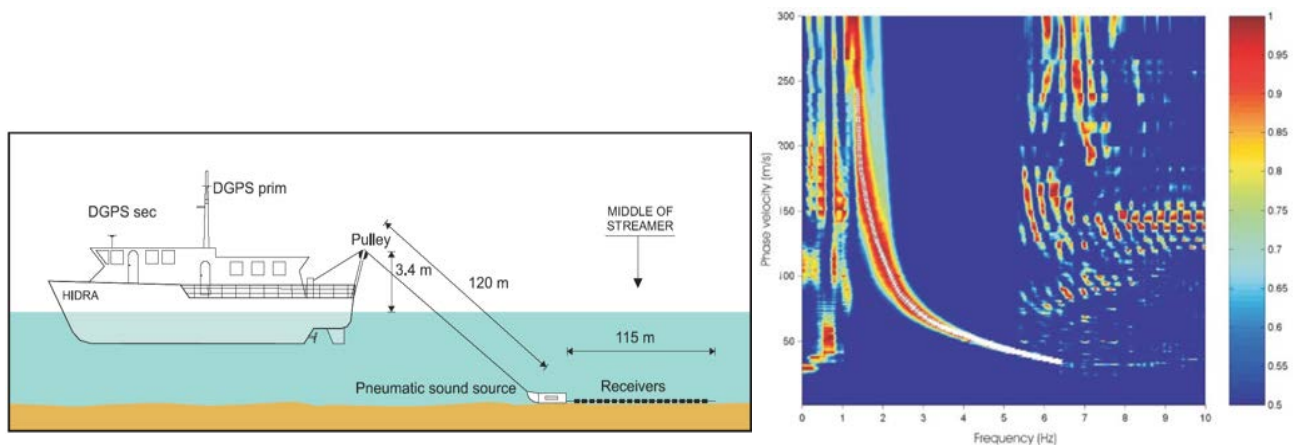


Fig. 3-3: Surface wave survey set-up for marine investigation. (Paoletti et al., 2010)

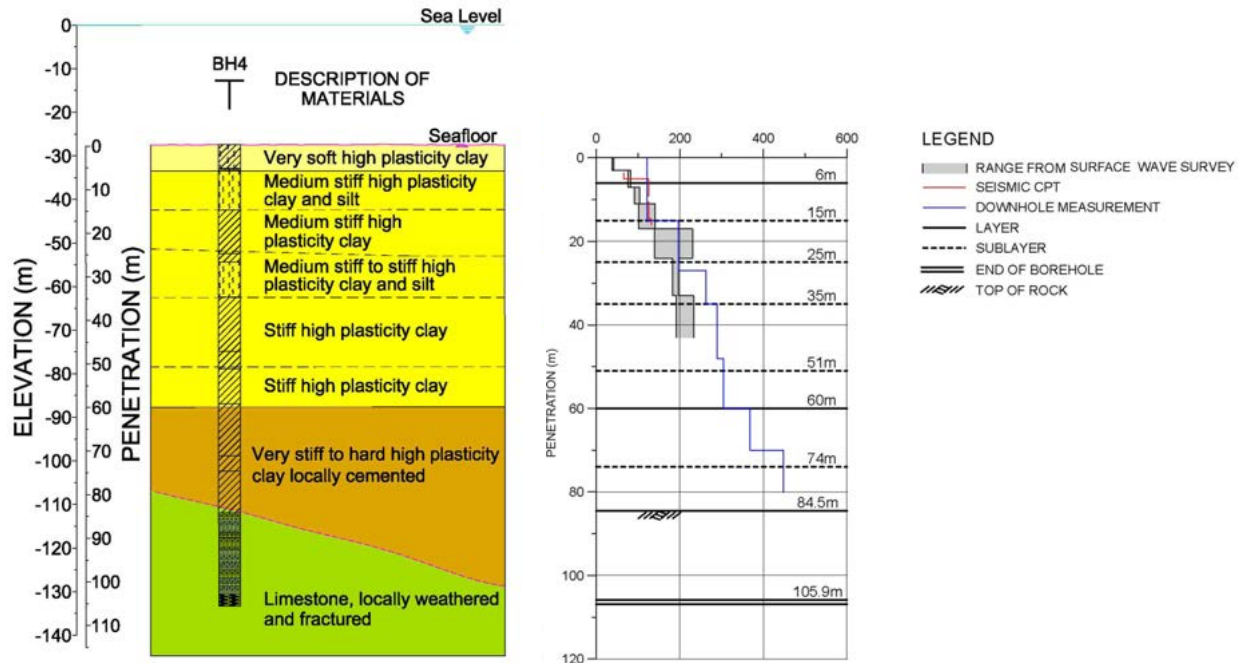


Fig. 3-4: Summary of shear wave velocity data, location BH4. (Paoletti et al., 2010)

3.2 Wave-propagation based techniques at different scales

Lai (2005) presented a comprehensive review of the application of surface waves to characterize materials at different scales. The term scales in this context refers to the size of the material being tested, which the same consideration adopted in this thesis. Typical applications at small scales are described in the ultrasonic literature for material characterization in a variety of materials engineering applications (e.g. Blake and Bond, 1990; Pecorari, 2001). At large scales, the applications are more oriented to investigate the structure of the Earth crust and of its upper mantle, like it has been typically done by seismologists who have long employed body and surface waves for this purpose (e.g. Lee and Solomon, 1979; Keilis-Borok, 1989; Aki and Richards, 2002). Finally, at intermediate scales, the use of surface waves for shallow characterization of geomaterials for geotechnical engineering purposes has been reported by Jones (1962), Stokoe et al. (1994), and Strobbia (2003), among others.

3.3 Geophysical techniques to study geomaterials – void detection

Near surface geophysical techniques (NSG-techniques) are applications of traditional geophysics to the shallower part of a medium. These techniques allow practitioners the possibility of dealing with sub-meter-scale depth and lateral resolution, and also the possibility of having confirmation of results by using traditional drilling techniques at some specific points (Everett, 2013). In real applications, it could be said the most widely used NSG-techniques in geotechnical engineering are the ones based on seismic-waves propagation (they will be referred to as seismic techniques from now on) and the ones based on electromagnetic waves propagation. High resolution seismic-waves propagation NSG-techniques have been developed and applied successfully to characterize a continuous medium. Also, very important technological advances have been achieved in electromagnetic-waves propagation techniques, like ground penetrating radar (GPR). However, in spite of the improvement in the NSG-techniques, the identification of sub-surface ground anomalies (e.g. voids) is still a challenging problem. In this paper, the focus will be on using seismic techniques like seismic reflection and multi-channel analysis of surface waves (MASW) to identify and characterize voids in a geomaterials medium.

3.3.1 Seismic reflection techniques

The use of seismic techniques for the detection of near-surface cavities was first reported in the late 1960s when oscillations with durations of one second or more and with narrow frequency bands were observed over cavities in lava and alluvium at depths shallower than 14 meters. This initial attempt in interpreting the seismic signals to identify cavities led to the identification of delays in arrival times and anomalous attenuation of seismic waves traversing cavities. For the data analysis, Fourier transform and autocorrelation were reported to be used successfully to detect these and similar resonant phenomena in noisy backgrounds; meanwhile, cross-correlation of proximate traces was less successful for this purpose. (Watkins et al., 1967)

Vesecky et al. (1980) reported the results of a comparative study including the application of electromagnetic techniques and seismic techniques (in this case cross-hole seismic) for tunnel detection. Their results showed that seismic P-waves suffer much less attenuation during propagation and produce more salient tunnel signatures for a given borehole separation. That study even concluded that seismic P-waves have significant advantages over electromagnetic waves for air-filled tunnels. The tunnel signatures were defined for the amplitude and for the phase of the signals recorded by the sensors. In some cases, amplitudes can be difficult to detect but phases could provide a more detectable signature. However, the authors advised that, by the time they reported the study, phase measurements had not been studied experimentally as a means of tunnel detection (Vesecky et al., 1980). Finally, they report the procedure utilized for signal processing, which consisted of applying a matched filter in the spatial frequency domain to detect the peak as an indication of the presence of tunnels.

Rechtien et al. (1995) discussed the same idea of identifying tunnel signatures from cross-hole tests and compared the field results with the theoretical solution. The results showed that the amplitudes of S-waves scattered from the tunnel were more than 20 dB smaller than the amplitudes of primary P-waves, so the former could be difficult to see in field data. The results also showed that amplitude reduction increased with frequency and tunnel size. The comparison of synthetic waveforms (from theory) to the real data (from the field) indicates that small changes in the tunnel cross-section do not affect the received waveform in a significant way.

Steeple and Miller (1987) reported the use of direct detection of shallow subsurface voids using high-resolution seismic-reflection techniques.

Branham and Steeples (1988) reported the use of high-resolution P-wave reflection seismology to locate water-filled cavities in a 1 m thick coal seam at depths of 9 m. They used a dominant frequency of 275 Hz to delineate the top of the coal seam. The authors claim this study is one of the first to locate water-filled coal mine cavities at depths of less than 30 m using high-resolution P-wave seismic reflection techniques.

Grandjean and Leparoux (2004) identified three different ways how a void can interact with the surrounding medium, so depending on the nature of the wave and the ratio wavelength to void-size, a void can: (i) act as a diffracting body, (ii) contribute to the masking of deeper reflections, or (iii) produce attenuation processes. They studied the problem of void detection by utilizing seismic reflection and surface waves analysis, while the former technique was effective, the latter was effective only when the void is very shallow. In the surface waves analysis, the phase characteristics of seismic signals are considered by computing the phase velocity of Rayleigh waves to perform the DLMO correction. The Rayleigh wave profile showed anomalies corresponding to cavities or shallow heterogeneities. Those anomalies could be due to phase perturbations but also to amplitude perturbations generated by cavities or heterogeneities, however, it was not possible to determine the physical origin of the anomaly on the profile.

Hickey et al. (2009) identified two reasons why seismic techniques are not widely used to characterize manmade subsurface structures like tunnels. First, the size of such a structures can be “small relative to the spatial sampling and the seismic wavelengths used in seismic surveying”; second, “the surrounding shallow subsurface soil is usually highly heterogeneous with respect to its mechanical properties”. They presented a seismic refraction tomography using a finite-frequency approach for high-contrast voids detection in the shallow subsurface. Their results showed that spatial distribution or ray coverage within the subsurface is an attribute that can be used for detecting and locating high-contrast voids.

Sloan et al. (2010) introduced three near-surface seismic methods, including “diffracted body waves, backscattered surface waves, and changes in reflection move-out velocities to detect voids directly or their effects on surrounding material properties using different parts of the wave-field.”

Schwenk et al. (2014) used the MASW testing approach “to study Rayleigh waves and the backscatter analysis of surface waves (BASW) to detect anomalies in the subsurface. Waves incident upon these discontinuities generate diffracted, reflected, or ‘backscattered’ waves. F-K filtering enhances backscattered energy, while dynamic linear

moveout corrections and a common receiver stack place the locus of these events at time zero. Separate moveout functions are designed around the fundamental and higher-mode dispersion trends”. Via the analysis of synthetic data, they demonstrated that “both velocity corrections result in proper location of a subsurface air-filled void. Correlation of the two moved-out gathers further constrained the lateral position of the void. This added localization and use of higher-mode dispersion is seen as the major discovery of this research. These conclusions were further tested, and shown repeatable, across several field data sets of known tunnel sites. This correlation technique allows greater interpretability and localization of anomalies in real-world scenarios”.

Keydar et al. (2018) considered the scenario in which every subsurface inhomogeneity is considered a possible diffractor. They proposed the separation of primary and multiple reflected waves, refracted waves and scattered/diffracted waves; then, they performed the imaging of the diffractors based on a spatial summation of the diffracted wavefield along diffraction time surfaces.

Zahari et al. (2018) performed an experimental field study to investigate the characteristic of reflected waves in the presence of a void in soil. They analyzed the amplitude wave pattern change with distance and identified the peaks in that contour plot as a clear indication of the presence of anomalies and even a good tool to approximate the size of the void.

3.3.2 Surface waves dispersion techniques

Besides the seismic reflection technique, the MASW test is an alternative seismic technique to characterize geomaterials. Park et al. (1999) reported the detection of near-surface voids by using surface waves. In this case, multiple numbers of shot gathers are collected over a certain surface distance like in the conventional seismic reflection common-depth-point (CDP) survey. Results showed higher values of phase velocities and higher attenuation in the signals for shot gathers collected with the source on top of the void, which could be due to the generation of higher modes. Thus, the main conclusion is that the existence of voids may play a similar role to the existence of a medium with a velocity inverse profile.

Phillips et al. (2002) used the SASW method with multiple receivers to detect underground voids and it has demonstrated to be very sensitive to receiver location relative to the underground void. In that way it is possible to examine the phase component of surface waves as they propagate, which allows the possibility to detect lateral inhomogeneities by analyzing the lateral energy component of the surface waves, and even to generate a dispersion curve in the event of noisy data.

Shokouhi and Gucunski (2003) studied the effect of different types of cavities by analyzing two graphical representations: first, the plot of power spectral amplitudes versus frequency and receiver location, and second, the plot of wavelet transform coefficients versus time and frequency. The results showed strong energy concentration right in front of a cavity in certain frequency bands in the first kind of plots. Furthermore, time and frequency signatures of waves reflected from near and far faces of the cavity can be clearly observed in the second kind of plots. These observations were used to locate and estimate the size of the cavity, so the wavelet transform seems to be a promising analysis tool for cavity detection and characterization.

Phillips et al. (2004) proposed the distance analysis of surface waves (DASW) method, which determines the horizontal homogeneity of a medium by analyzing the phase of surface waves with respect to distance. According with the results, the method is able to identify horizontal changes in medium properties and allowed to complement the spectral analysis of surface waves (SASW) method. The effectiveness of the method was probed through the comparison of a simplified theoretical solution and numerical simulations including different models and even including an underground void.

Gelis et al. (2005) presented an algorithm to simulate seismic wave propagation including a perfectly matched layer (PML) absorbing boundary condition to avoid reflection from the edges of the numerical model. PML boundary condition is different from the absorbing boundaries utilized by the software FLACTM, in which the boundaries could be perfectly absorbing only if the incident wave is oriented at least 30° with respect to the perpendicular of the absorbing boundary. The algorithm was then utilized to evaluate the effects of different empty cavity shapes and depths, and even to study the

effect of considering altered zones on top of a cavity. Gelis et al. (2005) proposed the analysis of “differential seismograms for both with and without cavities to find the specific frequency bands where the coherent energy is missing, and to relate it to the cavity depth, shape and degree of modification of the surrounding medium”.

Xia et al. (2007) used 2-D surface wave modeling to demonstrate that the diffractions due to a void on a homogenous half space were Rayleigh-wave diffractions because of their amplitude, velocity, and frequency. They derived a “travel-time equation of surface wave diffractions based on properties of surface wave and solved this equation for a phase velocity and depth to a void”. What they concluded is that in practice, only two diffraction times are necessary to define the depth to the top of a void and the average Rayleigh-wave velocity that generates the diffraction curve.

Ali et al. (2013) presented the results of 3D numerical simulations for the MASW test for a homogeneous medium with an underground cavity. Their goals were to investigate the effect of out of plain dimension of a cavity and to study the effect of cavity-receiver array misalignment on the surface responses. The numerical models showed that void–wave front interaction is a 3D phenomenon, so the out of plain dimension of the void has a significant effect on the surface responses. When the normalized wavelength is less than 3, the effect of void is less noticeable. They also concluded that “the alignment of receiver’s array and the void is a necessity for the successful application of MASW method in void detection”.

3.3.3 Guideline recommendations on selection of geophysical techniques

A guideline with recommendation on selection of near-surface geophysical techniques is presented in the appendices. This guideline is based solely on literature review, however, it is still useful for practitioners when dealing with site characterization where soft to very soft grounds are present.

4 Research Methodology

In this chapter the research methodology is discussed along with a breakdown of the necessary steps followed to ensure the achievement of the proposed research objectives. The research methodology was initially sketched and progressively modified while the research was progressing.

4.1 Main research activities

The main research activities are listed here and described in the following sections:

1. Preliminary research activities: introduction, problem statement, research objectives, theoretical background review, and literature background review.
2. Activity 1 – Parametric studies: based on numerical simulations, first for a hypothetical layered medium including soft soils in the top layer [Chapter 5], and second, for a realistic layered medium characterized from the CPTU test results [Chapter 6].
3. Activity 2 – Geomaterials characterization at large scales: based on field tests' results (sCPTU and MASW tests) along with numerical simulations replicating field conditions [Chapter 7].
4. Activity 3 – Geomaterials characterization at intermediate scales: based on laboratory tests' results obtained from a physical model (i.e. a sandbox) and numerical simulations to replicate waves propagation in it [Chapter 8].
5. Activity 4 – Geomaterials characterization at small scales: based on laboratory BE tests results, and also on numerical simulations results [Chapter 9]

4.2 Flowchart of the research methodology

Next, the flowchart for the methodology followed in this research is presented. This flow chart is intended to summarize all the step-by-step breakdown presented in the following sections.

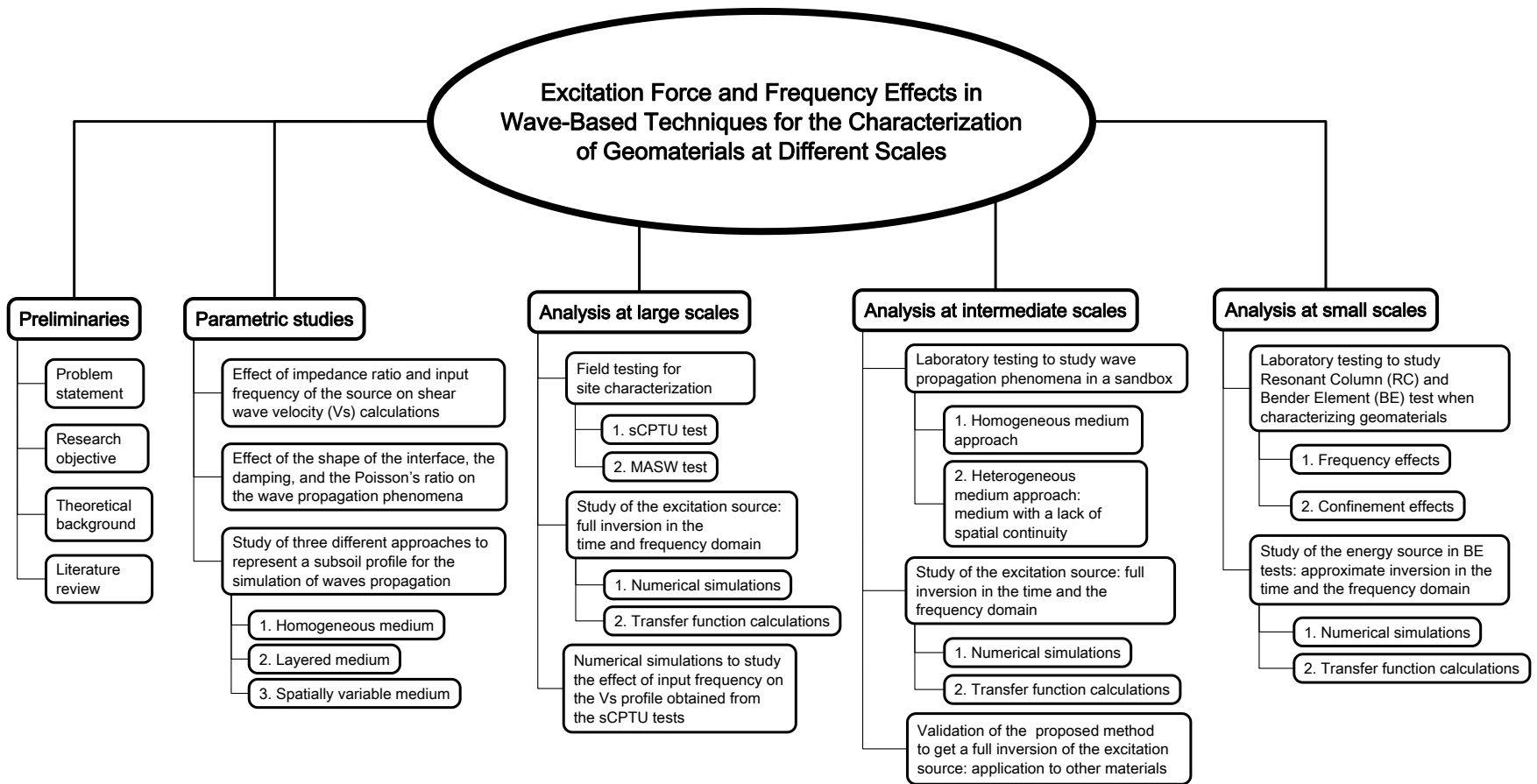


Fig. 4-1. Flowchart for the research methodology.

4.3 Parametric studies for the average shear wave velocity (v_{s-30})

4.3.1 Effect of impedance ratio between top materials and frequency content in the input source

The first approach to characterize geomaterials at large scales was done by using numerical models to simulate the propagation of seismic waves in a layered medium. A theoretical model composed of six layers of geomaterials overlaying a bedrock layer was defined. Then the theoretical value for the weighted average of shear wave velocity (v_s) was calculated.

To study the effect of impedance ratio between the first two top layers, the initial theoretical profile was modified to create nine variations of the numerical model, each one of those variations representing a new model in which the material in the first layer was replaced each time by a softer soil. In the end, the ten models (one initial model plus nine variations) had different materials in the first layer while the rest of the layers remained invariable in their properties. In this way, it was possible to study the effect of the impedance ratio between the top two layers on the results of weighted shear wave velocity in a layered medium.

The effect of frequency was also studied using the same numerical models. In this case, the parameter defining the frequency content in the input force was modified. Thus, each of the ten numerical models was then run applying four frequency contents. In this way, the numerical simulation for forty combinations of the impedance ratio and the frequency content were run. From the results of each model, the dispersion curve was generated and the v_s profile was obtained via mathematical inversion, and the weighted shear wave velocity (v_{s-30}) value was calculated. Then all the results were compared against the theoretical value of v_{s-30} .

The analysis of the results allowed the creation of a contours plot, in which any reasonable combination of impedance ratio and input frequency land in a normalized parameter that allows the estimation of deviation of weighted average of shear wave velocity (v_s) with respect to the theoretical value. If the impedance ratio had no effect on

the results, then the normalized parameter in the contour plot should take the exact value of 1.0, the same should happen for the input frequency content. Nonetheless, the contours plot clearly shows how the impedance ratio and input frequency affect the estimation of the weighted average of shear wave velocity (v_s).

The effect of some other parameters and conditions were also studied to illustrate how they affect the results of wave propagation. The other parameters studied were: the shape of the interface, the Poisson's ratio value, and the damping ratio value, which were analyzed by comparing changes in the frequency vs. wave number spectrum (F-K).

4.3.2 Effect of considering different approaches to spatially distribute the stiffness in the medium

In the previous research step, it was assumed that a layered medium was a good representation of soil properties distribution when dealing with the wave propagation phenomena. However, the layered medium is just a reasonable approach widely used when studying a variety of geotechnical engineering problems.

Other approaches to represent the soil profile properties are: first, to consider the medium is homogeneous, or second, to consider the medium is heterogeneous. The assumption of homogeneity is widely used to obtain the theoretical solution for problems dealing with a medium characterized by deterministic properties (i.e. an elastic homogeneous medium). Even though soils do not land in that category of materials, it is very common to see the use of that assumption in problems dealing with geomaterials. The second option is to consider the soil as a geomaterial with properties varying in space. This approach is complicated from a theoretical point of view, so that no exact solution actually exists for problems like seismic wave propagation in an spatially variable medium, thus, its use must be carefully considered.

Under these considerations, it was necessary to study the wave propagation phenomena in geomaterials for all the three approaches to define the properties' distribution inside the medium: first, the homogenous medium; second, the layered medium; third, the spatially variable medium. The way how the wave propagation phenomena was studied was by using numerical models, however, in this case the results

from field tests (i.e. MASW and sCPTU tests) were used to obtain the elastic properties of the soil profile in a real site. Then, the numerical models were created seeking to reproduce the field results (i.e. vertical displacements) obtained in the MASW field test.

The main challenge at this point was related to the characterization of the excitation force because the energy is not measured or estimated in any way in the field tests. Thus, the excitation force shape, amplitude, duration, and frequency content were defined, so that the real excitation force can be later used in numerical forward modeling. Some different shapes of pulses were tested, such as Lamb force pulse, sine pulse, semicircular pulse, and the Ricker wavelet pulse. The latter presented some advantages over the others and was chosen to be used as input force in the numerical models.

The results of these numerical simulations were useful to compare the wave propagation phenomena when the geomaterials' characterization at large scales followed different approaches (i.e. homogeneous, horizontally layered, or spatially variable medium). Then, by analyzing the field test results it is possible to conclude what is the best way to approach the medium characterization to study wave propagation in soils.

4.4 Characterization of geomaterials at large scales

4.4.1 sCPTU field test and numerical simulations to study the frequency effects on v_s results

The first two main steps in this research led to important conclusions when the characterization of geomaterials is pursued by using wave-propagation based methods. The first one shows how important impedance ratio and input frequency are in the results from seismic tests like the MASW. The second one compared three different approaches for the definition of the soil profile properties and allowed the definition of a range of frequencies suitable to represent field conditions for the MASW test.

In this third step, a novel methodology to further study the excitation force characterization is presented. This characterization is focused on finding the best fit possible in the frequency domain between the field data from sCPTU tests and the results from the numerical simulations in a layered medium. The results were promising in the

sense that in order to get a good match in the frequency domain it is not really necessary to get the match in the time domain, which could be very complicated in most cases for which the input source is unknown. By closely matching the frequency spectrums, the main shape of the input force pulse, along with its amplitude, and frequency parameters, could be properly defined.

Now, it is assumed that the frequency response in the field is approximately similar to the frequency response in the numerical model, thus, the transfer function for the numerical model is similar to the one for the field. Then, forward numerical modeling is done considering that the input source in the numerical model could be progressively modified until a good match is gotten between the numerical model and real field responses.

If the field medium is considered a linear invariant system (either the modeled or the real sandbox), the Fourier transform of the input can be calculated as the Fourier transform of the output divided by the transfer function. If the assumption that both transfer functions are similar enough is accepted, then the Fourier transform of the input in the real sandbox can be calculated as the Fourier transform of the output in the field, divided by the transfer function in the numerical model.

Once the excitation source is properly inverted, a parametric study is performed to evaluate the effect of input frequency content on the field tests results. This analysis lead to conclusions about the effect of introducing variations in the input force, when the shear wave velocity is sought.

4.5 Characterization of geomaterials at intermediate scales

4.5.1 MASW laboratory tests and numerical simulations to approach the input source inversion

At this point, the results in the research have allowed some progress in the characterization of input force of seismic tests frequently used in the field, however, in order to get a complete characterization of the source of energy in wave-propagation based tests, it is necessary to perform another set of experiments, this time in a controlled

environment (i. e. a laboratory). During the field test is quite complicated to control many variables governing the input energy, so the use of laboratory tests was a necessary step to take enough control in the seismic wave propagation test to properly get a characterization of the excitation force.

In this research step laboratory tests in a sandbox were performed. The use of cutting edge technology to read surface displacements (i.e. a laser vibrometer), along with the use of a calibrated ultrasonic transducer to control the input energy, made possible to perform controlled seismic wave propagation tests.

Before the laboratory tests, a set of numerical models were run to reproduce the wave propagation phenomena under the sandbox conditions. The initial excitation force used in this case was a sine pulse with a frequency of 54kHz. In the numerical model the input and output are perfectly know, thus, the calculation of a transfer function is possible and allows the understanding of the behaviour of the modeled sandbox as a linear invariant system.

Now, for the laboratory tests, an ultrasonic transducer was used to send energy into the sandbox at one point while the vertical displacements, obtained as the surface response in many other points of the sandbox, were read with a laser vibrometer. Because the ultrasonic transducer used as input excitation force was calibrated, its average response to an electrical pulse is well known.

If the real sandbox is also considered as a linear invariant system, the analysis of the frequency response could be performed by calculating its simplified transfer function as well. Such a calculation was easily done with the numerical models' input and output data, however, for the laboratory sandbox the only certain data is the response of the system while the input is still unknown. Because the transducer response in the calibration process was measured in air, the amplitude, shape, and frequency of the transducer response cannot be assumed to be exactly the same when the transducer is placed on top of the sandbox. It is believed that the input excitation force for the sandbox tests could be close to the transducer response in air, however, it cannot be considered as the exact same.

Now, by assuming the frequency response in the modeled sandbox is approximately similar to the frequency response in the real sandbox, it could be said that the transfer function for the numerical model is similar to the one for the real sandbox. This assumption is not exactly true when the input for the numerical model is a sine pulse, which is corroborated when responses in the real sandbox are compared with responses in the numerical model. They are very different from each other. However, a forward numerical modeling process could be done, in which the input source in the numerical model could be progressively modified until a good match is obtained between the numerical model and real sandbox responses.

By doing the same assumption about the system's linearity, if the sandbox is considered a linear invariant system, everything said about the calculation of the Fourier transform of the input signal could be replicated here. Thus, the transfer function method proposed to analyze field data is also applicable at a laboratory scale to study the results of the MASW tests performed on the sandbox.

To start the process of matching the time domain responses, the input force in the numerical model was modified. The average transducer response in air was assumed to be equal to the deformation of the surface at the input location in the model, then the deformation was converted to force by using the elastic properties of the material. The numerical simulation was performed and the transfer function for the numerical model was obtained. Later the Fourier transform of the response at one specific point in the real sandbox (i.e. a reference point) was divided by the transfer function previously obtained. The result was expected to be the Fourier transform of the input force in the real sandbox. That is why this input force was then used to repeat the numerical simulation and see if the responses in the time domain between the modeled and the real sandbox are similar. If that would have happened it could be said the input force was properly obtained; however, that was not the case.

A second trial included the modification of the real sandbox response by applying a windowing processing to the same signal obtained at the reference point. The windowed displacement signal was converted to force and used as input for the numerical model.

Next, the transfer function was calculated and the time domain responses were compared between modeled and real sandbox.

This process was repeated for different windows in the signal processing, and the input force was inverted every time until the time domain responses in the modeled and in the real sandbox matched. At that point it was concluded that the transfer function in the numerical model also represented the behaviour in the real sandbox, which means the input source is properly characterized in every single aspect (i.e. amplitude, shape, and frequency content).

Now that the path for obtaining the input source was cleared, the comparison of responses between the modeled and the real sandbox was performed at different locations on the sandbox, so that it was possible to understand if the transfer function obtained worked for every single point in the real sandbox.

The results showed that the transfer function obtained at the reference point does not work properly for all the sandbox surface points read with the laser, which was expected because that point is too close to the source and it is affected by the near field effect. A simplified analysis of displacements attenuation with distance from the source was done to define the near field. After that, the whole process was repeated to obtain another transfer function outside the near field. The latter transfer function works properly for most of the points away from the source and outside the near field.

At this point, it was concluded that the source characterization process was successful, and it could be replicated and tested in different materials or even at different scales.

4.6 Characterization of geomaterials at small scales

4.6.1 Results of RC and BE tests on laboratory samples

The analysis of wave-propagation based techniques to characterize materials at small scales was done by studying the results of resonant column (RC) tests and bender element (BE) tests. Laboratory tests were performed in three stages: first, performing BE

tests on a real sand sample; second, characterizing the bender element (BE) transmitter using a laser vibrometer; third, performing RC and BE tests on a reconstituted sample of fused quartz.

In addition, another set of numerical simulations was performed to replicate a two-dimensional (2D) approximation of the wave-field generated inside the sample in a BE test. The input force used for the numerical model was the actual horizontal and vertical displacements obtained from the BE calibration, which were converted into force in order to be applied at specific locations in the numerical model.

5 Characterization of geomaterials at large scales: layered medium approach – numerical study of the impedance ratio effect and the interface shape effect

In this chapter a numerical procedure to characterize geomaterials at large scales using a wave-propagation based method is presented. The main idea of the method is to focus on characterizing the soil profile in order to get the site characterization needed for a seismic design according to the building code in Canada. Then the analysis of the effect of impedance ratio for a range of geomaterials going from soft to very soft soils is made by studying the effect of the impedance ratio between adjacent layers, as well as the effect of the shape of the interface between layers, among others.

5.1 Detailed procedure

The detailed procedure followed in this chapter to characterize geomaterials at large scales involves numerical simulations, and field testing. The steps followed were:

1. Definition of preliminary aspects for the numerical simulation
 - a. Model geometry definition
 - b. Boundary and initial conditions
 - c. Mesh size and time step definition
 - d. Input force used for calibration
 - e. Calibration for surface wave propagation: damping selection
2. Numerical study of wave propagation in a horizontally layered medium
 - a. Analysis of effect of changes in the impedance ratio on the site classification (v_{s-30}) results
3. Numerical study of wave propagation in a non-horizontally layered medium
 - a. F-K spectrum results: analysis of the effect of changes in the shape of the interface between adjacent layers
 - b. F-K spectrum results: analysis of effect of changes in the impedance ratio, Poisson's ratio, input frequency, and damping parameter

5.2 Numerical model calibration

The use of a numerical model to simulate how seismic waves propagate inside and in the surface of a geomaterial requires the model to be properly defined in geometry, boundary, and initial conditions. Furthermore, the model also requires to be calibrated in order to fit the theoretical response expected in closed-solutions problems.

5.2.1 Model geometry definition

In this chapter the numerical model was defined to simulate the wave propagation phenomena at large scales, thus, their dimensions are meant to simulate a field test such as the MASW test. The numerical model is defined to be 40 meters long by 24 meters deep.

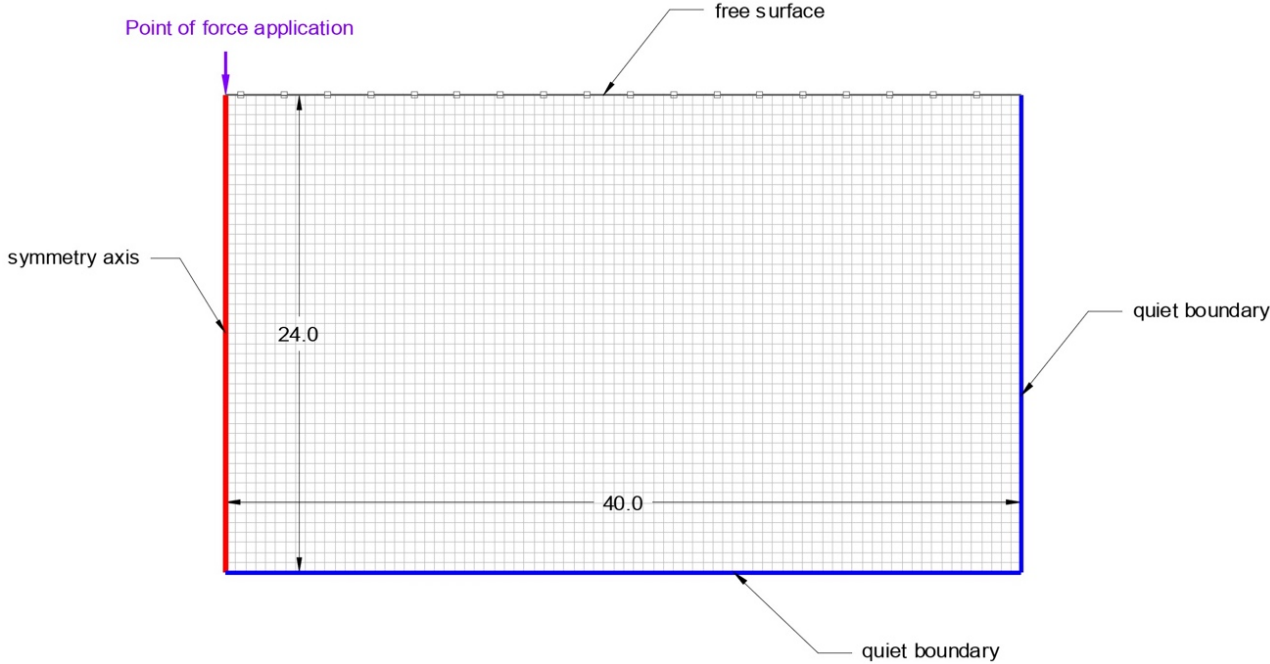


Fig. 5-1: Definition of geometry and boundaries for the numerical model.

5.2.2 Boundary and initial conditions

As the model is intended to simulate the real conditions of seismic tests in the field, the input force is considered to be a load applied on a single point, thus, a necessary condition for the model is to be axisymmetric, and the load to be applied in the symmetry axis. On that boundary corresponding to the symmetry axis, the horizontal displacements are restricted, so the points in that boundary can move only in the vertical direction.

For the boundaries corresponding to the bottom and the right end of the model, the condition of a quiet boundary is applied. This means the boundary absorbs the energy and does not allow its reflection back into the model, however, that kind of boundary has some conditions to be 100% effective, like the incident angle of the energy. Several formulations have been proposed. The software FLACTM uses the viscous boundary developed by (Kuhlemeyer and Lysmer, 1973), which is based on the use of independent dashpots in the normal and shear directions at the model boundaries (Itasca, 2000). As it is clearly stated in the user guide manual of the software, “the method is almost completely effective at absorbing body waves approaching the boundary at angles of incidence greater than 30°. For lower angles of incidence, or for surface waves, there is still energy absorption, but it is not perfect”. (Itasca, 2000)

For the initial conditions, the only consideration is the model is at rest before the load application actually starts. The load application time depends on the input frequency, however, it is always guaranteed that the numerical simulation lasts for at least the travel time taken for Rayleigh waves (the slower ones) to reach the right end of the model.

5.2.3 Mesh size and time step definition

As it was already explained, the wavelength (λ) determines the accuracy for wave propagation problems. Zerwer et al. (2002) suggested that element dimensions that are too large will filter high frequencies, whereas very small element dimensions can introduce numerical instability as well as require considerable computational resources. Thus, in order to avoid these issues Zerwer et al. (2002) recommend that an appropriate mesh size could be one-fifth of the minimum wavelength to use in the numerical model.

According to the criteria suggested by FLACTM (Itasca, 2000), for the numerical model is needed that the maximum mesh size is one-tenth of the wavelength. For geomaterials like soils, the wave velocity could range from values as low as 20 m/s up to values as high as 480 m/s. For different values of shear wave velocity (v_s) and for different values of frequency (f), it is possible to get different values of wavelength with this equation:

$$v_p = \lambda \times f \quad (5-1)$$

The calculation of values for mesh sizes following the criteria of one-tenth of wavelength are presented in Table 5-1 for various soils and for different frequencies. For all the numerical models the mesh was preferred to be regular, and its size was properly selected according with these results.

Table 5-1. Maximum mesh sizes for soils with different shear wave velocities and considering different frequencies to use in the numerical model

Soil Type	Soil Class	v_s (m/s)	<i>Maximum mesh size = one-tenth of wavelength ($\lambda/10$)</i> <i>(values of mesh size in meters for different frequencies in hertz)</i>					
			5 Hz	10 Hz	20 Hz	40 Hz	60 Hz	80 Hz
F	I	20	0.400	0.200	0.100	0.050	0.033	0.025
	II	40	0.800	0.400	0.200	0.100	0.067	0.050
	III	60	1.200	0.600	0.300	0.150	0.100	0.075
	IV	80	1.600	0.800	0.400	0.200	0.133	0.100
E	V	100	2.000	1.000	0.500	0.250	0.167	0.125
	VI	120	2.400	1.200	0.600	0.300	0.200	0.150
	VII	140	2.800	1.400	0.700	0.350	0.233	0.175
	VIII	160	3.200	1.600	0.800	0.400	0.267	0.200
	IX	180	3.600	1.800	0.900	0.450	0.300	0.225
D	1	240	4.800	2.400	1.200	0.600	0.400	0.300
	2	300	6.000	3.000	1.500	0.750	0.500	0.375
	3	360	7.200	3.600	1.800	0.900	0.600	0.450
C	4	420	8.400	4.200	2.100	1.050	0.700	0.525
	5	480	9.600	4.800	2.400	1.200	0.800	0.600
C	6	540	10.800	5.400	2.700	1.350	0.900	0.675
Bedrock	--	600	12.000	6.000	3.000	1.500	1.000	0.750

Besides the stability criterion recommended by FLACTM (Itasca, 2000), Zerwer et al. (2002) also recommend that an appropriate time step could be calculated by:

$$\frac{1}{10} \frac{\Delta x}{v_p} \leq \tau \leq \frac{\Delta x}{v_p} \quad (5-2)$$

where τ is the characteristic time; Δx is the mesh dimension; and v_p is the compressional wave velocity (Valliappan and Murti, 1984). Calculations of minimum time steps (characteristic times), following this criterion are presented in Table 5-2. These values were observed when defining the time steps for the numerical models.

Table 5-2. Minimum time steps to use in the numerical model

Minimum time steps in seconds (characteristic times calculated following Zerwer et al., 2002)					
5 Hz	10 Hz	20 Hz	40 Hz	60 Hz	80 Hz
0.002000	0.001000	0.000500	0.000250	0.000167	0.000125

Table 5-3. Maximum time steps to use in the numerical models

Maximum time steps in seconds (calculated following Itasca, 2000)					
5 Hz	10 Hz	20 Hz	40 Hz	60 Hz	80 Hz
0.003536	0.001768	0.000884	0.000442	0.000295	0.000221

5.2.4 Input force used for calibration

Since there is an analytical solution for the point load problem with the Lamb force, that was the input force used for the numerical model calibration. However, for the actual numerical simulations the sine pulse was used because it concentrates more energy at low frequencies and also because it allows a simpler definition of the central frequency.

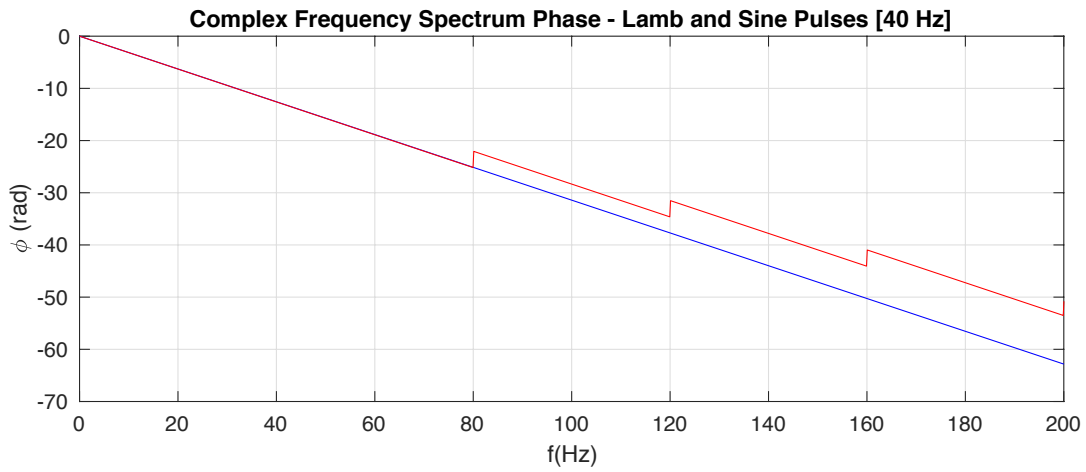
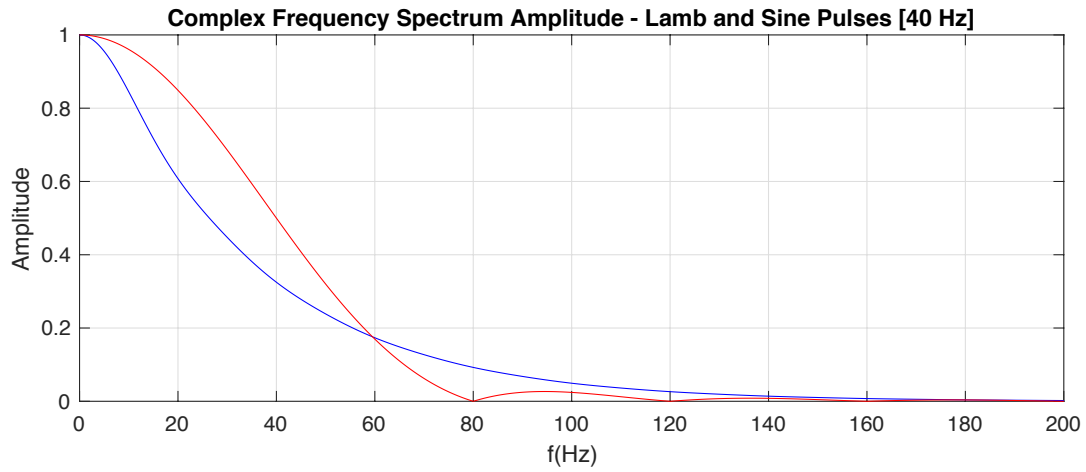
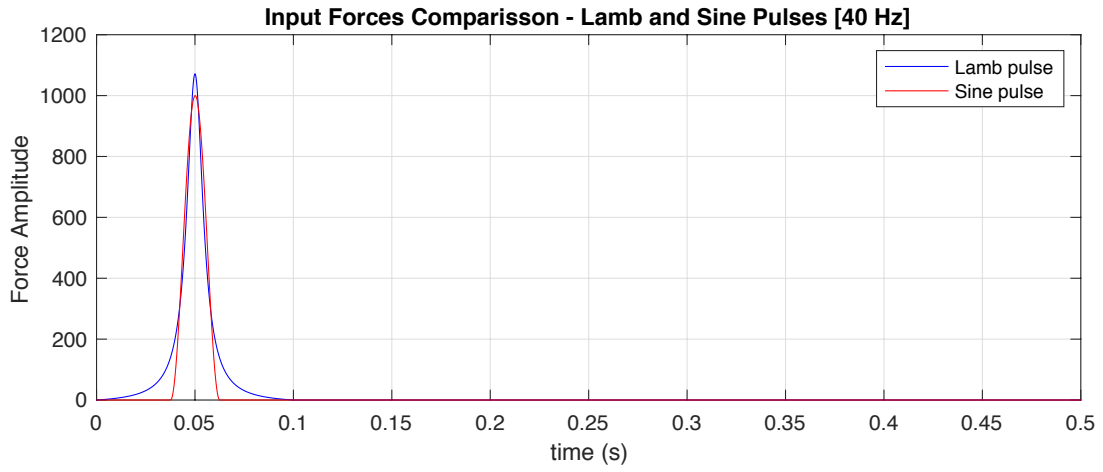


Fig. 5-2: Pulses used as input force in the model.

5.2.5 Calibration for surface wave propagation: damping selection

The analytical solution for surface wave propagation due to a point loaded with a Lamb force was compiled by Nasserri-Moghaddam (2006) and is presented in Table 5-4.

Table 5-4. Analytical solution for surface displacements due to a Lamb source point load (after Nasserri-Moghaddam, 2006)

Lamb source and solution - Axisymmetric - 3D :			
Parameters :	Source amplitude:	$Q_{bar} := 1000$	Source f content: $\tau := 0.00075$
	$a := \frac{1}{C_p}$	$b := \frac{1}{C_s}$	$c := \frac{1}{C_R}$ Wave slowness
	$\omega_{max} := 2 \cdot \pi \cdot f_{max}$	$h := \omega_{max} \cdot a$	$k := \omega_{max} \cdot b$ $\chi := \omega_{max} \cdot c$ Wave numbers
	$\alpha_1 := \sqrt{\chi^2 - h^2}$	$\beta_1 := \sqrt{\chi^2 - k^2}$	
Derivative of Rayleigh equation:	$F(\zeta) := 8 \cdot \zeta \cdot \left[\left(2 \cdot \zeta^2 - k^2 \right) - \sqrt{\zeta^2 - h^2} \cdot \sqrt{\zeta^2 - k^2} - \frac{\zeta^2}{2} \cdot \frac{\sqrt{\zeta^2 - k^2}}{\sqrt{\zeta^2 - h^2}} - \frac{\zeta^2}{2} \cdot \frac{\sqrt{\zeta^2 - h^2}}{\sqrt{\zeta^2 - k^2}} \right]$		
	$\psi(x, t) := \text{atan} \left(\frac{t - c \cdot x}{\tau} \right)$	$K := \frac{-k^2 \cdot \alpha_1}{F(\chi)}$	$H := \frac{-\chi \cdot (2 \cdot \chi^2 - k^2 - 2 \cdot \alpha_1 \cdot \beta_1)}{F(\chi)}$
Source function:	$Q(t) := \frac{Q_{bar}}{\pi} \cdot \frac{\tau}{t^2 + \tau^2}$	Delay := 750 Δt	$q_1 := Q(t_1 - \text{Delay})$
Vertical surface displacement far from source:	$u3_0(x, t) := \frac{K \cdot Q_{bar} \cdot c}{4 \cdot \pi \cdot G \cdot \tau^2} \cdot \sqrt{\frac{2 \cdot \tau}{c \cdot x}} \cdot \cos \left(\frac{\pi}{4} - \frac{3}{2} \cdot v(x, t) \right) \cdot \cos(v(x, t))^{\frac{3}{2}}$		
Horizontal surface displacement far from source:	$u1_0(x, t) := \frac{-H \cdot Q_{bar} \cdot c}{4 \cdot \pi \cdot G \cdot \tau^2} \cdot \sqrt{\frac{2 \cdot \tau}{c \cdot x}} \cdot \sin \left(\frac{\pi}{4} - \frac{3}{2} \cdot v(x, t) \right) \cdot \cos(v(x, t))^{\frac{3}{2}}$		

The aspects to consider when using the calculation scheme in Table 5-4 are related with the proper definition of material properties, frequency content factor for the source, and the dynamic time delay. A sample of the results obtained when using the analytical solution to calculate the vertical and horizontal displacement of the surface on a point away from the source, presented in Fig. 5-3.

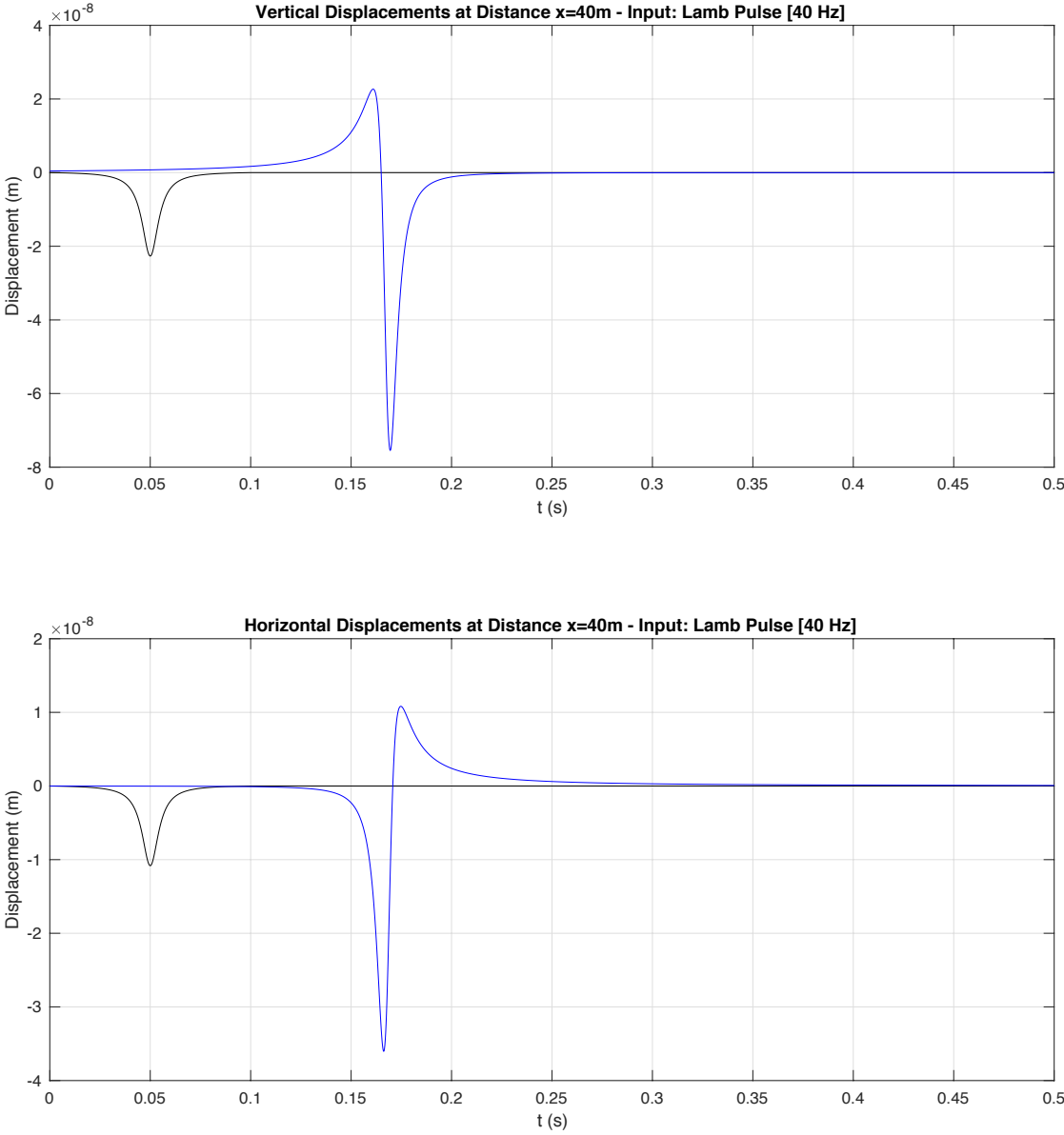


Fig. 5-3: Vertical and horizontal displacements at 40 meters from source, obtained with the analytical solution

For the damping selection a very low value was chosen, in this case 2% damping was applied at the central frequency of the input force.

The software to use for the numerical simulations is FLACTM version 2D, which is a two-dimensional explicit finite difference program for engineering mechanics computation, based on a Lagrangian calculation scheme (i.e. by calculating the difference of the kinetic and potential energies for a system at every time step). “This program simulates the behavior of structures built of soil, rock or other materials that may undergo plastic flow when their yield limits are reached”. (Itasca, 2000)

5.3 Numerical study of waves propagation in a horizontally layered medium

A hypothetical layered medium was used to evaluate the potential problems of using wave propagation based techniques to characterize soft to very soft soils. A soil profile was defined to involve all the soil types defined in the National Building Code of Canada (NRC, 2005). The issue emerges when the difference in acoustic impedance between adjacent materials is too high, to the point that the seismic waves get trapped in the soft layer and do not penetrate to allow the characterisation of the complete soil profile.

5.3.1 Model definition

An initial numerical model is defined to include six layers horizontally distributed. The materials' properties in the layers of the model were defined in such a way that they included different geomaterials ranging from soft soils to soft rock. The Poisson's ratio (ν) values were selected in such a way that it was guaranteed the elastic properties corresponded to partially saturated materials. Fig. 5-4 show the variation of wave velocities with respect to the Poisson's ratio. P-wave and R-wave velocities are normalized by S-wave velocity.

The impedance (Z) was calculated for shear waves and the impedance ratio was then calculated between adjacent layers.

$$I_z = \frac{Z_i}{Z_{i+1}} \quad (5-3)$$

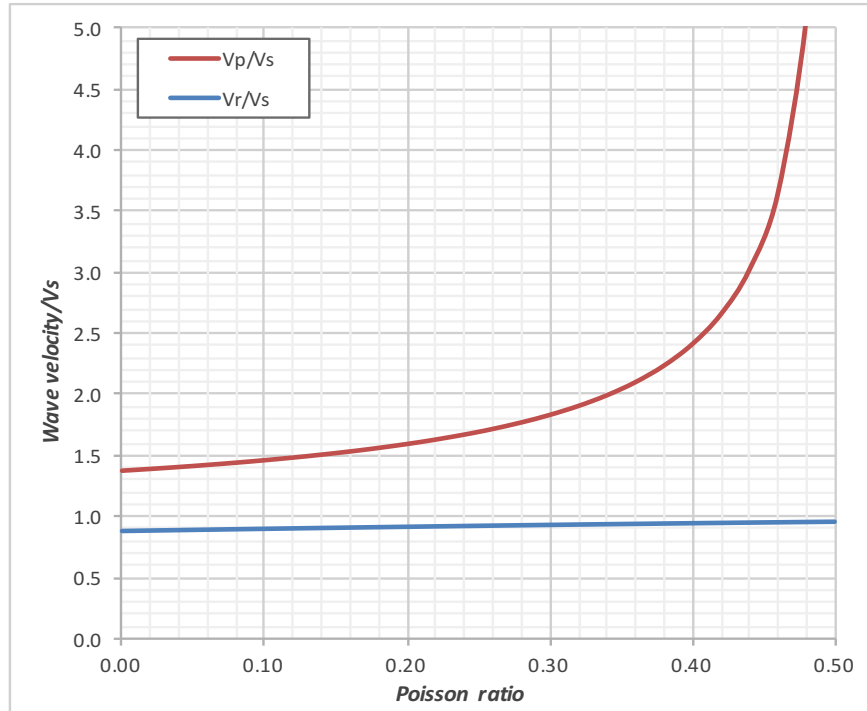


Fig. 5-4: Normalized wave velocity vs. Poisson's ratio

Geotechnical and dynamic properties of the geomaterials involved in the initial numerical model are presented in Table 5-5.

Table 5-5. Properties of materials in the initial numerical model

Layer (i)	ρ (Kg/m ³)	v_s (m/s)	ν	G (MPa)	K (MPa)	Z (MRayl)	I_z
1	2000	240	0.45	115.2	1113.6	0.48	0.78
2	2050	300	0.45	184.5	1783.5	0.62	0.81
3	2100	360	0.45	272.2	2630.9	0.76	0.84
4	2150	420	0.45	379.3	3666.2	0.90	0.86
5	2200	480	0.45	506.7	4899.8	1.06	0.87
6	2250	540	0.45	656.1	6342.3	1.22	0.81
7	2500	600	0.45	900.0	8700.0	1.50	--

A sketch of the geometry of the initial model is presented in Fig. 5-5, while the modified model is presented in Fig. 5-6. The wave propagation process was simulated by using an axisymmetric model and the input force was applied at the axis of symmetry.

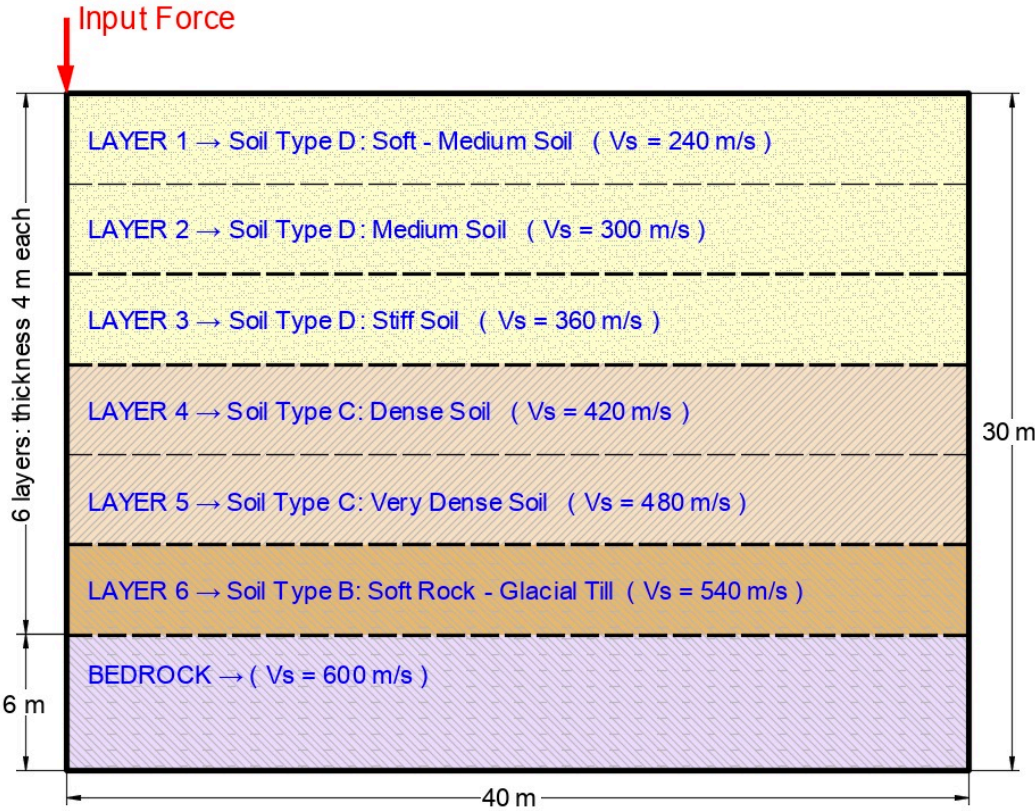


Fig. 5-5: Initial model for the numerical simulations of wave propagation in a hypothetical layered medium (after Díaz-Durán et al., 2018a)

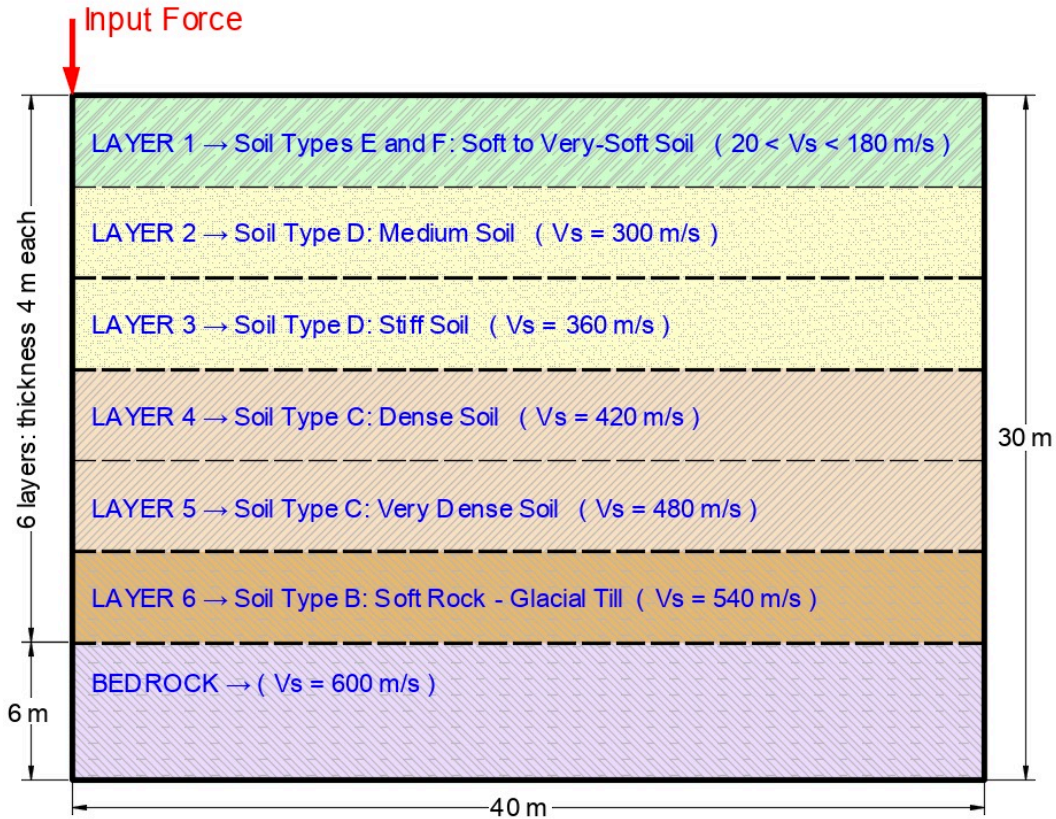


Fig. 5-6: Modified model for the numerical simulations (after Díaz-Durán et al., 2018a)

Lamb and sine pulses were used as input force. In order to generate different wavelengths in the material, different frequencies in the input force were used. At the end, Sine pulse was preferred over the Lamb pulse because the aforementioned better concentrates the energy at lower frequencies, which makes it more effective in penetrating the subsoil. In addition, the sine pulse allows a clear identification of the central frequency applied in the input force.

Once the initial model was run, the top layer was replaced by soft and very-soft materials which created impedance ratios between the first two layers ranging from 0.04 to 0.56 (see Table 5-6).

Table 5-6. Properties of soft to very soft soils in layer 1 of the numerical models

Soils in Layer 1	ρ (Kg/m ³)	v_s (m/s)	ν	G (MPa)	K (MPa)	Z (MRayl)	$I_z = \frac{Z_1}{Z_2}$
I	1100	20	0.499	0.44	1833.3	0.02	0.04
II	1200	40	0.499	1.92	1742.4	0.05	0.08
III	1300	60	0.498	4.68	1416.2	0.08	0.13
IV	1400	80	0.496	8.96	1117.5	0.11	0.18
V	1500	100	0.491	14.99	827.8	0.15	0.24
VI	1600	120	0.484	23.04	690.4	0.19	0.31
VII	1700	140	0.476	33.33	674.7	0.24	0.39
VIII	1800	160	0.465	46.10	643.2	0.29	0.47
IX	1900	180	0.452	61.58	627.7	0.34	0.56

As a result, in addition to the initial model nine more models were run, which allowed the analysis of the effect of variation of impedance of shear waves.

Very soft soils are the typical materials in wetlands, marshes and peats, which are very common in many regions of North America like northern Ontario (Canada). However, from the literature review, not too many studies reporting the geotechnical characterization of very-soft soils were found. For the dynamic properties it was even worst, because just one paper reporting characterization of very-soft materials in the laboratory was found; few papers are reporting correlation for dynamic properties and results of field tests like CPT.

5.3.2 Accuracy of the results for shear wave velocity inversion

To evaluate the accuracy of the models, waves velocities were measured in the travel-time curve and compared against the theoretical ones. In this case errors were defined as the difference between the theoretical velocities and the measured values. As a result, it can be said the errors are in most cases less than 1%, which is a good result showing the calibration of the model is highly reliable.

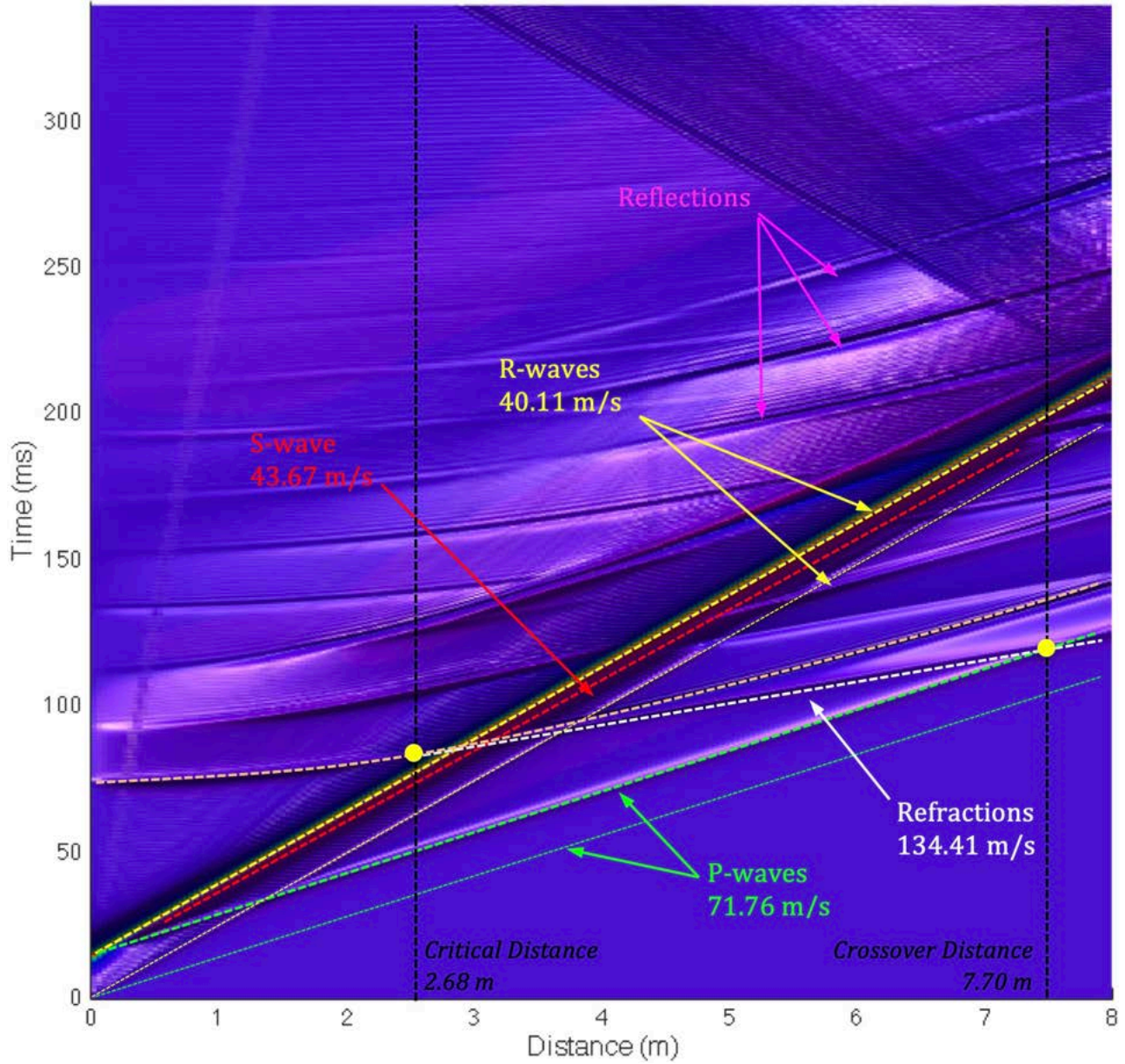


Fig. 5-7: Example of identification of seismic waves by using a travel-time plot for a model with impedance ratio $I_z = 0.10$.

Energy scattering in the numerical models simulating MASW tests could be analyzed in the Frequency vs. Wave Number spectrum (see right part of Fig. 5-8). From the results in the Frequency vs. Wave Number spectrum, the dispersion curve of Rayleigh wave velocity could be extracted.

From the dispersion curve an inversion process could be followed in order to get the shear wave velocity profile. An example of that dispersion curve is presented in the left part of Fig. 5-8.

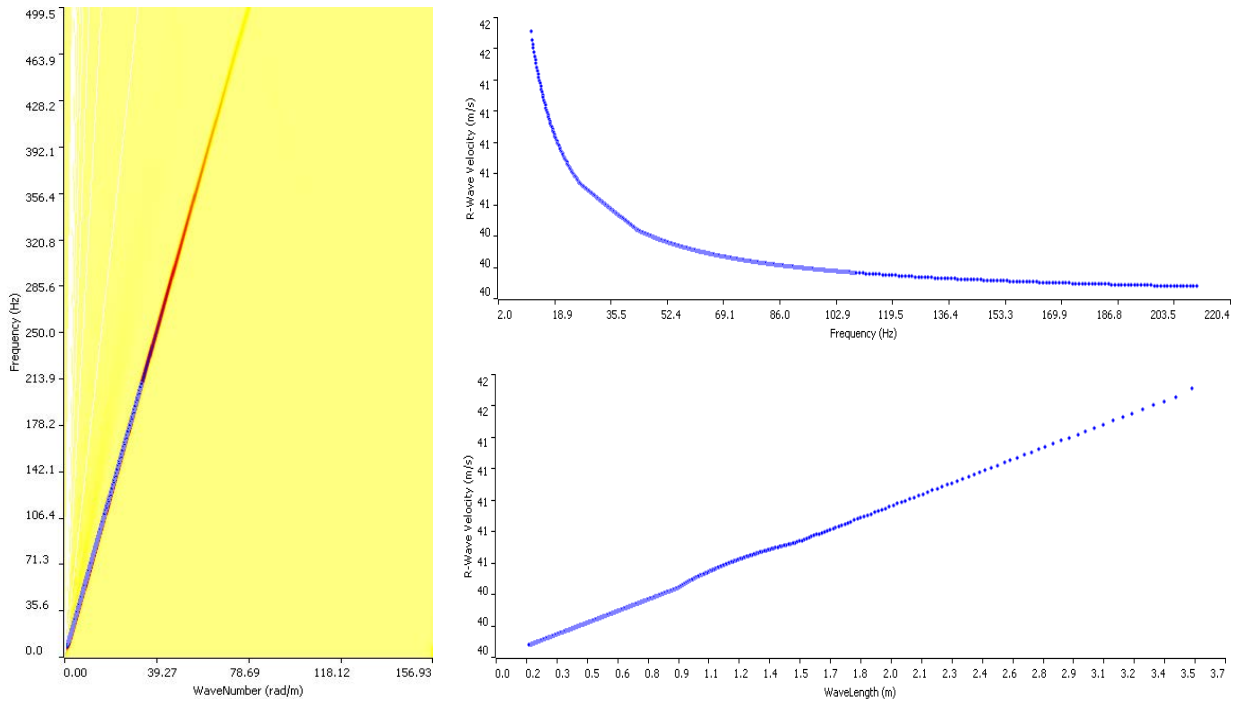


Fig. 5-8: F-K spectrum for a model with impedance ratio $I_z = 0.10$.

Root mean square error (RMSE) values between dispersion curves obtained from the numerical simulations and the theoretical dispersion curve were calculated when the spacing between adjacent channels was modified. From results presented in Table 5-7, it could be concluded that when the spacing between channels is 1.0 meter the RMSE value is the lowest one for most of the models.

Table 5-7. RMSE of dispersion curve for MASW models simulated with different spacing between channels (transducers). Input force was a sine pulse ($f_M=20\text{Hz}$).

Model	$I_z = \frac{Z_1}{Z_2}$	dx=0.6 (m)	dx=1.0 (m)	dx=2.0 (m)	dx=4.0 (m)	dx=8.0 (m)
Initial	0.78	3.53	3.97	3.98	4.01	4.85
IX	0.56	2.58	6.65	3.04	2.95	3.80
VIII	0.47	1.00	0.81	1.31	1.44	1.60
VII	0.39	0.89	0.78	0.79	1.12	1.15
VI	0.31	0.95	0.53	1.49	1.62	1.36
V	0.24	0.37	0.33	0.42	0.42	0.69
IV	0.18	0.56	0.65	0.80	0.97	1.51
III	0.13	1.97	1.90	2.05	2.59	2.38
II	0.08	2.44	2.46	2.92	3.40	3.36
I	0.04	2.97	--	3.30	3.25	5.15

In a similar way, RMSE values between dispersion curves obtained from the numerical simulations and the theoretical dispersion curve were calculated when the central frequency in the input force (sine pulse) was modified. From results presented in Table 5-7, it is concluded that for soft soils with impedance ratio between the two top layers $I_z > 0.15$, frequencies higher than 20 Hz in the input source will result in lower values for RMSE. On the other hand, for very-soft soils with impedance ratio between the two top layers $I_z < 0.15$, frequencies less than 20 Hz will result in higher values of RMSE.

Table 5-8. RMSE of dispersion curve for MASW models simulated with different frequencies in the input force (sine pulse). Spacing between channels was $dx=1.0\text{m}$.

Model	$I_z = \frac{Z_1}{Z_2}$	f = 5 (Hz)	f = 10 (Hz)	f = 20 (Hz)	f = 40 (Hz)
Initial	0.78	5.02	5.93	3.97	7.25
IX	0.56	3.37	9.11	6.65	1.89
VIII	0.47	2.17	8.26	0.81	0.85
VII	0.39	1.26	2.80	0.78	0.58
VI	0.31	6.04	2.28	0.53	1.26
V	0.24	5.29	2.18	0.33	1.84
IV	0.18	4.61	1.95	0.65	1.41
III	0.13	4.14	0.58	1.90	3.68
II	0.08	1.75	0.67	2.46	3.58
I	0.04	1.15	1.48	--	4.09

5.3.3 Evaluation of the results for v_{s-30}

The v_{s-30} is a parameter widely used for site characterization when a seismic design is needed. By analyzing the dispersion curves and performing the inversion of the soil profile of shear wave velocity, it is possible to calculate the values for the average shear wave velocity in the shallower 30 meters of a soil profile. If MASW is performed to obtain a soil v_s profile and the v_{s-30} value, the results show to be affected by the impedance ratio between materials in the two top layers. From results presented in Table 5-8, it could be concluded that the frequency in the input source actually has also an impact in the results.

The calculation of the v_{s-30} was done following the “Method 1” and “Method 2” explained in chapter 3 (see Equation 3-1 and Equation 3-2). Average shear wave velocity for the shallower 30 meters are presented in Table 5-9 for “Method 1” for different input frequencies and impedance ratios. Similar results obtained following “Method 2” are presented in Table 5-10. Each colored cell in this table corresponds to the result of the calculation for the v_{s-30} for the profile obtained from the inversion of the dispersion curve coming from one individual numerical simulation of the MASW test. Each simulation considers a model with one specific impedance ratio between the first two layers, and one specific central frequency in the input force.

The colored convention is explained here: Green colored cells correspond to the models allowing the resolution of four layers in the inversion process of the v_s profile; Yellow cells three layers; Orange cells two layers; and Red only one layer, thus, the MASW is ineffective in resolving the subsoil profile no matter what frequency is used in the input force.

A contour plot of the results of v_{s-30} following “Method 1” for different central frequencies in the input force and for different impedance ratios for the first two layers, is presented in Fig. 5-9. Similar results of v_{s-30} obtained following “Method 2” are presented in Fig. 5-11.

Table 5-9. Average shear wave velocity for the shallower 30 meters (v_{s-30} in m/s) following “Method 1”. Spacing between channels was $dx=1.0m$.

Model	$v_{s-Layer 1}$ (m/s)	$v_{s-30 (Real)}$ (m/s)	$I_z = \frac{Z_1}{Z_2}$	v_{s-30} for different Input Frequency (Hz)				Resolved Layers		
				5	10	20	40			
Initial	240	432	0.78	450	438	430	430	4		
IX	180	380	0.56	445	425	420	410		3	
VIII	160	421	0.47	440	420	380	370			2
VII	140	419	0.39	420	410	320	310			
VI	120	416	0.31	390	380	250	240	2		
V	100	413	0.24	340	290	200	190			
IV	80	411	0.18	280	230	180	180	1		
III	60	408	0.13	200	130	140	150			
II	40	405	0.08	120	90	90	90			
I	20	403	0.04	40	45	40	30			

Table 5-10. Average shear wave velocity for the shallower 30 meters (v_{s-30} in m/s) following “Method 2”. Spacing between channels was $dx=1.0m$.

Model	$v_{s-Layer 1}$ (m/s)	$v_{s-30 (Real)}$ (m/s)	$I_z = \frac{Z_1}{Z_2}$	v_{s-30} for different Input Frequency (Hz)				Resolved Layers		
				5	10	20	40			
Initial	240	393	0.78	409	398	391	391	4		
IX	180	334	0.56	384	367	363	354		3	
VIII	160	354	0.47	370	353	319	311			2
VII	140	340	0.39	341	333	260	252			
VI	120	322	0.31	302	295	194	186	2		
V	100	301	0.24	247	211	162	154			
IV	80	273	0.18	186	178	151	151	1		
III	60	237	0.13	146	106	121	130			
II	40	188	0.08	120	76	82	82			
I	20	116	0.04	35	39	35	26			

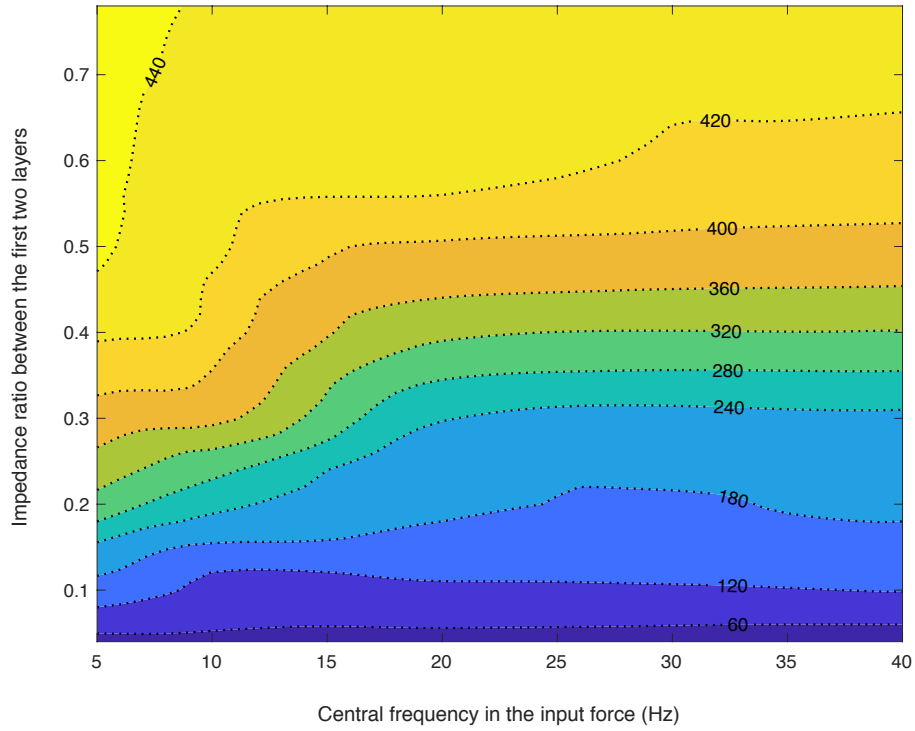


Fig. 5-9: Contours of shear wave velocity (v_{s-30} in m/s) following “Method 1”

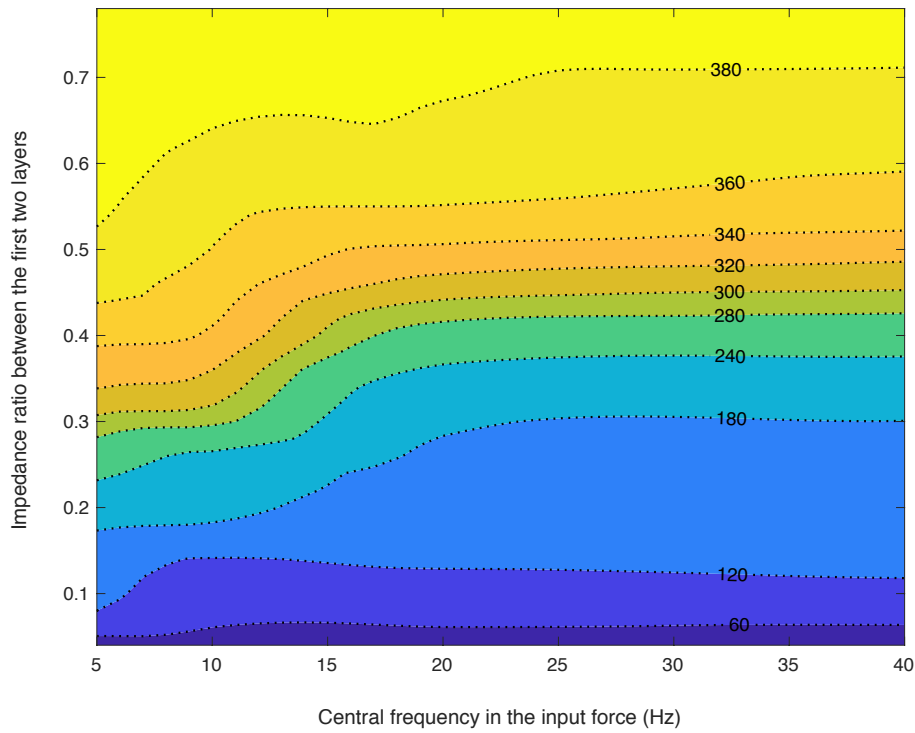


Fig. 5-10: Contours of shear wave velocity (v_{s-30} in m/s) following “Method 2”

The Table 5-11 presents the results of calculations of the theoretical v_{s-30} values for the ten numerical models simulated when materials in layer 1 are modified to change the impedance ratio (I_z). The calculations of fundamental period (T_0), and fundamental frequency (f_0) for the top layer are also presented as a reference.

Table 5-11. Theoretical values of shear wave velocity (v_{s-30}) for the ten models simulated with different impedance ratio between the two top layers

Material properties for Layer #1						Method 1	Method 2
Soil Type	Soil Class	v_s (m/s)	H (m)	T_0 (s)	f_0 (Hz)	v_{s-30} (m/s)	v_{s-30} (m/s)
F	I	20	4	0.800	1.25	402.7	115.5
	II	40	4	0.400	2.50	405.3	187.8
	III	60	4	0.267	3.75	408.0	237.4
	IV	80	4	0.200	5.00	410.7	273.5
E	V	100	4	0.160	6.25	413.3	300.9
	VI	120	4	0.133	7.50	416.0	322.4
	VII	140	4	0.114	8.75	418.7	339.8
	VIII	160	4	0.100	10.00	421.3	354.2
	IX	180	4	0.089	11.25	424.0	366.2
D	1	240	4	0.067	15.00	432.0	392.8

A large difference is obtained for the results between the two methods followed for the calculation of v_{s-30} . However, for both methods it has been identified there is an effect of the impedance ratio on the results of v_{s-30} . A contour plot of the results of normalized v_{s-30} following “Method 1” for different central frequencies in the input force and for different impedance ratios for the first two layers, is presented in Fig. 5-11. Similar results of normalized v_{s-30} obtained following “Method 2” are presented in Fig. 5-12.

When the v_{s-30} is normalized, it is easier to identify the threshold of impedance ratio for which a reduction in the estimated value of v_{s-30} could be considered relevant. By visual inspection of Fig. 5-11 and Fig. 5-12, it is clear that values of the impedance ratio lower than 0.5 lead to an underestimation of the average shear wave velocity v_{s-30} in the soil profile.

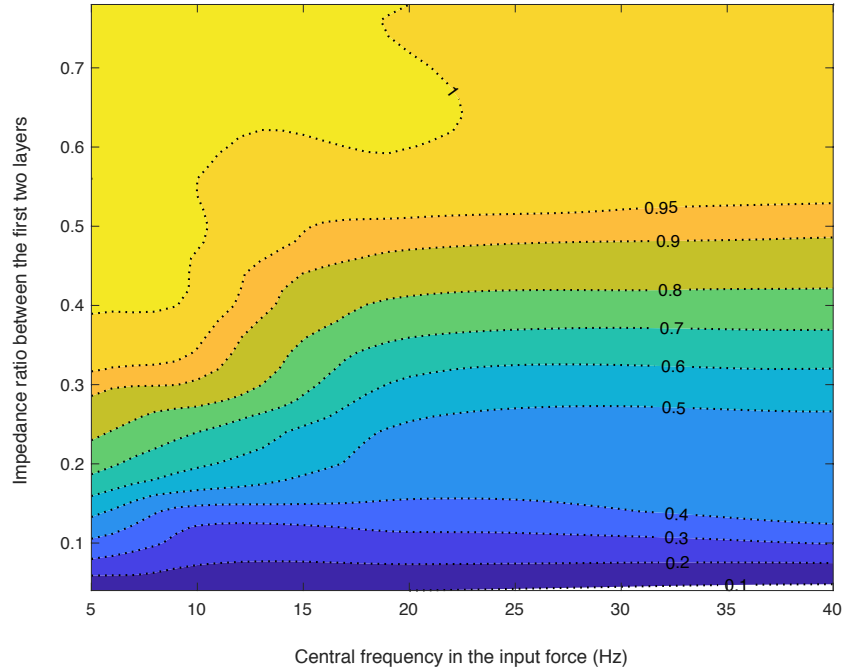


Fig. 5-11. Contours of normalized v_{s-30} (m/s) for different central frequencies in the input force and different impedance ratios for the first two layers. (“Method 1”)

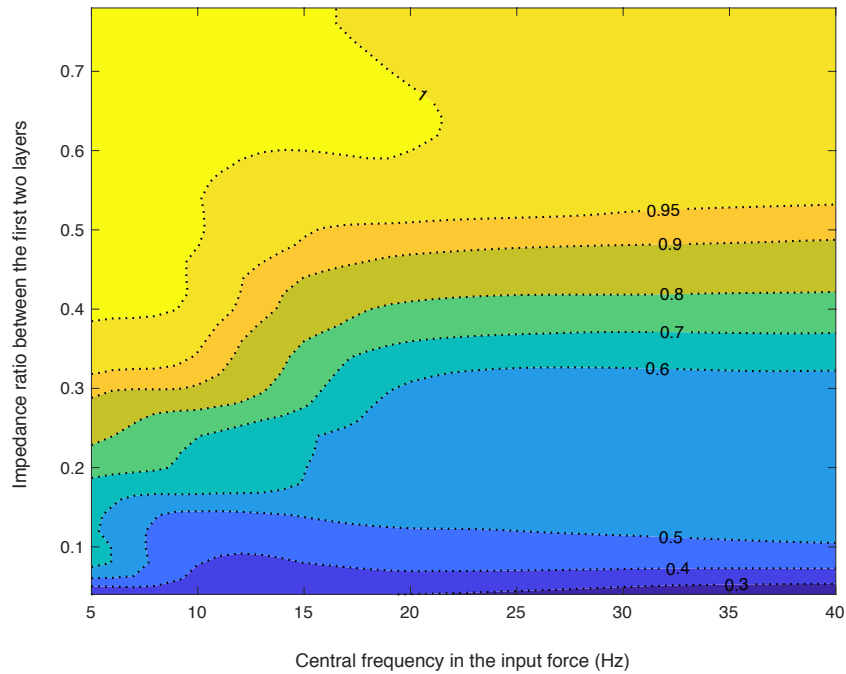


Fig. 5-12. Contours of normalized v_{s-30} (m/s) for different central frequencies in the input force and different impedance ratios for the first two layers. (“Method 2”)

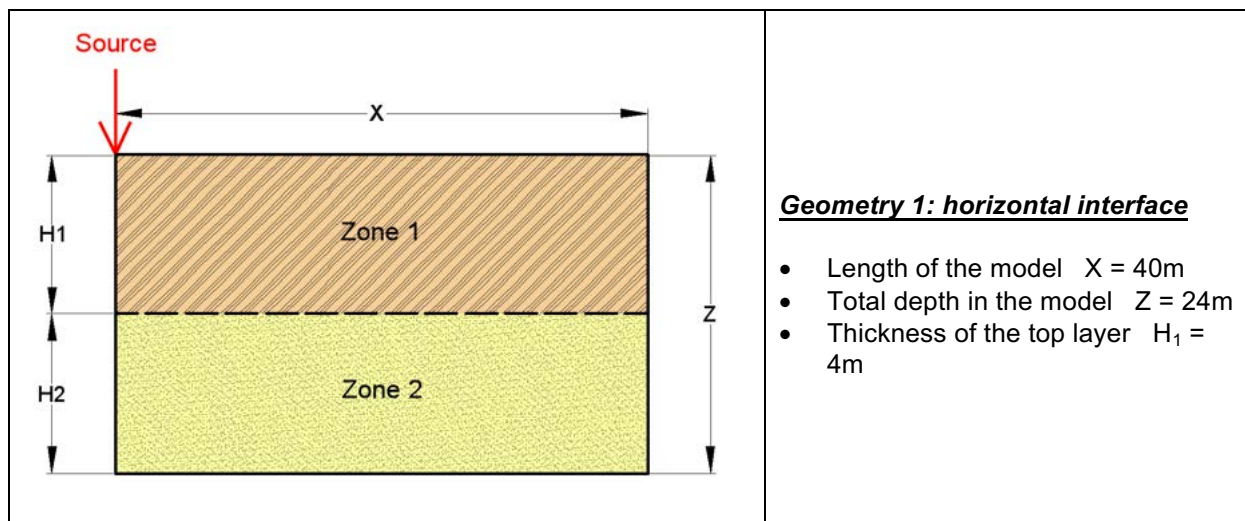
5.4 Numerical study of wave propagation in a non-horizontally layered medium

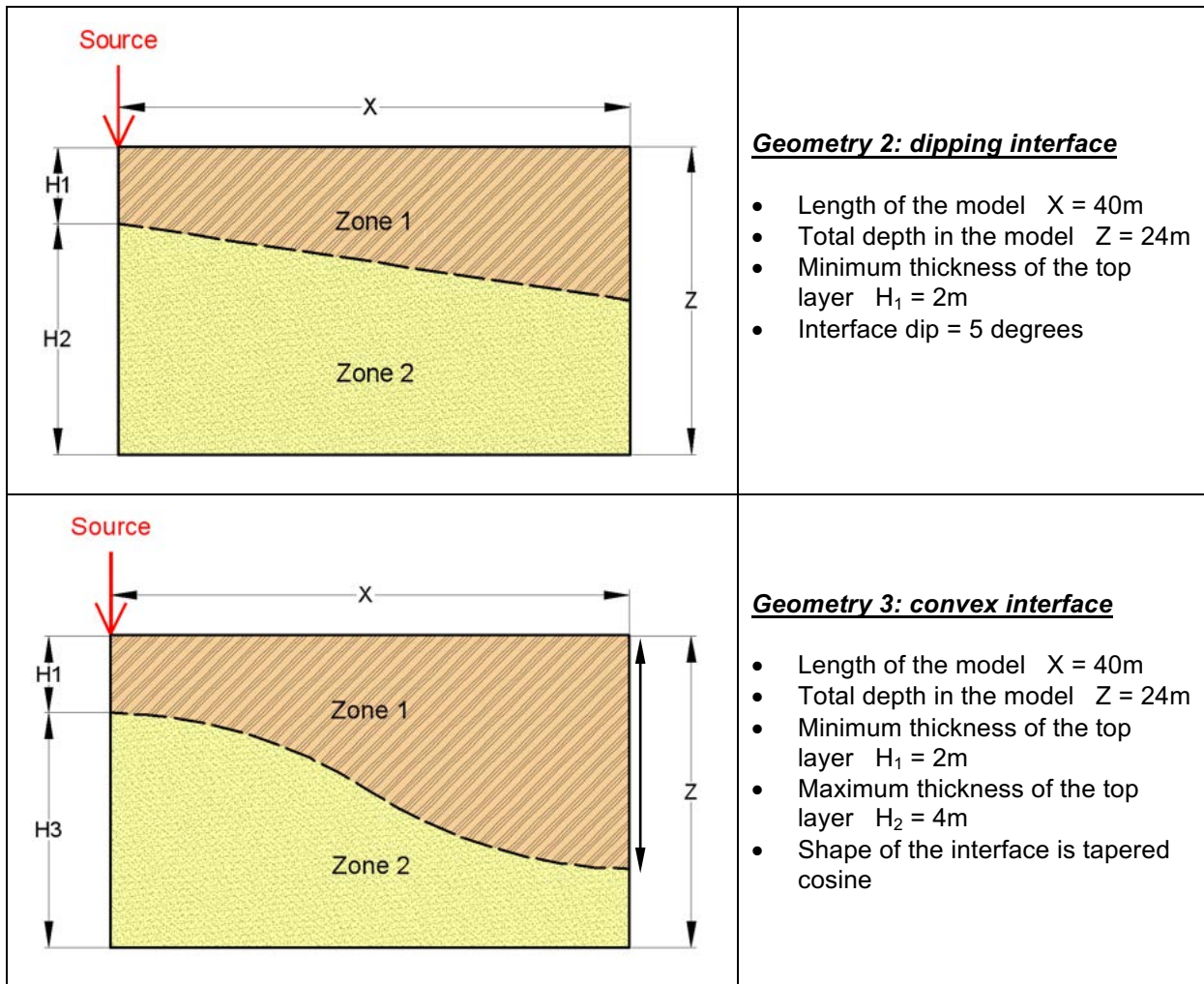
Factors other than impedance ratio actually affect wave propagation; for instance, Poisson's ratio, frequency content of the input source, damping, and the shape of the interface. In this numeral a preliminary study of the effect of some of these factors in the F-K results is presented. The analysis now it is confined to the two top layers and the interface between them. The material in the second-top layer is always a soil classified as type D, and class 1. The material in the top layer could be any of the nine geomaterials corresponding to the type E (soil classes V, VI, VII, VIII, and IX) and F (soil classes I, II, III, and IV), which properties were presented in Table 5-5 and Table 5-6.

5.4.1 Geometry definition for the numerical simulation

Three different geometries are considered for this simulations and the same materials defined in the previous section are used in this numerical models.

Table 5-12. Schematic geometries of the models to study the effect of the shape in the interface between the first two layers.





5.4.2 Effect of changes in impedance ratio for models with dipping interfaces

The effect of impedance ratio was widely studied in the previous section of this chapter. However, that study only considered a horizontal interface between materials. Variations in the impedance ratio also show an effect in the F-K spectrum when the interface is other than horizontal, some results are presented in Fig. 5-13. In those results the effect of reduction in the impedance ratio is presented for the models with dipping interfaces at 5° . From the F-K spectrums it could be concluded that the lower the impedance ratio, the larger the amount of energy spread due to the reflections along the P-wave.

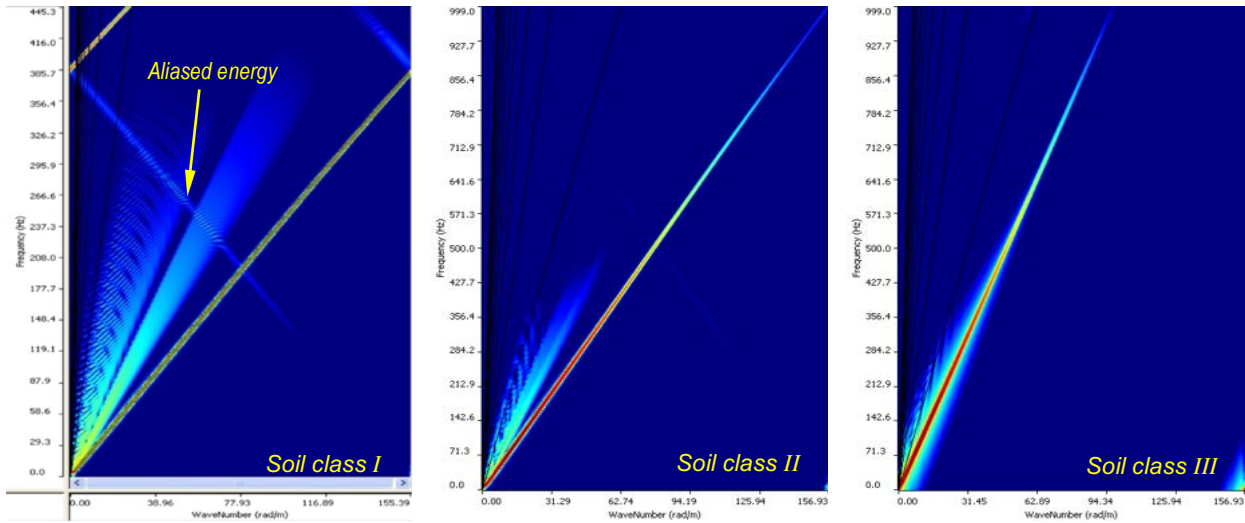


Fig. 5-13. Models with a 5° dipping interface: effect of reduction in the impedance ratio.

5.4.3 Effect of changes in the shape of interfaces

Three interfaces were considered for the numerical simulation of wave propagation. Models with different interfaces show different results in the F-K spectrum. Some selected results of F-K spectra for different interfaces are presented in Fig. 5-14. From the F-K spectra, it could be seen that dipping and concave interfaces do not show too much energy spread along the P-wave alignment, as the model with horizontal interface does.

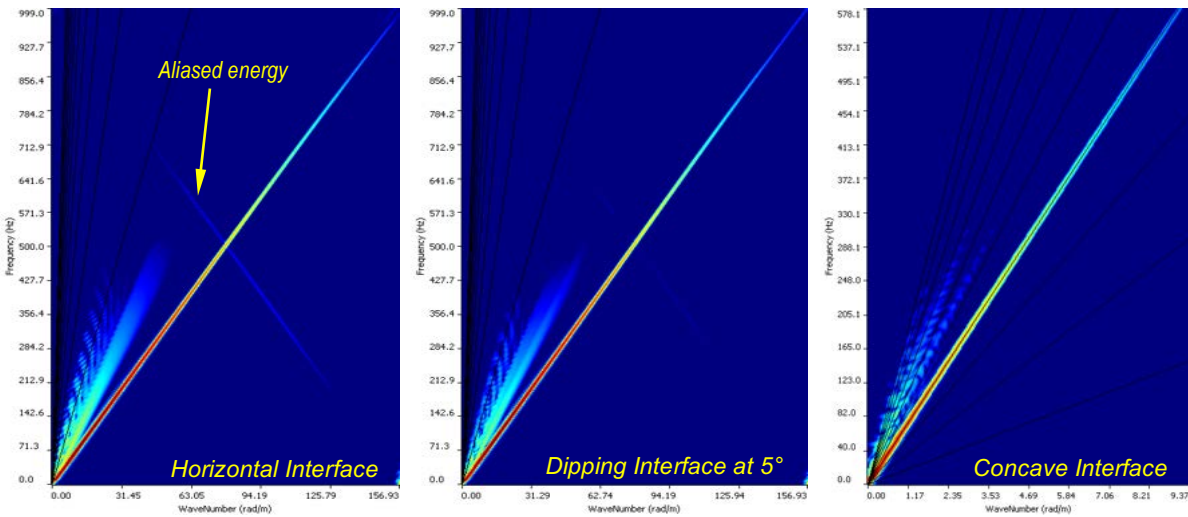


Fig. 5-14. Models with soil class II in top layer: effect of changes in the interface shape.

5.4.4 Effect of changes in Poisson's ratio

Factors other than impedance ratio actually affect wave propagation; for instance, Poisson's ratio. Variations in Poisson's ratio are analyzed for different combinations of material in the top two layers. The value of Poisson's ratio was modified in the materials in the top layer. Three values were selected in the range from 0.2 to 0.4, which covers the cases of sand and clays.

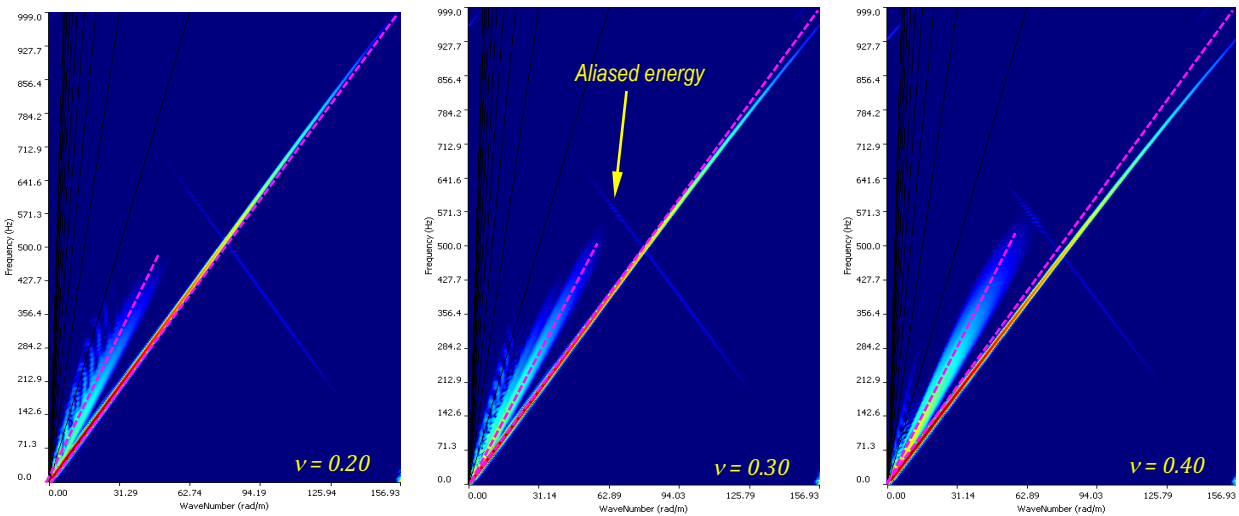


Fig. 5-15. Model with horizontal interface, soil in top layer was type F, class II: effect of Poisson's ratio in the F-K spectrum.

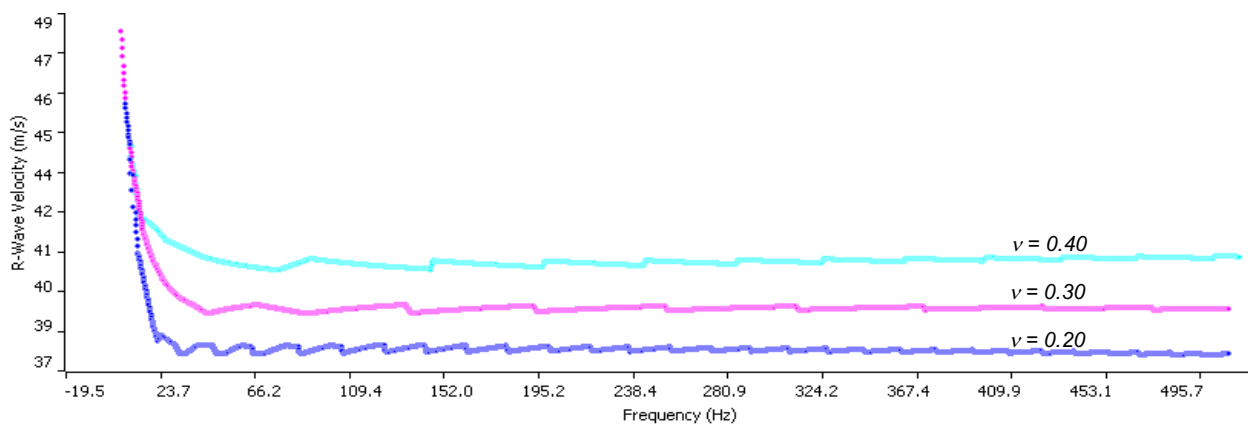


Fig. 5-16. Model with horizontal interface, soil in top layer was type F, class II: effect of Poisson's ratio in the dispersion curves.

From these plots is evident that any increment in Poisson’s ratio is generating an increment in wave velocity, which was expected. However, it is also clear that the higher the Poisson’s ratio, the higher the spreading of energy around the P-wave. Another effect is the curvature in the F-K energy concentration for high frequencies, which could be also understood as a dispersion effect for frequencies above 400 Hz.

5.4.5 Effect of changes in frequency content

The frequency content parameter is included in the Lamb source function (see Table 5-4). The modification of the parameter results in a modification of the shape of the Lamb source pulse in the time domain, which has also an effect on the frequency domain. Models with three different frequency content parameters were run to simulate the wave propagation phenomena. From Fig. 5-17 and Fig. 5-18 it is evident that any increment in parameter ϕ of Lamb force is creating a modification in frequency distribution in the FK Spectrum. The higher the parameter, the most concentrated the energy on lower frequencies. Furthermore, the lowest frequency content parameter also generates a higher amount of energy spreading along the P-wave, which could also be assimilated to multiples reflections.

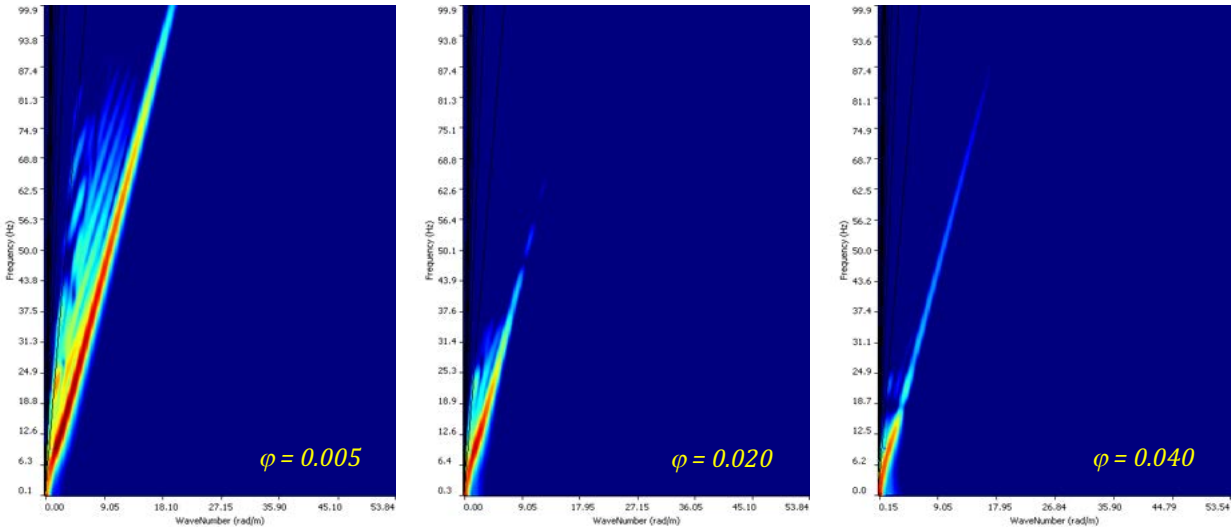


Fig. 5-17. Model with horizontal interface, soil in top layer was type F, class II: effect of frequency content in the F-K spectrum.

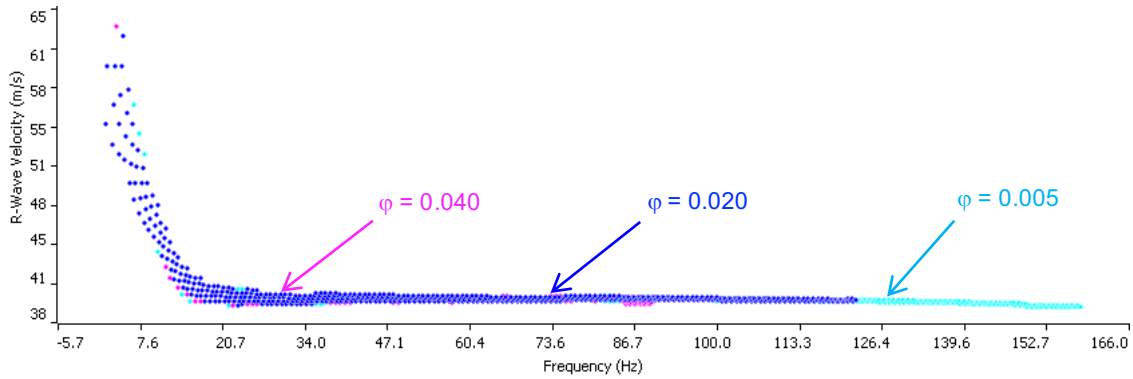


Fig. 5-18. Model with horizontal interface, soil in top layer was type F, class II: effect of frequency content in the dispersion curves.

5.4.6 Damping effect on the FK spectrum

Analysis of damping was also included in parametric study. FLACTM requires the definition of damping as Rayleigh damping, which includes mass and stiffness damping. To define those parameters some models were run with different values of damping and different frequencies. The conclusion is that the damping ratio must be variable depending on impedance ratio, so that the lower the latter, the higher the damping ratio needed to reduce the spreading of energy around the P-wave velocity in the FK spectrum.

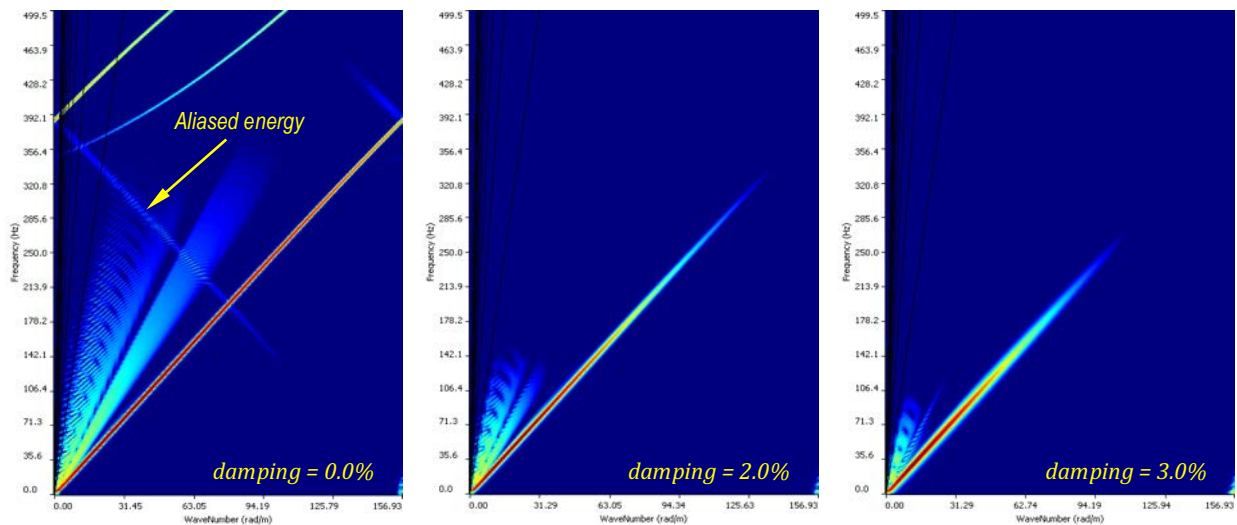


Fig. 5-19. Model with horizontal interface, soil in top layer was type F, class II: effect of damping increment in the F-K spectrum.

5.5 Conclusions

The results from the study of wave propagation on a horizontally layered medium led to the following conclusions:

- The higher the frequency in the input force, the lower the number of layers that can be obtained in a mathematical inversion process of the dispersion curve obtained from the MASW test.
- Impedance ratio between the two top layers with values lower than 0.5 showed reductions in the estimated value of the weighted average shear wave velocity. For instance, for impedance ratio values of 0.4 a reduction up to 20% in the average shear wave velocity were identified. Similarly, for impedance ratio values of 0.3 that reduction could be even higher up to 40% in the average shear wave velocity. Finally, for impedance ratio values of 0.2 the reduction in the average shear wave velocity could led to get values as low as 45% of the theoretical expected shear wave value.
- For frequencies above 15 Hz it could be concluded that impedance ratios about 0.5 are the minimum value required in order to properly obtain a v_{s-30} value for site characterization when using MASW test results to invert a soil profile of shear wave velocities.
- The frequency content in the input force also exhibited an effect in the weighted average of the shear wave velocity, as per mean frequencies below 15 Hz the threshold value for the impedance ratio gets reduced from 0.5 to 0.3, Thus, as long as the input frequency is less than 15 Hz it is possible to use the MASW technique in sites where the top layers have an impedance ratio of 0.3 or more.
- The spacing between channels has effect on the results of dispersion curves. For the model considered in this numerical study a spacing of 1.0 meter between channels leads to the lowest values of root mean square error (RMSE).

The results from the study of wave propagation on a non-horizontally layered medium led to the following conclusions:

- From the parametric study was evident that any increment in Poisson's ratio generated an increment in wave velocity. Furthermore, it can be concluded that the higher the Poisson's ratio, the higher the spreading of energy around the P-wave
- Interfaces other than the horizontal one exhibit lower spreading of energy around the P-wave
- About the frequency content, lower values of the mean input frequency generate a higher amount of energy spreading along the P-wave, which could also be assimilated to the multiples' reflections.
- The damping ratio must be variable depending on impedance ratio, so that the lower the latter, the higher the damping ratio needed to reduce the spreading of energy around the P-wave velocity in the FK spectrum.

6 Characterization of geomaterials at large scales: layered medium approach – field tests and numerical simulations

In this chapter, results from sCPT and MASW field test are used to define a soil profile in a real site, then for that profile, the numerical simulations are performed to characterize geomaterials at large scales. The main idea of the method is to focus on the analysis of some effects, in the results of site's characterization when seismic methods are used. Some of the effects analyzed are the changes in impedance ratio between adjacent layers, and the effect of the shape of the interface between layers, among others.

6.1 Detailed procedure

The detailed procedure followed in this chapter to characterize geomaterials at large scales involves only numerical simulations. The steps followed were:

1. sCPTU and MASW field tests
 - a. Test location
 - b. Soil profile from sCPTU tests
 - c. Soil profile from MASW tests
2. Numerical study of wave propagation
 - a. Analysis of a homogeneous medium
 - b. Analysis of a layered medium
 - c. Analysis of a spatially variable medium
3. Numerical study of frequency effects
 - a. Analysis of a homogeneous medium
 - b. Analysis of a layered medium
 - c. Analysis of a spatially variable medium

6.2 sCPTU and MASW field tests

Two different tests were performed in the field in order to obtain a characterization of the soil profile. Three seismic cone penetration tests with pore pressure measurement (sCPTU) were performed in order to characterize the material at some specific points of

the field, in addition, one line of multi-channel analysis of surface waves' tests (MASW) with different offset distances were performed to obtain a profile of shear wave velocities. The main goal of performing these near-surface geophysical seismic field tests was to obtain the soil profile of the shear wave velocity and a value for the v_{S-30} in a real site.

6.2.1 Location for the field testing

The field tests were performed in a geophysical testing place located close by the University of Waterloo South campus, as it is presented in Fig. 6-2. The testing place is located alongside the "Columbia lake" and the materials in the underground were expected to range from soft soils to medium-stiff soils in the shallower 30 meters.



Fig. 6-1: Field testing location

No samples were extracted from the soils in the testing place, thus, no laboratory tests were performed directly on these geomaterials and the only information available to characterize the soil profile is the one obtained from the near-surface geophysical seismic tests (sCPTU and MASW).

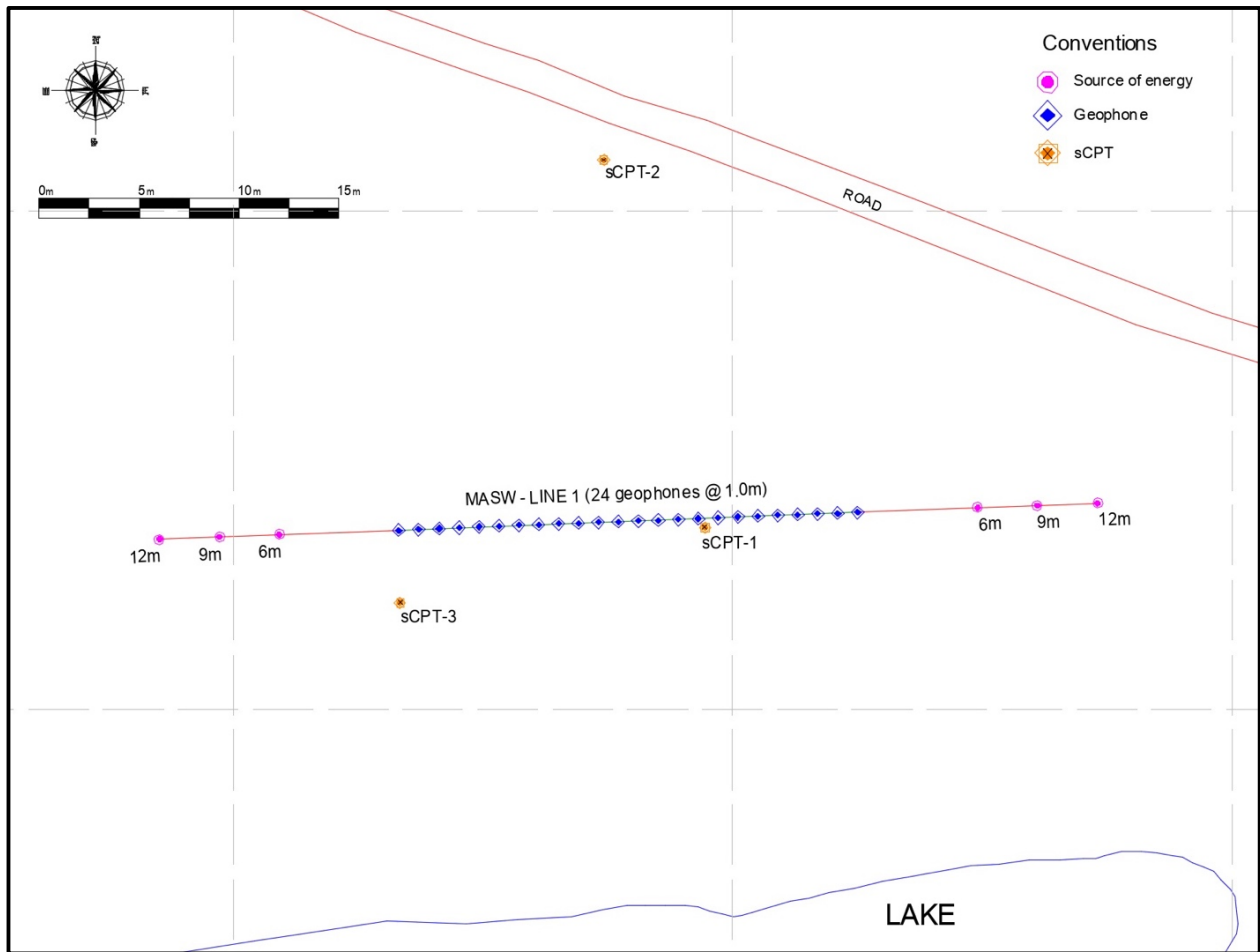


Fig. 6-2: Field setup for sCPTU and MASW tests

6.2.2 sCPTU tests

The first cone penetrometer test was performed in 1932, by then the cone was made using a 35 mm outside diameter gas pipe with a 15 mm steel inner push rod. In the following three decades some improvements were introduced to the cone test, among

them the modification of the cone geometry (i.e. Dutch cone in 1948) and the addition of the friction sleeve (i.e. adhesion jacket in 1953). In 1965 an electric driven cone was introduced, which highly improve the test reliability and formed the basis for the ASTM standard. Since then, many additional sensors have been added to the cone, among them piezometers and geophones or accelerometers are the most popular for geotechnical applications because they allow the measurement of pore pressure and seismic wave velocities, respectively (Robertson, 2015). A schematic of the seismic CPT (SCPT) procedure is shown Fig. 6-3.

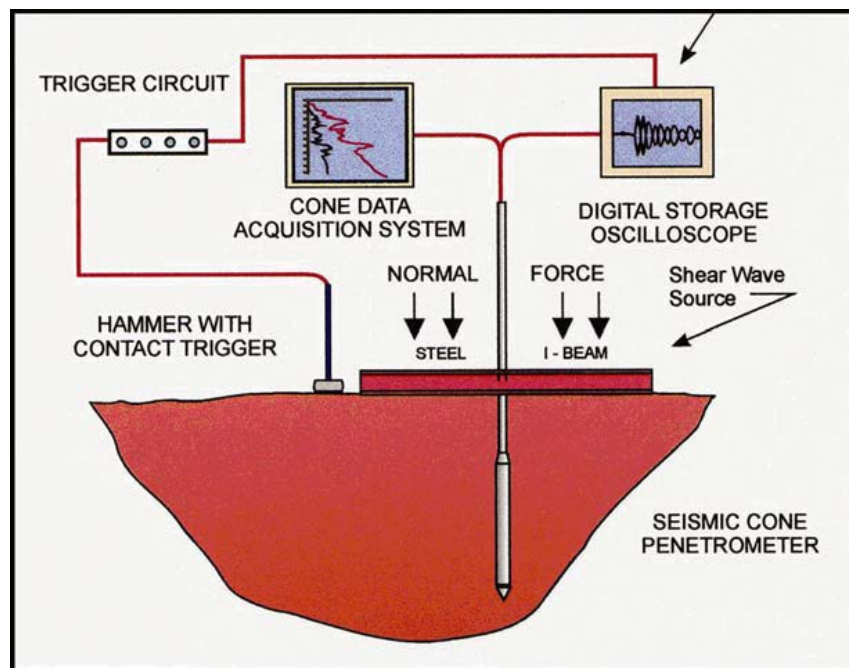


Fig. 6-3: Schematic of seismic CPT (SCPT) test procedure (Robertson, 2015)

The cone test and its variations have many considerations to be properly performed in the field, such as vertically control, rate of penetration, intervals of readings, calibration and maintenance, among others. Many of these considerations are addressed in the (ASTM D7400, 2017), others are presented in the documentation for the test procedure and interpretation by Robertson (2015).

The working principle for the cone penetration test, as it is presented by Robertson (2015), is quite simple. The total force acting on the cone (Q_C), divided by the projected area of the cone (A_C), produces the cone tip resistance (q_C). The total force acting on the friction sleeve (F_S), divided by the surface area of the friction sleeve (A_S), produces the sleeve resistance (f_S). The total cone resistance is $q_t = (q_C + f_S)$. In a piezocone, pore pressure is also measured, typically behind the cone in the (U_2) location, as shown in Fig. 6-3.

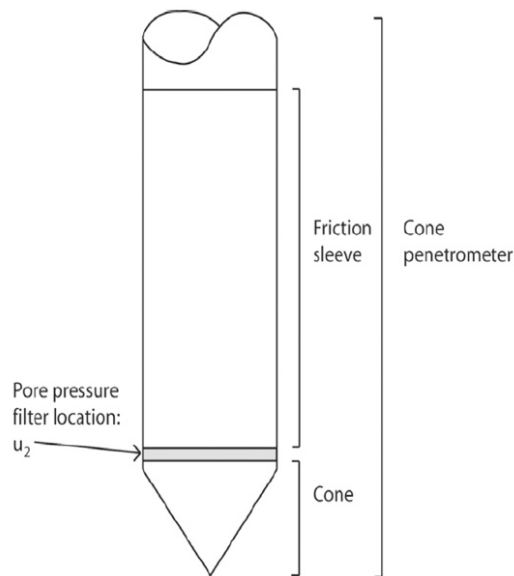


Fig. 6-4: Terminology for cone penetrometers (Robertson, 2015)

✓ CPTU: data acquisition in the field

Three different sCPTU tests were performed in order to obtain the tip resistance, the sleeve resistance, the pore pressure, and the shear wave velocity at some specific depths. The equipment used for these tests is shown in Fig. 6-6.



Fig. 6-5: Equipment used for the seismic cone penetration test (sCPTU)

The data obtained from the field was the cone tip resistance (q_c), the sleeve resistance (f_s), and the pore pressure (U). Typical baseline corrections were considered before and after the sounding. Because the tests sCPTU-1 was the closest one to the alignment of the MASW tests, that one was considered for the definition of the soil profile. The raw data obtained from these field tests are presented in Fig. 6-6 for the sCPTU-1, which went down up to a depth of 16 meters.

From these results and by using correlations it is possible to obtain a continuous profile of parameters such as elastic modulus (E), bulk modulus (K), shear modulus (G), and even the mass density (ρ). The Poisson's ratio value of 0.45 was selected to characterize these materials. The sCPTU equipment recorded values every centimeter of penetration, thus, in order to build a model from these data series, an average of each parameter was calculated every meter.

The total unit weight can be estimated from CPT results, such as the ones presented in Fig. 6-6 and the following relationship (Robertson, 2015):

$$\frac{\gamma}{\gamma_w} = 0.27 \left[\log \left(\frac{f_s}{q_t} \times 100 \right) \right] + 0.36 \left[\log \left(\frac{q_t}{p_a} \right) \right] + 1.236 \quad (6-1)$$

where (p_a) is the atmospheric pressure in same units of (q_t) .

The Young's modulus for non-cemented sands at low strains (0.1%) can be estimated by the following relationship (Robertson, 2015):

$$E = 0.015 \left[10^{(0.55 I_c + 1.68)} \right] \times (q_t - \sigma_{v_0}) \quad (6-2)$$

where (I_c) is the soil behavior type index (Robertson, 2015), and (σ_{v_0}) is the effective vertical stress. Finally, by adopting values for Poisson's ratio (ν) it is possible to obtain the shear modulus (G) and the bulk modulus (K).

$$G = \frac{E}{2(1+\nu)} \quad (6-3)$$

$$K = \frac{E}{3(1-2\nu)} \quad (6-4)$$

The results of these calculations are presented in Table 6-1. These values for elastic parameters were used in numerical models to carry out a preliminary set of numerical simulation of the wave propagation phenomena in a horizontally layered medium. It is important to keep in mind that the aforementioned strain level, at which the cone resistance was obtained, is about thousand times higher compared to the strain level generated in a typical seismic test. Thus, the elastic parameters obtained are not the proper ones to calculate the shear wave velocity value needed to characterize the site. Nonetheless, these preliminary simulations were useful to understand the effect of simplifying the characterization of a continuous medium by considering it as a horizontally layered medium.

Another use for these preliminary numerical models was the ability to simulate the relative effect on wave propagation when some sudden changes in the stiffness properties of a medium occur.

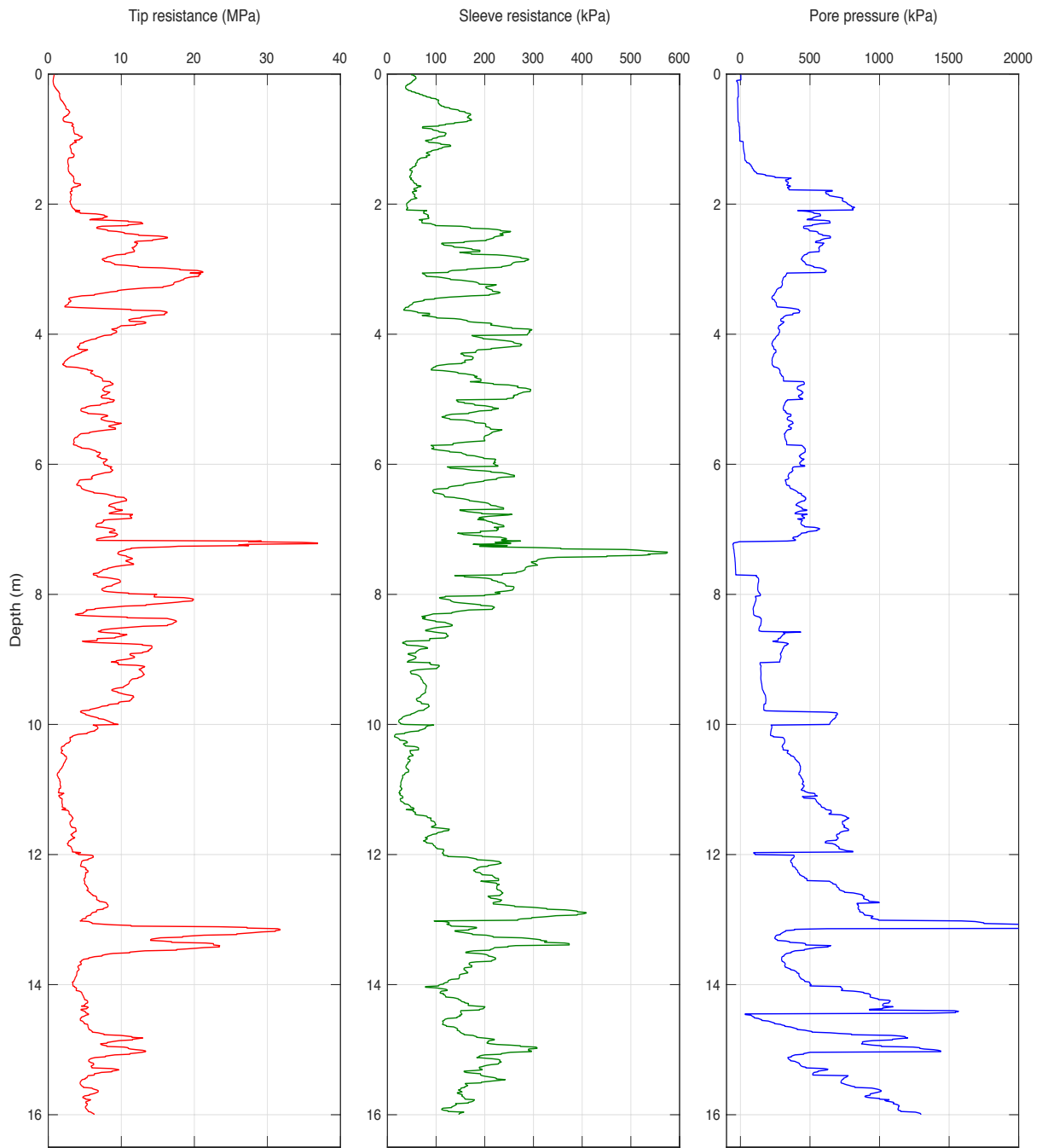


Fig. 6-6: Raw data from the seismic cone penetration test (sCPT-1)

Table 6-1. Material properties obtained from correlations with the cone resistance

Layer ID	Depth (m)		Thickness (m)	ρ (Kg/m³)	ν	<i>E</i> (MPa)	<i>G</i> (MPa)	<i>K</i> (MPa)	
1	0	-	1	1.0	1937	0.25	428.48	171.4	285.6
2	1	-	2	1.0	1937	0.25	250.24	100.1	166.8
3	2	-	3	1.0	1937	0.25	257.76	103.0	172.7
4	3	-	4	1.0	1937	0.25	229.99	92.0	153.3
5	4	-	5	1.0	1937	0.25	241.73	96.7	161.1
6	5	-	6	1.0	1937	0.25	280.01	112.0	186.7
7	6	-	7	1.0	1937	0.25	255.49	102.2	170.3
8	7	-	8	1.0	1937	0.25	323.27	129.3	215.6
9	8	-	9	1.0	1937	0.25	330.98	132.4	220.6
10	9	-	10	1.0	1937	0.25	337.27	134.9	224.9
11	10	-	11	1.0	1937	0.25	317.25	126.9	211.5
12	11	-	12	1.0	1937	0.25	359.51	143.8	239.7
13	12	-	13	1.0	1937	0.25	341.25	136.5	227.5
14	13	-	14	1.0	1937	0.25	403.73	161.5	269.1
15	14	-	15	1.0	1937	0.25	360.49	144.2	240.3
16	15	-	16	1.0	1937	0.25	381.75	152.7	254.5

6.2.3 MASW tests

For the testing designs, it is necessary to consider the geometry of the array, which includes:

- Spatial alignment of the geophones in the field: the common receiver midpoint geometry was used. (see Fig. 6-7)
- Spacing between adjacent geophones: the test used a 1-meter spacing array with 24 geophones, so the distance covered by the array was 23 meters.
- Offset distance between the excitation force and the first geophone in the array: the offset distances were 6 meters, 9 meters, and 12 meters.

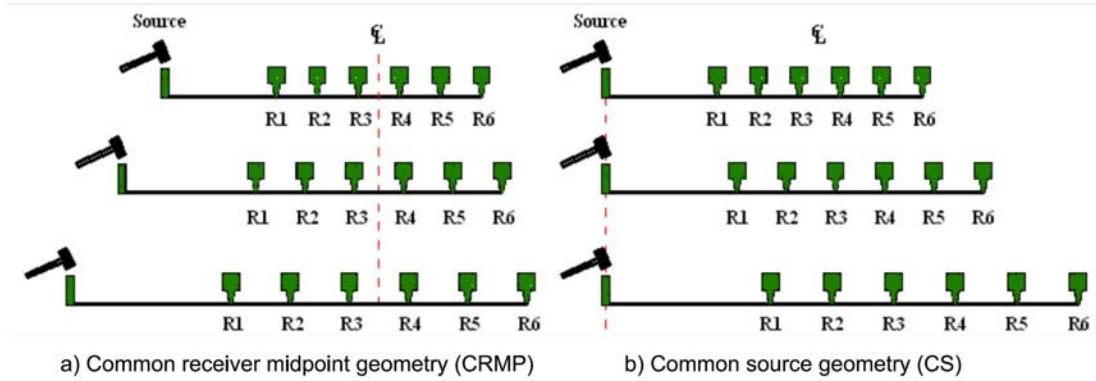


Fig. 6-7: Different arrays for the MASW test. (Nasseri-Moghaddam, 2006)

6.2.3.1 MASW test: data acquisition in the field

The parameters used for the data acquisition were:

- Spacing between adjacent geophones: $dx = 1\text{m}$
- Sampling rate for data collection: $dt = 0.25\text{ms}$
- Total time recorded: $T = 0.5\text{s}$

6.2.3.2 MASW test: data processing

The data processing was carried out in the time domain as well as in the frequency domain. In the time domain the processing involves the following operations:

Time domain processing

The raw data in time domain was processed by following standard signal processing operations such as:

- Direct component (DC) removal: a standard operation performed in signal processing to avoid DC bias when the signal is to be truncated or windowed.
- Denoising using wavelet decomposition: this operation uses the fact that the wavelet transform concentrates the main signal features in a few large-magnitude

wavelet coefficients, then, the wavelet coefficients with small values are considered to represent noise and they can be removed from the signal without affecting its quality.

- Low-pass filtering: the low-pass filter was used to remove some very low frequency components in the signals. The cut-off frequency was defined to be maximum 2Hz, and even in many cases there was no need to apply this filter to the signal.
- High-pass filtering: the high-pass filter was used in some cases where the signals showed high frequency noise that was not properly eliminated in the denoising process. The cut-off frequency was defined in each case to be at least twice the maximum frequency of interest in the signal analysis process.
- Signal windowing using a tapered cosine window: in this case the cosine fraction of the window was defined to be 10% in order not to have large tails at the initial and final part of the data being windowed. In Fig. 6-8 windows with different cosine fractions are presented to illustrate the effect of that parameter in the definition of the window. The key aspect was the definition of points B and C, which bound the plateau of the window and represent the part of the signal that remains intact after the operation.

An example of field data signals before and after processing is presented in Fig. 6-9.

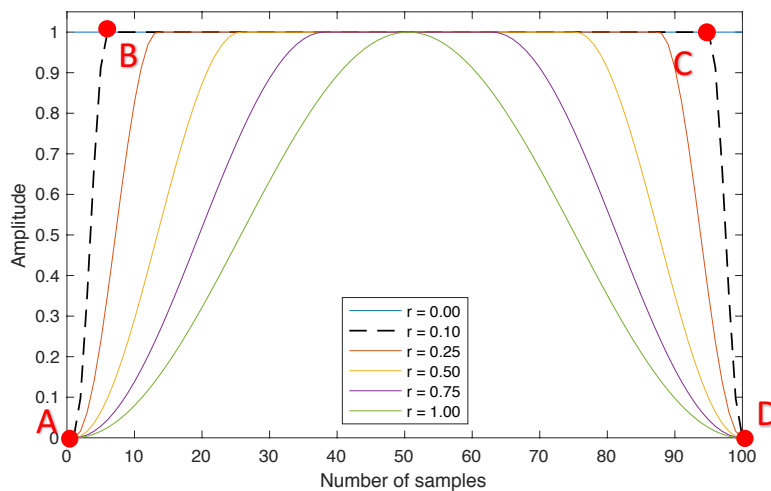


Fig. 6-8: Tapered cosine window for different cosine fractions (r)

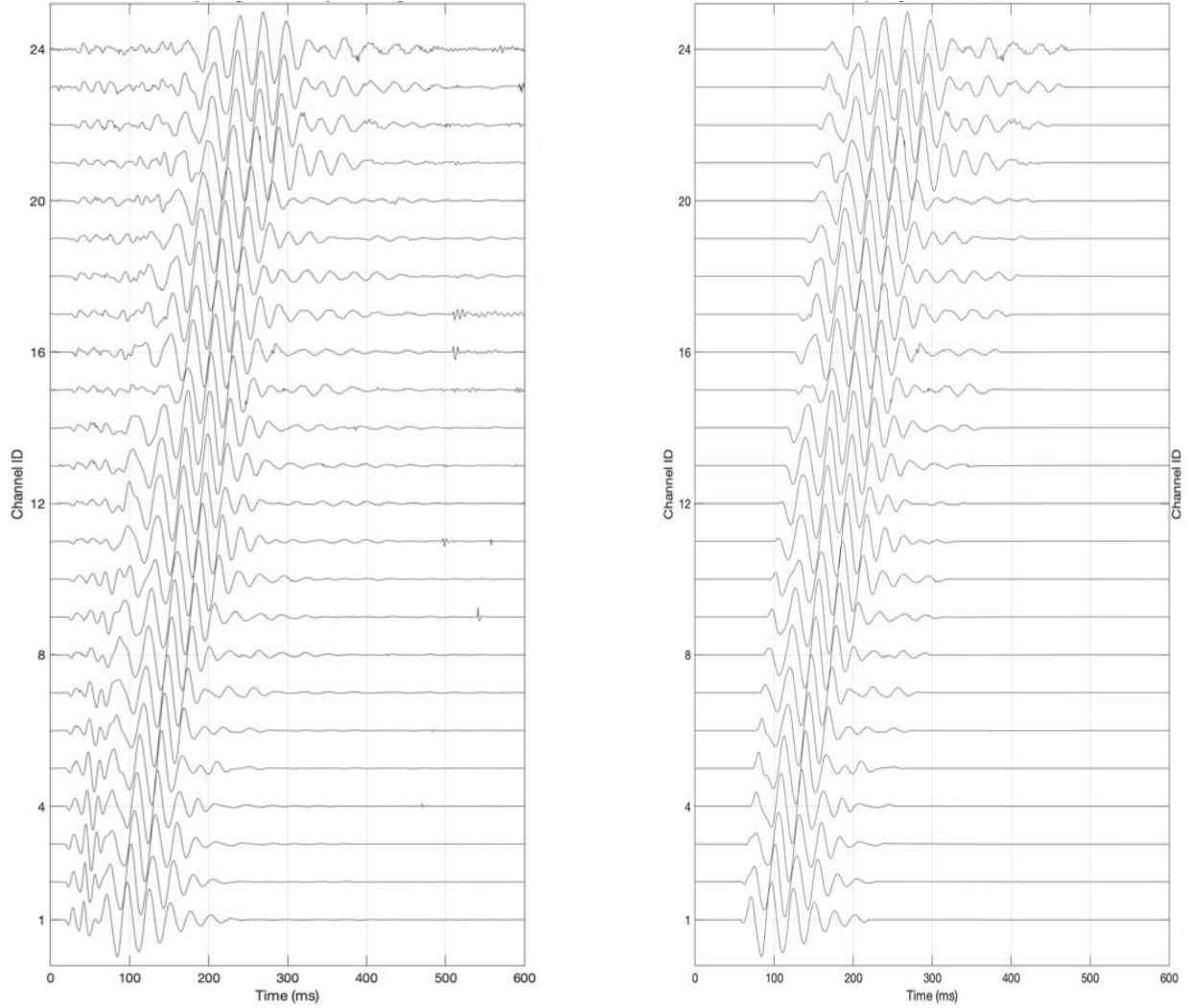


Fig. 6-9: Time domain signals before (left) and after (right) signal processing.

Frequency domain processing

In order to take the data from the time domain to the frequency domain the Fourier transform was used. An example of signals in the frequency domain before and after processing is presented in Fig. 6-10.

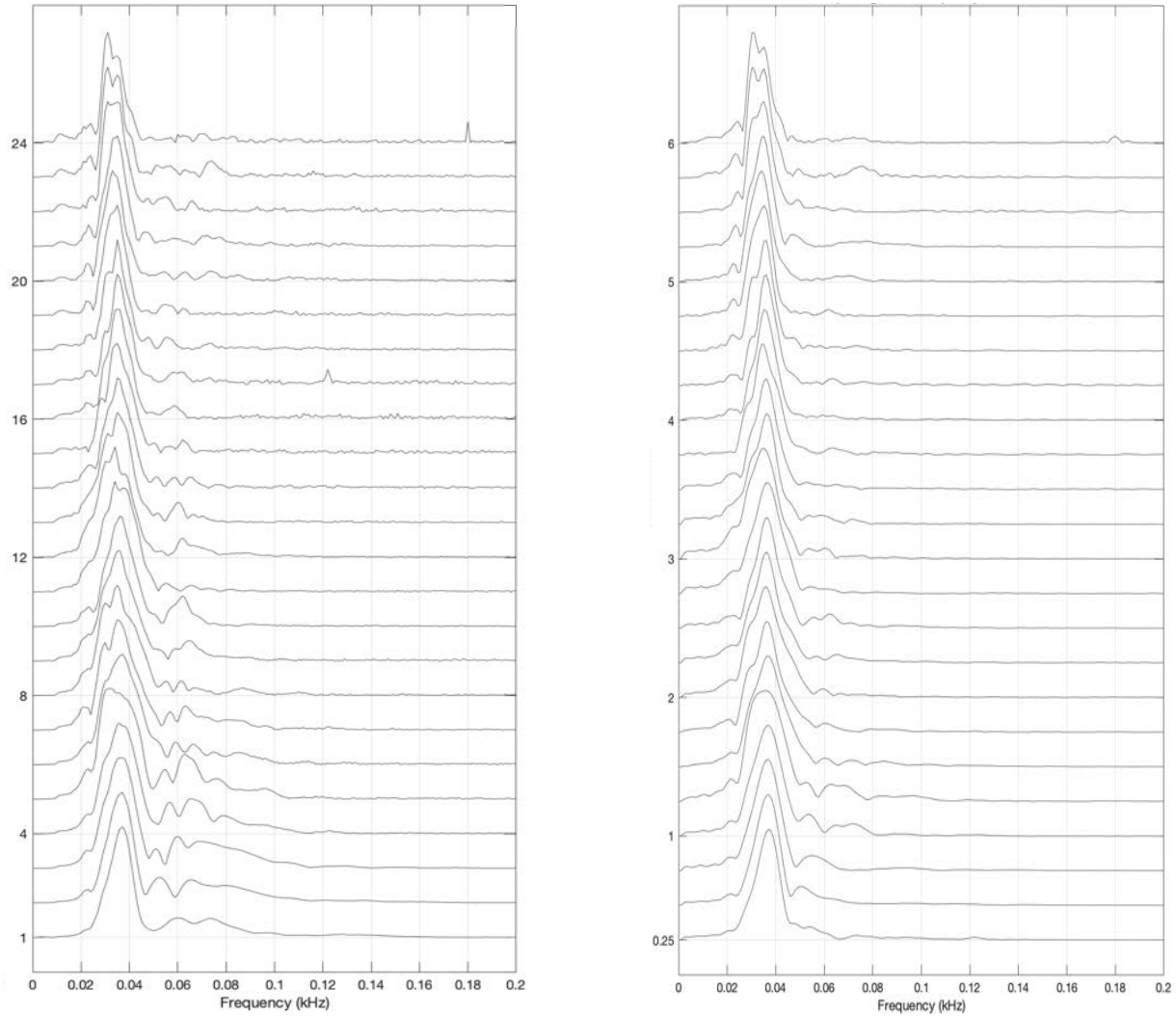


Fig. 6-10: Frequency domain signals before (left) and after (right) signal processing.

6.2.4 Travel-time plots and dispersion curves

In the following figures the travel time plots and the dispersion curves are presented for the results obtained in the MASW field test for different offset distance from excitation force to first receiver. The travel time plots the wave field generated by the excitation force, so it allows the identification of the wave trains corresponding to P-waves, shear waves and Rayleigh waves, also the identification of reflections and refractions should be possible, however sometimes the noise level masks those wave trains.

The dispersion curves show how the Rayleigh wave velocity changes with frequency, allowing also the identification of higher vibration modes. Theory of Rayleigh waves' propagation and dispersion curve calculation is well presented in Foti et al. (2014).

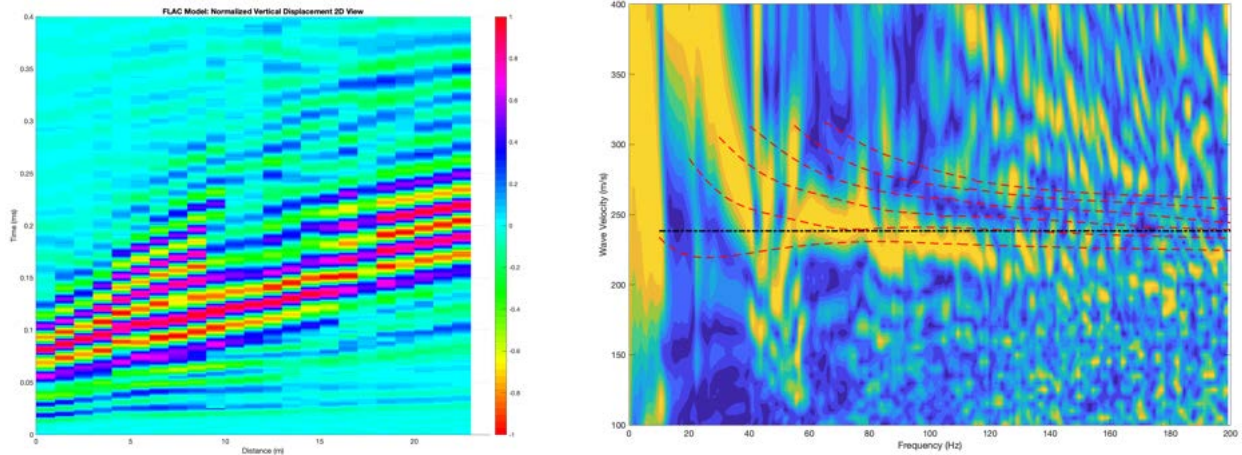


Fig. 6-11: Travel time plot (left) and dispersion curve (right) for MASW field test with source offset distance of 6m.

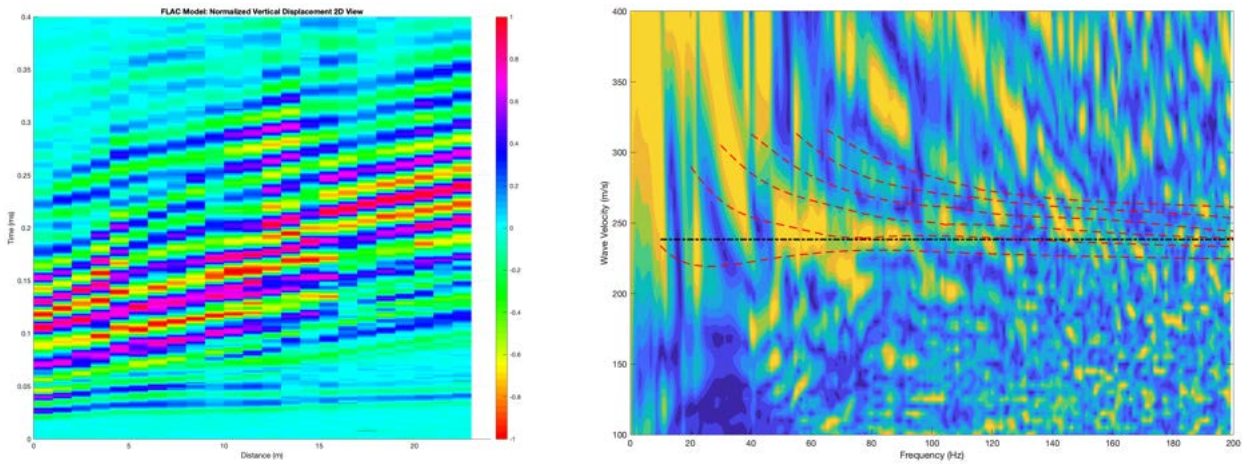


Fig. 6-12: Travel time plot (left) and dispersion curve (right) for MASW field test with source offset distance of 9m.

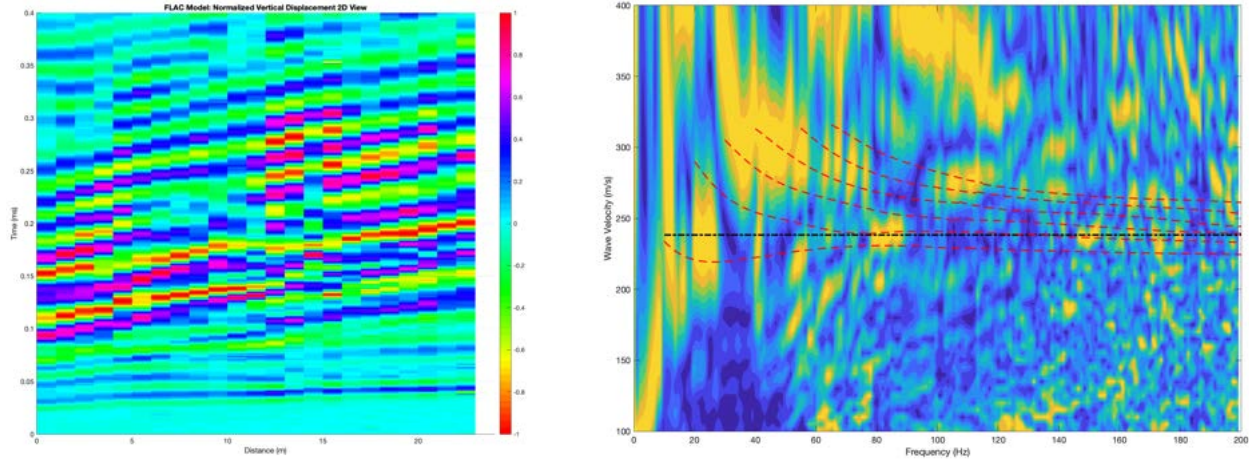


Fig. 6-13: Travel time plot (left) and dispersion curve (right) for MASW field test with source offset distance of 12m.

6.3 Numerical simulation to replicate field conditions

In the previous section the results from CPTU and MASW field tests were presented along with their interpretation to get the site characterization. In this section the results of three different sets of numerical simulations are presented. These numerical simulations are intended to replicate the field conditions of the field tests when different approaches are used to characterize the medium, which can allow a further parametric analysis.

The first set of numerical simulations was done following the easiest way to characterize a geomaterial medium, which is to approach it by considering it is homogeneous, so the average properties are used to define the density and strength parameters. On the other hand, the second set of numerical simulations followed the layered medium approach, which was used in the previous chapter and it is widely accepted in the geotechnical engineering practice for the definition of a geological-geotechnical model (GG-model). Finally, the third set of simulations considered the spatial variability of geomaterials' properties, approach for which the random field theory was used in order to define the spatial distribution of shear modulus inside the medium.

The results of these numerical simulations illustrated the differences obtained in the wave-field generated when different approaches are used to characterize the geomaterials' medium under study.

6.3.1 Numerical model definition

6.3.1.1 Dimensions and material properties

The same model geometry used in chapter 5 is used in this chapter, so the only difference is that now the material properties are those obtained from the field tests and that the layer thicknesses are now 1 meter in order to use the properties calculated in Table 6-1. For this numerical model no further numerical simulation was performed.

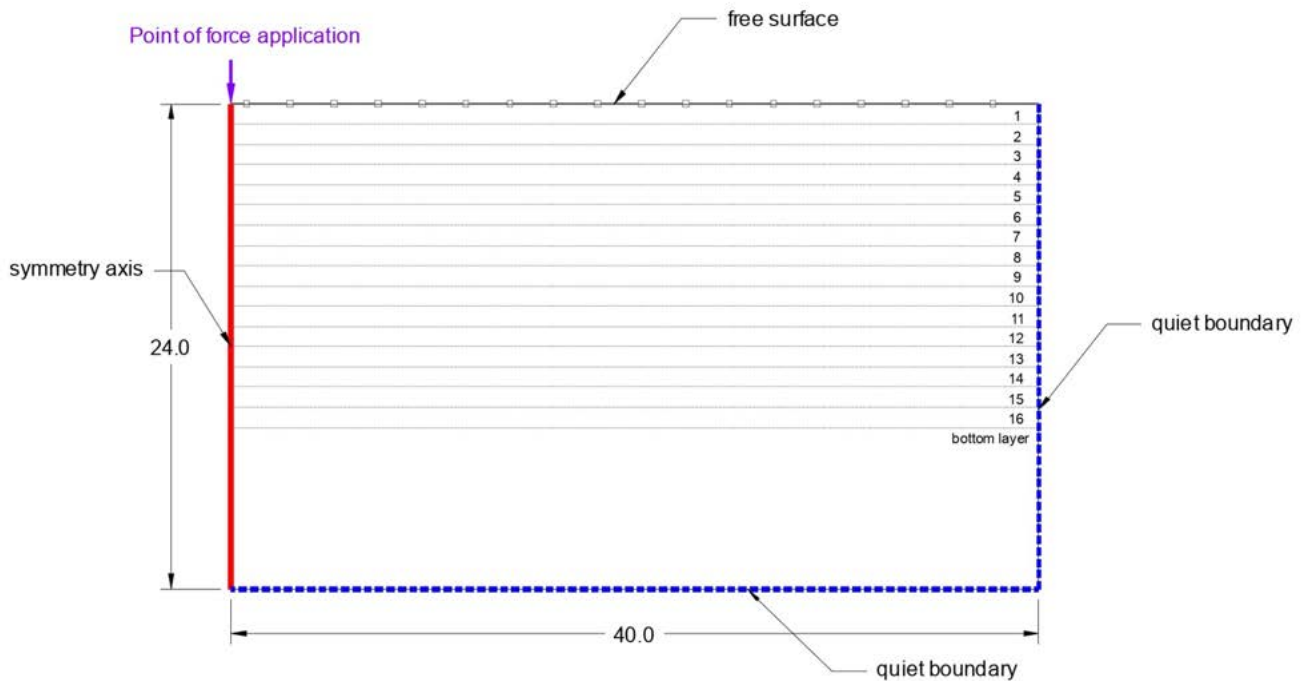


Fig. 6-14: Definition of geometry and boundary conditions for the numerical model.

6.3.1.2 Excitation force: Input force (Ricker wavelet)

Named for the American geophysicist Norman H. Ricker (1896–1980), the Ricker wavelet is a zero-phase wavelet, obtained as the second derivative of the Gaussian function or the third derivative of the normal-probability density function. (Sheriff, 2002)

Sheriff (2002) states that “a Ricker wavelet is often used as a zero-phase embedded wavelet in modeling and synthetic seismogram manufacture. The amplitude $f(t)$ of the Ricker wavelet with peak frequency f_M at time (t) is given by”:

$$f(t) = (1 - 2\pi^2 f_M^2 t^2) * e^{-(\pi^2 f_M^2 t^2)} \quad (6-5)$$

The frequency domain representation of the wavelet is given by,

$$F(f) = \left(\frac{2}{\sqrt{\pi}}\right) * \left(\frac{f^2}{f_M^3}\right) * e^{-\left(\frac{f^2}{f_M^3}\right)} \quad (6-6)$$

“Sometimes the period (somewhat erroneously referred to occasionally as the wavelength) is given as $(1/f)$, but since it has mixed frequencies, this is not quite correct, and for some wavelets is not even a good approximation” (Sheriff, 2002).

In this research the period will be referred as the characteristic period illustrated in Fig. 6-15 and defined by next equation:

$$T_D = \left(\frac{\sqrt{6}}{\pi f_M}\right) \quad (6-7)$$

In order to study the effect of frequency content on wave propagation results, five different Ricker pulses were used to define the input force, whose mean frequencies ranged from 22Hz to 160Hz. The time domain and the frequency domain representations for the Ricker pulses used to define the input force in these numerical simulations are shown in Fig. 6-16.

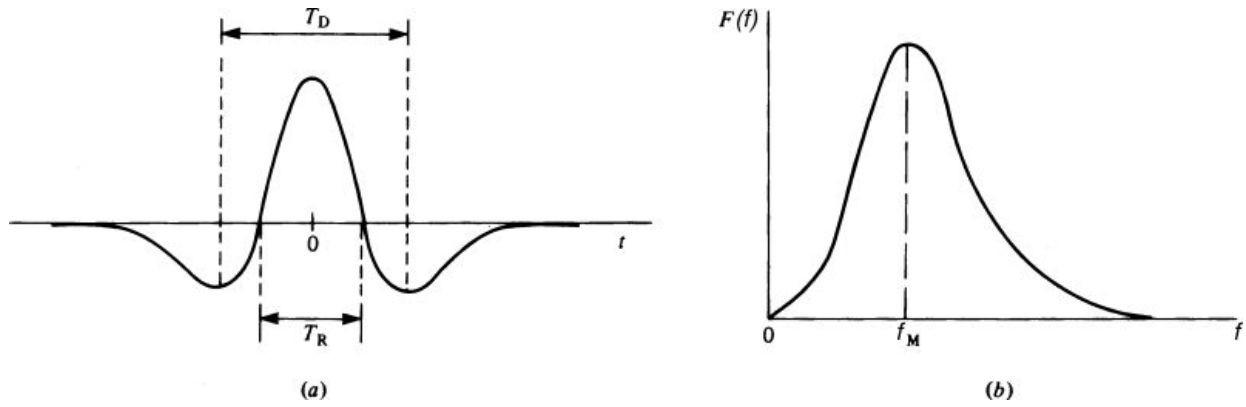


Fig. 6-15: Ricker wavelet used to define the shape of the force for the initial numerical models: (a) time domain, and (b) frequency domain (Sheriff, 2002)

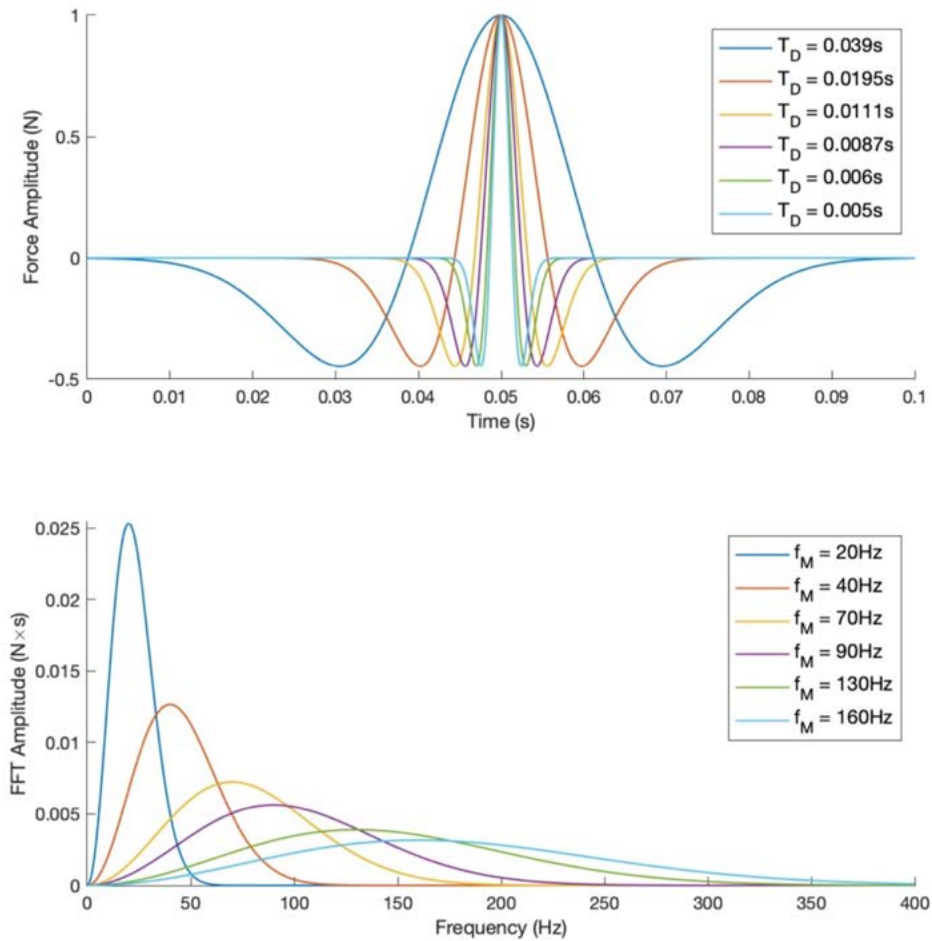


Fig. 6-16: Ricker wavelet force pulses with different mean frequencies

6.3.2 Approaches to represent the properties distribution inside a medium

Each one of the three approaches to represent the materials properties' distribution inside the medium was used to define the geometry for a numerical model. From the CPTU field test, the total depth of 16 meters of subsoil were characterized with elastic properties, so for the numerical simulations those 16 meters of soil will be simulated in three different ways: first, by taking the average of the properties in the whole 16 meters (i.e. homogeneous medium); second, by assuming the materials are distributed in 16 layers of one-meter thickness each (i.e. horizontally layered medium); third, by using random fields to spatially distribute the properties of the materials (i.e. heterogeneous medium). In all the three cases the 16 meters of material overlay a soil with properties equal to the maximum values obtained in the field CTPU field test.

6.3.2.1 Approach #1: homogeneous medium

The homogeneous medium is the simplest approach because it just takes the average of material properties to characterize the medium, which were presented in Table 6-1. The average of material properties for the first 16 meters, along with the adopted values for the bottom layer are presented in Table 6-2

Table 6-2. Material properties for a homogeneous medium

		ρ (Kg/m ³)	ν	E (MPa)	G (MPa)	K (MPa)
0 – 16 meters	Average (μ)	1937	0.25	318.7	127.5	212.5
	Standard deviation (σ)	---	---	60.8	24.3	40.5
16 – 24 meters	Adopted value ($\mu + 3\sigma$)	1937	0.25	501.0	200.4	333.9

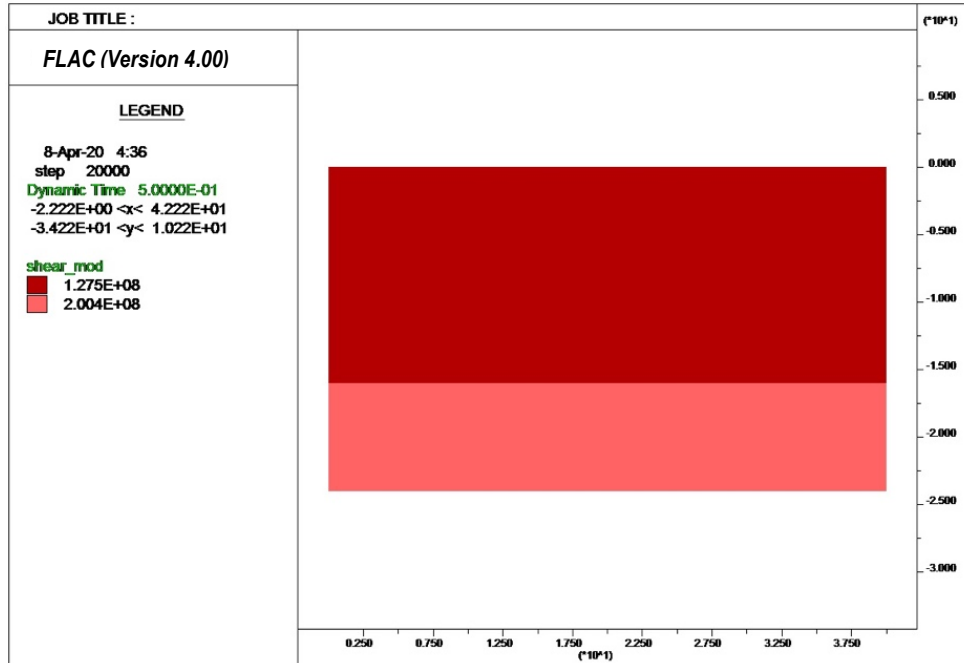


Fig. 6-17: Geometry for the numerical model considering a homogeneous medium.

6.3.2.2 Approach #2: horizontally layered medium

This approach considers 16 layers of one-meter thickness each, for which the properties were obtained from the field test (sCPTU) and were presented in Table 6-1. The properties for the bottom layer, which goes from 16 to 24 meters of depth, were the same presented in Table 6-2.

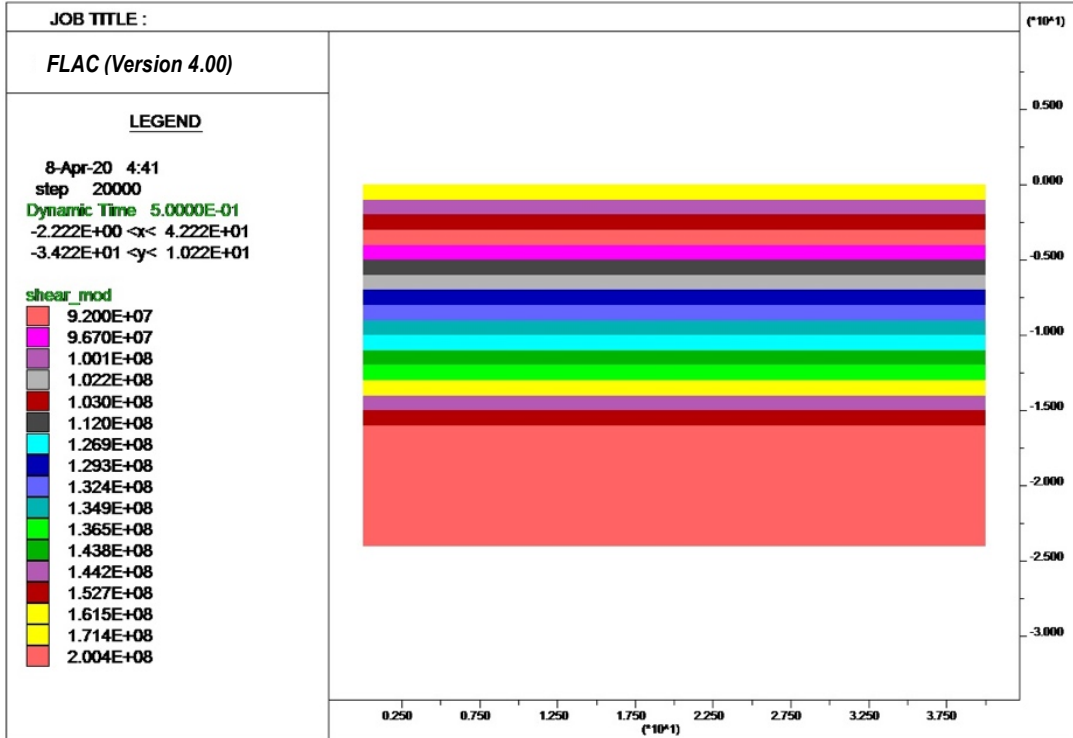


Fig. 6-18: Geometry for the numerical model using the horizontally layered medium.

6.3.2.3 Approach #2: spatially variable medium

In this approach the shear modulus inside the medium for the first 16 meters is assumed to be represented by a random field. An example of the model used for the numerical simulations in FLACTM is presented Fig. 6-19. As in the previous case, the properties for the bottom layer, which goes from 16 to 24 meters of depth, were the same presented in Table 6-2.

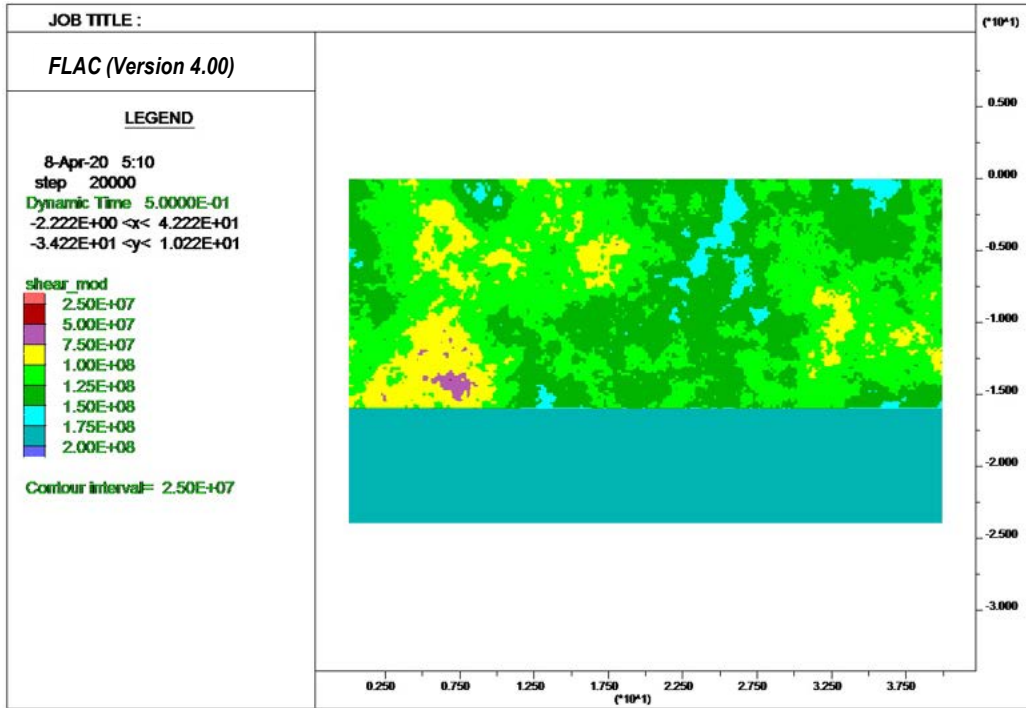


Fig. 6-19: Geometry for the numerical model using the spatially variable medium.

The random field generation is not a trivial issue, however, a deep study of the mathematics behind the generation techniques is out of the scope of this research. A good reference for the generation methods is Fenton and Griffiths (2008). The LU method (“Covariance Matrix Decomposition Technique”), as described in chapter 3 was used to generate the random fields to use in this research. The random field technique requires the average and standard deviation of the properties to get spatially distributed (i.e. the shear modulus), along with its correlation length. As there is no reported values for the correlation length of the shear modulus, it is necessary to perform a parametric study to understand how the correlation length affects the results for the wave-field generated. In order to ease the analysis of the results, the correlation length (L_c) is normalized with respect to the thickness of the materials under study, in this case ($H = 16m$).

Five different values for the normalized correlation length were used in this research. The actual random fields used for the numerical simulations are presented in Fig. 6-20 to Fig. 6-24.

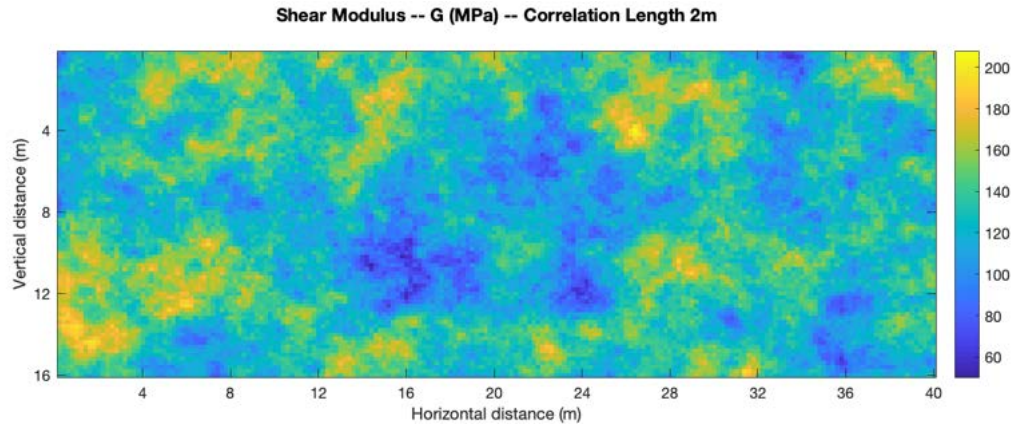


Fig. 6-20: Random fields for shear modulus (G) generated using LU decomposition technique with normalized correlation length (L_c / H) = 0.125.

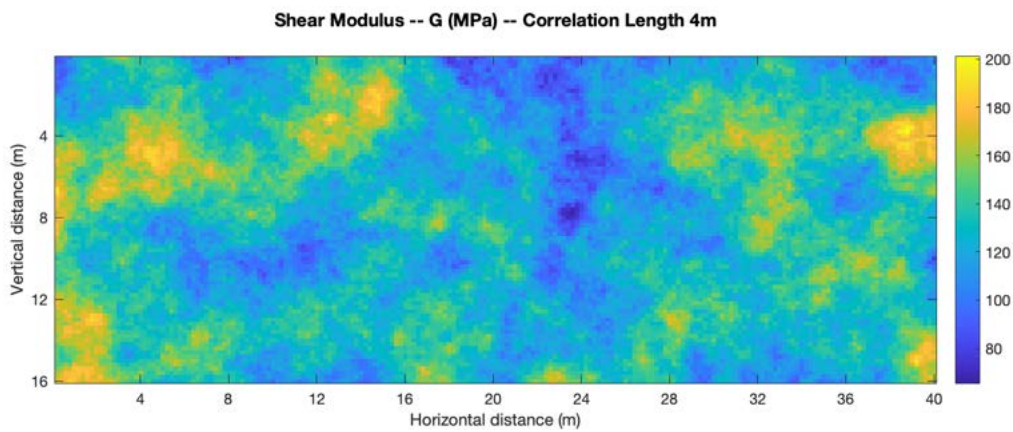


Fig. 6-21: Random fields for shear modulus (G) generated using LU decomposition technique with normalized correlation length (L_c / H) = 0.25.

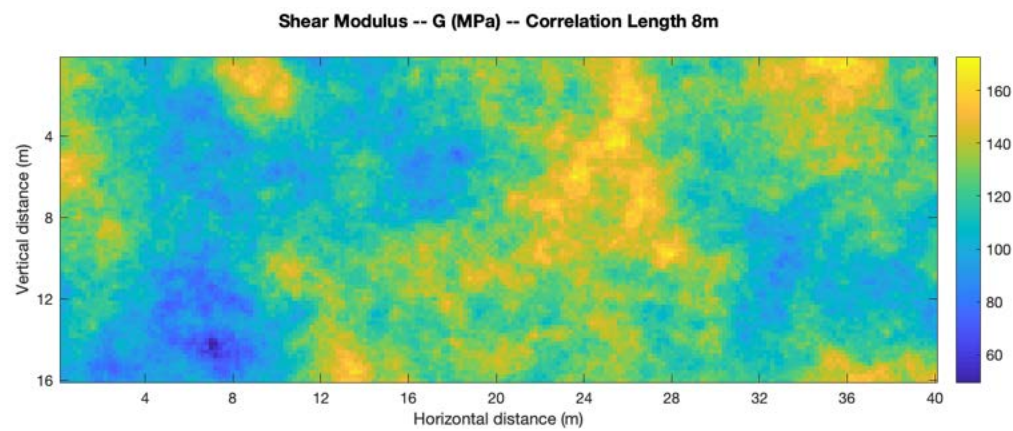


Fig. 6-22: Random fields for shear modulus (G) generated using LU decomposition technique with normalized correlation length (L_c / H) = 0.50.

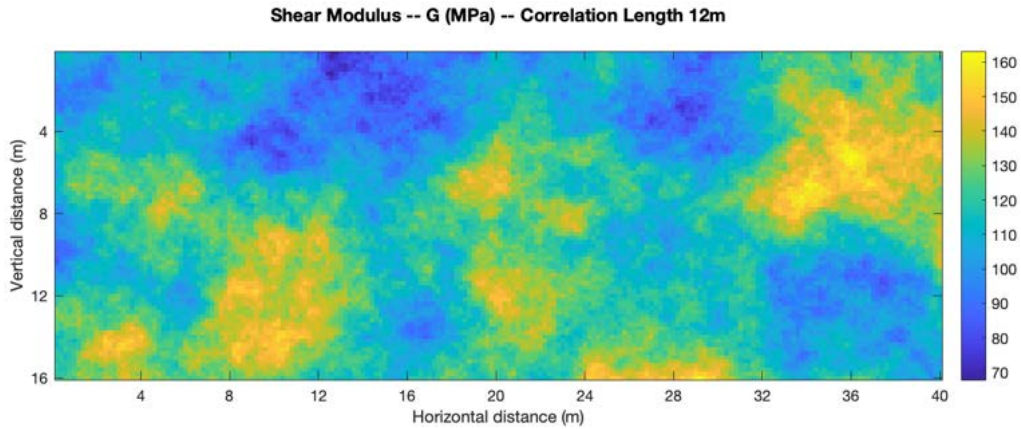


Fig. 6-23: Random fields for shear modulus (G) generated using LU decomposition technique with normalized correlation length (L_c / H) = 0.75.

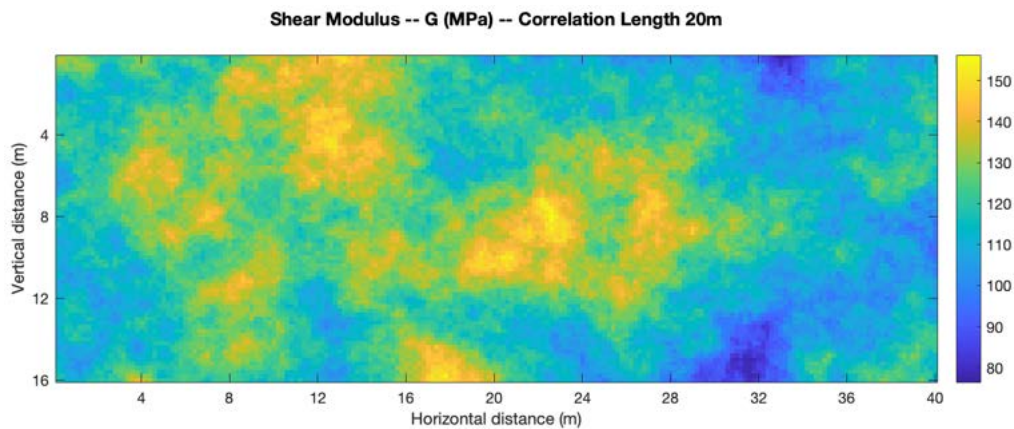


Fig. 6-24: Random fields for shear modulus (G) generated using LU decomposition technique with normalized correlation length (L_c / H) = 1.25.

6.3.3 Comparison of wave-field generated for different approaches for materials distribution

The results of numerical wave propagation for the three approaches used to characterize geomaterials are presented here.

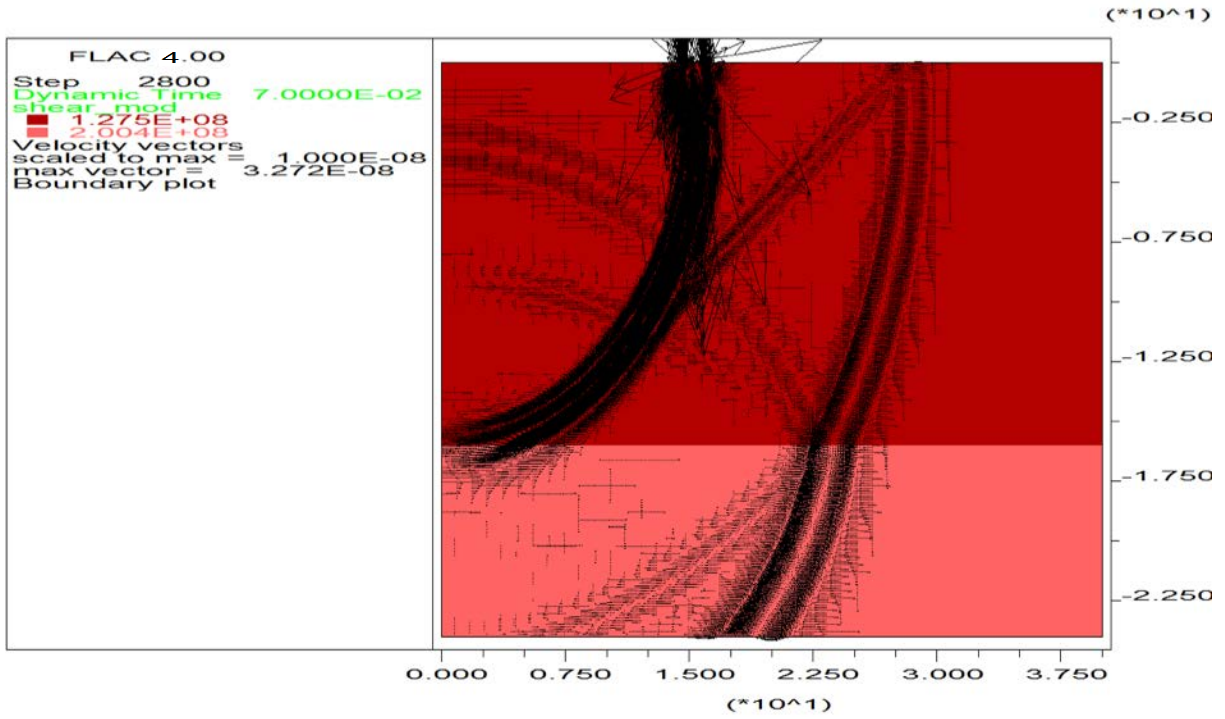


Fig. 6-25: Screenshot: numerical simulation of wave propagation in a 2-layers medium

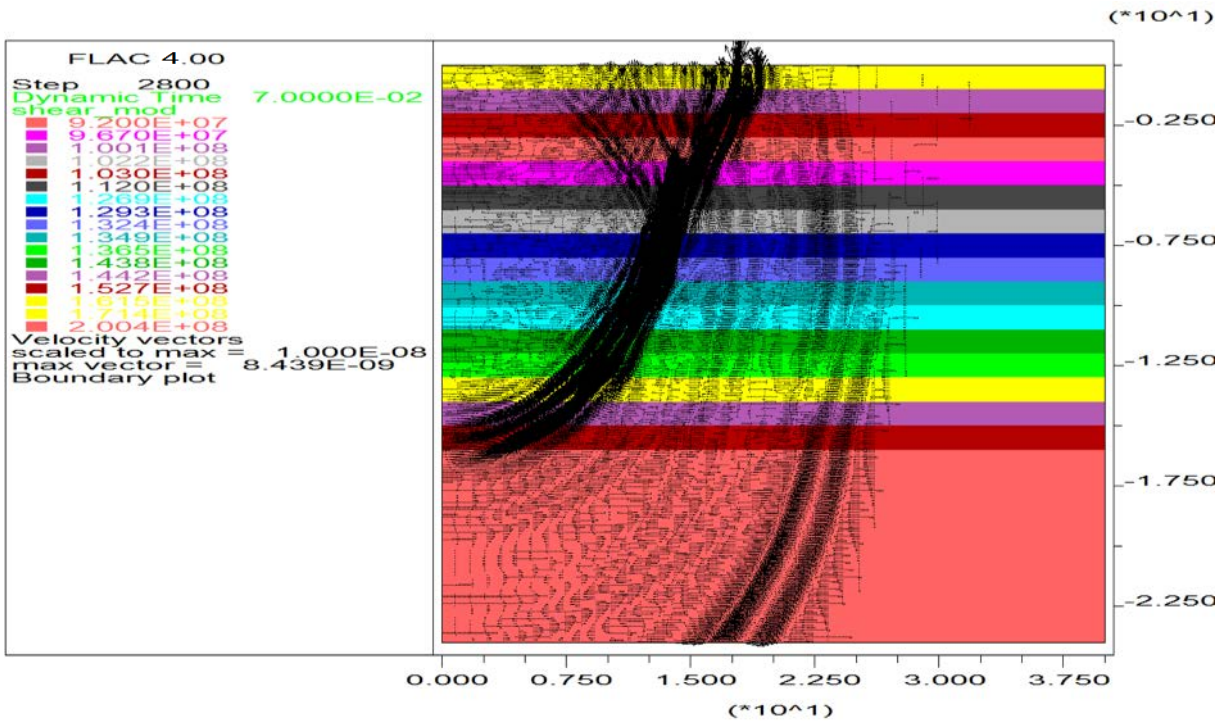


Fig. 6-26: Screenshot: numerical simulation of wave propagation in a 17-layers medium

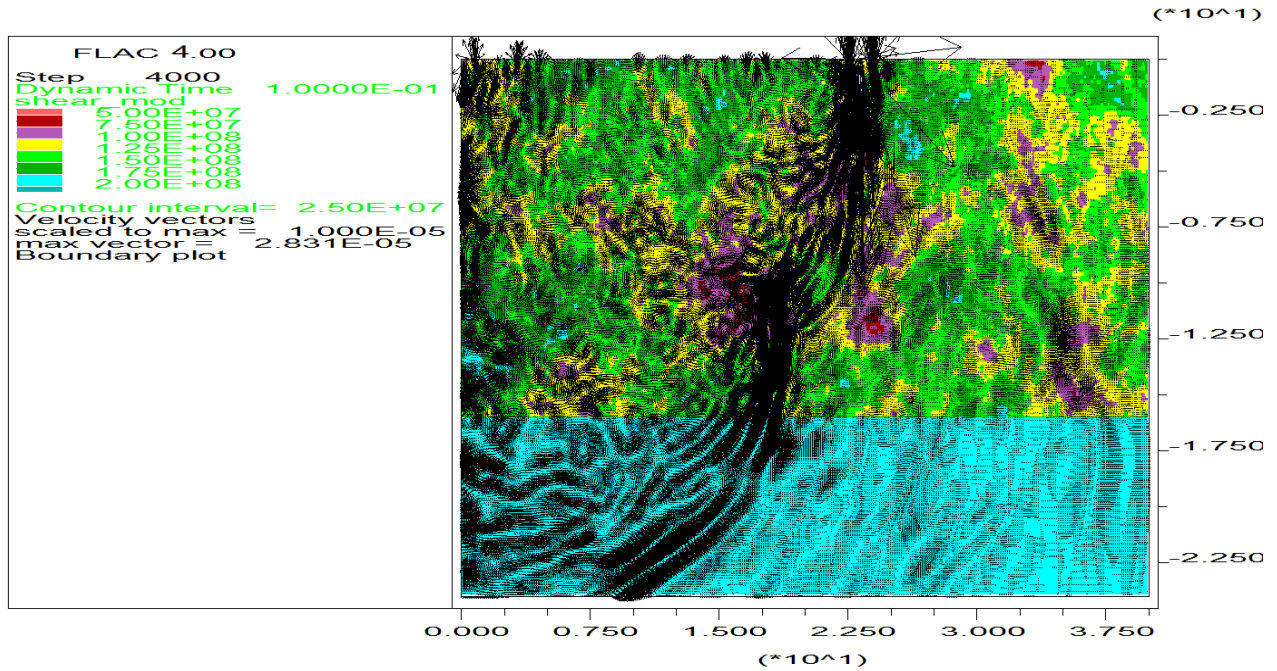


Fig. 6-27: Screenshot at 0.10s: numerical simulation of wave propagation in a spatially variable medium overlaying a homogeneous medium. The random field simulate the spatial variability of shear modulus – (G) (normalized correlation length is 0.125)

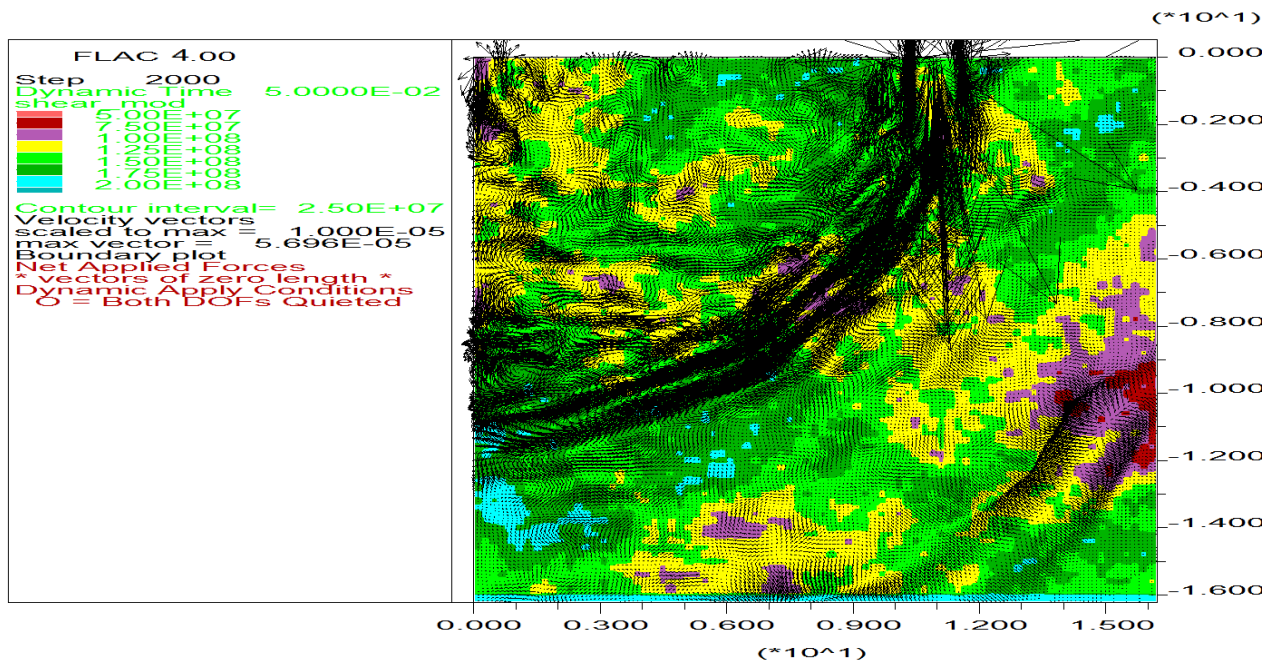


Fig. 6-28: Screenshot at 0.05s: numerical simulation of wave propagation in a spatially variable medium overlaying a homogeneous medium. The random field simulate the spatial variability of shear modulus – (G) (normalized correlation length is 0.125)

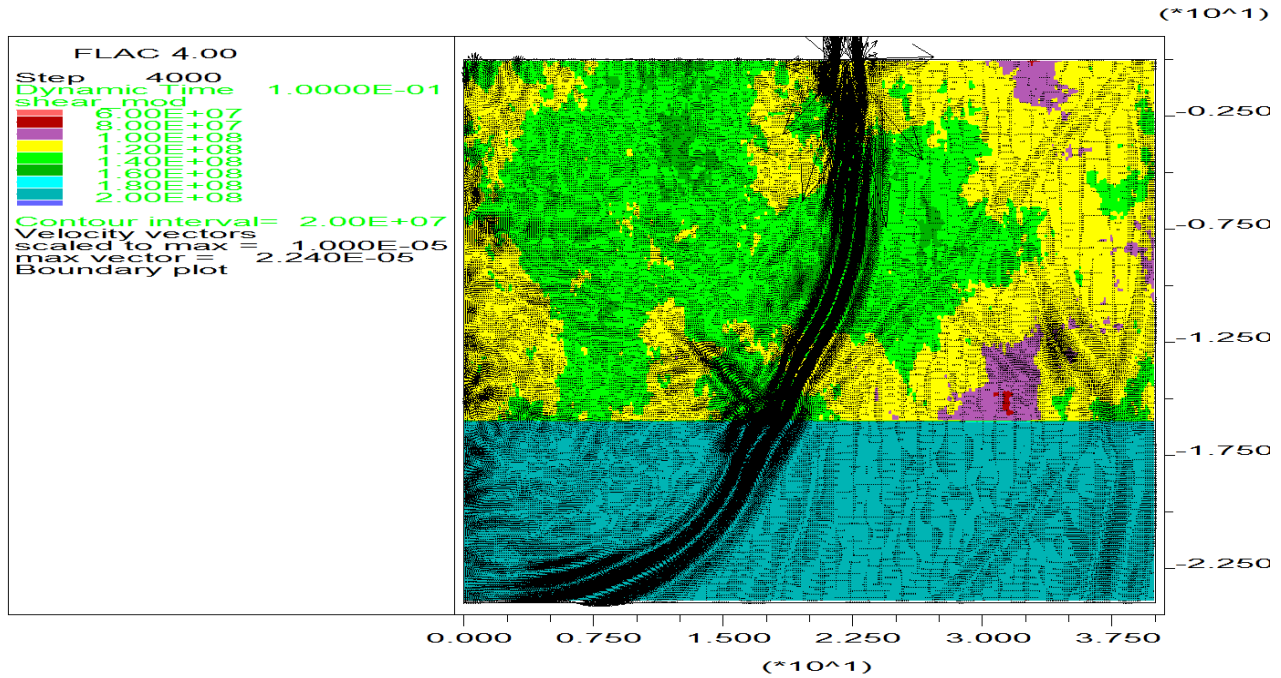


Fig. 6-29: Screenshot at 0.10s: numerical simulation of wave propagation in a spatially variable medium overlaying a homogeneous medium. The random field simulate the spatial variability of shear modulus – (G) (normalized correlation length is 1.25)

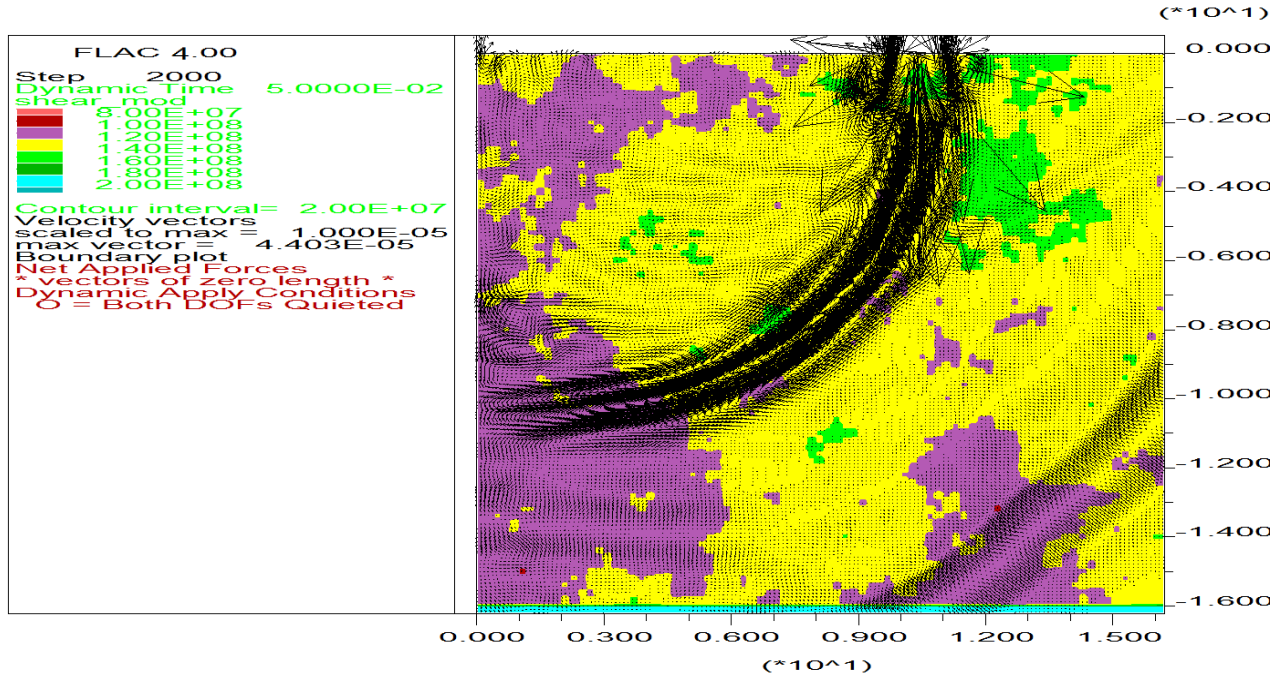


Fig. 6-30: Screenshot at 0.05s: numerical simulation of wave propagation in a spatially variable medium overlaying a homogeneous medium. The random field simulate the spatial variability of shear modulus – (G) (normalized correlation length is 1.25)

The previous section was plenty of figures showing differences in the wavefield generated by the same source for different approaches to characterize the medium. Special attention must be given to the results for the layered medium in Fig. 6-26, where reflections due to the impedance ratio between layers are evident. This fact was the main issue studied in the previous chapter.

A comparison of the vertical displacements on the surface for different models, and using different frequencies is presented in the following figures. Fig. 6-31 shows the vertical displacements at 10 meters from the excitation force and for different input frequencies when the medium is approached by a homogeneous model. What is interesting in this figure is how the arrivals for the v_s change for different frequencies, even when the medium is homogeneous. For instance, for the input frequency of 160 Hz, the flight time of the shear wave is identified to be 0.043 ms, while for the 60 Hz that flight time was identified at 0.044 ms, which means a difference about 2.3% is detected. Similarly, for the frequency of 20Hz the flight time of shear waves was identified to be 0.046 ms, which means an increment of about 5.5% in the travel time.

Similarly, Fig. 6-32 shows the vertical displacements at 10 meters from the excitation force and for different input frequencies when the medium is approached by a horizontally layered model. In this figure not just the arrivals of the v_s change for different frequencies, but also the reflection play an important role in the response of the medium, which can be observed in the frequency domain. For example, for the input frequency of 60 Hz the frequency spectrum seems to move its peaks to a lower frequency when the layered approach is used to characterize the medium. In this case, for the input frequency of 160 Hz, the flight time of the shear wave is identified to be 0.038 ms, while for the 60 Hz that flight time was identified at 0.042 ms, which means a difference about 10.5% is detected. Similarly, for the frequency of 20Hz the flight time of shear waves was identified to be 0.048 ms, which means an increment of about 14.3% in the travel time.

Fig. 6-33 shows the vertical displacements at 10 meters from the excitation force and for different input frequencies when the medium is approached by a spatially variable model (i.e. a random field). In this figure, the same effect of v_s arrivals changing with

frequency is observed. In addition, in this case, the random field had a normalized correlation length of 0.125 and its response is closer to the layered medium than to the homogeneous one. In this case, for the input frequency of 160 Hz, the flight time of the shear wave is identified to be 0.041 ms, while for the 60 Hz that flight time was identified at 0.042 ms, which means a difference about 2.7% is detected. Similarly, for the frequency of 20Hz the flight time of shear waves was identified to be 0.046 ms, which means an increment of about 7.7% in the travel time.

Fig. 6-34 shows the same result for a random field but in this case, the normalized correlation length is 1.25, which makes the response of the medium closer to the homogeneous medium than to the layered one. In this case, for the input frequency of 160 Hz, the flight time of the shear wave is identified to be 0.044 ms, while for the 60 Hz that flight time was identified at 0.045 ms, which means a difference about 2.1% is detected. Similarly, for the frequency of 20Hz the flight time of shear waves was identified to be 0.047 ms, which means an increment of about 4.7% in the travel time.

As it can be seen, variation in travel time (flight time) of shear waves increased for lower frequencies, which means the shear wave velocity is lower for lower frequencies.

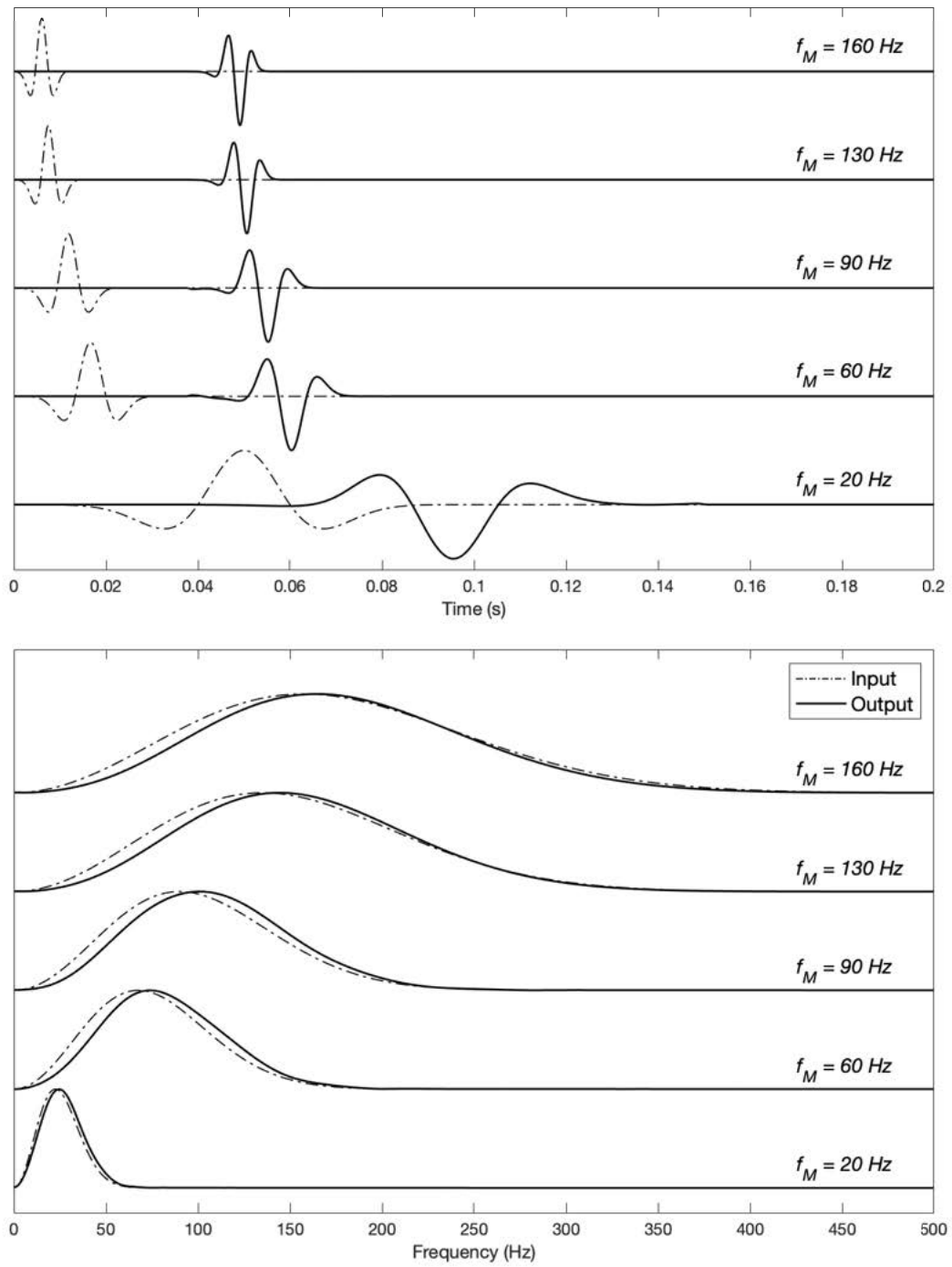


Fig. 6-31: Surface displacement at 10m from excitation force in time domain (up) and frequency domain (down). Response for different frequency contents in the input force in a 2-layers' medium.

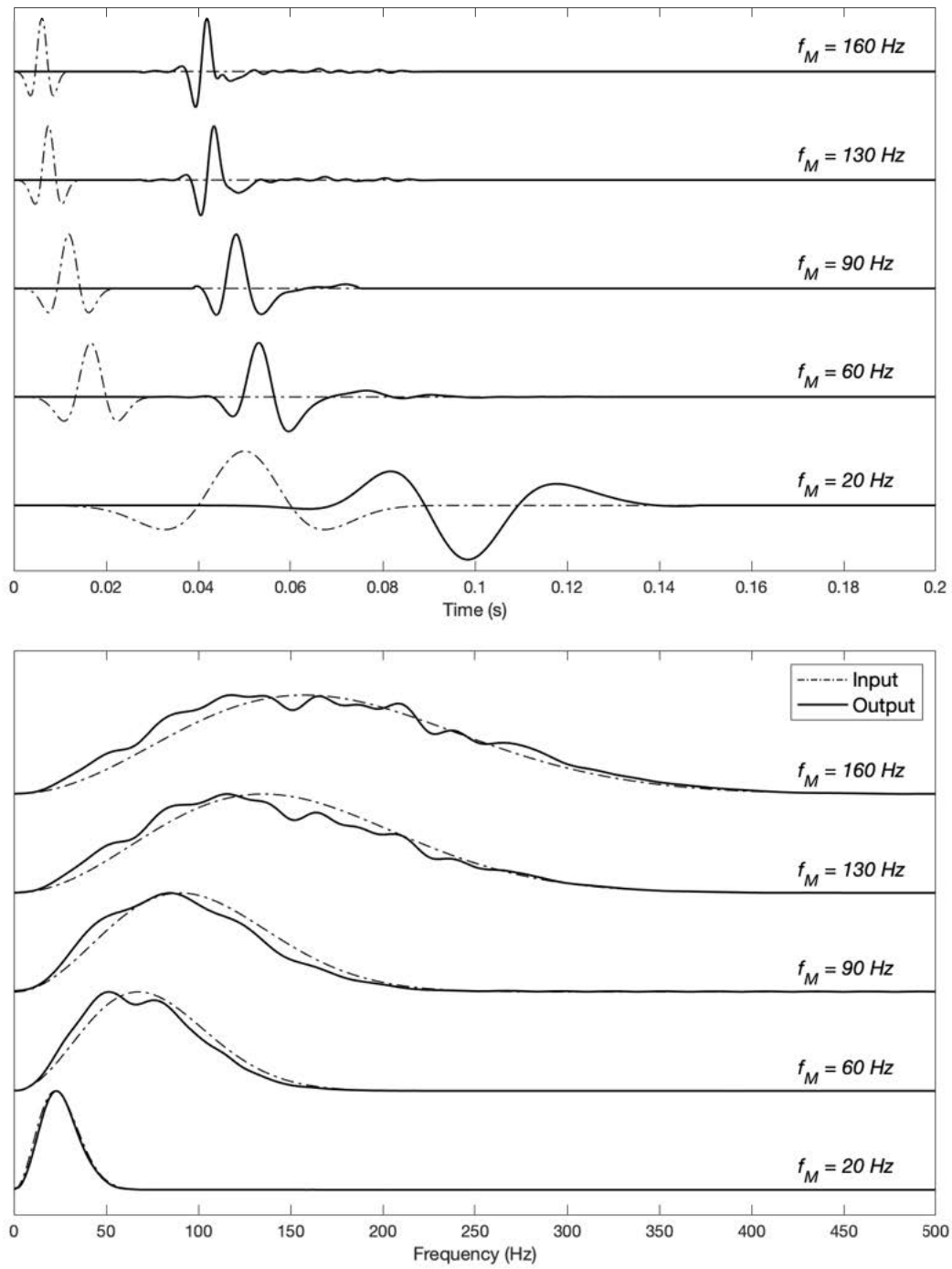


Fig. 6-32: Surface displacement at 10m from excitation force in time domain (up) and frequency domain (down). Response for different frequency contents in the input force in a 17-layers' medium.

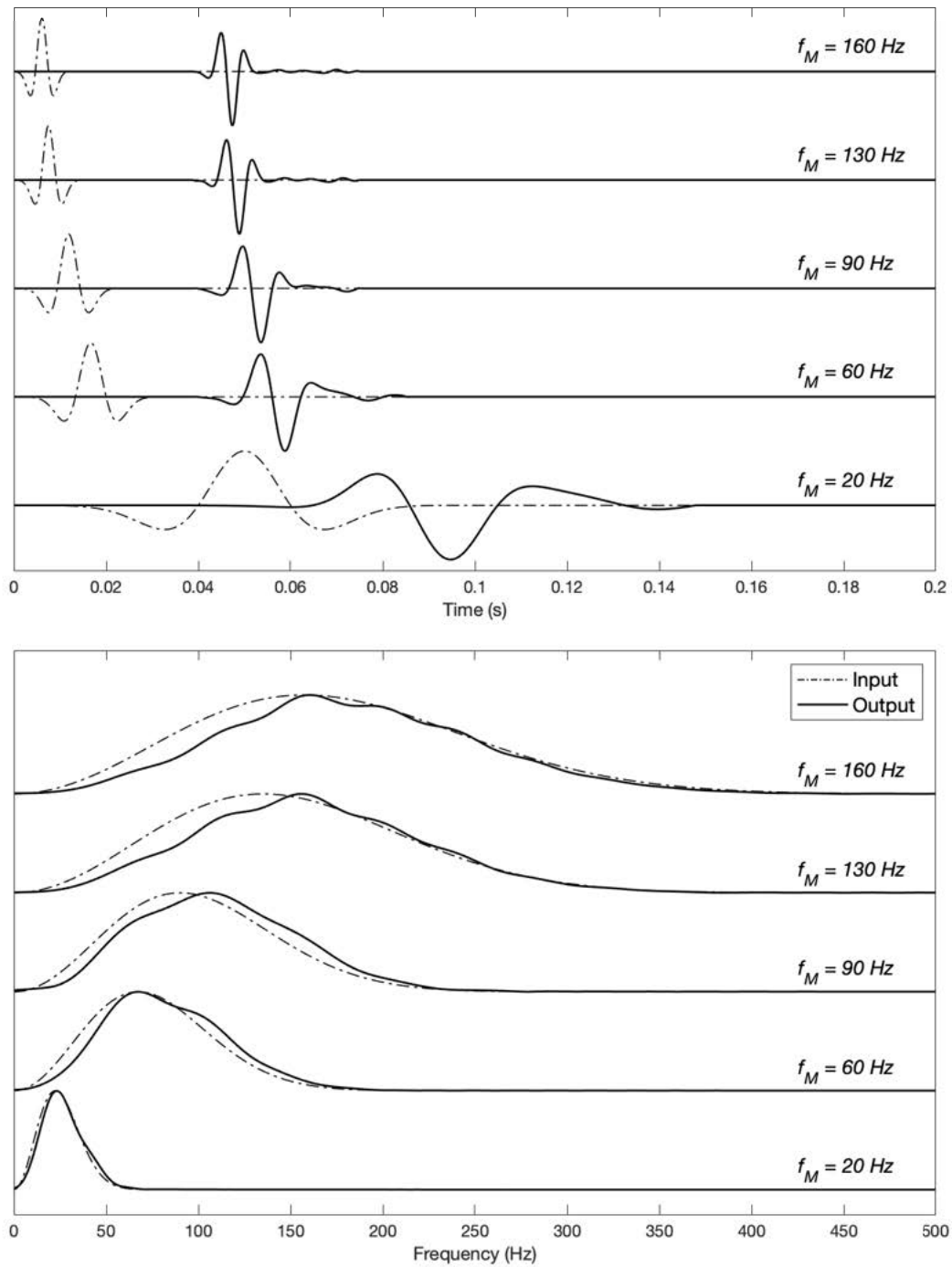


Fig. 6-33: Surface displacement at 10m from excitation force in time domain (up) and frequency domain (down). Response for different frequency contents in the input force in a spatially variable medium. Random field with normalized correlation length 0.125.

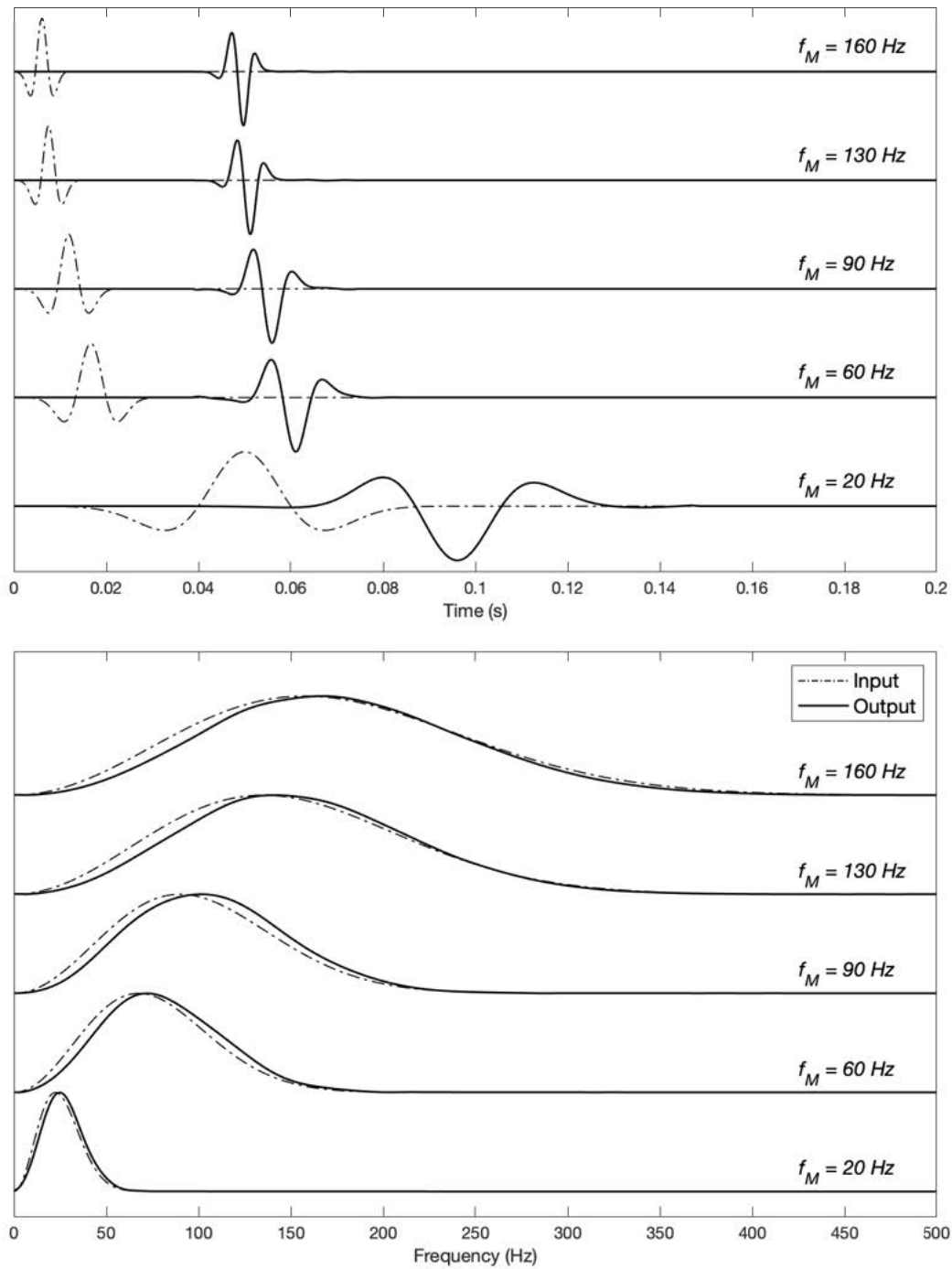


Fig. 6-34: Surface displacement at 10m from excitation force in time domain (up) and frequency domain (down). Response for different frequency contents in the input force in a spatially variable medium. Random field with normalized correlation length 1.25.

6.3.4 Effect of considering different approaches for the medium characterization

The analysis here consisted of comparing how the travel time curves and the dispersion curves changed when the spatial distribution of the stiffness properties inside the medium considers three different approaches. First, the medium was considered homogeneous, so that only two layers were included in the numerical model (the top layer is the homogeneous layer and the second layer is the bottom layer). Second, the layer was simulated as a layered medium with 16 layers plus the bottom layer (17 layers in total were included in the numerical models). Third, the medium was considered to exhibit a random distribution of stiffness, thus, the medium was assumed to spatially distribute the stiffness by following a random field.

An example of typical travel time curves are presented in Fig. 6-35 and Fig. 6-36.

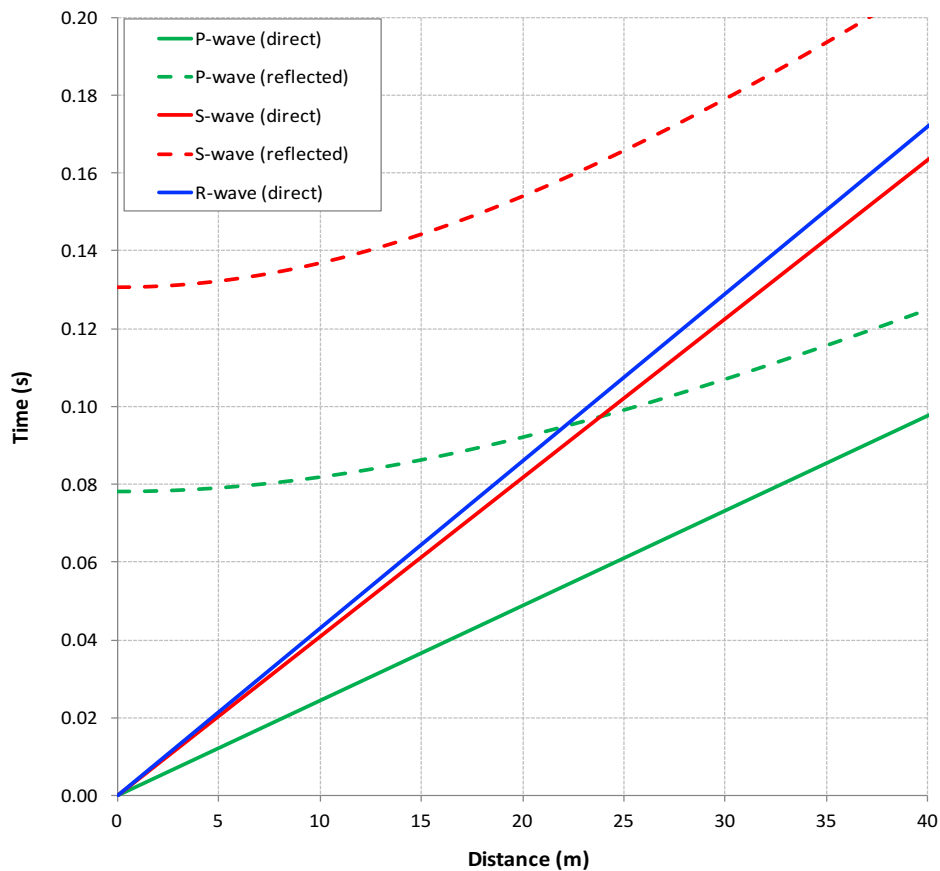


Fig. 6-35: Theoretical travel time curves for a 17-layers' model with horizontal interfaces

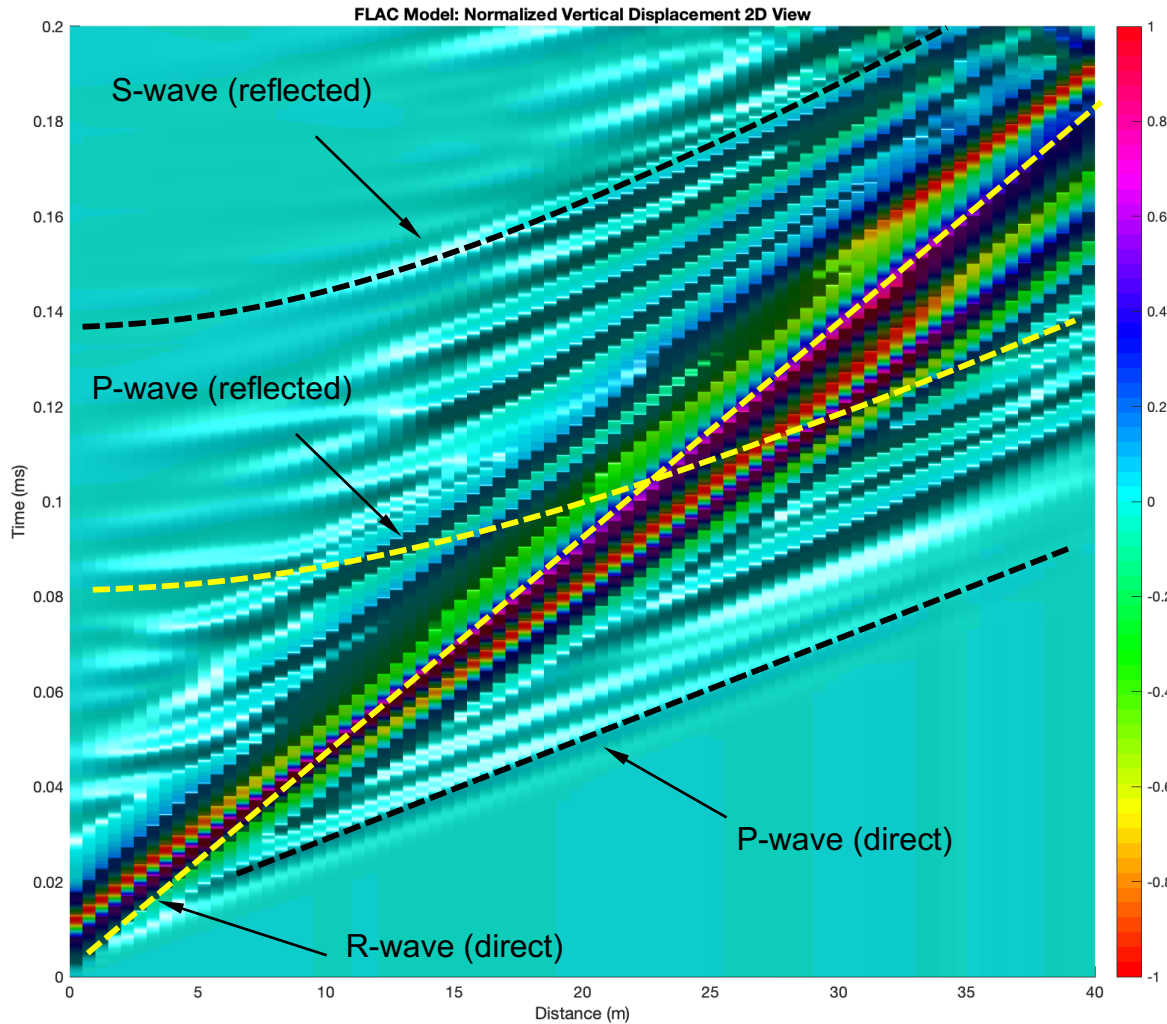


Fig. 6-36: Example of travel time plot obtained from a numerical simulation of wave propagation in a 17-layers model with horizontal interfaces

As it was mentioned before, the calibration of the numerical model was done by ensuring the response of the vertical displacements matched the values predicted by the theoretical solution. Furthermore, to get a second verification of the models' calibration, the dispersion curves obtained from the processing of the numerical results were compared against the theoretical curves obtained using the software SWANTM. (see Fig. 6-37 for the expected theoretical solution of the dispersion curves, and Fig. 6-38 for the dispersion curves obtained from the numerical simulations' results). The fundamental mode was compared as well as the first five higher modes.

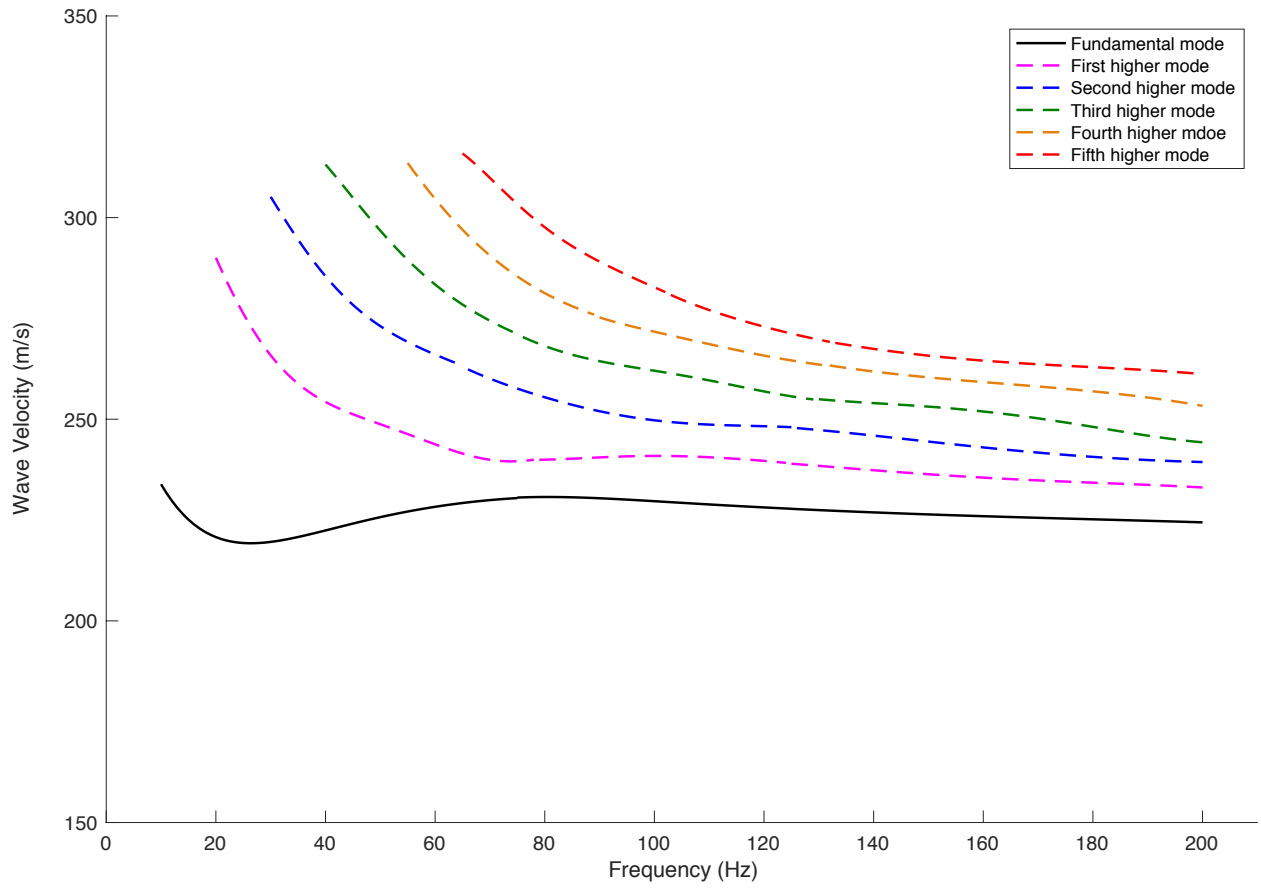


Fig. 6-37: Theoretical dispersion curve obtained from a numerical simulation of wave propagation in the 17-layers model with horizontal interfaces

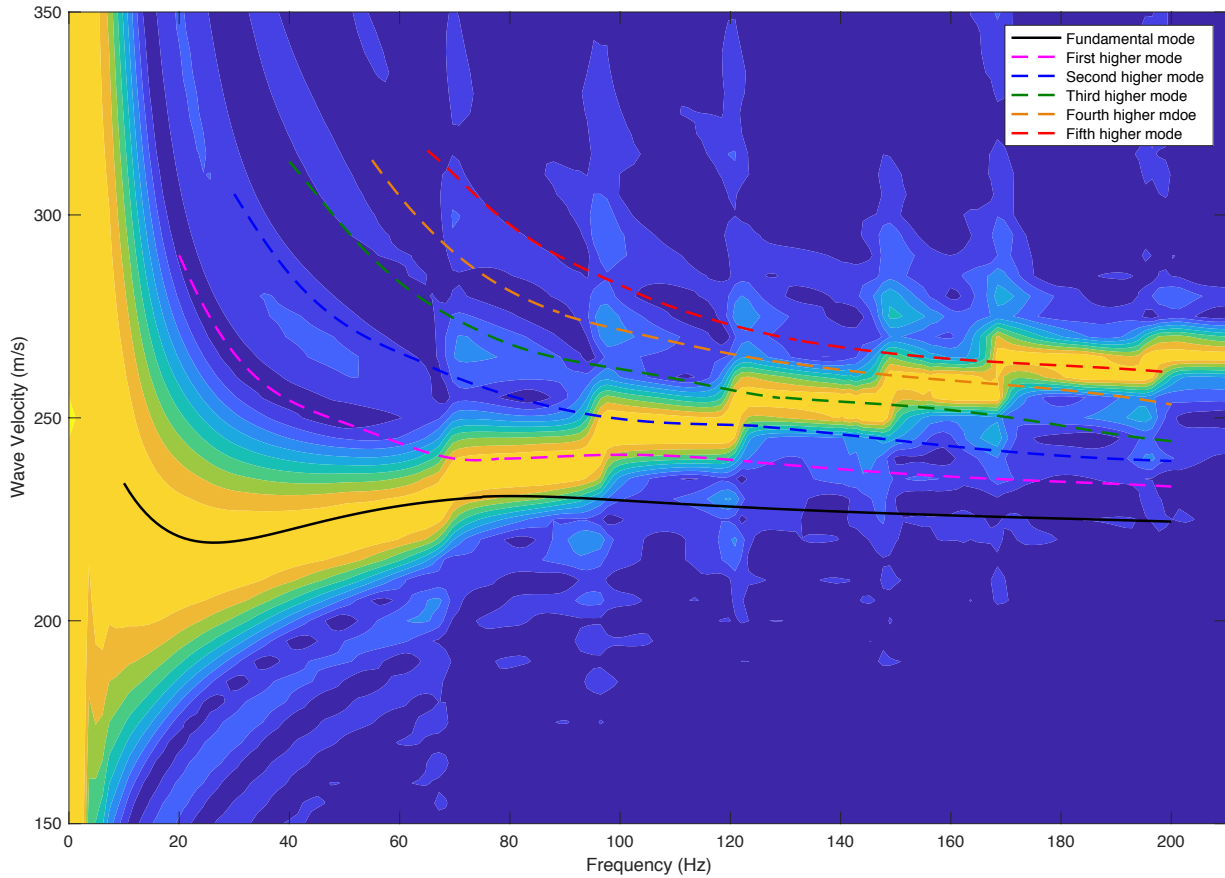
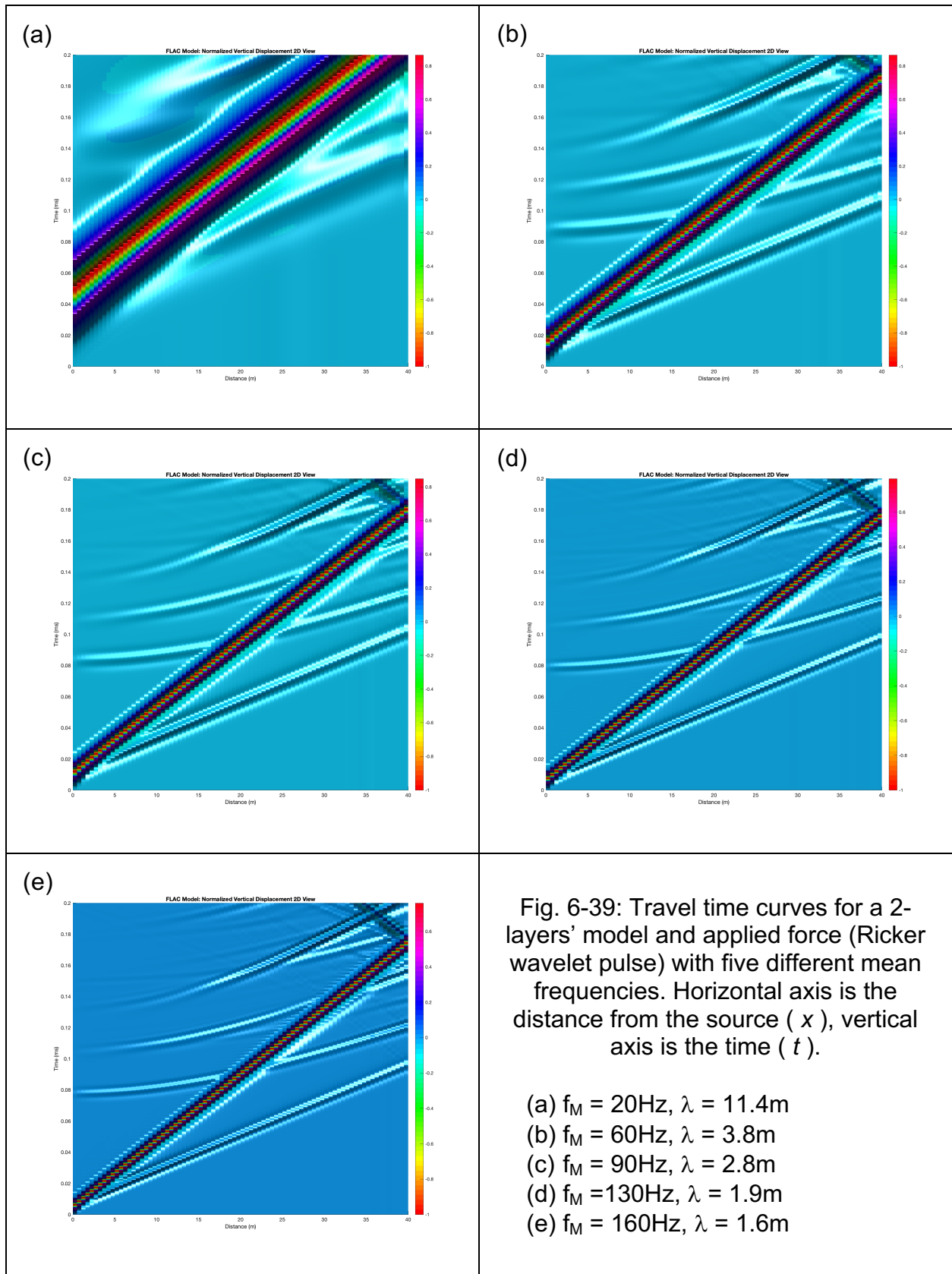
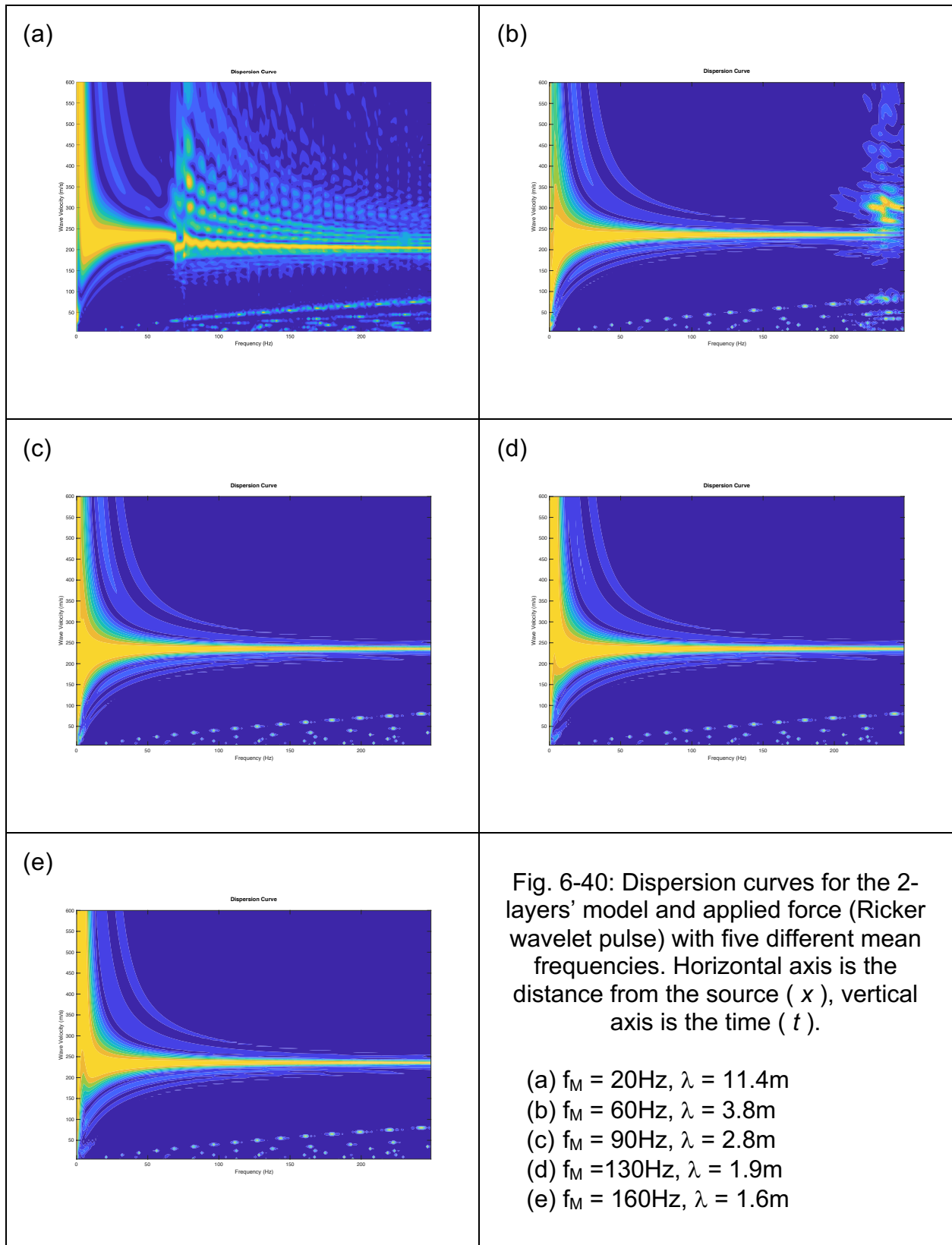


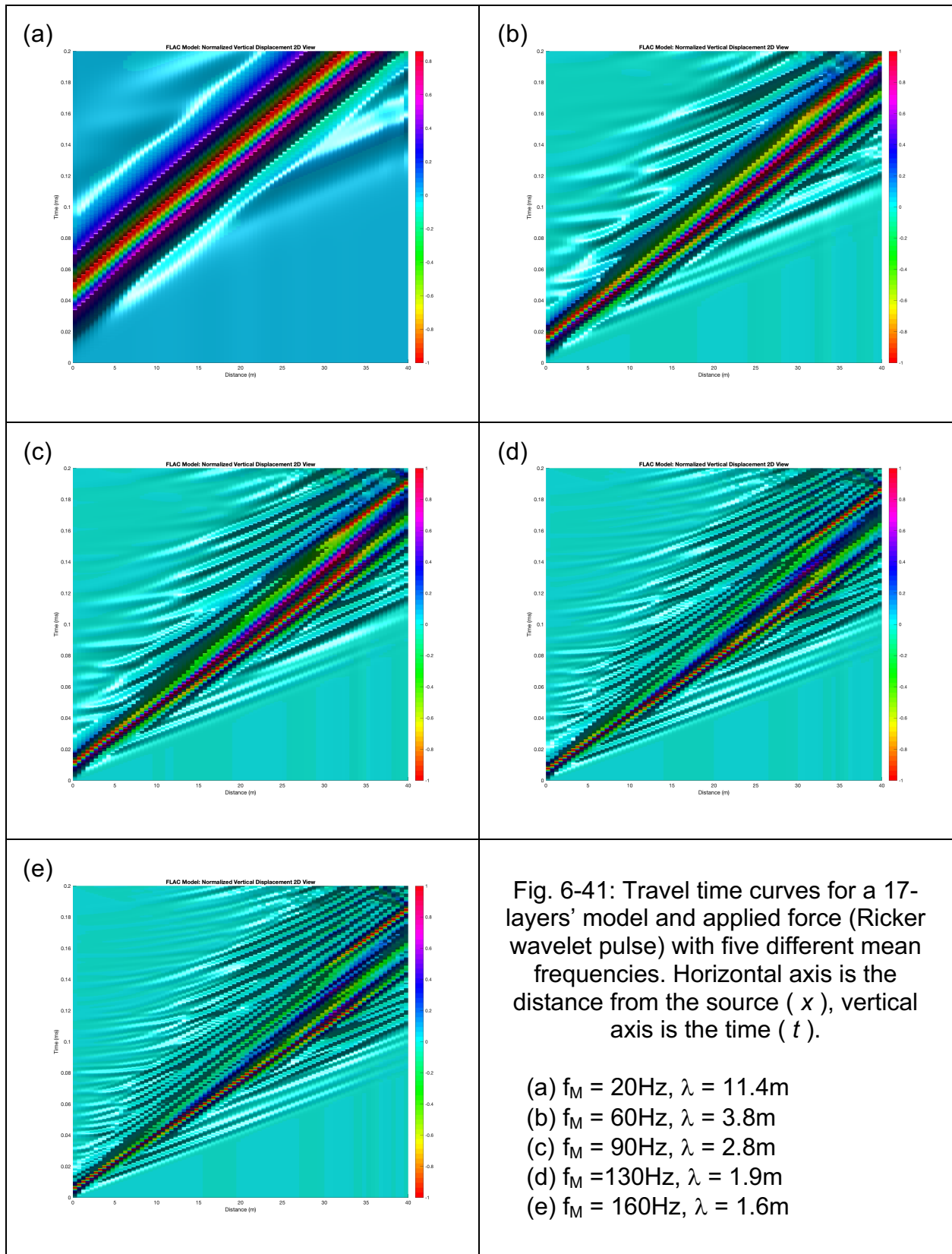
Fig. 6-38: Example of dispersion curve obtained from a numerical simulation of wave propagation in the 17-layers model with horizontal interfaces

All the results of travel time curves and dispersion curves for the approach of homogeneous medium and for the approach of horizontally layered medium, are presented in the following figures.

For the sake of the document, a sample of the results of travel time curves and dispersion curves for the approach in which the spatial distribution of material's properties follows a random field, and for five different input frequencies, is presented in the following figures. The full set of results is included in the Appendix A at the end of the document.







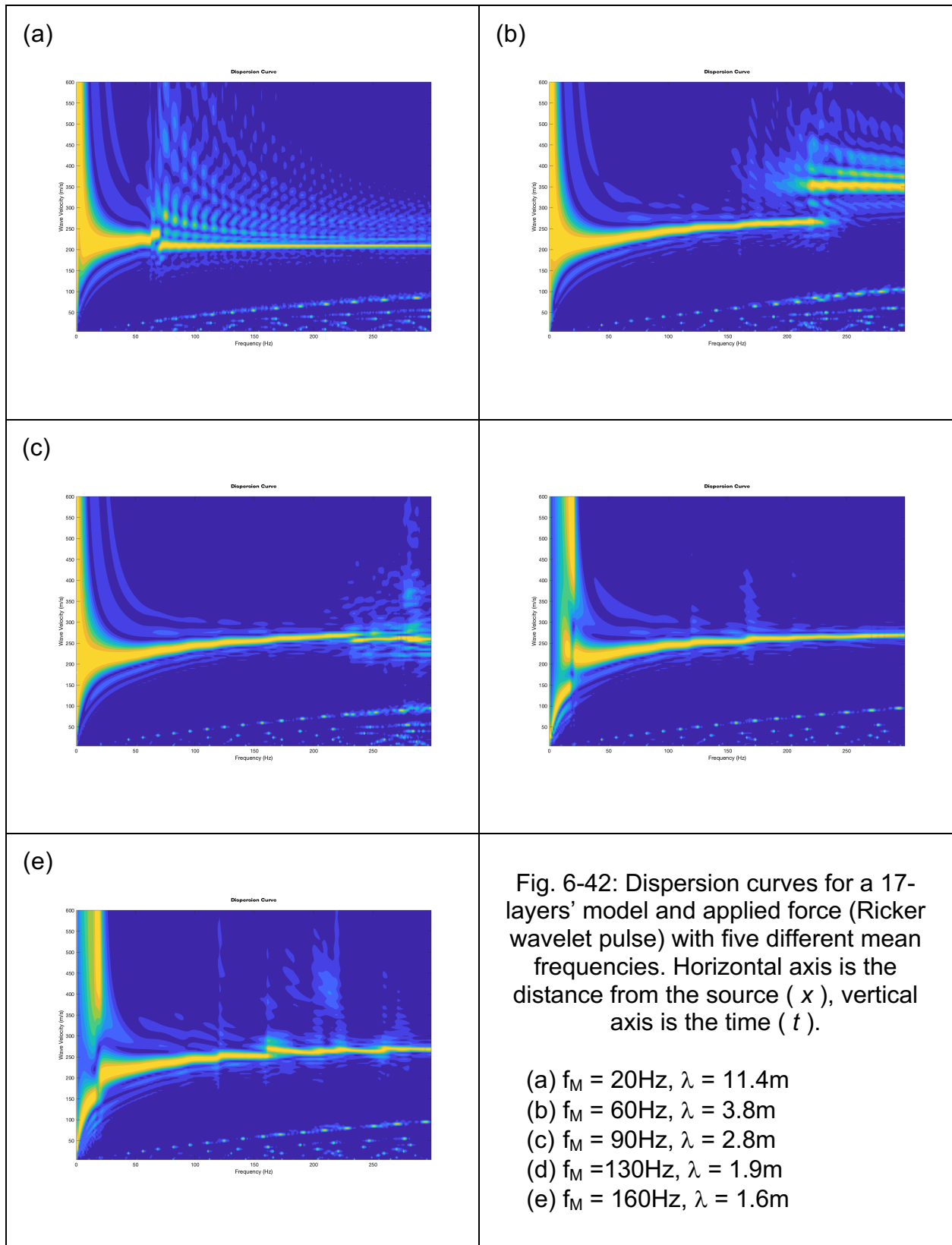


Fig. 6-42: Dispersion curves for a 17-layers' model and applied force (Ricker wavelet pulse) with five different mean frequencies. Horizontal axis is the distance from the source (x), vertical axis is the time (t).

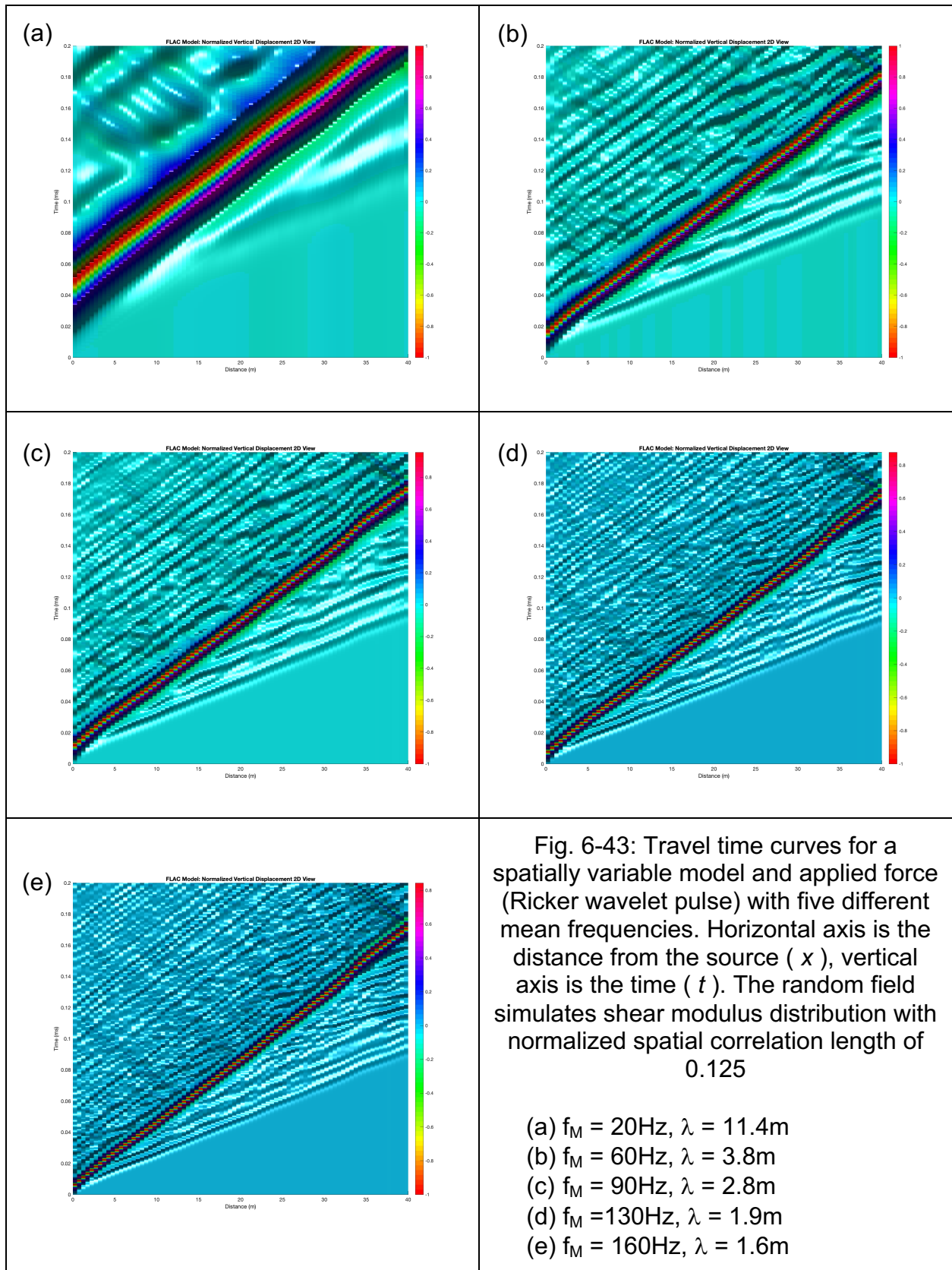


Fig. 6-43: Travel time curves for a spatially variable model and applied force (Ricker wavelet pulse) with five different mean frequencies. Horizontal axis is the distance from the source (x), vertical axis is the time (t). The random field simulates shear modulus distribution with normalized spatial correlation length of 0.125

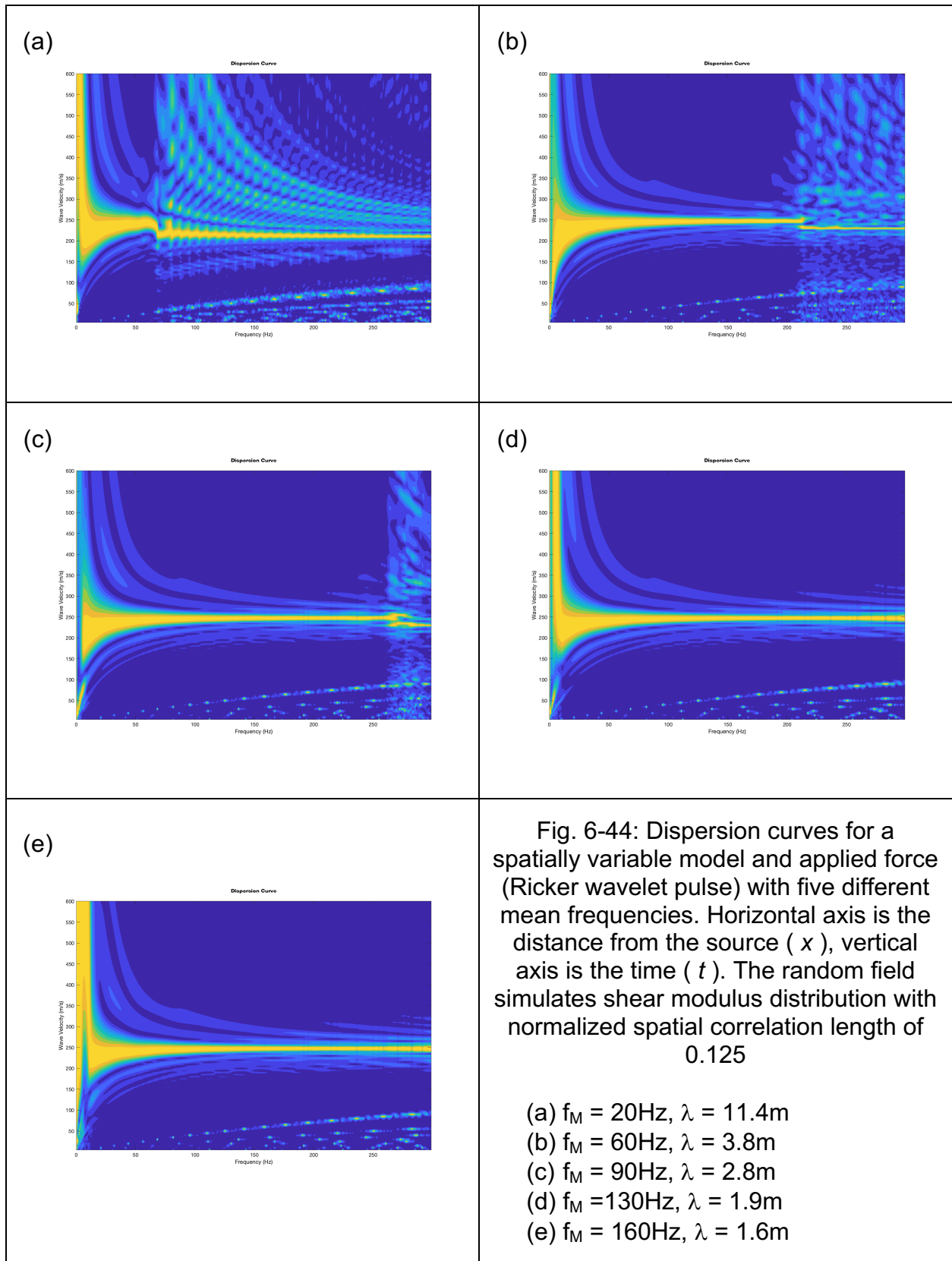
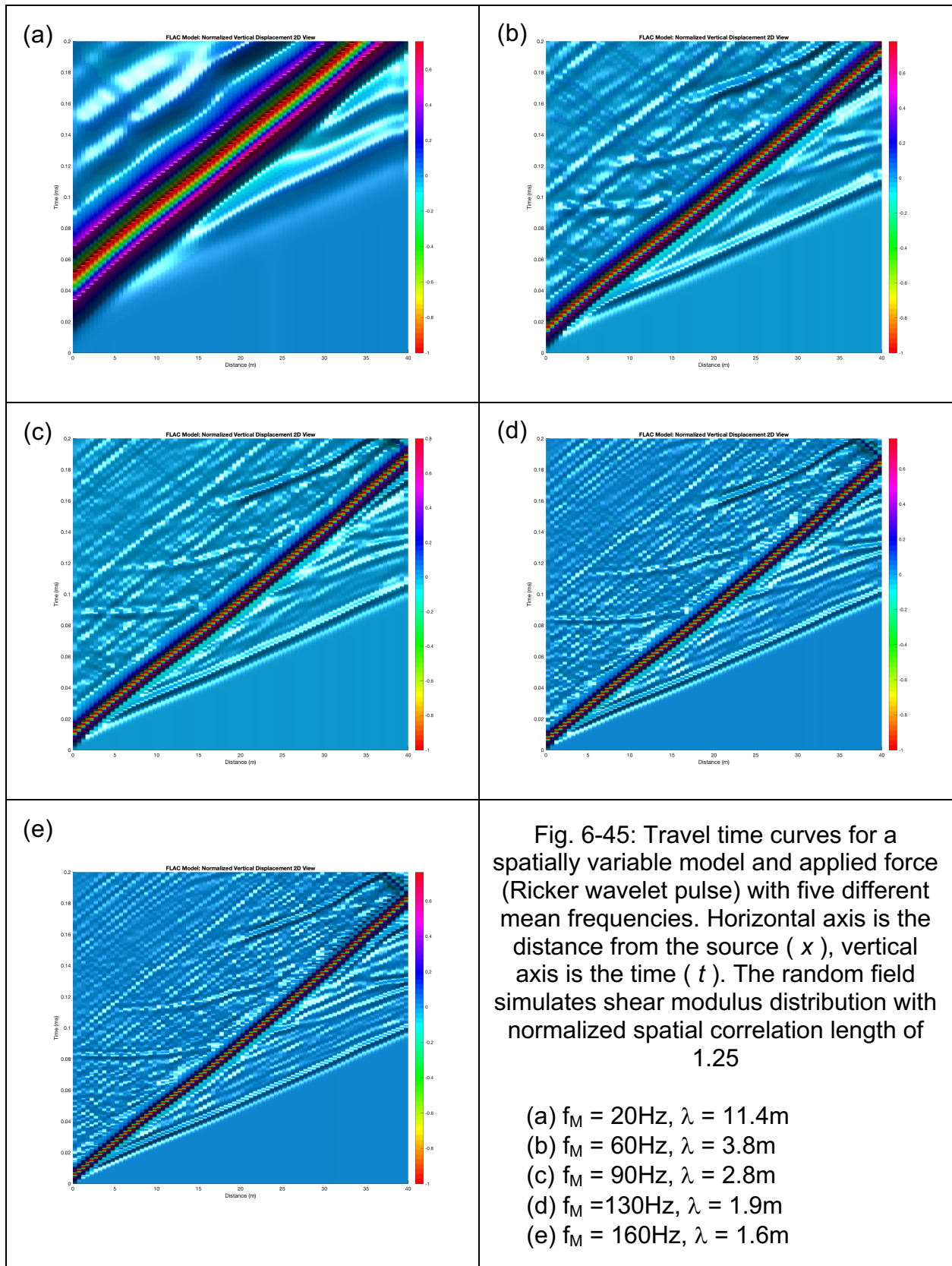


Fig. 6-44: Dispersion curves for a spatially variable model and applied force (Ricker wavelet pulse) with five different mean frequencies. Horizontal axis is the distance from the source (x), vertical axis is the time (t). The random field simulates shear modulus distribution with normalized spatial correlation length of 0.125



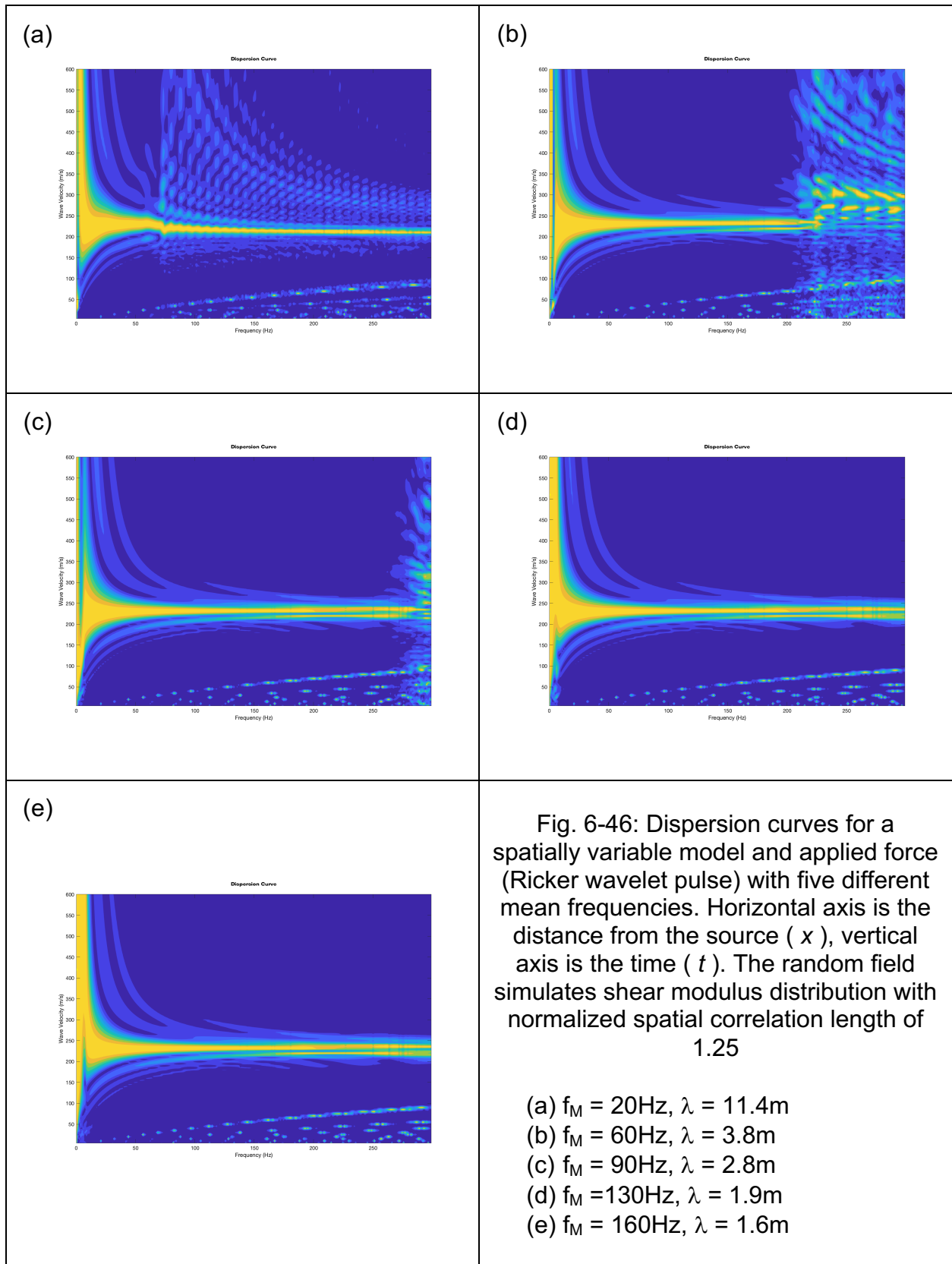


Fig. 6-46: Dispersion curves for a spatially variable model and applied force (Ricker wavelet pulse) with five different mean frequencies. Horizontal axis is the distance from the source (x), vertical axis is the time (t). The random field simulates shear modulus distribution with normalized spatial correlation length of 1.25

- (a) $f_M = 20\text{Hz}$, $\lambda = 11.4\text{m}$
- (b) $f_M = 60\text{Hz}$, $\lambda = 3.8\text{m}$
- (c) $f_M = 90\text{Hz}$, $\lambda = 2.8\text{m}$
- (d) $f_M = 130\text{Hz}$, $\lambda = 1.9\text{m}$
- (e) $f_M = 160\text{Hz}$, $\lambda = 1.6\text{m}$

6.4 Conclusions

This chapter presented the results for a large amount of numerical model considering different approaches to characterize the medium, as well as considering different frequencies in the input force.

The main conclusion obtained from this chapter is the fact that frequency seems to have an effect in the arrivals of the shear waves, no matter how the medium is approached (i.e. homogeneous, layered, or spatially variable). This fact is the motivation to study the effect of frequency content in the seismic field tests, which is presented in the next chapter.

In addition, the use of random fields could be beneficial in order to avoid the issues that arose when a layered medium is used to propagate seismic waves. However, the reader must be advised that in this chapter the random fields were unconditioned, and because of that, they are a bit far from the soil profile defined at the beginning of the chapter. That is another issue whose study will be presented in the next chapter.

7 Characterization of geomaterials at large scales: layered medium approach – analysis of frequency effects

The parametric studies presented in previous chapter were very illustrative about how some parameters affect the wave propagation in geomaterials when different approaches are considered (i.e. homogeneous medium, layered medium, and spatially variable medium). In this chapter, the layered medium approach is adopted in order to characterize a soil profile from the results obtained in the sCPTU field test. Then, numerical simulations are used to study the effect of frequency in the soil profile characterization.

7.1 Detailed procedure

The detailed procedure followed in this chapter to characterize geomaterials at large scales involves field testing and numerical simulations. The general steps followed are listed next and the complete and the detailed flowchart is presented in Fig. 7-1:

- Step 1 – Interpretation and processing of sCPTU field test results: it involves signal processing, numerical integration, near field analysis, and the interpretation of the test's results to obtain shear wave velocity profile
- Step 2 – Numerical simulations to approach the characterization of the excitation force: it requires the geometry and boundary conditions along with numerical simulation to identify the input force for the first approach in the inversion process.
- Step 3 – Frequency response analysis of the system: it includes transfer function calculations for the numerical model, source inversion for the field sCPTU system, and numerical simulation using the new force pulse. The analysis is done for horizontal accelerations and for horizontal displacements.
- Step 4 – Analysis of the effect of changes in the mean frequency of the input: includes the modification of the input force pulse obtained in inversion process in order to create a set of modified pulses with different input frequencies, then they are used in numerical simulation of the sCPTU tests to analyze the effect of changes in the input frequency.

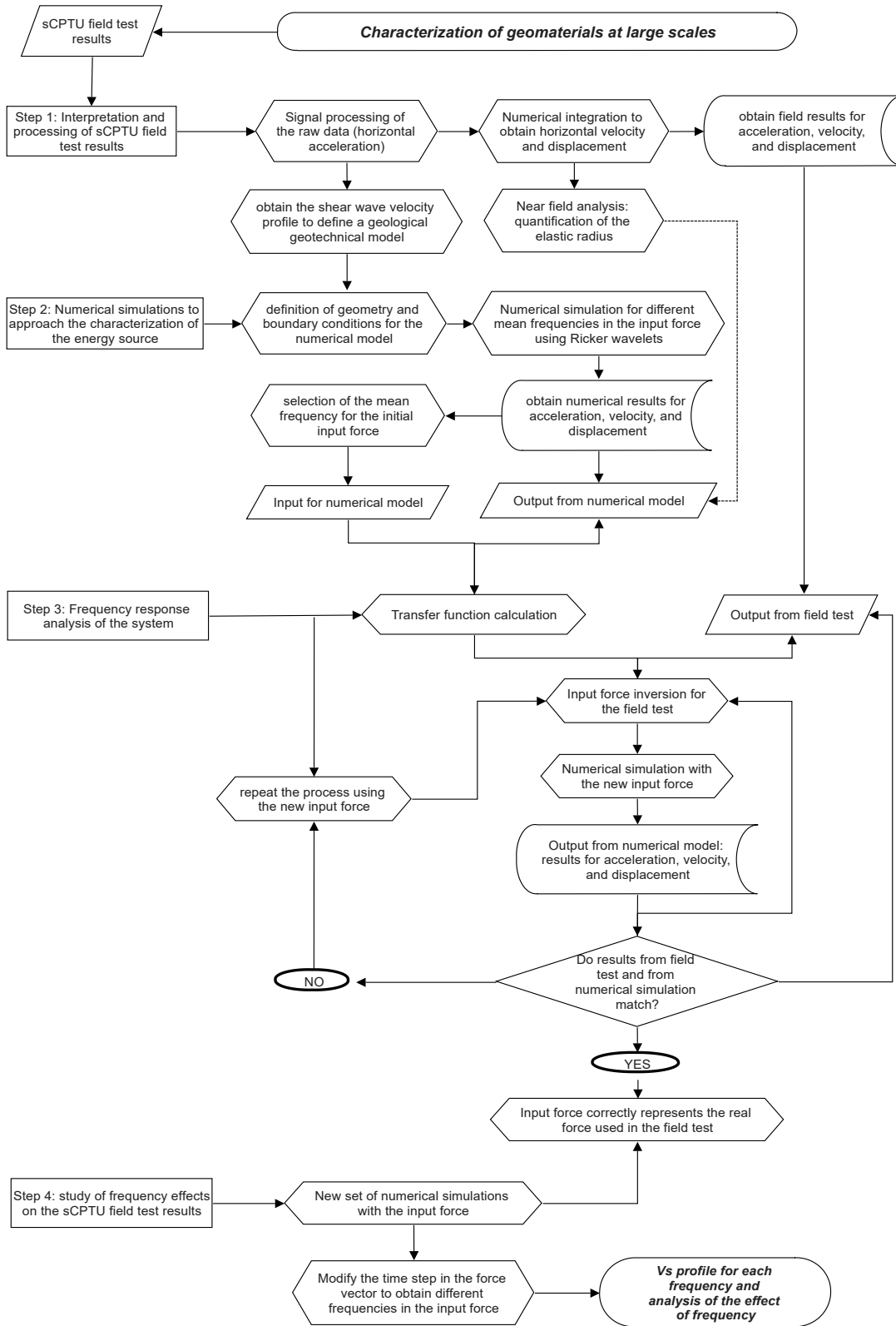


Fig. 7-1: Flow-chart of the procedure to characterize geomaterials at large scales

7.2 Step 1: interpretation and processing of sCPTU field test results

One part of the results of the sCPTU test was presented in Chapter 6 along with an explanation of how the test actually works and how the data was acquired. For the analysis presented in the previous chapter, the only data used were the cone tip resistance and the sleeve resistance. From those results, it was possible to obtain a profile of elastic properties to characterize materials and to create numerical models for the parametric study. In this chapter, the seismic records obtained from the sCPTU field test are now used to characterize the same materials and to create another set of numerical models seeking to study the effect of the input frequency in the test results from the sCPTU test.

7.2.1 Data acquisition in the field

As it was mentioned in chapter 6, three different sCPTU tests were performed in order to obtain the tip resistance, the sleeve resistance, the pore pressure, and the shear wave velocity at some specific depths. The equipment used to carry out the tests in the field was presented in Fig. 6-5. It corresponds to a commercial cone penetrometer machine equipped with a compact data logger which is able to continuously record both, cone tip and sleeve resistance, along with the pore pressure. So far the test has not included any seismic measurements, which require additional steps in the field.

The test configuration used in the field to record seismic data is presented in Fig. 7-2. In that case the probe is stop at the desired depth and then the metallic beams are hit using a sledge hammer to introduce seismic energy into the ground.

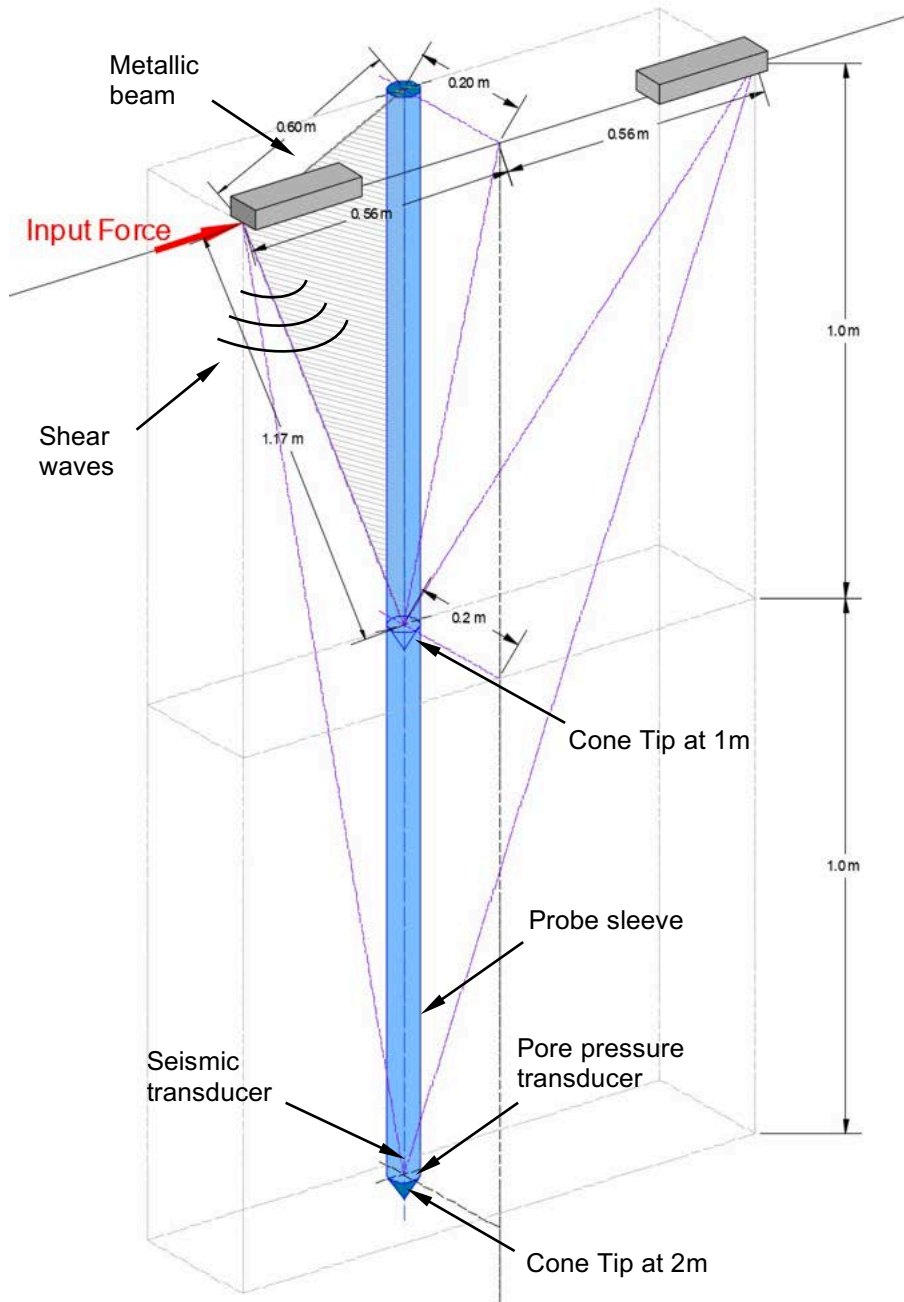


Fig. 7-2: Seismic cone penetration test (sCPTU) setup showing dimensions for the probe located at 1-meter depth and then when it was moved up to 2 meters' depth.

Typical baseline corrections were considered before and after the sounding. The pore water pressure was also measured during the test. Because the tests sCPTU-1 and sCPTU-3 were the closest ones to the alignment of the MASW tests, they were the only ones considered for the definition of the soil profile. The raw data obtained from these field tests are presented in Fig. 6-6 for the sCPTU-1, went down up to a depth of 16 meters.

As it was mentioned in the previous chapter, from these results and by using correlations with the cone resistance it is possible to obtain a continuous profile of parameters such as elastic modulus, bulk modulus, shear modulus, and even the mass density. However, it must be kept in mind the strain level at which the cone resistance is read, which is usually very high compared to the strain level generated by the typical wave-propagation phenomena in a seismic test. Thus, these results should not be used to estimate the absolute value of the shear wave velocity because it is highly probable to get an underestimation of its value. Nonetheless, the dynamic soil properties obtained in this way may be useful to understand some relative variations that could be expected in the wave-field generated in an sCPTU test.

The Poisson's ratio value of 0.45 was selected to characterize these materials. The sCPTU equipment recorded values every centimeter of penetration, thus, in order to build a model from these data series, an average of each parameter was calculated every meter. Finally, the results for sCPTU-1 were averaged every meter in depth.

The field results to consider in this chapter correspond to the seismic records of horizontal acceleration at different depths, which are used to obtain the shear wave velocity. An example of the time domain signals obtained in the field tests, along with their frequency spectra are presented in Fig. 7-3. During the field test, the metallic beams at each side of the cone penetrometer get hit three or four times per side in order to get a clearer response signal by taking the average of all the responses obtained each time the beam is hit.

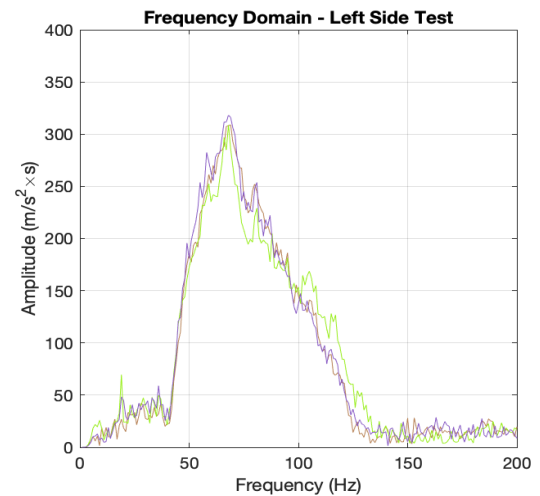
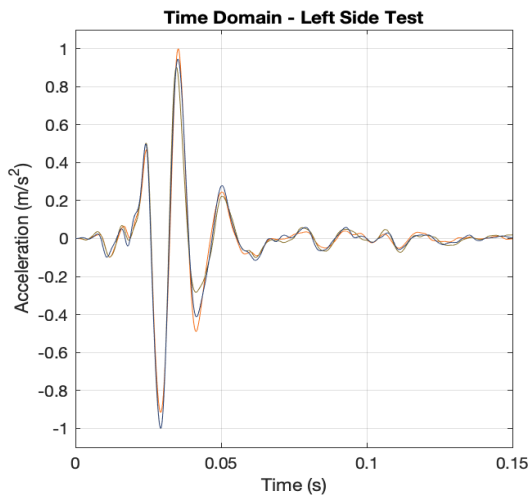
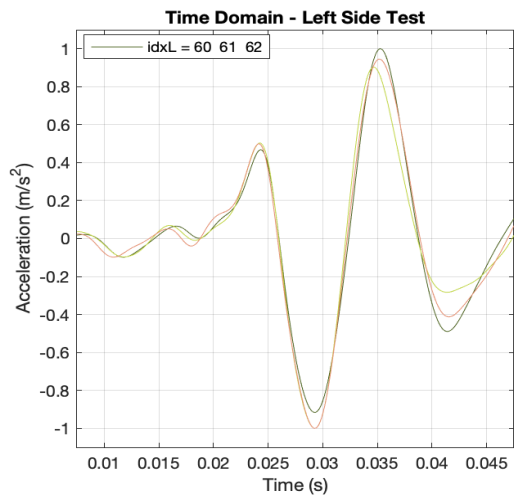
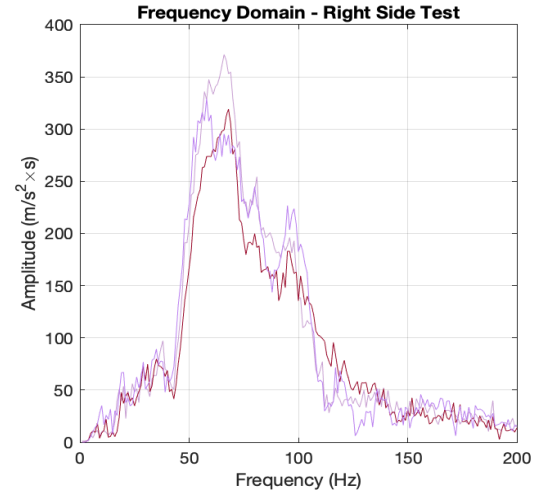
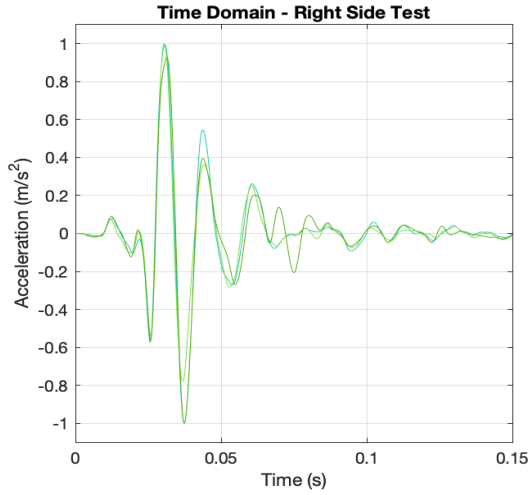
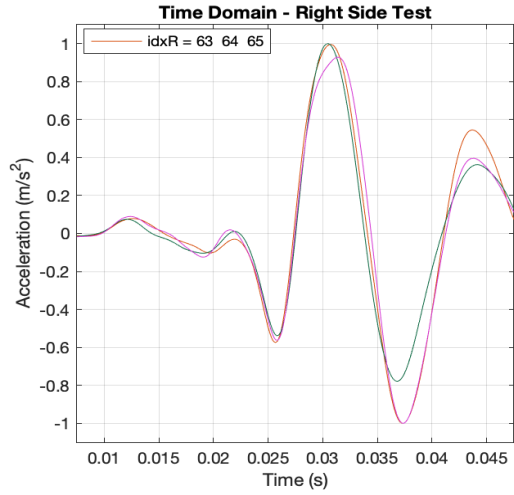


Fig. 7-3: Typical responses obtained from the sCPTU field test (for both, left and right side strikes): time domain (normalized) and frequency domain for horizontal acceleration at 4 meters' depth.

The raw data includes noise, so the records were processed by applying the following standard operations of signal processing:

1. Direct component removal
2. Signal denoising with the wavelet decomposition technique
3. Low-pass filter to remove relative high frequencies (i.e. higher than 200Hz)
4. High-pass filter to remove relative low frequencies (i.e. lower than 10Hz)
5. Signal detrending to remove erroneous linear trends in the data
6. Signal windowing using a tapered cosine window to clip the signal

After the signal processing, the acceleration data were numerically integrated using the cumulative trapezoidal method. This method approximates the area integration over an interval of the signal by splitting it down into trapezoids and accumulating the summation of areas of all the trapezoids over the signal length.

Typical results of horizontal acceleration data after signal processing, along with the results of numerical integration to obtain horizontal velocity, and horizontal displacement, are presented in Fig. 7-4. The results correspond to field data obtained at 4 meters' depth for the left-side sCPTU test.

From the time domain plots it is clear that the maximum and minimum values do not happen at the same time for acceleration, velocity, and displacement. This makes absolute sense since the maximum velocity must happen at the point when the change in displacement is maximum, and in a similar way, the maximum acceleration must correspond to the point where the change in velocity is maximum.

In the frequency domain, the peak frequency in the spectrum of the acceleration data is located in 67.75 Hz, then, after integration to obtain horizontal velocity the peak moves to 60.42 Hz. Similarly, after integration to obtain horizontal displacement the peak moves to 57.68 Hz.

Later in this chapter, the field data for horizontal acceleration, along with the results of the numerical integration to obtain velocity, and displacement, will be compared with the results of the same variables, that were obtained from numerical simulations.

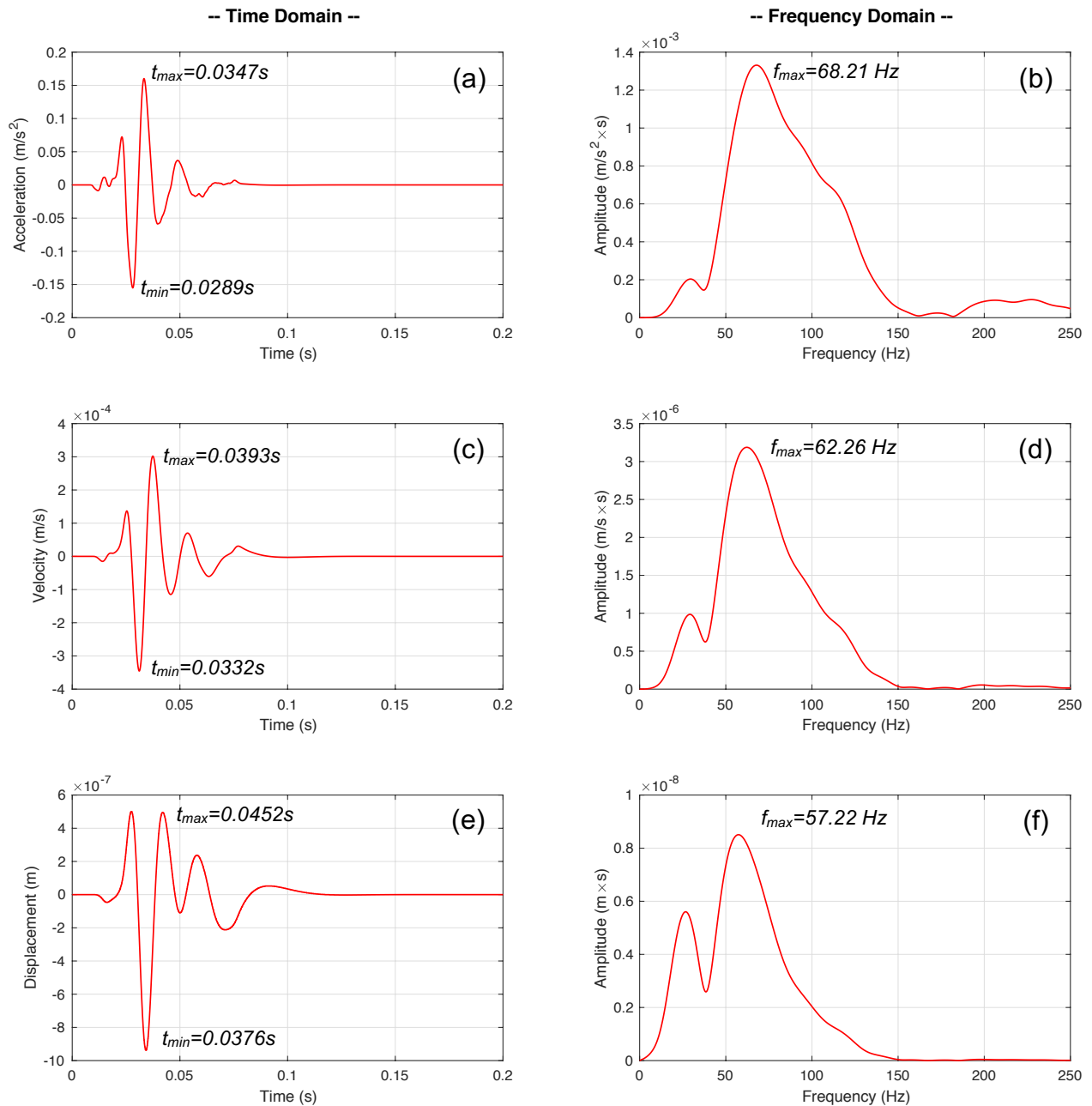


Fig. 7-4: Typical signals obtained from numerical integration of acceleration data from the sCPTU field test (left-side test at 4 meters' depth): time domain (left side plots) and frequency domain (right side plots). Plots (a) and (b) correspond to the horizontal acceleration data obtained in the field test. Plots (c) and (d) correspond to the horizontal velocity data obtained from numerical integration of horizontal acceleration data. Plots (e) and (f) correspond to the horizontal displacement data obtained from numerical integration of horizontal velocity data (i.e. double integration of acceleration data).

7.2.2 Near field analysis

The first issue to consider for the analysis of data from the sCPTU test is the estimation of the near field for the wave-field generated in this test. The analysis of radiation patterns for seismic waves generation is an issue out of the scope of this research.

The quantification of the near field generated by the input energy is not a trivial issue. Immediately after the force is applied to the medium the energy starts propagating following a nonlinear process. Lay and Wallace (1995), defined the concept of “elastic radius” (r_e) as the distance from the source at which a spherical surface exists and beyond which infinitesimal strain theory is valid. Thus, on that spherical surface and beyond, the elastic displacements and strains due to the effective pressure force, $F(t)$, can be properly estimated. That concept of elastic radius is somehow assimilated to the near field, in the sense that after that distance the elastic theory can be applied.

If it is assumed that the energy applied in the sCPTU test propagates following a spherical pattern inside the medium, it is a common practice to calculate the amplitude decay of body waves using a decay rate given by:

$$Amp(r) = \frac{1}{(r)} \quad (7-1)$$

where (r) is the distance from the excitation force.

Beyond the elastic radius, the three-dimensional equations of motion for an elastic solid, obtained from equilibrium requirements (Eq. 2-7), can be reduced to a one-dimensional wave equation (Lay and Wallace, 1995):

$$\frac{\partial^2 \phi}{\partial r^2} - \frac{1}{\alpha^2} \frac{\partial^2 \phi_p}{\partial t^2} = -4\pi F(t) \delta(r_e) \quad (7-2)$$

where (ϕ_p) is the displacement potential and $F(t)$ is the effective force function applied at the elastic radius (r_e). (Lay and Wallace, 1995) presented the following expression as the solution for the potential displacement.

$$\phi_p(r, t) = -\left(\frac{1}{\bar{r}}\right) * F \left[t - \left(\frac{\bar{r}}{\alpha}\right) \right] \quad (7-3)$$

where (\bar{r}) is the effective distance from the elastic radius $(r - r_e)$.

The first term on the right side of the Equation (7-3) is well known as the potential decay for body waves. Nonetheless, that decay rate is only applicable after the elastic radius, as for the near field the energy decays much faster. For many applications in traditional geophysics, the elastic radius is negligible when it is compared with the distance from the source. However, for near-surface geophysics applications, that assumption is not always acceptable and a proper quantification of the near field is needed.

Now, the data obtained in the sCPTU field tests corresponds to acceleration, no displacement. Strictly speaking, the concepts of elastic radius and potential decay, or decay rate, are related to the displacement potential, (ϕ) . Thus, displacement values should be obtained to quantify the near field, which were already calculated by applying a numerical integration technique to the acceleration data. However, no much difference was found when the decay is analyzed in acceleration data or displacement data.

If the depth of the near field in the sCPTU is assumed to be equal to the aforementioned elastic radius, the amplitude decay rate beyond that threshold can be calculated with the following expression:

$$Amp(r) = \frac{1}{(r-r_e)} \quad (7-4)$$

where the term $(r - r_e)$ is interpreted as the distance from the source subtracted by the elastic radius.

In the Fig. 7-5 the theoretical amplitude decay with depth is presented for different values of near field depth (elastic radius). Because the spatial resolution of data obtained in the field test was 1 meter, the results are presented for entire values of depth ranging from 0 to 4 meters.

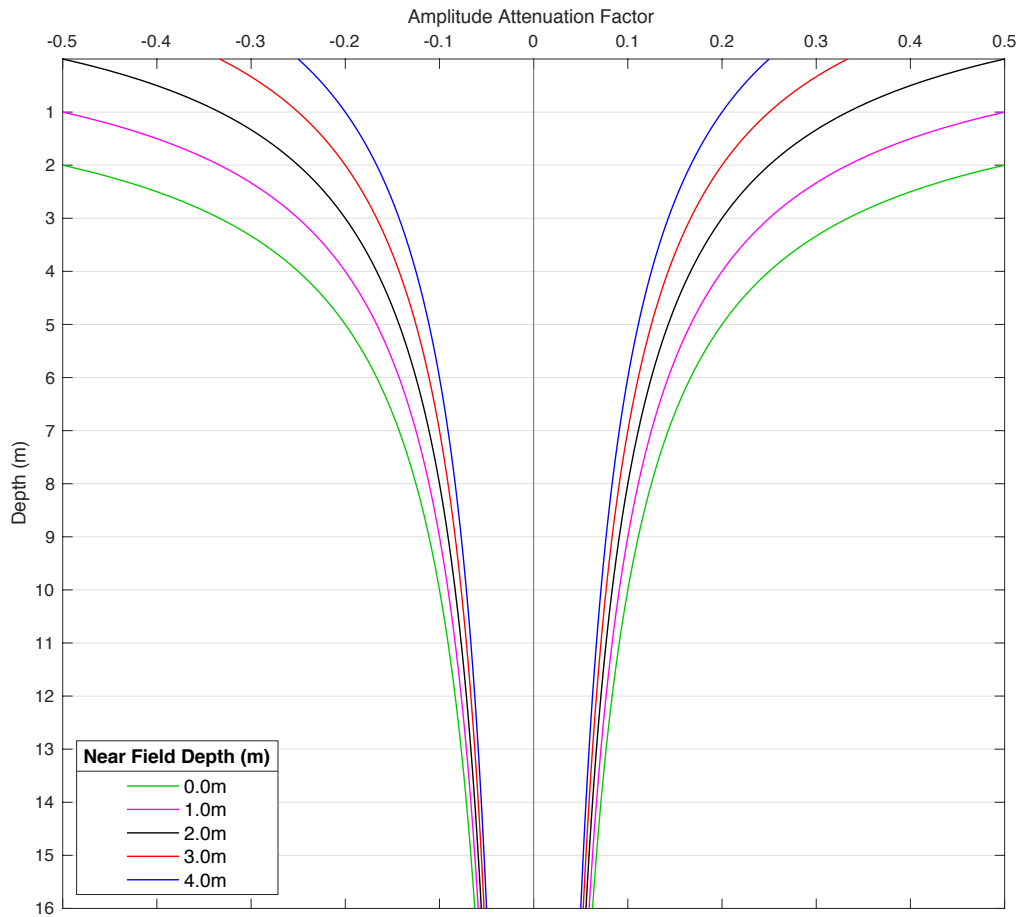


Fig. 7-5: Theoretical amplitude decay of body waves with respect to depth for different values of near field depth (elastic radius).

Now, the data obtained from the field test must be compared with the theoretical calculations of amplitude decay, the best match will define a quantification for the near field in the sCPTU test.

The maximum and minimum amplitudes of horizontal acceleration are obtained from the average signals at each individual depth and from each side in the field test (i.e. right side test or left side test). In these tests there was no record at the depth of 0 meters (i.e. ground level). The maximum and minimum values of acceleration obtained at 1-meter depth are out of the scale of the plot presented in Fig. 7-6 and their actual values are indicated in the plot.

The root-mean-square errors (RMSE) were calculated for the amplitude decay of horizontal acceleration considering different values of near field depth (elastic radius). These results are presented in Table 7-1. Considering there are four values of RMSE at each depth, one for each side of the test (left and right), and also one for maximums and one for minimum amplitude values, the average RMSE was calculated and it is presented in Fig. 7-7.

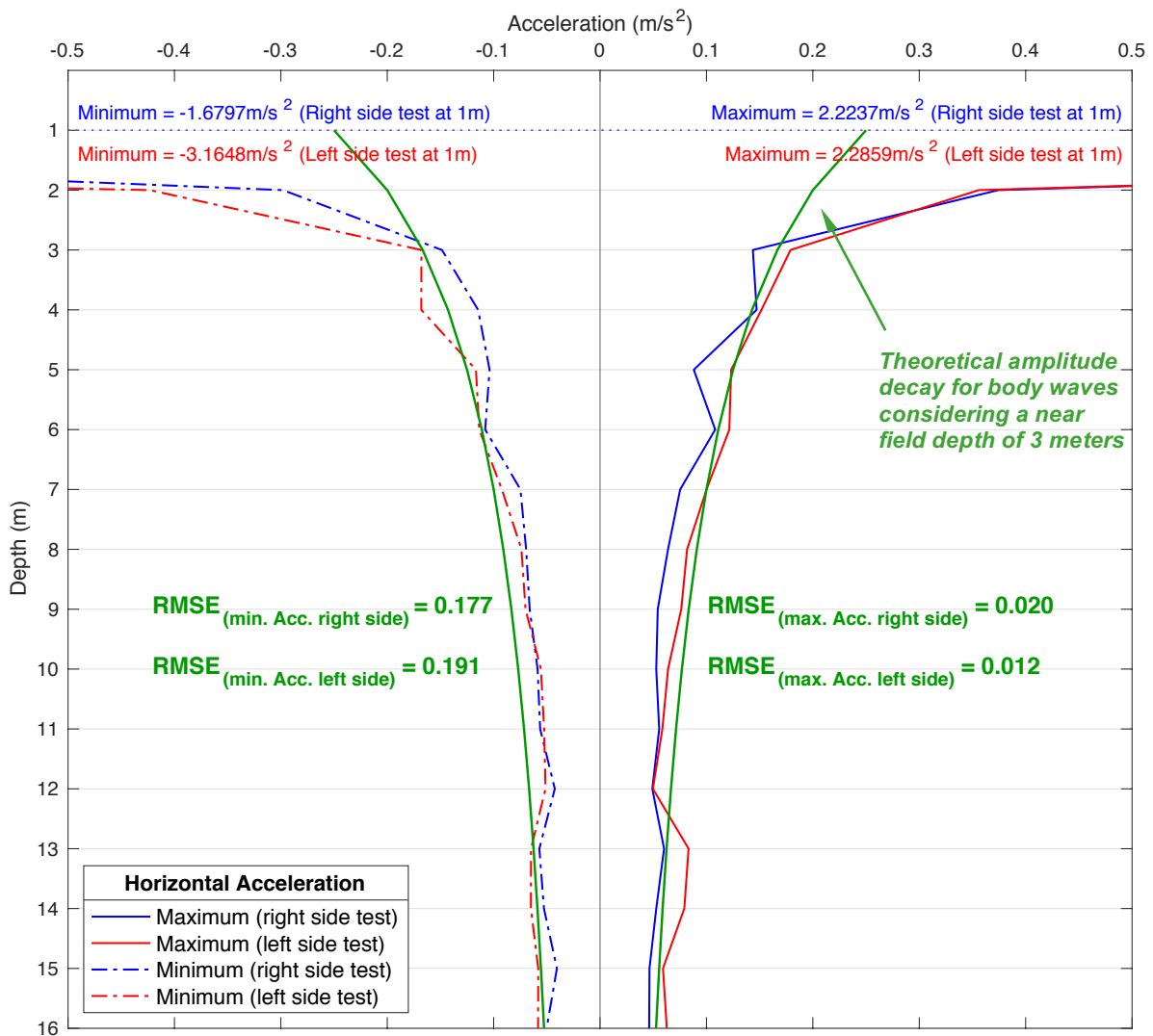


Fig. 7-6: Fitting of amplitude decay for horizontal accelerations data with respect to depth when a near field depth (elastic radius) of 3 meters is considered.

Table 7-1. Root mean square error for amplitude decay of maximum and minimum horizontal acceleration in the field test sCPTU #1 (left side and right side tests)

Near Field Depth (m)	RMSE for maximum acc. (right side test)	RMSE for maximum acc. (left side test)	RMSE for minimum acc. (right side test)	RMSE for minimum acc. (left side test)	Average RMSE
0.0	0.474	0.489	0.551	0.911	0.911
1.0	0.433	0.448	0.600	0.958	0.958
2.0	0.044	0.031	0.232	0.262	0.262
3.0	0.020	0.012	0.177	0.191	0.191
4.0	0.015	0.015	0.153	0.166	0.166
5.0	0.011	0.018	0.153	0.138	0.145

As it was expected, the RMSE values calculated between the field data and the theoretical decay curve show a reduction for deeper values of the near field. No guidance or criteria about how to define the correct value of near field depth for the sCPTU test was found in the literature. That is why in this research it is proposed that the elastic radius or the near field depth is taken at the depth where the RMSE values start following a smooth linear trend (see Fig. 7-7).

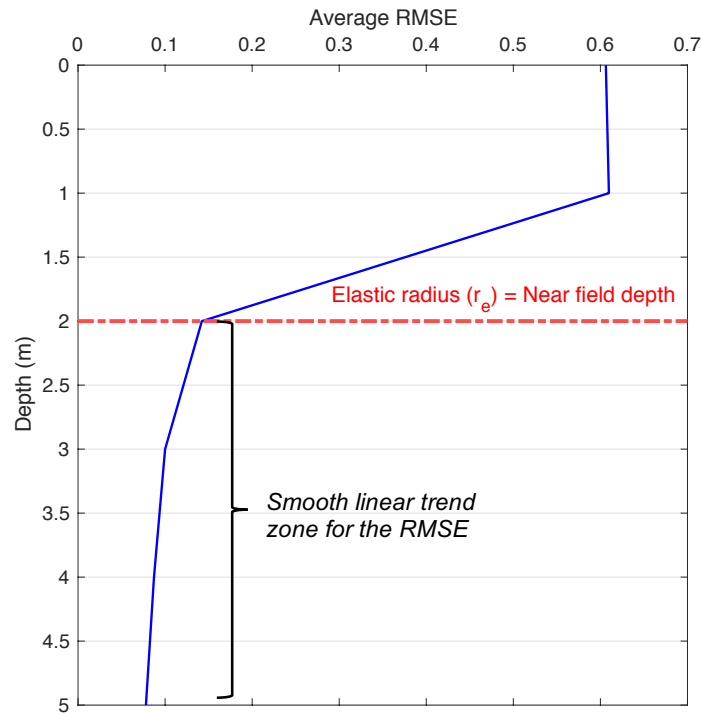


Fig. 7-7: Variation of RMSE with depth of the near field (elastic radius).

This result is critical for the sCPTU interpretation and for the rest of the analysis to be discussed later in this chapter. Having quantified the near field depth, it is possible to do a frequency response analysis considering the field testing site, beyond the elastic radius, behaves as a linear system. That will be presented later in this chapter.

7.2.3 Data interpretation according to ASTM standard

The specific ASTM standard to guide practitioners carrying out the seismic cone penetration test is designated as the downhole seismic testing (ASTM D7400, 2017). The test method is focused on the determination of the interval velocities from arrival times and relative arrival times of compression (P) waves and vertically (SV) and horizontally (SH) oriented shear seismic waves which are generated near surface and travel down to an array of vertically installed seismic sensors.

The P-wave and S-wave velocities are directly related to elastic parameters of the geomaterial being tested (i.e. Poisson's ratio, shear modulus, bulk modulus, and Young's modulus). Accurate in-situ P-wave and S-wave velocity profiles are essential in geotechnical foundation designs. These parameters are used in soil behaviour under both static and dynamic conditions. The fundamental assumptions in this kind of test are: first, that the geomaterial being tested is laterally homogeneous, so in that way the source wave train trajectories can be approximated to Snell's law of refraction; second, the medium is assumed to have transverse isotropy. (ASTM D7400, 2017)

A fundamental aspect to consider when testing soft soils is the fact that usually the P-wave velocity of the soil is less than the P-wave velocity of water (i.e. 1450 m/s), thus, the P-wave velocity identifiable in the signals will be controlled by the water rather than by the soil's skeleton.

An important caution made by the ASTM D7400 (2017) is that under the water table the behaviour is not exactly matching the theory, because the P-waves travel through solids and water and the measured velocity of P-waves is affected by the water, but S-waves travel only through solids and the measured velocity of S-waves is unaffected by the

water, so elasticity theory formulas correlating between the two using Poisson's ratio may not apply. (ASTM D7400, 2017)

The seismic signals of horizontal acceleration recorded at different depths in the field test are displayed in Fig. 7-10, along with an interpretation of the velocities profile made in accordance with the ASTM standard.

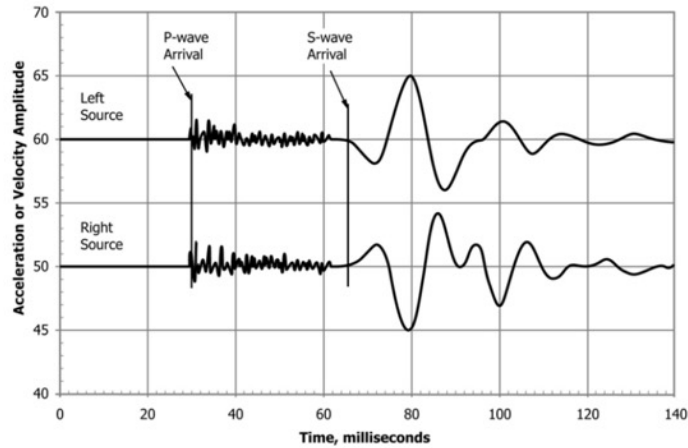


Fig. 7-8: Impulse seismic source produces P and S waves trains (ASTM D7400, 2017)

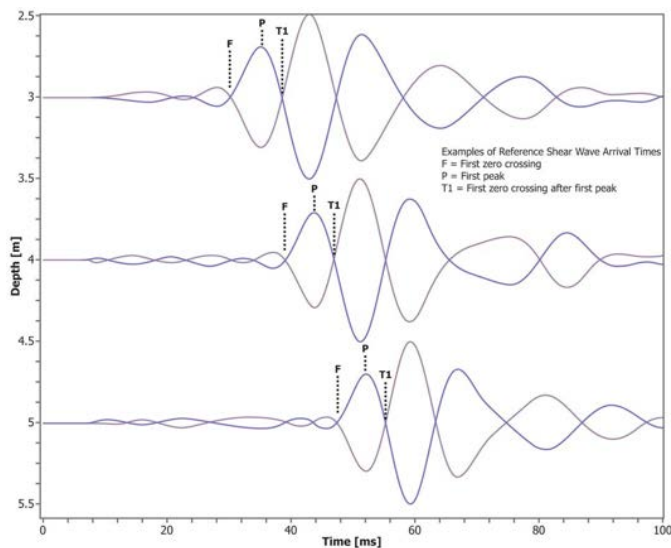


Fig. 7-9: Typical downhole shear wave arrival traces (signals with reversed polarity) (ASTM D7400, 2017)

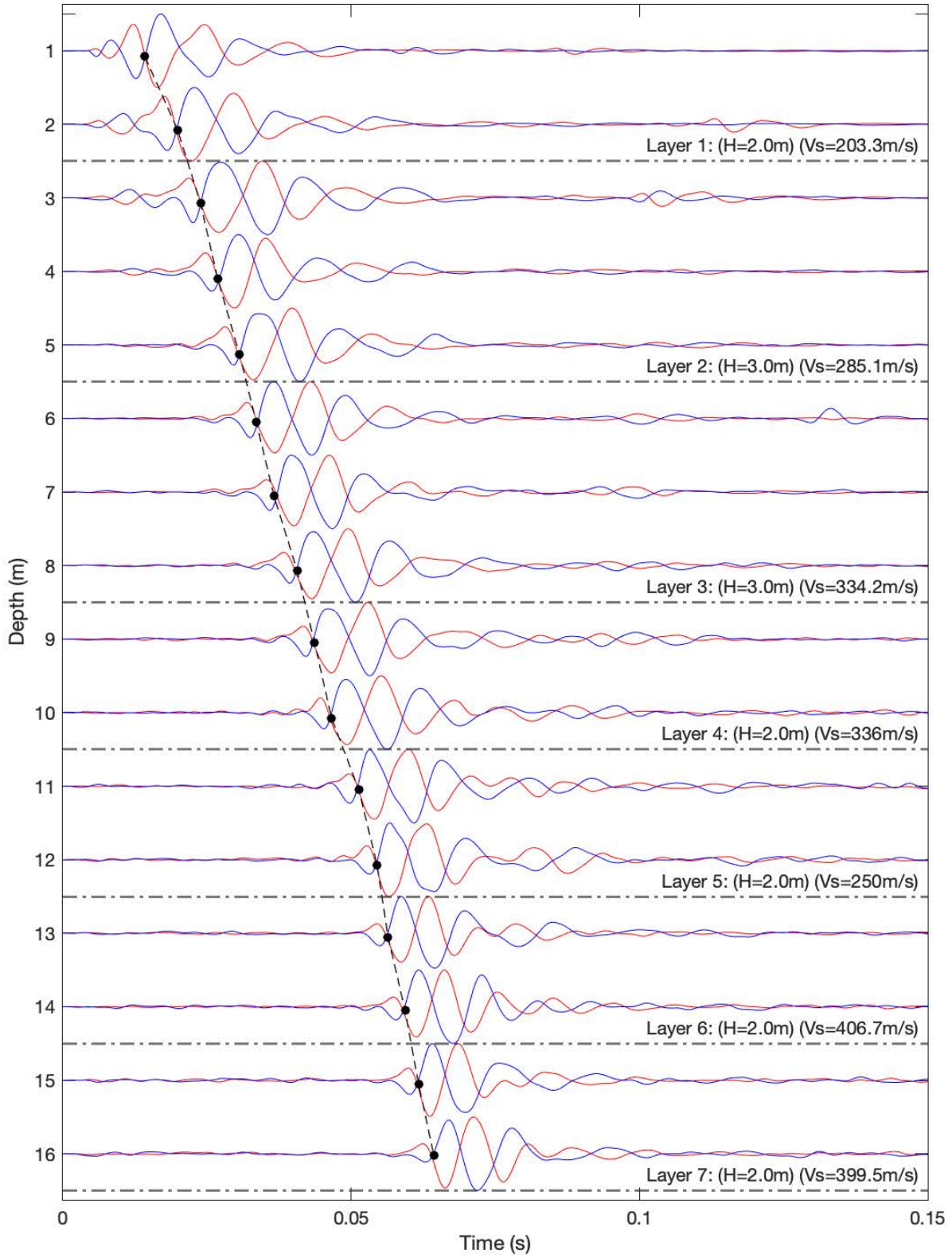


Fig. 7-10: Shear wave velocity (v_s) profile interpretation of the field test sCPTU #1 in accordance with (ASTM D7400, 2017)

In the previous chapter, the soil profile was characterized using the values of elastic parameters obtained by correlations with the cone resistance (tip and sleeve resistance). Now, in this chapter, after the interpretation of the seismic records the soil profile was characterized by profiling the shear wave velocity (see Fig. 7-10). With these results, it is possible to modify the numerical model used in Chapter 6 in order to fine-tune the values of shear wave velocity along with the associated elastic properties (i.e. shear modulus, and bulk modulus). The idea is to get a numerical model which is able to properly replicate the results obtained in the sCPTU field test. That task will be presented in the following section.

7.3 Step 2: numerical simulations to approach the characterization of the excitation force

The same FLACTM model created in chapter 6 to study the wave propagation phenomena when different approaches are considered for the soil profile, is now modified in this section seeking to replicate the sCPTU field test results. Considering that the numerical model was properly calibrated in chapter 6, no further calibration was done for the model. The purpose here is to get the best match possible between the signals of horizontal acceleration obtained in the field test and the signals obtained in a numerical simulation. The challenging part is the definition of the excitation force for the numerical models because there was no characterization of the actual source used in the field test, so the process is done by progressively modifying the input force in the numerical model.

7.3.1 Numerical model definition

In order to start the simulation, process a set of then numerical models was run using a Ricker wavelet as the input force. For each numerical model the mean frequency was modified in order to have a wide range of responses in the numerical model to compare with the field results. The explanation of the Ricker wavelet was presented in chapter 6 and plots of this kind of pulses were presented in time and frequency domain in the Fig. 6-16. In Table 7-2 the mean frequency for the Ricker pulses used to define the excitation force in the numerical model are presented, which are ranging from 50Hz to 84Hz, the

corresponding characteristic periods are also presented in the Table 7-2. The characterization of materials after the adjustment of the properties in the numerical model calibrated in chapter 6 are presented in Table 7-3. These properties define the numerical model to be used to replicate the results of the sCPTU field test.

Table 7-2. Mean frequency and characteristic period for different Ricker pulses used to define the excitation force in the numerical models.

<i>Model ID</i>	f_M (Hz)	T_D (s)
1	50	0.0156
2	54	0.0144
3	58	0.0134
4	63	0.0124
5	65	0.0120
6	68	0.0115
7	72	0.0108
8	76	0.0100
9	80	0.0100
10	84	0.0090

Table 7-3. Material properties from the seismic records of the sCPTU field test

<i>Layer ID</i>	<i>Depth</i> (m)	<i>Thickness</i> (m)	ρ (Kg/m ³)	ν	<i>E</i> (MPa)	<i>G</i> (MPa)	<i>K</i> (MPa)	v_s (m/s)	v_p (m/s)
1	0 - 1	1	1937	0.25	146.1	58.5	97.4	173.7	300.9
2	1 - 2	1	1937	0.25	146.1	58.5	97.4	173.7	300.9
3	2 - 3	1	1937	0.25	305.2	122.1	203.5	251.1	434.8
4	3 - 4	1	1937	0.25	543.4	217.4	362.3	335.0	580.3
5	4 - 5	1	1937	0.25	340.0	136.0	226.7	265.0	459.0
6	5 - 6	1	1937	0.25	563.3	225.3	375.5	341.1	590.7
7	6 - 7	1	1937	0.25	520.0	208.0	346.7	327.7	567.6
8	7 - 8	1	1937	0.25	293.5	117.4	195.7	246.2	426.5
9	8 - 9	1	1937	0.25	541.3	216.5	360.9	334.4	579.1
10	9 - 10	1	1937	0.25	552.4	221.0	368.3	337.8	585.0
11	10 - 11	1	1937	0.25	217.3	86.9	144.8	211.8	366.9
12	11 - 12	1	1937	0.25	478.7	191.5	319.1	314.4	544.6
13	12 - 13	1	1937	0.25	1355.2	542.1	903.4	529.0	916.3
14	13 - 14	1	1937	0.25	556.3	222.5	370.9	338.9	587.1
15	14 - 15	1	1937	0.25	876.6	350.6	584.4	425.5	737.0
16	15 - 16	1	1937	0.25	689.4	275.8	459.6	377.3	653.5
17	16 - 24	8	2000.0	0.25	1399.4	559.8	932.9	529.0	916.3

7.3.2 Numerical simulation results for different frequencies in the input force

In Fig. 7-11 some examples of the results for the horizontal acceleration at 4 meters' depth in the numerical model are compared with the results obtained in the sCPTU field test. The comparison is presented both in the time and the frequency domain.

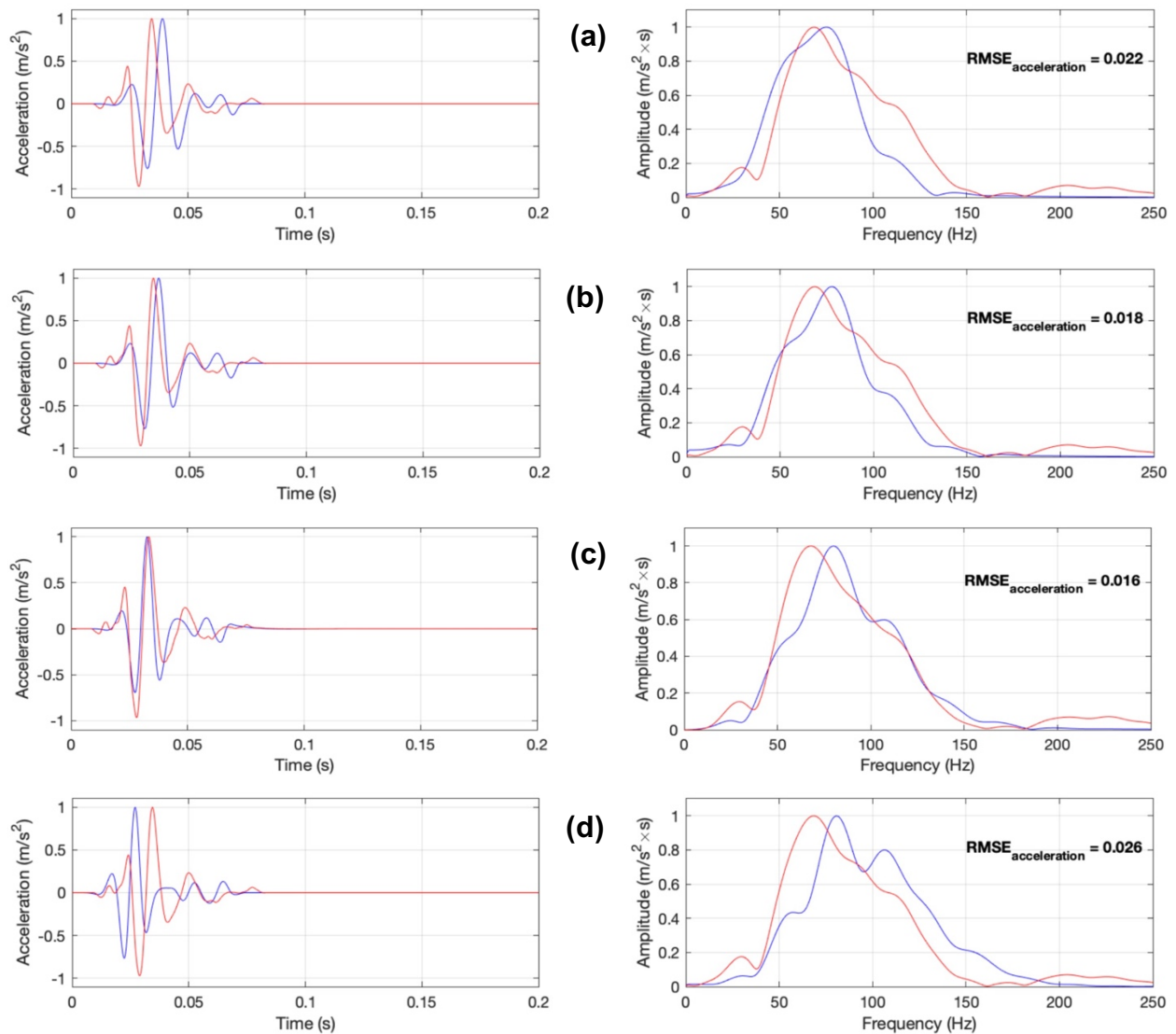


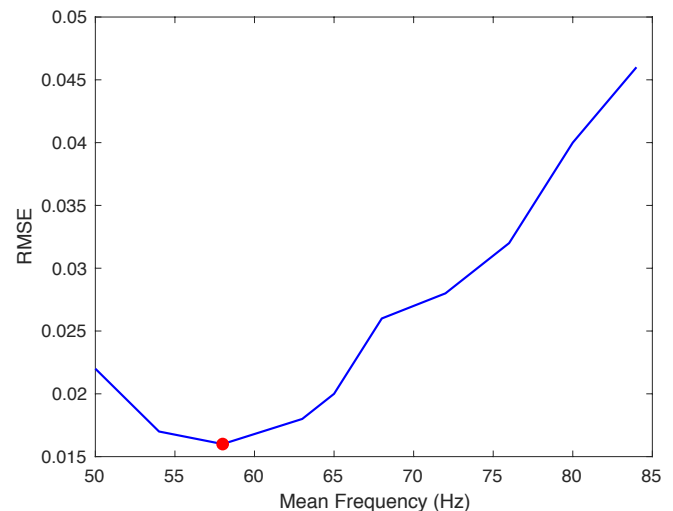
Fig. 7-11: Comparison between data of horizontal acceleration at 4 meters' depth obtained from the field sCPTU test (red) and from the numerical simulations (blue) when different peak frequencies are used in the input force (Ricker pulse): a) 50Hz, b) 54Hz, c) 58Hz, d) 68Hz

At this point it is not expected a good match in the time domain, because the shape of the source was perfectly symmetrical pulse and mathematically defined by an equation, which is not exactly what happens when the sledge hammer hits the metallic beam in the sCPTU field test. Nonetheless, in the frequency domain the match is expected to be better, so the RMSE was calculated between the amplitude of the Fourier transform of the field acceleration data and the data obtained from the numerical models. By a simple visual inspection, it could be said that the response of the numerical model to the Ricker pulse with mean frequency of 58Hz has a spectrum with similar shape to the spectrum for the field data. However, the RMSE for the ten numerical models were calculated and plotted to define the input frequency in the numerical model that generates horizontal acceleration with the best fit to the field data in the frequency domain.

The results of the RMSE calculated in the frequency domain for the ten models are presented in Table 7-4, for which is clear that the minimum RMSE is obtained for the model with input pulse corresponding to a Ricker wavelet with mean frequency of 58Hz. The minimum value is demarked by a red point in the left side figure.

Table 7-4. RMSE values obtained from comparison of frequency spectrums of field data and numerical simulation data with different mean frequencies in the input pulse.

Model ID	f_M (Hz)	RMSE
1	50	0.022
2	54	0.018
3	58	0.016
4	63	0.018
5	65	0.020
6	68	0.026
7	72	0.028
8	76	0.032
9	80	0.040
10	84	0.046



In Fig. 7-12 the results of acceleration, velocity, and horizontal displacements obtained at 4 meters' depth from the numerical simulation, are compared against the results obtained from the field test. In the case of horizontal acceleration from the field test, the signal is the result of applying signal processing to the raw data recorded during the sCPTU test, while for the horizontal velocity and displacement, the signals were obtained from the numerical integration process described in a previous section.

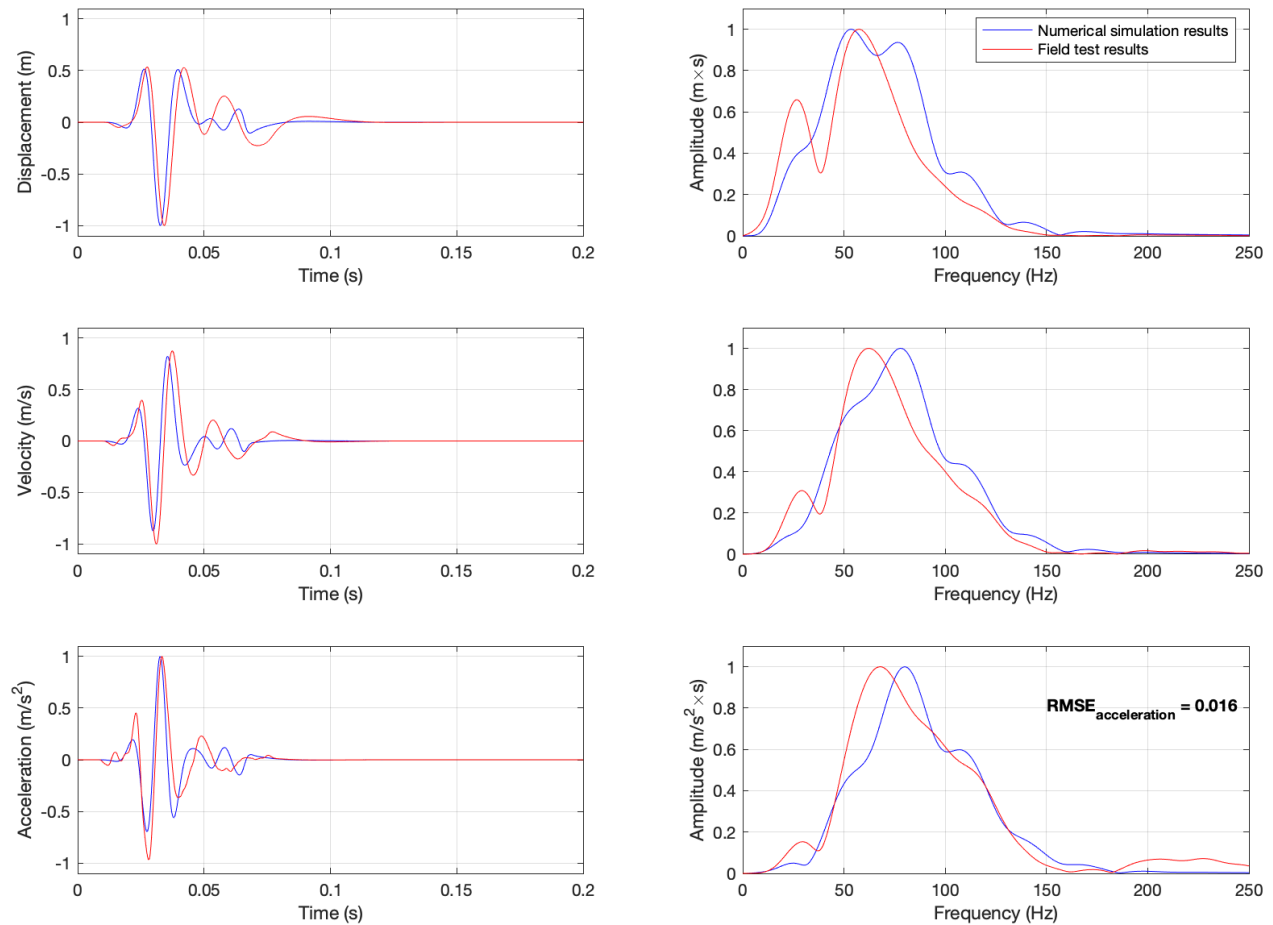


Fig. 7-12: Responses at 4 meters' depth obtained from the field test (red) and from the numerical simulation (blue) when the input pulse has mean frequency of 58Hz. For the field test response, the data recorded in the field was acceleration, while velocity and displacement were obtained by numerical integration.

From the results of this set of numerical simulations, the one important conclusion that can be extracted is the actual value for the mean frequency in the Ricker wavelet used as input force, which generates acceleration signals that match the field records with the minimum RMSE in the frequency domain, that frequency was found to be 58Hz.

Even though the acceleration signals do not match very well in the time domain, the match in the frequency domain is considered to be good enough to calculate the frequency response function (a simplification of the transfer function). Also the displacement data exhibits a good fit between numerical results and the results of the numerical integration of field sCPTU data, so displacements are the other variable to be considered as the output of the system. This analysis will be presented in the next sections.

7.4 Step 3: frequency response analysis of the system (sCPTU field test)

In linear invariant systems theory, the transfer function involves both, the phase response of the system, and the frequency response. The latter could be calculated as the ratio between frequency spectrums obtained using the Fourier transform. However, to calculate the full transfer function, the Laplace transform must be used for calculations, rather than the Fourier transform. This simple consideration is not trivial and complicates the analysis quite a lot, because in order to use Laplace transform the continuity in the input and output functions is needed, which is not the case for discrete data obtained in the sCPTU tests.

In order to make the analysis feasible, in this research it is considered that the frequency response analysis is good enough to represent the behaviour of the system, which is true in many cases as long as the frequency response is dominant over the phase response. Thus, it must be clear that whenever a transfer function is mentioned in this research, just the frequency response is considered because it is being calculated via Fourier transform rather than Laplace transform.

The sketch of the sCPTU test and the soil medium, both together interpreted as a linear invariant system is presented in Fig. 7-13.

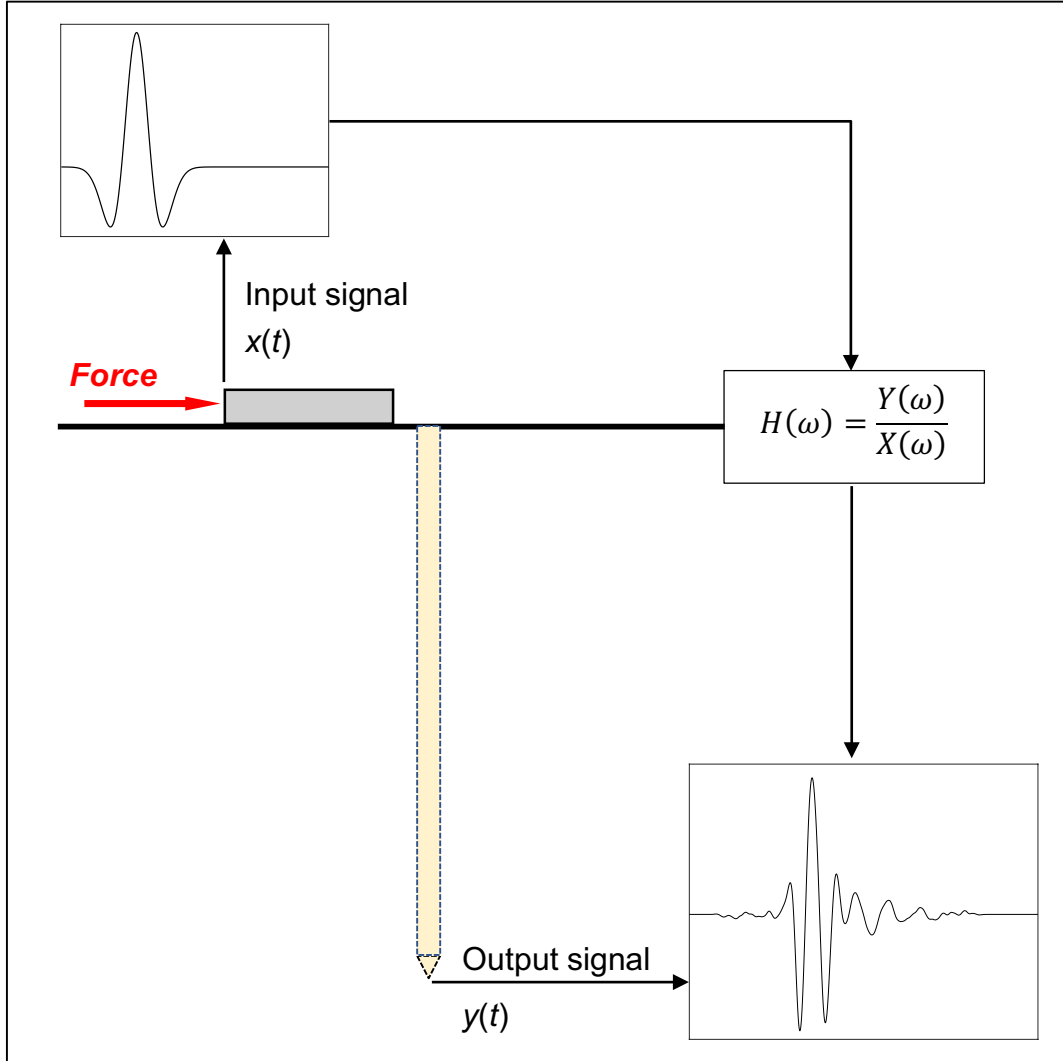


Fig. 7-13: sCPTU field test system and definition of input and output signals to be involved in the transfer function calculation.

The transfer function for this system is given by the following expression:

$$H(\omega) = \frac{Y(\omega)}{X(\omega)} \quad (7-5)$$

where $Y(\omega)$ is the Fourier transform of the output signal (system's response), and $X(\omega)$ corresponds to the Fourier transform of the input signal (system's excitation). The transfer

function can be easily calculated for the numerical models because the input and the output are well known. However, for the field test is not the same because the input (i.e. the excitation force characterization) is unknown, the only certain data in the field test is the output, which in this case corresponds to the horizontal acceleration.

At this point, the immediate goal is to obtain the transfer function that characterizes the sCPTU test in the field, which means the characterization of the real input force is needed. If a numerical model properly represents what happens in the field, then its input force would correspond to the real input force used in the sCPTU field test. In this research a process to obtain the real input source characterization using numerical modeling is proposed and explained next as a list of tasks:

- (a) Use the field results from the sCPTU test to build a numerical model that represents the soil profile. The geometry of the medium and its elastic properties must be as closer to the reality as possible.
- (b) Identify the depth of the near field and select a point beyond that threshold to perform the calculation of transfer function.
- (c) Assume the input force has the shape of a Ricker wavelet and find a mean frequency (f_M) close to the peak frequency of the field data.
- (d) Run a numerical model using that input force and obtain the output of the model for the point selected in numeral (2).
- (e) Calculate the first transfer function for the numerical model.

$$H_{model_1}(\omega) = \frac{Y_{model_1}(\omega)}{X_{model_1}(\omega)} \quad (7-6)$$

- (f) Assume the transfer function for the model also characterize the sCPTU field test system, then calculate the Fourier transform of the input force as it follows:

$$H_{SCPT_1}(\omega) = H_{model_1}(\omega) = \frac{Y_{SCPT_1}(\omega)}{X_{SCPT_1}(\omega)} \quad (7-7)$$

$$X_{SCPT_1}(\omega) = \frac{Y_{SCPT_1}(\omega)}{H_{model_1}(\omega)} \quad (7-8)$$

(g) Obtain the input force in the time domain by taking the inverse Fourier transform:

$$x_{SCPT_1}(t) = IFFT[X_{SCPT_1}(\omega)] = IFFT\left[\frac{Y_{SCPT_1}(\omega)}{H_{model_1}(\omega)}\right] \quad (7-9)$$

(h) Run a numerical simulation using the input force just obtained: $x_{SCPT_1}(t)$

(i) Calculate the second transfer function for the numerical model.

$$H_{model_2}(\omega) = \frac{Y_{model_2}(\omega)}{X_{SCPT_1}(\omega)} \quad (7-10)$$

(j) Recalculate the Fourier transform of the input force estimated for the field test by taking the Fourier transform of the output for the field test divided by the transfer function of the numerical model, as it follows:

$$H_{SCPT_2}(\omega) \approx H_{model_2}(\omega) = \frac{Y_{SCPT_1}(\omega)}{X_{SCPT_2}(\omega)} \quad (7-11)$$

$$X_{SCPT_2}(\omega) = \frac{Y_{SCPT_1}(\omega)}{H_{model_2}(\omega)} \quad (7-12)$$

(k) Obtain the time domain of the input force estimated for the field test by taking the inverse Fourier transform:

$$x_{SCPT_2}(t) = IFFT[X_{SCPT_2}(\omega)] = IFFT\left[\frac{Y_{SCPT_1}(\omega)}{H_{model_2}(\omega)}\right] \quad (7-13)$$

(l) Calculate the final transfer function for the sCPTU field test system:

$$H_{SCPT}(\omega) = \frac{Y_{SCPT}(\omega)}{X_{SCPT_2}(\omega)} \quad (7-14)$$

The results for the tasks 1 to 4 were already presented in previous sections of this chapter, so in the following numerals, the results of tasks 5 to 12 are explained and the summary of the results is presented in Fig. 7-15.

7.4.1 Excitation force inversion when the horizontal acceleration is used as the output for the assimilated linear invariant system

In order to calculate the transfer function for the numerical model it is necessary to define the input and the output of the system, then, their corresponding Fourier transforms must be calculated. The transfer function is then computed as the ratio between the Fourier transforms of the output and the input. The Fig. 7-14 shows the input signal, which is defined by the Ricker wavelet pulse obtained in previous section, with a mean frequency of 58Hz. In the time domain the signal is clear the maximum amplitude of the horizontal force applied to the model, which in this case was 1kN.

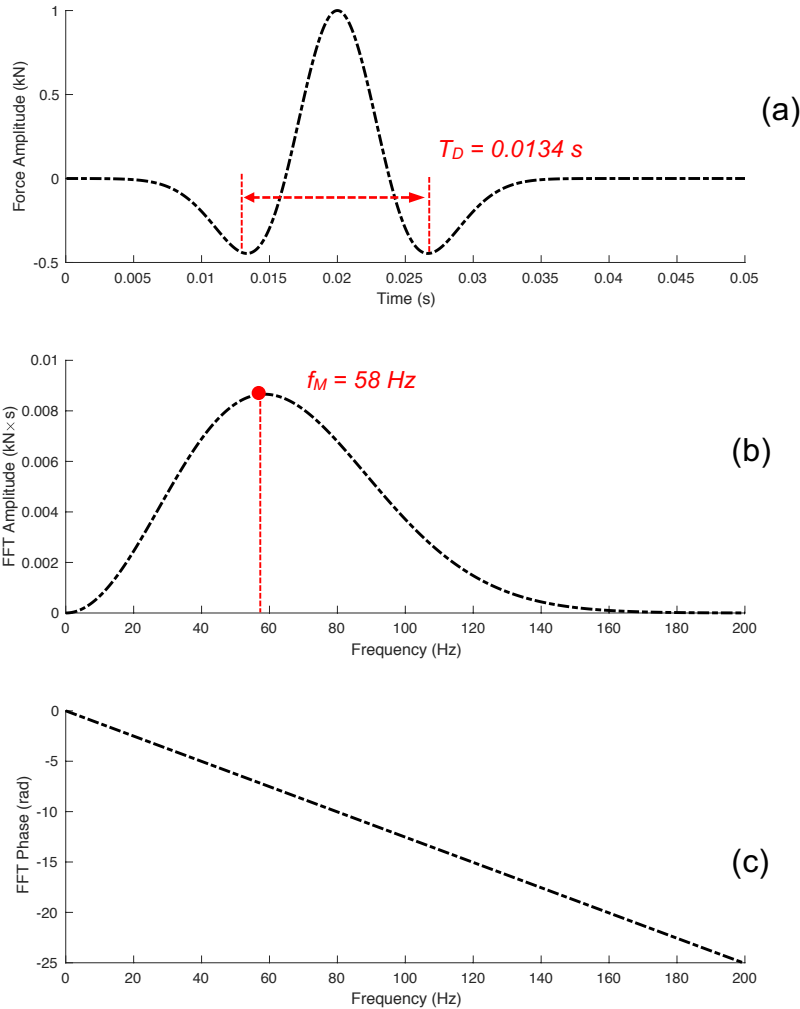


Fig. 7-14: Input pulse (Ricker wavelet) with mean frequency of 58Hz.

For the output signal, the horizontal acceleration at a given selected depth is taken as the system's response. Considering the results of the near field analysis developed in section (7.2.2), the elastic radius or near field depth for the sCPTU field test was estimated to be 2 meters. Thus, the point for the output signal and for the transfer function calculation must be selected beyond that threshold. For this analysis the point for the output signal was chosen at 4 meters' depth, which correspond to the signals presented in Fig. 7-12.

The result of all the mathematical and numerical operations for the inversion of the excitation force are shown in Fig. 7-15 and the content of every plot in that figure is explained next.

- (a) Initial input force used for the numerical model.
- (b) Fourier transform of the initial input force for the numerical model.
- (c) Inverse discrete Fourier transform of (b) in order to obtain back the input force used in the numerical model.
- (d) Output horizontal acceleration obtained at 4 meters' depth in the numerical model.
- (e) Fourier transform of the horizontal acceleration in (d).
- (f) Inverse discrete Fourier transform of (e) in order to obtain back the output horizontal acceleration obtained from the numerical model at 4 meters' depth.
- (g) Amplitude of the transfer function calculated by taking the absolute value of the division of Fourier transform of the output (e), divided by the Fourier transform of the input (b).
- (h) Fourier transform of the input force used in the numerical model: now it is obtained by dividing the Fourier transform of the output horizontal acceleration obtained from the numerical model at 4 meters' depth (e), into the transfer function obtained for the numerical model (g).
- (i) Inverse Fourier transform of (h) to obtain the inverted input signal. The plot compares the original initial input force and the one obtained via the inversion process. This operation proves the numerical process followed to invert the input force actually works when the transfer function of the numerical model is used.

- (j) Output horizontal acceleration obtained from the sCPTU field test at 4 meter's depth.
- (k) Fourier transform of the horizontal acceleration in (j).
- (l) Inverse discrete Fourier transform of (k) in order to obtain back the output horizontal acceleration obtained from the sCPTU field test at 4 meter's depth.
- (m) Amplitude of the transfer function calculated by taking the absolute value of the division of Fourier transform of the output (e), divided by the corrected Fourier transform of the input shown in (b). The aforementioned correction deals with the fact that the Fourier transform of the input can actually exhibit some zeros (roots), or some very small values, which makes the division to take very high values. Those high values may create a numerical result biased in the input force inversion, so to avoid the problem the Fourier transform of the input is added by an epsilon (ϵ) value. The epsilon value is selected to be between 0% and 5% of the maximum amplitude in the Fourier transform of the input.
- (n) Fourier transform of the input force estimated for the sCPTU field test: it is obtained by dividing the Fourier transform of the output horizontal acceleration obtained from the sCPTU field test at 4 meters' depth (k), into the corrected transfer function obtained for the numerical model (m).
- (o) Inverse Fourier transform of (n) to obtain the estimation of the inverted input force in the sCPTU field test. This result will be used as the input force in the numerical model for the next iteration.

A way to assess the results obtained in this analysis, is by actually comparing the horizontal acceleration at the 4 meters' depth from the numerical model against the sCPTU field recorded data. The comparison was done in the time domain, as well as in the frequency domain, all along with the respective transfer function. The input force and the output horizontal acceleration in the time domain, both from the numerical model and from the sCPTU field test are presented in Fig. 7-16 (a). As it can be seen, the match in the time domain response (i.e. horizontal acceleration) is not quite exact, however it is good enough to see the shape in the response is similar and the arrivals for the shear waves are very good. Nonetheless, the amplitude in the response is still too different.

These results should not be surprising as this was the first iteration and the input force for the numerical model was a Ricker wavelet.

Fig. 7-16 (b) shows the input force and the output horizontal acceleration in the frequency domain, both from the numerical model and from the sCPTU field test. From these Fourier spectra it is clear that the signal response from the numerical simulation shows higher energy than the one from the sCPTU field test, which is caused for an input force higher than it should be applied in the numerical model. Fig. 7-16 (c) shows the transfer function calculated both for the numerical model and for the field test results.

The previously discussed results (i.e. the ones shown in Fig. 7-15 and Fig. 7-16) correspond to the first iteration in the excitation force inversion process, as it was presented in the flowchart in Fig. 7-1. The same process was repeated two more times, each time using the input force obtained in the previous iteration as the initial input force for the numerical model. The results are presented in Fig. 7-17 and Fig. 7-18 for the second iteration, as well as in Fig. 7-19 and Fig. 7-20 for the third iteration. The same results presented in Fig. 7-20 are presented for all the depths between 2 meters and 16 meters (i.e. beyond the elastic radius) in a video that can be accessed in the following link https://youtu.be/KhfZP_IR-Ug.

All the input forces involved in this inversion process are compared both in the time domain and in the frequency domain, the results are shown in Fig. 7-21. In order to evaluate the convergence in the iteration process, the root mean squared error (RMSE) is calculated and the values displayed in the plots. Although the responses in the time domain (i.e. horizontal acceleration) are getting closer in shape and amplitude, in Fig. 7-21 it is clear that the input force changes shape and amplitude in the time domain showing a non-convergent process.

At this point there were two ways to actually proceed: first, to continue repeating the inversion process until the input force does not change much and the output response; second, to repeat the process but now using horizontal displacement instead of horizontal acceleration as the output of the system. The decision was made to take the second branch and the results are analyzed in the next section of this chapter.

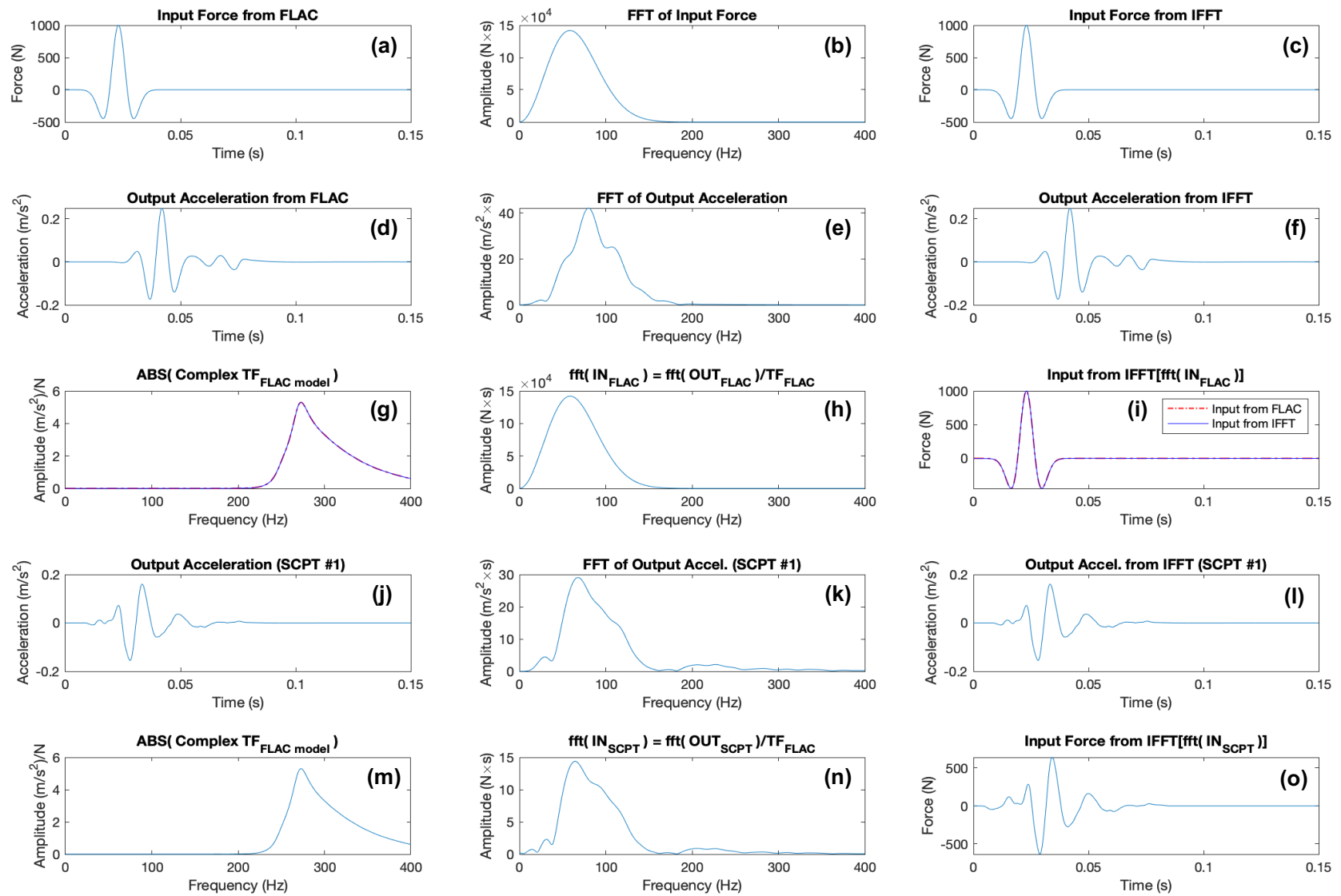


Fig. 7-15: Inversion process to obtain the input force when acceleration is used as the system's output (first iteration)

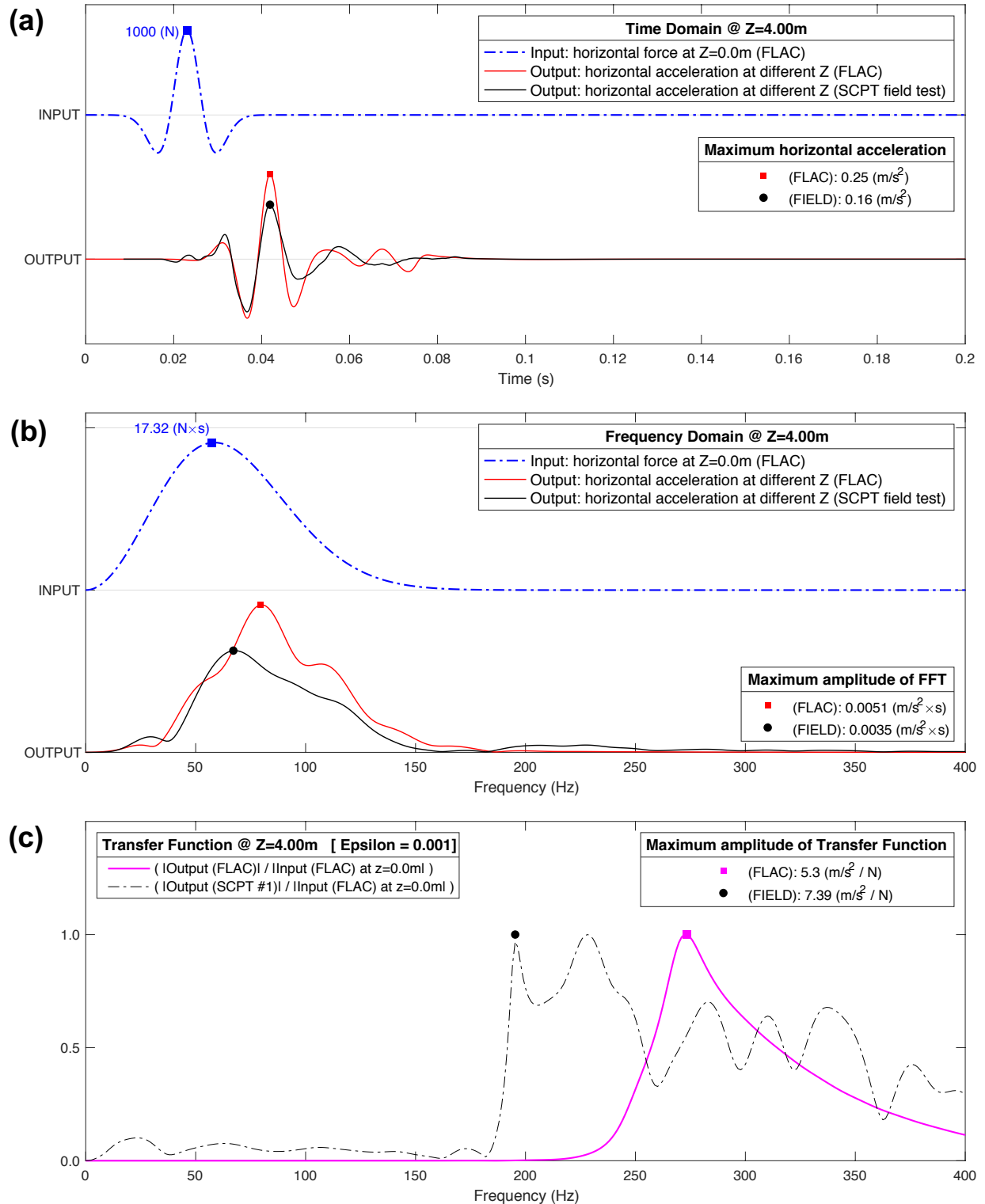


Fig. 7-16: Comparison of results of horizontal acceleration from sCPTU field test and from numerical model when the input force was approached by a Ricker wavelet with mean frequency of 58Hz.

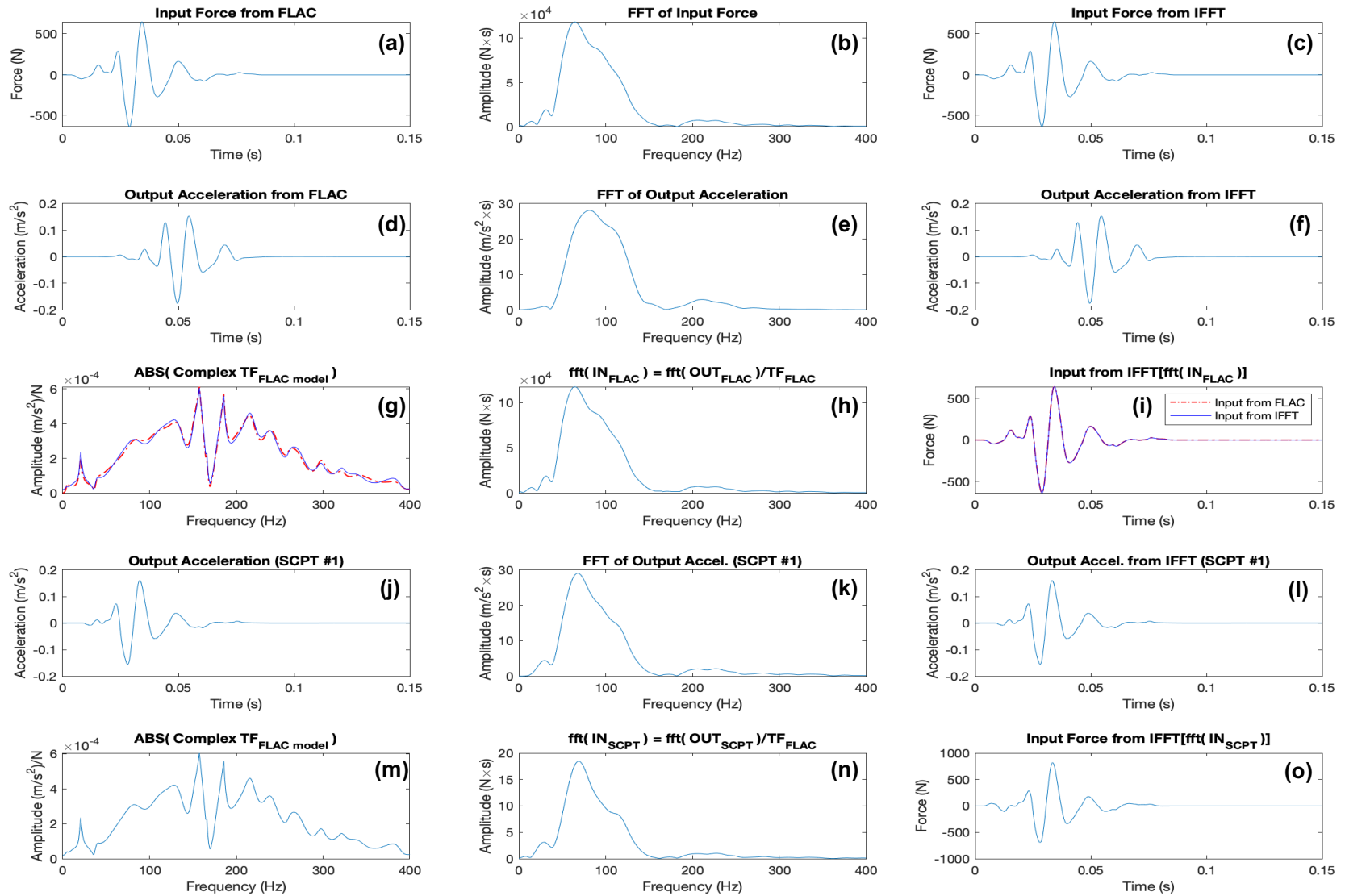


Fig. 7-17: Inversion process to obtain the input force when acceleration is used as the system's output (second iteration)

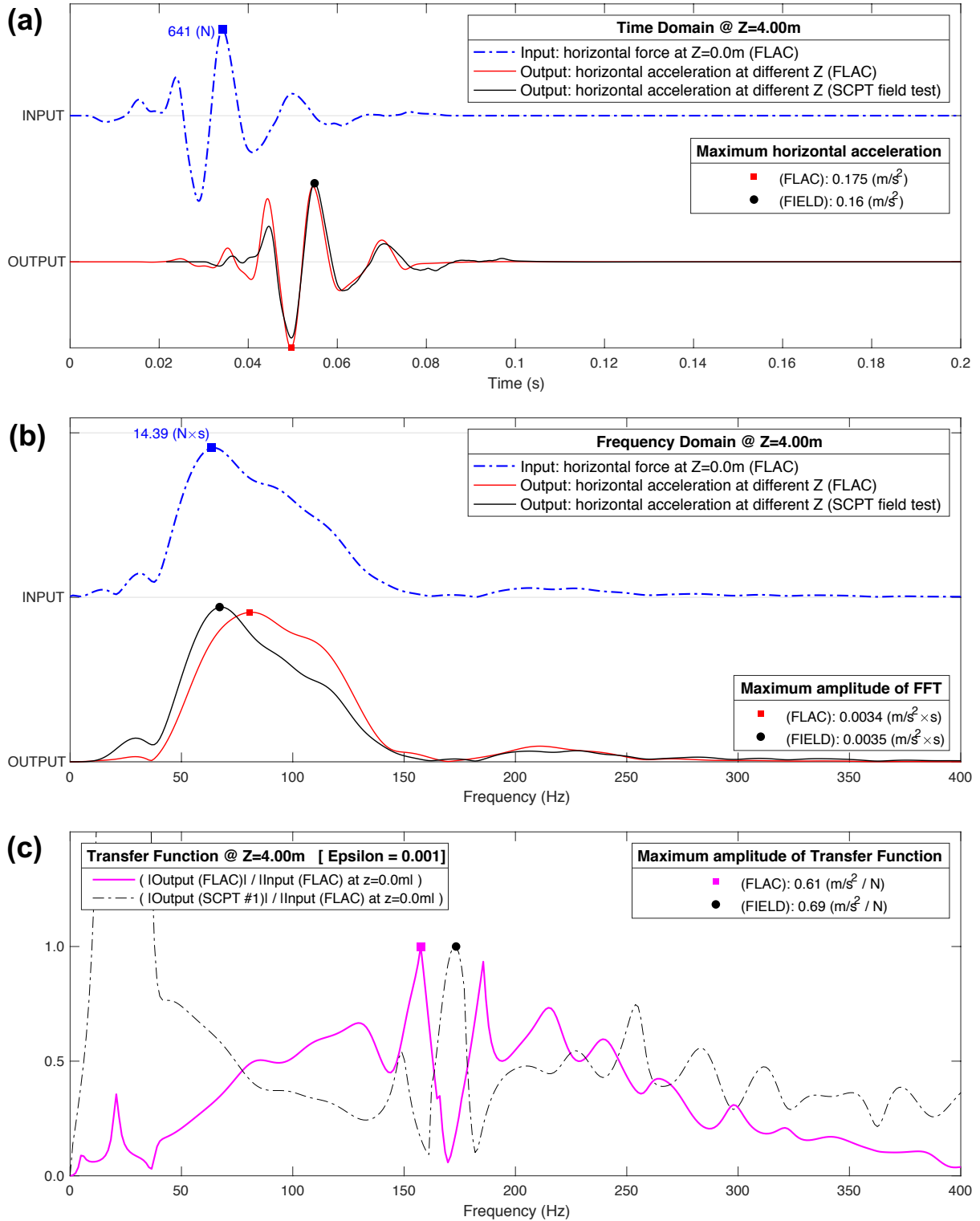


Fig. 7-18: Comparison of results of horizontal acceleration from sCPTU field test and from numerical model, the input force corresponds to the result obtained from the first iteration of the excitation force inversion process.

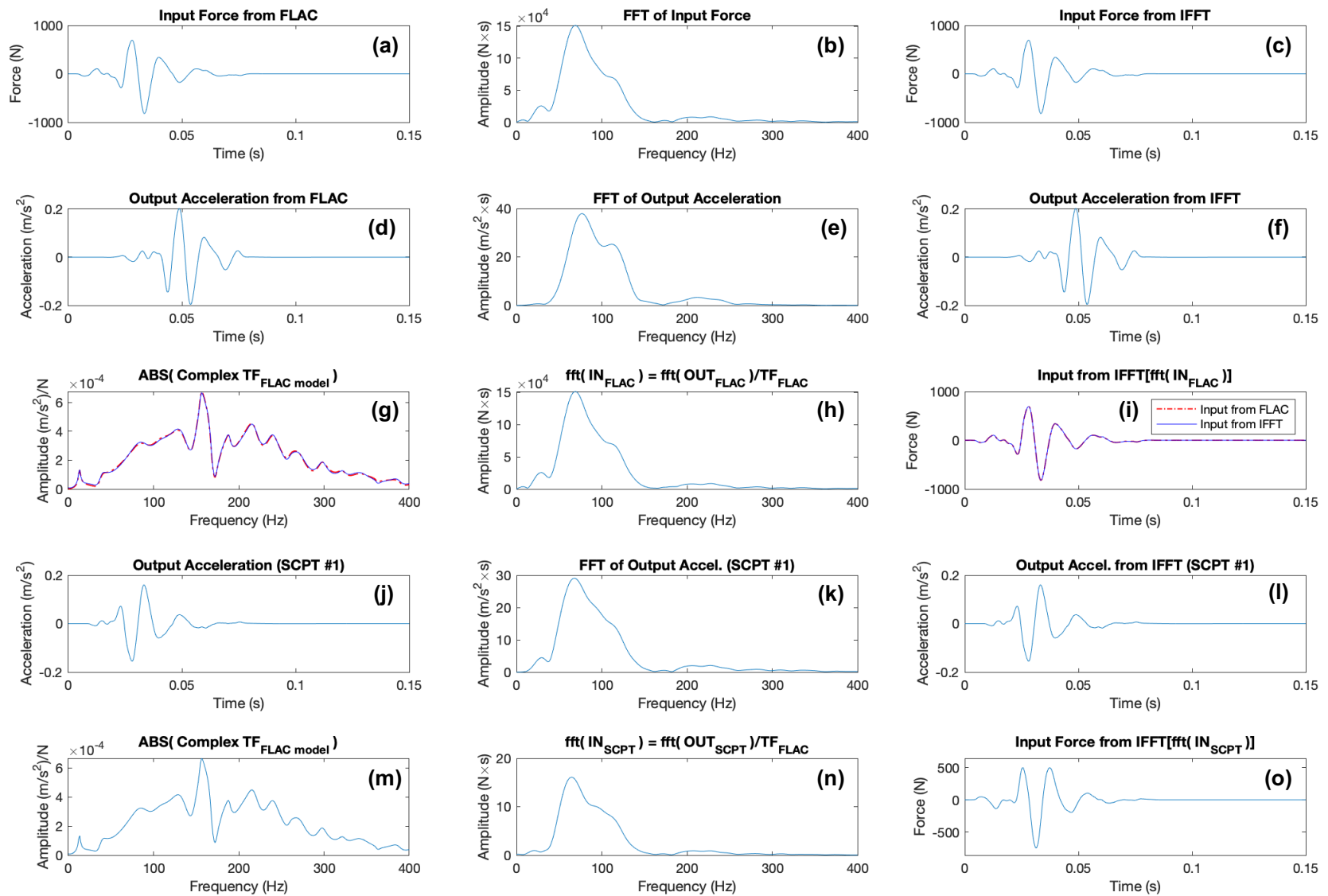


Fig. 7-19: Inversion process to obtain the input force when acceleration is used as the system's output (third iteration)

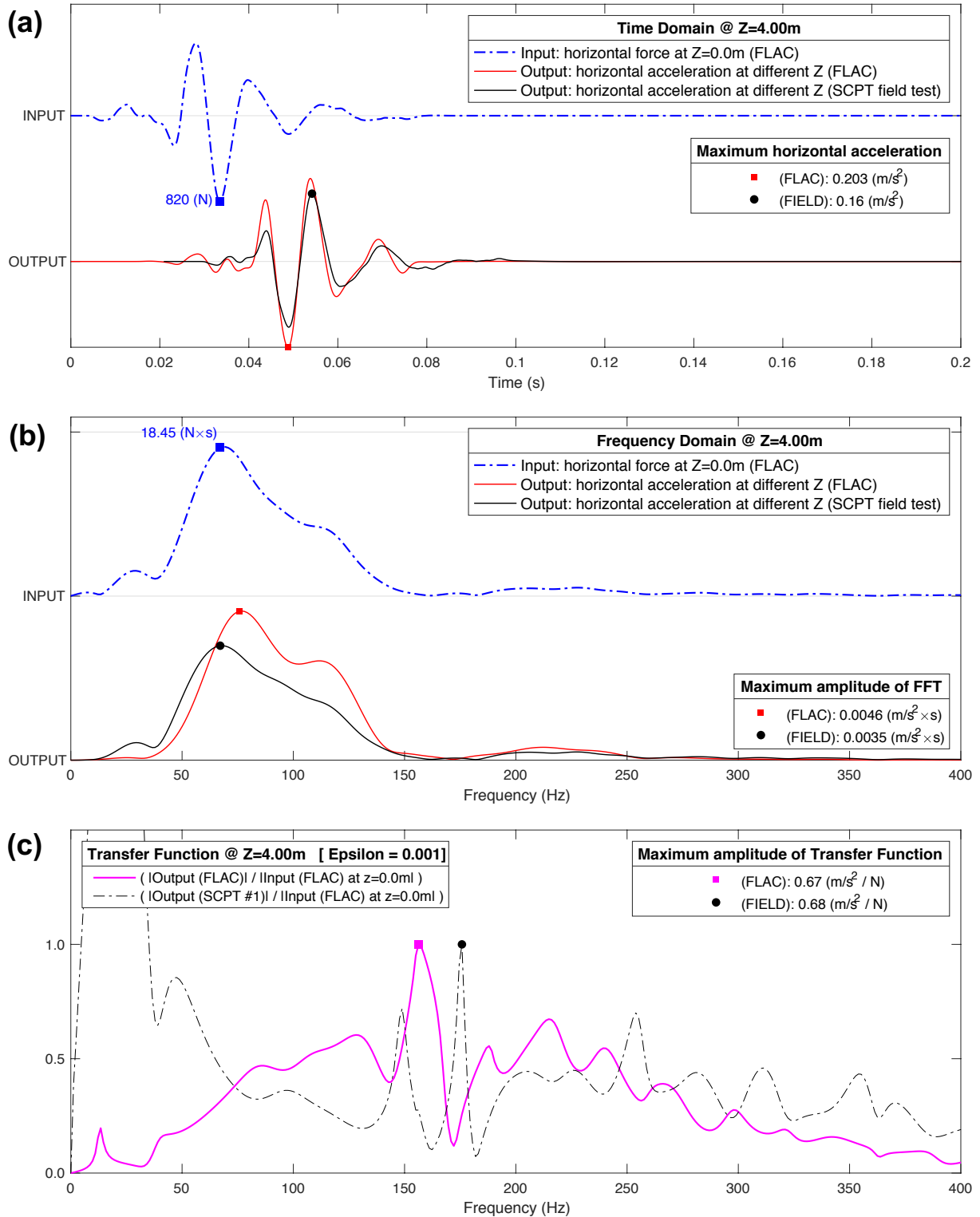


Fig. 7-20: Comparison of results of horizontal acceleration from sCPTU field test and from numerical model, the input force corresponds to the result obtained from the second iteration of the excitation force inversion process.

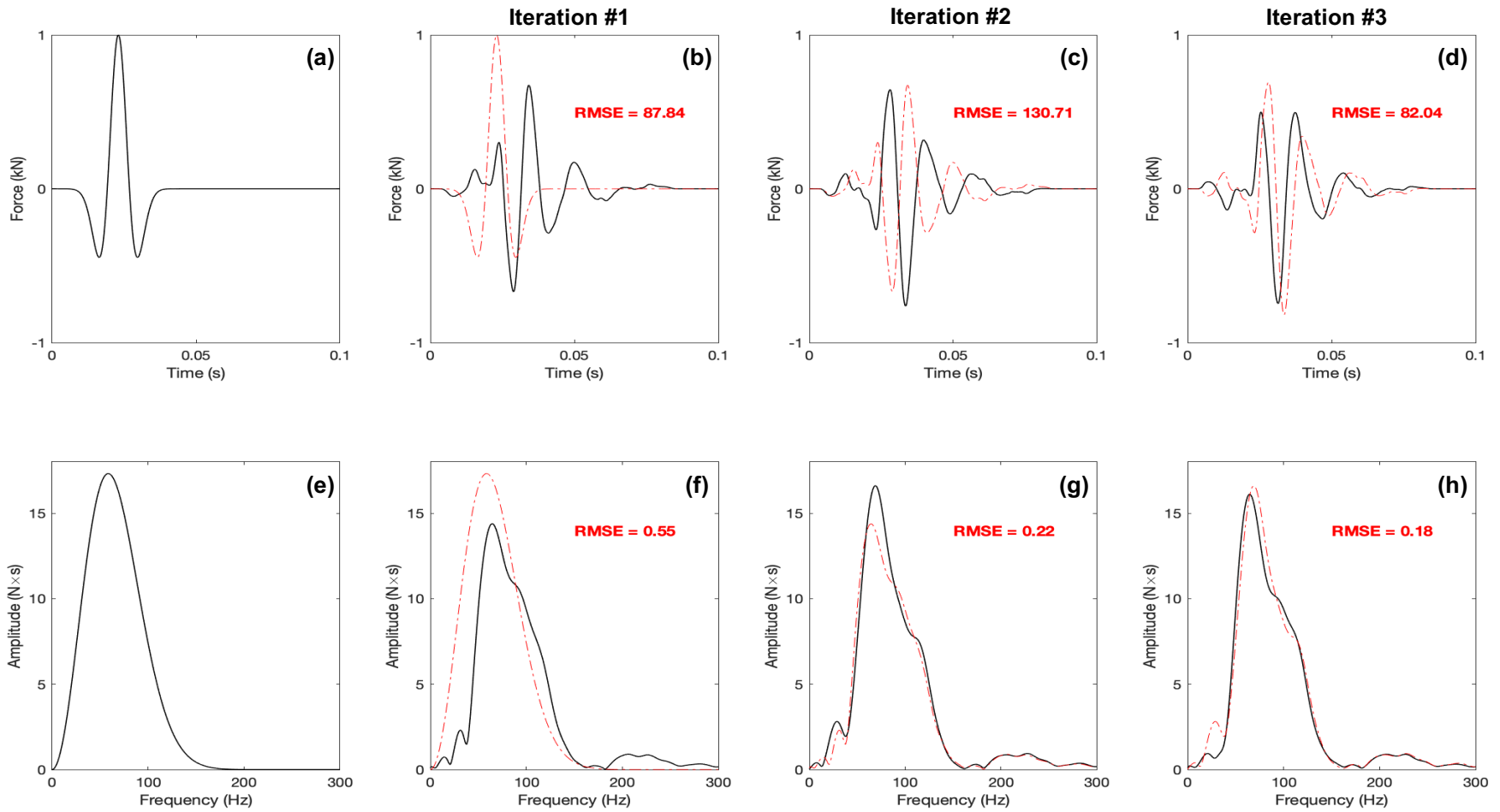


Fig. 7-21: Comparison of input forces used for the numerical simulations through IFFT inversion when acceleration is used as output of the system. The result shown in plot (d) corresponds to the force after three iterations in the inversion process. At each iteration, the dashed red lines correspond to the input force in the previous iteration and it is plotted to facilitate the comparison of results between successive iterations.

7.4.2 Excitation force inversion when the horizontal displacement is used as the output for the assimilated linear invariant system

In this section the same process presented in the flowchart of Fig. 7-1 was followed, just that in this case the output considered for the analysis is the horizontal displacement. For the numerical models, the horizontal displacements were obtained at the same depths that it was done for horizontal acceleration. In the case of the field data obtained from the sCPTU test, as it was explained before, the original data recorded in the field was horizontal acceleration, so horizontal displacement was obtained by numerical integration, as it was explained earlier in this chapter.

The initial force used to start the iteration process was the same used in the previous section (i.e. a Ricker wavelet with mean frequency in 58Hz, see Fig. 7-14). The results for all the operations in the first iteration of the inversion process are presented in Fig. 7-22, the comparison of response at 4 meters' depth is presented in Fig. 7-23. In a similar way, the results for the second iteration are presented in Fig. 7-24 and Fig. 7-25, while for the third iteration the results are presented in Fig. 7-26 and Fig. 7-27. The same results for all the depths between 2 meters and 16 meters (i.e. beyond the elastic radius) in a video that can be accessed in the following link https://youtu.be/g_WmUoXv74s.

After three iterations the results are showing almost a perfect match for the horizontal displacement at 4 meters' depth, both in the time domain and in the frequency domain. Also, a comparison of the input forces obtained from the inversion after every iteration is presented in Fig. 7-28. As it is clear, three iterations are enough to show how the input force converges to the shape shown in Fig. 7-28 (d) with an RMSE value of about 7N. In this case it is clear how iteration by iteration the RMSE gets drastically reduced, showing an evident convergence both in the time and in the frequency domain. The difference in the maximum amplitude in the time domain (i.e. maximum horizontal displacement), is about 11% when the data from the sCPTU field test is taken as reference. Similarly, the difference in the maximum amplitude in the frequency domain is less than 1%. These results could be considered a good match, so the force shown in Fig. 7-28 (d) may be considered the input force used in the sCPTU field test.

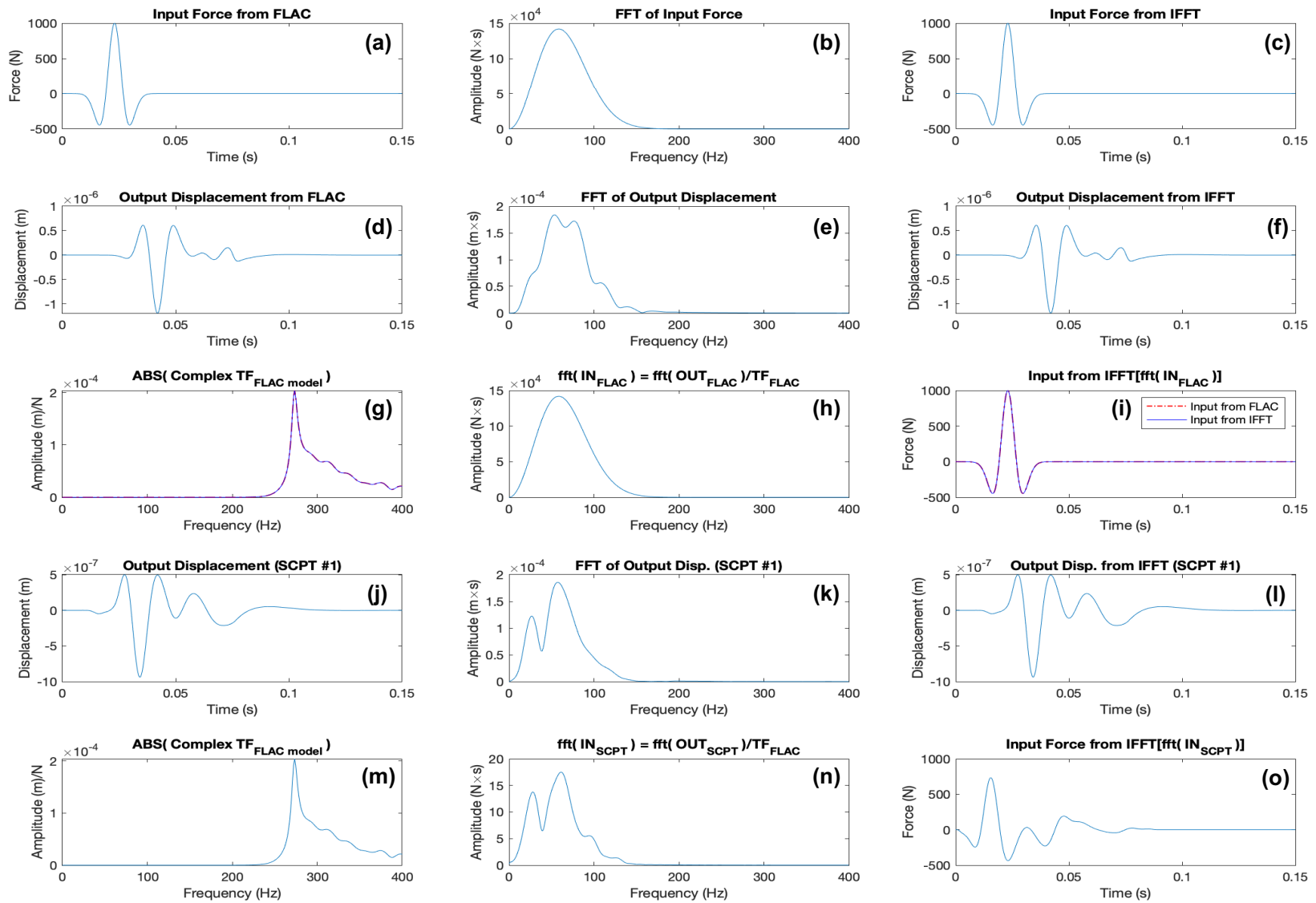


Fig. 7-22: Inversion process to obtain the input force when displacement is used as the system's output (first iteration)

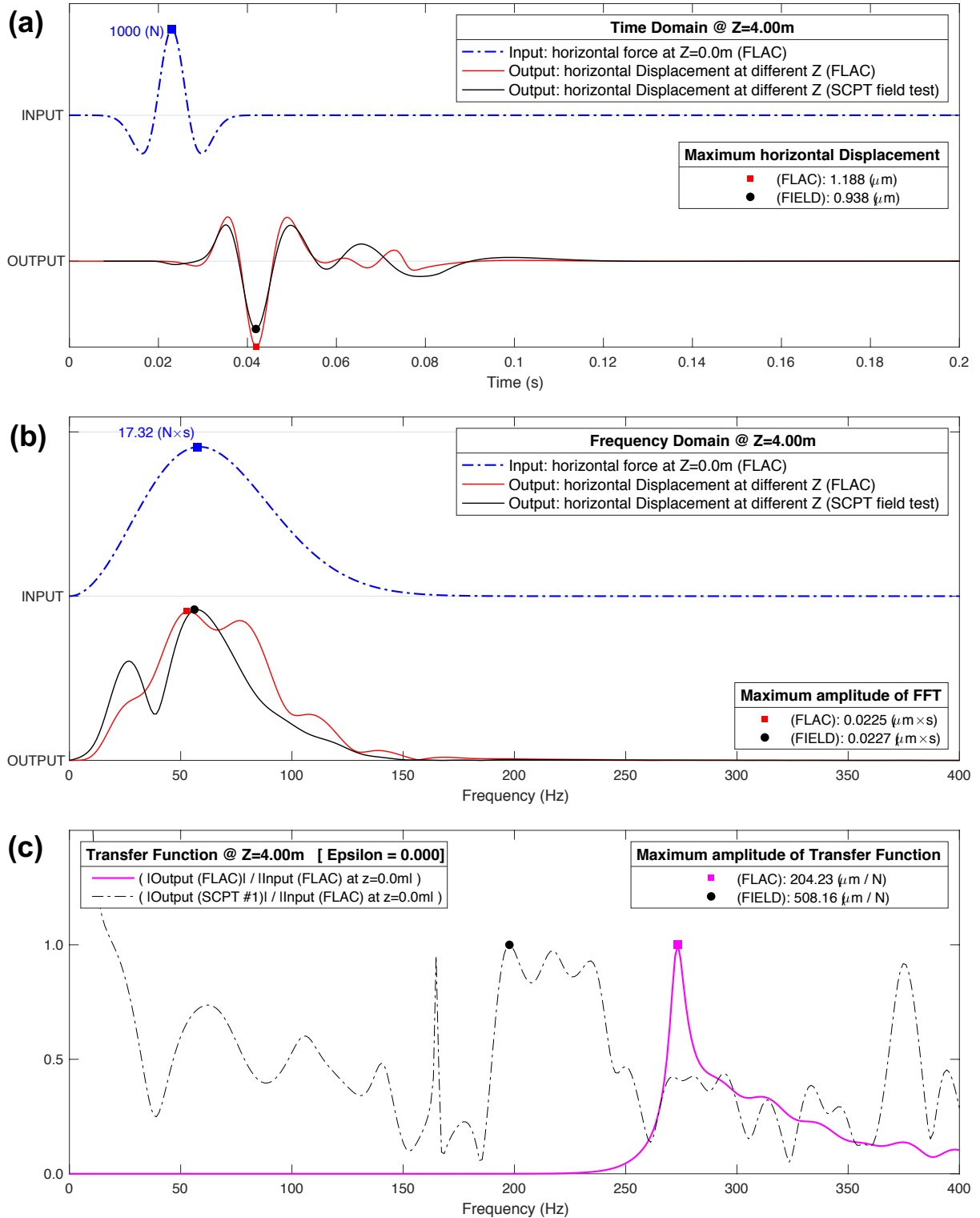


Fig. 7-23: Comparison of results of horizontal displacement from sCPTU field test and from numerical model, the input force corresponds to a Ricker wavelet with mean frequency of 58Hz.

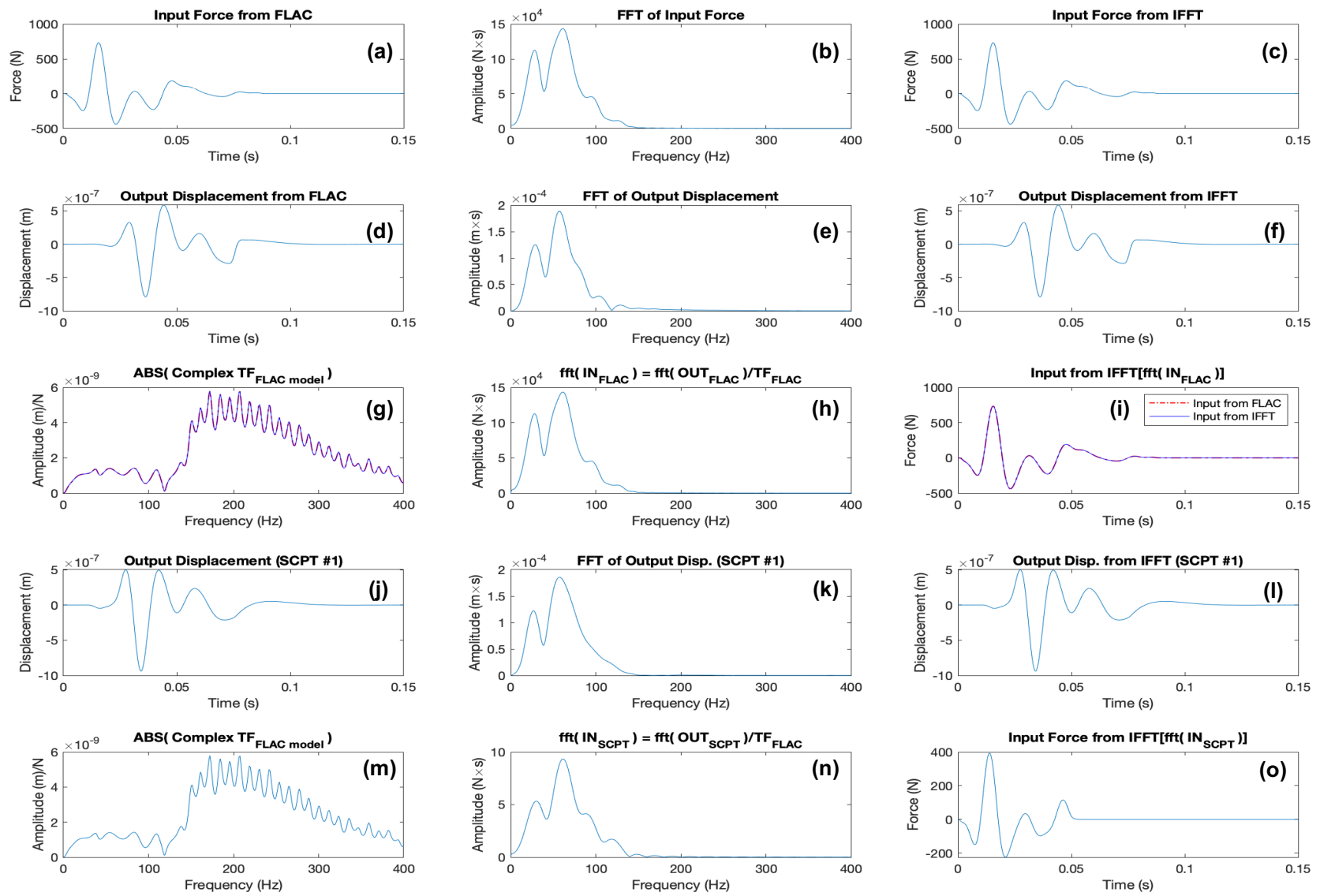


Fig. 7-24: Inversion process to obtain the input force when displacement is used as the system's output (second iteration)

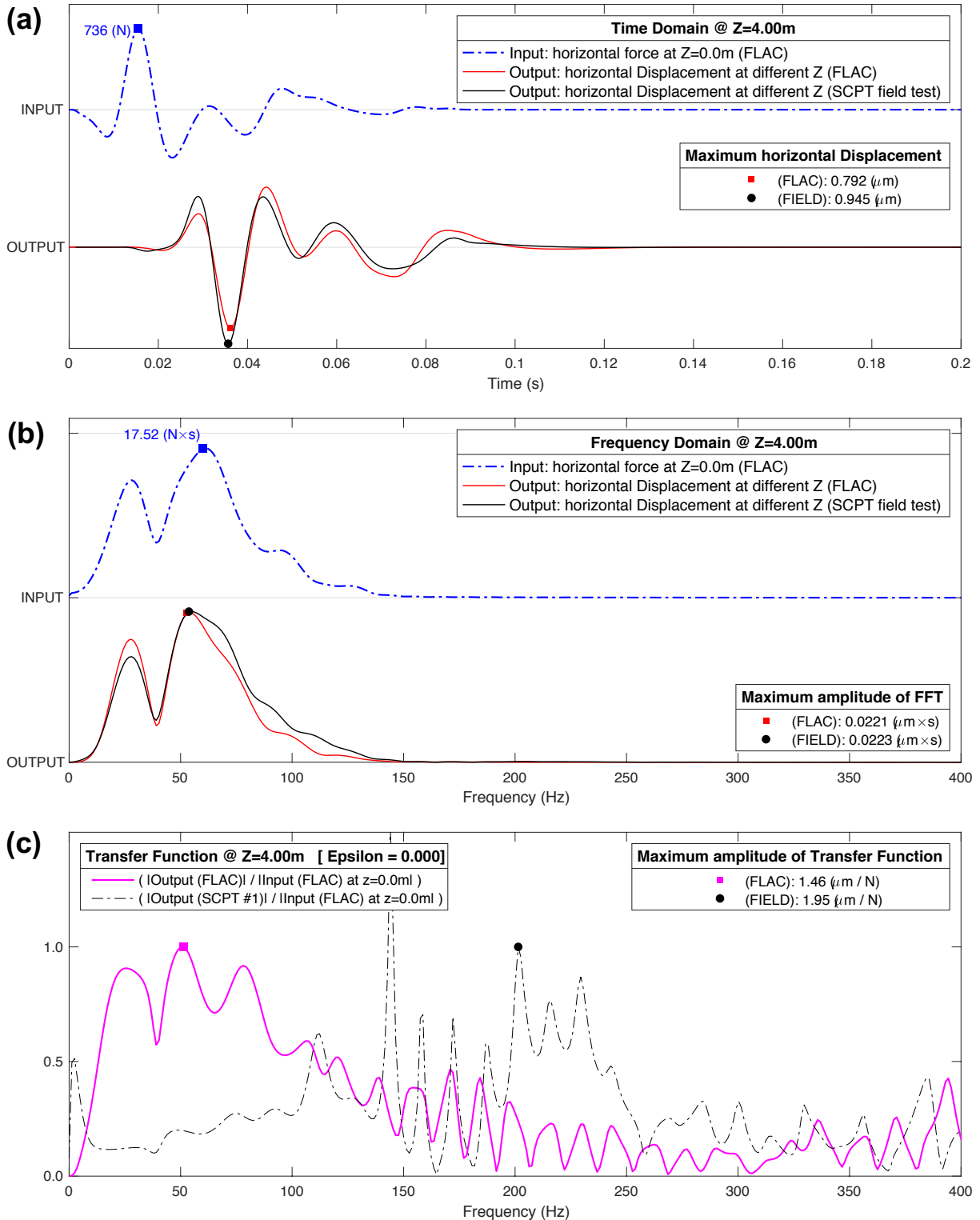


Fig. 7-25: Comparison of results of horizontal displacement from sCPTU field test and from numerical model, the input force corresponds to the result obtained from the first iteration of the excitation force inversion process.

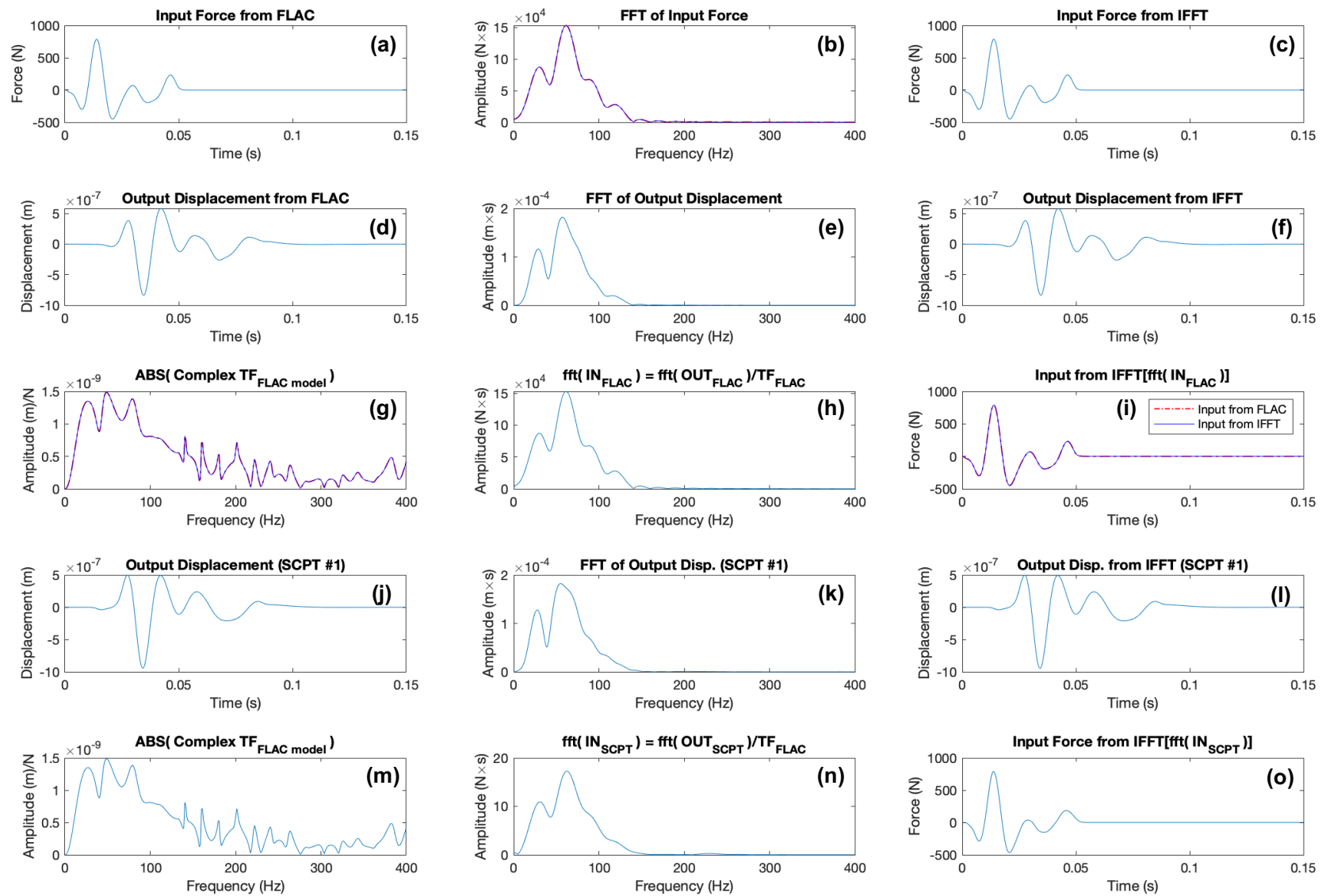


Fig. 7-26: Inversion process to obtain the input force when displacement is used as the system's output (third iteration)

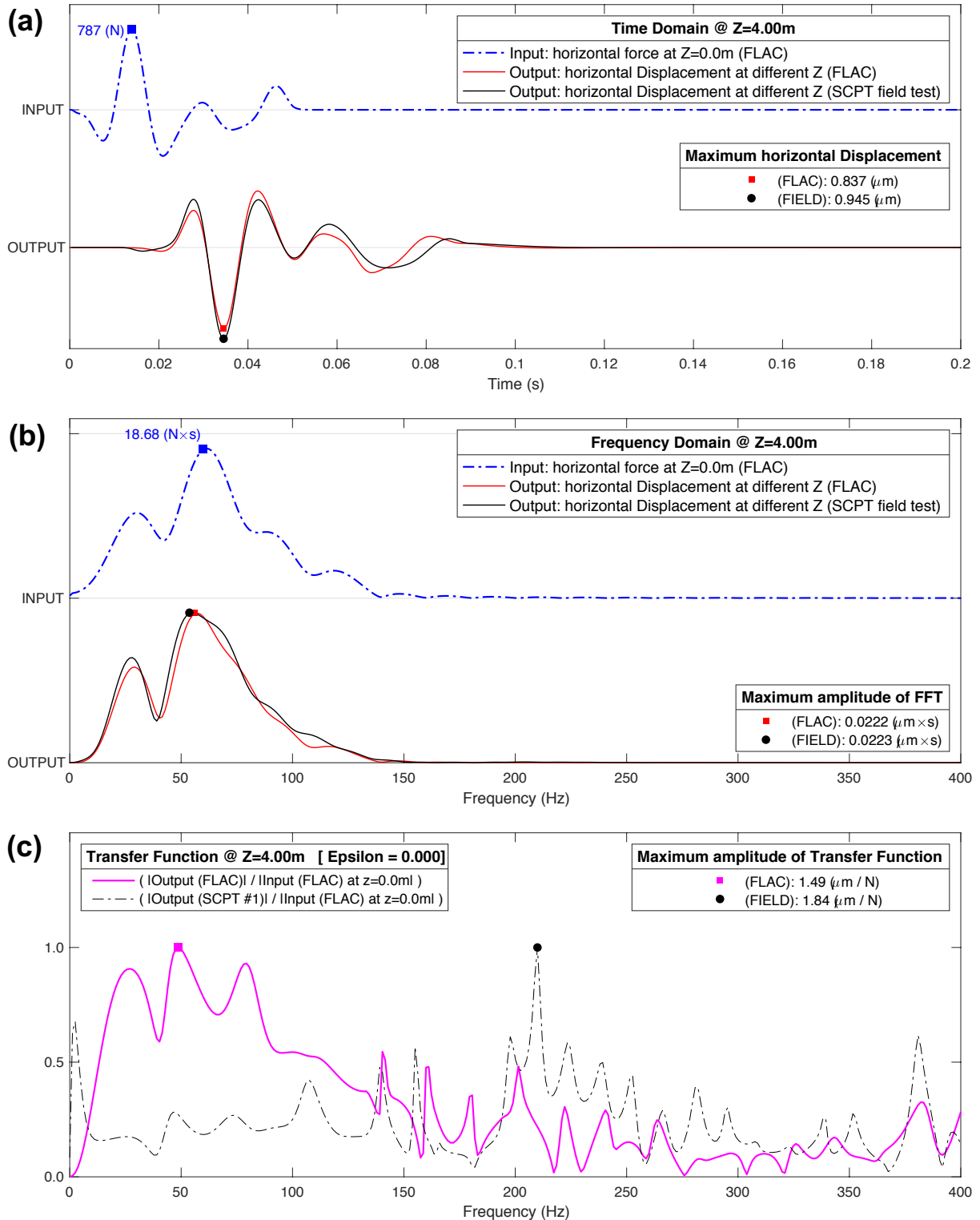


Fig. 7-27: Comparison of results of horizontal displacement from sCPTU field test and from numerical model, the input force corresponds to the result obtained from the second iteration of the excitation force inversion process.

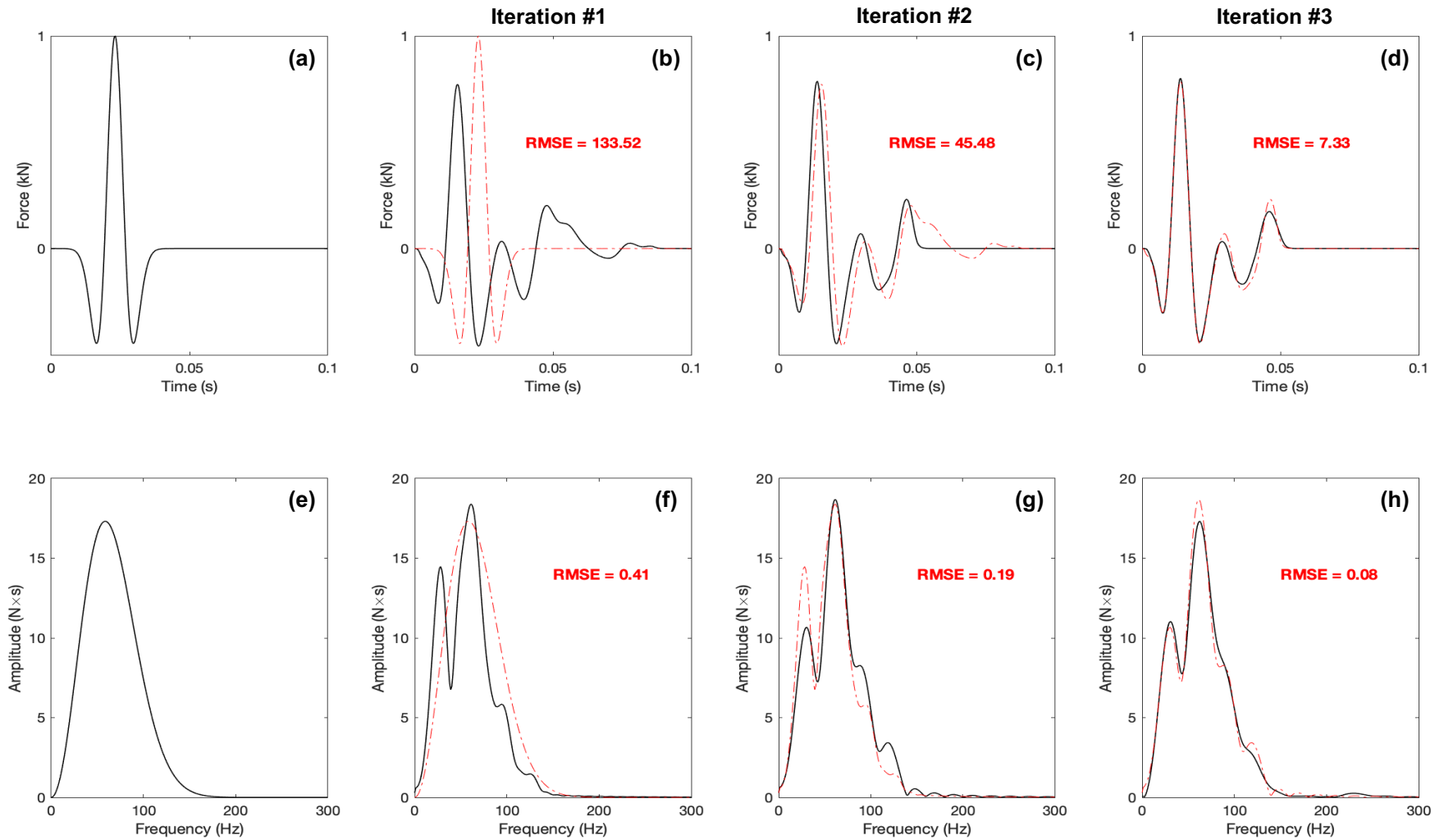


Fig. 7-28: Comparison of input forces used for the numerical simulations through IFFT inversion when the horizontal displacement is used as the output of the system. The result shown in plot (d) corresponds to the force after three iterations in the inversion process. At each iteration, the dashed red lines correspond to the input force in the previous iteration and it is plotted to facilitate the comparison of results between successive iterations.

7.5 Step 4: analysis of the effect of changes in the frequency of the input in the sCPTU field test

In the previous sections of this chapter the characterization of the excitation force used in the sCPTU field test was done by studying the transfer functions in the numerical models along with the field data. The inversion process led to an input force fully characterized in the time domain (i.e. amplitude, shape, duration and time step), and in the frequency domain (i.e. the peak frequency). Now, by modifying the input force it is possible to a variety of force pulses with different frequency contents; this can be easily done by changing the time step in the force vector.

In this section the results of a new set of numerical models are analysed in order to understand the effect of frequency on the results of the sCPTU field test. The time step used to define the input force in the inversion process was $5(\mu s)$ and it is named here $dt_{initial}$, then it is just multiplied by a factor to ensure the new frequency content of the input force is also modified. The new time steps and the correspondent peak frequencies are presented in Table 7-5, and their representation in the time and the frequency domain are shown in Fig. 7-22.

Table 7-5. Modified input forces for the analysis of the effect of frequency.

Model ID	dt (μs)	f_p (Hz)
1	$0.65 * dt_{initial} = 3.25$	95.4
2	$0.75 * dt_{initial} = 3.75$	82.7
3	$0.85 * dt_{initial} = 4.25$	72.9
4	$1.00 * dt_{initial} = 5.00$	62.0
5	$1.20 * dt_{initial} = 6.00$	51.7
6	$1.50 * dt_{initial} = 7.50$	41.3
7	$2.00 * dt_{initial} = 10.0$	31.0

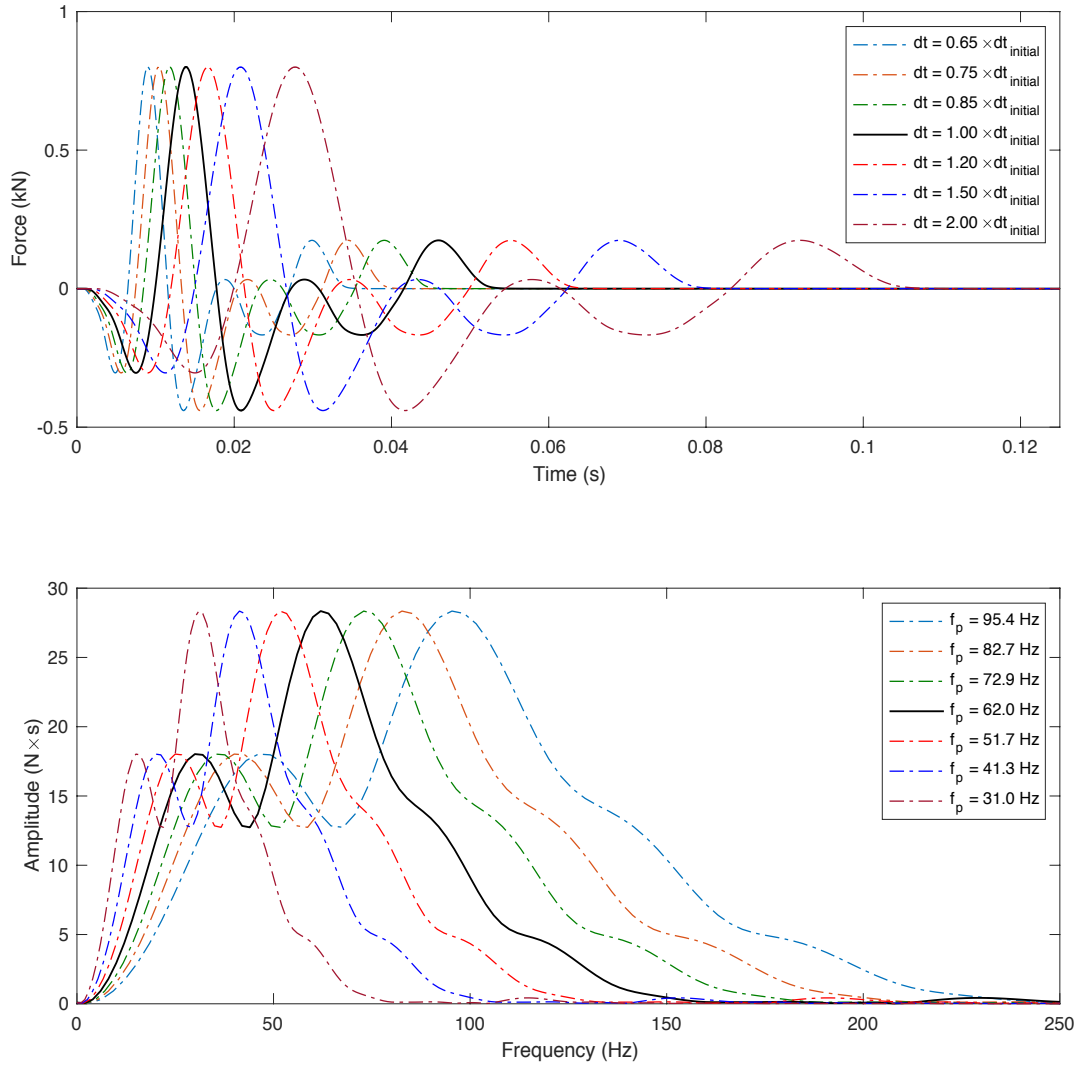


Fig. 7-29: Modified input forces for the analysis of the effect of frequency on sCPTU field test results

The modified input forces were used to run numerical models and to get the response at different depths, these results are compared with the ones recorded in the field test. The difference between the numerical models and the field data for different frequencies allowed the understanding of the effect of frequency content in the input force for the sCPTU field test. The results of the numerical simulation for all the aforementioned frequencies are presented in Fig. 7-30 to Fig. 7-36.

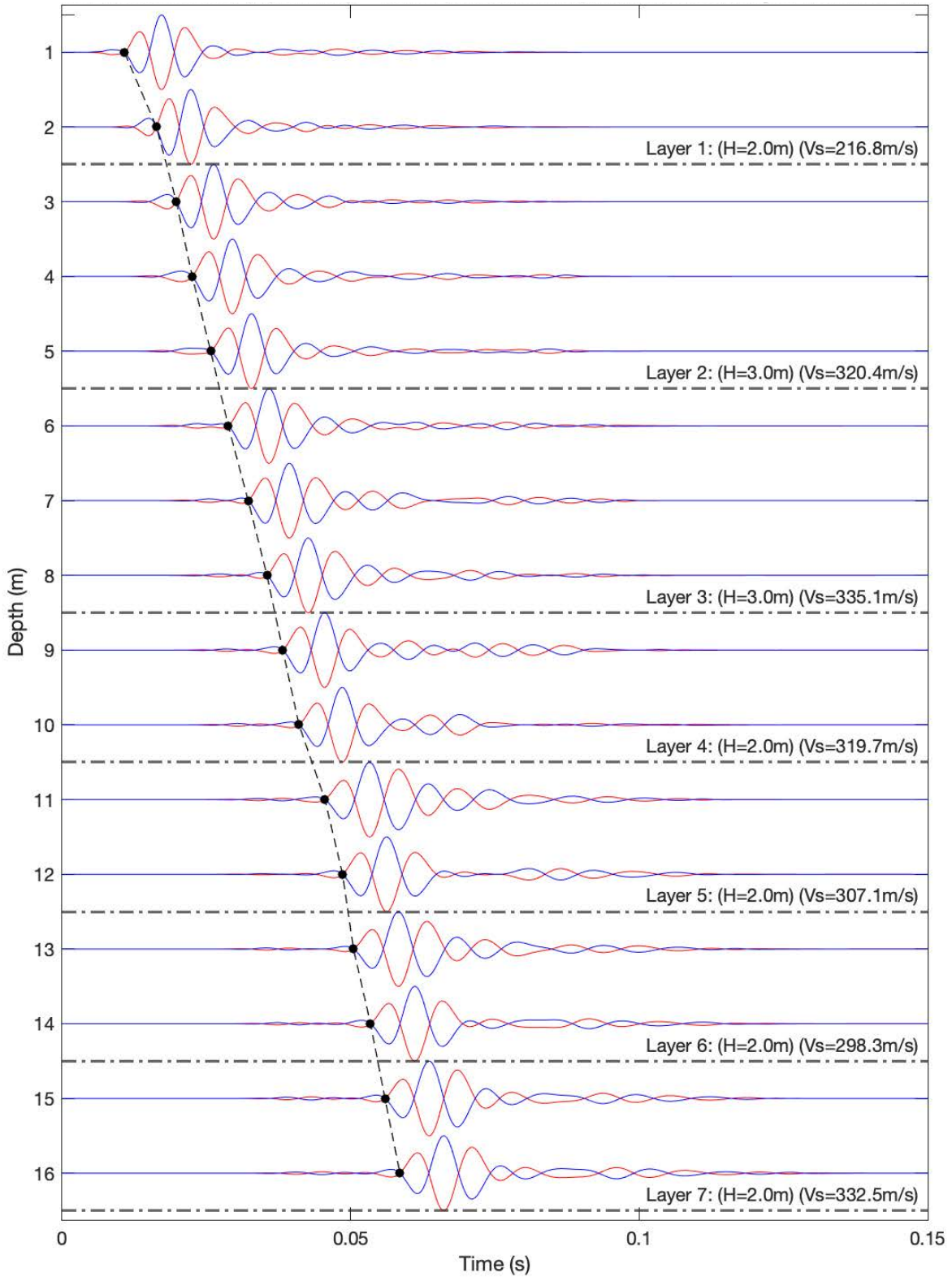


Fig. 7-30: Shear wave velocity (v_s) profile interpretation following ASTM D7400 (2017). Numerical model of sCPTU test: force input with frequency peak = 31.0Hz

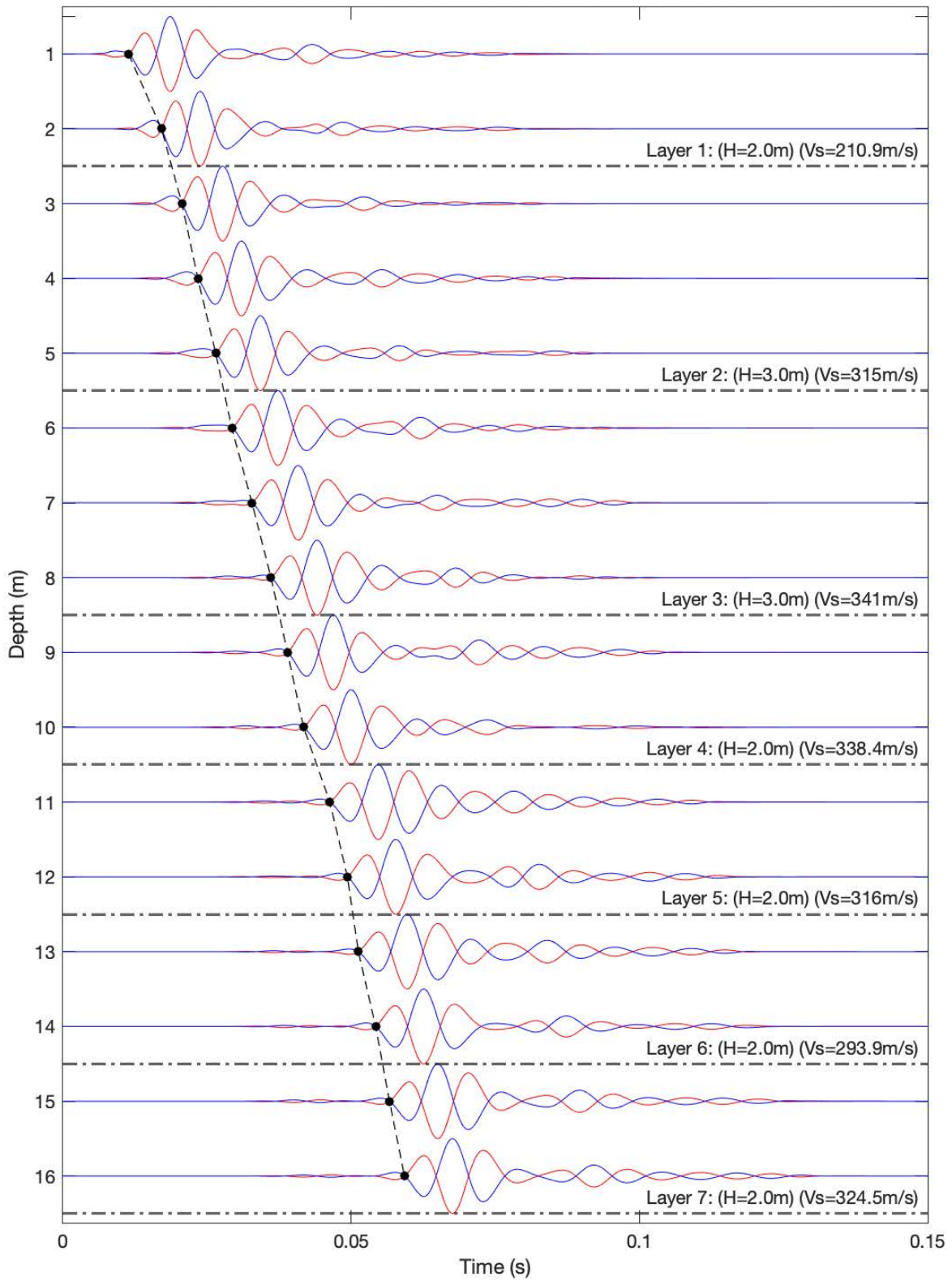


Fig. 7-31: Shear wave velocity (v_s) profile interpretation following ASTM D7400 (2017). Numerical model of sCPTU test: force input with frequency peak = 41.3Hz

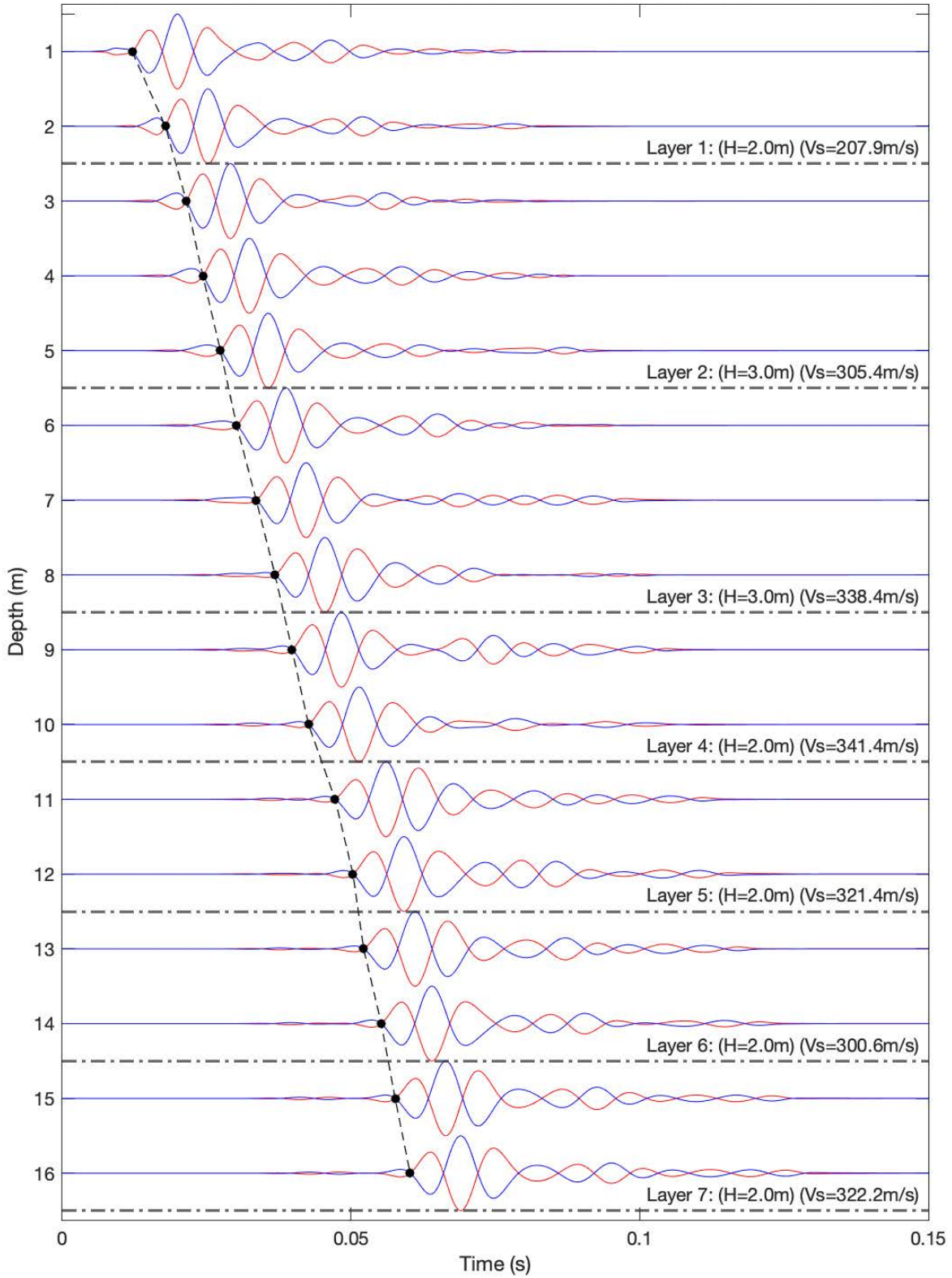


Fig. 7-32: Shear wave velocity (v_s) profile interpretation following ASTM D7400 (2017). Numerical model of sCPTU test: force input with frequency peak = 51.7Hz

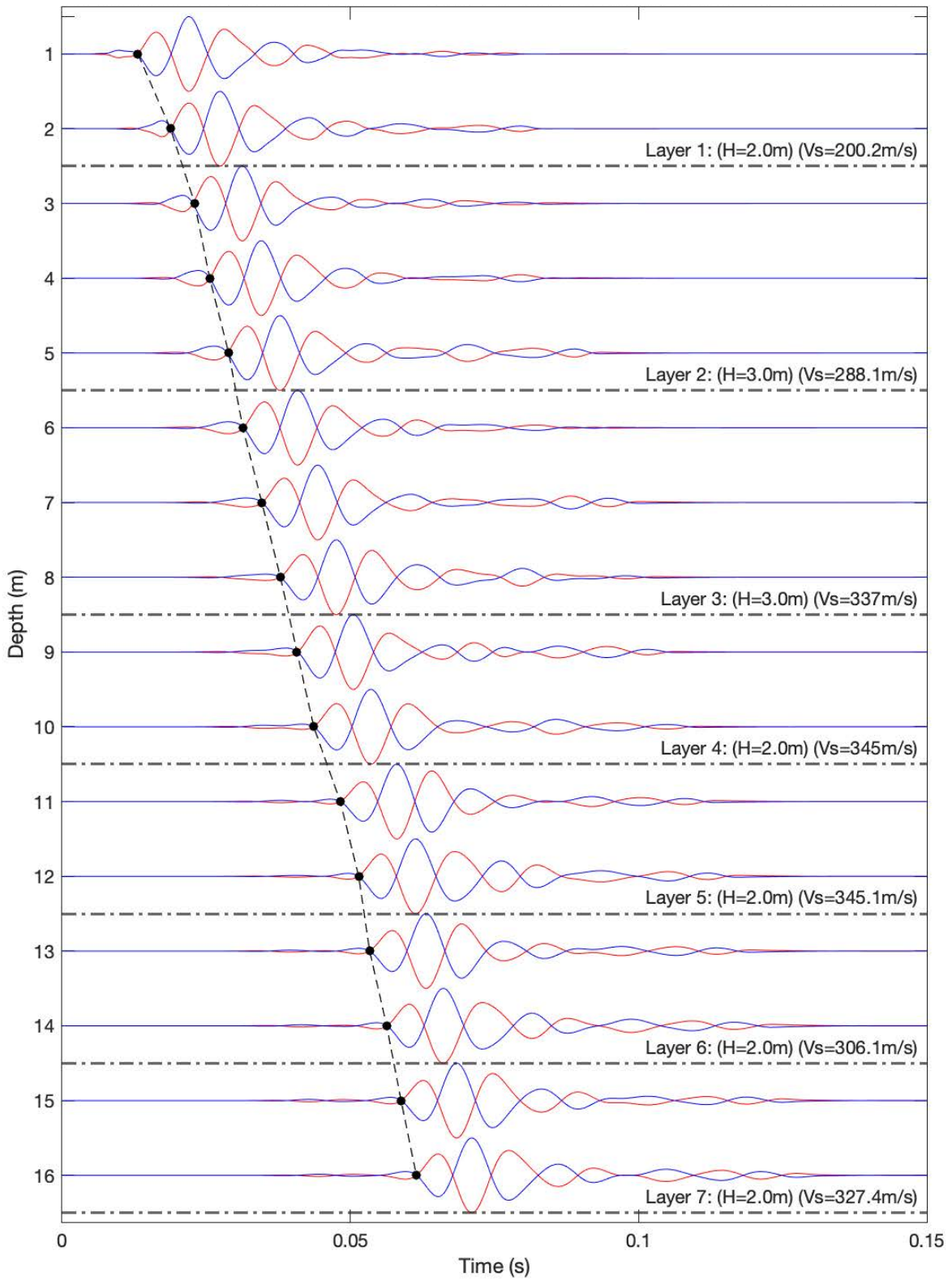


Fig. 7-33: Shear wave velocity (v_s) profile interpretation following ASTM D7400 (2017). Numerical model of sCPTU test: force input with frequency peak = 62.0Hz

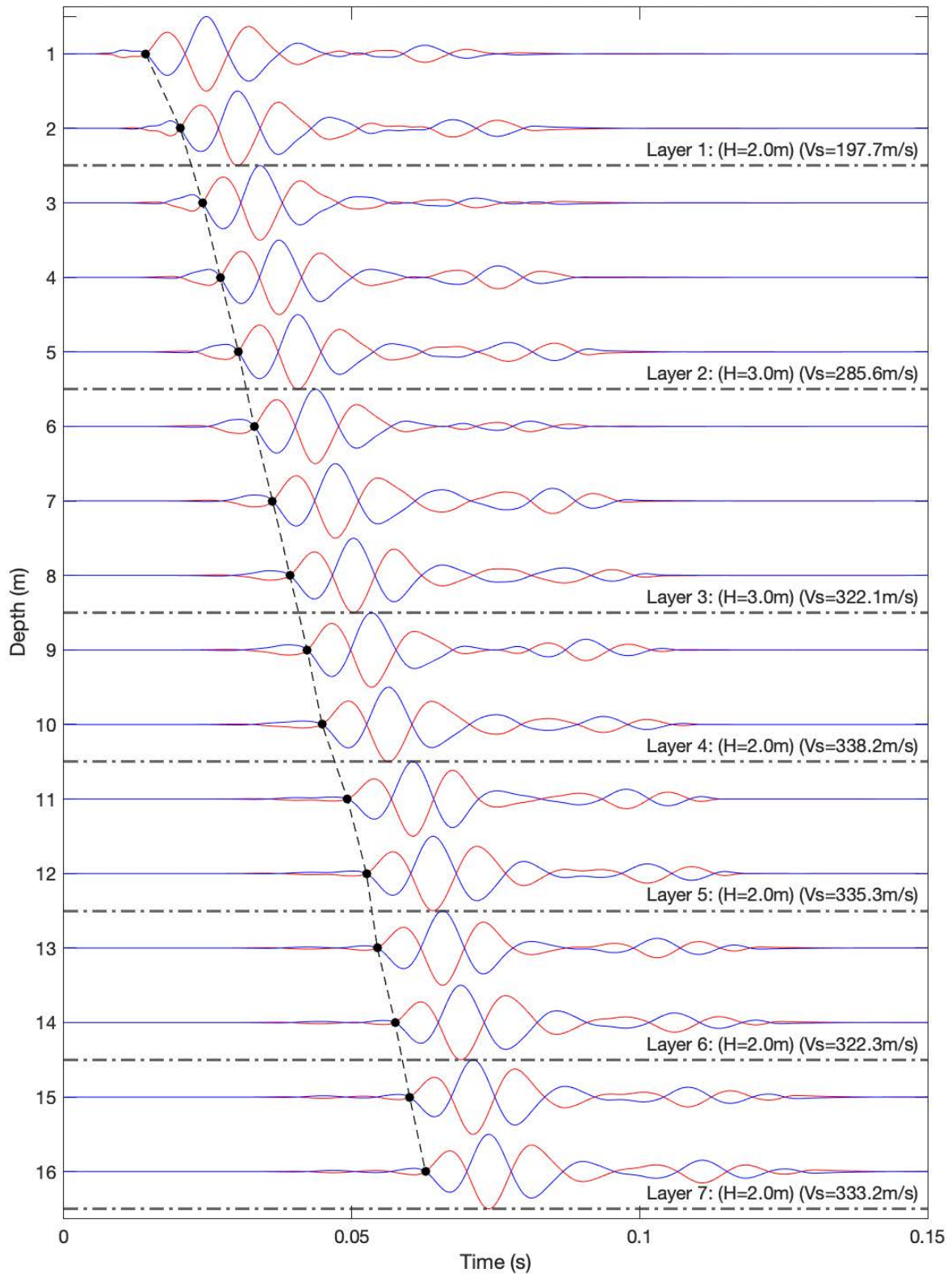


Fig. 7-34: Shear wave velocity (v_s) profile interpretation following ASTM D7400 (2017). Numerical model of sCPTU test: force input with frequency peak = 72.9Hz

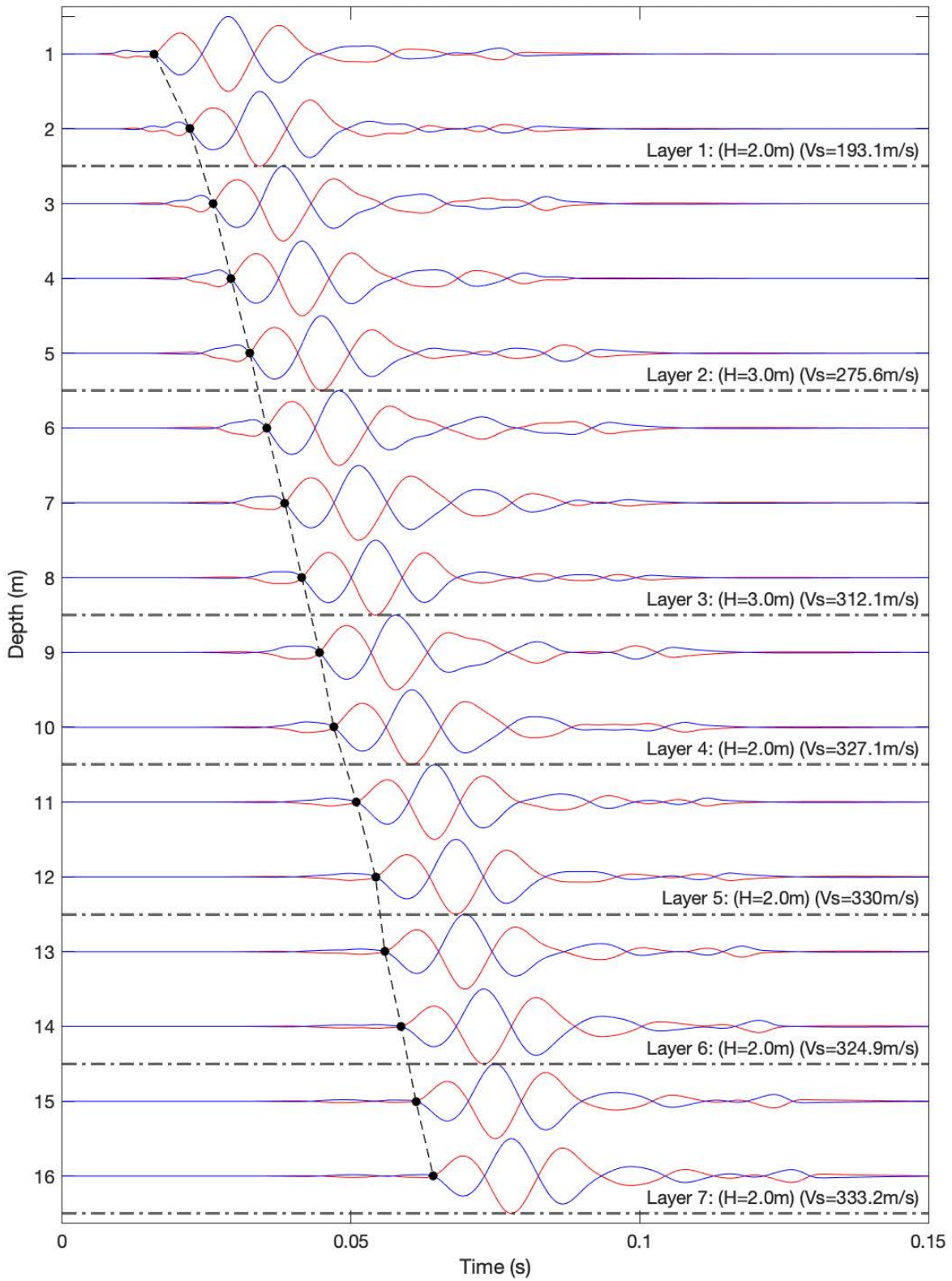


Fig. 7-35: Shear wave velocity (v_s) profile interpretation following ASTM D7400 (2017). Numerical model of sCPTU test: force input with frequency peak = 82.7Hz

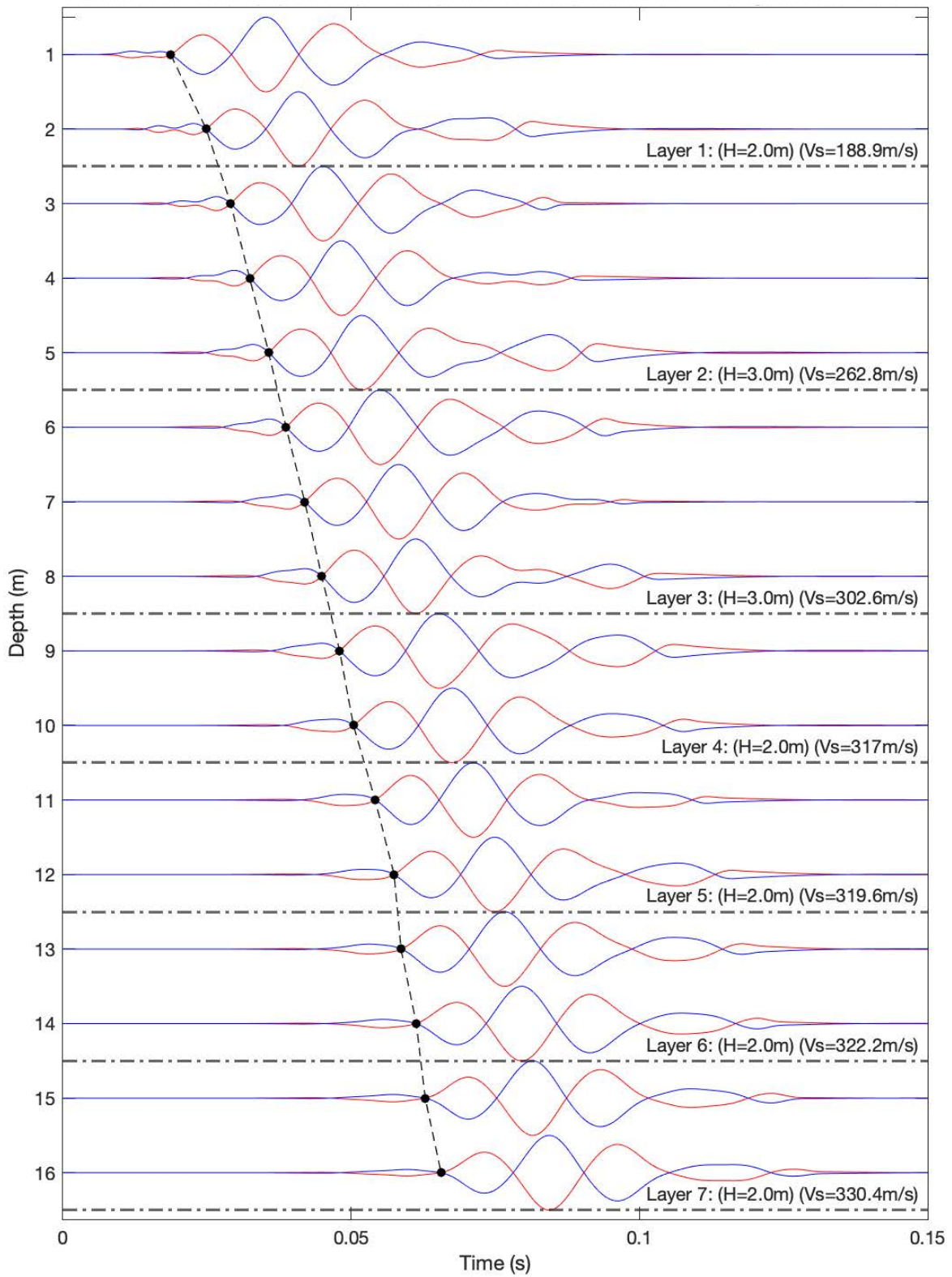


Fig. 7-36: Shear wave velocity (v_s) profile interpretation following ASTM D7400 (2017). Numerical model of sCPTU test: force input with frequency peak = 95.4Hz

Table 7-6. Results for the sCPTU field test and for the numerical simulations

Depth (m)	Distance from Source	Time to first zero crossing in sCPTU test (field data and numerical simulations for different frequencies peaks in the input force)							
		SCPT (field test)	f_{peak} 31.0Hz	f_{peak} 41.3Hz	f_{peak} 51.7Hz	f_{peak} 62.0Hz	f_{peak} 72.9Hz	f_{peak} 82.7Hz	f_{peak} 95.4Hz
1	1.0198	0.01420	0.01870	0.01595	0.01420	0.01315	0.01210	0.01140	0.01080
2	2.0100	0.01990	0.02485	0.02205	0.02020	0.01880	0.01785	0.01710	0.01635
3	3.0067	0.02387	0.02910	0.02610	0.02410	0.02300	0.02150	0.02065	0.01980
4	4.0050	0.02685	0.03240	0.02925	0.02715	0.02560	0.02435	0.02340	0.02255
5	5.0040	0.03062	0.03570	0.03250	0.03030	0.02890	0.02740	0.02650	0.02575
6	6.0033	0.03355	0.03870	0.03535	0.03305	0.03135	0.03020	0.02930	0.02880
7	7.0029	0.03660	0.04195	0.03855	0.03625	0.03465	0.03360	0.03280	0.03225
8	8.0025	0.04066	0.04490	0.04150	0.03925	0.03788	0.03685	0.03610	0.03550
9	9.0022	0.04365	0.04800	0.04455	0.04225	0.04075	0.03980	0.03895	0.03825
10	10.0020	0.04661	0.05040	0.04700	0.04485	0.04365	0.04265	0.04175	0.04105
11	11.0018	0.05133	0.05415	0.05095	0.04925	0.04825	0.04725	0.04630	0.04555
12	12.0017	0.05451	0.05745	0.05425	0.05255	0.05145	0.05035	0.04935	0.04860
13	13.0015	0.05640	0.05865	0.05585	0.05445	0.05335	0.05220	0.05125	0.05050
14	14.0014	0.05935	0.06130	0.05870	0.05750	0.05630	0.05525	0.05425	0.05345
15	15.0013	0.06170	0.06285	0.06125	0.06005	0.05880	0.05765	0.05665	0.05595
16	16.0012	0.06435	0.06560	0.06425	0.06280	0.06145	0.06025	0.05925	0.05855

Table 7-7. Shear wave velocity obtained from the sCPTU field test and from the numerical simulations

Layer ID	Thickness (m)	v_s (m/s)	v_s (m/s) from numerical simulations with different frequency contents in the input force						
		SCPT (field test)	$f_{peak} = 31.0\text{Hz}$	$f_{peak} = 41.3\text{Hz}$	$f_{peak} = 51.7\text{Hz}$	$f_{peak} = 62.0\text{Hz}$	$f_{peak} = 72.9\text{Hz}$	$f_{peak} = 82.7\text{Hz}$	$f_{peak} = 95.4\text{Hz}$
1	2.0	203.3	188.9	193.1	197.7	200.2	207.9	210.9	216.8
2	3.0	285.1	262.8	275.6	285.6	288.1	305.4	315.0	320.4
3	3.0	334.2	319.6	330.0	335.3	345.1	321.4	316.0	307.1
4	2.0	336.0	361.6	362.1	356.4	346.5	344.7	353.9	360.3
5	2.0	250.0	283.3	275.1	257.9	253.6	256.5	259.7	261.6
6	2.0	406.7	496.0	437.9	396.9	406.0	400.1	401.4	406.0
7	2.0	399.5	453.3	359.5	377.1	388.2	399.8	399.8	392.1
	v_s (weighted)	315.6	332.1	317.0	314.7	318.0	318.6	321.5	322.3
	RMSE	0.0	44.0	24.2	12.6	7.4	10.4	15.7	20.5

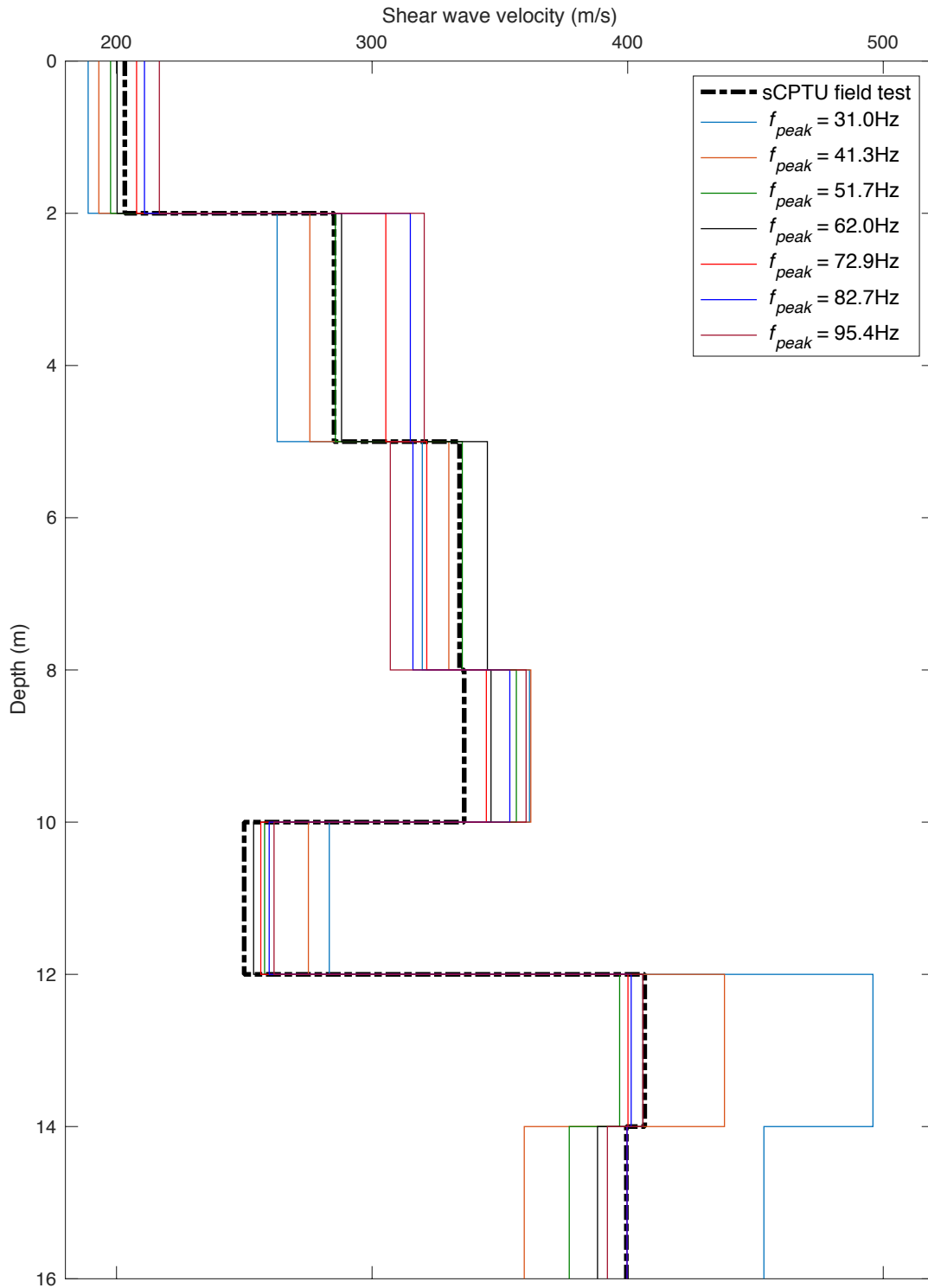


Fig. 7-37: Shear wave velocity profile: sCPTU field test and numerical simulations with different frequency content in the input force

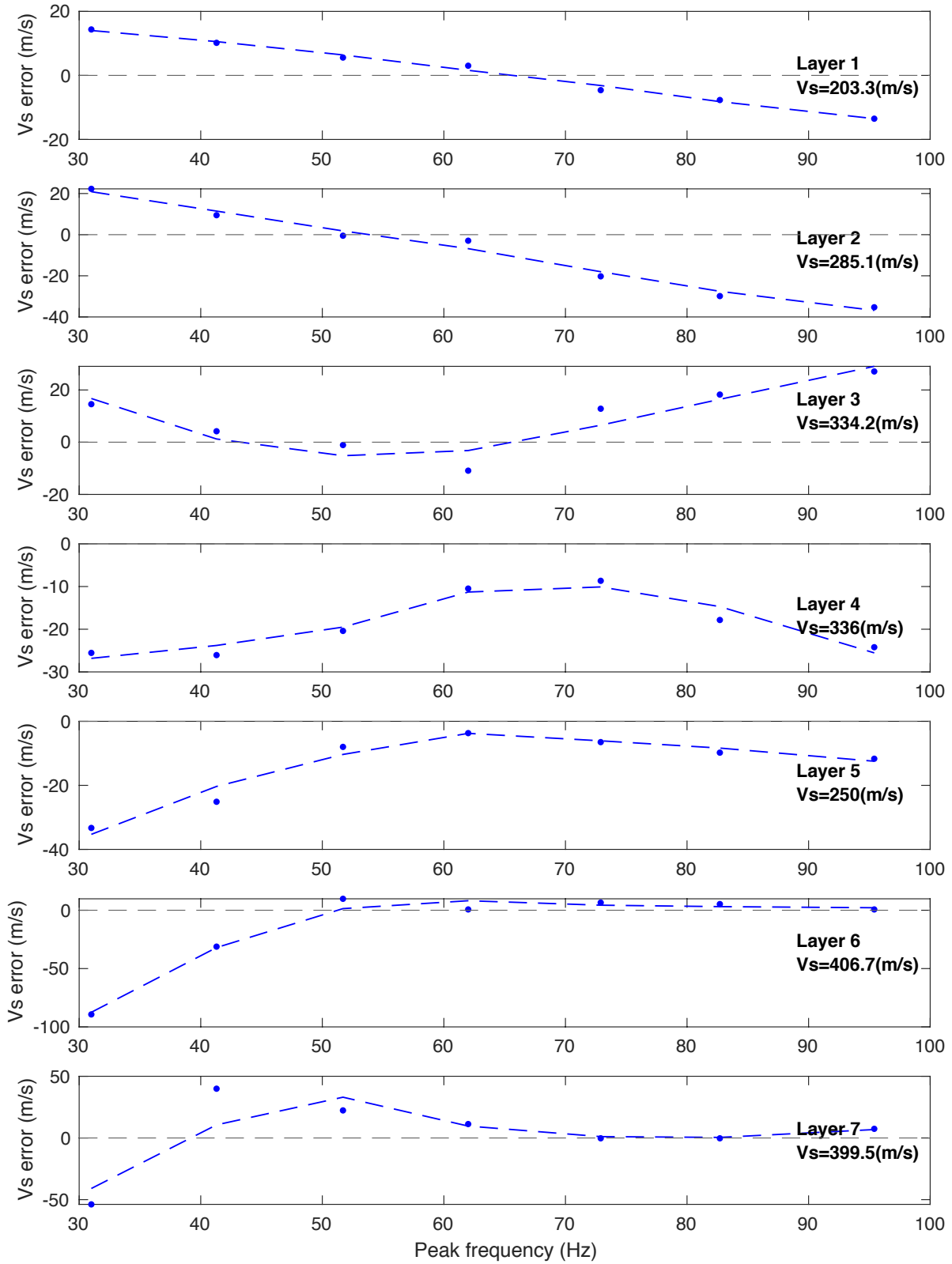


Fig. 7-38: Error in v_s estimation for each layer identified in the sCPTU interpretation

The calculation of wavelengths expected for different materials is presented in Table 7-8. These results are helpful in the interpretation of the RMSE values previously calculated because they allow to see how deep the waves actually penetrate when they reach every layer in the soil profile.

Table 7-8. Wavelength for materials in different layers and different frequencies

Layer ID	Thickness (m)	v_s (m/s)	Wavelength λ (m)						
			f_{peak} 31.0Hz	f_{peak} 41.3Hz	f_{peak} 51.7Hz	f_{peak} 62.0Hz	f_{peak} 72.9Hz	f_{peak} 82.7Hz	f_{peak} 95.4Hz
1	2.0	203.3	6.6	4.9	3.9	3.3	2.8	2.5	2.1
2	3.0	285.1	9.2	6.9	5.5	4.6	3.9	3.4	3.0
3	3.0	334.2	10.8	8.1	6.5	5.4	4.6	4.0	3.5
4	2.0	336.0	10.8	8.1	6.5	5.4	4.6	4.1	3.5
5	2.0	250.0	8.1	6.1	4.8	4.0	3.4	3.0	2.6
6	2.0	406.7	13.1	9.8	7.9	6.6	5.6	4.9	4.3
7	2.0	399.5	12.9	9.7	7.7	6.4	5.5	4.8	4.2

From the interpretation of Fig. 7-39 it is clear that the two top layers exhibit a similar response to the frequency variation, which is for the lower frequencies the shear wave velocity is underestimated, while for the higher frequencies it is overestimated. For the four deeper layers the effect of the input frequency goes the other way around, for the lower frequencies the shear wave velocity is overestimated, while for the higher frequencies it is underestimated.

7.6 Analysis for a spatially variable medium

So far in this chapter, all the results have been obtained from numerical models built under the assumption that the geomaterials in the field are distributed in horizontal layers (i.e. layered medium approach). Other approach to characterize the medium is by considering the properties are spatially variable, as it was preliminary studied in the previous chapter.

As a final exercise in this chapter, the input force obtained from the excitation force inversion process was used as the input force in a numerical model, now taking into

account the spatial variability of the shear modulus. However, few considerations were necessary and are explained here:

1. The random fields used in chapter 6 were not conditioned, meaning they are not applicable for a case when the property being spatialized has been measured at specific locations. In that case the random field must be generated using a conditioned distribution which respects the measured values.
2. In a first stage of the random field generation, it was not generated for the whole thickness of 16 meters at once as it was done in the previous chapter. Instead, a separated conditioned random field was generated for each one of the seven layers identified in the shear wave profile obtained from the interpretation of the sCPTU field test.
3. In a second stage of the random field generation, the seven random fields (i.e. one per layer), were combined to create a unique random field for the 16 meters. In order to ensure smooth transitions between adjacent layers, the first two rows and last two rows in adjacent layers were averaged.

The values of mean and standard deviation of the shear modulus for the materials inside each layer are summarized in Table 7-9. The result obtained from the conditioned random field generation process is presented in Fig. 7-39.

Table 7-9. Materials properties for the conditioned random field generation.

Layer ID	Thickness (m)	Mass Density	Poisson's ratio	G_{mean} (MPa)	$G_{std. deviation}$ (MPa)
1	2.0	1936.8	0.25	79.7	30.0
2	3.0	1936.8	0.25	151.8	62.5
3	3.0	1936.8	0.25	180.6	44.8
4	2.0	1936.8	0.25	160.4	59.3
5	2.0	1936.8	0.25	260.3	52.3
6	2.0	1936.8	0.25	326.7	69.0
7	2.0	1936.8	0.25	352.2	64.1

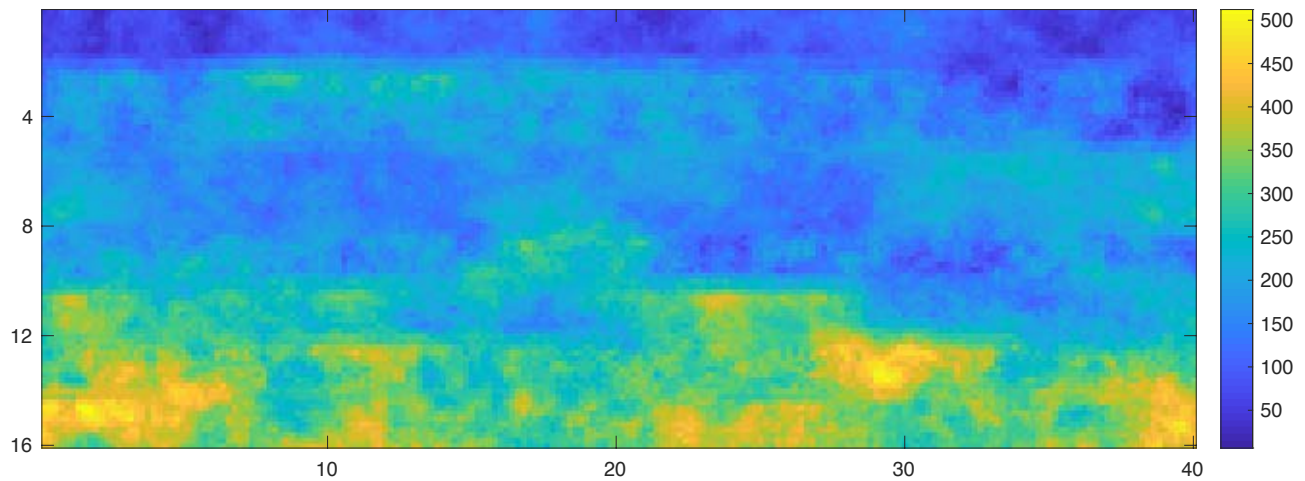


Fig. 7-39: Conditioned random field for the simulation of the sCPTU test. The normalized correlation length was 1.25.

The result obtained in the generation process for the conditioned random field looks very different when it is compared with the non-conditioned random fields generated in the chapter 6, as they were presented in Fig. 6-20 to Fig. 6-24. In this case the conditioned random field respects the trend identified in the sCPTU field test results, which was the desired result.

In Fig. 7-40 the results of acceleration, velocity, and horizontal displacements obtained at 4 meters' depth from the numerical simulation including the conditioned random field, are compared against the results obtained from the sCPTU field test. As it was pointed before, in the case of horizontal acceleration from the field test, the signal is the result of applying signal processing to the raw data recorded during the sCPTU test, while for the horizontal velocity and displacement, the signals were obtained from the numerical integration process described in a previous section.

The input force used for the numerical simulation was the same obtained after three iterations in the layered medium (see Fig. 7-28 (d)). The comparison of results from the numerical model at 4 meters' depth, against the results obtained in the sCPTU field

test are presented in Fig. 7-41. The same results for all the depths between 2 meters and 16 meters (i.e. beyond the elastic radius) are presented in a video that can be accessed in the following link <https://youtu.be/bnqqC46pxol>.

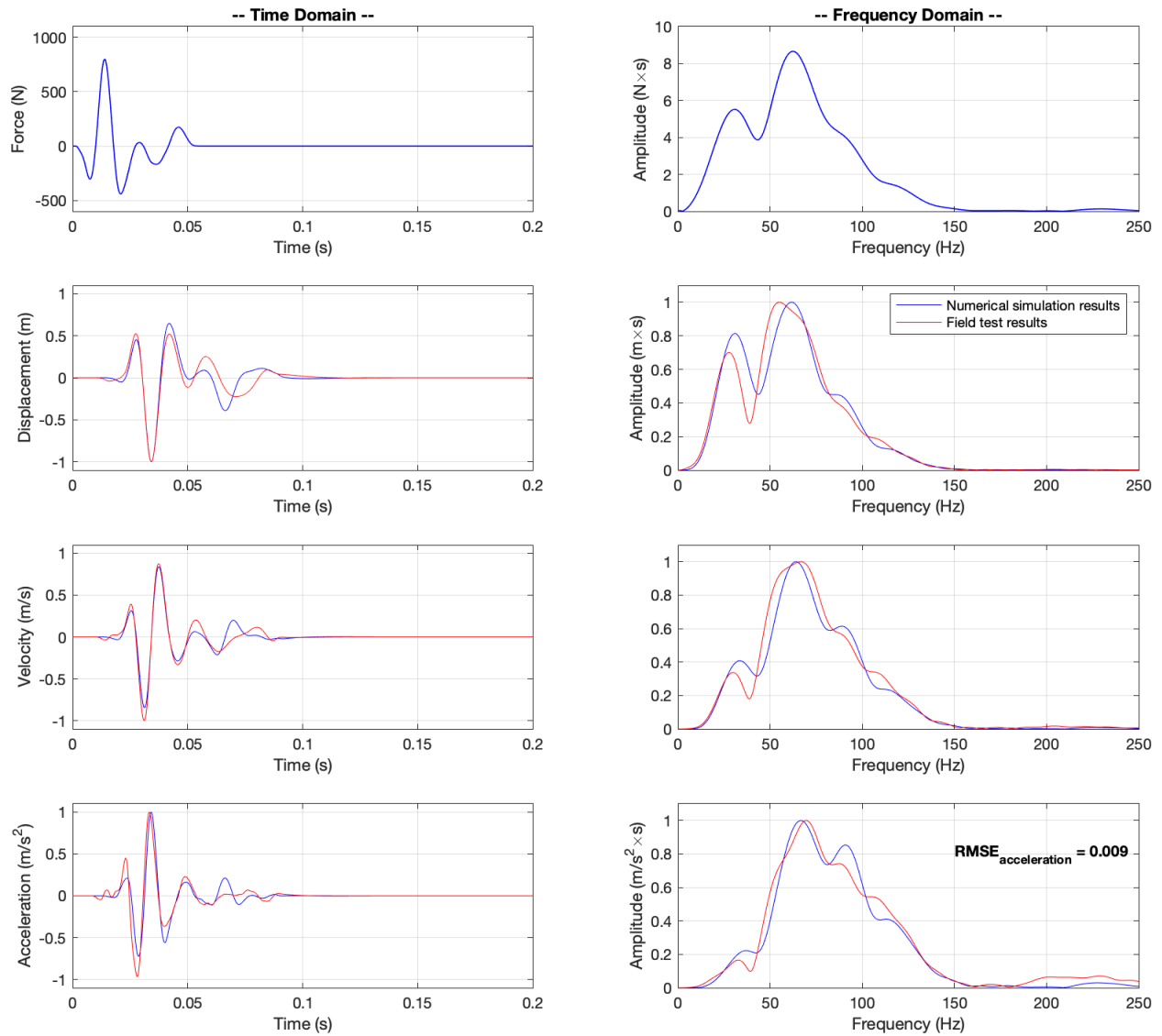


Fig. 7-40: Response at a 4 meters' depth for numerical model with random fields

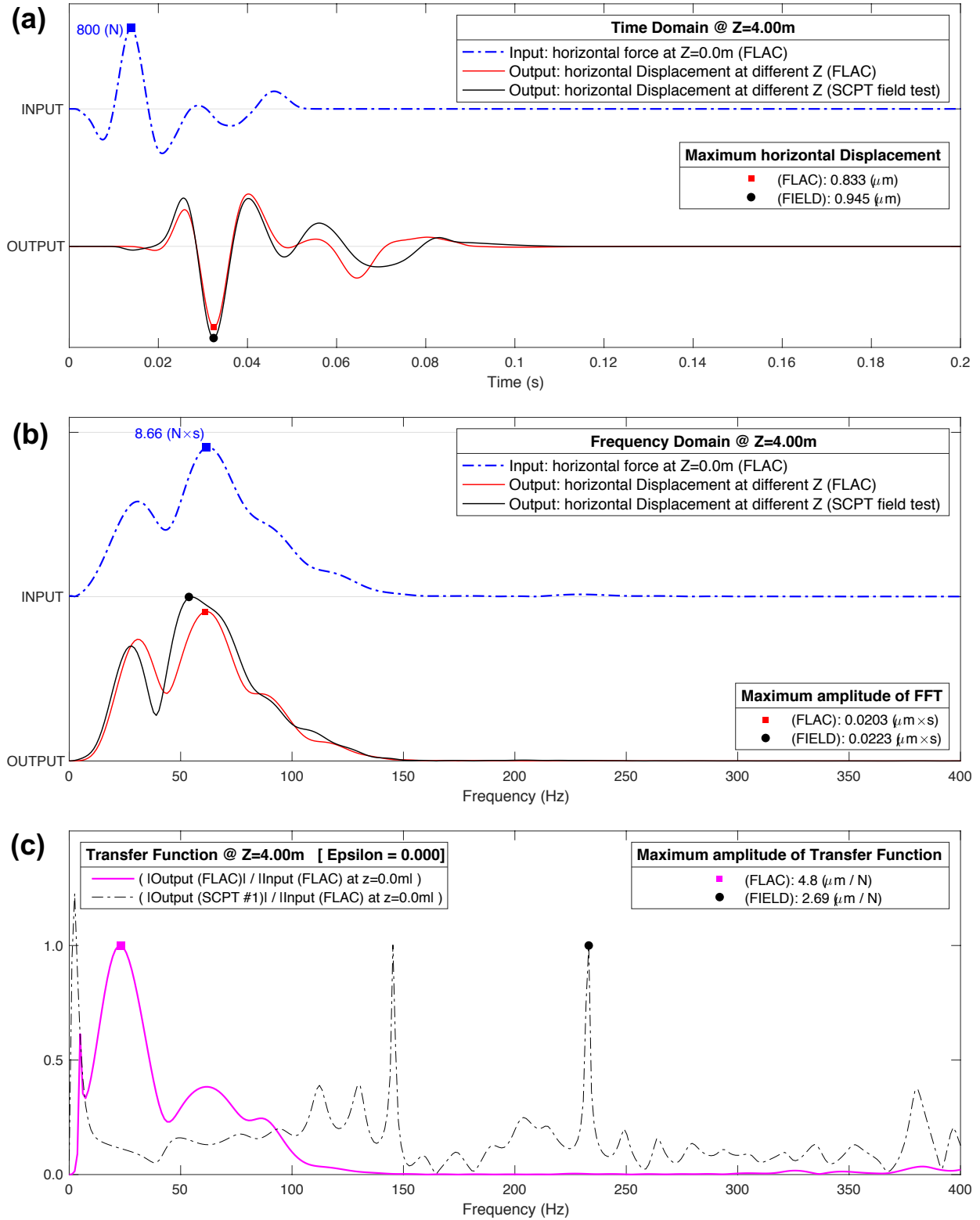


Fig. 7-41: Response at a 4 meters' depth for numerical model including a conditioned random fields

7.7 Conclusions

The work done in this chapter was very extensive and the conclusions obtained will be drawn section by section in order to ease the reader its comprehension:

- From the analysis of the results of the sCPTU field test:
 - The mean frequency in the horizontal acceleration data is about 68 Hz, which corresponds to a wavelength of about 3.0 meters in the first layer of the soil profile. The v_s value for the first layer is 203.3 m/s.
 - After the numerical integration of the acceleration data it was possible to obtain velocity and displacement for the sCPTU field test. For the horizontal velocity the mean frequency was about 62 Hz, while for the displacement it was about 57 Hz. Thus, the mean frequency in the response depends on the variable considered to be the output of the system.
 - The analysis of near field effect led to a value of 3 meters for the elastic radius, which means in this case the near field is estimated to reach a depth equivalent to two thirds of the full thickness of the first layer.
- From the preliminary numerical simulations:
 - The Ricker wavelet was an excellent option to make an initial assumption of the input force.
 - In this research, a complete set of numerical simulations was run to test different frequencies in the input force defined by a Ricker wavelet, at the end the best match between numerical results and field results was obtained for a Ricker wavelet with a mean frequency of 58 Hz, which is very close to the mean frequency in the displacements obtained from integration of the field data of horizontal acceleration.
 - For future applications of this method of analysis is not necessary to run a complete set of numerical models to define the first approximation of the input force, because the mean frequency in the displacement data from the field test is an excellent starting point.
- From the proposed method to obtain the characterization of the input force:

1. A method proposed to obtain the characterization of the input force was presented in this chapter and its results were also analysed. The main benefits of the method are:
 - a. No need of getting extra information, just the typical sCPTU field test data.
 - b. A simple Ricker wavelet can be used as the initial input force to start the iterative process.
 - c. The method converges very fast so that no more than three iterations are enough.
 - d. Once the input force is properly inverted, parametric studies can be performed using the exact force or some controlled modifications of it. For instance, the frequency content can be modified by a simple change in the time step in the force vector.
2. The main drawbacks of the method are:
 - a. The method seems to work better for displacement data rather than acceleration data. The problem is that many sCPTU commercially available equipment use accelerometers, or electromagnetic geophones, so they record either acceleration, or velocity.
 - b. The numerical integration of the signals needs to be carefully done in order to ensure a proper detrending in the data and a proper baseline correction individually for each recorded data.
3. The results shown the effectiveness of the proposed technique to invert the excitation force used in the sCPTU field test. Its ability to actually replicate the results obtained in the field by using numerical simulations is very good.
 - From the study of the effect of variations in the input frequency:
4. The two top layers exhibit a similar response to the frequency variation, which is for the lower frequencies the shear wave velocity is underestimated, while for the higher frequencies it seems to be overestimated.
5. For deeper layers the effect of the input frequency goes the other way around, for the lower frequencies the shear wave velocity is overestimated, while for the higher frequencies it is underestimated.

8 Characterization of geomaterials at intermediate scales: homogeneous approach vs. lack of spatial continuity approach (void detection)

In the previous chapter the analysis of data from the sCPTU field test, as well as the results from numerical simulations, along with a novel method proposed to invert the input excitation force, were used to characterize geomaterials at large scales. The excitation force obtained was then used to study the effect of frequency on v_s results. Most of the analyses in the previous chapter were done for a medium in which the materials' properties were distributed in a horizontally layered model. In the last section of the chapter, the study of a spatially variable medium considering a conditioned random field was presented in order to show the potential of including stochastic analysis in wave propagation methods for the characterization of geomaterials at large scales.

In this chapter, the same method proposed for the input excitation force inversion, was followed to characterize the excitation force in a sandbox model in the laboratory which is considered to be a more controlled environment. The idea here is not just to characterize the geomaterials in the sandbox, but also to validate the suggested method to obtain the inversion of the input force when it is applied at different scales and for different materials. In this case a sandbox was used to study the propagation of waves generated by ultrasonic transducers with a variety of resonance frequencies, and then the vertical displacements were measured at different points in the surface of the sandbox following a linear array and using a laser vibrometer.

Finally, the potential of the method is explored to characterize a medium with a lack of spatial continuity by repeating the tests on one side of the sandbox where a void was intentionally made at the time when the sandbox was built.

8.1 Detailed procedure

The detailed procedure followed in this chapter to characterize geomaterials at intermediate scales involves laboratory testing and numerical simulations. The general steps followed are basically the same used in the previous chapter, with light variations,

like the inclusion of the ultrasonic transducer calibration, and subtraction of the study of the frequency effect on v_s results. The detailed flowchart is presented in Fig. 8-1.

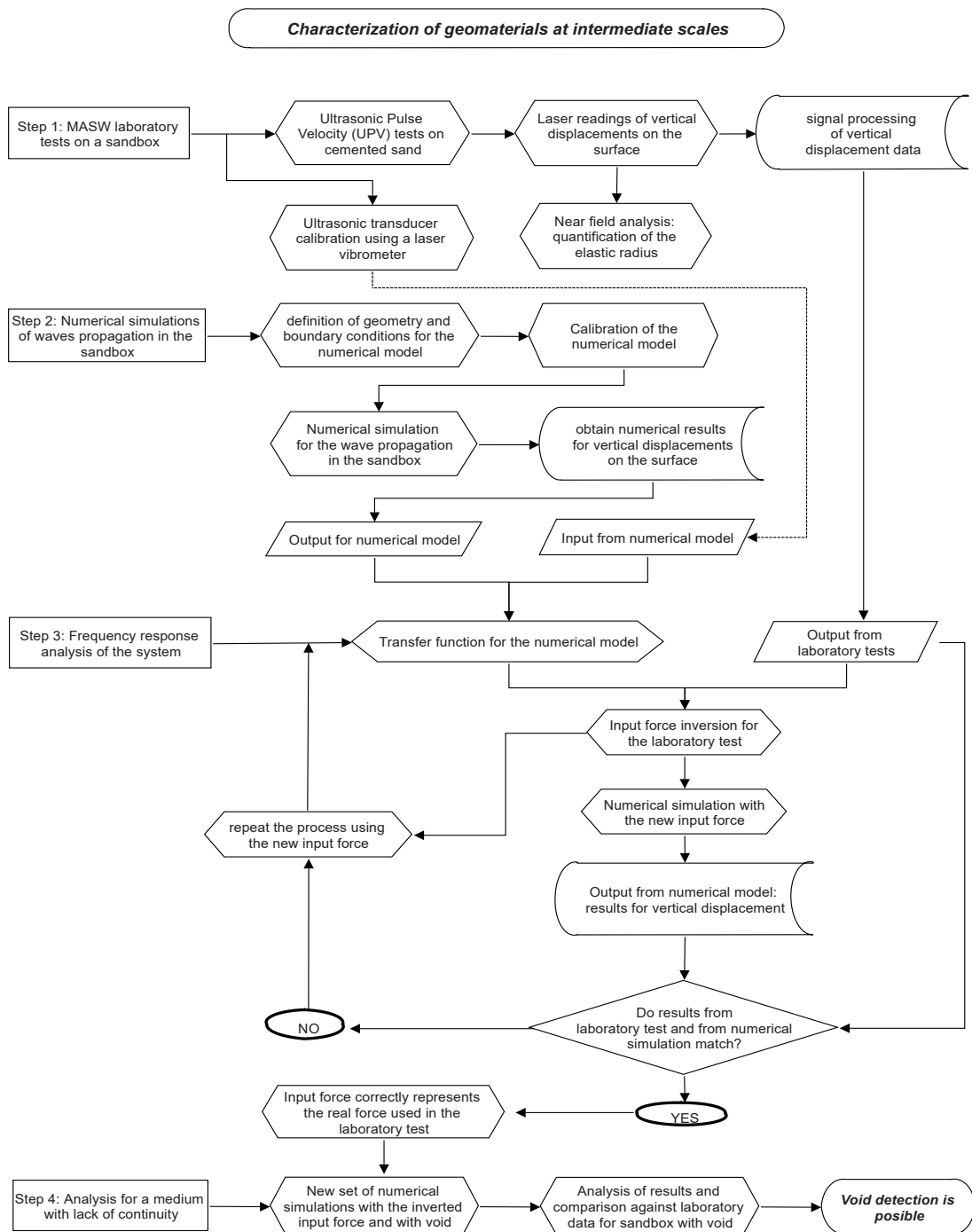


Fig. 8-1: Flowchart of the procedure to characterize geomaterials at intermediate scales

8.2 Step 1: MASW laboratory tests in the sandbox

The sandbox model used in the laboratory was composed of two layers of sand, the upper layer was a cemented sand and the lower one was a loose sand. The drawing with the actual dimensions of the physical model in the laboratory is shown in Fig. 8-2.

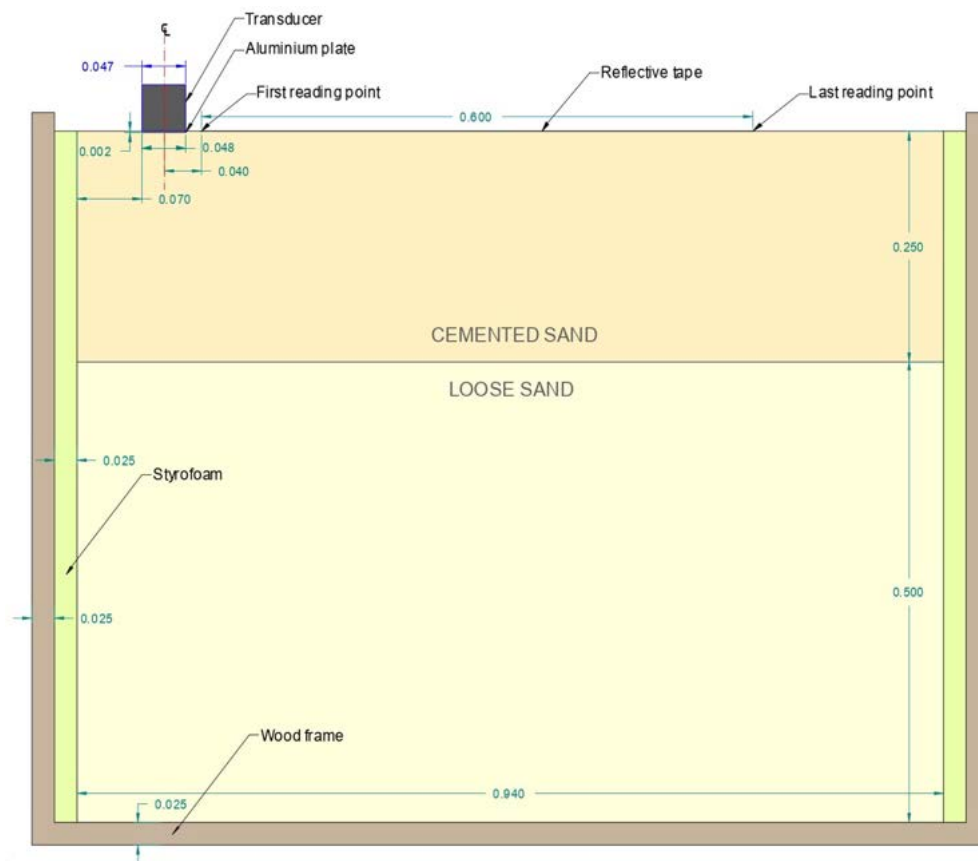


Fig. 8-2: Sketch of the sandbox used in the laboratory

Nasseri-Moghaddam (2006) performed some studies on the very sandbox model used in this research, and reported some of the material properties. For the lower layer the material was characterized as a loose sand with mean grain size $D_{50} = 0.15$ mm, mass density $\rho = 1600$ kg/m³, Poisson's ratio $\nu = 0.25$, elasticity modulus $E = 230.4$ MPa, and bulk modulus $K = 153.6$ MPa; consequently, the corresponding wave velocities were reported to be: $v_{p\text{-wave}} = 416$ m/s, $v_{s\text{-wave}} = 240$ m/s, and $v_{R\text{-wave}} = 221$ m/s.

For the upper layer the material was characterized as a cemented sand consistent of fine sand mixed with about 10% of gypsum based cement. Ali (2015) also reported results for a laboratory seismic test in the same sandbox. He found the Rayleigh wave velocity for the upper layer was $v_{R-wave} = 1074$ m/s, however, a full set of properties for the upper layer was not properly reported. In order to properly characterize the elastic properties of the upper layer material a set of test was performed in the laboratory.

8.2.1 Ultrasonic pulse velocity (UPV)

In order to better characterize the material in the upper layer, a hole was drilled and a core sample of the cemented sand was extracted, then a basic laboratory test was performed on that sample to determine the mass density of the cemented sand, which was found to be $\rho = 1615$ (kg/m³). To measure the P-wave velocity, ultrasonic pulse velocity (UPV) tests were performed at two different frequencies: 54kHz, and 150kHz. Wiciak et al. (2017) studied the effect of length and diameter of the specimen when the UPV test is performed in cemented materials. They recommend that the length (L) of tested specimens should exceed more than one wavelength (λ_p) (i.e. the same suggestion made by ASTM), however, they found that specimens with length over three wavelengths allow a better identification of the wave arrivals. They also studied the effect of diameter of the specimen (ϕ) and showed that increasing diameter of the specimen improves the peaks observed in the frequency spectra. Thus, from those results it can be said that the higher the value of the ratios (L/λ_p) and (ϕ/λ_p), the more reliable the UPV results are.

For the characterization of the cemented sand, the results of the ultrasonic pulse velocity (UPV) tests were in average $v_p = 1668.2$ m/s for the test at 54kHz, and $v_p = 1737.6$ m/s for the test at 150kHz. With these results the wavelengths are calculated to be $\lambda_p = 30.9$ mm and $\lambda_p = 11.6$ mm, respectively. The length of the core sand sample for UPV test was $L = 103.5$ mm, so the ratio length to wavelength (L / λ_p) was 3.3 for the 54kHz test, and 8.9 for the 150kHz test. On the other hand, the diameter of the specimen was $\phi = 53.4$ mm in average, so the ratio diameter to wavelength (ϕ / λ_p) was 1.7 for the 54kHz

test and 4.6 for the 150kHz test. Thus, these results corroborate what was reported by Wiciak et al. (2017), the results from the UPV test depend on the (L/λ_p) and (ϕ/λ_p) ratios and they need to be verified by another test, that is why the results of the MASW test will be used to determine the wave velocities by analyzing the time domain seismograms.

8.2.2 Multi-channel analysis of surface waves (MASW) tests

8.2.2.1 Experimental setup

In order to perform the MASW test in the laboratory, the following aspects were considered:

- The input energy was applied by an ultrasonic transducer in full contact with a setting plate on the horizontal surface of the sandbox. A function generator was connected to the transducer and an electric pulse was sent to the transducer through a piezo-driver to increase the power in the signal.
- The coupling between the setting plate and the cemented sand was done with a strong epoxy glue to ensure the reference location for the input source had not modification during the tests.
- The placing of the transducer was carefully done to ensure the center of the transducer coincided with the center of the setting plate. The coupling between the transducer and the setting plate was done with ultrasonic gel.
- The array geometry was a straight line of 61 points with horizontal spacing of 10mm (for reference see Fig. 8-2). The first reading point was located at 40mm from the center of the setting plate where the transducer was placed.
- The vertical displacements on the surface of the sandbox were recorded using a laser vibrometer. The non-contact technology of the laser ensured there was an effective reading of the true vertical displacement.
- To ensure a proper reflection of the laser beam, a reflective tape was stick to the surface of the sandbox. Because the tape did not stand by itself, it was necessary to use additional coupling. After many trials, it was found that the best coupling for the reflective tape was obtained with water-based wall sealer paint.

- Vertical displacements at every reading point were measured separately because the laser head had to get manually displaced from one reading point to the next one. The movement was carefully done and controlled by measuring the distance with a caliper in order to ensure the spacing between reading points was always the same (10mm).
- The laser vibrometer was configured to record data with the following parameters:
 - Time step: 15.62 μ s
 - Sampling frequency: 6.4 MHz
 - Recorded time: 5.12 ms
- The test was performed on two alignments, one on the sound side of the sandbox, the second on the other side of the sandbox, on top of where the void is expected.

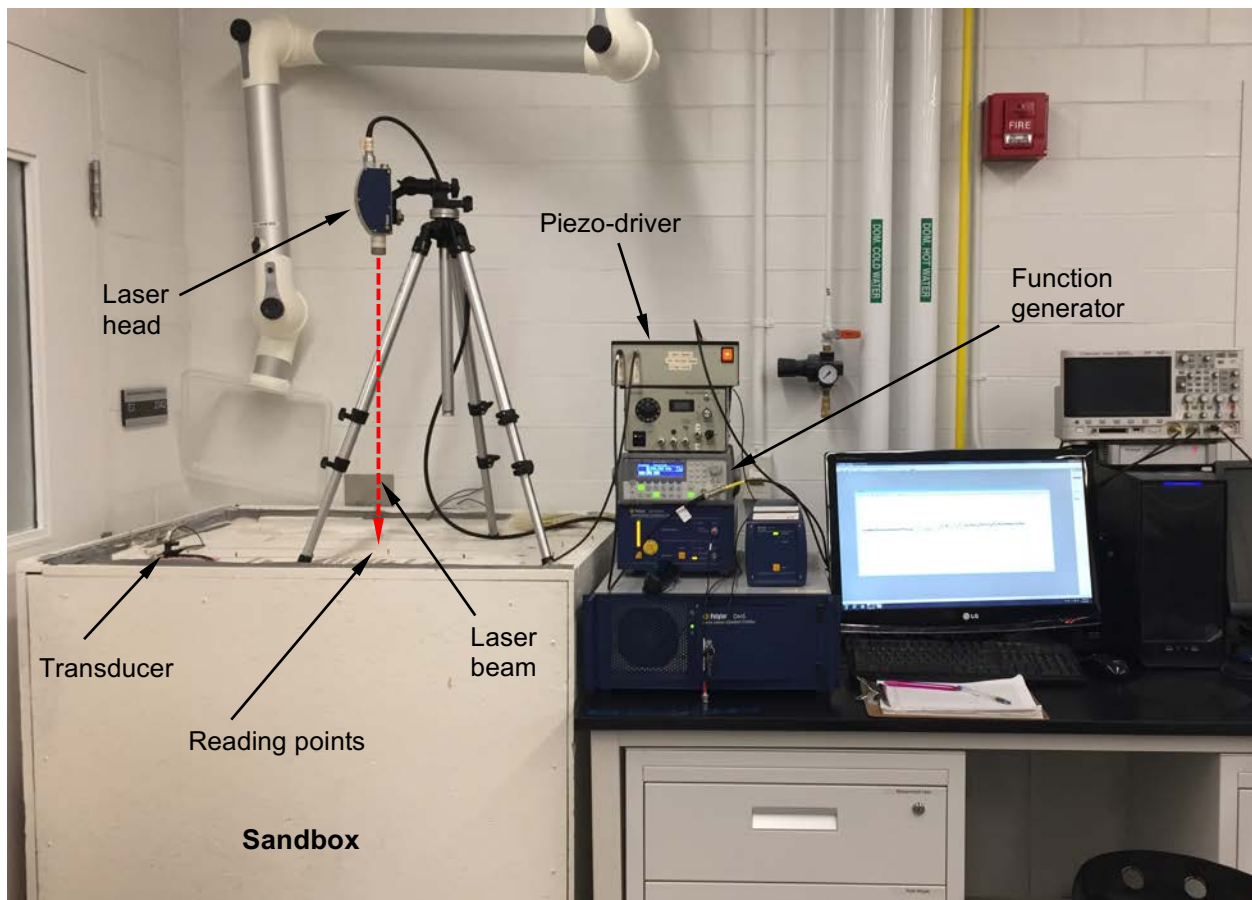


Fig. 8-3: Laboratory setup for laser reading of vertical displacements

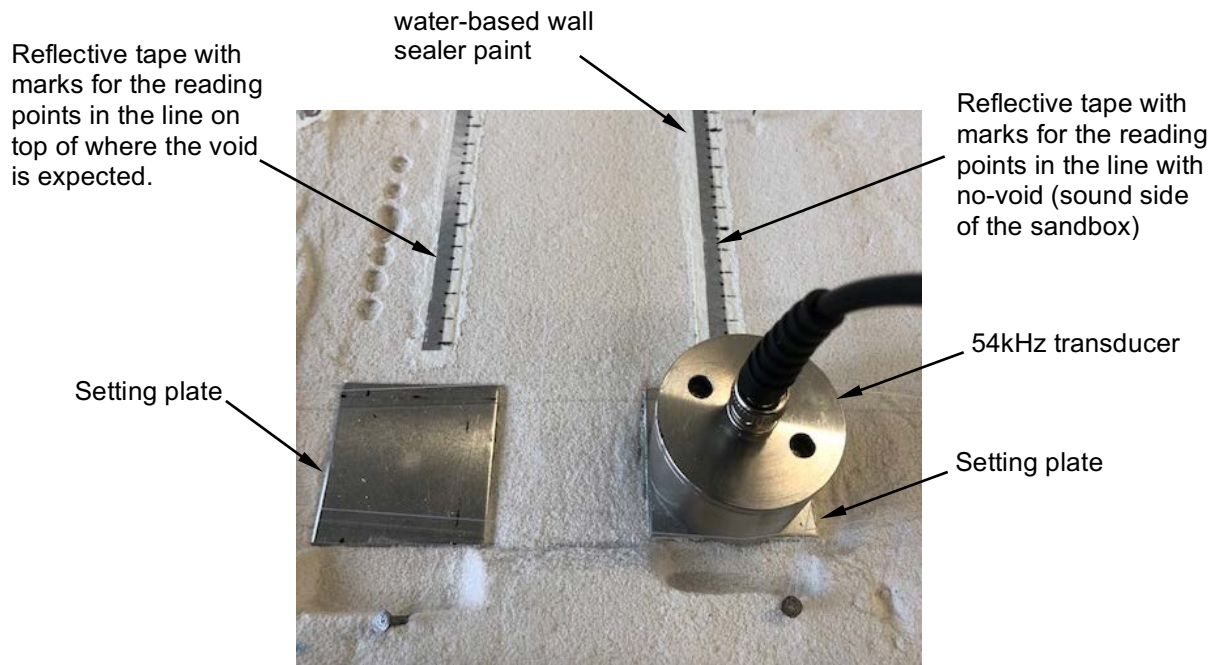


Fig. 8-4: Transducer placement and reflective tape

The function generator used in this tests was an HP33120A model. It was used to generate an input voltage signal send to the transmitter through a piezo driver to increase its power; this input signal was also monitored on an oscilloscope.

The laser vibrometer device used in this research was a single point vibrometer developed by Polytec Inc., which operates on the principle of the heterodyne interferometer to obtain the characteristics of the mechanical vibrations (Polytec, 2013). The beam radiating from the laser head was properly pointed each time at the respective target point on the sandbox surface, which reflected back the laser beam because of the reflective tape stuck to the surface. A phase modulation of the laser light is generated by the displacement amplitudes of the target because of the Doppler effect. Then, the vibration decoder recovers this modulation and converts it into signals that can be displayed on a computer screen. In addition, frequency modulation could be used to get velocity information. The laser vibrometer is capable of measuring displacements with frequencies up to 24 MHz (Polytec, 2013).

8.2.2.2 Experimental procedure

Actual vibrations of the sandbox surface were measured in vertical direction at 61 points. For each measurement, an average of 2000 time signals is saved as the representative time signal. The standard deviation of the 2000 time signals varied from 0.08 to 0.12 for length of the time signals. The input pulse sent from the function generator to the transducer was a 90 degrees out of phase Sine pulse as it is shown in Fig. 8-5.

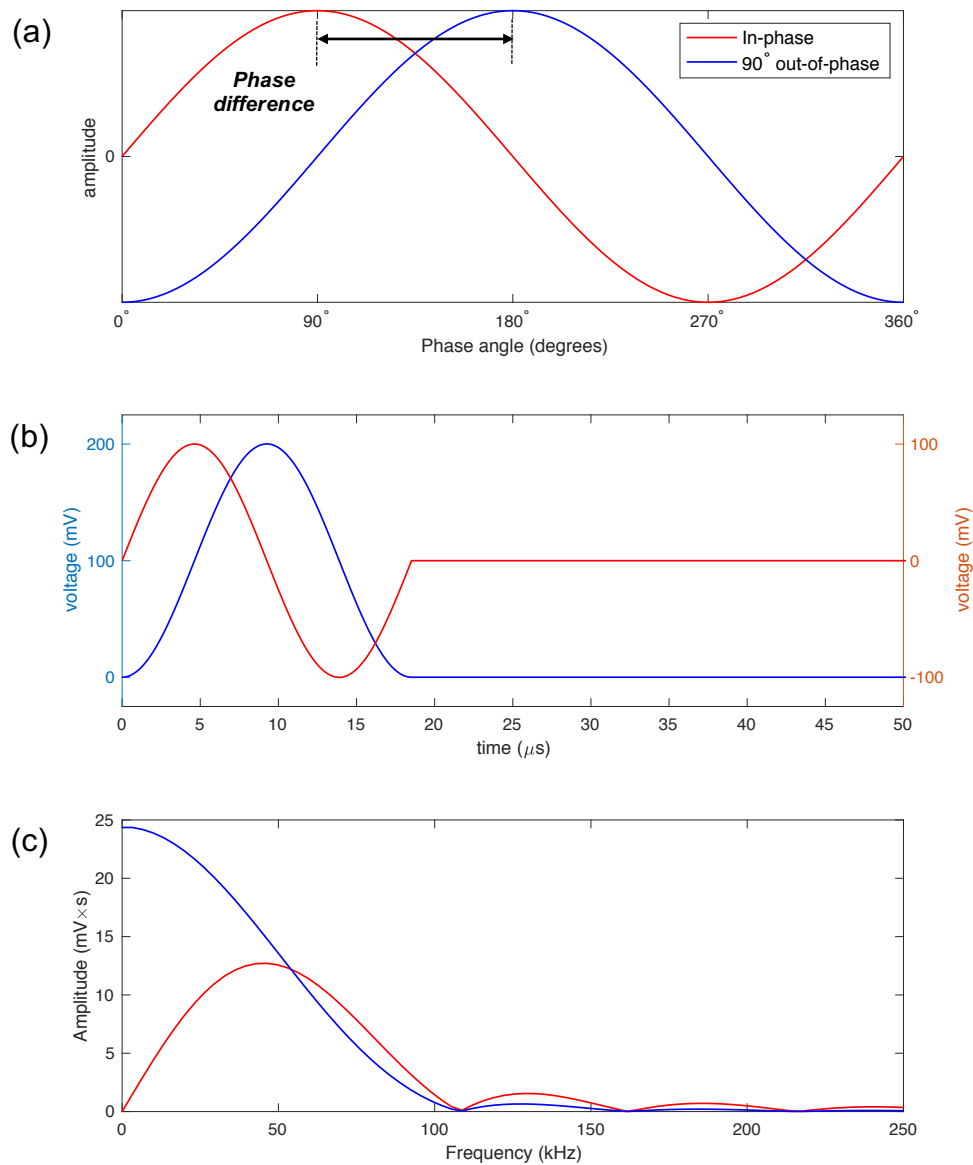


Fig. 8-5: Comparison of sine pulses in-phase and out-of-phase

In Fig. 8-5 (b) a comparison of the input pulses is presented when the in-phase and the out-of-phase sine are used. A sine pulse 90 degrees out-of-phase was preferred over the in-phase pulse because the former concentrates more energy in the low frequency range, as it could be seen in Fig. 8-5 (c). It must be remembered that low frequencies correspond to large wavelengths, which means the lower the frequency, the deeper the penetration of the surface waves. In addition, it is clear that the side lobes in the frequency spectrum are reduced for the out-of-phase pulse, which means the leakage of energy is reduced.

The MASW test in the sandbox was performed for many different input frequencies in the transducer, which ranged from 10kHz to 250kHz. Different transducers were used according to the input frequency targeted, the rest of the test setup was kept the same.

8.2.2.3 Analysis of results

A preliminary of the results was performed by analyzing the raw seismograms in the sandbox, with the only purpose of identifying the P-wave velocity and S-wave velocity values for the cemented sand in the upper layer. A typical raw seismogram is presented in Fig. 8-6. The results obtained for tests at different frequencies, along with the respective calculation of elastic properties for the cemented sand, are summarized in the Table 8-1.

Table 8-1. Wave velocities for cemented sand: interpretation from the raw seismograms of the test performed in the line with no void

<i>Frequency (kHz)</i>	10	20	36	54	72	100	150	200	250	<i>Average</i>
<i>v_p (m/s)</i>	1984.0	1983.0	1997.0	1998.0	2000.0	1978.0	1988.0	2048.0	2085.0	2006.8
<i>v_s (m/s)</i>	1162.0	1167.0	1164.0	1176.0	1173.0	1172.0	1186.0	1210.0	1195.0	1178.3
<i>v_R (m/s)</i>	1068.0	1068.0	1070.0	1076.0	1078.0	1076.0	1080.0	1106.0	1095.0	1079.7
<i>α</i>	1.71	1.70	1.72	1.70	1.71	1.69	1.68	1.69	1.74	1.70
<i>Poisson's ratio (ν)</i>	0.239	0.235	0.243	0.235	0.238	0.229	0.224	0.232	0.255	0.237
<i>Shear Moduli G (MPa)</i>	2180.6	2199.5	2188.2	2233.5	2222.1	2218.3	2271.7	2364.5	2306.3	2242.4
<i>Bulk Moduli K (MPa)</i>	3449.5	3418.0	3523.1	3469.1	3497.2	3360.9	3353.8	3621.1	3945.8	3514.0
<i>Elastic Moduli E (MPa)</i>	5403.3	5433.0	5438.5	5516.6	5501.2	5454.9	5559.7	5825.6	5790.6	5547.2
<i>Constrained Moduli M (MPa)</i>	6357.1	6350.6	6440.6	6447.1	6460.0	6318.7	6382.7	6773.8	7020.8	6503.9

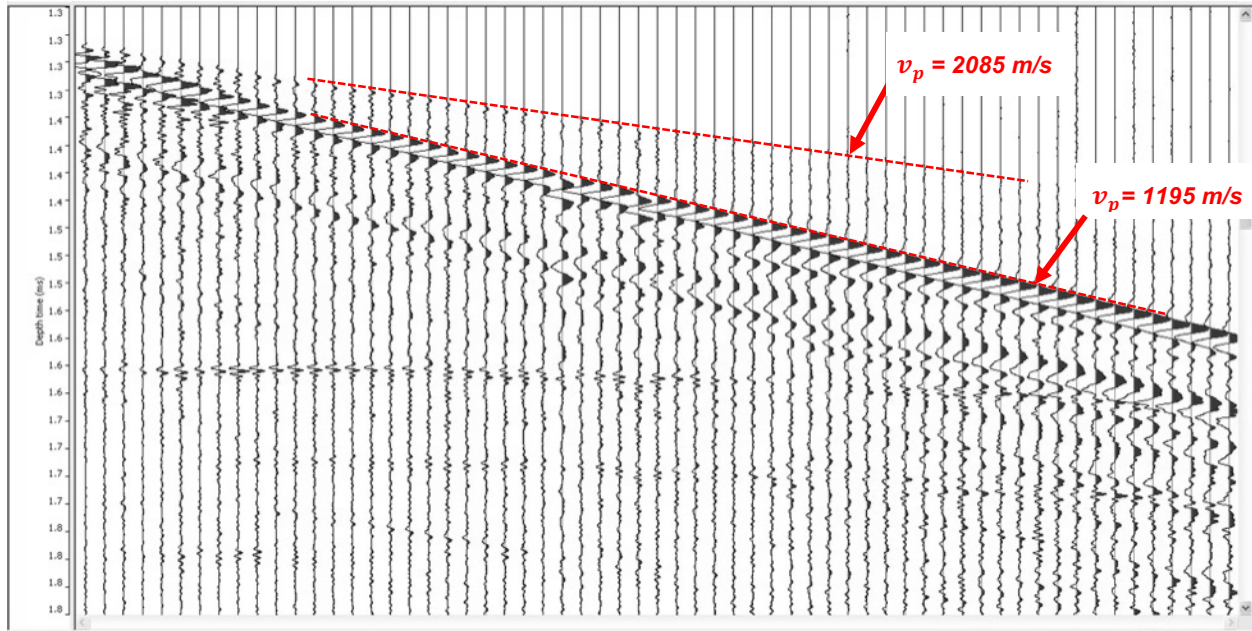


Fig. 8-6: Example of raw seismogram for the seismic test in the sandbox for the alignment with no void (Input Frequency was 250kHz)

For the identification of the arrivals, the first eleven (11) channels (i.e. reading points) were dropped, as well as the last nine (9). The first channels were dropped to avoid the near field effect, and the last ones to avoid the far field effect. This issues will be the matter of further analysis later in this chapter (i.e. next section).

Average values of wave velocities were then considered for the numerical models. The adopted values were $v_p=2006.8$ m/s, $v_s=1178.3$ m/s, and $v_R=1079.7$ m/s. Also the Poisson's ratio value was calculated taken the average from the table $\nu = 0.24$. All the moduli were calculated from the adopted values of wave velocities and Poisson's ratio. Thus, the elastic modulus was $E = 5547.2$ MPa, the shear modulus was $G = 2242.4$ MPa, the bulk modulus was $K = 3514.0$ MPa, and the constrained modulus was $M = 6503.9$ MPa. The variation of wave velocity with the input frequency is presented in Fig. 8-7 for the compressional wave velocity, and in the Fig. 8-8 for the shear and Rayleigh wave velocities.

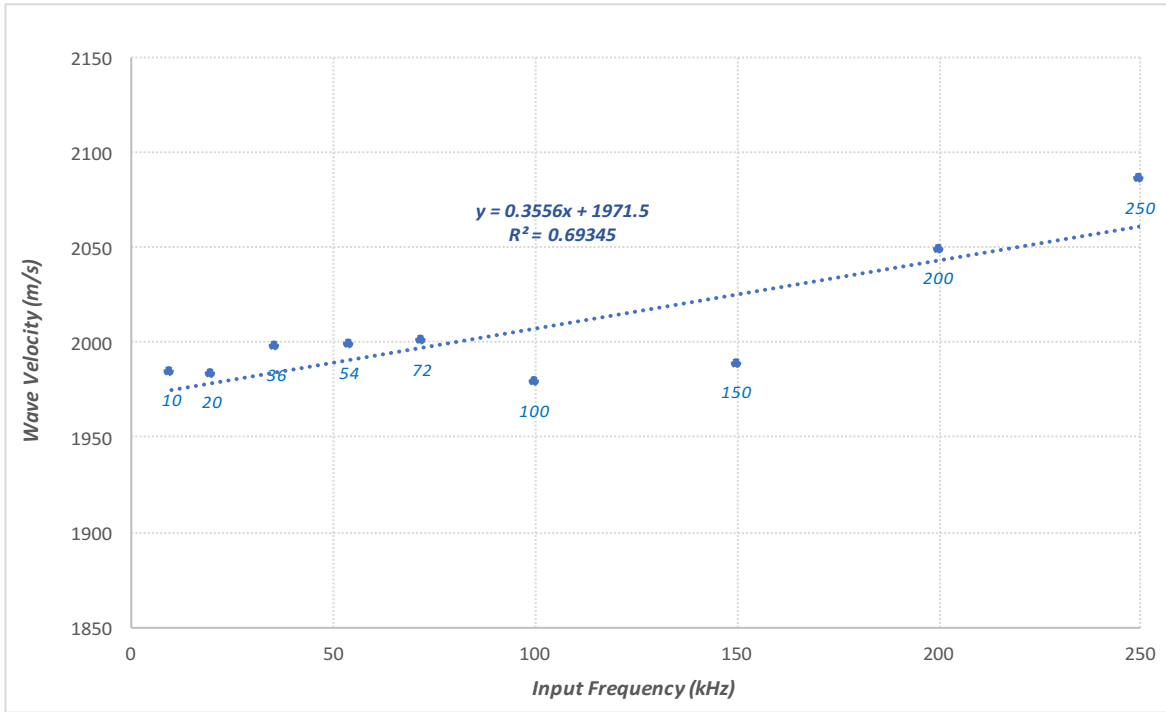


Fig. 8-7: Variation of v_p with the input frequency

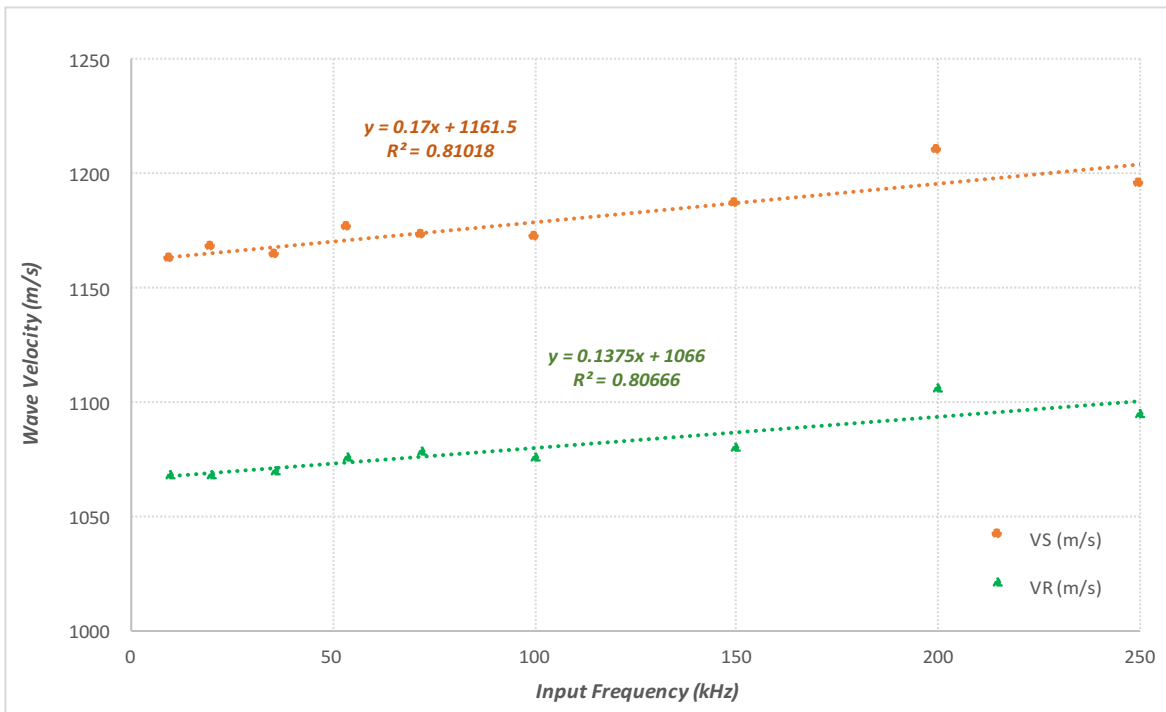


Fig. 8-8: Variation of v_s and v_R with the input frequency

8.2.3 Near field and far field identification

Fig. 8-9 shows the maximum and minimum amplitudes of the vertical displacement for each channel in each one of the two alignments on the surface of the sandbox. By plotting these values against the distance to the excitation force, it is possible to identify the near-field zone and the far-field zone. The limit of the near-field was identified to be located at 0.15 meters from the center of the excitation force, bounding the zone where the maximum and minimum displacements exhibit irregular behavior (i.e. ups and downs in the plot). In a similar way, the far-field zone was identified to correspond to the last 0.09 meters of the arrays, where the amplitudes exhibit an extraneous increasing trend which can be caused by the reflections from the end boundary of the sandbox.

In addition to the near and far-field identification, in Fig. 8-9 is possible to identify the presence of the void by the irregularities in the plot. Thus, the zone where the curves do not follow a regular trend are identified as the zone where the void is located.

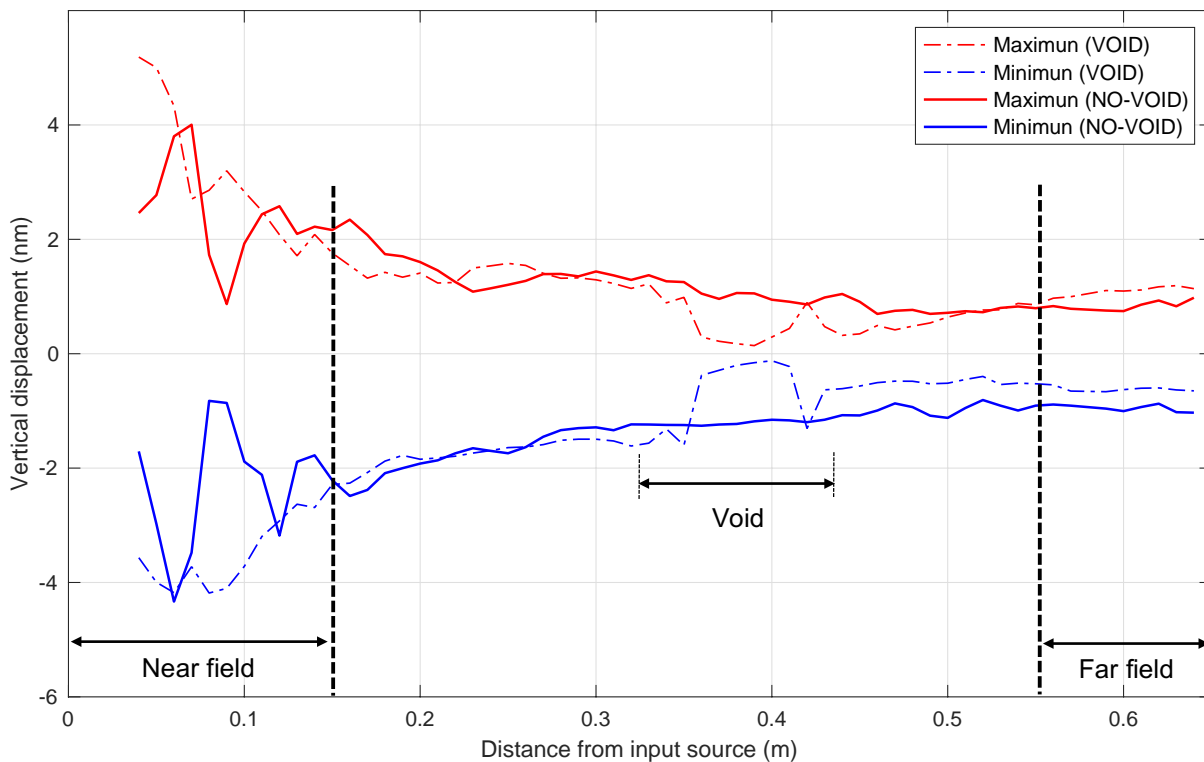


Fig. 8-9: Maximum and minimum amplitudes for all the locations tested in the sand box.

8.2.4 Transducer characterization using a laser vibrometer

Taking advantage of the laser vibrometer, the transducers used in the laboratory testing were characterized. The procedure was quite simple, the same electric input pulse used in the MASW test was sent to the transducer while it was in contact with air (i.e. a sine pulse 90° out-of-phase). Then, the displacements perpendicular to the transducers face were measured following the reading pattern shown in Fig. 8-6. With this reading pattern, 161 points were recorded and mapped to get the actual distribution of the response in the face of the transducers.

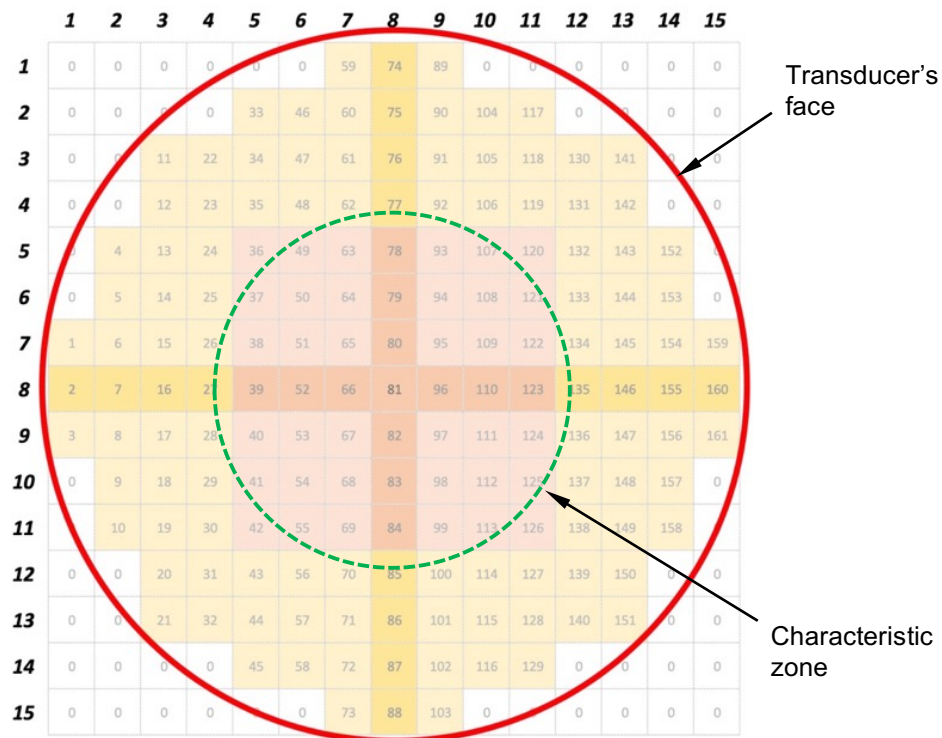


Fig. 8-10: Grid definition for the reading point in the transducers' face

In order to analyze the distribution of the maximum displacements in the transducer's face, average of the responses along the four radius highlighted (dark yellow) in Fig. 8-6 were taken, and then plotted with respect to the distance from the center of the transducer. Fig. 8-7 shows the average response along the radius of the

transducer of 54kHz. As it is clear in that figure, the first half of the radius exhibit a slight variation in the maximum amplitudes, meaning that the central part of the transducer could be used as the characteristic zone governing the behavior of the transducer's face.

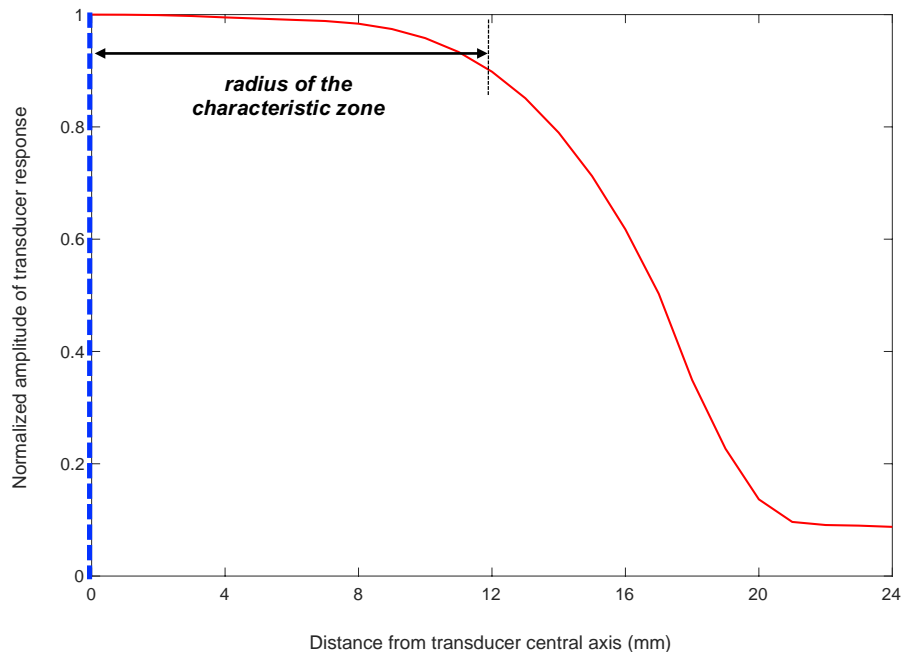


Fig. 8-11: Distribution of the maximum displacements for the 54kHz

Finally, the characterization of the transducer is done by taken averages of the signals recorded at each point inside the characteristic zone. The central part of the transducer carries most of the energy getting converted into displacement (it was estimated to be about 67%). Fig. 8-12 (a) shows the average time domain response for the characteristic zone of the transducer, along with the input pulse sent from the function generator. As it can be seen, for an input pulse of amplitude 200 mV, a maximum displacement of 63.39 nm was obtained in average. The frequency spectrums for the average response of the transducer and for the input pulse are presented in Fig. 8-12 (b). Finally, Fig. 8-12 (c) shows the transfer function for the transducer of 54 kHz. The same results for the transducer with resonance at 20 kHz are presented in Fig. 8-13, and for the transducer with resonance at 150 kHz in Fig. 8-14.

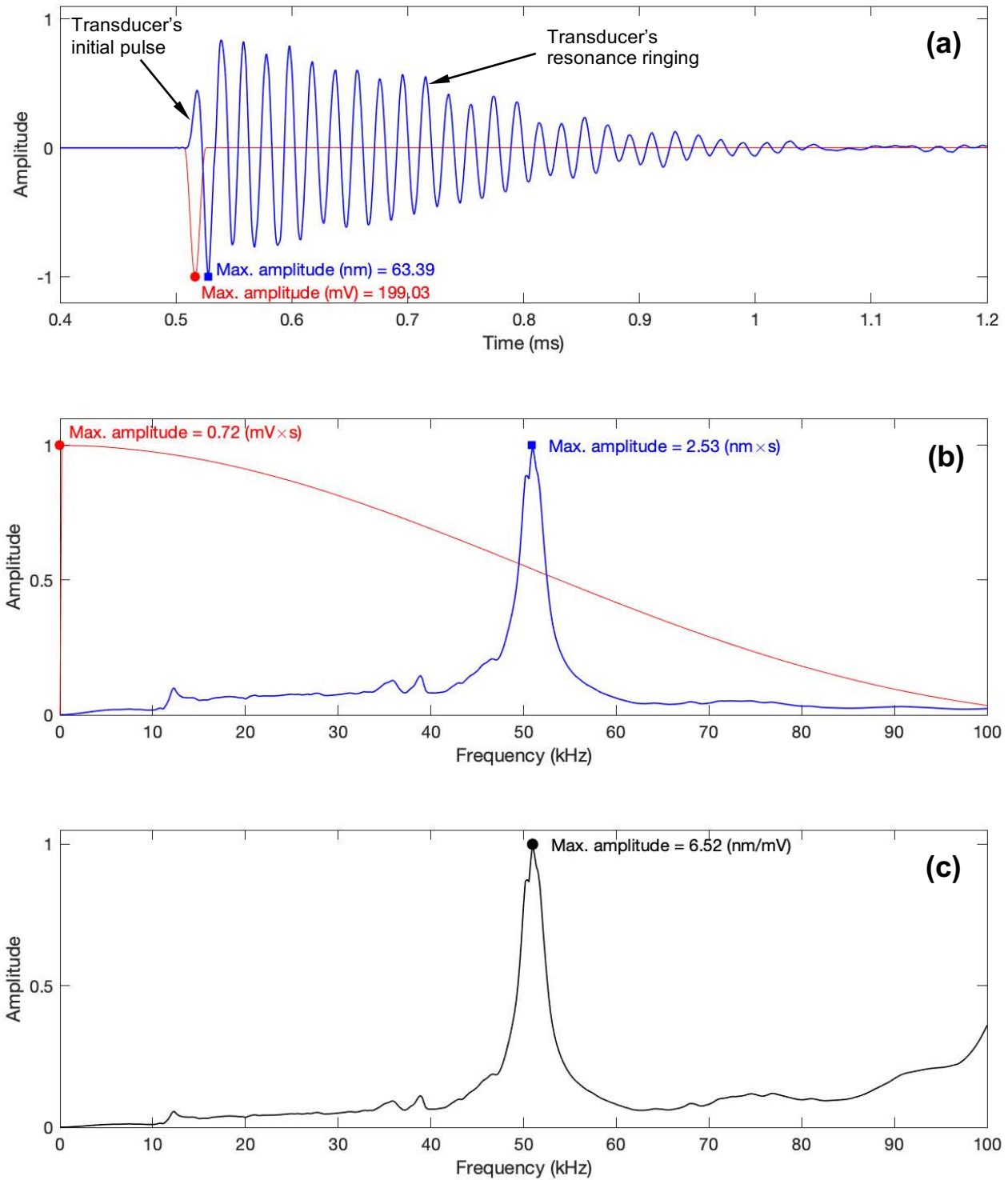


Fig. 8-12: Input pulse (red) and average response (blue) in the time domain (a), the frequency domain (b), and transfer function (c) for the characteristic zone of the transducer with resonant frequency of 54 kHz.

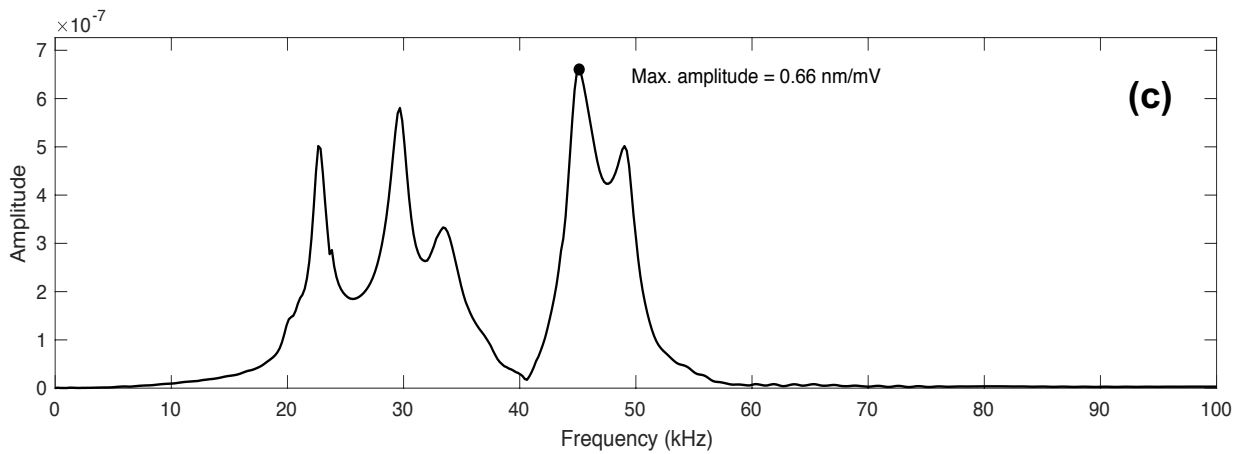
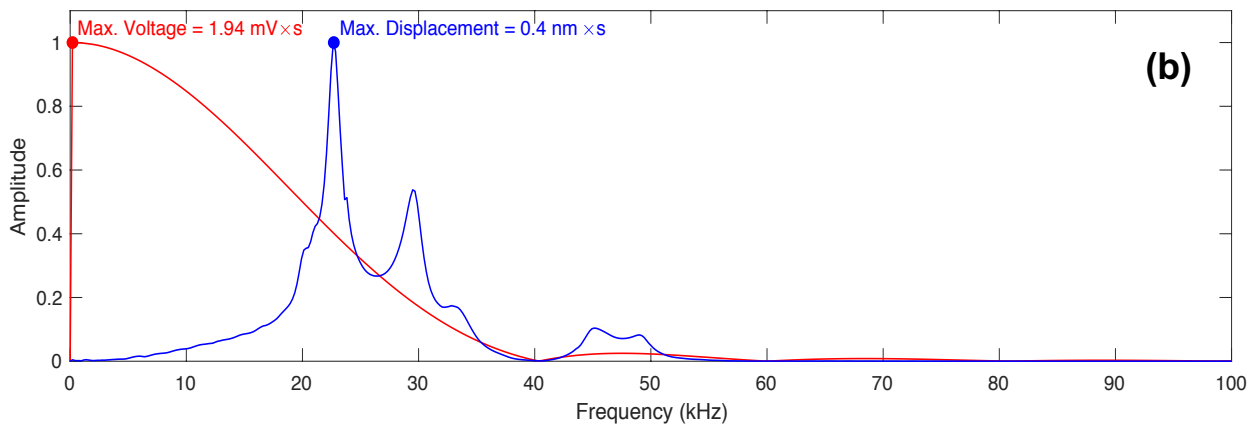
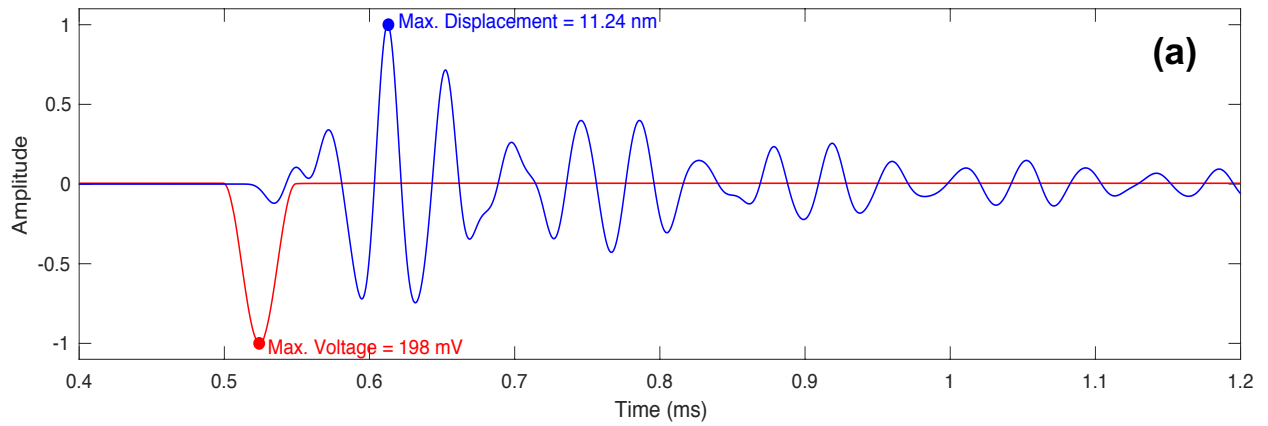


Fig. 8-13: Input pulse (red) and average response (blue) in the time domain (a), the frequency domain (b), and transfer function (c) for the characteristic zone of the transducer with resonant frequency of 20 kHz.

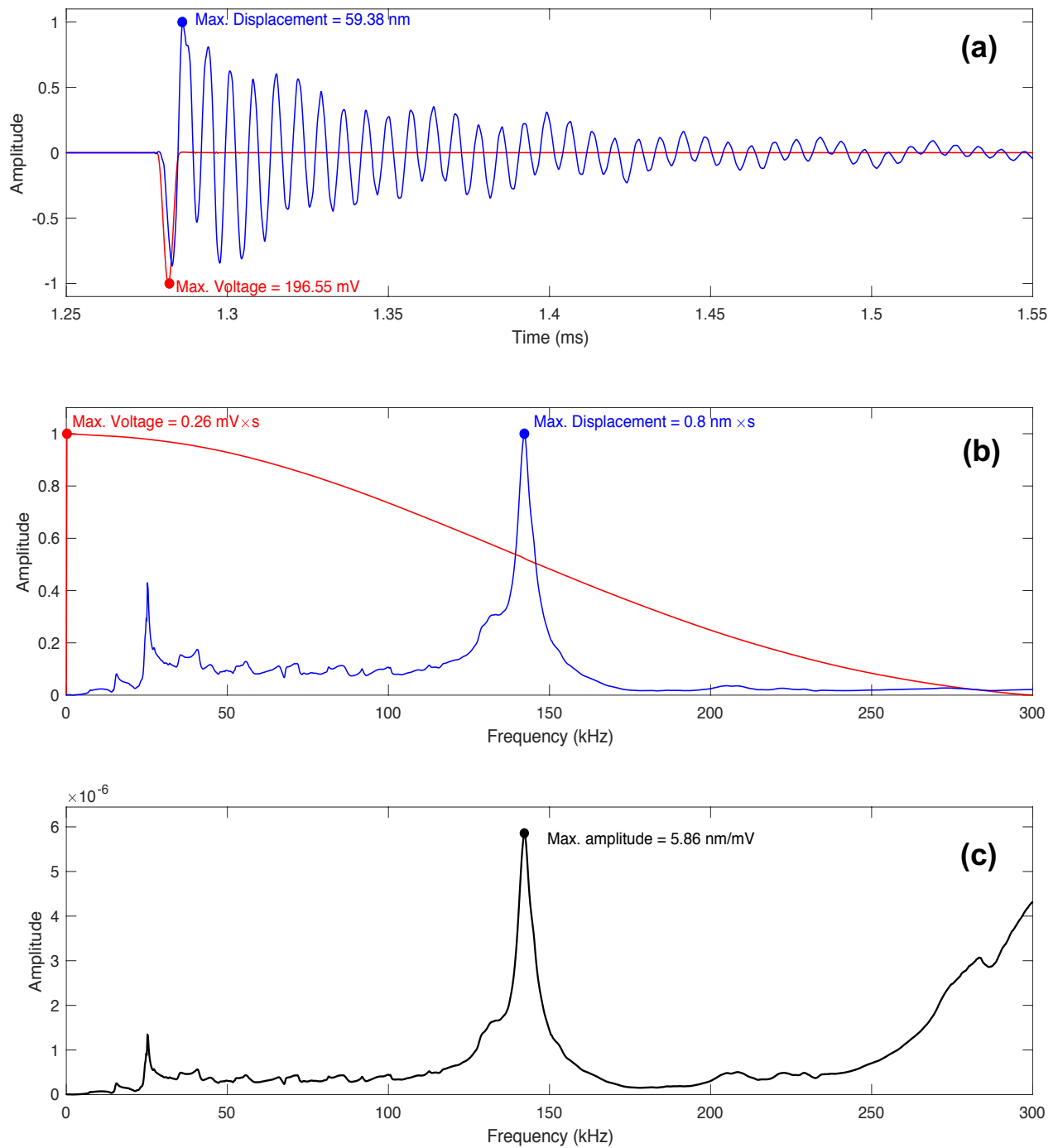


Fig. 8-14: Input pulse (red) and average response (blue) in the time domain (a), the frequency domain (b), and transfer function (c) for the characteristic zone of the transducer with resonant frequency of 150 kHz.

Another important conclusion that can be extracted from previous plots is related to the real resonant frequencies in the transducer used in this research. The first transducer used have a nominal resonance frequency at 54kHz, however, from Fig. 8-12 (b) it is clear that the true resonance frequency is 52 kHz. For the second transducer, which was supposed to have resonance frequency at 20kHz, however, from Fig. 8-13 (b) the true resonance frequency was 22 kHz. Finally, for the transducer with nominal resonance frequency at 150 kHz, the true resonance frequency extracted from Fig. 8-14 was 142 kHz.

8.3 Step 2: numerical simulation of waves propagation in the sandbox

Numerical simulations for a homogeneous medium (i.e. with no void) and for a non-homogeneous one (i.e. with void) were carried out using the finite differences software FLACTM. For the calibration process of the model, the input source was a Lamb force applied at one specific point on the surface, then the model's response was compared against the theoretical solution presented in Table 5-4, exactly in the same way that was done for the numerical models calibrated in previous chapters.

8.3.1 Material properties

In MASW tests, the medium properties and the excitation source govern the wavefield propagated through the medium. The properties of the medium are presented next and were obtained from the analysis of raw seismograms in a previous section:

- Compressional wave velocity: $v_p = 2006.8 \text{ m/s}$
- Shear wave velocity: $v_s = 1178.3 \text{ m/s}$
- Rayleigh wave velocity: $v_R = 1079.7 \text{ m/s}$
- Poisson's ratio $\nu = 0.24$
- Elastic modulus: $E = 5547.2 \text{ MPa}$
- Shear modulus: $G = 2242.4 \text{ MPa}$
- Bulk modulus: $K = 3514.0 \text{ MPa}$
- Constrained modulus: $M = 6503.9 \text{ MPa}$.

8.3.2 Geometry of the model

The geometry of the model used the exact dimensions of the sandbox already existent in the laboratory in order to properly replicate wave propagation inside it. That sandbox was built by disposing sandy materials in two layers. The lower layer is about 0.55 meters thick and corresponds to a loose silica sand, while the upper layer is about 0.25 meters thick and was made of gypsum-based cemented silica sand. The other dimensions of the box are presented in Fig. 8-2.

Fig. 8-15 illustrates a general sketch of the two-dimensional axisymmetric model used for the simulations. Fig. 8-15 (a) shows the side of the sandbox without void, while the Fig. 8-15 (b) shows the location and embedment depth of the void.

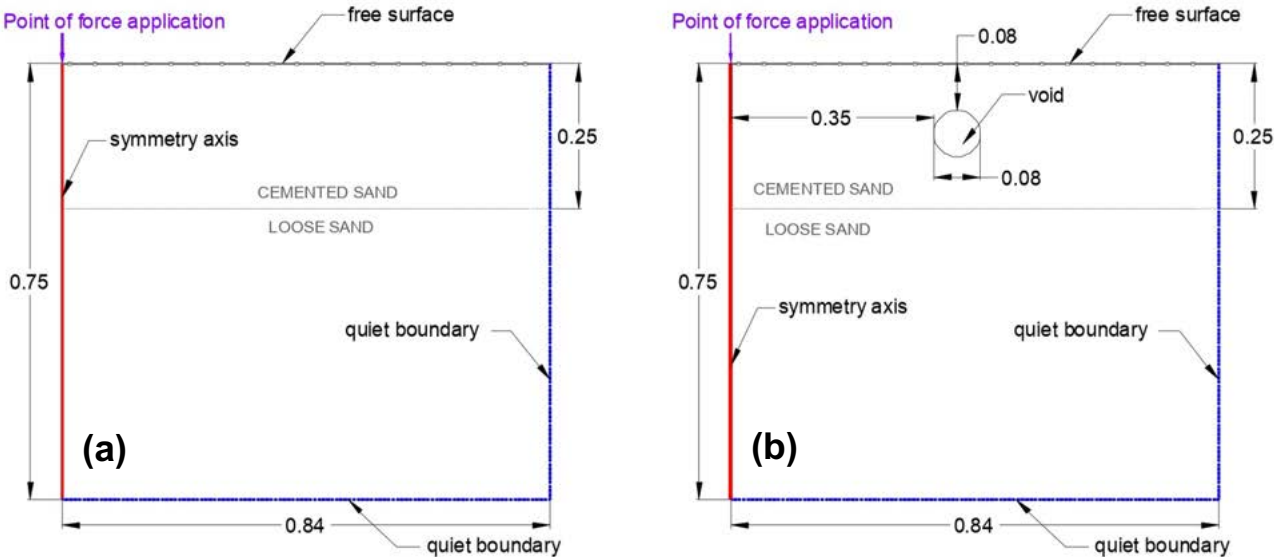


Fig. 8-15: Geometry for the numerical models built to replicate the wave propagation phenomena in the sandbox, for a homogeneous medium (left) and for a medium with a lack of continuity represented by a void (right)

In this model the parameters were adjusted to match the theoretical solution of a Lamb force, and to verify that the model accurately replicates the propagation of surface waves in a semi-infinite medium with the theoretical velocity. The model consists of a

uniform grid in its whole extension. The axis of symmetry was the left end boundary of the model. Quiet boundaries were defined at the right end and bottom. As mentioned by Ali (2015) “To effectively reduce the reflections of R-waves, the boundaries of the numerical model are practically positioned as far from the void as possible”.

The distance between the receivers is exactly the same used in the MASW laboratory test (i.e. 10mm) and the boundary is selected to ensure that the reflections from the boundary are not greater than the main Rayleigh wave arrival at any receivers. Reflections from the boundaries can be expected in the time signals recorded on the surface. However, as Ali et al. (2011) pointed out “reflections from R-wave generated after the interaction of the main R-wave event with the void are practically not affected by boundary reflections because of their geometrical attenuation”.

8.3.3 Boundary and initial conditions

For the boundaries corresponding to the bottom and the right end of the model, the condition of a quiet boundary is applied. For the initial conditions, the only consideration is the model is at rest before the load application actually starts. The load application time depends on the input frequency, however, it is always guaranteed that the numerical simulation lasts for at least the travel time taken for Rayleigh waves (the slower ones) to reach the right end of the model.

8.3.4 Mesh size and time step definition

As it was already explained, the wavelength (λ) determines the accuracy for wave propagation problems. The criteria suggested by FLACTM (Itasca, 2000) for the numerical model is guaranteed that the maximum mesh size has to be one-tenth of the wavelength. For geomaterials like cemented sand, the Rayleigh wave velocity is about 1080 m/s. As it was analyzed for previous numerical models, for different values of shear wave velocity (V_s) and for different values of frequency (f), it is possible to get different values of wavelength, so the calculation of values for mesh sizes following the criteria of one-tenth of wavelength were done for different frequencies. For all the numerical models the mesh

was preferred to be regular, and its size was properly selected according with these results.

8.3.5 Calibration of the numerical model

Lamb source is applied to calibrate the model (Lamb, 1904). The force function applied to the left boundary is:

$$f(t) = \frac{F_b}{\pi} \frac{\tau}{(t^2 + \tau^2)} \quad (8-1)$$

In Equation 8.1, F_b and t are constants that modify the amplitude and the frequency content of the force function, respectively. Rectangular voids of variable width and embedment depth are introduced in the numerical models. The distance from the source to first (offset distance) and last receivers are 0.04 m and 0.64 m, respectively, matching the same conditions for the laboratory tests. Surface responses are recorded from a total of 61 recording points.

Further, the calibration of the numerical model is performed by changing model parameters such that the responses measured from numerical model without void matches well with the theoretical model. Fig. 8-16 shows the input force used for the calibration of the model in the time and the frequency domain, along with a sine pulse 90 degrees out-of-phase, which was used as a reference to ensure the input pulse had the desired central frequency. This comparison is done because in the sine pulse is perfectly possible to control the mean frequency, while in the Lamb pulse the best that can be done is just an approximation.

An example of the vertical and horizontal responses obtained from the theoretical solution, as it was presented in Table 5-4, for a distance of 0.5 meters from the excitation source is presented in Fig. 8-17.

For the calibration of this model a series of numerical simulation were performed to define the damping parameters to be used for this model. Fig. 8-18 presents the results of a comparison of responses in numerical models when different central frequencies are

considered for the Rayleigh damping. For central frequencies between 46 kHz and 68 kHz no significant difference was found.

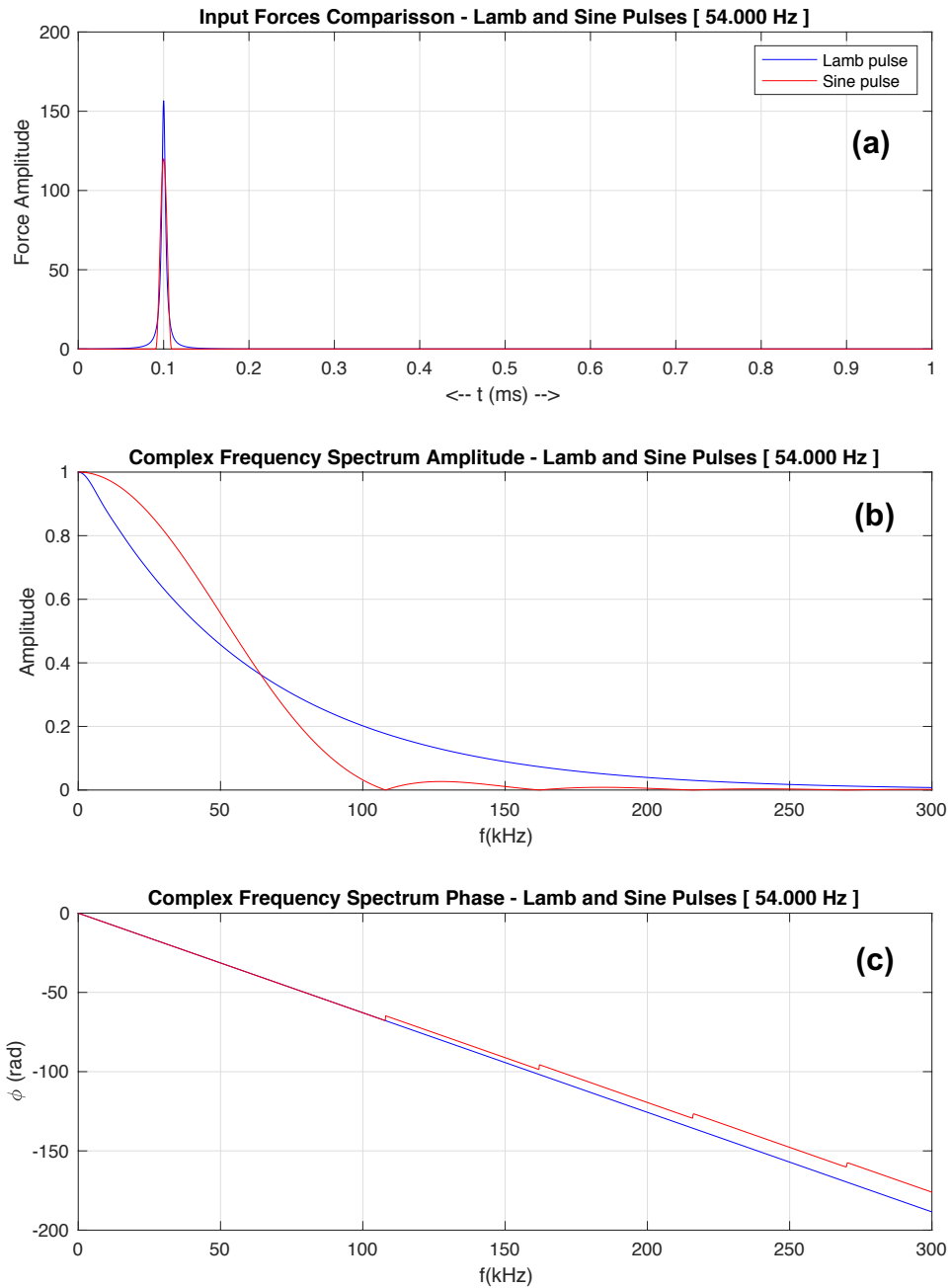


Fig. 8-16: Input force used to calibrate the numerical model seeking to replicate the wave propagation in the sandbox

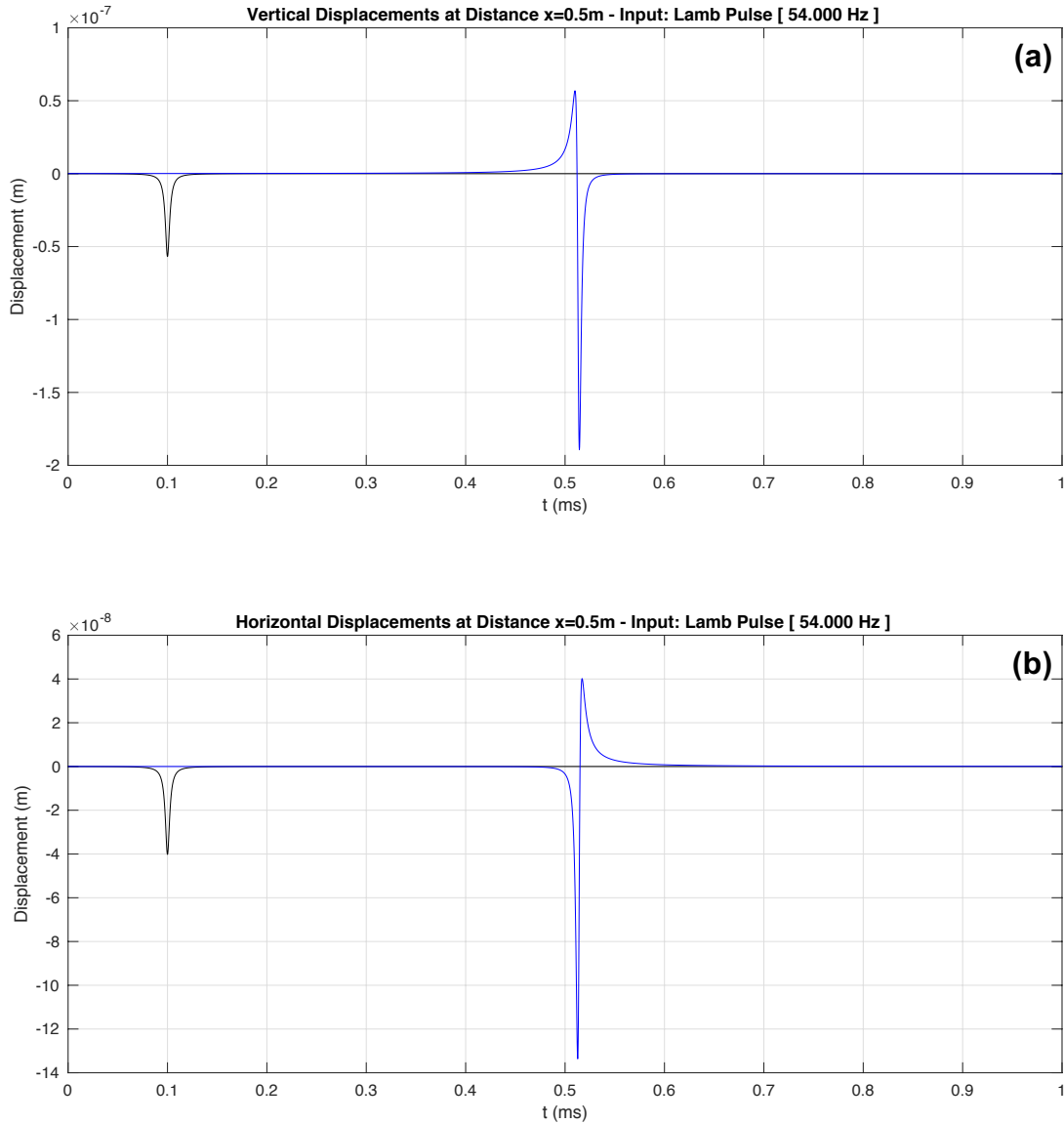


Fig. 8-17: Vertical and horizontal displacements from the theoretical solution at 0.5 meters from the excitation source.

Fig. 8-19 and Fig. 8-20 show the results of a comparison of responses in numerical models when different damping ratios are considered. The comparison of results for values ranging from 0% to 5% showed how the damping affect the response, not just in killing some specific frequencies, but also in reducing the amplitude of the whole signal. Form these results it was concluded the best damping ratio for the model was 4% applied at a central frequency of 54 kHz.

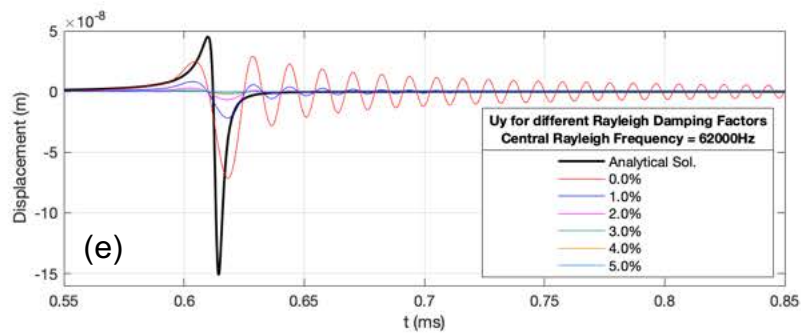
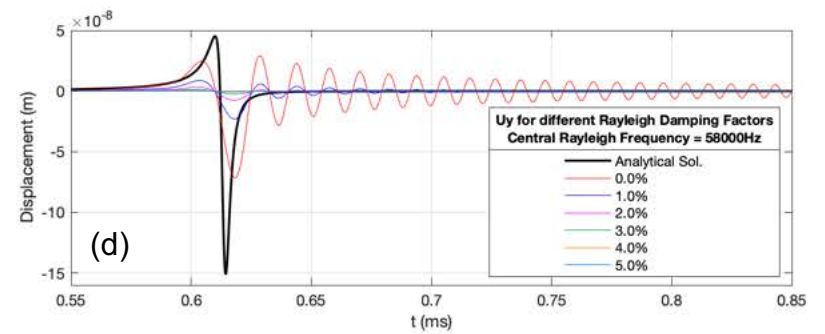
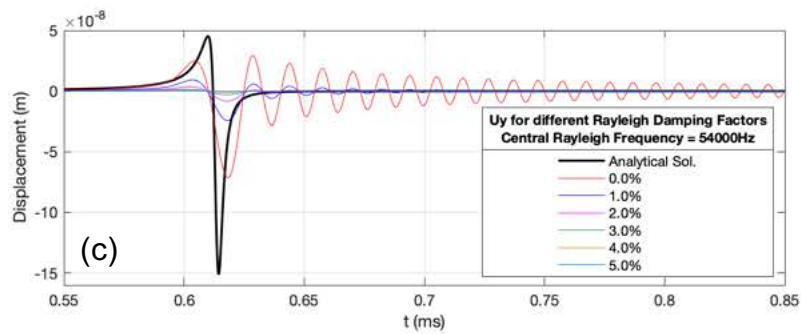
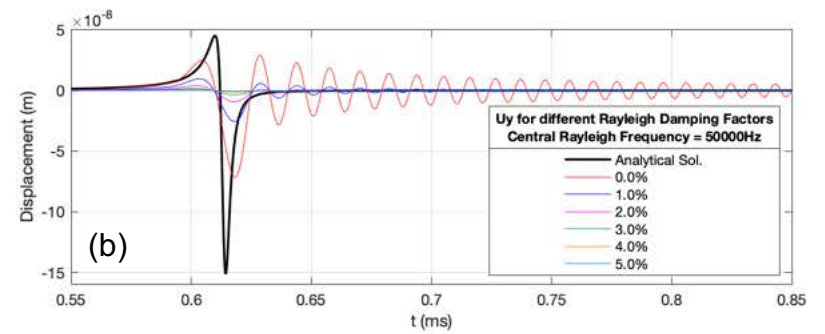
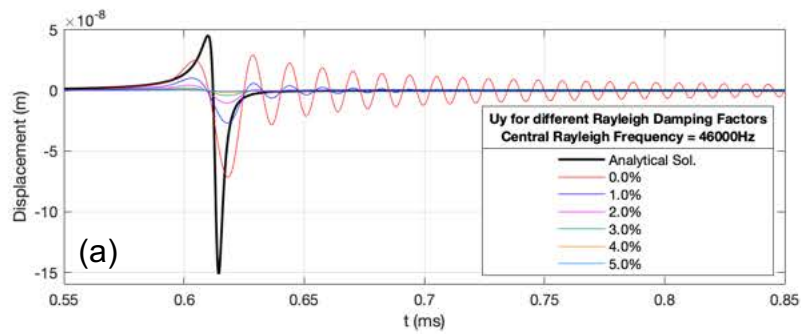


Fig. 8-18: Vertical displacements on surface (U_y) at 0.5 meters from the excitation source for different Rayleigh central frequencies: (a) 46kHz, (b) 50kHz, (c) 54kHz, (d) 58kHz, and (e) 62kHz.

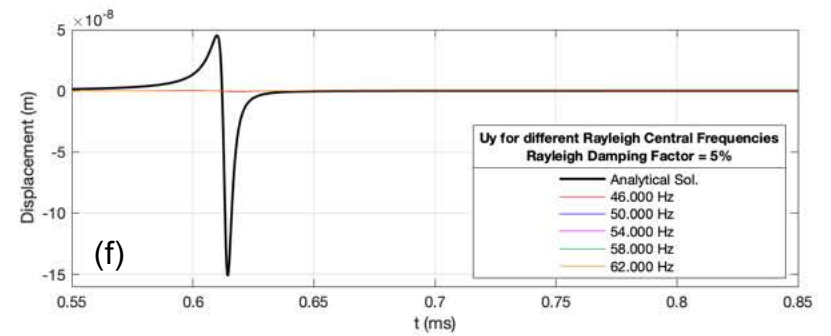
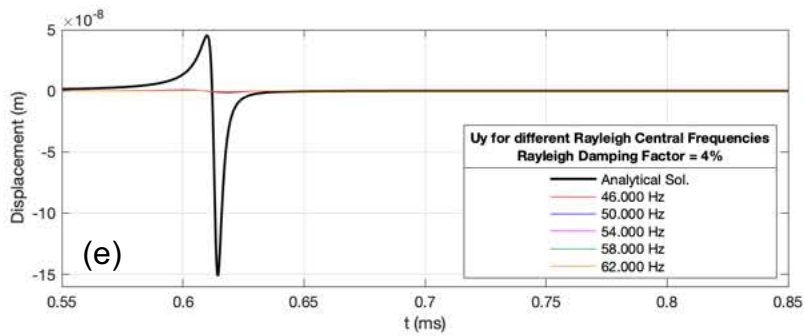
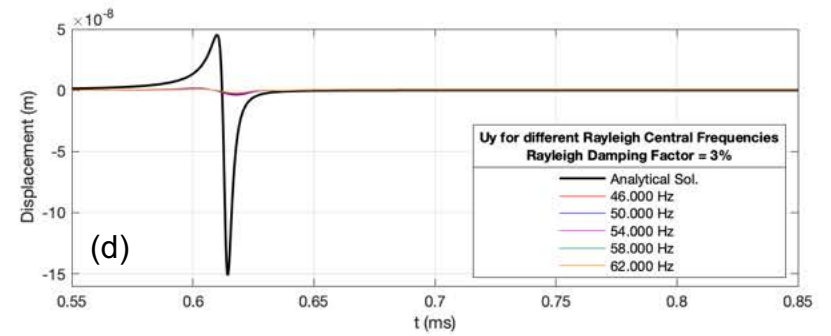
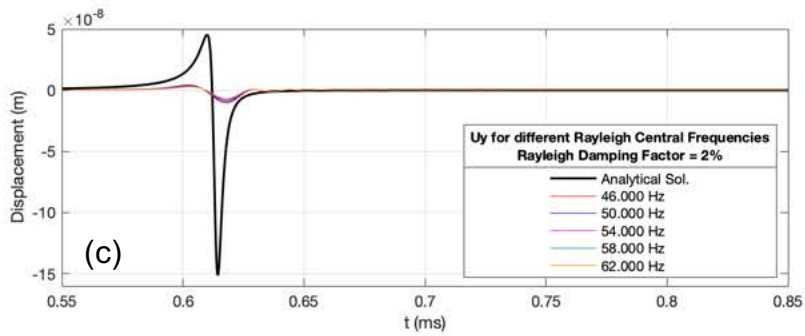
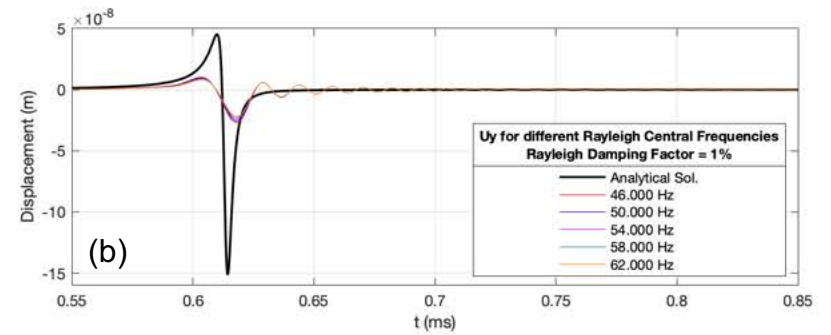
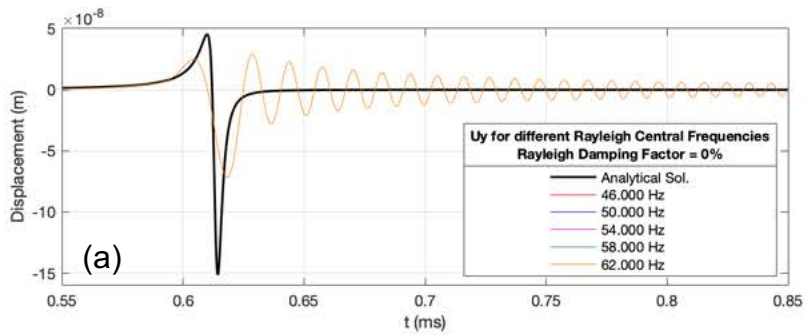


Fig. 8-19: Vertical displacements on surface (U_y) at 0.5 meters from the excitation source for different Rayleigh damping ratios: (a) 0%, (b) 1%, (c) 2%, (d) 3%, (e) 4%, and (f) 5%. (general view)

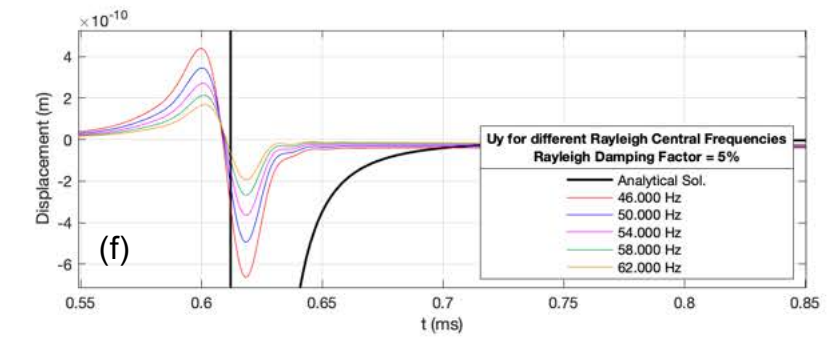
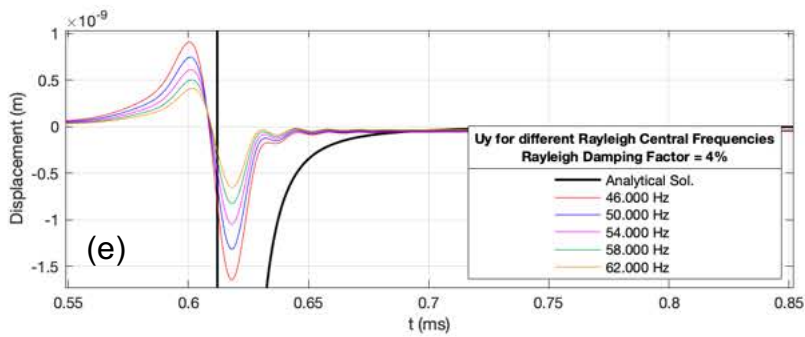
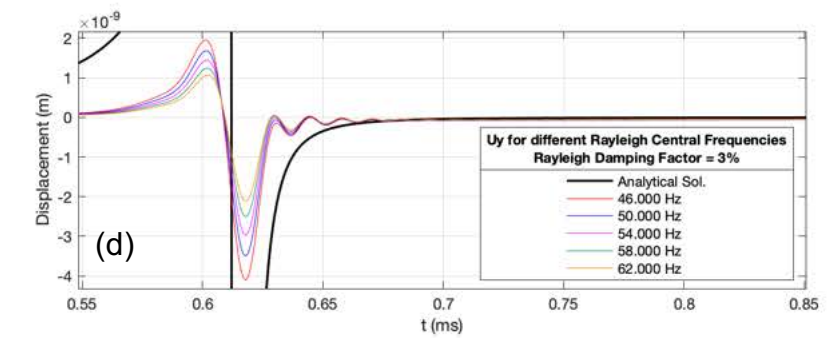
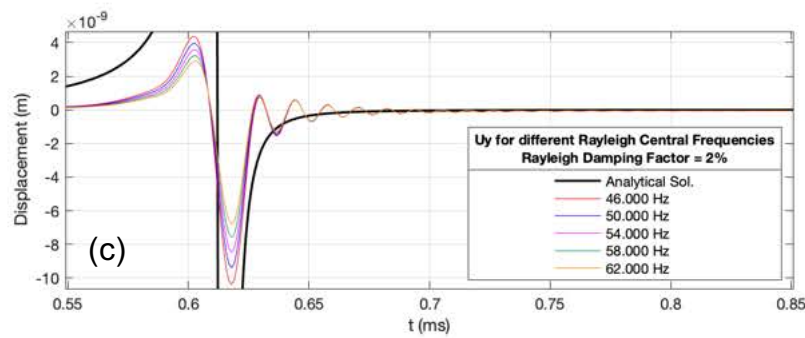
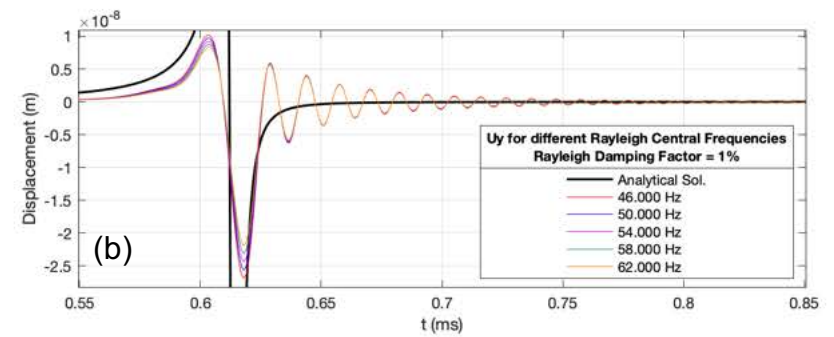
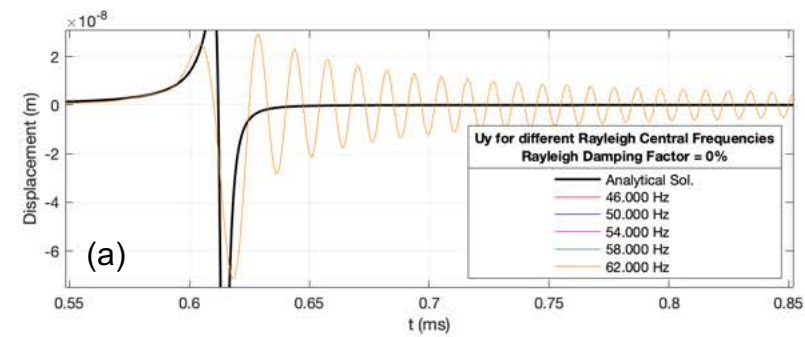


Fig. 8-20: Vertical displacements on surface (U_y) at 0.5 meters from the excitation source for different Rayleigh damping ratios: (a) 0%, (b) 1%, (c) 2%, (d) 3%, (e) 4%, and (f) 5%. (zoomed view)

A final issue to consider in the model calibration is the precision of the wave velocities that can be extracted from the model results. Fig. 8-21 shows a raw seismogram of vertical displacements for a model using the damping parameters previously defined. In that figure the identification of S-wave fronts and P-wave fronts is possible, the error for the velocities determined in this seismogram was less than 0.3% with respect to the theoretical values previously defined for the materials.

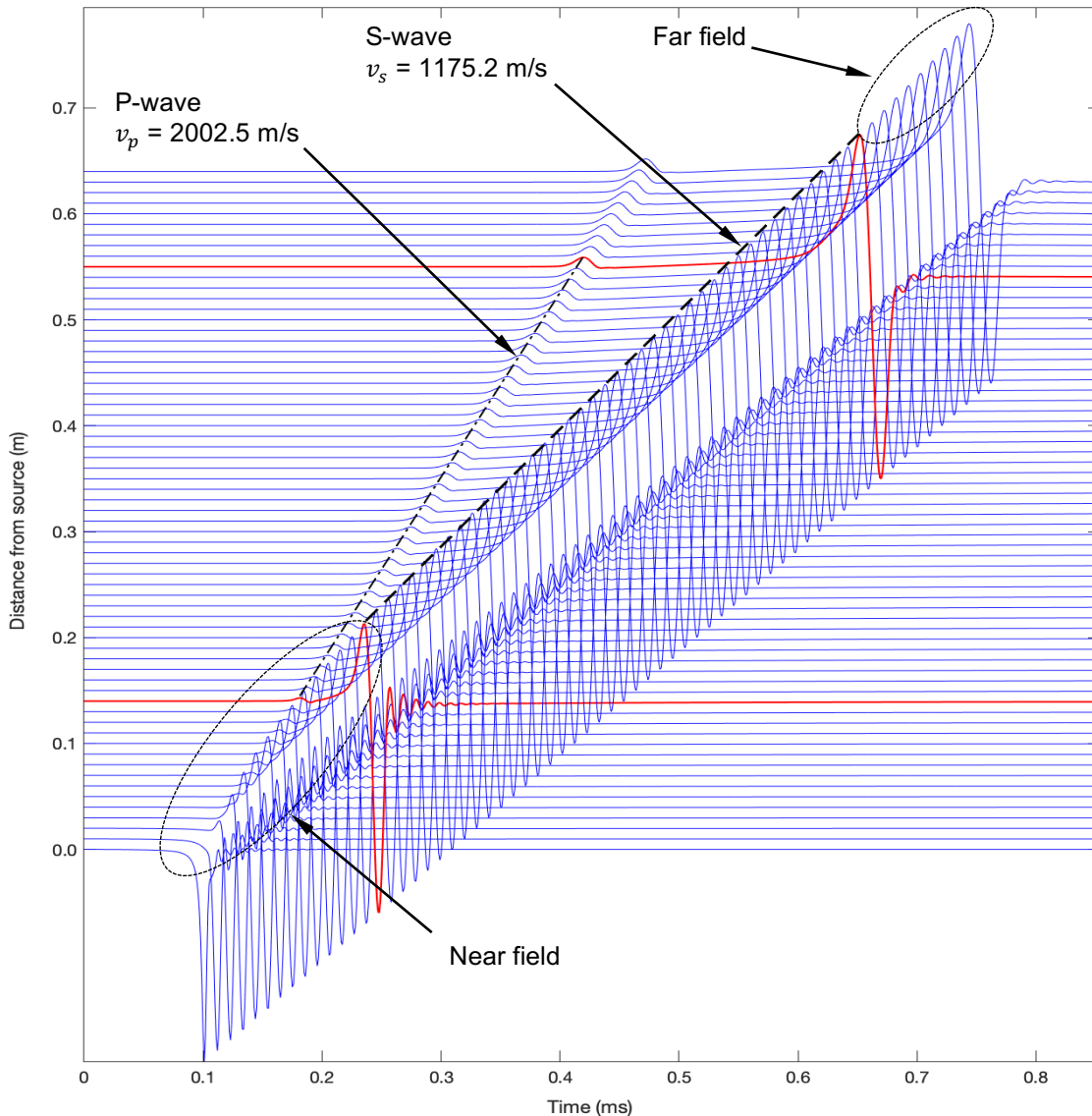


Fig. 8-21: Raw seismogram of vertical displacements from the numerical model to identify the near field zone, the far field zone, and the P-wave and S-wave.

The previous analysis demonstrated that the model is perfectly calibrated, not just reproducing the theoretical response to a Lamb pulse, but also generating seismograms with the expected wave velocities. In addition, the identification of the near field and far field zones was possible by inspecting the distances for which the S-wave does not exhibit a perfectly straight alignment of the peaks. It was found that for the first 0.15 meters the peaks in the S-wave do not follow that alignment, which matches extremely well with the analysis of near field based on amplitudes decay presented in a previous section.

8.4 Step 3: frequency response analysis

The same analysis performed in the chapter 7 for the excitation source characterization in the sCPTU field test were now performed for the sandbox. Fig. 8-22 shows the conceptual model for the assimilated linear system in the sandbox

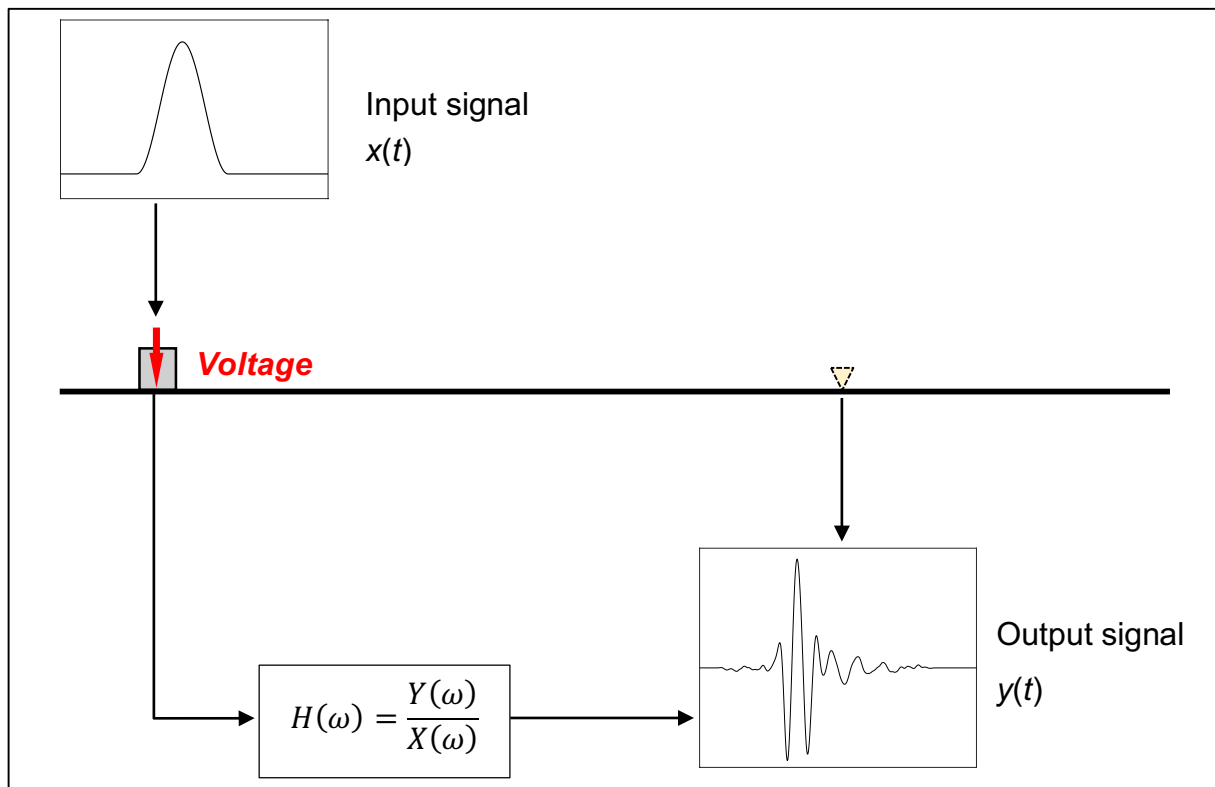


Fig. 8-22: MASW laboratory test system and definition of input and output signals to be involved in the transfer function calculation.

The transfer function for the sandbox MASW test system is given by the following expression:

$$H(\omega) = \frac{Y(\omega)}{X(\omega)} \quad (8-2)$$

where $Y(\omega)$ is the Fourier transform of the output signal (system's response), and $X(\omega)$ corresponds to the Fourier transform of the input signal (system's excitation).

At this point, the immediate goal is to obtain the transfer function that characterizes the MASW test in the sandbox, which means the characterization of the real input force is needed. The process to obtain the real input source characterization using numerical modeling is proposed and explained next as a list of tasks:

- (a) Use the laboratory MASW test results from the sandbox to build a numerical model that represents the soil profile. The geometry of the medium and its elastic properties must be as closer to the reality as possible.
- (b) Identify the distance for the near field and select a point beyond that threshold to perform the calculation of transfer function. In this case a point 0.15 meters away from the center of the excitation source was considered.
- (c) Assume the input force has the same shape of the transducer response in air and convert the displacement into force. In this case the transducer response signal is windowed using a tapered cosine.
- (d) Run a numerical model using that input force and obtain the output of the model for the point selected in numeral (2).
- (e) Calculate the first transfer function for the numerical model.

$$H_{model_1}(\omega) = \frac{Y_{model_1}(\omega)}{X_{model_1}(\omega)} \quad (8-3)$$

- (f) Assume the transfer function for the model also characterize the sandbox MASW test system, then calculate the Fourier transform of the input force as it follows:

$$H_{MASW_1}(\omega) = H_{model_1}(\omega) = \frac{Y_{MASW_1}(\omega)}{X_{MASW_1}(\omega)} \quad (8-4)$$

$$X_{MASW_1}(\omega) = \frac{Y_{MASW_1}(\omega)}{H_{model_1}(\omega)} \quad (8-5)$$

(g) Obtain the input force in the time domain by taking the inverse Fourier transform:

$$x_{MASW_1}(t) = IFFT[X_{MASW_1}(\omega)] = IFFT\left[\frac{Y_{MASW_1}(\omega)}{H_{model_1}(\omega)}\right] \quad (8-6)$$

(h) Run a numerical simulation using the input force just obtained: $x_{MASW_1}(t)$

(i) Calculate the second transfer function for the numerical model.

$$H_{model_2}(\omega) = \frac{Y_{model_2}(\omega)}{X_{MASW_1}(\omega)} \quad (8-7)$$

(j) Recalculate the Fourier transform of the input force estimated for the field test by taking the Fourier transform of the output for the field test divided by the transfer function of the numerical model, as it follows:

$$H_{MASW_2}(\omega) \approx H_{model_2}(\omega) = \frac{Y_{MASW_1}(\omega)}{X_{MASW_2}(\omega)} \quad (8-8)$$

$$X_{MASW_2}(\omega) = \frac{Y_{MASW_1}(\omega)}{H_{model_2}(\omega)} \quad (8-9)$$

(k) Obtain the time domain of the input force estimated for the MASW laboratory test by taking the inverse Fourier transform:

$$x_{MASW_2}(t) = IFFT[X_{MASW_2}(\omega)] = IFFT\left[\frac{Y_{MASW_1}(\omega)}{H_{model_2}(\omega)}\right] \quad (8-10)$$

(l) Calculate the final transfer function for the sandbox MASW test system:

$$H_{MASW}(\omega) = \frac{Y_{MASW}(\omega)}{X_{MASW_2}(\omega)} \quad (8-11)$$

The results obtained in this process are presented in the following figures. Extra details with the whole set of plots similar to the ones presented in chapter 7 can be found in the appendices.

8.4.1 Inversion process with initial force obtained from transducer's response

The first iteration in the excitation source inversion process used the windowed signal obtained from the transducer response in air. The transducer response had two main components: the initial pulse, and the resonance ringing, as they were identified in Fig. 8-12. After some trial and errors, it was decided the best way to window the transducer response was by eliminating almost completely the transducer's ringing.

Fig. 8-24 presents the results of the first iteration, which shows a very clean transfer function for the system, however the match between displacements in the numerical model and the sandbox MASW tests was not quite good. The result of all the mathematical and numerical operations for the inversion of the excitation force are shown in Fig. 8-24 and the content of every plot in that figure is explained next.

- (a) Initial input force used for the numerical model. This is the transducer response signal after the tapered cosine window.
- (b) Fourier transform of the initial input force for the numerical model.
- (c) Inverse discrete Fourier transform of (b) in order to obtain back the input force used in the numerical model.
- (d) Output vertical displacement obtained at 0.15 meters' away from source in the numerical model.
- (e) Fourier transform of the vertical displacement in (d).
- (f) Inverse discrete Fourier transform of (e) in order to obtain back the output vertical displacement obtained from the numerical model at 0.15 meters' away from the source.
- (g) Amplitude of the transfer function calculated by taking the absolute value of the division of Fourier transform of the output (e), divided by the Fourier transform of the input (b).
- (h) Fourier transform of the input force used in the numerical model: now it is obtained by dividing the Fourier transform of the output vertical displacement obtained from the numerical model at 0.15 meters' away from the source (e), into the transfer function obtained for the numerical model (g).

- (i) Inverse Fourier transform of (h) to obtain the inverted input signal.
- (j) Output vertical displacement obtained from the sandbox MASW laboratory test at 0.15 meter's away from the source.
- (k) Fourier transform of the vertical displacement in (j).
- (l) Inverse discrete Fourier transform of (k) in order to obtain back the output vertical displacement obtained from the sandbox MASW laboratory test at 0.15 meter's away from the source.
- (m) Amplitude of the transfer function calculated by taking the absolute value of the division of Fourier transform of the output (e), divided by the corrected Fourier transform of the input shown in (b). The aforementioned correction deals with the fact that the Fourier transform of the input can actually exhibit some zeros (roots), or some very small values, which makes the division to take very high values. Those high values may create a numerical result biased in the input force inversion, so to avoid the problem the Fourier transform of the input is added by an epsilon (ϵ) value. The epsilon value is selected to be between 0% and 5% of the maximum amplitude in the Fourier transform of the input.
- (n) Fourier transform of the input force estimated for the sandbox MASW laboratory test: it is obtained by dividing the Fourier transform of the output vertical displacement obtained from the sandbox MASW laboratory test at 0.15 meters' away from the source (k), into the corrected transfer function obtained for the numerical model (m).
- (o) Inverse Fourier transform of (n) to obtain the estimation of the inverted input force in the sandbox MASW laboratory test. This result will be used as the input force in the numerical model for the next iteration.

Fig. 8-25 shows the results of the second iteration, in which the force does not seem to be converging and the transfer function started getting corrupted when it is compared to the initial one. At this point it was concluded that the transducer's response was not the best option to use as the initial force for the inversion process.

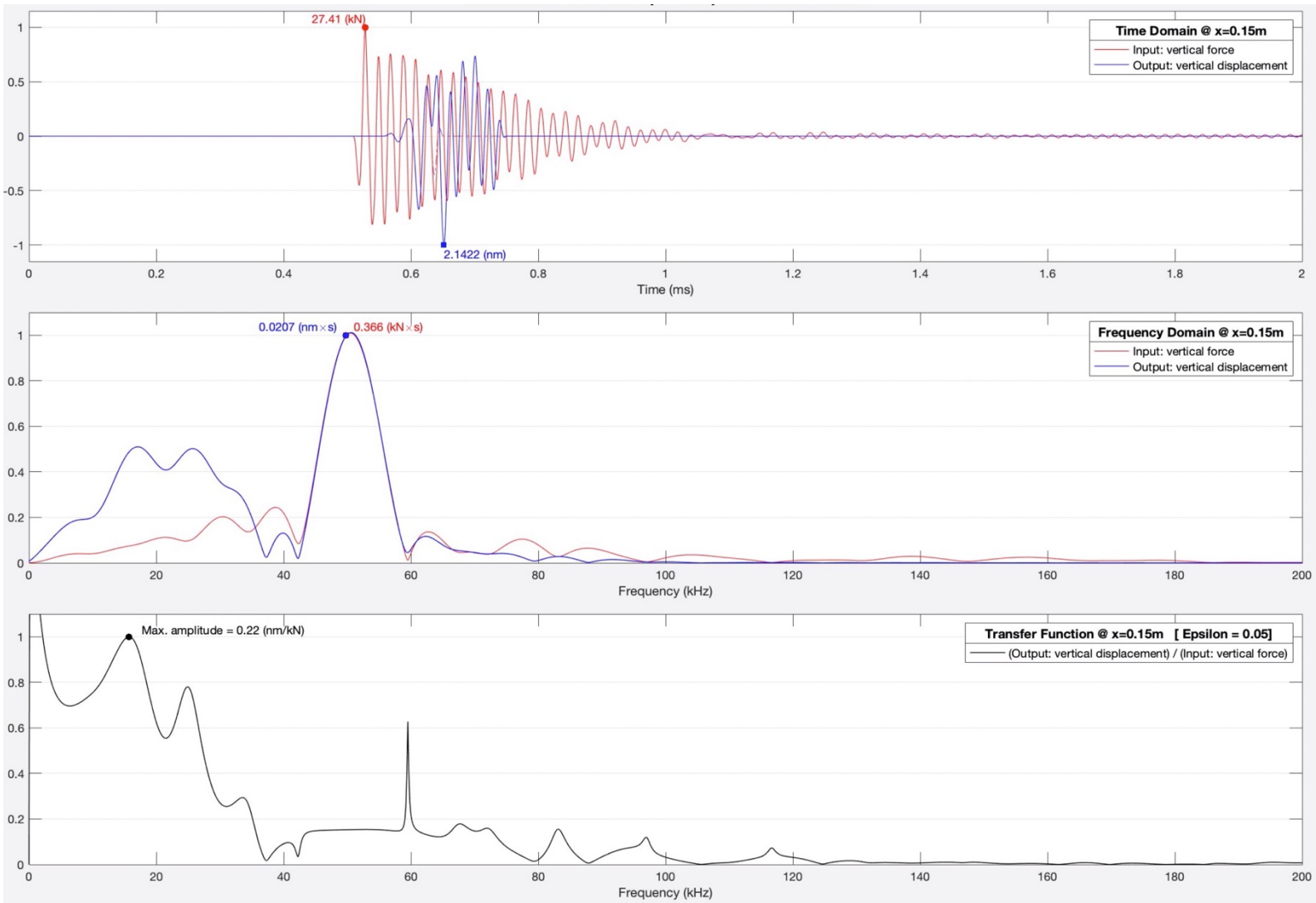


Fig. 8-23: Time domain and frequency domain for the input (transducer's response) and for the output (vertical displacement) at 0.15m for the excitation source. The transfer function is also presented.

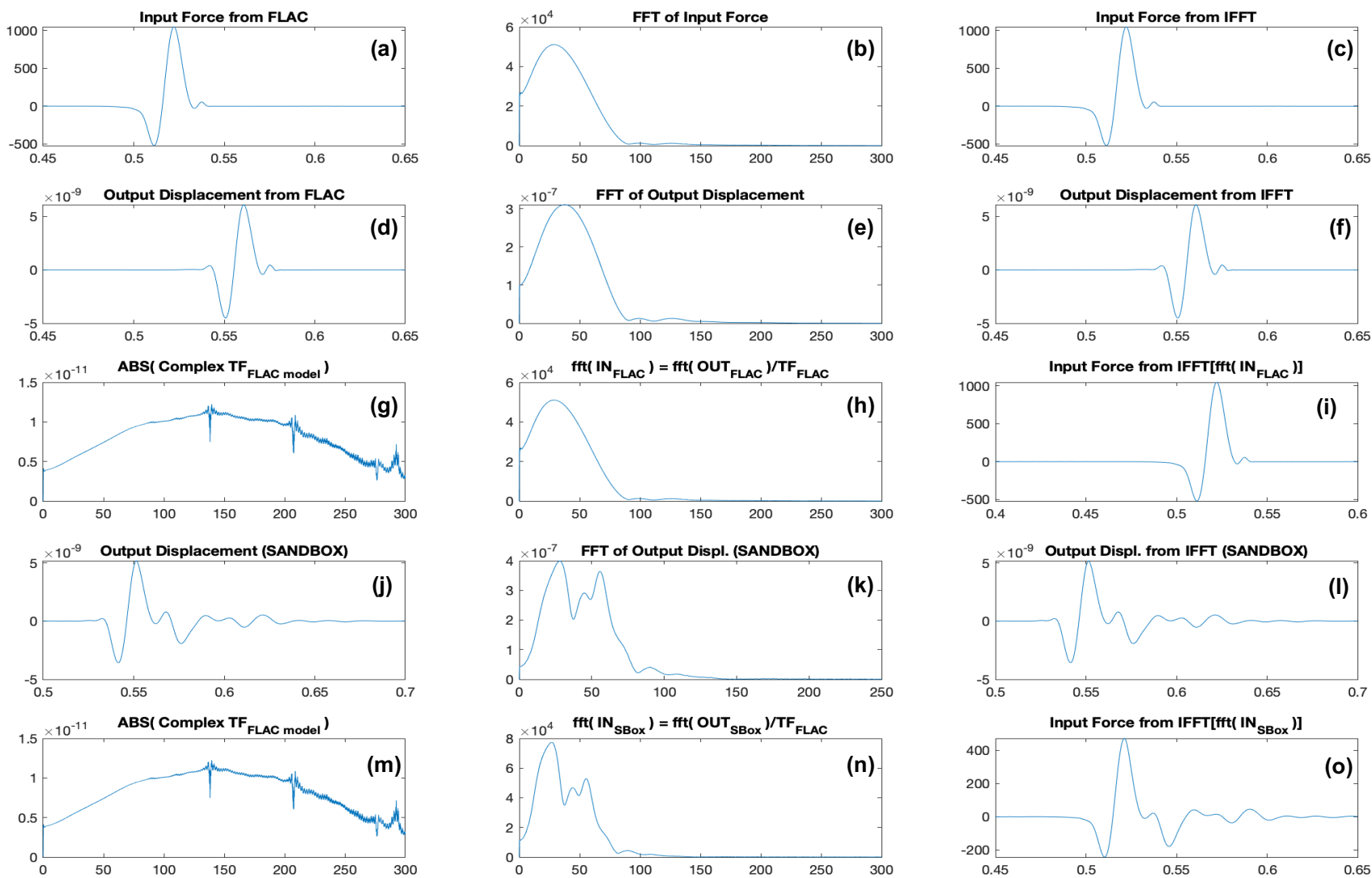


Fig. 8-24: Inversion of the excitation source in the sandbox MASW test (First iteration). The initial input was the transducer's response signal.

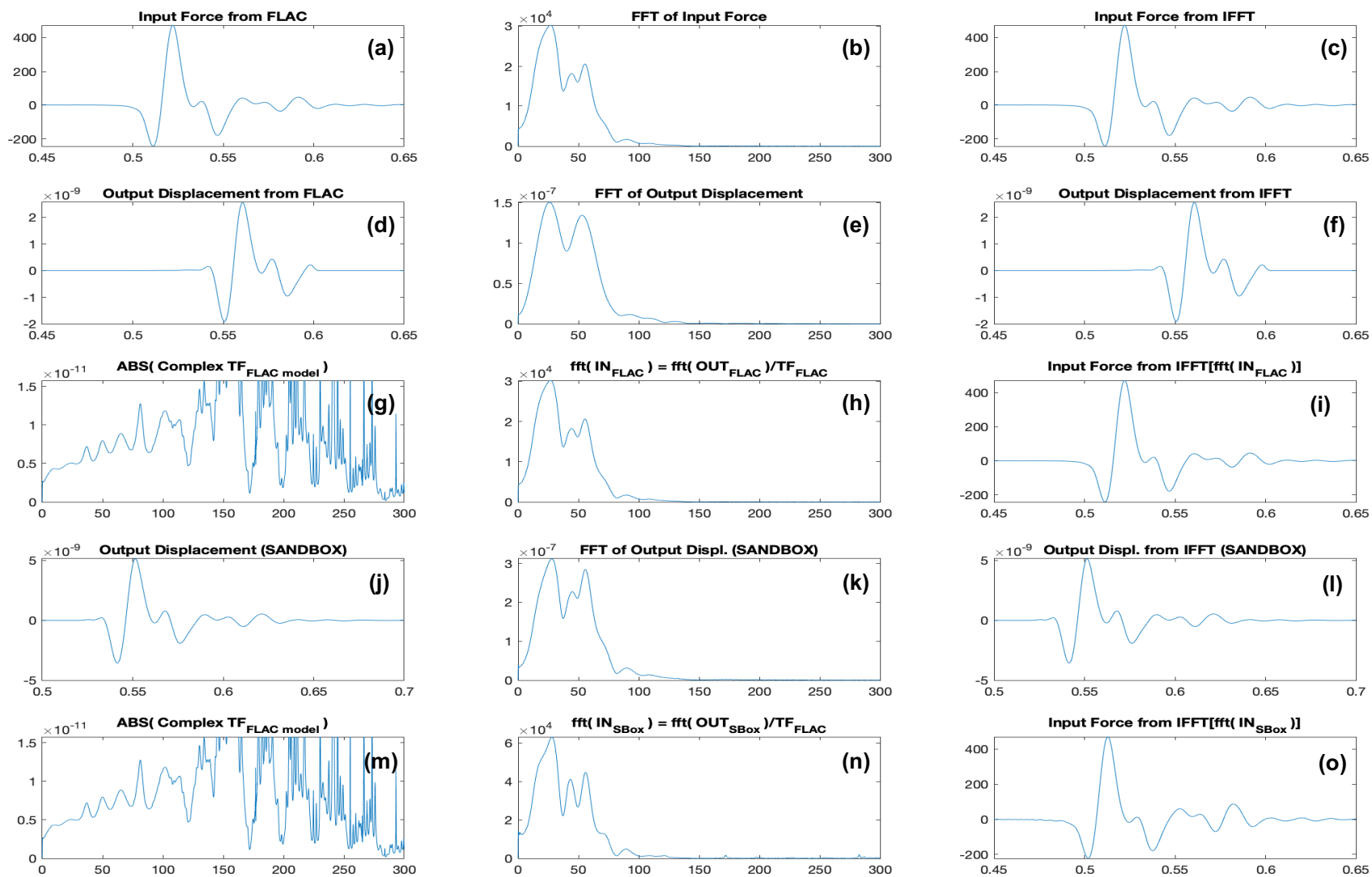


Fig. 8-25: Inversion of the excitation source in the sandbox MASW test (second iteration). The initial input was the transducer's response signal.

8.4.2 Inversion process with initial force obtained from vertical displacements in the sandbox: alignment with void

The next step was to consider the vertical displacement in the first recorded point in the sandbox to define the shape of the input force, that point was located at 0.04 meters away from the center of the excitation source. These results are presented in Fig. 8-27 for the first iteration and Fig. 8-28 for the second iteration.

Fig. 8-29 shows a comparison of outputs obtained from the laboratory MASW sandbox test at 0.04 meters away from the source, against the output obtained from the numerical model using the force obtained after two iterations. Similarly, Fig. 8-30 shows a comparison of outputs obtained from the laboratory MASW sandbox test at 0.15 meters away from the source, against the output obtained from the numerical model using the force obtained after two iterations. The full set of responses at different distances from the source can be seen in a video in the following link: <https://youtu.be/ZqVXxiYNOb0>

An sketch of the sandbox with void is presented in Fig. 8-26.

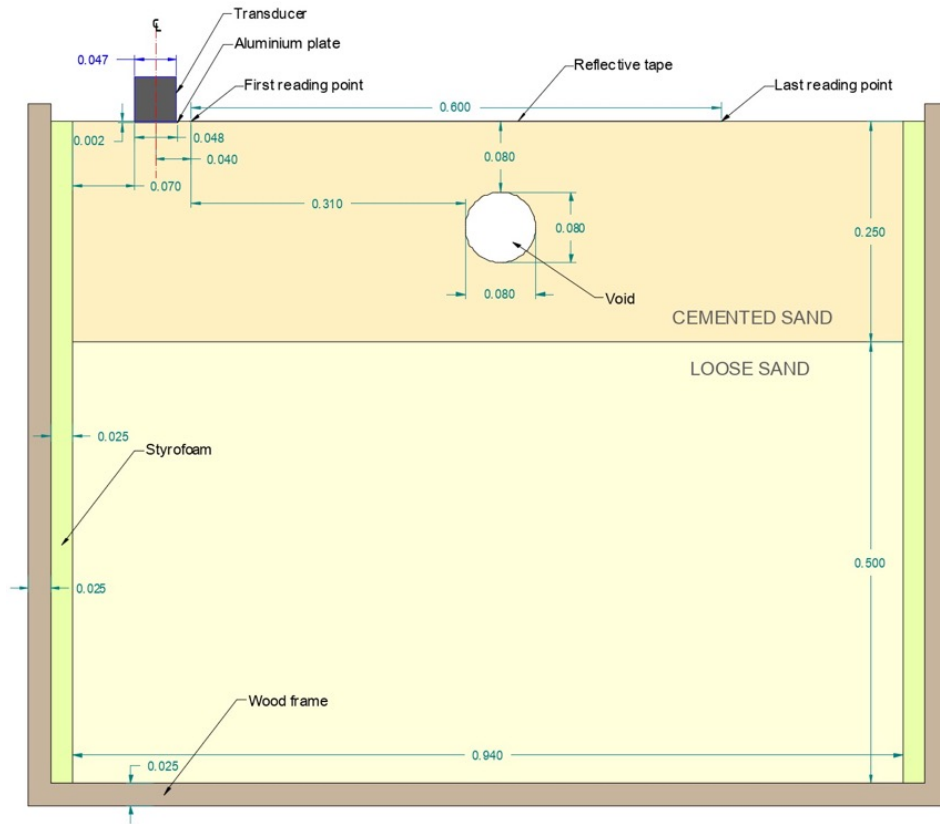


Fig. 8-26: Sketch of the sandbox with a lack of continuity (void) in the upper layer

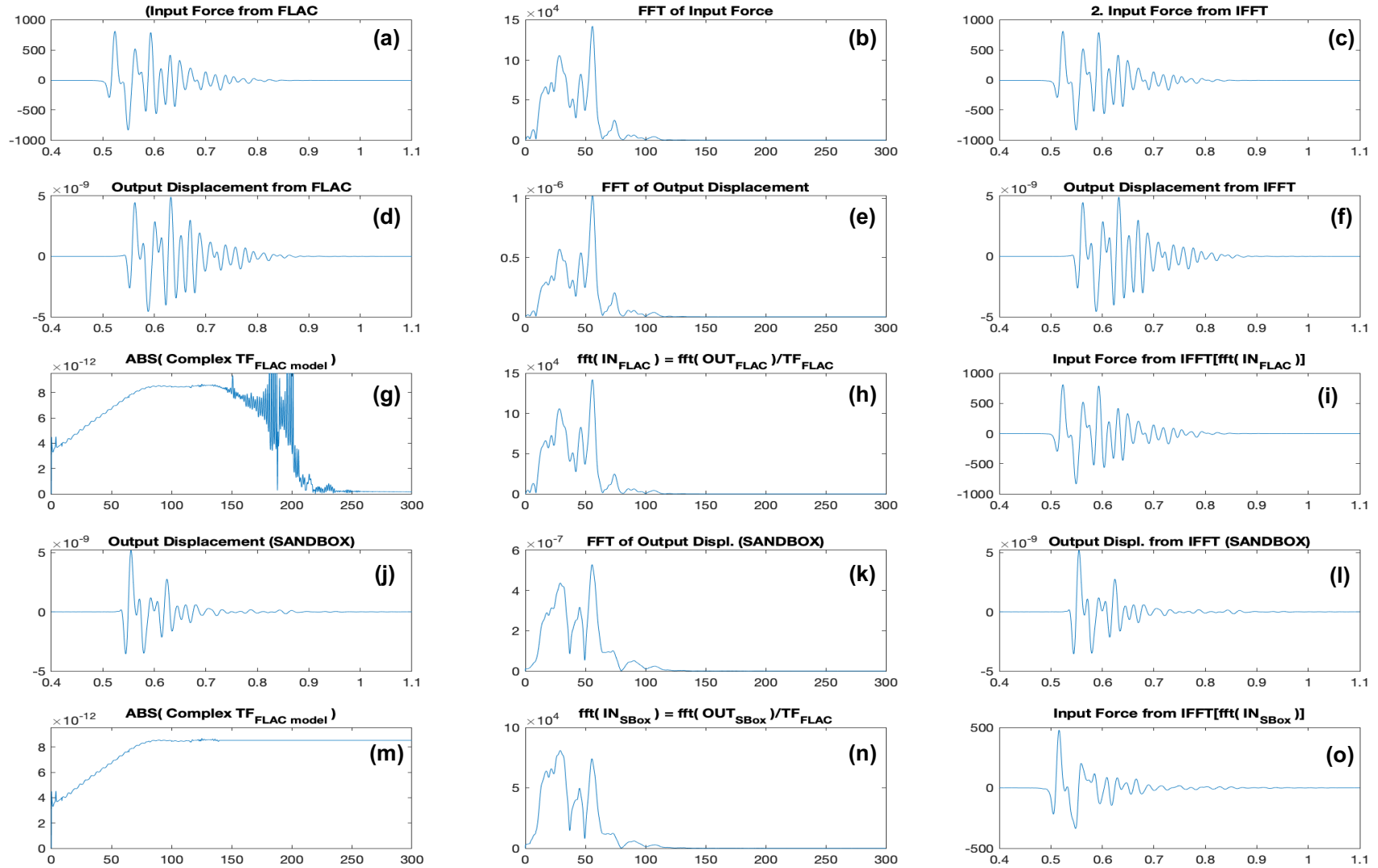


Fig. 8-27: Inversion of the excitation source in the sandbox MASW test (First iteration). The initial input was the vertical displacement in the sandbox (with void) at 0.04m away from the excitation source.

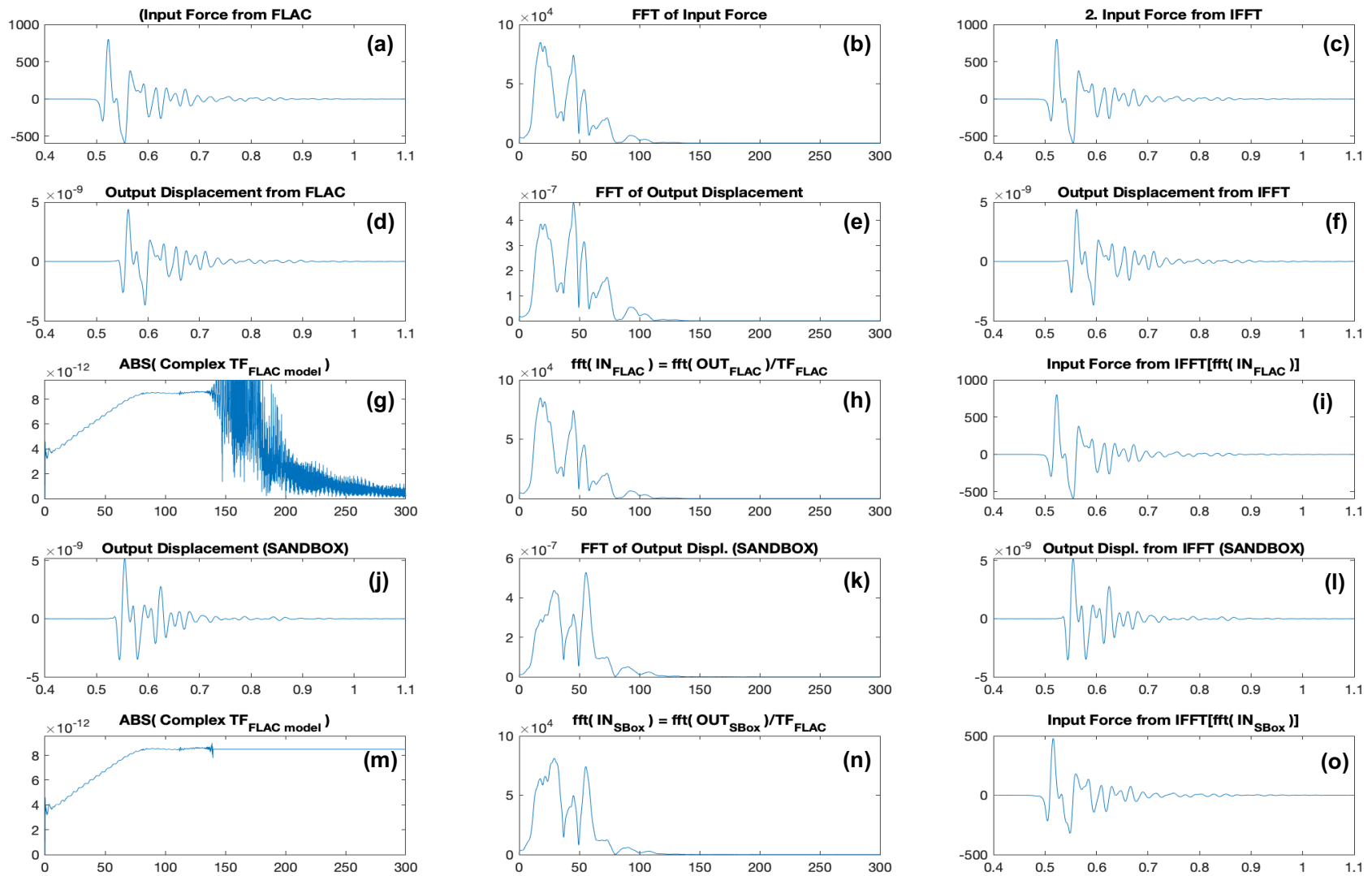


Fig. 8-28: Inversion of the excitation source in the sandbox MASW test (second iteration). The initial input was the vertical displacement in the sandbox (with void) at 0.04m away from the excitation source.

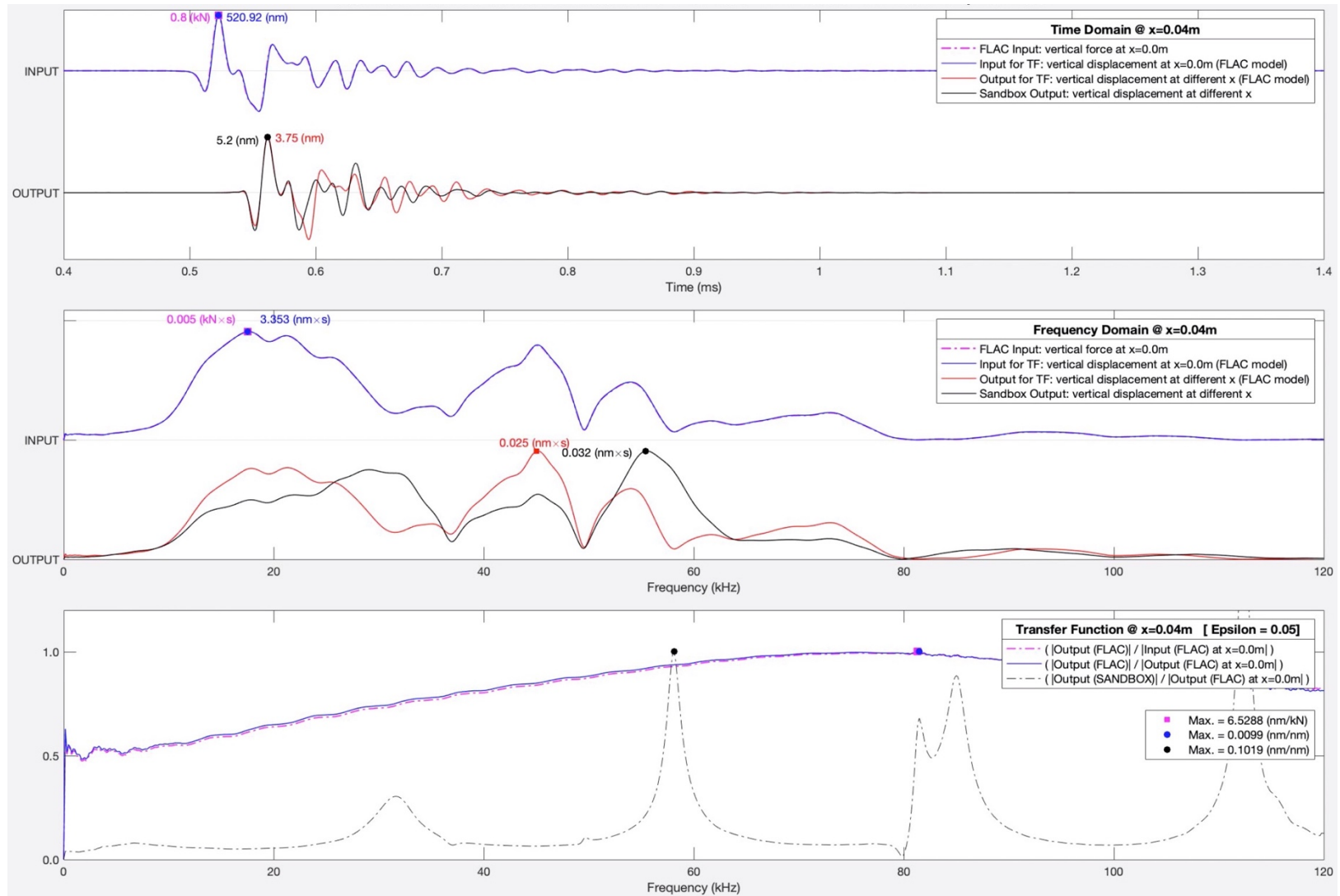


Fig. 8-29: Comparison of outputs from the sandbox (with void) in the laboratory and from the numerical models at 0.04 meters away from the source. The input force was obtained after two iterations in the inversion process.

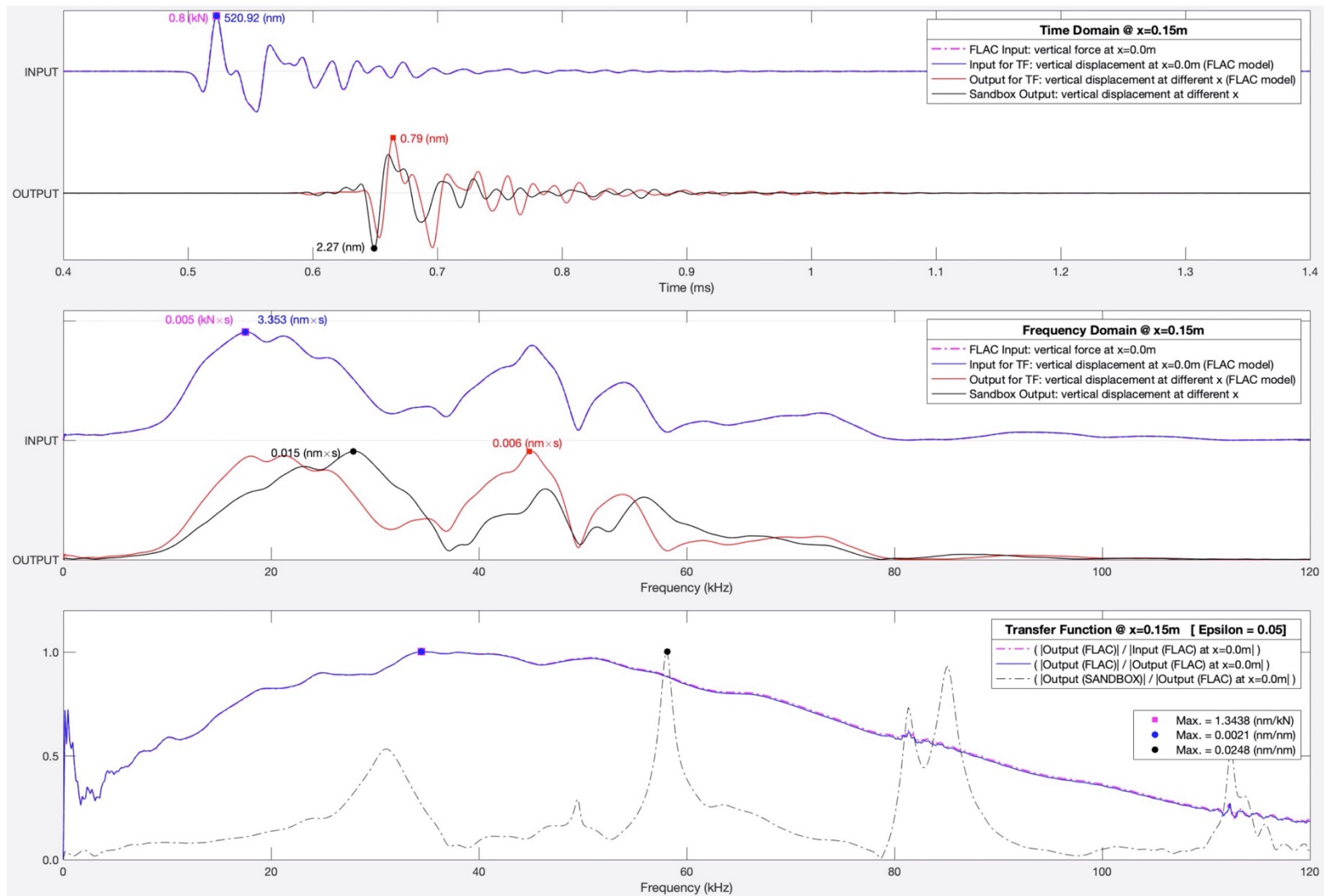


Fig. 8-30: Comparison of outputs from the sandbox (with void) in the laboratory and from the numerical models at 0.15 meters away from the source. The input force was obtained after two iterations in the inversion process

8.4.3 Inversion process with initial force obtained from vertical displacements in the sandbox: alignment without void

In this case no iterations were performed because the force already inverted in the previous section was considered to be applicable for this alignment. Fig. 8-29 shows a comparison of outputs obtained from the laboratory MASW sandbox test at 0.04 meters away from the source, against the output obtained from the numerical model using the force obtained after two iterations. Similarly, Fig. 8-30 shows a comparison of outputs obtained from the laboratory MASW sandbox test at 0.15 meters away from the source, against the output obtained from the numerical model using the force obtained after two iterations.

The full set of responses at different distances from the source can be seen in a video in the following link: <https://youtu.be/VnYTSpxZ0tQ>

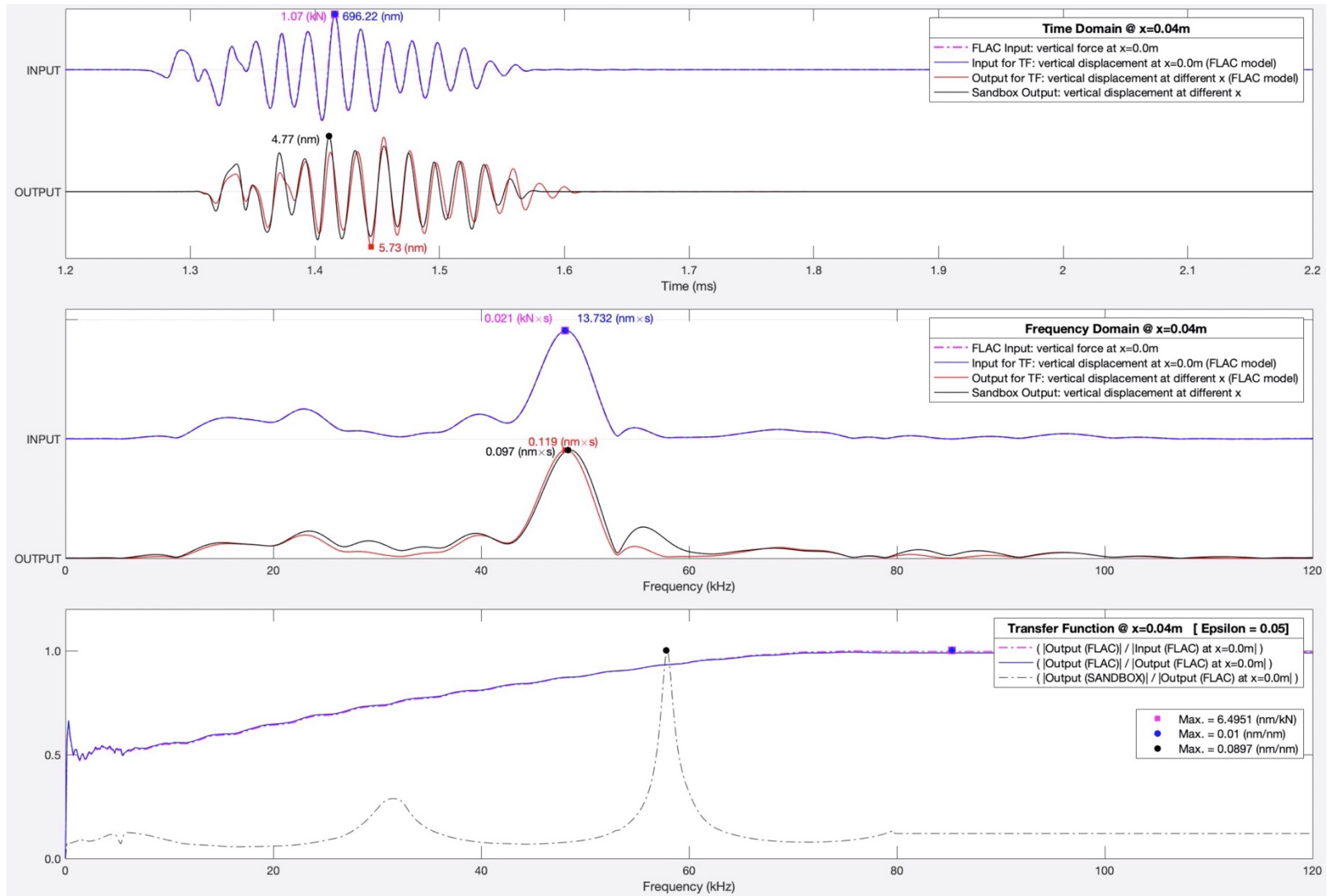


Fig. 8-31: Comparison of outputs from the sandbox (without void) in the laboratory and from the numerical models at 0.04 meters away from the source. The input force was obtained after two iterations in the inversion process.

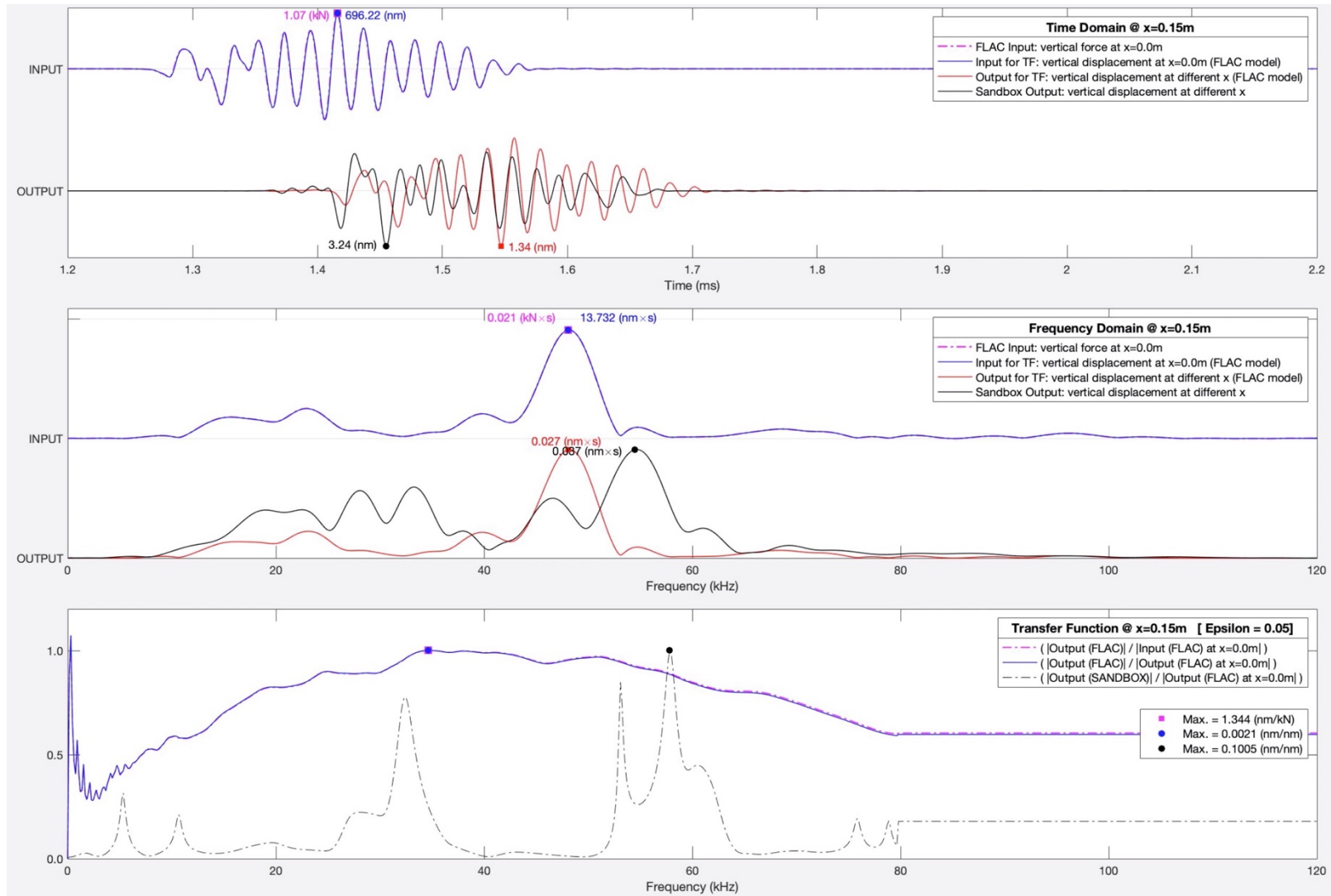


Fig. 8-32: Comparison of outputs from the sandbox (without void) in the laboratory and from the numerical models at 0.15 meters away from the source. The input force was obtained after two iterations in the inversion process.

8.5 Step 4: analysis for a medium with lack of continuity

The results from the inversion of the excitation source are very good for the sandbox in the alignment with void (i.e. a heterogeneous medium), however, for the alignment without void there is no good match between the output obtained from the numerical simulations and the output obtained from the actual MASW laboratory test. This matter requires further investigation.

Nonetheless, an effective way to actually identify the void, other than the analysis of amplitudes presented in a previous section of this chapter, is by analyzing the cross-correlation of the input and the output in the system.

The main effect that a lack of continuity in a homogeneous medium creates in the response signals of vertical displacements, above the actual void location is the appearance of diffracted wave fronts, similar to the reflections in a seismogram. So, by doing the correlation analysis is possible to see where that correlation is missed in order to locate the feature creating distortion in the wave propagation.

Fig. 8-33 show the cross correlation between input and output for different distances away from the source. It was found that when the response signals are windowed to remove the aforementioned diffractions, the maximum correlation indexes aligned very well, so by comparing the point before and after windowing the signals it is possible to establish the location of the void.

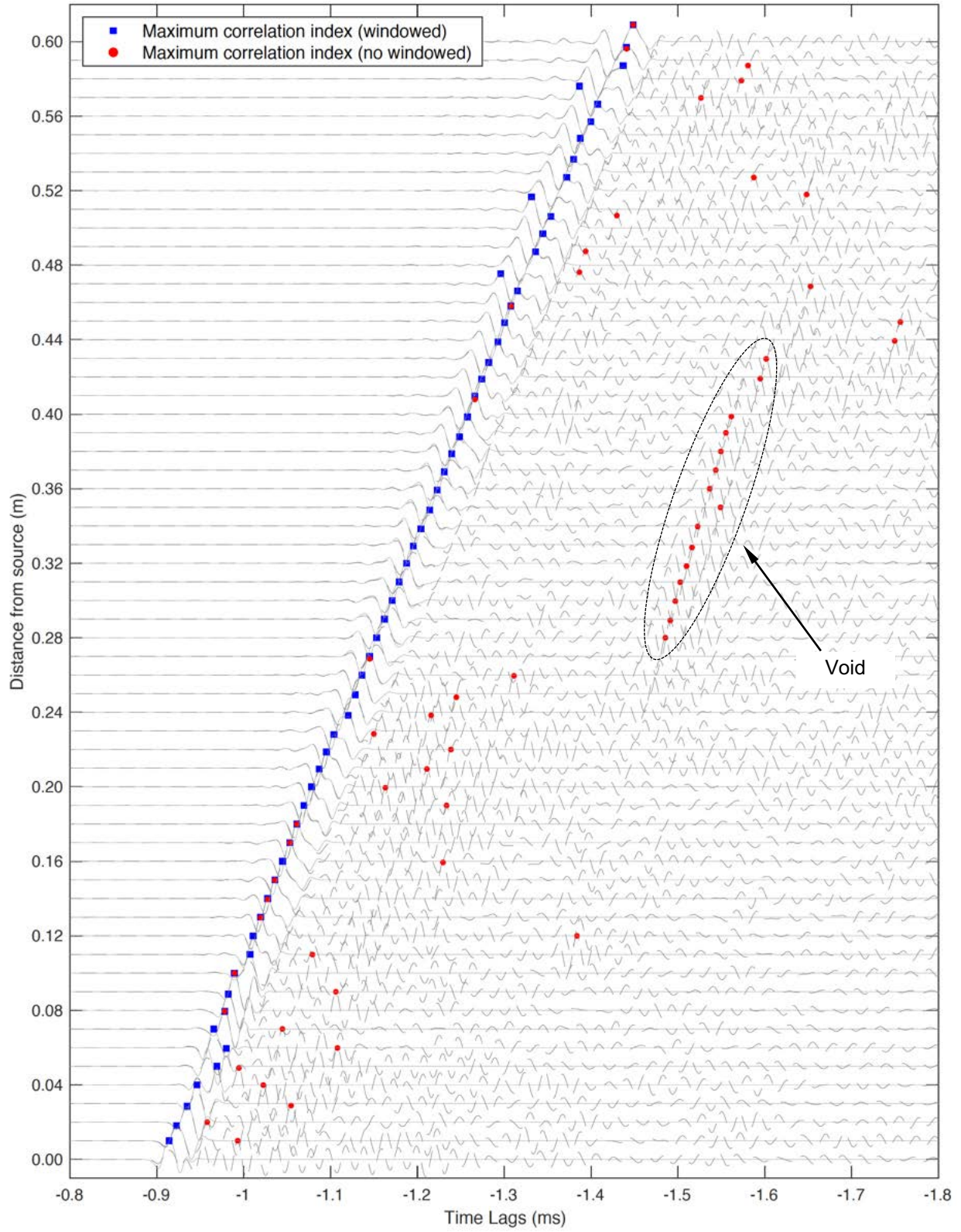


Fig. 8-33: Cross-correlation sandbox alignment with void

8.6 Conclusions

The analysis of raw seismograms, both from numerical simulations and from the MASW test in the sandbox, was very useful for the determination of the velocities in the cemented sand, as well as in the confirmation of the length of the near field. It was found that inside the near field the peaks corresponding to the S-waves in the signals at different locations, do not follow a straight line, which allows the determination of the near field extension just by determining the location where that alignment of points starts.

It is important to highlight the fact that the wave velocities computed from the arrivals and distances in the raw seismograms for the MASW test in the laboratory, showed that the frequency used has an effect on the velocity obtained. The higher the frequency, the higher the velocity. This fact aligns very well with the results obtained from the UPV test in a sample of cemented sand, for which the very same phenomena was observed.

The characterization of the ultrasonic transducers using a high frequency laser vibrometer, allowed to understand the distribution of maximum displacements in the face of the transducer, which led to the definition of a characteristic zone which is in average a good representation of the transducer response.

The use of the transducer's response in air to define the initial input force to start the inversion process seeking to obtain the excitation source in the MASW test in the laboratory was not successful. This could be due to three issues: first, the behaviour of the transducer in when in contact with the setting plate in the sandbox is no quite close to its behaviour in air; secondly, the near field effect distorts the input energy in such a way that when the wave front reaches the elastic radius (i.e. the near filed boundary), the signal is completely different to the one introduced by the transducer; thirdly, in the numerical model the source is applied at one specific point (i.e. point load), while in the sandbox the transducers apply the force in a specific area, that in this case can be assimilated to the area of the setting plate (i.e. $A = 0.048 \times 0.048 = 0.0023 \text{m}^2$).

The method proposed in the previous chapter was successfully implemented here to get the inversion of the excitation source. This time it was used in different materials

(e.g. cemented sand) and also at a different scales of analysis. These facts demonstrated how versatile is the method to get the inversion of the excitation source in a seismic wave propagation test. Nonetheless, further research is required in order to improve the process, for example in defining what should be used as the initial force.

The responses obtained from the numerical simulation using the input force obtained in the inversion process works very well for the point at 0.04 meters away from the source, which means it works well inside the near field zone. However, it does not work well for the point beyond the near field. This means that one inverted source is not able to resolve the displacements in the whole alignment, so, different sources must be inverted to replicate the system's response inside the near field and outside it.

The cross-correlation analysis between the input obtained from the inversion of the excitation source, and the output vertical displacements in the real sandbox, were useful to locate the void.

9 Characterization of geomaterials at small scales: bender element tests for v_s estimation in homogeneous laboratory samples

In this research, the term “small scale” is used in the context of the characterization of geomaterials using typical laboratory samples, either obtained from traditional sampling techniques in the field (i.e. intact samples), or built on in the lab (i.e. reconstituted samples). The measurement of shear wave velocity (v_s) in geomaterials samples can be performed by a variety of laboratory tests, like the resonant column (RC) test and bender element (BE) test, among others. In this chapter these tests were used to study the effect of confinement pressure, strain level, and input frequency on the determination of wave velocities, not just shear wave velocity, but also compressional wave velocity.

9.1 Detailed procedure

The detailed procedure followed in this chapter to characterize geomaterials at large scales involves field testing and numerical simulations. The general steps followed are listed next and the complete and the detailed flowchart is presented in Fig. 7-1:

- Stage 1 – BE test to characterize a sand sample under different confinement pressures and for different frequencies
- Stage 2 – Characterization of the BE transmitter using a laser vibrometer to identify different vibration modes for horizontal and vertical displacements.
- Stage 3 – RC and BE tests under different confinements, different strain levels in the RC, and for different input frequencies in the BE test.
- Stage 4 – Transfer function calculations to understand the response at different stage in the BE test. This stage also involves numerical simulations of the BE test.

In the Fig. 9-1 the flowchart of the detailed procedure followed in this chapter to characterize geomaterials at small scales is presented. The results of stages 1 and 2 were used as the core of a paper done in collaboration with Dr. Ferreira and Dr. da Fonseca, from University of Porto. The results of stage 3 were used in another paper, this time in collaboration with Dr. Irfan at University of Waterloo. This is the reason why this chapter has additional background and literature review.

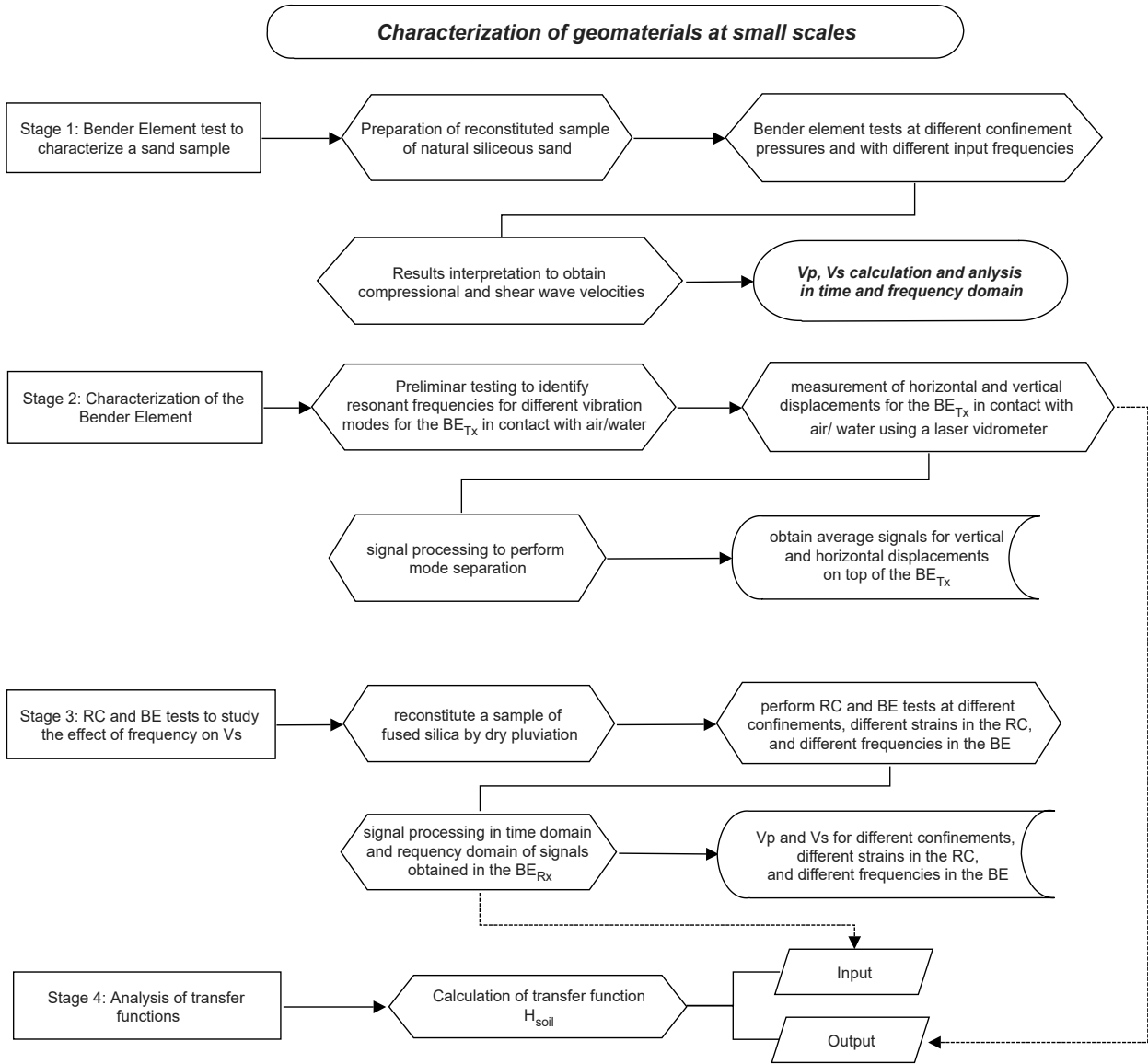


Fig. 9-1: Flowchart of the detailed procedure followed to characterize geomaterials at small scales

9.2 Bender element (BE) test

The BE test uses two piezo-ceramic transducers (the bender elements) which are carefully inserted at the opposite ends of the sample, then, an input voltage signal is applied to the transducer at one end (the transmitter) and the response to that signal is recorded at the other end (the receiver). The piezo-ceramic transducers are composed of two thin plates, rigidly bonded to a central metallic sheet and to electrodes on its outer

surfaces, as shown in Fig. 9-2. In order to induce a flexural deformation in the piezo-ceramic plates, the wiring connection must be made according to their polarization directions. This connection must be carefully done, because any change in the wiring connection derives in a different behaviour of the bender element.

Lings and Greening (2001) reported how by changing the wiring connection of the piezo-ceramic plates, it is possible to induce extensional deformation rather than flexural deformation. This simple change derived in the well-known bender-extender element (BEE), which allows the measurement of shear and compressional waves via the change in the wiring connection.

Independent of the wiring connection, the voltage applied to the transmitter makes the piezo-ceramic element bending back and forth, introducing a mechanical energy disturbance that allows the propagation of mechanical waves into the tested sample. At the other end of the sample, those mechanical waves make the receiver to bend as well, in this case making the piezo-ceramic elements to generate an output voltage signal.

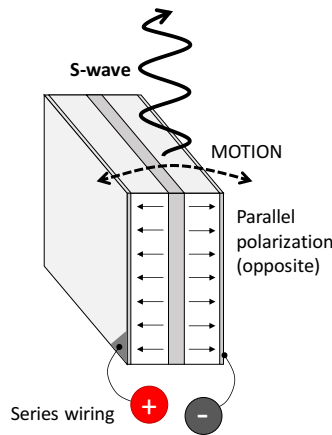


Fig. 9-2: Schematic of the wiring connection in a BE (Ferreira et al., 2020)

The calculation of wave velocity in BE test is very straight forward, it simply takes the distance between transducers and divides into the travel time (Dyvik and Madshus 1985). Despite its simplicity and its low cost, there is not yet a standardized procedure for BE testing, mainly because the complex behaviour of waves generated inside the sample is still not fully understood. For the test it is usually recommended to use a range of input

frequencies where a predominantly flexural movement of the BE transmitter is excited, thus resulting in the transmission of clear shear waves. In contrast, the use of high frequencies is usually discouraged, as these tend to induce a more complex behaviour; due to the stronger participation of compressional waves. Nonetheless, the use of high frequencies has been reported to be advantageous to measure compressional wave velocities. (Ferreira et al., 2020)

The behaviour of the bender elements inside a geomaterial sample is been studied by few researchers. Rio (2006) used a laser velocimeter to measure the response of transmitters and compare their behaviour in air and under embedded conditions inside a synthetic rubber specimen. As expected, when bender elements are embedded, the natural frequency and damping ratio of transmitter vibration are greater and the amplitude of vibration is less than the corresponding quantities measured when the bender elements are free (in air). Pallara et al. (2008) reported the use of a laser vibrometer to measure the response of a transmitter in air and showed that the shape of the transmitter response is different from the shape of the input signal. Irfan (2019) reported the use of a laser vibrometer and a transparent soil to measure the behaviour of bender elements under confinement conditions. The same kind of transparent soil was previously characterized by (Ezzein and Bathurst 2011), who found its mechanical properties were similar to those of granular soils with angular particles.

In this chapter, the contributions made to develop a new approach for the combined measurement of compressional (v_p) and shear (v_s) wave velocities using the traditional BE test, are presented. This approach was initially motivated from experimental evidence in a variety of geomaterials tested by Ferreira et al. (2020), and subsequently validated by the author of this thesis by using laser measurements of the BE behaviour under different excitation frequencies. A detailed analysis of the transducer movement with respect to the input frequency allows the validation of the type of waves being generated and measured in a BE test, which consequently confirms the soil response encountered when different frequencies were used by Ferreira et al. (2020).

The main advantage of the proposed approach is its versatility to obtain compressional (v_p) and shear (v_s) wave velocities with traditional bender elements via a simple change in the input frequency, no change in the wiring connection is needed. The effect of changing the input frequency in the transmitter is the excitation of higher modes of vibration, which was understood once the vibration modes of the bender element were identified and properly separated using signal processing.

9.3 Background

9.3.1 Shear wave velocity

The main advantage of using shear waves to characterize soils is the fact that the shear modulus only depends on the skeleton shear stiffness (G_{sk}), and it is not affected by the bulk stiffness of the pore fluid (Ferreira et al., 2020). While shear wave velocity (v_s) is defined as the ratio between the shear modulus of the soil (G_{soil}) and its mass density (ρ_{soil}), compressional wave velocity is defined by the ratio between the constraint modulus (M_{soil}) and its mass density (ρ_{soil}).

$$v_s = \sqrt{\frac{G_{soil}}{\rho_{soil}}} \quad (9-1)$$

$$v_p = \sqrt{\frac{M_{soil}}{\rho_{soil}}} \quad (9-2)$$

The constraint modulus (M_{soil}) depends on the bulk modulus (B_{soil}) and the shear modulus of the soil (G_{soil}), as follows:

$$M_{soil} = B_{soil} + \frac{4}{3}G_{soil} \quad (9-3)$$

The bulk modulus of the soil is defined as the sum of the bulk moduli of the suspension (B_{sus}), and bulk moduli of the skeleton (B_{sk}).

$$B_{soil} = B_{sus} + B_{sk} \quad (9-4)$$

The suspension is the mixture of the fluid in the pores and the solid grains or particles. It is characterized by its bulk moduli (B_{sus}), which can be computed from the porosity (n), the bulk modulus of water (B_w) and bulk modulus of the solid grains (B_g).

$$B_{sus} = \left[\frac{n}{B_w} + \frac{1-n}{B_g} \right]^{-1} \quad (9-5)$$

On the other hand, the bulk modulus of the skeleton (B_{sk}) is calculated from the shear modulus of the soil (G_{soil}) and the Poisson's ratio, as follows:

$$B_{sk} = \frac{2}{3} G_{soil} \left(\frac{1+\nu}{1-2\nu} \right) \quad (9-6)$$

A more detailed description on these concepts and fundamentals for saturated and unsaturated soils is presented in Santamarina et al. (2005).

9.3.2 Estimation of shear wave velocity in BE tests

In a conventional BE test, the shear wave travel time t_s is computed as the time difference between the input signal $x(t)$ from the transmitter and the output signal $y(t)$ from the receiver (Fig. 9-3). Irfan (2019) mentioned that travel time is associated with transfer function H_{soil} which is calculated as the ratio between the frequency spectrum of the output signal $Y(\omega)$ and the input signal $X(\omega)$. However, time delays are introduced at different stages in a BE test because of multiple transfer functions involved (Wang et al. 2007).

It is important to clarify that in linear invariant systems the ratio between frequency spectrums is just the frequency response of the system, not the transfer function. In order to define the transfer function, it is necessary to calculate also the phase response of the system, not just the frequency response. Thus, Laplace transform must be used for calculations, rather than Fourier transform. This simple consideration complicates the analysis quite a lot because in order to use Laplace transform the continuity in the input and output functions is needed, which is not the case for discrete data obtained in BE tests. In order to make the analysis feasible, it is considered that frequency response analysis is good enough, which is true in many cases as long as the frequency response

is dominant over the phase response. Further analysis to obtain a true transfer function of the BE-sample system is out of the scope of this research, so it must be clear that whenever a transfer function is mentioned, just the frequency response is considered because the calculation is done via Fourier transform rather than Laplace transform.

The multiple time delays at different stages in a BE test and their associated transfer functions are shown in Fig. 9-3 (Irfan, 2019).

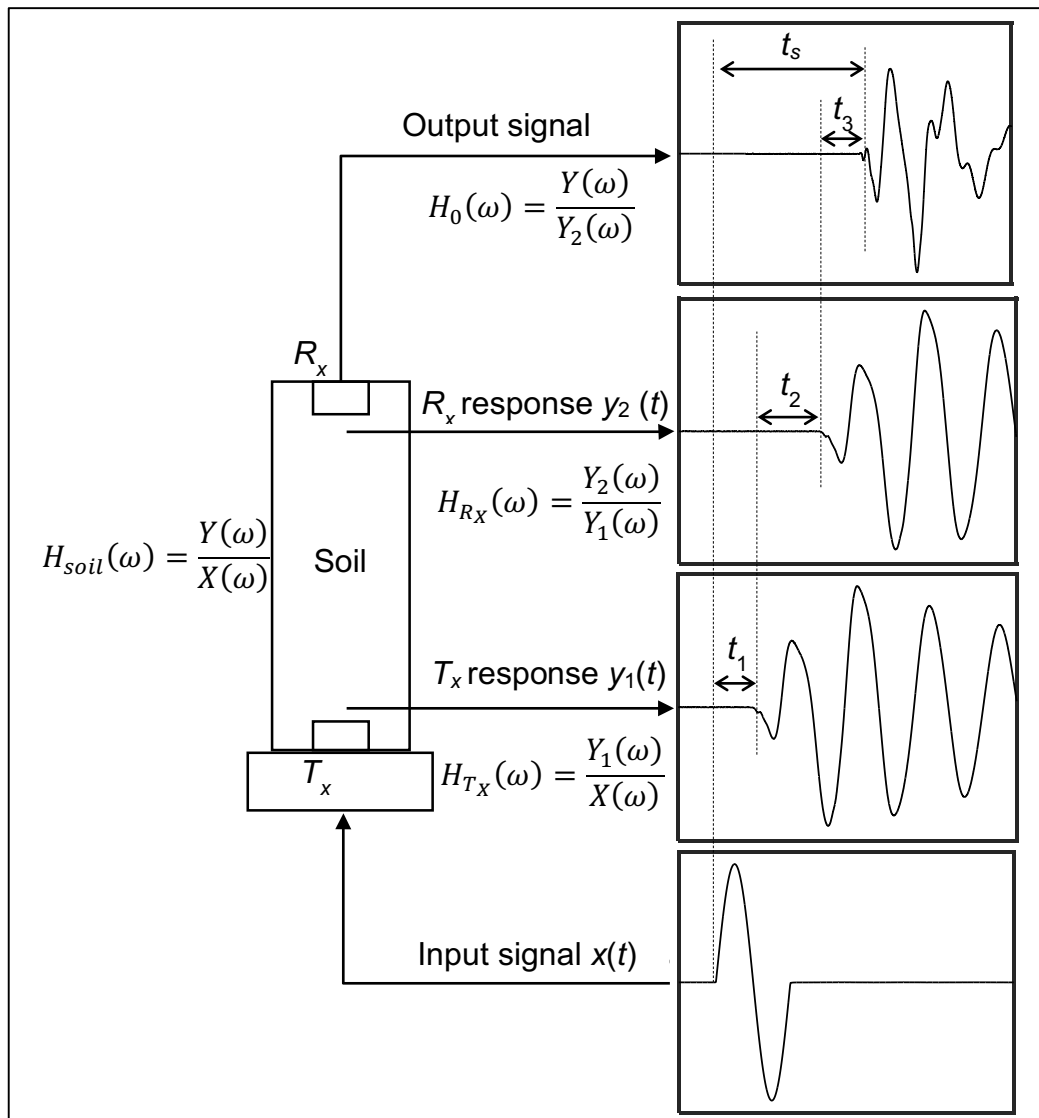


Fig. 9-3: Shear wave arrival times and transfer functions at different stages in a conventional BE test setup (after Irfan, 2019)

First, t_1 is the time delay between the input voltage and the transmitter response with the transfer function (H_{Tx}). Second, t_2 is the delay between the transmitter and receiver responses with the transfer function (H_{Rx}). Finally, t_3 is the delay between the receiver response and the output voltage with the transfer function (H_0). Most of the studies in BE testing have focused on improving the accuracy of t_s because of the difficulty in measuring t_1 , t_2 , and t_3 and their transfer functions; therefore, the reliability of conventional BE test results has been dependent on the accuracy of the measured t_s . (Irfan, 2019)

For the determination of travel time (t_s), a variety of methods both in the time and the frequency domain have been proposed. The simplest method is the computation of time interval between input and output signals in the time domain, which involves the assumption of plane wave propagation without the consideration of reflected or refracted waves (Irfan, 2019). More elaborate techniques, supported by signal processing and frequency domain analysis are available, like the method based on computation of cross-correlation between input and output signals, proposed by Viggiani and Atkinson (1995).

Although the travel time determination is by far more complex, different proposals for the definition of the travel distance have also been suggested (Fam and Santamarina, 1995, Porovic, 1995, Viggiani and Atkinson, 1995, Rio, 2006). Nevertheless, as pointed by Ferreira et al. (2020), the effective distance is most commonly taken as the bender elements tip-to-tip distance, which generally corresponds to the height of the soil specimen at the time of testing subtracted by the protrusion of each BE on either side.

9.3.3 Bender element vibration

It was very common to assume the simplification that a BE vibrates as a cantilever beam (Lee and Santamarina 2005). Under this assumption, the resonance frequency of the n^{th} mode of vibration of a BE in air can be estimated by the following expression (Clough and Penzien, 2003):

$$f_n = \frac{(k_{Ln})^2}{2\pi(\alpha L_b)^2} \sqrt{\frac{E_b I_b}{\rho_b A_b}} \quad (9-7)$$

where:

- k_{L_n} : characteristic number that depends on n and the boundary conditions
- A_b, L_b, I_b, ρ_b : area, length, area moment of inertia, and mass density of BE
- E_b : Young's modulus of the piezo-ceramic element
- α : is the effective length factor ($\alpha = 1$ if the BE is perfectly fixed to the base)

Now, if the BE is considered to be embedded in soil, the resonance frequency of its first mode of vibration can be estimated following the expression (Lee and Santamarina, 2005):

$$f_1 = \frac{1}{2\pi} \sqrt{\frac{1.875^4 \left[\frac{E_b I_b}{(\alpha L_b)^3} \right] + \eta E_s L_b}{\rho_b A_b \alpha L_b + (\rho_s b^2 L_b) \beta}} \quad (9-8)$$

where:

- ρ_s and E_s are the mass density and Young's modulus of the soil
- β : factor related to the volume of soil affecting the vibration of BE
- η (≈ 2) is the mean displacement influence factor at the soil-BE interface


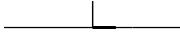
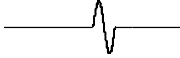

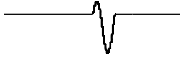




9.3.4 Input signal selection for BE test

The selection of the shape of the electric signal to be used as input, is not a trivial issue. The input signal is generated by the function generator, then it is sent directly or via an amplifier to the transmitter bender element. The most common input signal configurations reported in the literature are summarized in Table 9-1.

Most early studies using BEs (Dyvik and Madshus, 1985, Bates, 1989) employed single square-wave pulses, as this signal has a very sharp, well-defined start. While this instantaneous variation of voltage can be mathematically expressed and electrically reproduced by a digital function generator, mechanical devices and materials with finite mass and stiffness cannot respond in such manner. Due to the presence of inertia forces,

it is not possible to obtain instantaneous variations in motions, equivalent to infinite accelerations (Rio, 2006). Moreover, the initial sharp rise of the signal results in a very broad frequency content with no particular main frequency. In addition, it is yet unclear how the transmitter BE actually responds to this excitation. As a result, the response signal provided by the receiver is more difficult to compare with the square input signal sent by the function generator.

Table 9-1. Typical BE electrical input excitations (after Ferreira, 2009)

Input wave shape		Reference
	Square or step signal	Dyvik & Madshus (1985), Fam & Santamarina (1995)
	Impulse signal	Lee & Santamarina (2005)
	Sine wave	Viggiani & Atkinson (1995), Brignoli et al. (1996)
	Sine pulse [90° phase shift]	Pennington et al. (2001)
	Distorted sine wave [typically 30° phase shift]	Jovicic et al. (1996)
	Forced oscillation [sine wave cycles at resonance frequency]	Jovicic et al. (1996)
	Continuous sine wave of constant frequency	Greening & Nash (2004)
	Sine sweep of frequencies [typically 100 Hz to 20 kHz]	Greening & Nash (2004), Ferreira et al. (2007)
	Stochastic random noise	Roesler (1979), Santos et al. (2007)

Tallavó et al. (2009) presented a novel methodology for the dynamic characterization of ultrasonic transmitters, which uses different types of excitation pulses (input signals) and computes the theoretical Fourier spectra, and then applies the complex exponential method to extract the dynamic properties of the transmitter from transient time signals. They also analyzed the power spectra for one-cycle of square, sine, triangle, and saw-tooth pulses; according with their results the magnitude of the

frequency spectrum of a square pulse is about two times that of the sine pulse, whereas, for the square and triangle pulses, that ratio is about three. Thus, the ratios in the frequency spectrum magnitudes are practically the same as the ratios of the total energies computed in the time domain.

Even though the square pulse carries more energy than the sine pulse, the shape of the frequency spectrum is smoother for the latter because it concentrates the energy around one central frequency and reduces the appearance of ridges in the tails of the spectrum; which eases the interpretation of BE test results in the frequency domain. That is why in this research the sine pulse was chosen over the others.

9.4 Experimental procedure

The experimental procedure presented here was developed in the first three stages. The first stage corresponding to the laboratory tests carried out by Ferreira et al. (2020) at the University of Porto (Portugal), for which the author of this thesis contributed with the signal processing and data analysis. The second stage corresponds to the bender element characterization, which was solely done by the author of this thesis. Finally, the third stage of testing was done in collaboration with Irfan (2019) and involved the testing of a transparent soil sample, which was reconstituted by dry pluviation in the laboratory at the University of Waterloo. For this last stage, both resonant column (RC) and bender element (BE) tests were carried out simultaneously.

There is a fourth stage, which is not experimental, and it is focused in the calculation of transfer functions in the BE test.

9.4.1 Experimental setup and testing: Stage 1

At this stage the goal was to characterize a real geomaterial by using BE tests at different confinements. Ferreira et al. (2020) reported the results for BE tests carried out on a natural siliceous sand from the Lisbon region, collected at the pilot site of “LIQUEFACT” project (da Fonseca et al., 2019). The tested sample corresponded to a loose sand specimen which was prepared by dry pluviation, at a high void ratio, close to e_{max} . The

specimen was molded to about 100 mm of height and 50 mm of diameter. Some mechanical properties of this geomaterial are presented in Table 9-2.

Table 9-2. Mechanical properties of the soil sample (after Ferreira et al., 2020)

Soil properties	Values
specific gravity	$G_s=2.64$
void ratio (minimum)	$e_{\min} = 0.54$
void ratio (maximum)	$e_{\max} = 0.84$
finer content	2.9%
Uniformity index	$C_{U.Index} = 2.16$
Curvature index	$C_{C.Index} = 0.90$

For these tests, Ferreira et al. (2020) applied a series of isotropic confining stresses, at two different state conditions: dry and fully saturated. The confining effective stresses were 10, 30, 50, 75, 100, 150, 200, 250, 300, 350, 400 kPa. The percolation involved two phases: (i) percolation with CO₂, and (ii) percolation with de-aired water. The saturation was performed increasing both the back-pressure and the cell pressure, at a constant effective stress of 10 kPa, until 300 kPa of back-pressure. To check the specimen's saturation, both Skempton's B-value and the compressional wave velocity (v_p) were measured. The specimen was considered fully saturated for values of B higher than 0.97 and values of v_p above 1500 m/s. Ferreira et al. (2020)

Ferreira (2009) reported the measurement of compressional and shear wave velocities using the aforementioned series-connected single pair of bender elements, the test was repeated for each confining stress level. The input signals used in this tests were sine-wave pulses and, based on the methodology described by da Fonseca et al.(2009), four different input frequencies were used, selected according to the observed response signals. In this case, for S-wave measurement, the input frequencies of 1, 2, 4, 6 and 8 kHz were used, while for P-wave measurement, frequencies of 25, 50, 75 and 100 kHz were applied. The identification of the arrival time of both seismic waves was made considering the first direct arrival of the output wave, common to all input frequencies. In

this approach, it is assumed that the travel time of the seismic waves is not significantly affected by the input frequency. Ferreira et al. (2020)

9.4.2 Experimental setup and testing: Stage 2

For this stage the goal was to characterize the bender element transducer itself. In order to take readings of the actual displacements for the bender element (BE), a state-of-the-art laser vibrometer was used in laboratory tests. The setup for these tests included a BE transmitter on air, the same BE transmitter on water, peripheral electronics and a laser vibrometer. Except for the peripheral electronics, all the other devices and tools needed for the tests were set over an isolation table, which ensured there was no external vibrations affecting the readings during the tests.

Schematics of the experimental setup for the BE transducer characterization on air and on water is shown in Fig. 9-4.

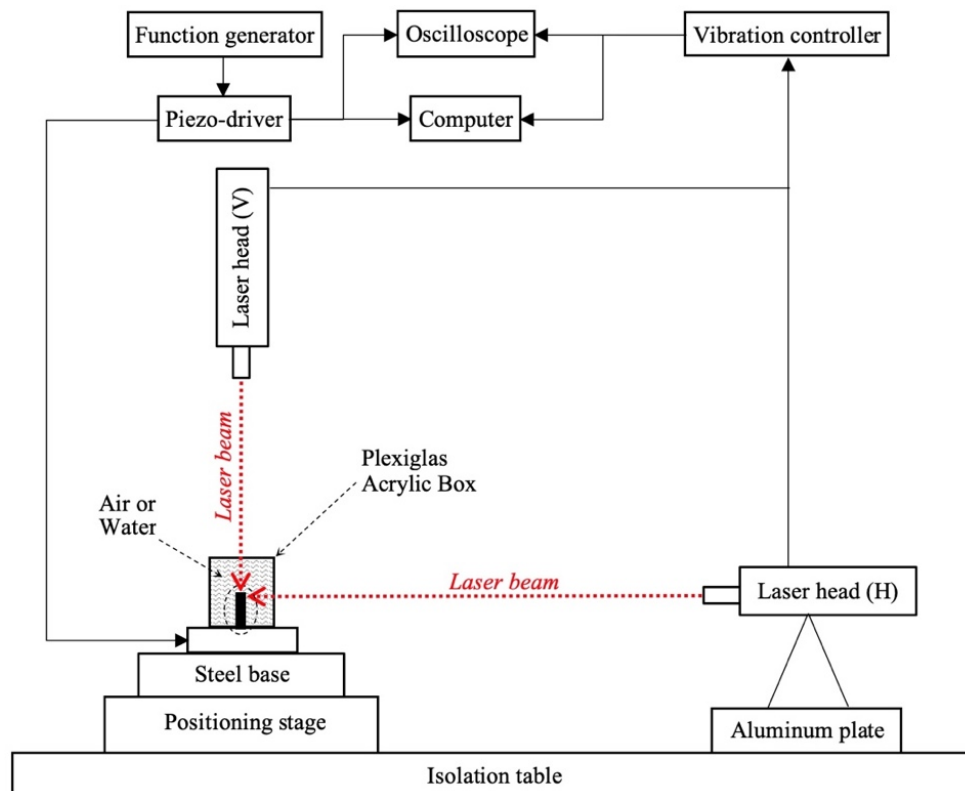


Fig. 9-4: Schematic of the experimental setup for laser measurements in air and water

A function generator (FG) was used to generate an input voltage signal, which was sent to the BE transducer, passing first through a piezo-driver in order to be amplified. The amplified signal induced the vibration and movement of the BE and its displacements were measured using a laser vibrometer.

Displacement readings were taken at different points along the top-center edge of the BE for the vertical alignment of the laser beam and also along the top-side edge of the BE for the vertical alignment of the laser beam. The laser head was vertically or horizontally oriented, according with the direction of the displacement being measured at the time of the test. Readings were taken following a pattern, which consisted of a horizontal row of 27 points with spacing of 0.5 mm, so that the full length of the BE was covered. The same pattern was followed for vertical and for horizontal readings. The laser head was managed by a controller device to assure precision in the measured points. A reflecting paper was glued onto the BE top and side surfaces to enhance maximum signal quality of the laser measurements. The length of the laser beam was set at 0.5 m for all tests and the time signals were recorded for a total time of 2.5 ms with a sampling frequency of 25.6 MHz.

Actual vibrations of the BE transmitter are measured in air and water. For each measurement, an average of 2000 time signals is saved as the representative time signal. The BE transducer tested in the laboratory had the following dimensions: length 13.7 mm, height 5.3 mm, and thickness 1.9 mm. Schematics of a 3D view of the actual BE transducer tested is shown in Fig. 9-5.

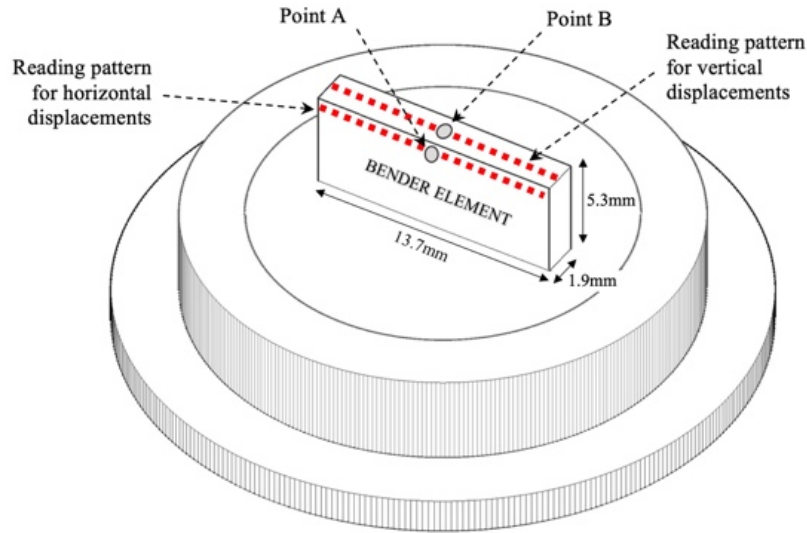


Fig. 9-5: Alignment of reading patterns at BE edges for vertically and horizontally oriented laser beams

9.4.3 Experimental setup and testing: Stage 3

For the third stage of testing a sample of fused quartz (the same material used to make the transparent soil by Irfan, 2019) was reconstituted using the dry pluviation technique and then it was tested in the laboratory with the collaboration of Irfan (2019). The sample was tested in the resonant column under different confinement pressures ranging from 35 kPa to 600 kPa, and for each confinement, a series of BE tests were carried out for frequencies of 10kHz and 50kHz using a one-cycle sine pulse as the input signal. In addition, the BE test was performed for different strain levels in the RC while the confinement was kept constant at 50kPa.

For the RC test, a modified Stokoe-type resonant column was used with a fixed-free configuration. The built-in source in the spectrum analyzer (HP-35670A) was used to apply a sinusoidal sweep input voltage which is amplified by a power amplifier (Bogen GS-250) because the output voltage amplitude of the built-in source is limited. The amplified input voltage is used to induce alternating current in the coils which are mounted on the driving plate. This alternating current causes the magnets to vibrate which in turn

cause torsional excitations on the soil sample. The response of the specimen to these torsional excitations is characterized in terms of the acceleration of the accelerometers (PCB 353A78 and PCB 353B65) mounted on the driving plate. The current in the coils and the acceleration are amplified and filtered (200 Hz low pass) using a filter amplifier (Krohn-Hite 3384) before being sent to the spectrum analyzer for transfer function calculations; the spectrum analyzer calculates the transfer function in real time. Resonance frequency and damping ratio of the soil specimen are estimated from the transfer function. (Irfan, 2019)

The RC driving system with the soil specimen is placed in a confinement chamber. A pneumatic pressure panel (Brainard and Kilman), which has a maximum confinement capacity of 700 kPa, is used to exert the confinement on the soil sample. Axial strain of the specimen is monitored using a Linear-Voltage-Displacement-Transducer (LVDT) (Trans-Tek, 0242-0000 D-6) which is mounted on the driving plate.

Schematics of the experimental setup for the RC and BE test on fused quartz is shown in Fig. 9-6.

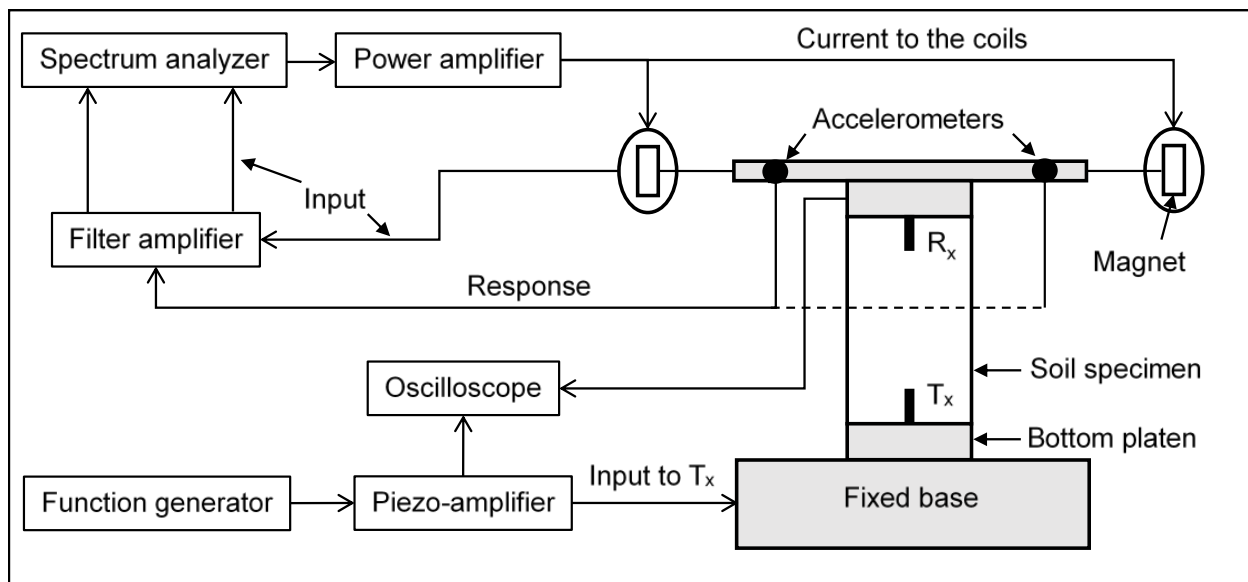


Fig. 9-6: Schematic of resonant column and bender element tests (after Irfan, 2019)

9.5 Testing results

The results obtained for each one of the testing stages is presented and analyzed next.

9.5.1 Testing results: Stage 1

The general overview of the evolution of the seismic velocities with confining isotropic stress is illustrated in Fig. 9-7 for dry and saturated conditions, for the sand sample reconstituted in the laboratory Ferreira et al. (2020). The evolution for v_p in saturated conditions is not presented due to the fact that for different confinement pressures that wave velocity does not change much and in average takes the value of 1600 m/s, which makes sense since the whole pores inside the sample are filled with water.

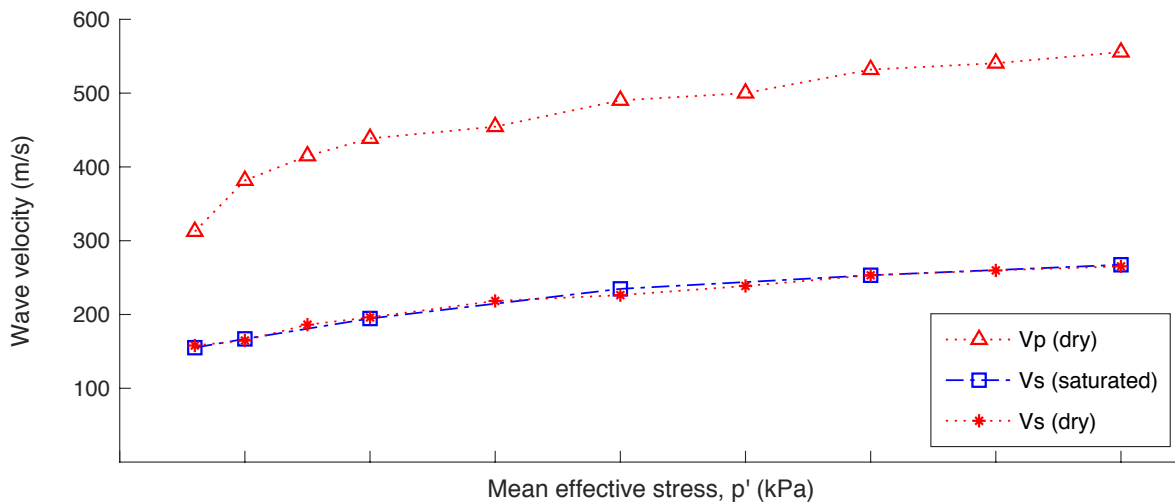


Fig. 9-7: v_s and v_p evolution with isotropic confinement (after Ferreira et al., 2020)

From Fig. 9-7, it is clear that the evolution of shear-wave velocities (v_s) with increasing stresses exhibit the similar trend, whether in dry or saturated conditions. A similar evolution, expressed by the obtained stress exponents, can be observed for compression-wave velocities (v_p), but only in dry conditions (exponent β of 0.20).

The BE signals obtained for different input frequencies, are compared for tests when the sample was under 100 kPa isotropic confinement, for dry and for saturated

conditions, in terms of P-waves (Fig. 9-8) and S-waves (Fig. 9-9). It was found that lower frequencies are more effective to identify the arrival of S-waves, while the higher frequencies are more effective to identify the arrival of P-waves.

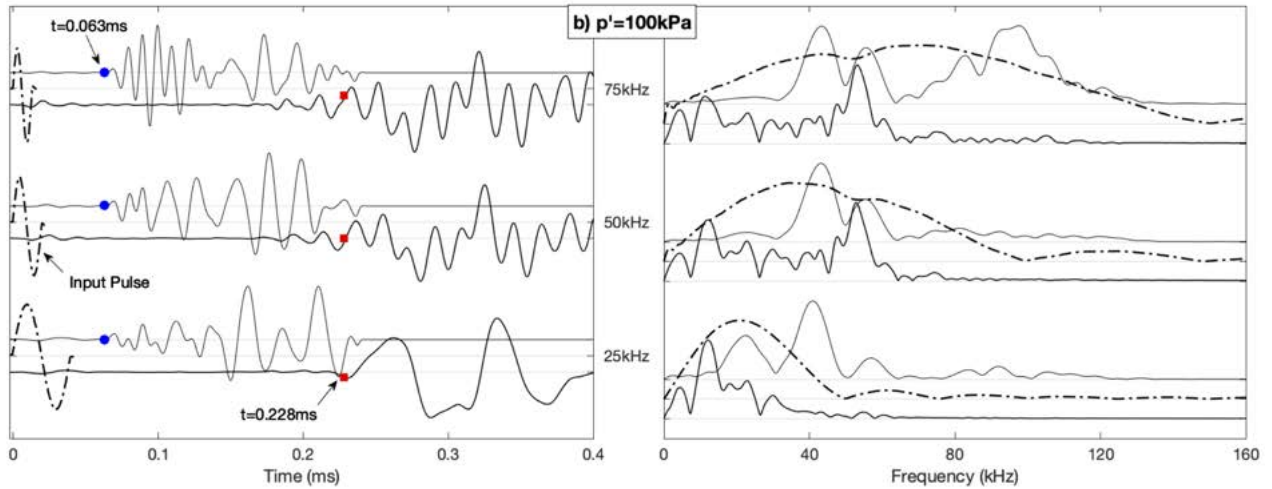


Fig. 9-8: BE results for P-waves in dry (thick lines) and saturated (thin lines) conditions, using different input frequencies for effective confining isotropic stresses of 100 kPa.

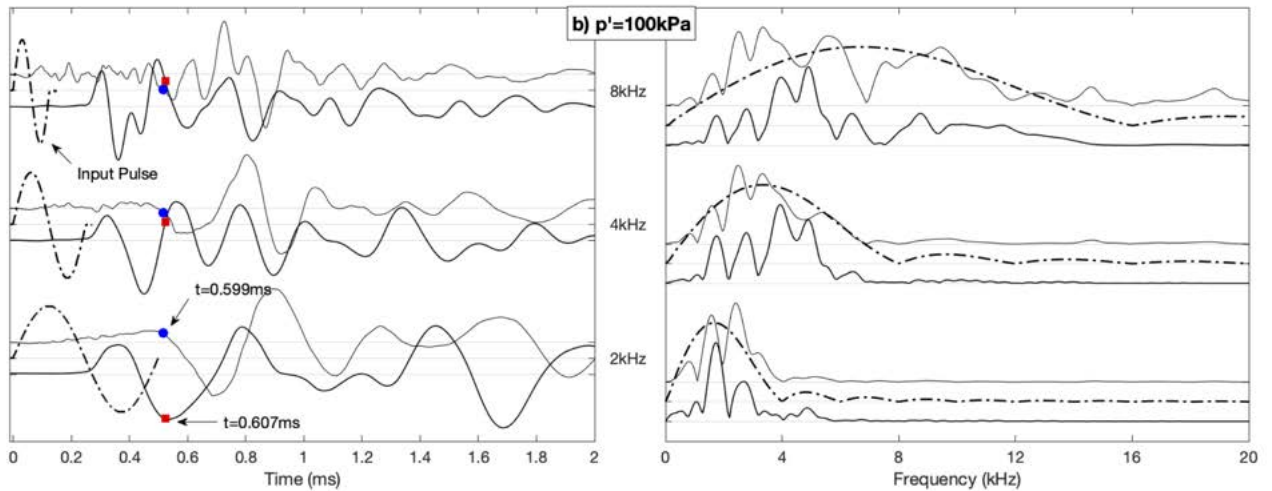


Fig. 9-9: BE results for S-waves in dry (thick lines) and saturated (thin lines) conditions, using different input frequencies for effective confining isotropic stresses of 100 kPa.

These two sets of BE measurements evidence significant changes in shape and amplitude of the received waves due to the change in saturation conditions. In dry conditions, the output signals at low frequencies, corresponding to S-waves, are complex and difficult to interpret, not only due to the higher wave dispersion, but also due to the proximity to the travel times of the two waves, since t_p is nearly half of t_s . In saturated conditions, the S-wave signals exhibit lower amplitudes, but are simpler, therefore easier to interpret.

From Fig. 9-10, it can be seen that the frequency spectra confirm the observed differences in the signals, in terms of amplitude and natural frequency. At 50 kHz input frequency, the BE output signal changes to a much sharper spectrum after saturation, centered near 20 kHz. Similar response is obtained for 75 kHz input frequency, however in this case the natural frequency in saturated conditions reaches 50 kHz, at an even higher amplitude.

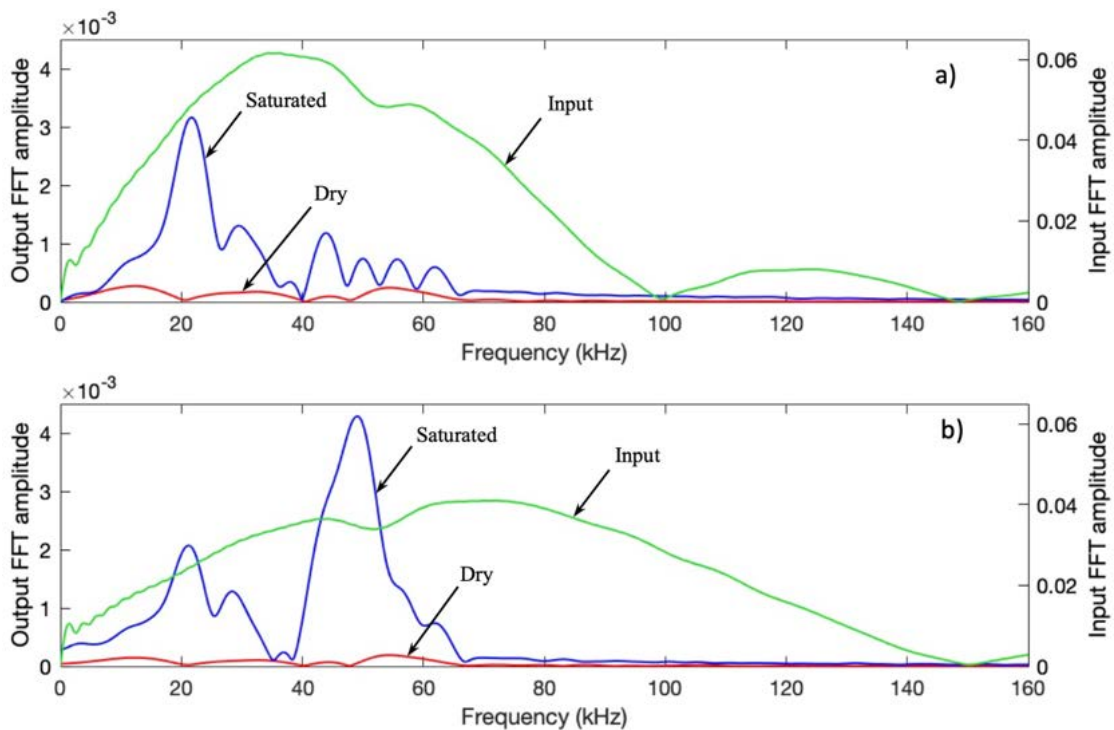


Fig. 9-10: Frequency spectra for BE signals for 50kHz (a) and 75kHz (b) input frequencies, for dry and saturated conditions, at 100 kPa confining stress

What is important to highlight from these results, is the fact that all of these measurements were obtained with a single BE transducer, simply by adjusting the input wave frequencies. Which means that without any modification to the wiring, just by changing the input frequency it is possible to get both, P-waves and S-waves' velocities. In order to better understand this result, a second stage of experimental work was done and its results are discussed in the next section, which dealt with the characterization of the BE transmitter when it is excited by different input frequencies.

9.5.2 Testing results: Stage 2

The first step for this stage in the laboratory testing, was to identify the resonance frequencies for the first three vibration modes (f_1 , f_2 , and f_3) of the BE. They were identified by sending a sinusoidal sweep to the BE with a range of frequencies going from 4 kHz to 100 kHz and then analyzing the frequency response. The sinusoidal sweep test was performed using a spectrum analyzer (HP-35670A) which calculates the transfer function between two signals in real time.

The horizontal displacements' readings were taken at one point in the middle of the top-side edge of the BE (point A in Fig. 9-5). The vertical displacements' readings were taken at one point in the middle of the top-center edge of the BE (point B in Fig. 9-5). The horizontal and vertical displacements readings were taken with the laser vibrometer and the signals were processed to obtain the frequency spectrums. From the frequency spectrum it was possible to get the resonant frequencies for horizontal displacements and for vertical displacements.

The power spectrums for the horizontal displacements of the BE are presented in Fig. 9-12. For the BE in contact with air, the resonant frequencies identified were: $f_{H1(air)} = 12kHz$, $f_{H2(air)} = 29kHz$, and $f_{H3(air)} = 48kHz$. Likewise, for horizontal displacements under water the resonant frequencies identified were: $f_{H1(water)} = 10kHz$, $f_{H2(water)} = 25kHz$, and $f_{H3(water)} = 40kHz$.

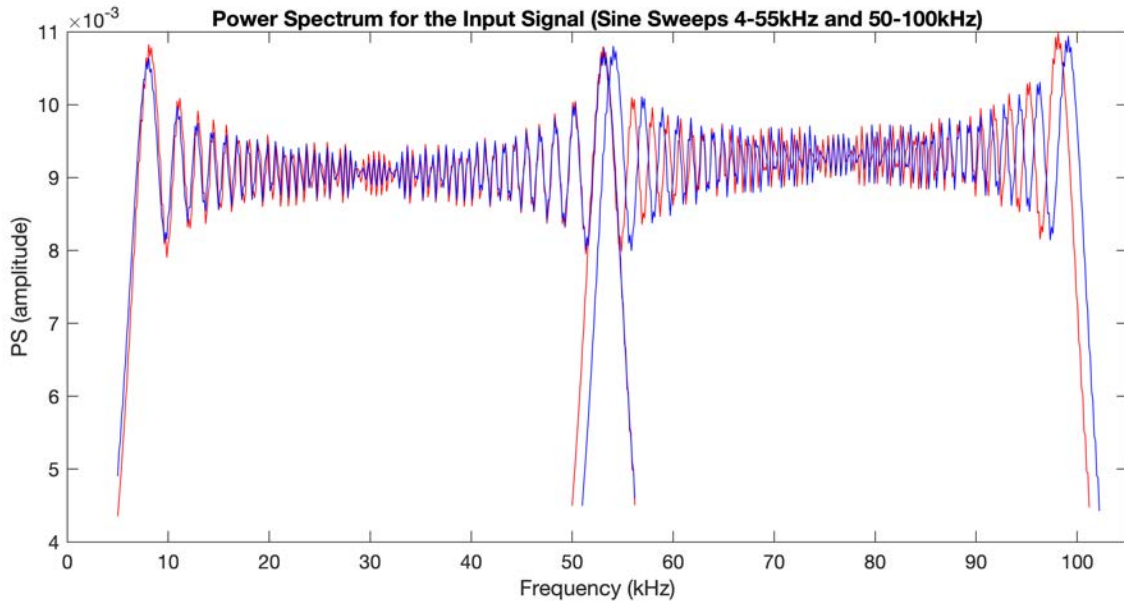


Fig. 9-11: Power spectrum for the input signal (4 to 100 kHz Sine sweep) used to measure horizontal displacements of BE tested on air (red) and on water (blue)

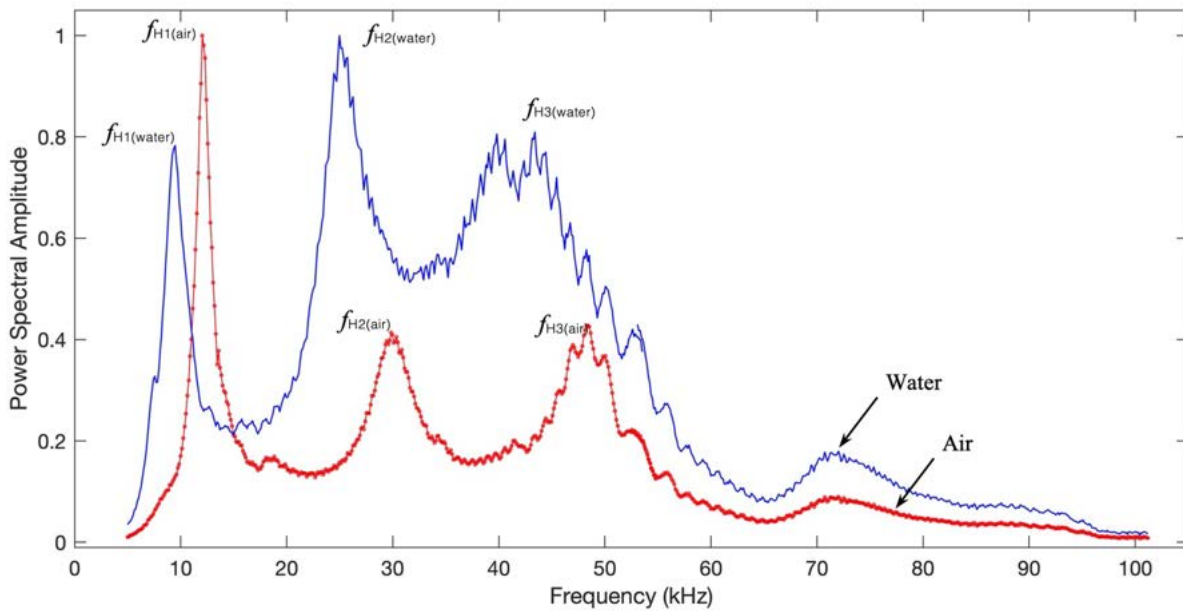


Fig. 9-12: Frequency spectrum for horizontal displacements of BE tested under a 4 to 100 kHz Sine sweep

The power spectrums for the vertical displacements of the BE are presented in Fig. 9-14. For the BE in contact with air, the resonant frequencies identified for vertical displacements were: $f_{V1(air)} = 12kHz$, $f_{V2(air)} = 48kHz$, and $f_{V3(air)} = 82kHz$. Likewise, for vertical displacements under water the resonant frequencies identified were: $f_{V1(water)} = 40kHz$, $f_{V2(water)} = 46kHz$, and $f_{V3(water)} = 62kHz$.

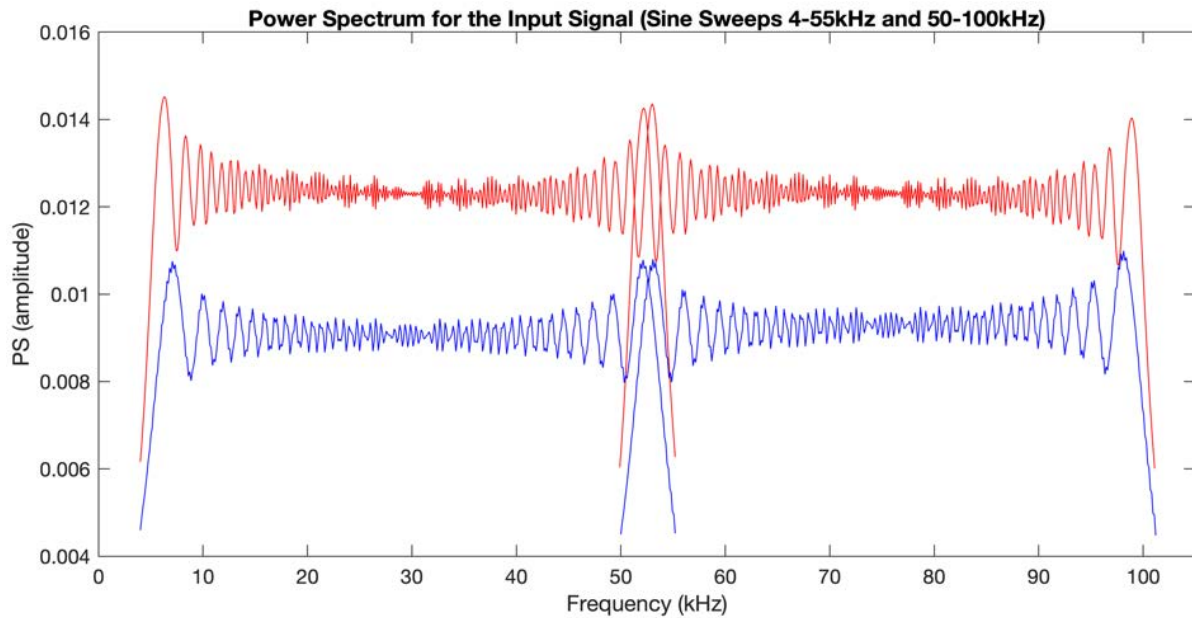


Fig. 9-13: Power spectrum for the input signal (4 to 100 kHz Sine sweep) used to measure vertical displacements of BE tested on air (red) and on water (blue)

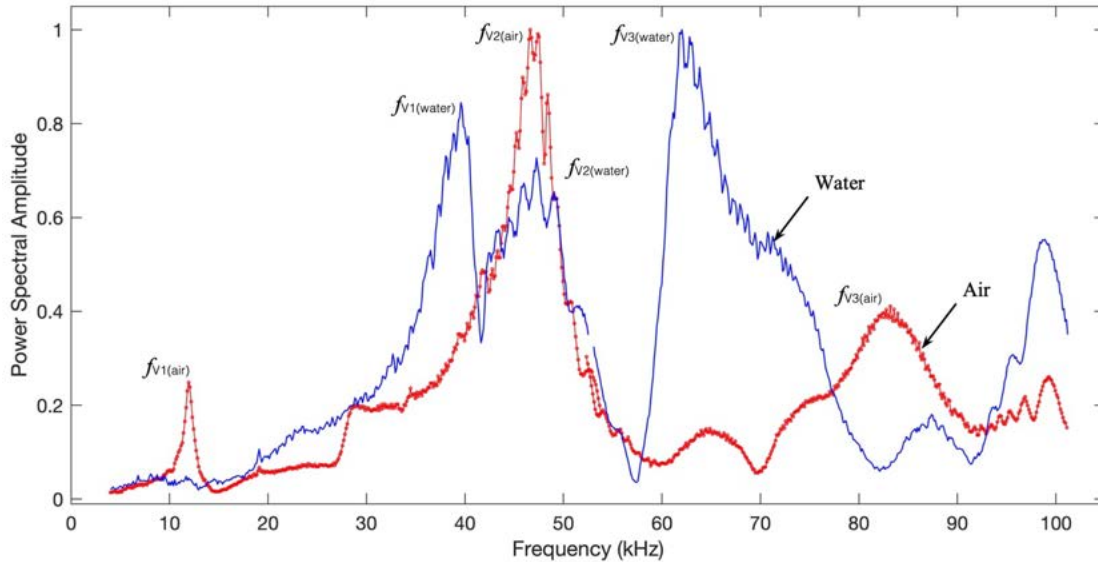


Fig. 9-14: Frequency spectrum for vertical displacements of BE tested under a 4 to 100 kHz Sine sweep

The second step in the laboratory testing for this stage, was to use each resonant frequency as the central frequency (f_c) of a sine pulse which was used as input to measure the BE response in air and in water. By using different central frequencies, it is possible to excite different vibration modes in the BE. The amplitude for the sine pulse in the input signal was 10 Volts peak-to-peak (V_{PP}). For each resonance frequency, vertical and horizontal displacements were measured on top edge and side edges of the BE for points with a spacing of half of a millimeter. The displacement signals were processed in order to filter each mode according to the central input frequency.

The laser readings were done following the same procedure and changing the central frequency for the input pulse. The frequencies used correspond to those previously identified as resonant frequencies. An example of signals obtained from the laser readings is presented in Fig. 9-15. The frequency spectra for the raw data corresponding to BE displacements while in contact with air, and when a sine pulse was used as input signal at different frequencies are presented in Fig. 9-16.

In order to understand the behaviour of the BE vibration modes, it is necessary to perform the mode separation. A fastest and effective technique to do so is by studying the frequency spectrum of displacements in different directions and for different frequencies in the input signals. Once the peaks corresponding to the resonant frequencies are identified in each spectrum (i.e. for each displacement orientation and for each input frequency), a bandpass filter is used to isolate the vibration mode.

The frequency spectrum of filtered signals after mode separation is presented in Fig. 9-17. In those spectrums, it is possible to see clearly the vibration modes separation, which means the corresponding filtered time signals only contain the displacement components for the targeted mode of the BE. Thus, the mode shapes can be properly seen not just in the time domain, but in the frequency domain.

There are many other techniques to perform mode separation, such as the continuous wavelet transform, the short time Fourier transform, or the synchro-squeezed wavelet transform, among others. A deep study of those techniques is out of the scope of this research, however, a fast verification of the results obtained from the vibration mode separation with band-pass filtering was done by comparing those results against the results from the continuous wavelet and from the synchro-squeezed wavelet transform. An example of the results obtain with those techniques is presented in Fig. 9-18, which correspond to the vertical displacements in the middle top point of top edge of the BE.

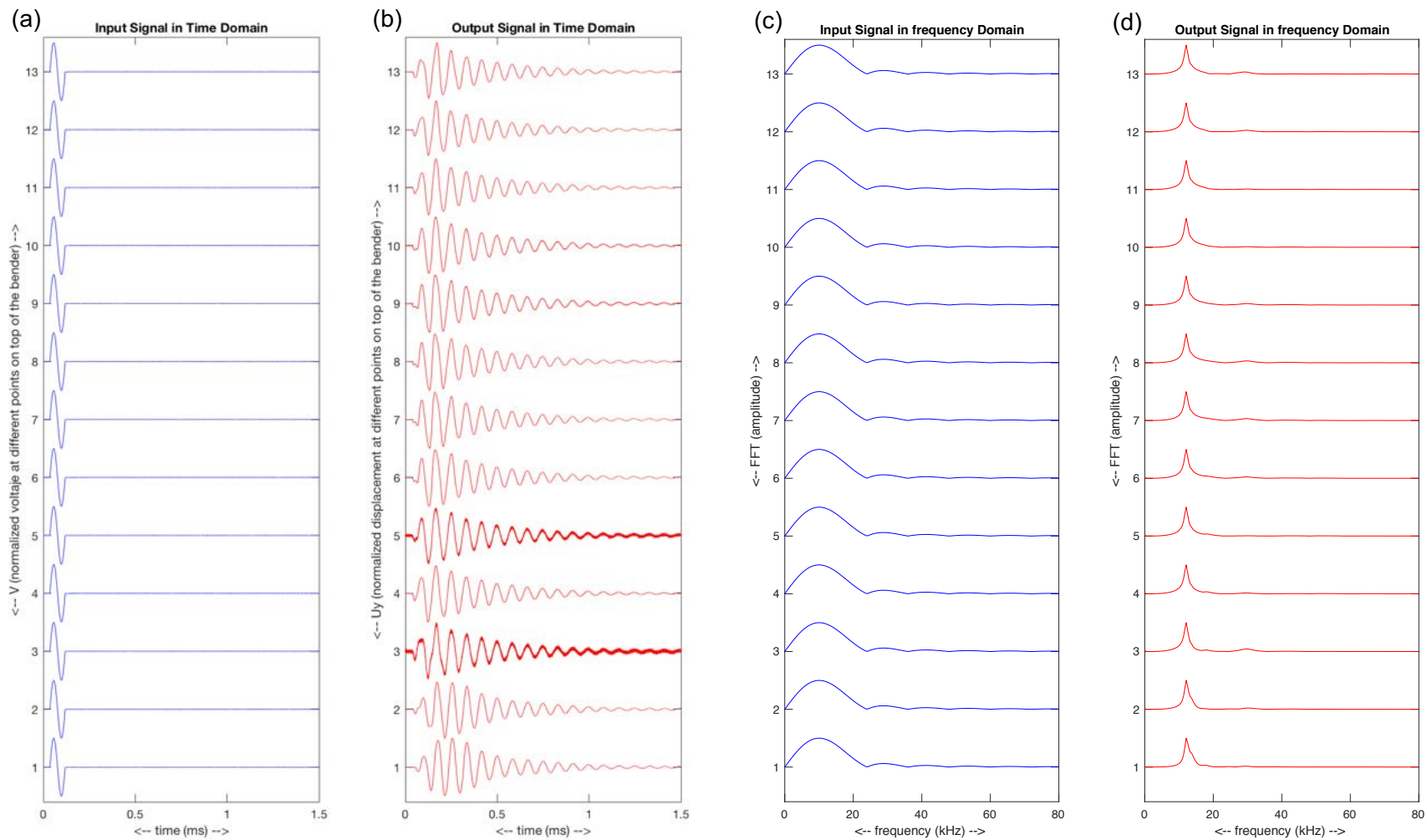


Fig. 9-15: Example of signals obtained from the laser readings. In this case horizontal displacements were read at 13 different locations on top edge of the BE for an input frequency of 12kHz: a) Input signal in the time domain, b) Output signal in the time domain c) Input signal in the frequency domain, and d) Output signal in the frequency domain.

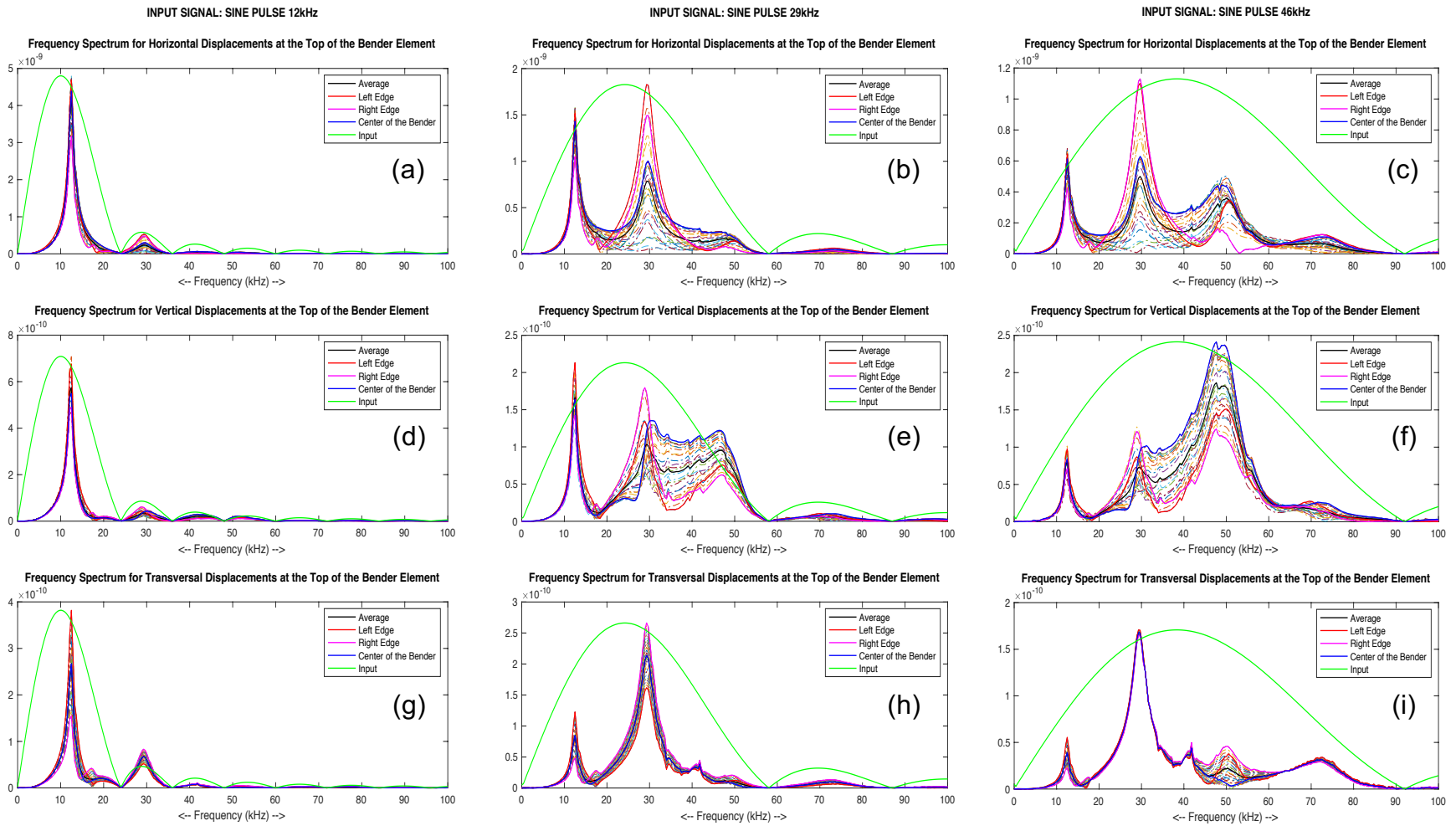


Fig. 9-16: Fourier transform of the raw time signals for bender element (BE) displacement measured with the laser in different orientations and for different frequencies in the input signals.

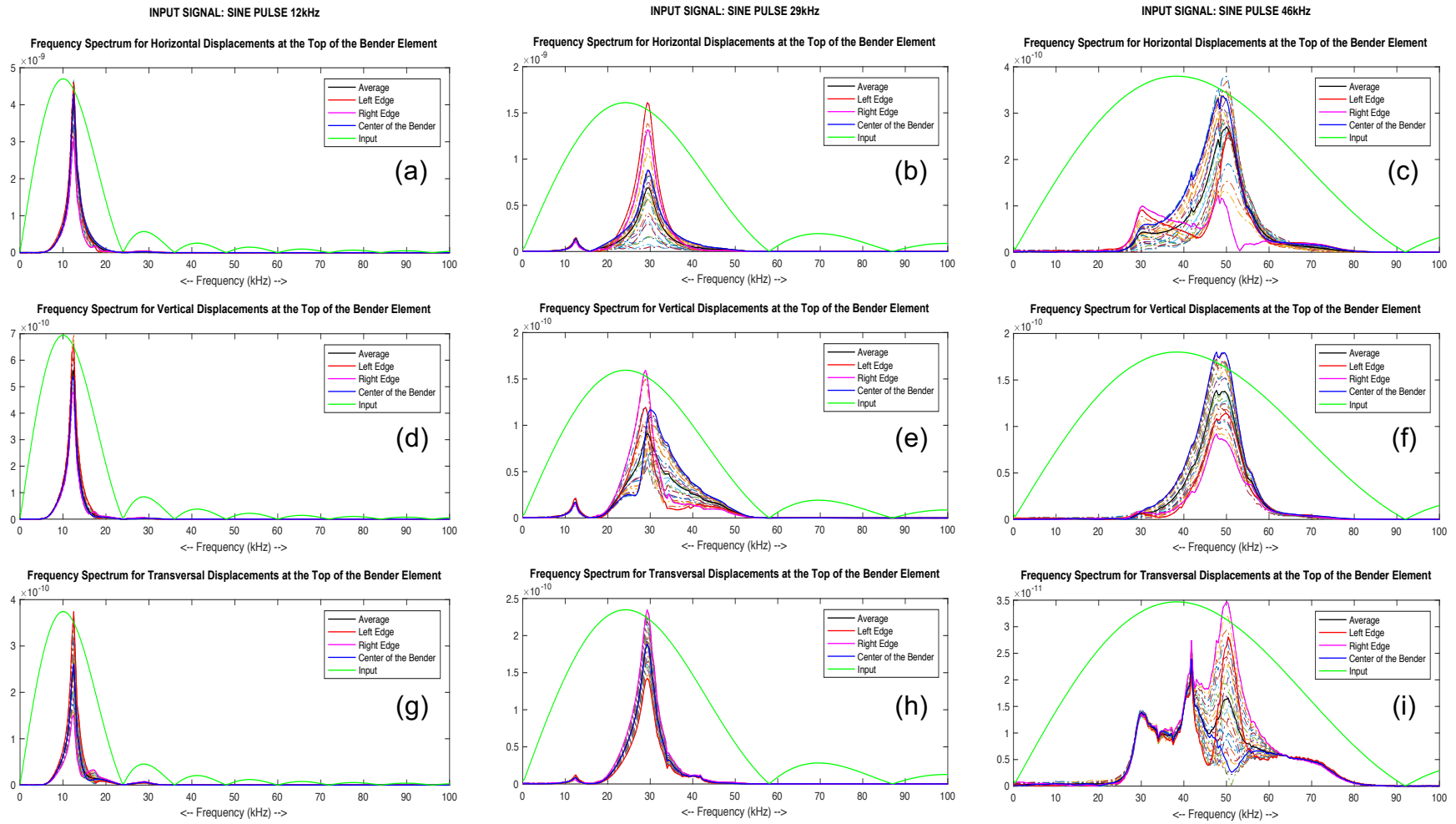


Fig. 9-17: Fourier transform of the filtered time signals for bender element (BE) displacement measured with the laser in different orientations and for different frequencies in the input signals. The signals were filtered to isolate vibration modes.

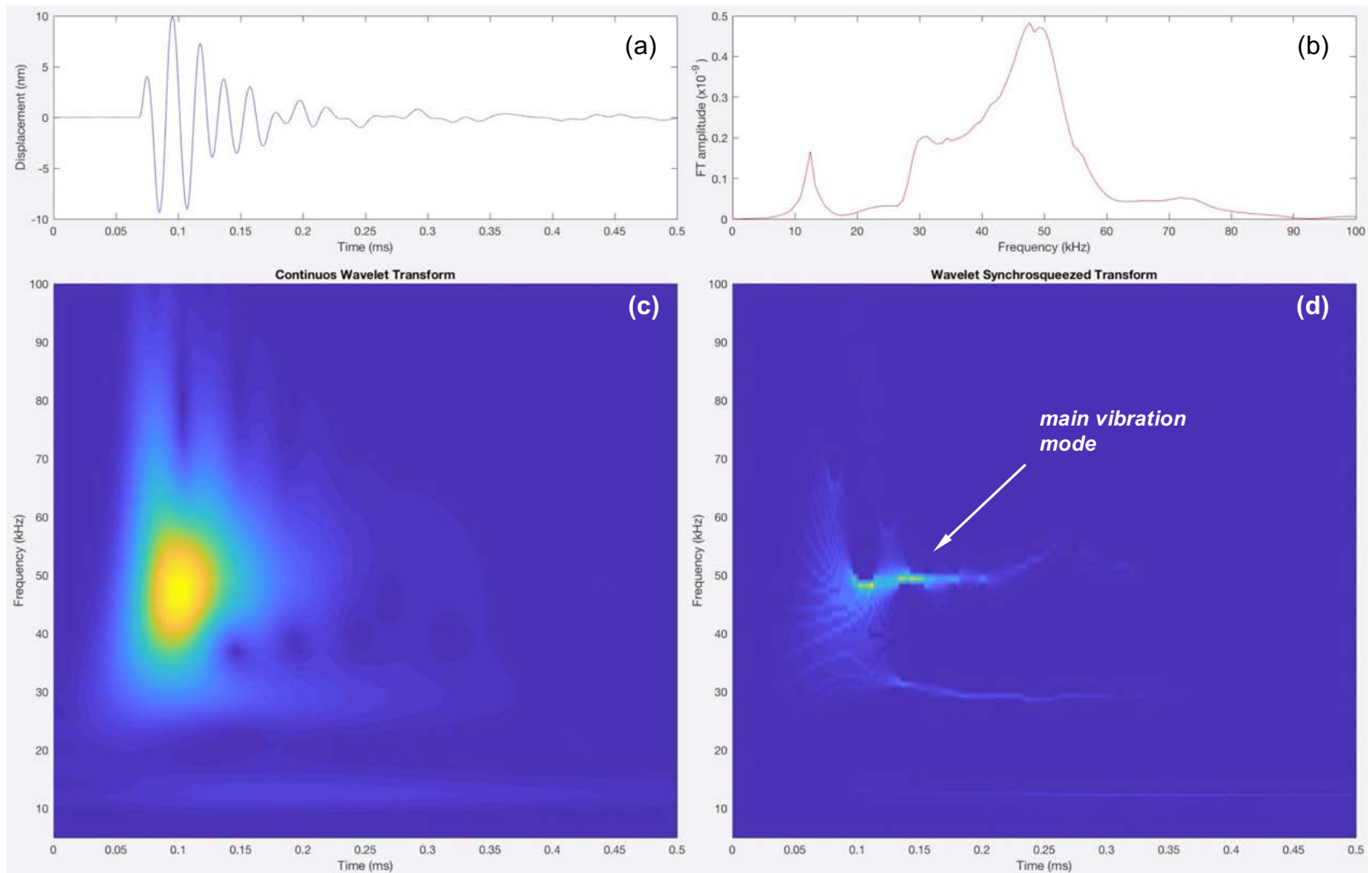


Fig. 9-18: Vibration modes separation using continuous wavelet transform (c) and wavelet synchro-squeezed transform for vertical displacements in the middle point on top edge of the BE. The input frequency was 46kHz.

In Fig. 9-19 and Fig. 9-20, the first and third vibration modes are presented for the envelopes of the vertical (down) and horizontal (left) displacements on top of the BE, along the full length of its top edge. As a reference, the top edge of the bender element at rest is represented by a red line in the plots.

For the vertical displacements, corresponding to a compression-extension deformation, the maximums for the first mode are relatively low; however, for the third mode, which was mainly excited by a frequency of 46kHz, the vertical displacements are roughly twice the values obtained for the first mode. This means the higher the input frequency, the more important the vertical displacements become in the BE vibration, which corresponds to an increase in the compressional components of the transmitted wave.

In turn, the observed maximum horizontal displacements decrease considerably with the frequency increase, from the first to the third mode, which evidence a reduction in the flexural component of the transmitted wave.

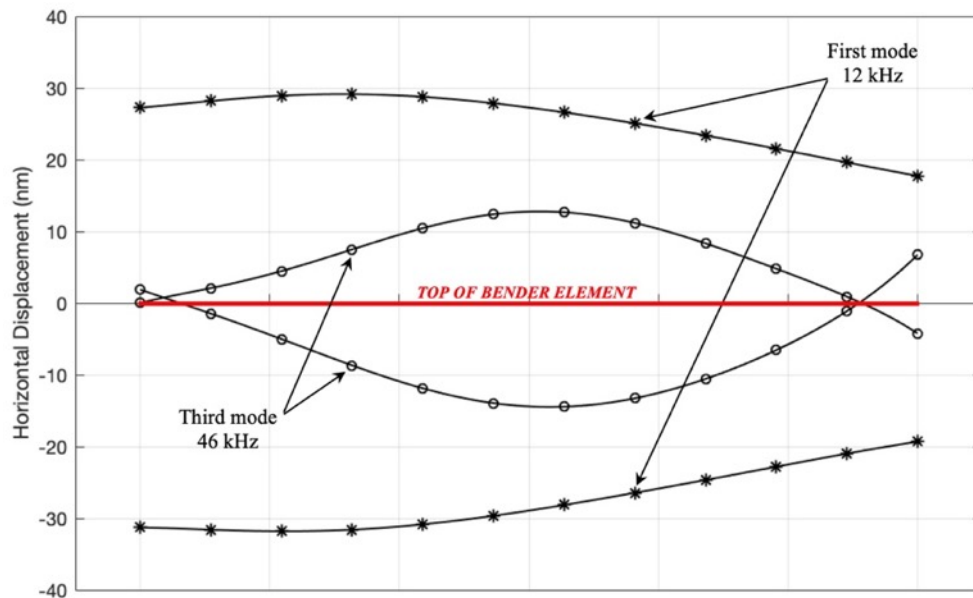


Fig. 9-19: First and third vibration modes for horizontal displacements on top of the BE, along its length while it was in contact with air

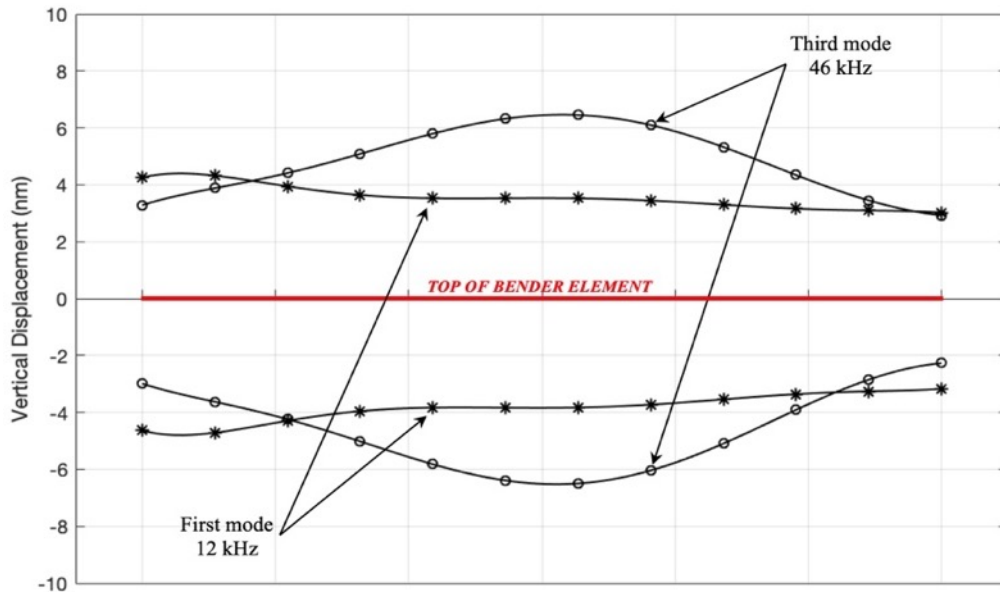


Fig. 9-20: First and third vibration modes for vertical displacements on top of the BE, along its length while it was in contact with air

The results obtained in these laser measurement tests demonstrate how the input frequency strongly affects the BE movement. These results also explain why it is possible to identify the P-wave arrival when high frequencies are used in the BE test. As the high frequencies tend to excite more the third mode, rather than the first or the second, more energy is oriented in vertical direction creating a stronger P-wave front, which allows its detection in the receiver BE.

In order to see the actual behaviour of the bender element in three dimensions (3D), an additional set of measurements was taken all along the front, top, and lateral sides of the BE using the laser vibrometer. Displacements were always read in the direction perpendicular to each of the faces of the BE. The reading pattern followed to measure displacements on each of the three faces of the BE is presented in Fig. 9-21.

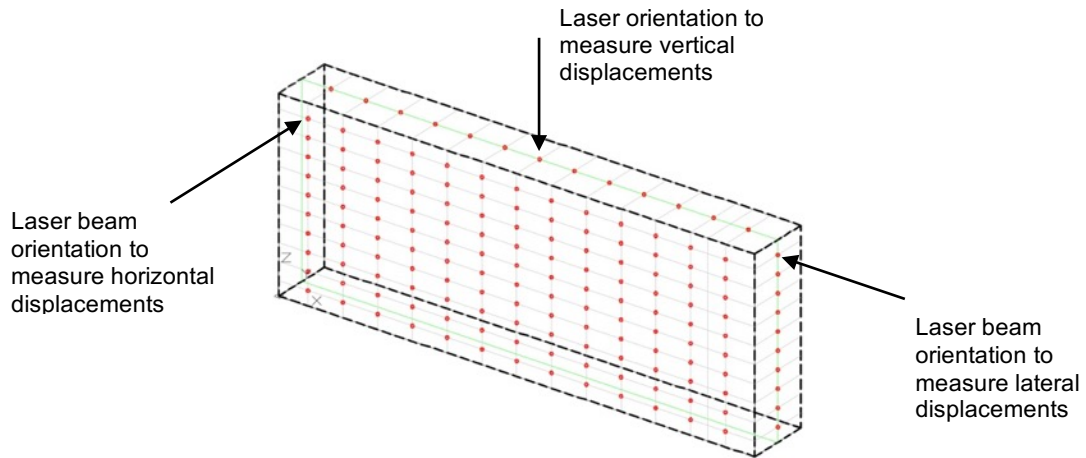


Fig. 9-21: Pattern of points used to read 3D displacements in the BE

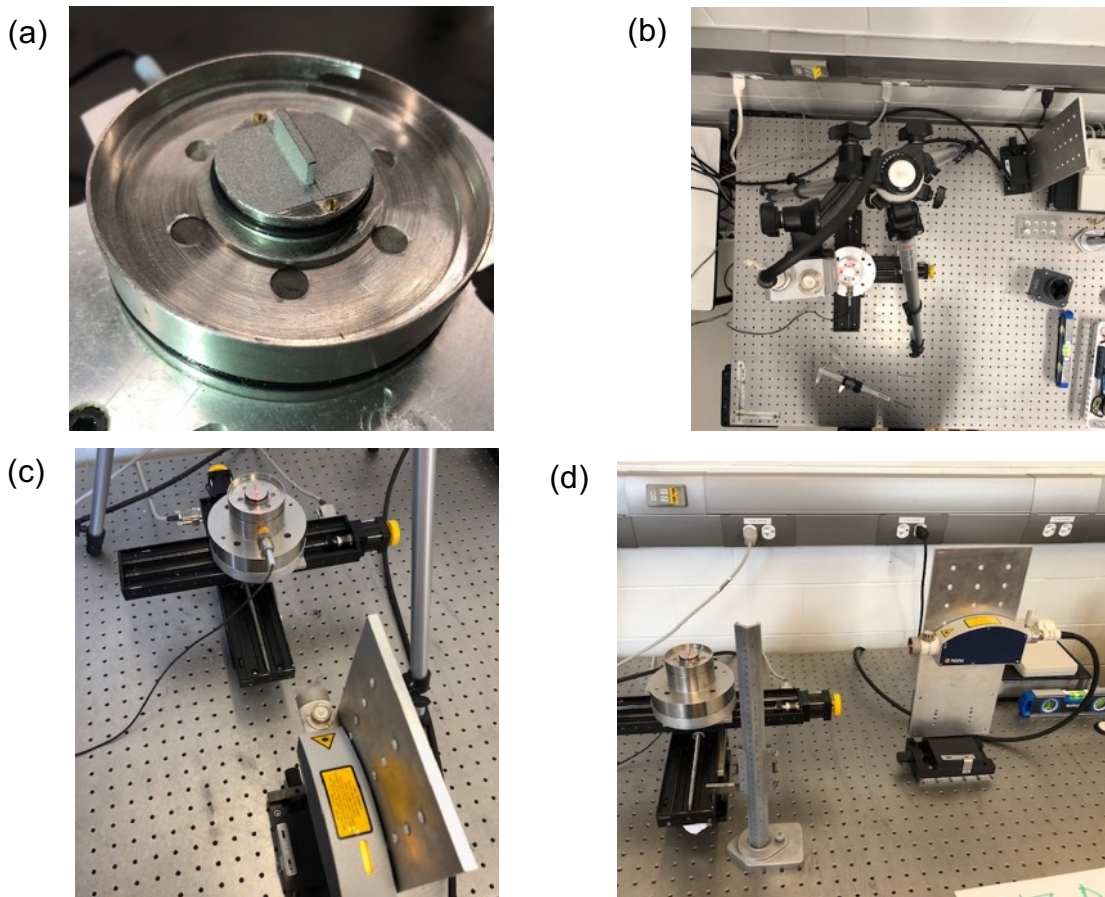


Fig. 9-22: Setup for laser readings under different orientations: (a) detailed view of BE, (b) Top readings, (c) lateral readings, (d) horizontal readings.

As it was shown in previous plots, horizontal displacements are almost one order of magnitude higher than vertical displacements (see Fig. 9-19 and Fig. 9-20). Thus, in order to appreciate the difference in behaviour when vertical displacements are considered to characterize the BE, two set of videos were created using the displacement readings to see the actual behaviour of the BE in three dimensions. The first set of videos was made showing just the horizontal displacements, which are associated to the flexural model of BE. The second set of videos was made including both, horizontal and vertical displacements. The links to access the videos are presented in Table 9-3.

Table 9-3. Links to access the videos of displacements measured using a laser vibrometer while the BE was in contact with air.

<i>Content of the video</i>	<i>Input frequency</i>	<i>Link</i>
2D flexural mode: horizontal displacements	12 kHz	https://youtu.be/1I5Q1JkdQmA
	29 kHz	https://youtu.be/qelwSkal-1w
	46 kHz	https://youtu.be/uHUmuaU1K2E
3D movie: vertical and horizontal displacements	12 kHz	https://youtu.be/SY95CG1A3PQ
	29 kHz	https://youtu.be/qHV8MgN0DqU
	46 kHz	https://youtu.be/xirilha8Aco

Screenshots of the videos showing the first and third vibration modes for horizontal displacements (flexural mode) on top of the BE along its length, while it was tested in contact with air area shown in Fig. 9-23.

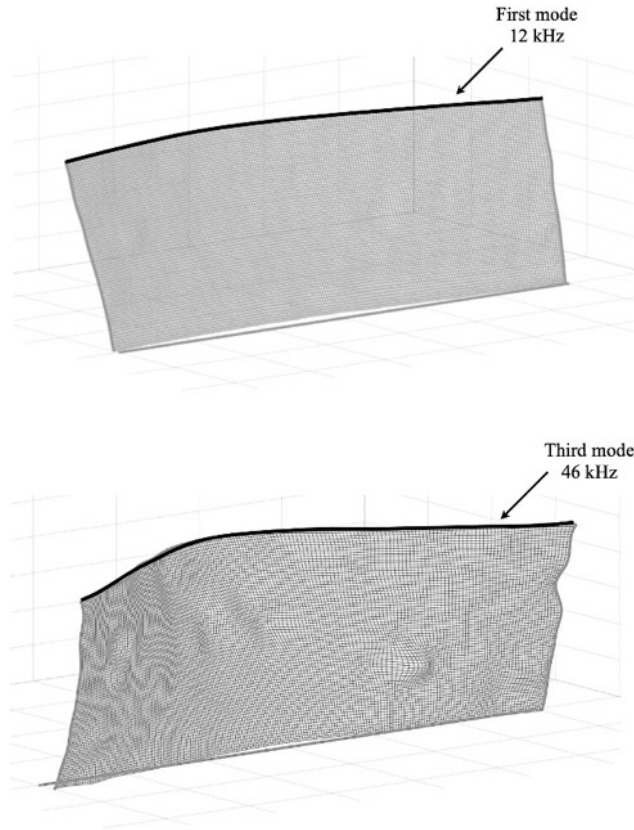


Fig. 9-23: First and third vibration modes for horizontal displacements.

9.5.3 Testing results: Stage 3

In order to see how the confinement level and the input frequency affect the results in the BE tests, the results were plotted in the time and the frequency domain. The circle filled dots in Fig. 9-24 (a) represent what is believe to be the arrival for the shear waves in the BE tests. According with these arrival times and considering the travel distance (tip-to-tip distance in the BE-soil system) the v_s values were obtained ranging from 230 m/s at low confinement and low frequency (35kPa and 10kHz) to 447 m/s at high confinement and high frequency (600kPa and 50kHz). The resonant frequencies for the transparent-soil sample were obtained for different confinements from the RC test results, and the dominant frequencies in the BE test results were obtained from the frequency spectrums,

i.e. Fig. 9-24 (b); then the calculations of the wavelengths, both in RC and BE tests, were performed and compared to identify particular patterns.

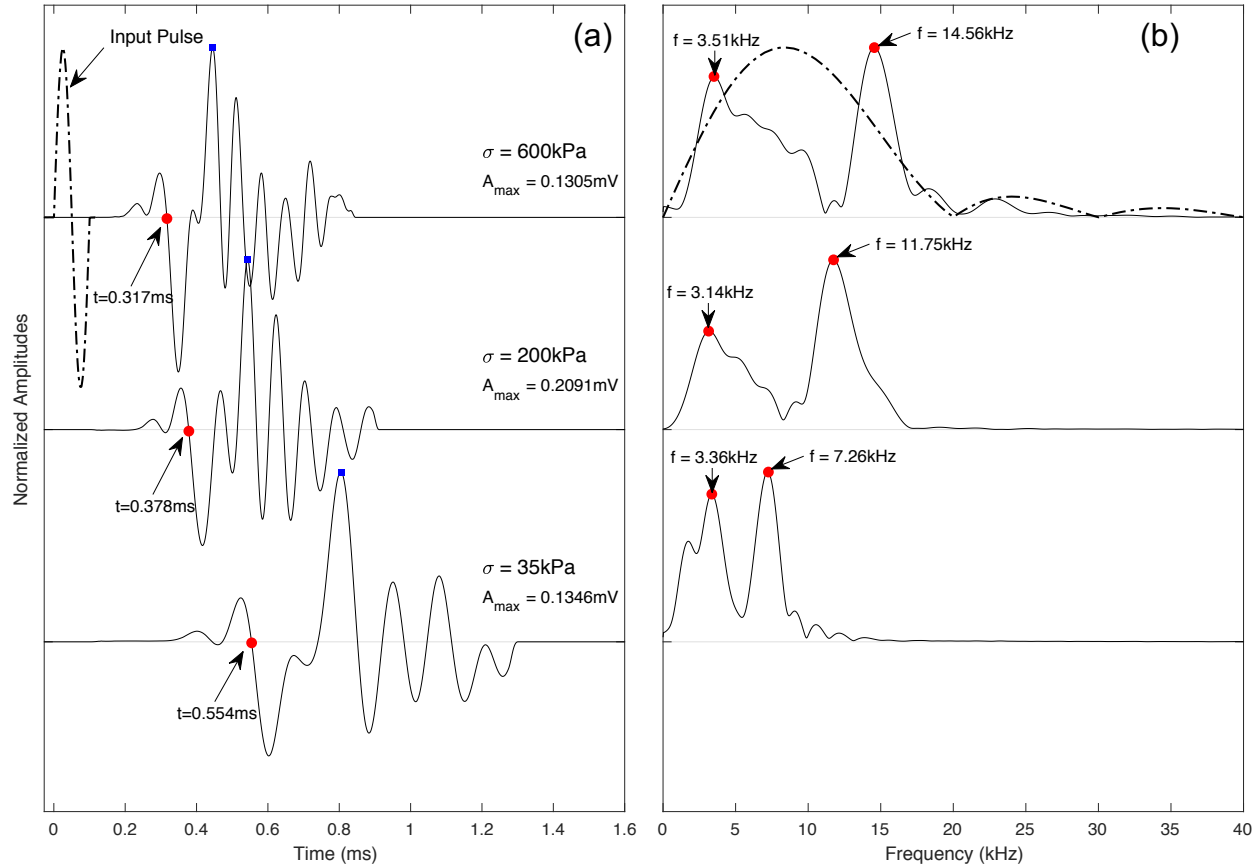


Fig. 9-24: (a) BE-Rx responses to sine pulse (10 kHz) at different confinements (b) frequency spectrum of the time signals in (a)

For the RC test at low confinement (35 kPa) the resonant frequency of the fused quartz sample (the granular material used by Irfan (2019) to make the transparent-soil) was $f_{0_RC-Low} = 47.9\text{ Hz}$ and the shear wave velocity $v_{s_RC-Low} = 203.7\text{ m/s}$, these values lead to a wavelength value of $\lambda_{RC-Low} = 4.25\text{ m}$; when the sample was under high confinement (600 kPa) the results for the resonant frequency, the shear wave velocity, and the wavelength were: $f_{0_RC-High} = 91.0\text{ Hz}$, $v_{s_RC-High} = 386.4\text{ m/s}$, and $\lambda_{RC-High} = 4.25\text{ m}$, respectively. It was clear that the values of wavelength were practically constant for

the RC test under different confinements, and the ratio between the length of the sample ($L_{RC} = 0.142\text{m}$) and the wavelength was $(L/\lambda) \approx (1/30)$.

In a similar way, for the BE test at low confinement (35 kPa) the dominant frequency in the BE-soil system was $f_{BE-Low} = 7.3$ kHz and the shear wave velocity calculated was $v_{s_BE-Low} = 237.7$ m/s, these values lead to a wavelength value of $\lambda_{BE-Low} = 0.0327$ m; when the sample was under high confinement (600 kPa) the results for the dominant frequency, the shear wave velocity, and the wavelength were: $f_{BE-High} = 14.6$ kHz, $v_{s_BE-High} = 415.1$ m/s, and $\lambda_{BE-High} = 0.0285$ m. It is clear that the values of wavelength in the BE test are decreasing, while the shear wave velocity and the dominant frequency are increasing with the confinement level. The ratio between the length of the sample, which corresponds in this case to the aforementioned tip-to-tip distance ($L_{BE}=0.132\text{m}$), and the wavelength for the low confinement case was $(L/\lambda)_{Low} = 4.03$, while for the high confinement case was $(L/\lambda)_{High} = 4.63$.

In the frequency spectrums, it is clear the presence of two peaks. Each of these peaks is associated with different characteristics of the BE-soil system; in the case of the first peak, it is associated with the compressional and the shear wave fronts arriving at the BE receiver; on the other hand, the second peak is associated with the resonant frequency of the BE itself. If the BE-soil system is assimilated to a damped forced harmonic oscillator system, then it is possible to associate the resonant frequency of the system with a given value of damping ratio. Thus, any change in the resonant frequency of the system will lead to a change in the damping ratio as well.

The dominant frequency obtained from the BE test results (Fig. 9-24 (b)) is associated with the resonance frequency of the BE itself, rather than the resonance of the whole BE-soil system. That dominant frequency corresponds to the second peak in the frequency spectrums in Fig. 9-24 (b) and its evolution with increasing confinement pressure is well fitted to a power trendline ($R^2 = 0.99$) with a stress-dependency exponent β of 0.25. At low confinement (35 kPa) the dominant frequency was 7.2 kHz, then, as the pressure increased to the highest value considered in the tests (600 kPa), the dominant frequency rose to 14.6 kHz. The change in the dominant frequency (i.e. the resonance

frequency of the BE) is due to the decreased damping ratio caused by the increasing confinement pressure for the BE-soil system. The damping ratio is a parameter widely used to measure the energy dissipation characteristics of soils, so it is known that by increasing the confining pressure a decrease in damping ratio is created.

The BE test was also carried out for different strain levels in the RC while the confinement pressure was kept constant at 50kPa. The shear strain level in the RC was increased from $7.0E-06\%$ to $4.7E-04\%$. The (a) plot in the Fig. 9-25 shows the time domain response for the BE test under different strain levels, while the (b) plot shows the frequency spectrums. In the frequency spectrums it can be seen how they remain almost invariable for different strain levels when the RC system was off.

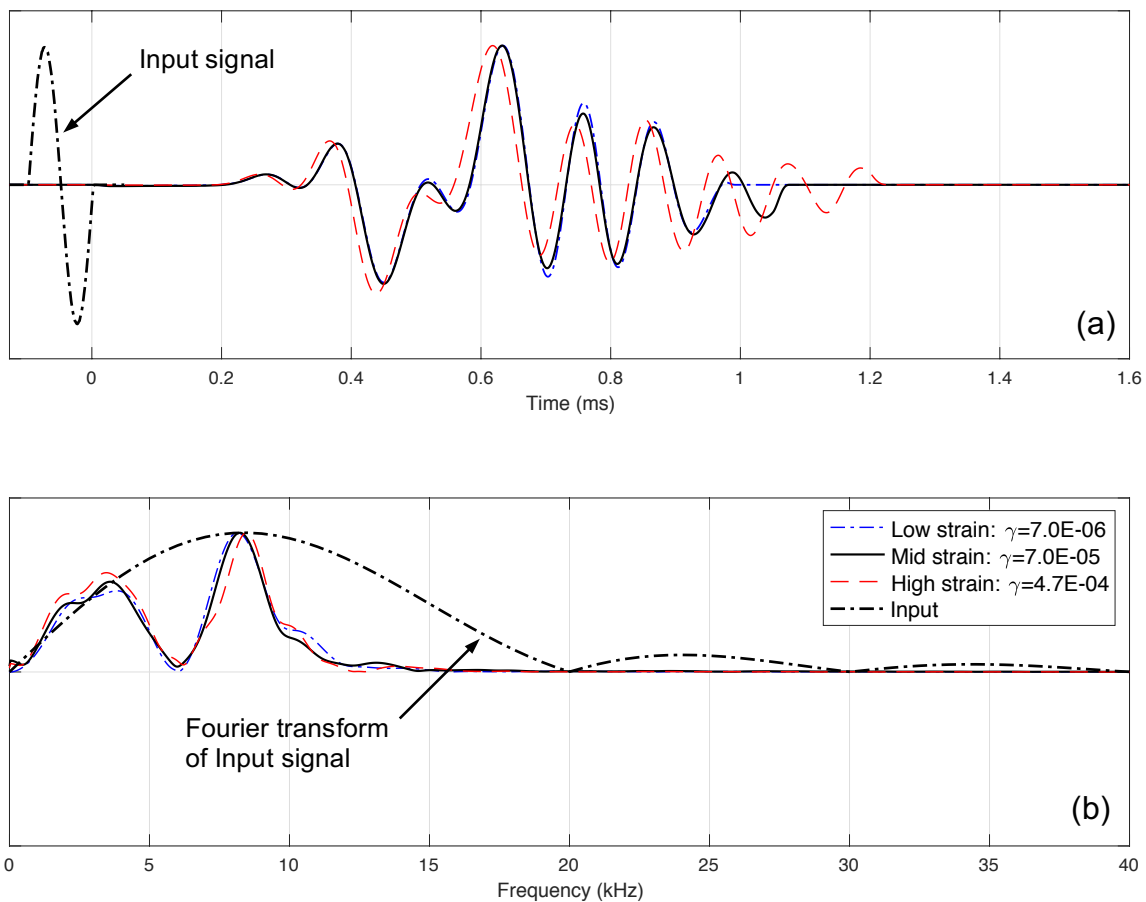


Fig. 9-25: (a) BE-Rx responses to sine pulse (10 kHz) at different strain levels for dry condition (b) frequency spectrum of the time signals in (a)

In Fig. 9-26 the compressional wave velocity values obtained from the BE tests and the shear wave velocity values obtained from RC tests, are plotted for different confinement levels and for the two input frequencies used in the BE testing program (10kHz and 50kHz). For all the results the wave velocity values and the confinement values are very well fitted to power trend-lines with R^2 values ranging between 0.99 and 1.00. For the v_s values obtained from RC test the stress-dependency exponent obtained for dry condition was $b = 0.23$ and the R^2 value was 0.997. On the other hand, for the BE tests the stress-dependency exponents obtained were $b=0.20$ when the input frequency was 10 kHz and $b=0.25$ when the input frequency was 50 kHz, while the R^2 values were 0.991 and 0.986 respectively.

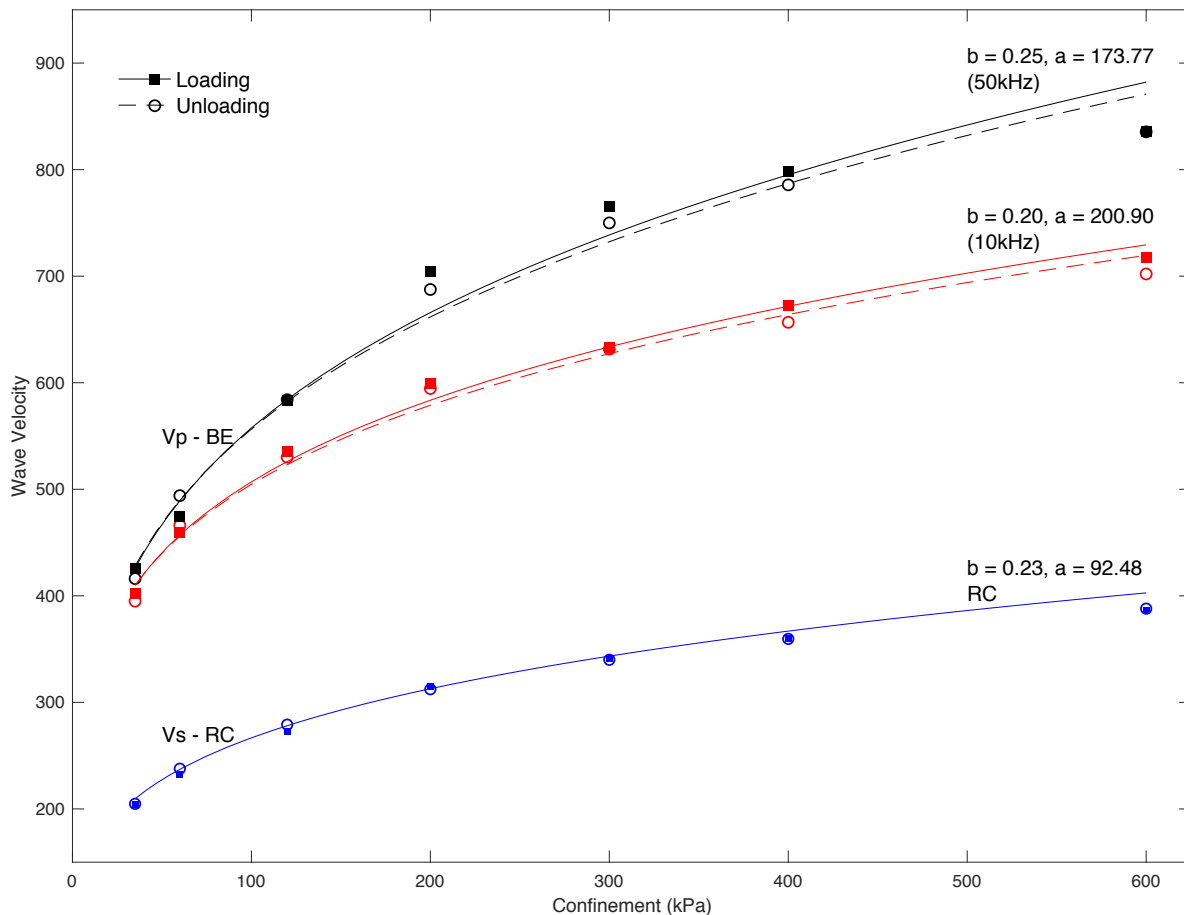


Fig. 9-26: Shear wave velocity (BE and RC) and compressional wave velocity of fused quartz at different confinements

In a similar way, in Fig. 9-27 the shear wave velocity values obtained from the BE and RC tests are plotted for different confinement levels and for the two input frequencies used in the BE testing program. In general, it could be said that the v_s values obtained in the BE test at 10 kHz were about 10% higher than the v_s values obtained in the RC test; for the BE test at 50 kHz the v_s values were about 15% higher than the v_s values obtained in the RC test. Also in this case, all the results of v_s values and the confinement values are very well fitted to power trend-lines with stress-dependency exponents $b=0.20$ when the input frequency was 10 kHz and $b=0.21$ when the input frequency was 50 kHz, while the R^2 values were 0.99 in both cases. These stress-dependency exponents for v_s values are within the typical values for natural sands reported by Cho et al. (2006), and Ramos et al. (2019), which is another proof that the fused silica behaves like a natural sand.

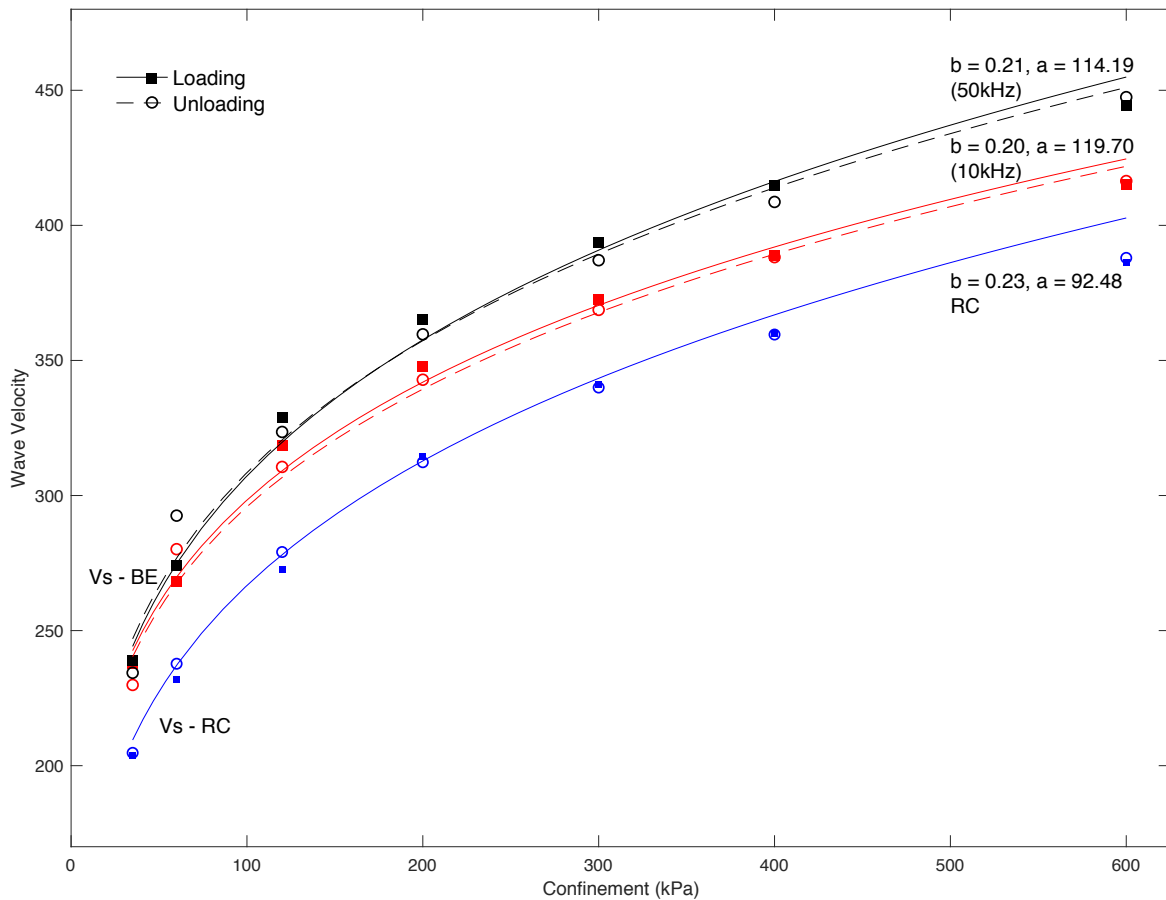


Fig. 9-27: Shear wave velocity (BE and RC) of fused quartz at different confinements

The Poisson's ratio values (ν) were also calculated from the v_s and v_p values obtained in the RC and BE tests with different input frequencies. When the v_p values from the BE tests and the v_s values from the RC test were considered, the Poisson's ratio values ranged from 0.33 to 0.36 for the case of input frequency of 10 kHz in the BE; for the 50kHz input frequency in the BE, the Poisson's ratio values ranged from 0.37 to 0.40. Similarly, when both the v_p and the v_s values were taken from the BE tests, the Poisson's ratio values ranged from 0.23 to 0.25 for the case of input frequency of 10 kHz in the BE, and from 0.24 to 0.32 for the 50kHz input frequency in the BE.

Fig. 9-28 shows the time domain signals obtained from the BE test when the sample was at 50 kPa of confinement pressure, and for different shear strain levels in the RC. In this case the BE test was performed while the RC test was running.

For this test, the strain level in the RC rose from 3.3E-06% to 3.7E-04% and the results shown that the BE sees a picture of the deformation and not the full strain level imposed by the RC test. Thus, the arrivals for P-waves (square filled points) do not change at all for different strain levels in the RC tests. Nonetheless, the S-wave arrivals (circle filled points) do change accordingly with the strain level showing shorter arrivals for the test at low shear strain ($\gamma = 3.30E-06$) and larger values of arrival time for the test at high shear strain ($\gamma = 3.70E-04$).

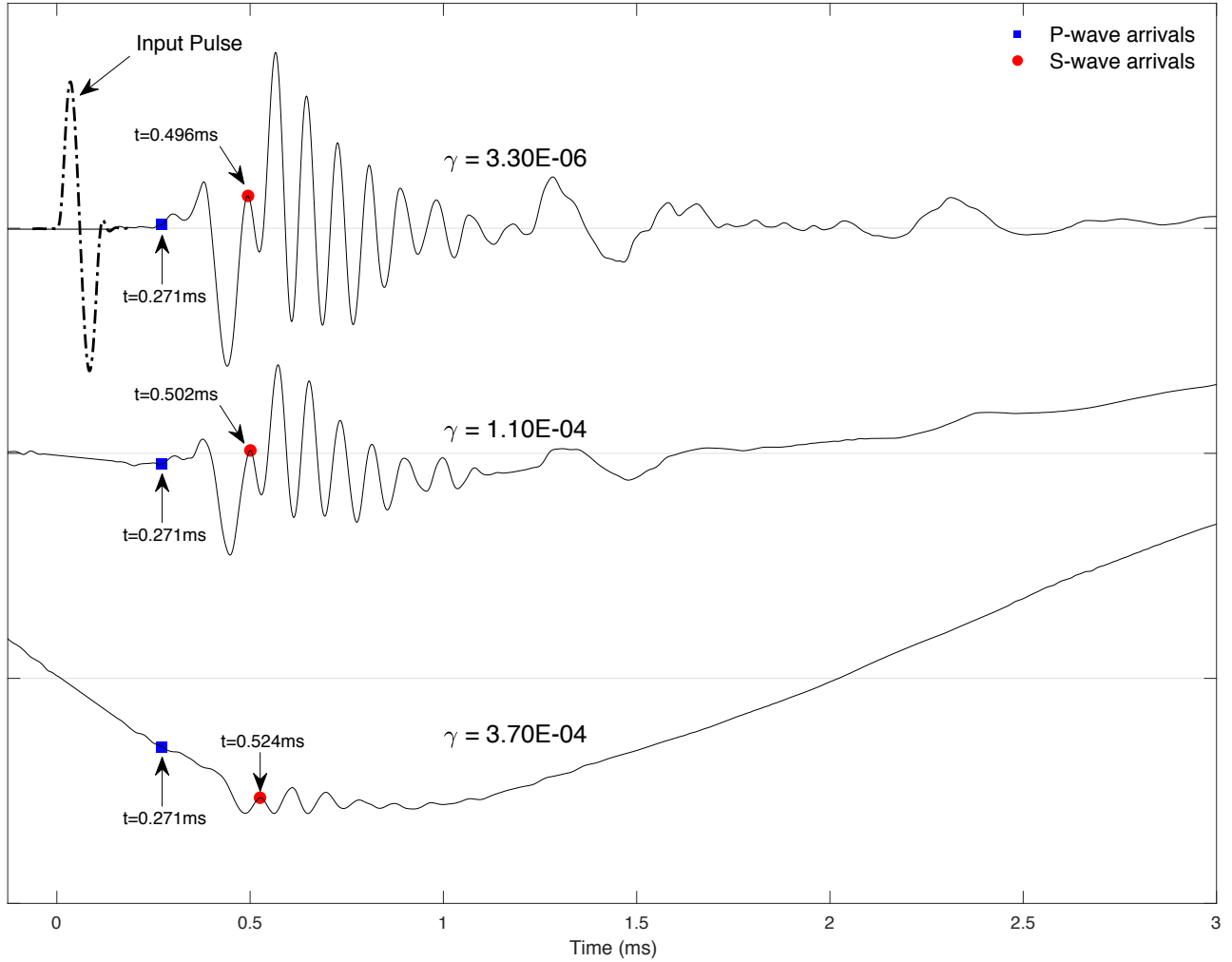


Fig. 9-28: BE-Rx response at different strain levels (RC system turned on). In the lower plot the amplitude was amplified by a factor of 10. In the middle plot the amplitude was amplified by a factor of 4. In the upper plot the amplitudes were not amplified at all.

Fig. 9-29 shows the squared normalized values of the shear wave velocity ($v_s^2_{\{norm.\}}$), which are linearly related to the shear stiffness moduli values, for different shear strain levels.

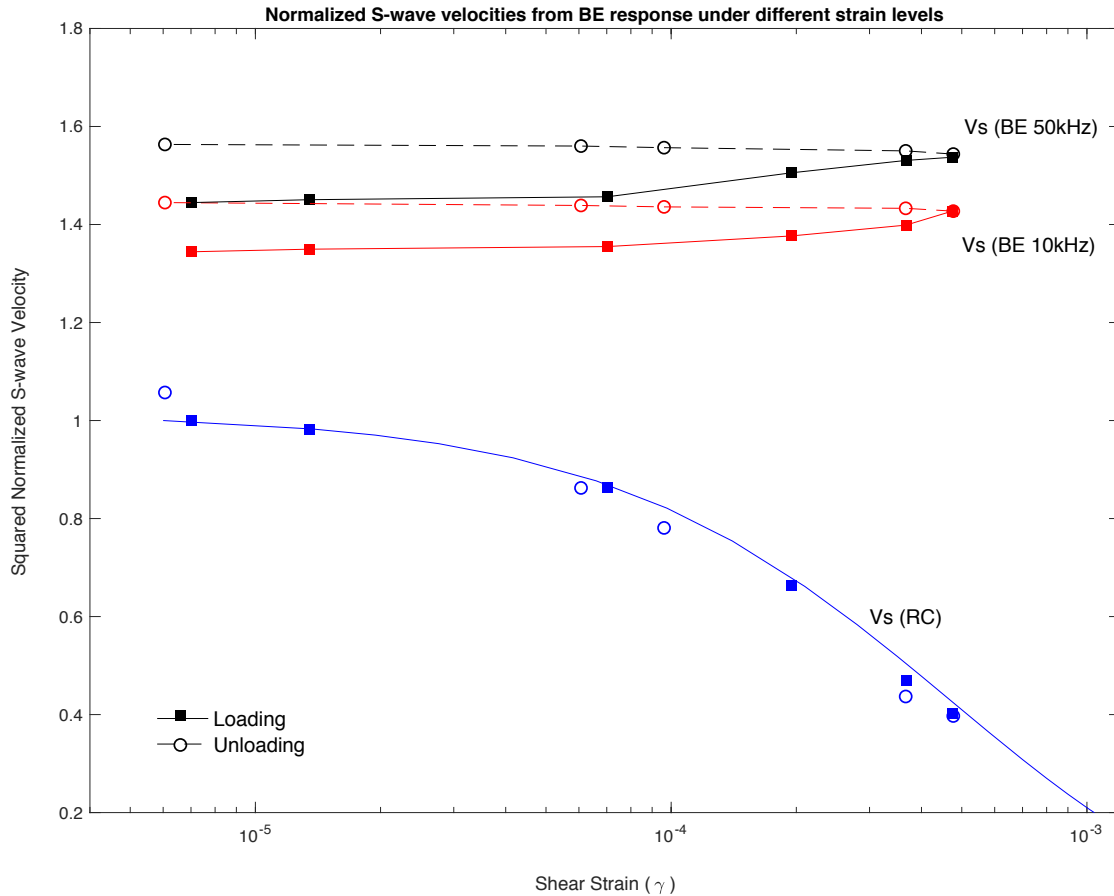


Fig. 9-29: Normalized shear wave velocities at different strain levels using BE and RC tests (sine pulse input frequencies: 10 and 50 kHz)

As it can be seen, for the loading and unloading process at different strain levels and with different input frequencies, the results of $v_s^2_{\{norm.\}}$ are basically the same, which means there is no relevant effect of the strain level in the assessment of v_s values from the BE test.

9.6 Transfer function calculations

In Fig. 9-3 the different transfer functions in a bender element test were presented as they were identified by Irfan (2019). The usual BE tests performed in stages 1 and 3 allow the calculation of the general transfer function H_{soil} . In order to compute the other transfer functions (H_{Tx} , H_{Rx} , H_0), it is necessary to get their respective inputs and outputs, which are identified in Table 9-4.

Table 9-4. Identification of input and output for all the transfer functions in a BE test

<i>Transfer Function</i>	<i>Input</i>	<i>Output</i>
H_{soil}	Electric pulse (sine pulse) [V]	Electric response signal [V]
H_{Tx}	Electric pulse (sine pulse) [V]	Displacement [nm]
H_{Rx}	Displacement [nm]	Displacement [nm]
H_0	Displacement [nm]	Electric response signal [V]

9.6.1 Transfer function for the whole BE system (H_{soil})

Fig. 9-30 shows the input and output signals in the BE test obtained in the stage 3 of the experimental procedure. The input was a sine pulse with frequency of 10 kHz.

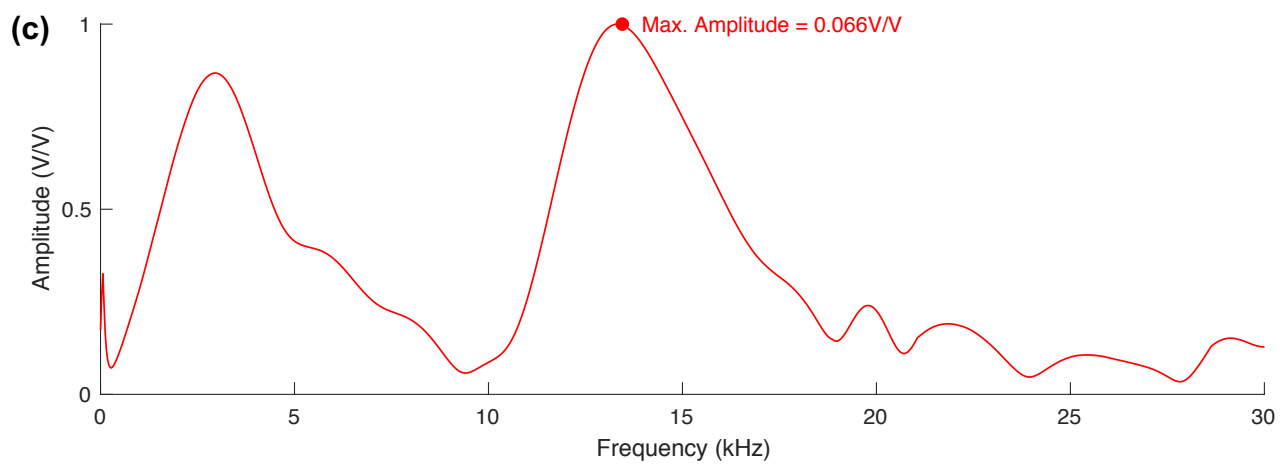
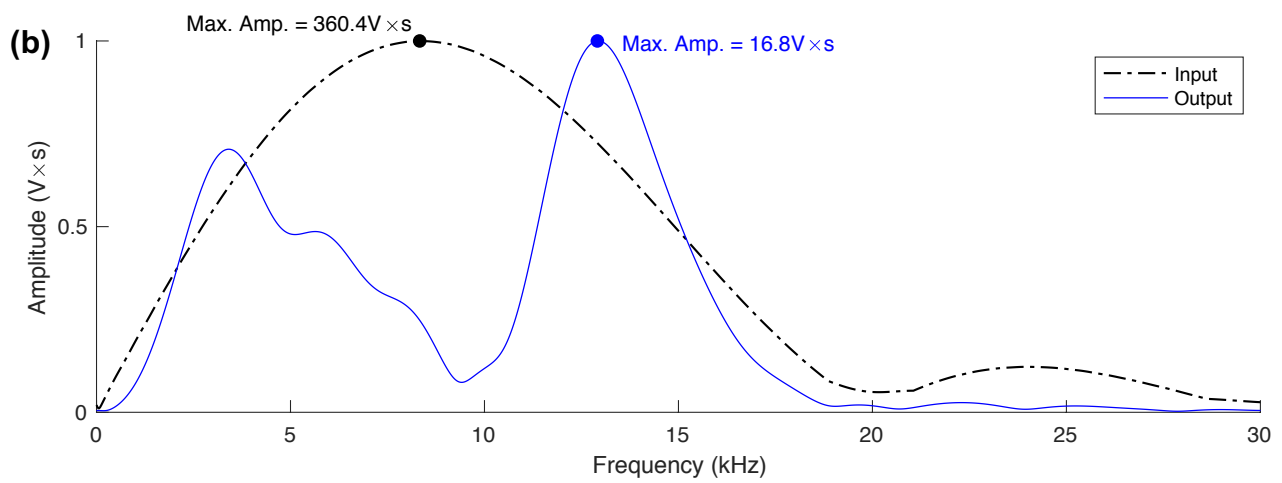
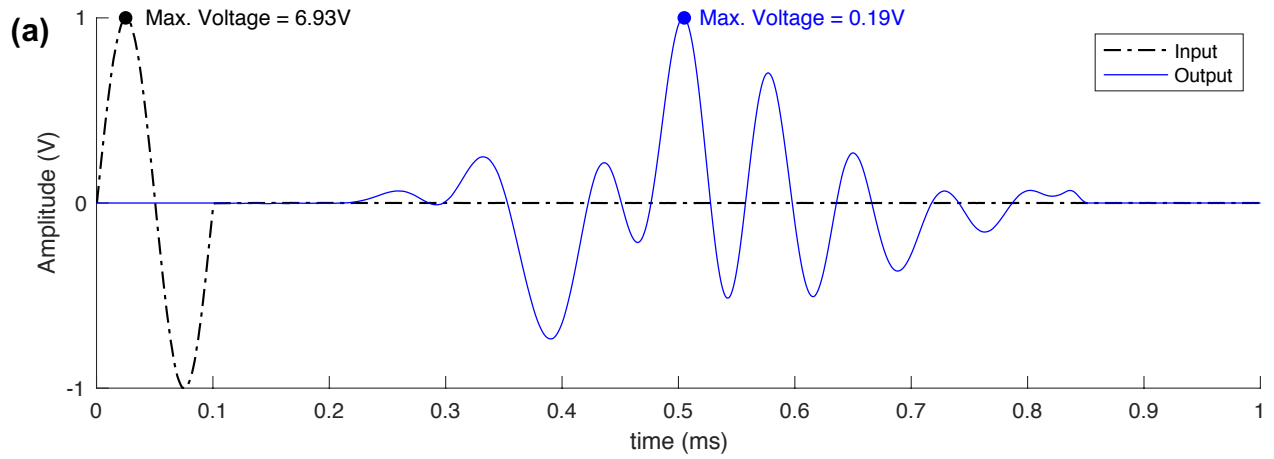


Fig. 9-30: Transfer function H_{soil}

9.6.2 Transfer function for the BE transmitter (H_{Tx})

Taken advantage of the results obtained in the second stage of the experimental procedure, in which the BE transmitter was characterized using a laser vibrometer, now is possible to calculate the transfer function. In this case the input a sine pulse as it is presented in Fig. 9-31, while the for the output there are two options: first, to consider vertical displacements on top of the BE transmitter; second, to use the horizontal displacements on the top edge of the BE, or at any other height with respect to the BE base (see Fig. 9-32 and Fig. 9-33).

For the calculation of the transfer function only the average vertical and horizontal displacements on top of the BE transmitter were considered for the case when it was in contact with air. The results of those calculations are presented in Fig. 9-34 for horizontal displacements and Fig. 9-35 for vertical displacements.

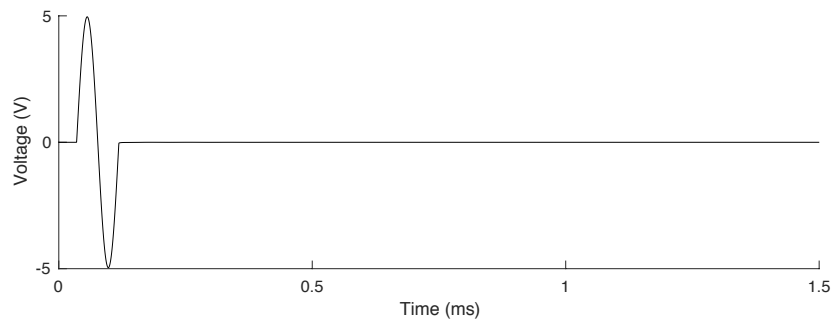


Fig. 9-31: Sine 12 kHz: Input signal to measure horizontal and vertical displacements

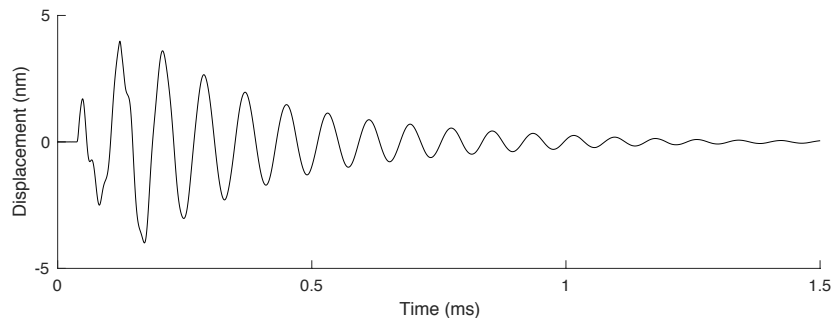


Fig. 9-32: Average vertical displacement on top edge of the BE, the input was a sine pulse at 12 kHz.

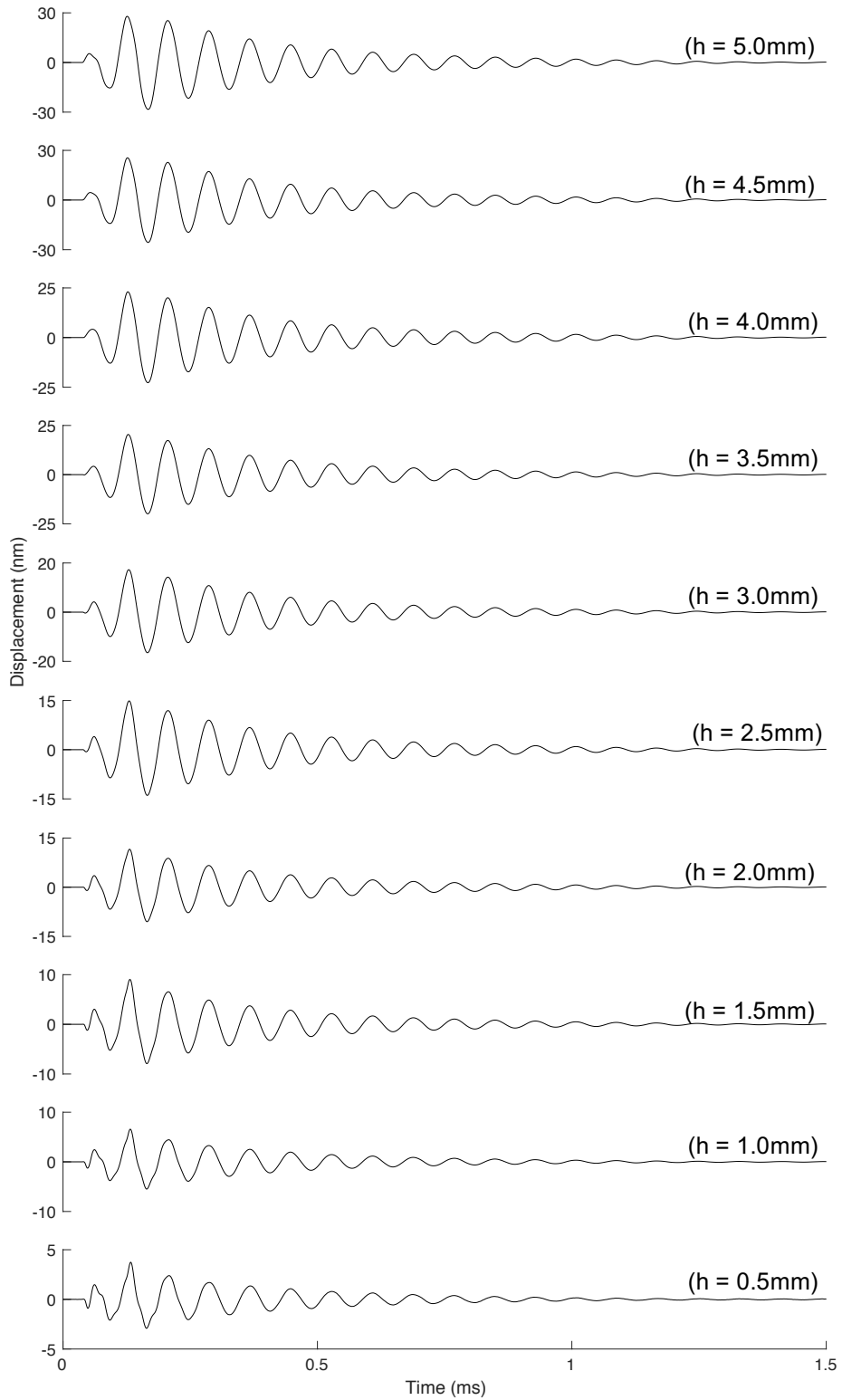


Fig. 9-33: Average signals of horizontal displacement at different heights from the base of the BE (input was a sine pulse at 12 kHz), measurements on air.

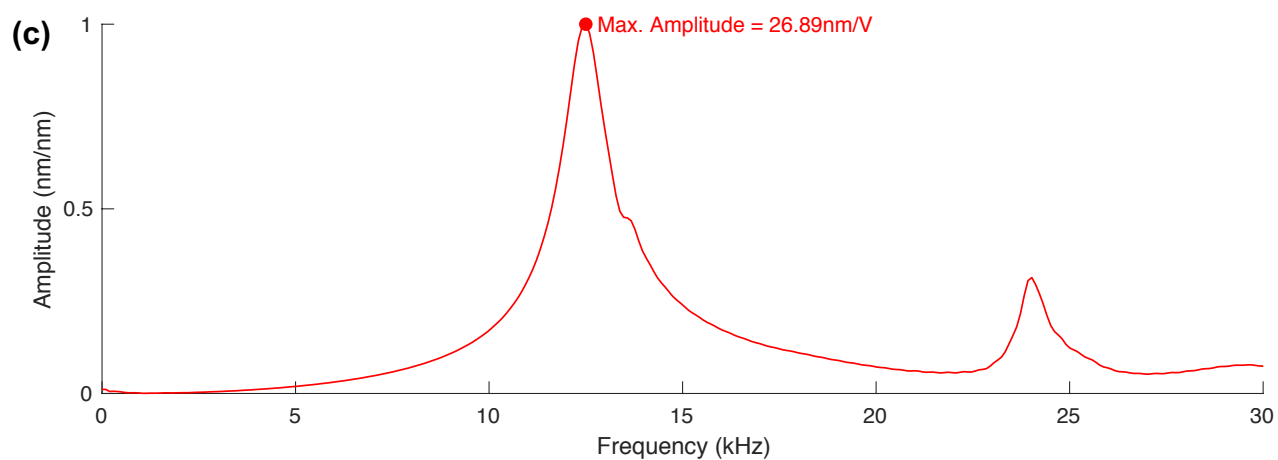
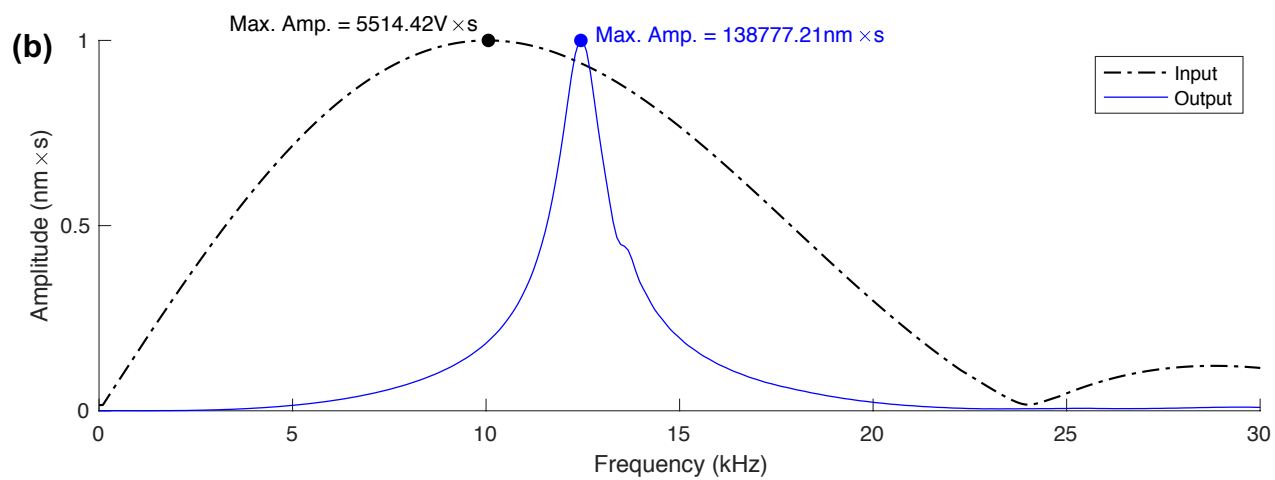
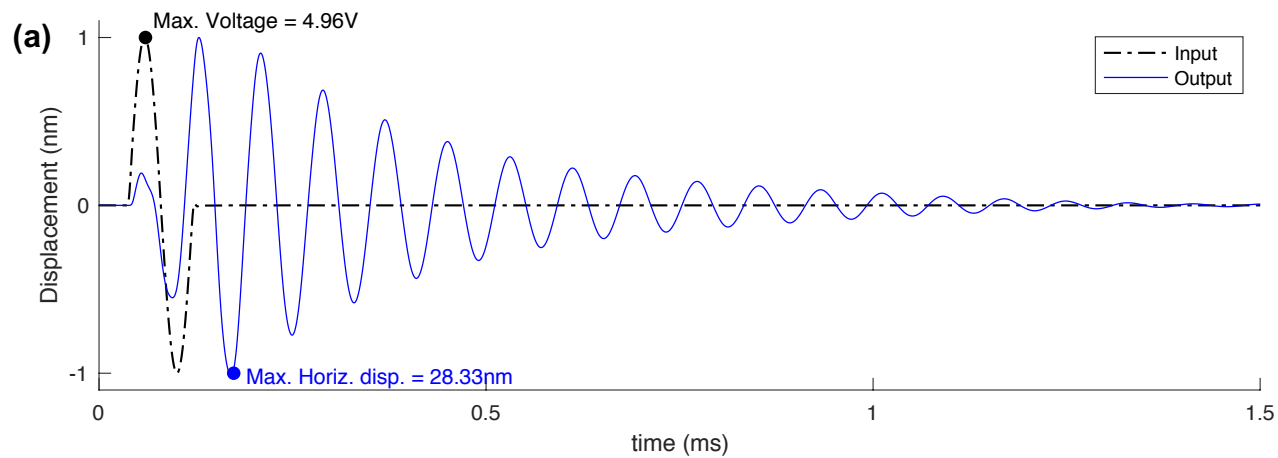


Fig. 9-34: Transfer function H_{Tx} (output was the horizontal displacements signal)

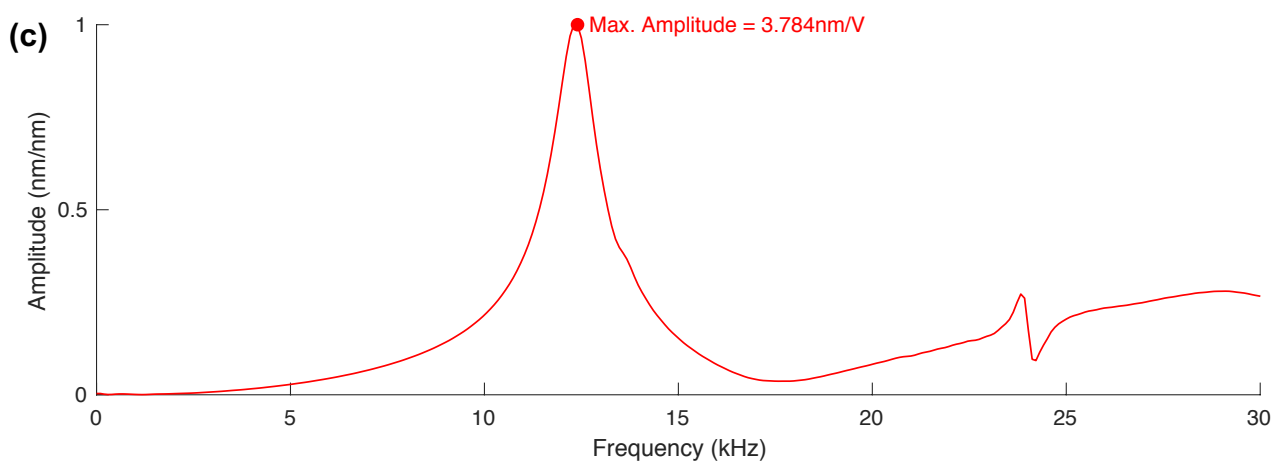
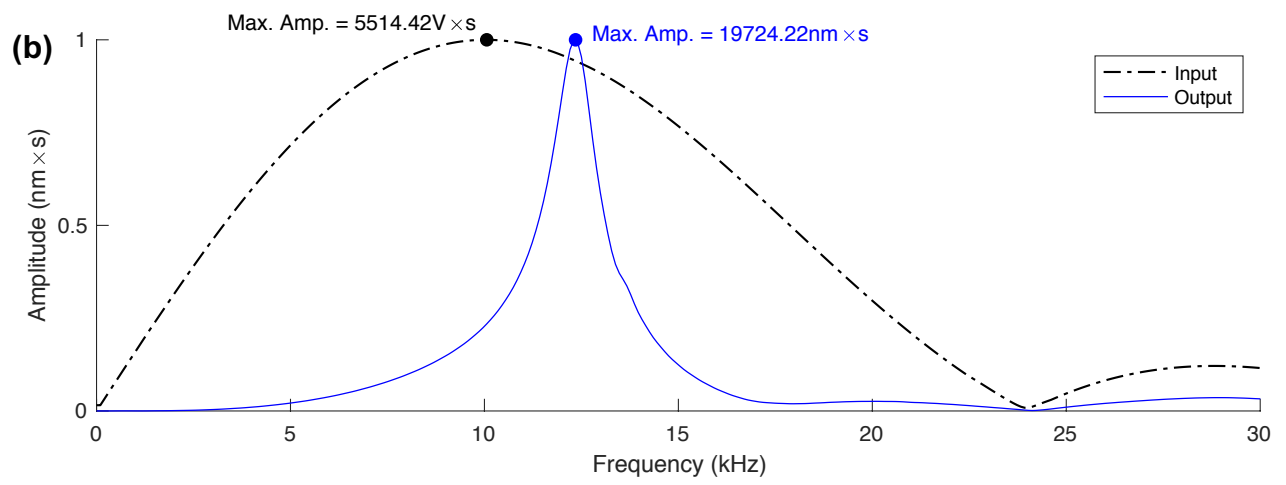
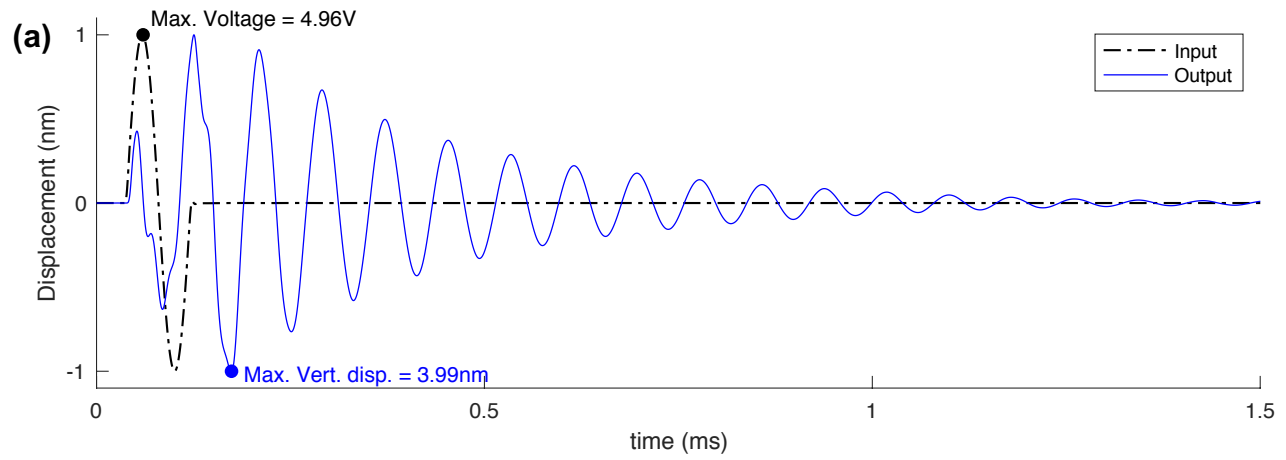


Fig. 9-35: Transfer function H_{Tx} (output was the vertical displacements signal)

9.6.3 Transfer function for the BE receiver (H_{Rx})

Irfan (2019) reported the measurement of horizontal displacements in a BE transmitter inside a transparent soil y under confinement. However, there is still no practical way of reading displacements in the BE receiver, mainly due to the complexity of the setup required in the lab to ensure the laser reading under confinement. As a first approach to the calculation of the transfer function for the receiver, a preliminary numerical model was built in order to simulate the wave propagation problem corresponding to the BE test.

Table 9-5 presents a summary of the properties of the fused silica used for the reconstitution of the sample for the BE test in the stage 3 of the experimental procedure. These properties were used for the numerical model, so that it reproduces the same sample tested in the BE and RC.

Table 9-5. Properties of reconstituted sample of fused quartz

Sample property	Value
Height	$H = 0.142$ m
Diameter	$\varnothing = 0.067$ m
Mass density	$\rho = 1262.12$ Kg/m ³
Confinement pressure	$\sigma_0 = 300$ kPa
v_p from BE test at 10kHz	$v_{p-BE} = 633.7$ m/s
v_s from BE test at 10kHz	$v_{s-BE} = 370.4$ m/s
v_s from RC test at 300 kPa	$v_{s-RC} = 318.1$ m/s
Alpha parameter	$\alpha = \frac{V_p}{V_s} = \sqrt{\frac{2(1-\nu)}{(1-2\nu)}} = 1.71$
Poisson's ratio	$\nu = \frac{\alpha^2 - 2}{2(\alpha^2 - 1)} = 0.24$
Elastic modulus	$E_{BE} = 429.62$ MPa
Bulk modulus	$K_{BE} = 275.96$ MPa
Shear modulus	$G_{BE} = 173.16$ MPa

In order to define the damping ratio to use in the numerical model, the logarithmic decrement method was used in the input signals. The points selected for the procedure, along with the results are displayed in Fig. 9-36. Considering these results, a value of 4% was used as damping ratio for the numerical model.

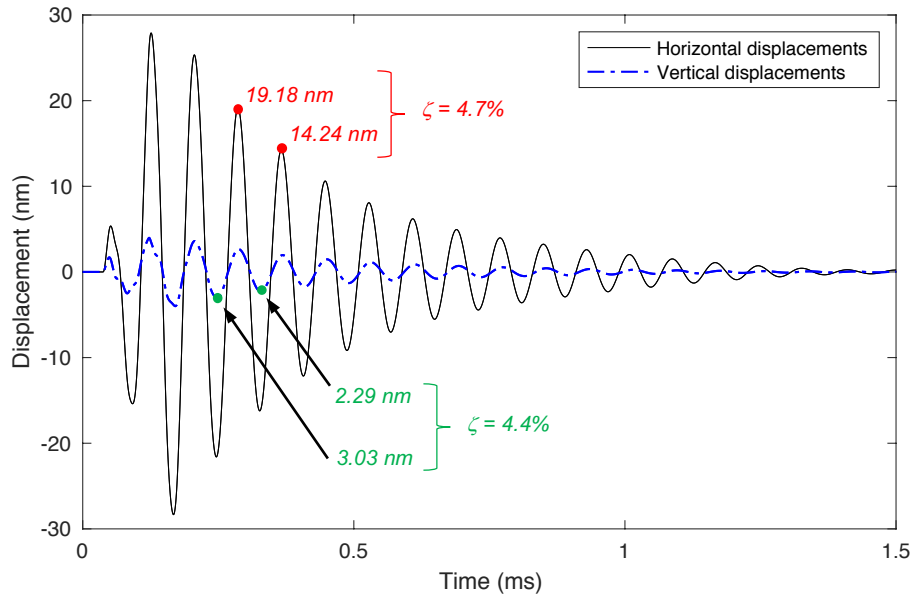


Fig. 9-36: Damping ratios calculation for BE horizontal and vertical displacements (input was a sine pulse at 12 kHz), measurements of air.

The software used for the numerical simulation was FLACTM, the same finite differences program used in previous chapters. The boundary conditions used are quite simple, the top and bottom border of the model are considered to be restricted in their vertical and horizontal movement, as it actually happens in the BE test in the laboratory. The rest of the borders (i.e. the vertical ones) were free boundaries.

Fig. 9-37 (Screenshot at 0.200ms) and Fig. 9-38 (Screenshot at 0.465ms) show partial results of the numerical simulation of BE test (fused quartz sample). For this numerical model the horizontal and vertical displacements measured with the laser for BE transmitter characterization (as they were presented in previous section) were converted to force and used as input forces at different heights in the BE transmitter (see the blue arrows). A video for the full simulation of the BE test can be accessed in this link: <https://youtu.be/cGZr4oMAuGo>.

Fig. 9-39 and Fig. 9-40 show the signals obtained in the numerical simulation for the horizontal and vertical displacements on top of the BE receiver.

Dynamic Time 2.0000E-04
Density
■ 1.200E+03
■ 1.262E+03
Velocity vectors
scaled to max = 5.000E-02
max vector = 1.147E-02
Boundary plot
Net Applied Forces
max vector = 3.619E+00

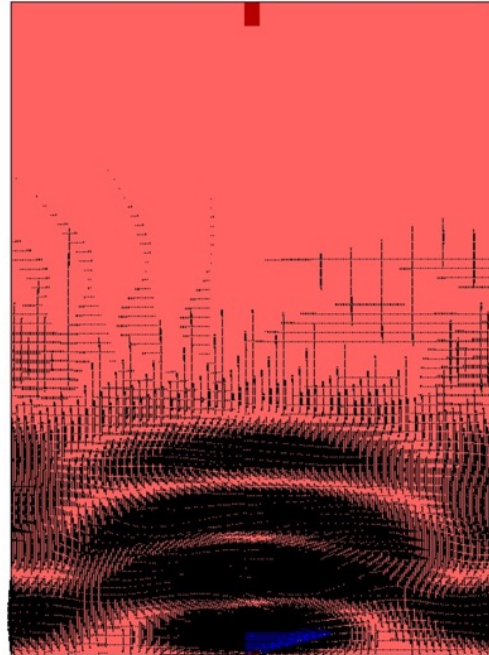


Fig. 9-37: Screenshot at 0.200ms: numerical simulation of BE test (fused quartz reconstituted sample).

Dynamic Time 4.6500E-04
Density
■ 1.200E+03
■ 1.262E+03
Velocity vectors
scaled to max = 5.000E-02
max vector = 3.550E-03
Boundary plot
Net Applied Forces
max vector = 5.129E+00

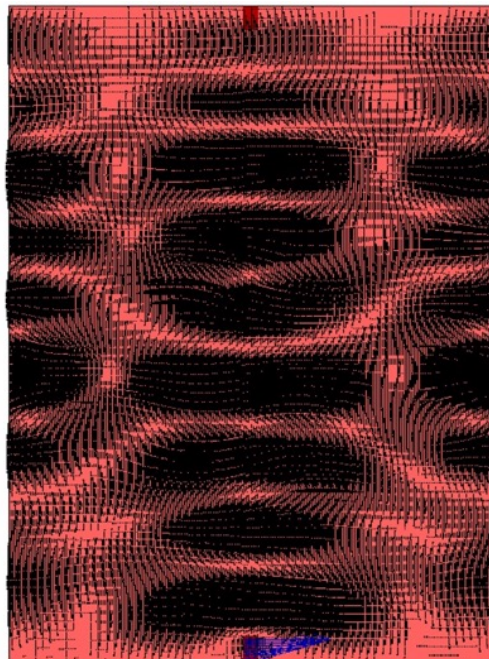


Fig. 9-38: Screenshot at 0.465ms: numerical simulation of BE test (fused quartz reconstituted sample).

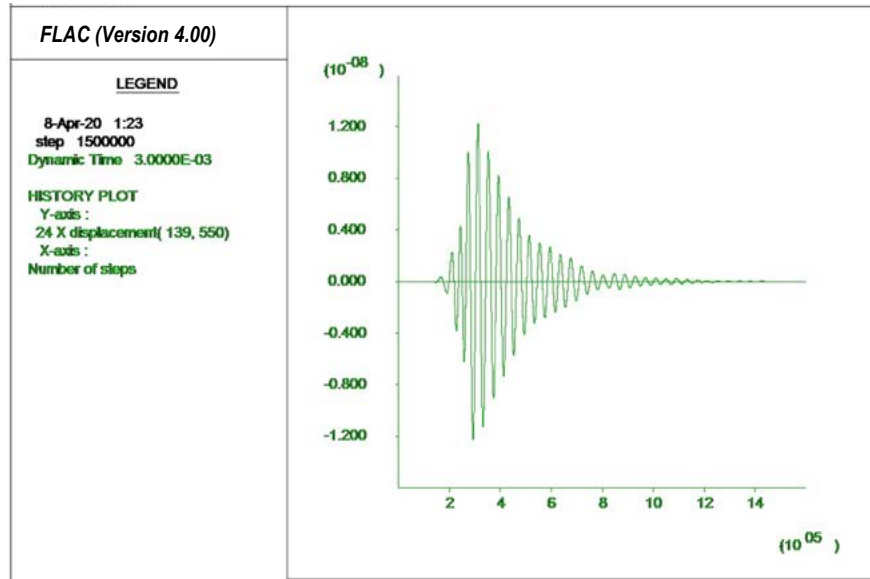


Fig. 9-39: Numerical simulation: Horizontal displacements on top of the BE receiver.

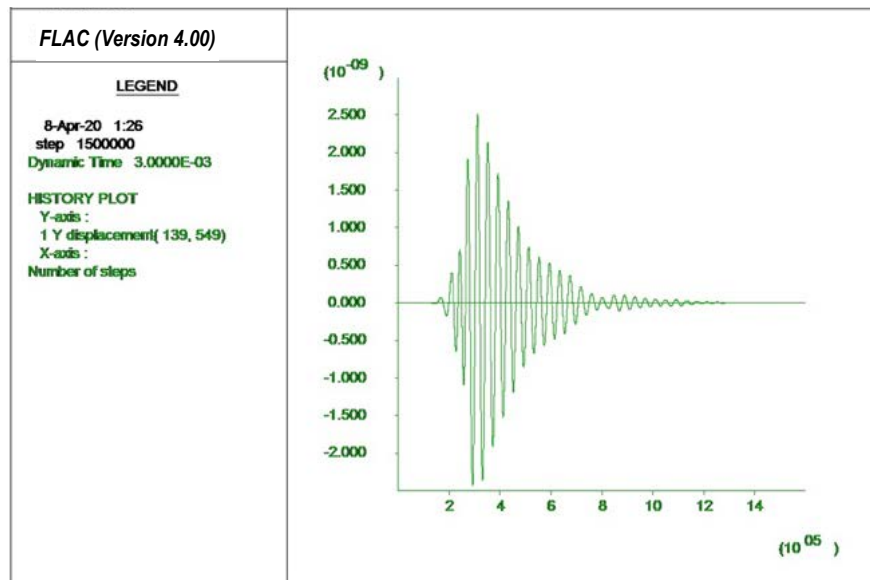


Fig. 9-40: Numerical simulation: Vertical displacements on top of the BE receiver.

Next, the calculations of the transfer functions for the BE receiver are presented. First, for the case of the horizontal displacements considered as the output of the system (Fig. 9-41), and second, for the case of the vertical displacements (see Fig. 9-42)

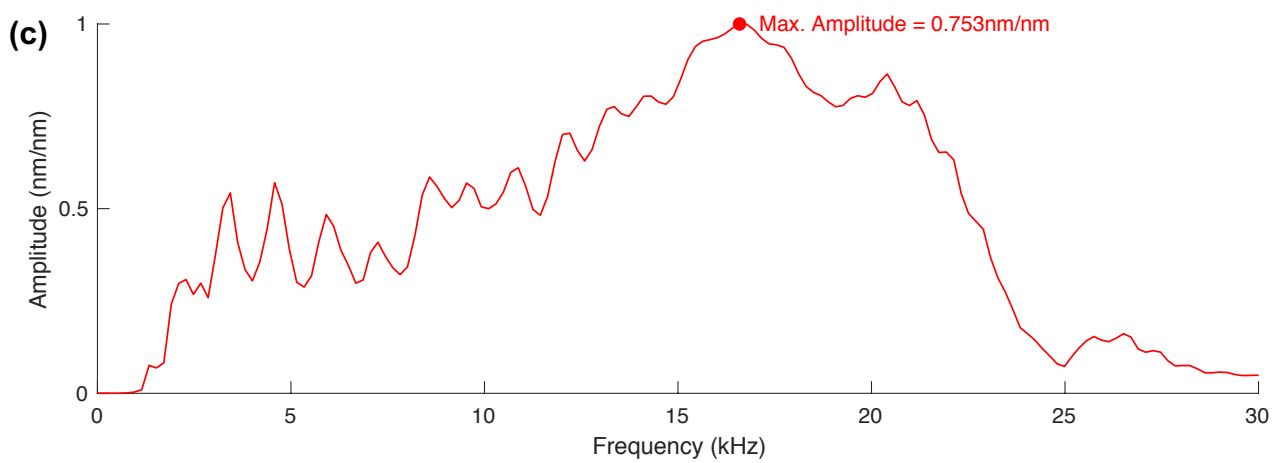
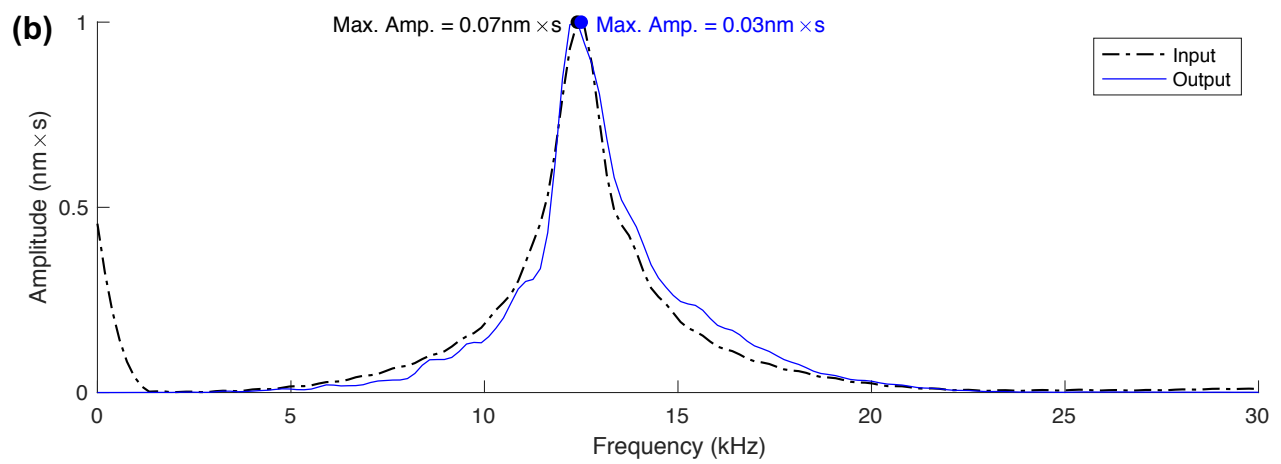
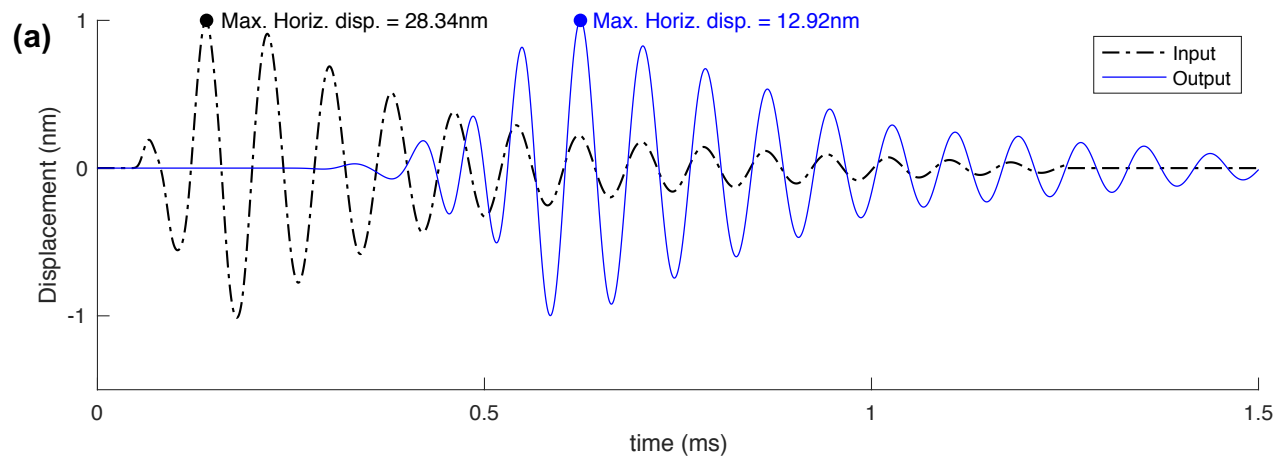


Fig. 9-41: Transfer function H_{Rx} (output was the horizontal displacements signal)

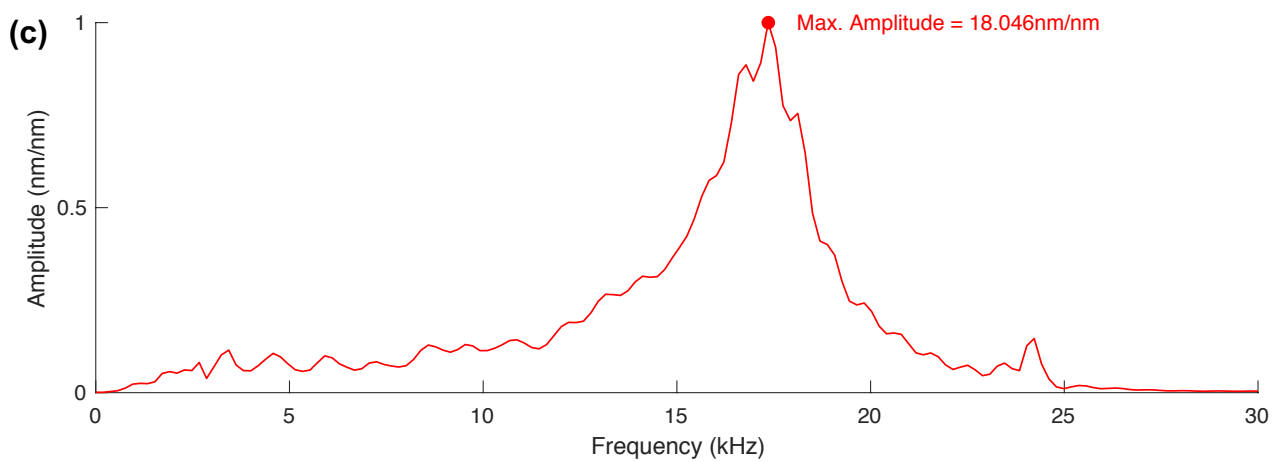
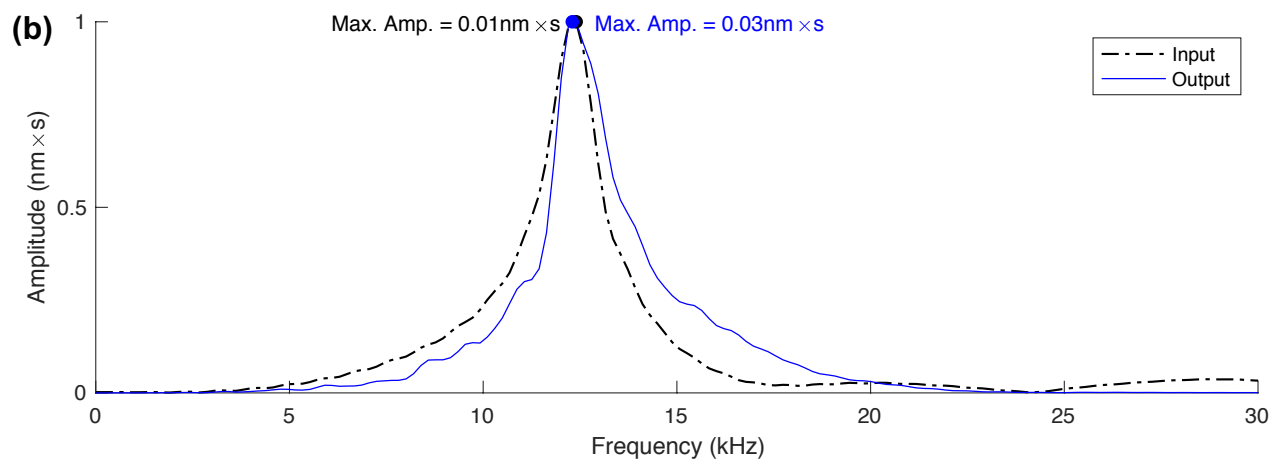
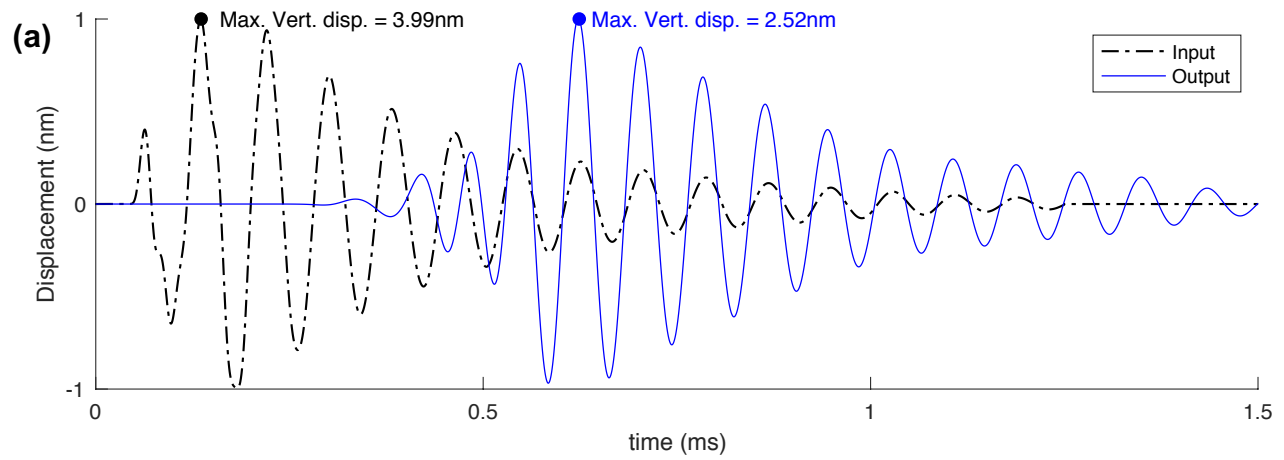


Fig. 9-42: Transfer function H_{Rx} (output was the vertical displacements signal)

From these transfer functions is clear that H_{soil} exhibits the same shape as the Fourier transform of the output signal. In the frequency spectrums, there are two peaks, the first one is associated with the compressional and the shear wave fronts arriving at the BE receiver, and the second peak is associated with the resonant frequency of the BE itself, which is close to 12.9 kHz.

The idea of breaking down the system into subsystems, lead to a more detailed analysis. Thus, it is possible to understand the intermediate responses by analyzing the intermediate transfer functions. If the subsystem are considered to be connected in series, the general transfer function can be understood as the convolution of the subsystems' transfer functions, as it follows:

$$H_{soil} = H_{Tx} * H_{Rx} * H_0 \quad (9-9)$$

$$\frac{Y_0(\omega)}{X(\omega)} = \frac{Y_1(\omega)}{X(\omega)} * \frac{Y_2(\omega)}{Y_1(\omega)} * \frac{Y_0(\omega)}{Y_2(\omega)} \quad (9-10)$$

In Fig. 9-34 for the calculation of the transfer function (H_{Tx}), which corresponds to the BE transmitter, it is clear that the Fourier transform of the output has a peak around 12.5 kHz, very close to the 12.9kHz peak identified for the general transfer function (H_{soil}). The difference in the tests conditions between the two aforementioned transfer functions is the confinement pressure of 300kPa that was applied to the sample in the tests used for the calculation of the transfer function (H_{soil}). Thus, the change in the resonant frequency of the BE transmitter is due to that confinement pressure.

In Fig. 9-42 it is clear that for the calculation of the transfer function (H_{Rx}), which corresponds to the BE receiver, both Fourier transforms (i.e. input and output) have the same peak around 12.5 kHz, which was the frequency identified in the transfer function (H_{Tx}). This means, when the waves propagate inside the soil, from the transmitter (T_X) to the receiver (R_X), there is no effect in the resonant frequency of the bender element transducers. If this is true, what is expected in the receiver is that its resonant frequency is very close to the resonant frequency when the receiver is tested in contact with air.

However, the real response of the BE receiver must be evaluated when it is under confinement pressure, which can be done with the procedure reported by Irfan (2019).

9.7 Conclusions

The conclusions here are presented stage by stage, as the chapter was developed:

Stage 1

- This research confirmed that the input frequency in a BE test plays an important role in the detection of P-wave arrivals.
- High frequencies (i.e. 25 – 75 kHz) demonstrated to be more effective to identify P-wave arrivals, while low frequencies (i.e. 2 – 8 kHz) seem to be more adequate for the detection of S-wave arrivals.
- All of these measurements were obtained with a single BE transducer, simply by adjusting the input wave frequencies. Which means that without any modification to the wiring.

Stage 2

- The results obtained in these laser measurement tests to characterize de BE transmitter, also demonstrated how the input frequency strongly affects the BE movement.
- These results also explain why it is possible to identify the P-wave arrival when high frequencies are used in the BE test.
- As the high frequencies tend to excite more the third mode, rather than the first or the second, more energy is oriented in vertical direction creating a stronger P-wave front, which allows its detection in the receiver BE.
- It is important to consider that horizontal displacements are almost one order of magnitude higher than vertical displacements on top of the BE transmitter.

Stage 3

- In the frequency spectrums of the BE results obtained when the tests were performed with different input frequencies, it is clear the presence of two peaks.

Each of these peaks is associated with different characteristics of the BE-soil system; in the case of the first peak, it is associated with the compressional and the shear wave fronts arriving at the BE receiver; on the other hand, the second peak is associated with the resonant frequency of the BE itself.

- In the frequency spectrums of the BE results obtained when the tests were performed under different strain levels, it was found there is almost no effect of the strain level when the RC system was off. However, when the RC system is turned on, it was found the strain level affects the S-wave arrivals showing shorter arrivals for the test at low shear strain ($\gamma = 3.30\text{E-}06$) and larger values of arrival time for the test at high shear strain ($\gamma = 3.70\text{E-}04$).

Stage 4: Transfer function calculations

- The general transfer function H_{soil} exhibits two peaks, the first one is associated with the compressional and the shear wave fronts arriving at the BE receiver, and the second peak is associated with the resonant frequency of the BE itself, which is close to 12.9 kHz.
- In the transfer function (H_{Tx}), which corresponds to the BE transmitter, it is clear that the Fourier transform of the output has a peak around 12.5 kHz, very close to the 12.9kHz peak identified for the general transfer function (H_{soil}). The difference is expected to be associated to the confinement pressure in the tests used to calculate (H_{soil}). This result is preliminary and just indicative of what is expected when the BE transmitter is calibrated under confinement.
- In the transfer function (H_{Rx}), which corresponds to the BE receiver, both Fourier transforms (i.e. input and output) have the same peak around 12.5 kHz, which was the frequency identified in the transfer function (H_{Tx}). This means, when the waves propagate inside the soil sample, from the transmitter (T_x) to the receiver (R_x), there is no effect in the resonant frequency of the bender element transducers.

10 Conclusions

All around the world, construction codes include requirements related to the dynamic site classification for seismic design purposes. In order to properly classify a construction site, the quantification of the dynamic properties of geomaterials is a fundamental task that can be addressed both with field and laboratory tests. However, in the current practice, there are gaps that are not yet covered by the theory supporting the laboratory and field testing.

Examples of those gaps are the lack of understanding of the effect of the impedance ratio between the top layers of the media, the effect of the frequency content of the input source used in the tests, as well as other issues related to the testing scale. The combination of these issues may lead to an incorrect site classification, which will necessarily affect the seismic designs.

The research presented in this thesis addressed the three gaps identified in the previous paragraph in order to improve the characterization of geomaterials using methods based on the propagation of mechanical waves. The results are relevant because they have practical applicability, not just for research purposes but also for practitioners in the field.

Generally speaking, the results of the thesis were satisfactory because they showed the research objectives were achieved. First, the effects of the impedance ratios between top layers on the propagation of surface waves were evaluated using calibrated numerical models to establish limitations in the applicability of the MASW test. Second, a new methodology for the characterization of the excitation source in seismic wave testing was presented and proved to work using laboratory, field, and numerical simulation results. Third, the participation of P-waves in the response of typical bender element testing was demonstrated by studying the effect of frequency in the excitation of different vibration modes.

10.1 Effects of impedance ratio among layers on wave propagation results

The results from the study of wave propagation on a horizontally layered medium led to the conclusions that the impedance ratio has an important effect on the results of the MASW tests. First, for impedance ratio between the two top layers with values lower than 0.5, it was found that the estimated value of the weighted average shear wave velocity is highly underestimated. Secondly, the combination of high frequency in the input force, and low impedance ratio led to an important reduction in the number of layers that can be resolved in a mathematical inversion process of the dispersion curve obtained from the MASW test.

Impedance ratio between the two top layers with values lower than 0.5 showed reductions in the estimated value of the weighted average shear wave velocity. For instance, for impedance ratio values of 0.4 a reduction up to 20% in the average shear wave velocity were identified. Similarly, for impedance ratio values of 0.3 that reduction could be even higher up to 40% in the average shear wave velocity. Finally, for impedance ratio values of 0.2 the reduction in the average shear wave velocity could led to get values as low as 45% of the theoretical expected shear wave value.

Thus, from these results a straight forward conclusion is drawn: the MASW test is not applicable to characterize sites for which the impedance ratio between the top two layers is less than 0.5. A proper selection of the frequency must be performed in order to facilitate the method in the resolution of layers from the inversion of the dispersion curve.

A final recommendation for practitioners in the field is to evaluate the effect of the spacing between channels on the results of dispersion curves. For the model considered in this numerical study a spacing of 1.0 meter between channels leads to the lowest values of root mean square error (RMSE), however this spacing must be optimized in the field for each specific case.

10.2 Effects of frequency and medium approach on wave propagation results

The results of numerical simulations considering different approaches to characterize the medium (i.e. homogeneous, layered, spatially variable), as well as considering different

frequencies in the input force, led to the conclusion that the input frequency in field seismic test like MASW has an effect in the arrivals of the shear waves, no matter how the medium is approached (i.e. homogeneous, layered, or spatially variable).

In average, for the input frequency of 160 Hz, the flight time of the shear wave is identified to varies between 0.038 and 0.043 ms, which means the shear wave velocities vary between 263 and 232 m/s, respectively. For the 60 Hz that flight time was identified to varies between 0.042 and 0.045 ms, which means the shear wave velocities vary between 238 and 222 m/s, respectively. These results lead to differences between 2.1% and 11.1% in the travel time, and between 4.4% and 9.5% in the shear wave velocity. Similarly, for the frequency of 20Hz the flight time of shear waves was identified to varies between 0.046 and 0.049 ms, which means the shear wave velocities vary between 217 and 204 m/s, respectively. These differences leads to increments between 4.7% and 14.5% in the travel time, and also lead to reduction between 7.8% and 8.1% in the shear wave velocity, when the results for 20Hz are compared against the results for 60Hz. These results confirm the fact that the input frequency has an effect on the shear wave velocity values.

In addition, the use of random fields could be beneficial in order to avoid the issues that arose when a layered medium is used to propagate seismic waves. However, the unconditioned random fields are not appealing to the modeling of real soils conditions, so it is suggested to consider the conditioned random fields for geotechnical engineering purposes in problems dealing with wave propagation.

10.3 Characterization of the excitation source for field and laboratory seismic testing

The analysis of raw seismograms, both from numerical simulations and from the MASW test in the field and in the laboratory, is very useful for the determination of the body wave velocities and for the estimation of the length of the near field. It was found that inside the near field the peaks corresponding to the S-waves in the signals at different locations, do not follow a straight line, which allows the determination of the near field extension just by determining the location where that alignment of points starts.

It is important to highlight the fact that the wave velocities computed from the arrivals and distances in the raw seismograms for the MASW test, showed that the input frequency used in the test has an effect on the velocity obtained. Furthermore, the velocity increases with the increase in frequency as predicted from Fourier analysis because high frequencies are required to represent sharp arrivals in time domain. Thus, the higher the input frequency, the higher the velocity obtained. This fact aligns very well with the results obtained from the UPV test in a sample of cemented sand, for which the very same phenomena was observed.

The method proposed to perform the excitation source inversion was successfully implemented both in the field and in the laboratory. By using the method at different scales and in different materials, it was demonstrated the versatility of the method to get the inversion of the excitation source in a seismic wave propagation test. Nonetheless, further research is required in order to improve the process, for example in defining what should be used as the initial force to optimize the iteration process.

From the applicability of the proposed method in the field, three iterations were needed to obtain an estimation of a force with RMSE value less than 1% (7.33N) of the maximum amplitude in the force (800 N).

A very important issue to highlight here, is the fact that the new methodology proposed for the inversion of the excitation source is relevant for practitioners and researchers because it will allow a proper calibration of numerical models to run parametric studies and to extend the benefits of real field or laboratory tests at a very low extra cost.

In the laboratory the responses obtained from the numerical simulation using the input force obtained in the inversion process works very well inside the near field zone. However, it does not work well for the point beyond the near field. This means that one inverted source is not able to resolve the displacements in the whole alignment, so, different sources must be inverted to replicate the system's response inside the near field and outside it.

The cross-correlation analysis between the input obtained from the inversion of the excitation source, and the output vertical displacements in the real sandbox, were useful to locate the void.

10.4 Study of participation of P-waves in the results from BE testing

This research confirmed that the input frequency in a BE test plays an important role in the detection of P-wave arrivals. High frequencies (i.e. 25 – 75 kHz) demonstrated to be more effective to identify P-wave arrivals, while low frequencies (i.e. 2 – 8 kHz) seem to be more adequate for the detection of S-wave arrivals. All of these measurements were obtained with a single BE transducer, simply by adjusting the input wave frequencies. Which means that without any modification to the wiring.

The characterization of the BE transmitter was possible by using a high-frequency laser vibrometer. The vibration modes separation was also performed to demonstrate how the input frequency strongly affects the BE movement. These results also explain why it is possible to identify the P-wave arrival when high frequencies are used in the BE test. As the high frequencies tend to excite more the third mode, rather than the first or the second, more energy is oriented in vertical direction creating a stronger P-wave front, which allows its detection in the receiver BE.

In the frequency spectrums of the BE results obtained when the tests were performed with different input frequencies, it is clear the presence of two peaks. Each of these peaks is associated with different characteristics of the BE-soil system; in the case of the first peak, it is associated with the compressional and the shear wave fronts arriving at the BE receiver; on the other hand, the second peak is associated with the resonant frequency of the BE itself.

In the frequency spectrums of the BE results obtained when the tests were performed under different strain levels, it was found there is almost no effect of the strain level when the RC system was off. However, when the RC system is turned on, it was found the strain level affects the S-wave arrivals showing shorter arrivals for the test at

low shear strain ($\gamma = 3.30\text{E-}06$) and larger values of arrival time for the test at high shear strain ($\gamma = 3.70\text{E-}04$).

The general transfer function H_{soil} exhibits two peaks, the first one is associated with the compressional and the shear wave fronts arriving at the BE receiver, and the second peak is associated with the resonant frequency of the BE itself, which is close to 12.9 kHz. In the transfer function (H_{Tx}), which corresponds to the BE transmitter, it is clear that the Fourier transform of the output has a peak around 12.5 kHz, very close to the 12.9kHz peak identified for the general transfer function (H_{soil}). The difference is expected to be associated to the confinement pressure in the tests used to calculate (H_{soil}). This result is preliminary and just indicative of what is expected when the BE transmitter is calibrated under confinement.

In the transfer function (H_{Rx}), which corresponds to the BE receiver, both Fourier transforms (i.e. input and output) have the same peak around 12.5 kHz, which was the frequency identified in the transfer function (H_{Tx}). This means, when the waves propagate inside the soil sample, from the transmitter (T_X) to the receiver (R_X), there is no effect in the resonant frequency of the bender element transducers.

10.5 Main contributions and their implications in the construction industry

The construction industry is a very dynamic one. It almost never has the time to perform research while the building process is in progress, that is why that industry is grateful to all the contributions done by researchers interested in improving the current practice.

To ensure any infrastructure meets the requirements of the construction code, the builder engineers trust the design engineers, who at their time do their best to design in such a way that infrastructure does not fail when a seismic event hits the construction site. However, all those efforts may end being in vain if the knowledge base for the designs is not correct.

10.5.1 MASW test: impedance ratio effect for the determination of (v_{S-30})

Through numerical simulations, this research demonstrated how the use of the MASW field tests to characterize a site exhibiting materials with an important difference in acoustic impedance, may lead to incorrect results of the parameter (v_{S-30}). This result is a warning for field practitioners who are used to blindly perform that test to characterize any site without considering the impedance ratio effect.

Now, when proposing the use of the MASW technique, practitioners must consider performing the test using different frequency contents in the excitation source by following next recommendations:

1. First, the use of a high frequency is recommended in order to capture the response of the shallower layer only and to calculate the shear wave velocity for the first meter in depth (v_{S-1}). The use of small hammers and short impacts is recommended to ensure the input force is rich in high frequencies.
2. Second, a lower frequency must be used to progressively penetrate to the next layer and determine the (v_{S-2}). In this case the use of a bigger hammers may help in generating lower frequencies.
3. Third, the impedance ratio calculation must be done in order to establish how feasible is to continue with the test for that specific site.
4. If the impedance ratio, as defined in this thesis, is lower than 0.5, the MASW may not be the best technique to characterize the dynamic properties of the site, specifically the (v_{S-30}).

By following this process, practitioner will be able to analyze the results as the MASW test progresses in its penetration depth and to make the decision if the results are going to be reliable or not. At this point, it is important to highlight the fact that ensuring the right frequency content in the input source is not a mechanical process and it requires for the practitioner to be educated about how the concept of wavelength for different materials. It is key to keep in mind that for the same kind of excitation source different wavelengths will be generated depending on the stiffness and density of the materials being tested.

10.5.2 sCPTU test: source characterization

For the sCPTU test in the field, a new methodology for the characterization of the excitation source in seismic wave testing was presented and proved to work using laboratory, field, and numerical simulation results. The advantages of this methodology are related to the characterization of the input source in the time and frequency domain. Once the source is properly characterized, many options arise for further analysis, like the frequency effect on the results obtained for the shear wave velocity profile.

The following recommendations may help laboratory technicians in taking advantage of the proposed methodology:

1. First, the sCPTU test must be performed in the field being careful about the precision in-depth location of the probe, as well as about the distance between the metallic beam being hit and the point where the probe is getting introduced.
2. Second, the medium being tested must be carefully analyzed in order to properly identify significant geometrical characteristics that could impact the wave propagation process.
3. Third, a numerical model representing the physical medium must be built and calibrated in order to ensure it is a proper model to simulate wave propagation.
4. Fourth, a set of numerical simulations must be run using different mean frequencies to cover a wide range of possible frequencies used in the field test. The Ricker wavelet seems to work well to define the shape of the input force in the numerical models.
5. Fifth, the data obtained from the field must be analyzed in the time and the frequency domain and compared to the results from the numerical models.
6. Sixth, the inversion of the input source could be obtained by using the transfer function technique, which will allow to properly define the input force in the time and the frequency domain.

Once the input force is obtained, many possible analyses could be performed numerically by using the geometry representing the field conditions and the input force inverted. This thesis presented the study of the effect of frequency as an example of the possibilities that the new methodology allows.

10.5.3 BE test: source characterization

In the case of the BE test, this research demonstrated how the confinement pressure and the input frequency affect the results obtained for the shear wave velocity (v_{S-1}). Furthermore, the participation of P-waves in the response of typical bender element testing was demonstrated to be more significant when the input frequency is close to the resonant frequency of the third vertical vibration mode.

The following recommendations may help laboratory technicians in taking advantage of this discovery:

1. First, the BE itself requires a calibration process using a signal analyzer to make it vibrate under a chirp signal with a wide band of frequencies.
2. Second, by using a laser vibrometer it is possible to recognize the resonance frequencies for the different vibration modes of the BE both in horizontal and vertical directions.
3. Once the BE is calibrated, it is possible to perform the test at different frequencies without any change in the wiring. The bender element must include a curve describing the change in the resonance frequency of the BE with the change in confinement pressure.
4. The results at low frequencies will allow the identification of shear waves. It is key to keep in mind that low frequencies (i.e. below 2 kHz) excite more the first mode that has its main displacement component in the horizontal direction, which is better for the generation of shear waves inside the sample.
5. The results at low frequencies will allow the identification of shear waves. Likewise, higher frequencies (i.e. above 20kHz) tend to excite more the third mode of vibration, which has an important component in the vertical direction and creates an important front of P-waves.

The threshold values for the detection of shear waves or compressional waves are proposed based on the experience gained in this research, however, the calibration process of each bender must suggest more precise values.

10.6 Future research

Some areas where further research is required are listed below:

- The results obtained for the analysis of the effect of impedance ratios must be validated in the field in order to verify the threshold value beyond which is not feasible the use of MASW tests.
- Generation of conditioned random fields to properly approach the distribution of soil properties in a real construction site needs further investigation. The correlation length is key parameter in the generation of the conditioned random field.
- The inversion process to obtain the excitation source characteristics must be performed independently for points inside and out of the elastic radius. Thus, at least one processing is necessary to characterize the energy propagation in the near field zone, and one other process to characterize the energy propagation in the elastic zone.
- The study of MASW technique and cross-correlation analysis could be improved in order to better apply the identification of gaps inside a continuous media.

References

1. AASHTO, 2007. Load and Resistance Factor Design Movable Highway Bridge Design Specifications. AASHTO.
2. Abraham, J.D., Cannia, J.C., 2011. Airborne electromagnetic surveys for 3D geological mapping.
3. Aki, K., Richards, P.G., 2002. Quantitative seismology. University Science Books.
4. Al-Eqabi, G.I., Herrmann, R.B., 1993. Ground roll: A potential tool for constraining shallow shear-wave structure. *Geophysics* 58, 713–719.
5. Ali, H., 2015. Study of Laboratory and Field Techniques to Measure Shear Wave Parameters - Frequency Effects. UWSpace.
6. Ali, H., Cascante, G., Nasser-Moghaddam, A., Harrap, R., 2013. Effect of underground cavities on surface waves: 3D-Numerical modeling.
7. Ali, H., Nasser-Moghaddam, A., Cascante, G., 2011. Use of numerical simulation for the identification of underground voids using the MASW test, in: Pan-Am CGS Geotechnical Conference. CGS, Toronto.
8. Arango, I., 1980. Ingeniería Sísmica aplicada a problemas geotécnicos. II Seminario Colombiano de Geotecnia 1.
9. ASTM D1586, 2011. Standard Test Method for Standard Penetration Test (SPT) and Split-Barrel Sampling of Soils. ASTM International.
10. ASTM D2573, 2018. Standard Test Method for Field Vane Shear Test in Saturated Fine-Grained Soils.
11. ASTM D3441, 2016. Standard Test Method for Mechanical Cone Penetration Testing of Soils. ASTM International.
12. ASTM D4719, 2020. Standard Test Methods for Prebored Pressuremeter Testing in Soils.
13. ASTM D5311, 2013. Standard Test Method for Load Controlled Cyclic Triaxial Strength of Soil. ASTM International.
14. ASTM D5777, 2018. Standard Guide for Using the Seismic Refraction Method for Subsurface Investigation.

15. ASTM D5783, 2018. Standard Guide for Use of Direct Rotary Drilling with Water-Based Drilling Fluid for Geoenvironmental Exploration and the Installation of Subsurface Water-Quality Monitoring Devices.
16. ASTM D6151, 2015. Standard Practice for Using Hollow-Stem Augers for Geotechnical Exploration and Soil Sampling.
17. ASTM D6635, 2015. Standard Test Method for Performing the Flat Plate Dilatometer.
18. ASTM D7128, 2018. Standard Guide for Using the Seismic-Reflection Method for Shallow Subsurface Investigation.
19. ASTM D7400, 2017. Standard Test Methods for Downhole Seismic Testing.
20. Avwenagha, E., Arong, T., Overare, B., Okunuwadje, S., Osokpor, J., 2014. Classification and compaction characteristics of lateritic soils of Warri, Delta State, Nigeria. *Advances in Applied Science Research* 5, 451–457.
21. Baroni, M., de Almeida, M.S.S., 2013. In situ and laboratory parameters of extremely soft organic clay deposits, in: *Geotechnical and Geophysical Site Characterization: Proceedings of the 4th International Conference on Site Characterization ISC-4*. Taylor & Francis Books Ltd, pp. 1611–1619.
22. Bates, C.R., 1989. Dynamic soil property measurements during triaxial testing. *Géotechnique* 39, 721–726.
23. Blake, R.J., Bond, L.J., 1990. Rayleigh wave scattering from surface features: wedges and down-steps. *Ultrasonics* 28, 214–228.
24. Boaga, J., Cassiani, G., Strobbia, C.L., Vignoli, G., 2013. Mode misidentification in Rayleigh waves: Ellipticity as a cause and a cure. *Geophysics* 78, EN17–EN28.
25. Boaga, J., Vignoli, G., Deiana, R., Cassiani, G., 2014. The influence of subsoil structure and acquisition parameters in MASW mode mis-identification. *Journal of Environmental and Engineering Geophysics* 19, 87–99.
26. Borchardt, R.D., 1994. The Loma Prieta, California, Earthquake of October 17, 1989: Strong Ground Motion. US Government Printing Office Washington, DC.
27. Branham, K.L., Steeples, D.W., 1988. Cavity detection using high-resolution seismic reflection methods. *Min. Eng.(Littleton, Colo.);(United States)* 40.
28. Camacho-Tauta, J.F., Cascante, G., Viana da Fonseca, A., Santos, J.A., 2015. Time and frequency domain evaluation of bender element systems. *Géotechnique* 65, 548–562.

29. Campanella, R.G., Stewart, W.P., 1992. Seismic cone analysis using digital signal processing for dynamic site characterization. *Canadian Geotechnical Journal*. <https://doi.org/10.1139/t92-052>
30. Campanella, R.G., Stewart, W.P., Roy, D., Davies, M.P., 1994. Low strain dynamic characteristics of soils with the downhole seismic piezocone penetrometer, in: *Dynamic Geotechnical Testing II*. ASTM International.
31. Cho, G.-C., Dodds, J., Santamarina, J.C., 2006. Particle shape effects on packing density, stiffness, and strength: natural and crushed sands. *Journal of geotechnical and geoenvironmental engineering* 132, 591–602.
32. Comina, C., Foti, S., Boiero, D., Socco, L.V., 2011. Reliability of VS₃₀ evaluation from surface-wave tests. *Journal of Geotechnical and Geoenvironmental engineering* 137, 579–586.
33. Cox, C., 1992. Satellite imagery, aerial photography and wetland archaeology: an interim report on an application of remote sensing to wetland archaeology: the pilot study in Cumbria, England. *World Archaeology* 24, 249–267.
34. da Fonseca, A.V., Ferreira, C., Fahey, M., 2009. A framework interpreting bender element tests, combining time-domain and frequency-domain methods. *Geotechnical Testing Journal* 32, 91–107.
35. da Fonseca, A.V., Ferreira, C., Ramos, C., Molina-Gómez, F., 2019. The geotechnical test site in the greater Lisbon area for liquefaction characterisation and sample quality control of cohesionless soils. *AIMS Geosciences* 5, 325.
36. Daubechies, I., Lu, J., Wu, H.-T., 2011. Synchrosqueezed wavelet transforms: An empirical mode decomposition-like tool. *Applied and Computational Harmonic Analysis* 30, 243–261. <https://doi.org/10.1016/j.acha.2010.08.002>
37. de Almeida, M.S.S., Marques, M.E.S., Baroni, M., 2010. Geotechnical parameters of very soft clays from CPTu.
38. Deng, Y., Zhou, A., Yu, X., Chen, Y., Zhang, D., 2019. Geomaterials in Geotechnical Engineering. *Advances in Civil Engineering* 2019, 8614305. <https://doi.org/10.1155/2019/8614305>
39. Díaz-Durán, F., Cascante, G., Pandey, M., 2018a. Numerical Investigation of Impedance Variation Effect on Surface-Waves' Propagation for Characterization of Very Soft Soils, in: *GeoEdmonton*. Edmonton, Alberta, pp. 343–344.
40. Díaz-Durán, F., Cascante, G., Pandey, M., 2018b. Effect of Input-Source Frequency Content on Results from Seismic Techniques for the Vs Profile Definition in Spatially Variable Soils. *Symposium on the Application of Geophysics to Engineering and Environmental Problems 2018*.

41. Donoghue, D., Shennan, I., 1988. The application of remote sensing to environmental archaeology. *Geoarchaeology* 3, 275–285.
42. Dorman, J., Ewing, M., Oliver, J., 1960. Study of shear-velocity distribution in the upper mantle by mantle Rayleigh waves. *Bulletin of the Seismological Society of America* 50, 87–115.
43. Dyvik, R., Madshus, C., 1985. Lab Measurements of G_m x Using Bender Elements, in: *Advances in the Art of Testing Soils under Cyclic Conditions*. ASCE, pp. 186–196.
44. Everett, M.E., 2013. *Near-surface applied geophysics*. Cambridge University Press.
45. Ewing, W.M., Jardetzky, W.S., Press, F., Beiser, A., 1957. Elastic waves in layered media. *Physics Today* 10, 27. <https://doi.org/10.1063/1.3060203>
46. Fam, M., Santamarina, C., 1995. Study of geoprocesses with complementary mechanical and electromagnetic wave measurements in an oedometer. *Geotechnical Testing Journal* 18, 307–314.
47. Fang, H.-Y., Daniels, J.L., 2006. *Introductory geotechnical engineering: an environmental perspective*. CRC Press.
48. Fenton, G.A., Griffiths, D.V., 2008. *Risk Assessment in Geotechnical Engineering*. Wiley.
49. Ferreira, C., 2009. *The use of seismic wave velocities in the measurement of stiffness of a residual soil*. University of Porto.
50. Ferreira, C., Díaz-Durán, F., da Fonseca, V., Cascante, G., 2020. New approach to simultaneous VS and VP measurements using bender elements. *ASTM Geotechnical Testing Journal* (paper submitted - under revision).
51. Ferreira, C., Martins, J.P., Correia, A.G., 2014. Determination of the small-strain stiffness of hard soils by means of bender elements and accelerometers. *Geotechnical and Geological Engineering* 32, 1369–1375.
52. Finn, W.L., Wightman, A., 2003. Ground motion amplification factors for the proposed 2005 edition of the National Building Code of Canada. *Canadian Journal of Civil Engineering* 30, 272–278.
53. Foti, S., 2004. Using transfer function for estimating dissipative properties of soils from surface-wave data. *Near Surface Geophysics* 2, 231–240.
54. Foti, S., 2002. Numerical and experimental comparison between 2-station and multistation methods for spectral analysis of surface waves. *Rivista Italiana di Geotecnica*.

55. Foti, S., Lai, C.G., Rix, G.J., Strobbia, C., 2014. Surface Wave Methods for Near-Surface Site Characterization. Taylor & Francis.
56. Glangeaud, F., Mari, J.L., Mars, J., 1998. Dispersive seismic wave tools in geophysics, in: 4th EEGS Meeting. European Association of Geoscientists & Engineers, p. cp-43-00163.
57. Grandjean, G., Leparoux, D., 2004. The potential of seismic methods for detecting cavities and buried objects: experimentation at a test site. *Journal of Applied Geophysics* 56, 93–106.
58. Grigoryan, V., 2012. Fourier Series and Numerical Methods [WWW Document]. MATH 124B/215B. URL <http://web.math.ucsb.edu/~grigoryan/124B/> (accessed 11.12.15).
59. Haeni, F.P., 1988. Application of seismic-refraction techniques to hydrologic studies. Department of the Interior, US Geological Survey.
60. Hardin, B.O., Black, W., 1969. Closure on vibration modulus of normally consolidated clay. *Journal of Soil Mechanics & Foundations Div.*
61. Hart, R., Han, Y., 2006. FLAC Training Course Basic Concepts and Recommended procedures for geotechnical numerical analysis related to nuclear waste isolation.
62. Haykin, S., Van Veen, B., 2007. Signals and systems. John Wiley & Sons.
63. Hickey, C.J., Schmitt, D.R., Sabatier, J.M., Riddle, G., 2009. Seismic measurements for detecting underground high-contrast voids. Presented at the Symposium on the Application of Geophysics to Engineering and Environmental Problems 2009, Society of Exploration Geophysicists, pp. 929–936.
64. Hirai, H., 1992. Analysis of Rayleigh waves in saturated porous elastic media by finite element method. *Soil Dynamics and Earthquake Engineering* 11, 311–326.
65. Huang, N.E., Shen, Z., Long, S.R., Wu, M.C., Shih, H.H., Zheng, Q., Yen, N.-C., Tung, C.C., Liu, H.H., 1998. The empirical mode decomposition and the Hilbert spectrum for nonlinear and non-stationary time series analysis. *Proceedings of the Royal Society of London. Series A: mathematical, physical and engineering sciences* 454, 903–995.
66. Hunter, J.A., Motezedian, D., 2006. Shear wave velocity measurements for soft soil earthquake response evaluation in the eastern Ottawa region, Ontario, Canada, in: Symposium on the Application of Geophysics to Engineering and Environmental Problems 2006. Society of Exploration Geophysicists, pp. 1282–1295.
67. Idriss, I.M., Dobry, R. u, Sing, R.D., 1978. Nonlinear behavior of soft clays during cyclic loading. *Journal of geotechnical and geoenvironmental engineering* 104.

68. Irfan, M., 2019. Advancements in bender-element testing - frequency effects (PhD. Thesis).
69. Itasca, C.G., 2000. FLAC 4.0 User's Manual. Minneapolis, USA.
70. Ivanov, J., Tsoflias, G.P., Miller, R., Xia, J., 2009. Practical aspects of MASW inversion using varying density. 22nd EEGS Symposium on the Application of Geophysics to Engineering and Environmental Problems.
71. Jones, D.M., 2008. Geophysical Survey in Archaeological Field Evaluation (Swindon, UK: English Heritage).
72. Jones, R., 1962. Surface wave technique for measuring the elastic properties and thickness of roads: theoretical development. *British Journal of Applied Physics* 13, 21.
73. Jung, H.S., Cho, C.G., Chun, B.S., 2010. The engineering properties of surface layer on very soft clay of the south coast in Korea, in: 2nd International Symposium on Cone Penetration Testing.
74. Jung, J.W., Kim, H.S., Kim, B.C., Park, I.B., Mok, Y.J., 2008. In-Situ Stiffness Evaluation of Soft Ground Using Bender Elements, in: 14th World Conference on Earthquake Engineering (第十四届国际地震工程会议). 中国地震学会, p. A-X.
75. Kalteziotis, N.A., Tsiambaos, G., Sabatakakis, N., Zervogiannis, H., 1990. Prediction of soil dynamic parameters from pressuremeter and other in situ tests. pressuremeters. Presented at the Third international symposium, organised by the british geotechnical society, Telford (Thomas) Limited, Oxford university.
76. Kawaguchi, T., Tanaka, H., 2008. Formulation of Gmax from reconstituted clayey soils and its application to Gmax measured in the field. *Soils and foundations* 48, 821–831.
77. Keilis-Borok, V.I., 1989. Recording, identification, and measurement of surface wave parameters, in: *Seismic Surface Waves in a Laterally Inhomogeneous Earth*. Springer, pp. 131–182.
78. Keydar, S., Shtivelman, V., Arzi, A., 2018. Three-Dimensional Seismic Diffraction Imaging for Detecting Near-Surface Inhomogeneities.
79. Kim, H., 2005. Spatial variability in soils: Stiffness and Strength. Georgia Institute of Technology, Atlanta, GA.
80. Knutsen, M., 2014. On determination of Gmax by bender element and cross-hole testing. Institutt for bygg, anlegg og transport.

81. Kovach, R.L., 1978. Seismic surface waves and crustal and upper mantle structure. *Reviews of Geophysics* 16, 1–13.
82. Kramer, S.L., 1996. *Geotechnical earthquake engineering*. Pearson Education India.
83. Ku, T., Mayne, P.W., 2013. Evaluating the in situ lateral stress coefficient (K_0) of soils via paired shear wave velocity modes. *Journal of geotechnical and geoenvironmental engineering* 139, 775–787.
84. Kuhlemeyer, R.L., Lysmer, J., 1973. Finite element method accuracy for wave propagation problems. *Journal of Soil Mechanics & Foundations Div* 99.
85. Kulhawy, F.H., Mayne, P.W., Electric Power Research, I., Cornell University. *Geotechnical Engineering, G.*, 1990. *Manual on Estimating Soil Properties for Foundation Design*.
86. Kumar, P., Fofoula-Georgiou, E., 1997. Wavelet analysis for geophysical applications. *Reviews of geophysics* 35, 385–412.
87. Kumar, S.S., Krishna, A.M., Dey, A., 2013. Parameters Influencing Dynamic Soil Properties: A Review Treatise. *National Conference on Recent Advances in Civil Engineering*.
88. Lai, C.G., 2005. Surface waves in dissipative media: Forward and inverse modelling, in: *Surface Waves in Geomechanics: Direct and Inverse Modelling for Soils and Rocks*. Springer, pp. 73–163.
89. Lai, C.G., Rix, G.J., 1998. Simultaneous inversion of Rayleigh phase velocity and attenuation for near-surface site characterization.
90. Lai, C.G., Wilmański, K., 2005. *Surface Waves in Geomechanics: Direct and Inverse Modelling for Soils and Rocks*. CISM International Centre for Mechanical Sciences. <https://doi.org/10.1007/3-211-38065-5>
91. Lamb, H., 1904. I. On the Propagation of Tremors over the Surface of an Elastic Solid. *Philosophical Transactions of the Royal Society of London. Series A, Containing papers of a mathematical or physical character* 203, 1–42.
92. Lay, T., Wallace, T.C., 1995. *Modern global seismology*. Elsevier.
93. Lee, W.B., Solomon, S.C., 1979. Simultaneous inversion of surface-wave phase velocity and attenuation: Rayleigh and Love waves over continental and oceanic paths. *Bulletin of the Seismological Society of America* 69, 65–95.

94. Li, J.P., Yan, S.A., Tang, Y.Y., 2001. The application of wavelet analysis method to civil infrastructure health monitoring, in: *International Conference on Wavelet Analysis and Its Applications*. Springer, pp. 393–397.
95. Likitlersuang, S., Teachavorasinskun, S., Surarak, C., Oh, E., Balasubramaniam, A., 2013. Small strain stiffness and stiffness degradation curve of Bangkok Clays. *Soils and Foundations* 53, 498–509.
96. Lindberg, R., 2011. The Black Boxes of Science and Engineering [WWW Document]. URL <https://www.youtube.com/watch?v=1jPJt-q83k0&feature=youtu.be> (accessed 12.17.15).
97. Lings, M.L., Greening, P.D., 2001. A novel bender/extender element for soil testing. *Géotechnique* 51, 713–717.
98. Lo Presti, D.C.F., 1997. Damping ratio of soils from laboratory and in situ tests," in "Seismic behaviour of ground and geotechnical structures, in: *Proc. of Special Technical Session on Earthquake Geotech. Engrg., 14th Int. Conf. on SMFE*. Balkema, pp. 391–400.
99. Lowrie, W., 2007. *Fundamentals of Geophysics*.
100. Luna, R., Jadi, H., 2000. Determination of dynamic soil properties using geophysical methods, in: *Proceedings of the First International Conference on the Application of Geophysical and NDT Methodologies to Transportation Facilities and Infrastructure—Geophysics*. pp. 3–1.
101. Malagnini, L., Herrmann, R.B., Mercuri, A., Opice, S., Biella, G., Franco, R. de, 1997. Shear-wave velocity structure of sediments from the inversion of explosion-induced Rayleigh waves: comparison with cross-hole measurements. *Bulletin of the Seismological Society of America* 87, 1413–1421.
102. Manolis, G.D., 2002. Stochastic soil dynamics. *Soil Dynamics and Earthquake Engineering* 22, 3–15.
103. Massad, F., 1994. Properties of marine sediments. *Solos do Litoral do Estado de São Paulo* 99–128.
104. Mayne, P.W., 2007. Cone penetration testing. *Transportation Research Board*.
105. McGillivray, A.V., 2007. Enhanced integration of shear wave velocity profiling in direct-push site characterization systems. *Georgia Institute of Technology*.
106. Mitsch, W., Gosselink, J.G., 1993. *Wetlands, 2nd Edition*. ed. John Wiley, New York.

107. Nasser-Moghaddam, A., 2006. Study of the effect of lateral inhomogeneities on the propagation of Rayleigh waves in an elastic medium. University of Waterloo, Waterloo, Ontario.
108. NEHRP, 1994. Recommended provisions for seismic regulations for new buildings. Building Seismic Safety Council, Washington.
109. NRC, 2005. National Building Code of Canada. National Research Council, Ottawa, Ontario.
110. Nwankwoala, H.O., Amadi, A.N., Ushie, F.A., Warmate, T., Eze, C.J., 2014. Determination of subsurface geotechnical properties for foundation design and construction in Akenfa community, Bayelsa state, Nigeria. *American Journal of Civil Engineering and Architecture* 2, 130–135.
111. Oh, S.H., Park, D.S., Kim, B.J., Kim, E.J., Mok, Y.J., 2008. Laboratory measurements of stiffness of soft clay using bender elements, in: *The 14th World Conference on Earthquake Engineering*. pp. 1–8.
112. Pallara, O., Mattone, M., LO PRESTI, D.C., 2008. Bender elements: bad source–good receiver, in: *4th International Symposium on Deformation Characteristics of Geomaterials*. IOS, pp. 697–702.
113. Paoletti, L., Mouton, E., Liposcak, I., 2010. Comparison of Underwater MASW, Seismic CPT, and Downhole Methods: Offshore Croatia, in: *GeoFlorida 2010: Advances in Analysis, Modeling & Design*. pp. 1100–1107.
114. Park, C.B., 2020. Park Seismic [WWW Document]. Seismic Site Characterization (Vs30m). URL <http://www.parkseismic.com/SSC-HowToCalculateVs30m.html> (accessed 3.1.20).
115. Park, C.B., Miller, R.D., Miura, H., 2002. Optimum field parameters of an MASW survey. *Proceedings of the Society of Exploration Geophysicists (SEG) Japan Tokyo 22*, 23.
116. Park, C.B., Miller, R.D., Xia, J., 1999. Detection of Near-Surface Voids Using Surface Wave, in: *Symposium on the Application of Geophysics to Engineering and Environmental Problems 1999*. pp. 281–286.
117. Park, C.B., Miller, R.D., Xia, J., Ivanov, J., 2007. Multichannel analysis of surface waves (MASW)—active and passive methods. *The Leading Edge* 26, 60–64.
118. Pecorari, C., 2001. Scattering of a Rayleigh wave by a surface-breaking crack with faces in partial contact. *Wave motion* 33, 259–270.
119. Peters, R.D., 2002. Toward a Universal Model of Damping--Modified Coulomb Friction. arXiv preprint physics/0208025.

120. Phillips, C., Cascante, G., Hutchinson, D., 2002. The Innovative Use of Seismic Surface Waves for Void Detection and Material Characterization.
121. Phillips, C., Cascante, G., Hutchinson, D.J., 2004. Evaluation of horizontal homogeneity of geomaterials with the distance analysis of surface waves. *Canadian Geotechnical Journal* 41, 212–226. <https://doi.org/10.1139/t03-085>
122. Polytec, 2013. User's manual of OFV-2570 vibration controller.
123. Porovic, E., 1995. Investigations of soil behaviour using a resonant-column torsional-shear hollow cylinder apparatus. Ph. D. Thesis, Imperial College, University of London.
124. Pradhan, T.B., Tatsuoka, F., Horii, N., 1988. Simple shear testing on sand in a torsional shear apparatus. *Soils and Foundations* 28, 95–112.
125. Prasad, M., Zimmer, M.A., Berge, P.A., Bonner, B.P., 2004. Laboratory measurements of velocity and attenuation in sediments. LLNL Rep. UCRL-JRNL 205155, 34.
126. Ramos, C., Ferreira, C., Molina-Gómez, F., da Fonseca, A.V., 2019. Critical state lines of Portuguese liquefiable sands, in: *E3S Web of Conferences*. EDP Sciences, p. 06003.
127. Rechten, R.D., Greenfield, R.J., Ballard, R.F., 1995. Tunnel signature prediction for a cross-borehole seismic survey. *GEOPHYSICS* 60, 76–86. <https://doi.org/10.1190/1.1443765>
128. Rio, J.F.M.E., 2006. Advances in laboratory geophysics using bender elements. University of London.
129. Rix, G.J., 1990. Experimental study of factors affecting the spectral-analysis-of-surface-waves method.
130. Rix, G.J., Lai, C.G., Foti, S., 2001. Simultaneous measurement of surface wave dispersion and attenuation curves. *Geotechnical Testing Journal* 24, 350–358.
131. Robertson, P.K., 2016. Cone penetration test (CPT)-based soil behaviour type (SBT) classification system—an update. *Canadian Geotechnical Journal* 53, 1910–1927.
132. Robertson, P.K., 2015. CPT for Quality Control (QC) of Ground Improvement (Deep Compaction). Webinar# 13 Dec.
133. Robertson, P.K., 2009. Performance based earthquake design using the CPT. *Proc. IS-Tokyo* 3–20.

134. Robertson, P.K., Campanella, R.G., Wightman, A., 1983. SPT - CPT Correlations. *Journal of Geotechnical Engineering*. [https://doi.org/doi:10.1061/\(ASCE\)0733-9410\(1983\)109:11\(1449\)](https://doi.org/doi:10.1061/(ASCE)0733-9410(1983)109:11(1449))
135. Rodríguez-Ordoñez, J.A., 1994. A New Method for Interpretation of Surface Wave Measurements in Soils.
136. Roy, N., Jakka, R.S., 2017. Near-field effects on site characterization using MASW technique. *Soil Dynamics and Earthquake Engineering* 97, 289–303.
137. Salami, B.M., Falebita, D.E., Fatoba, J.O., Ajala, M.O., 2012. Integrated geophysical and geotechnical investigation of a bridge site-A case study of a swamp/creek environment in south east Lagos, Nigeria. *Ife Journal of Science* 14, 75–82.
138. Santamarina, J.C., Fratta, D., 2005. Discrete signals and inverse problems. *An Introduction for Engineers and Scientists*. UK: Wiley & Sons.
139. Santamarina, J.C., Rinaldi, V.A., Fratta, D., Klein, K.A., Wang, Y.-H., Cho, G.C., Cascante, G., 2005. A survey of elastic and electromagnetic properties of near-surface soils. *Near-surface geophysics* 1, 71–87.
140. Scholte, J.G., 1942. On the Stoneley wave equation. *Proceedings of the Koninklijke Nederlandse Akademie van Wetenschappen* 45, 20–25.
141. Schwenk, J.T., Sloan, S.D., Miller, R.D., Ivanov, J., 2014. Correlation of the backscatter analysis of surface waves method (BASW) for anomaly detection, in: *SEG Technical Program Expanded Abstracts 2014*. Society of Exploration Geophysicists, pp. 2029–2035.
142. Seed, H.B., Wong, R.T., Idriss, I.M., Tokimatsu, K., 1986. Moduli and damping factors for dynamic analyses of cohesionless soils. *Journal of geotechnical engineering* 112, 1016–1032.
143. Seedsman, R., Gordon, N., Aziz, N., 2009. Analytical tools for managing rock fall hazards in Australian coal mine roadways. *Final Report-ACARP Project C 14029*, 132p.
144. Sheriff, R.E., 2002. *Encyclopedic dictionary of applied geophysics*. Society of exploration geophysicists.
145. Shibata, T., Soelarno, D.S., 1978. Stress-strain characteristics of clays under cyclic loading, in: *Proceedings of the Japan Society of Civil Engineers*. Japan Society of Civil Engineers, pp. 101–110.
146. Shibuya, S., Tanaka, H., 1996. Estimate of elastic shear modulus in Holocene soil deposits. *Soils and foundations* 36, 45–55.

147. Shokouhi, P., Gucunski, N., 2003. Application of Wavelet Transform in Detection of Shallow Cavities by Surface Waves, in: Symposium on the Application of Geophysics to Engineering and Environmental Problems 2003. pp. 813–831.
148. Shtivelman, V., Marco, S., Reshef, M., Agnon, A., Hamiel, Y., 2005. Using trapped waves for mapping shallow fault zones. *Near Surface Geophysics* 3, 91–97.
149. Sloan, S.D., Peterie, S.L., Ivanov, J., Miller, R., McKenna, J.R., 2010. Void Detection Using Near-Surface Seismic Methods, in: *Advances in Near-Surface Seismology and Ground-Penetrating Radar*. Society of Exploration Geophysicists, pp. 201–218.
150. Steeples, D.W., Miller, R.D., 1987. Direct detection of shallow subsurface voids using high-resolution seismic-reflection techniques, in: *Multidisciplinary Conference on Sinkholes and the Environmental Impacts of Karst*. 2. pp. 179–183.
151. Stewart, W.P., 1992. *In situ measurement of dynamic soil properties with emphasis on damping*. University of British Columbia.
152. Stokoe, K.H., Wright, S.G., Bay, J.A., Roesset, J.M., 1994. Characterization of geotechnical sites by SASW method, in: *Geophysical Characterization of Sites*. pp. 15–25.
153. Stoneley, R., 1924. Elastic waves at the surface of separation of two solids. *Proceedings of the Royal Society of London. Series A, Containing Papers of a Mathematical and Physical Character* 106, 416–428.
154. Strobbia, C., 2003. *Surface wave methods: acquisition, processing and inversion*. Torino: Politecnico di Torino.
155. Sun, J.I., Golesorkhi, R., Seed, H.B., 1988. Dynamic moduli and damping ratios for cohesive soils. Earthquake Engineering Research Center, University of California Berkeley.
156. Taipodia, J., Baglari, D., Dey, A., 2019. Effect of source characteristics on the resolution of dispersion image from active MASW survey. *Indian Geotechnical Journal* 49, 314–327.
157. Takaki, C.N., de Mello, L., Bilfinger, W., 2013. Geotechnical Properties of soft to very soft clays of the left bank of the Port of Santos, in: *Geotechnical and Geophysical Site Characterization: Proceedings of the 4th International Conference on Site Characterization ISC-4*. Taylor & Francis Books Ltd, pp. 1591–1599.
158. Tallavó, F., Cascante, G., Pandey, M., 2009. New Methodology for Source Characterization in Pulse Velocity Testing. *Geotechnical Testing Journal* 32, 1–16.
159. Terzaghi, K., Peck, R., 1948. *Soil Mechanics in Engineering Practice*. Wiley, New York.

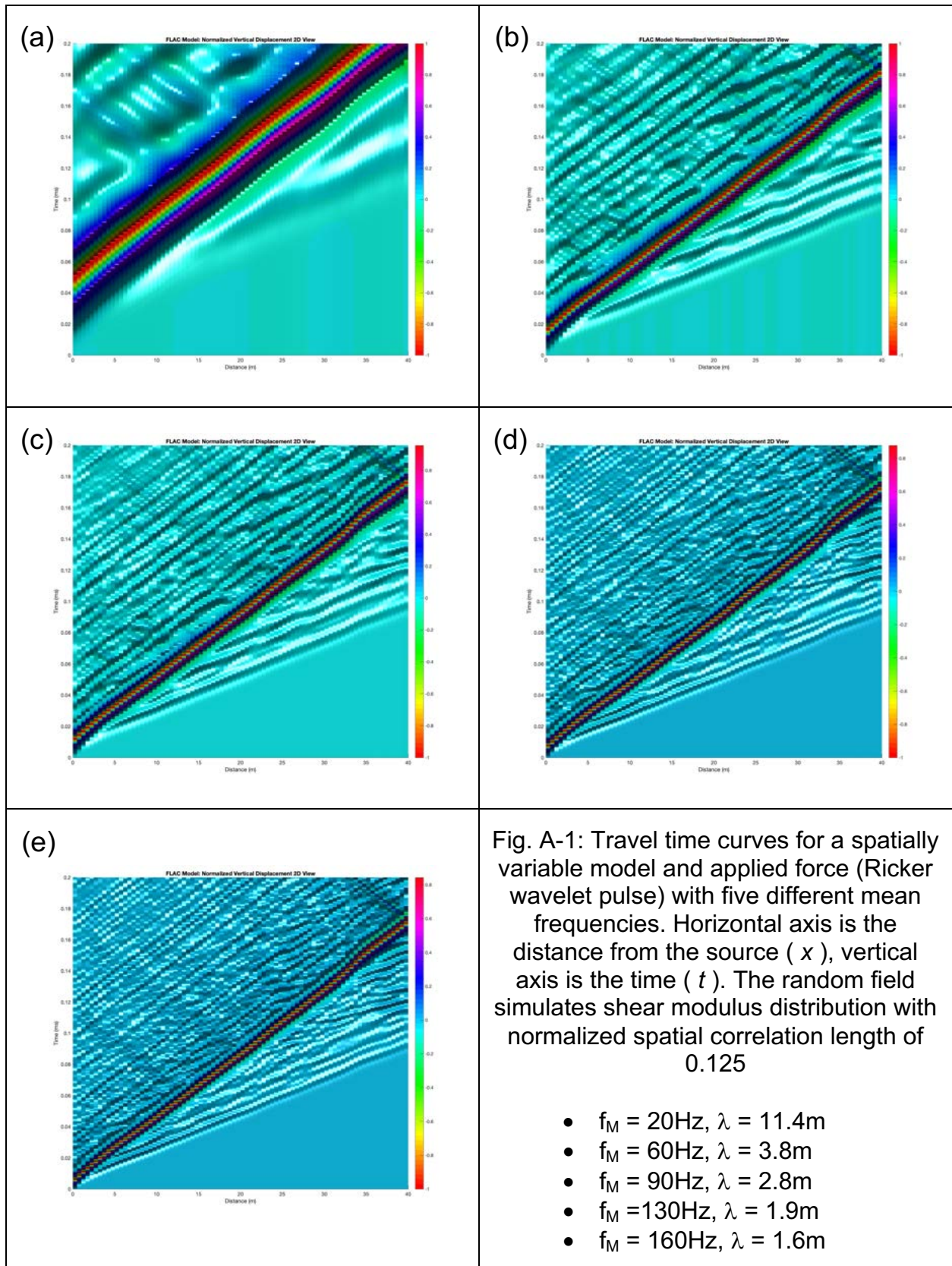
160. Terzaghi, K., Peck, R.B., Mesri, G., 1996. Soil mechanics in engineering practice. John Wiley & Sons.
161. Thurber Eng. Ltd., 2013. Evaluation of Geophysical Techniques for Site Characterization Highway 407E Extension (No. 19-2805–11). Report to Ministry of Transportation Ontario, Canada.
162. Tokimatsu, K., 1998. Effects of lateral ground movements on failure patterns of piles in the 1995 Hyogoken-Nambu earthquake, in: Proc. A Speciality Conf., Geotechnical Earthquake Engineering and Soil Dynamics III.
163. Tomic, J., 2017. Are Love-and Rayleigh seismic waves detectable in Groningen?
164. UCB, 2015. TeachEngineering [WWW Document]. Engineering Design Process. URL <https://www.teachengineering.org> (accessed 11.12.15).
165. Valliappan, S., Murti, V., 1984. Finite element constraints in the analysis of wave propagation problems.
166. Van Der Hilst, R., Burdick, Scott, 2010. 12.510 Introduction to Seismology. Spring 2010.
167. Vesecky, J.F., Nierenberg, W.A., Despain, A.M., 1980. Tunnel detection. SRI International - Arlington, VA.
168. Viggiani, G., Atkinson, J.H., 1995. Interpretation of bender element tests. *Géotechnique* 45, 149–154.
169. Viktorov, I.A., 1967. Rayleigh and Lamb waves, physical theory and applications. Moscow: Acoustics Institute, Academy of Science of the USSR.
170. Vucetic, M., Dobry, R., 1991. Effect of Soil Plasticity on Cyclic Response. *Journal of Geotechnical Engineering*.
171. Watkins, J.S., Godson, R.H., Watson, K., 1967. Seismic detection of near-surface cavities (Report No. 599A), Professional Paper.
172. Whiteley, R.J., 1994. Seismic refraction testing-a tutorial, in: *Geophysical Characterization of Sites*. pp. 45–47.
173. Wiciak, P., Cascante, G., Polak, M., 2017. Sensor and Dimensions Effects in Ultrasonic Pulse Velocity Measurements in Mortar Specimens. *Procedia Engineering* 193, 409–416. <https://doi.org/10.1016/j.proeng.2017.06.231>
174. Winkler, K., Nur, A., Gladwin, M., 1979. Friction and seismic attenuation in rocks. *Nature* 277, 528–531.

175. Wood, C.M., Cox, B.R., 2012. A comparison of MASW dispersion uncertainty and bias for impact and harmonic sources, in: *GeoCongress 2012: State of the Art and Practice in Geotechnical Engineering*. pp. 2756–2765.
176. Woods, R., 1994. Laboratory Measurement of Dynamic Soil Properties, in: Ebelhar, R., Drnevich, V., Kutter, B. (Eds.), *Dynamic Geotechnical Testing II*. ASTM International, West Conshohocken, PA, pp. 165–190. <https://doi.org/10.1520/STP13212S>
177. Woods, R.D., 1978. Measurement of dynamic soil properties, in: *From Volume I of Earthquake Engineering and Soil Dynamics--Proceedings of the ASCE Geotechnical Engineering Division Specialty Conference, June 19-21, 1978, Pasadena, California*. Sponsored by Geotechnical Engineering Division of ASCE
178. Xia, J., Miller, R.D., Park, C.B., 1999. Estimation of near-surface shear-wave velocity by inversion of Rayleigh waves. *Geophysics* 64, 691–700.
179. Xia, J., Nyquist, J.E., Xu, Y., Roth, M.J.S., Miller, R.D., 2007. Feasibility of detecting near-surface feature with Rayleigh-wave diffraction. *Journal of Applied Geophysics* 62, 244–253. <http://dx.doi.org/10.1016/j.jappgeo.2006.12.002>
180. Xie, Q., Xuan, B., Peng, S., Li, J., Xu, W., Han, H., 2008. Bandwidth empirical mode decomposition and its application. *International Journal of Wavelets, Multiresolution and Information Processing* 6, 777–798.
181. Youdeowei, P.O., Nwankwoala, H.O., 2013. Suitability of soils as bearing media at a freshwater swamp terrain in the Niger Delta. *Journal of geology and mining research* 5, 58–64.
182. Zahari, M.N.H., Madun, A., Dahlan, S.H., Joret, A., Abidin, M.H.Z., Mohammad, A.H., Omar, A.H., 2018. Experimental Detection and Characterization of Void using Time-Domain Reflection Wave. Presented at the *Journal of Physics: Conference Series*, IOP Publishing, p. 012102.
183. Zerwer, A., Cascante, G., Hutchinson, J., 2002. Parameter Estimation in Finite Element Simulations of Rayleigh Waves. *Journal of Geotechnical and Geoenvironmental Engineering* 128, 250–261. [https://doi.org/doi:10.1061/\(ASCE\)1090-0241\(2002\)128:3\(250\)](https://doi.org/doi:10.1061/(ASCE)1090-0241(2002)128:3(250))

Appendices

Appendix A: Result of Numerical Simulations for Random Field Models

In this appendix, the results for the numerical simulations including random fields with different normalized correlation lengths are presented. These results are the same kind of results presented in Chapter 5. In this appendix, the results for numerical simulations involving random fields with normalized correlation lengths other than 0.125 and 1.25 are presented along with their correspondent dispersion curves.



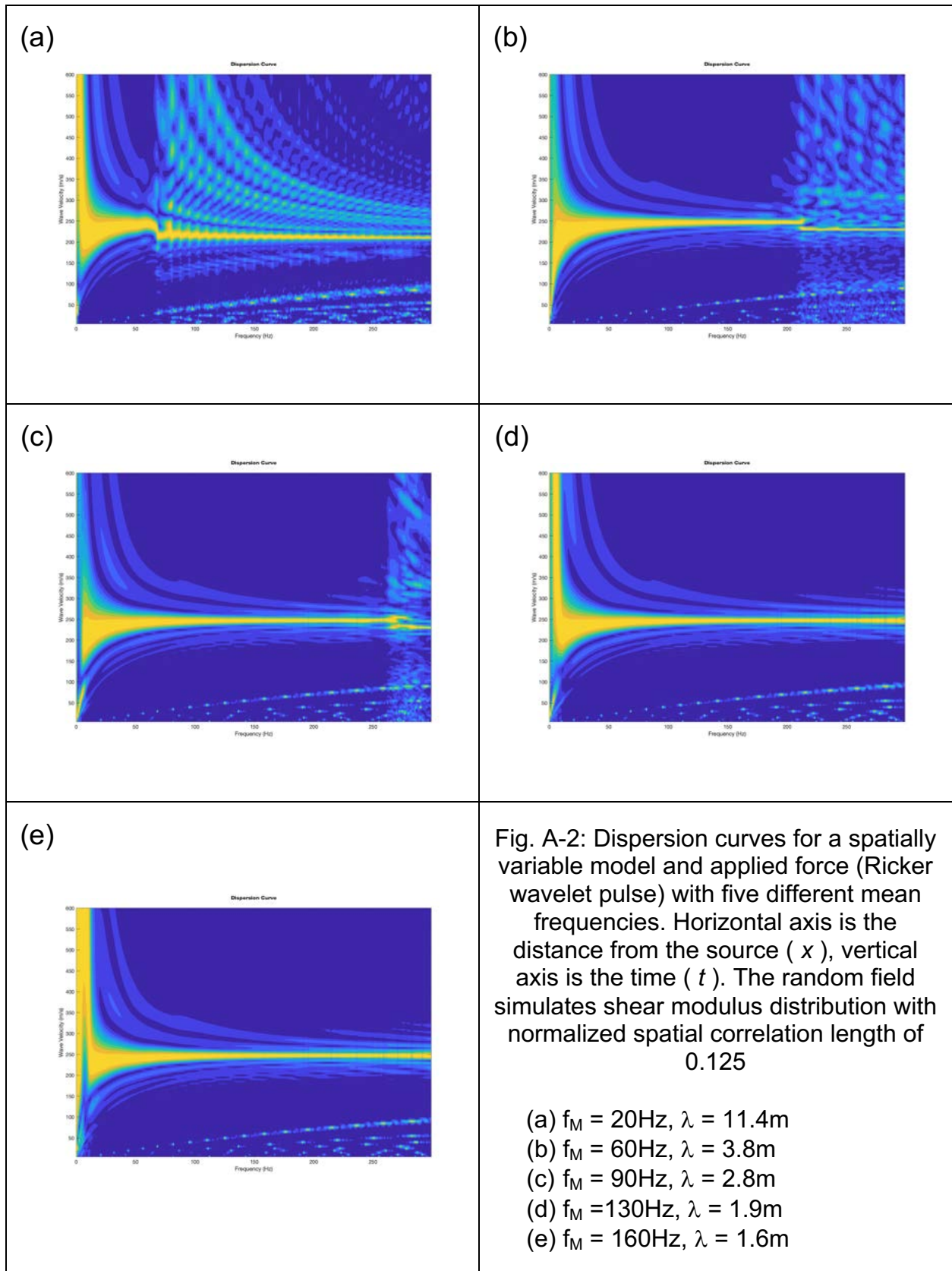
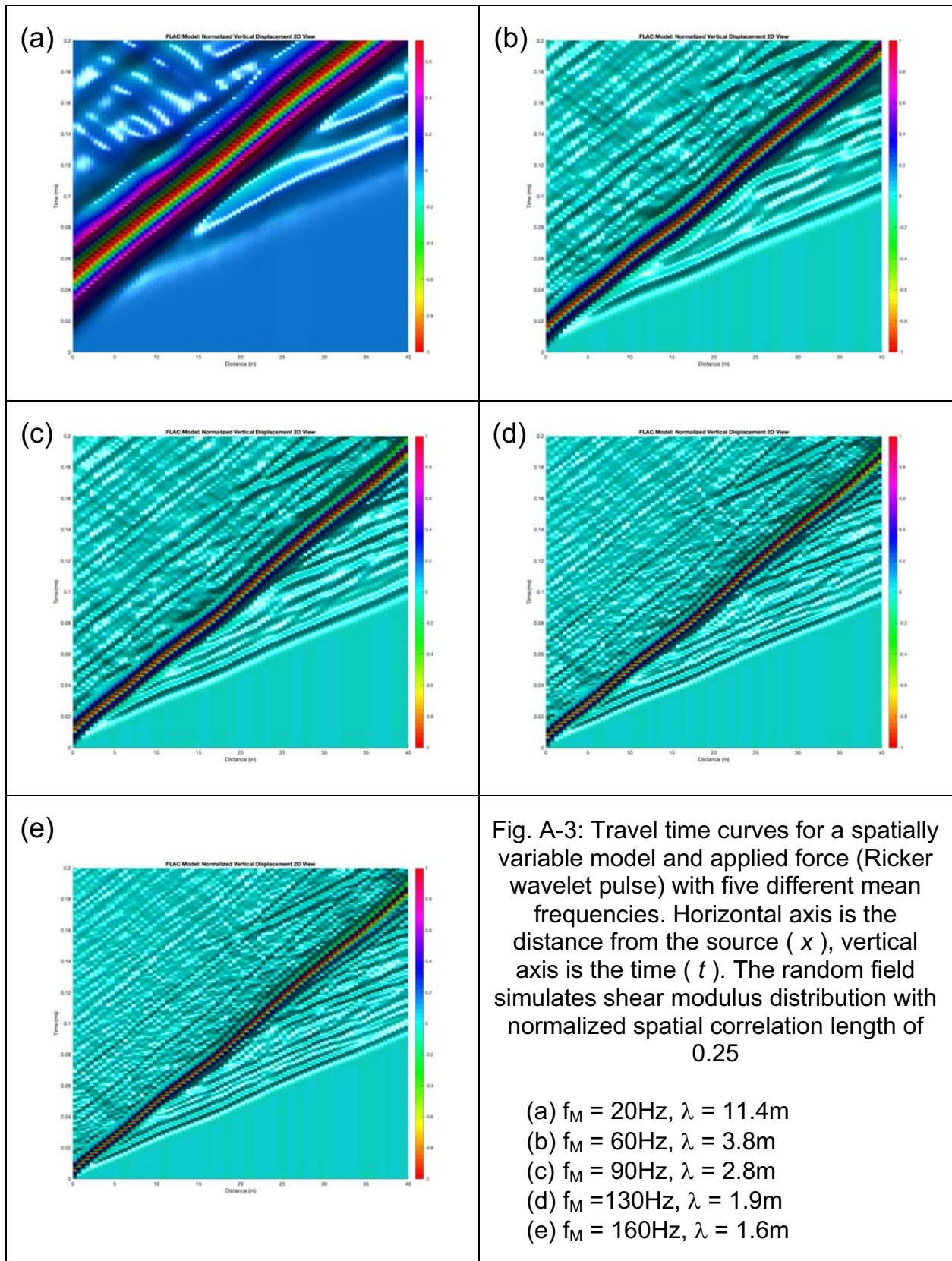


Fig. A-2: Dispersion curves for a spatially variable model and applied force (Ricker wavelet pulse) with five different mean frequencies. Horizontal axis is the distance from the source (x), vertical axis is the time (t). The random field simulates shear modulus distribution with normalized spatial correlation length of 0.125

- (a) $f_M = 20\text{Hz}$, $\lambda = 11.4\text{m}$
- (b) $f_M = 60\text{Hz}$, $\lambda = 3.8\text{m}$
- (c) $f_M = 90\text{Hz}$, $\lambda = 2.8\text{m}$
- (d) $f_M = 130\text{Hz}$, $\lambda = 1.9\text{m}$
- (e) $f_M = 160\text{Hz}$, $\lambda = 1.6\text{m}$



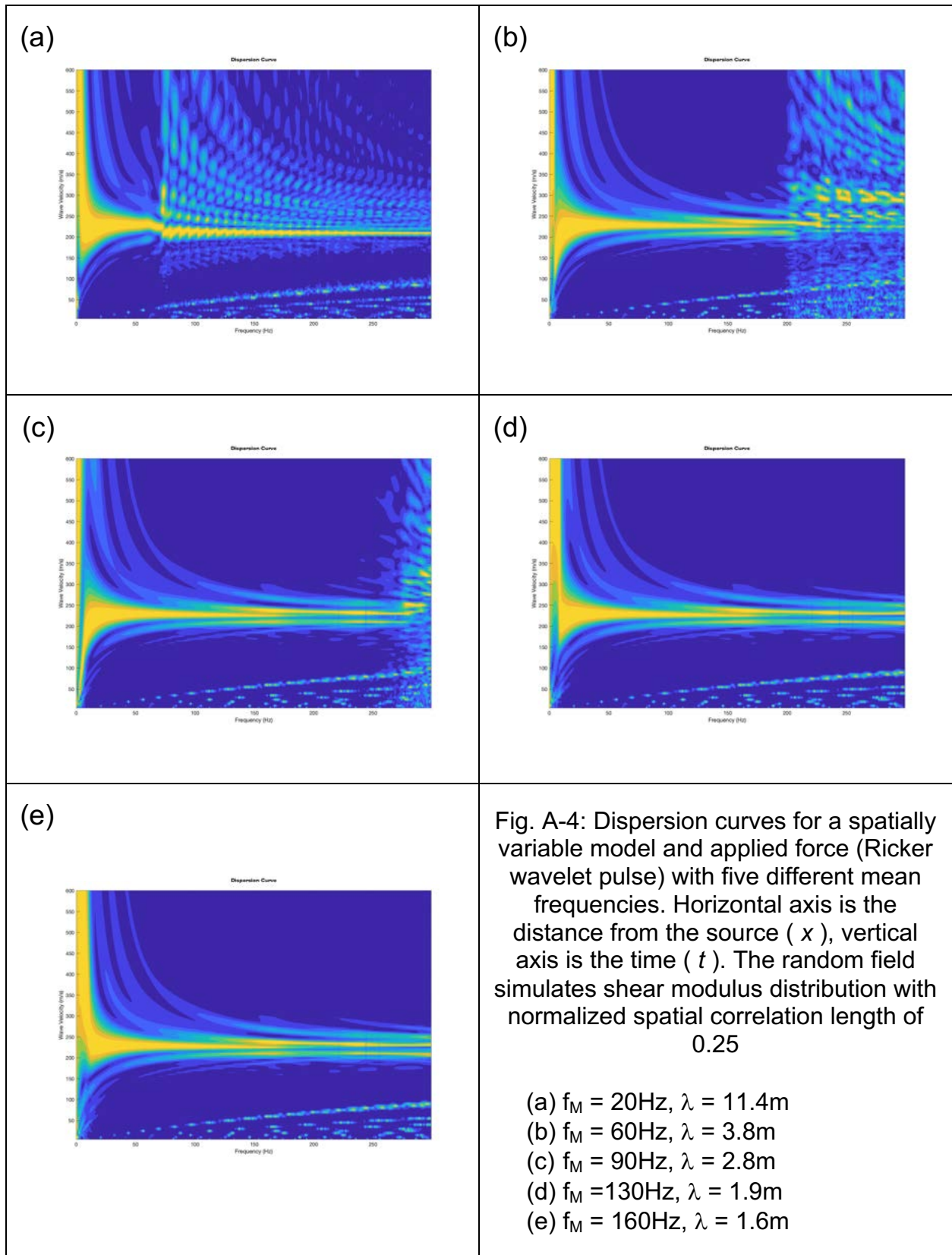


Fig. A-4: Dispersion curves for a spatially variable model and applied force (Ricker wavelet pulse) with five different mean frequencies. Horizontal axis is the distance from the source (x), vertical axis is the time (t). The random field simulates shear modulus distribution with normalized spatial correlation length of 0.25

- (a) $f_M = 20\text{Hz}$, $\lambda = 11.4\text{m}$
- (b) $f_M = 60\text{Hz}$, $\lambda = 3.8\text{m}$
- (c) $f_M = 90\text{Hz}$, $\lambda = 2.8\text{m}$
- (d) $f_M = 130\text{Hz}$, $\lambda = 1.9\text{m}$
- (e) $f_M = 160\text{Hz}$, $\lambda = 1.6\text{m}$

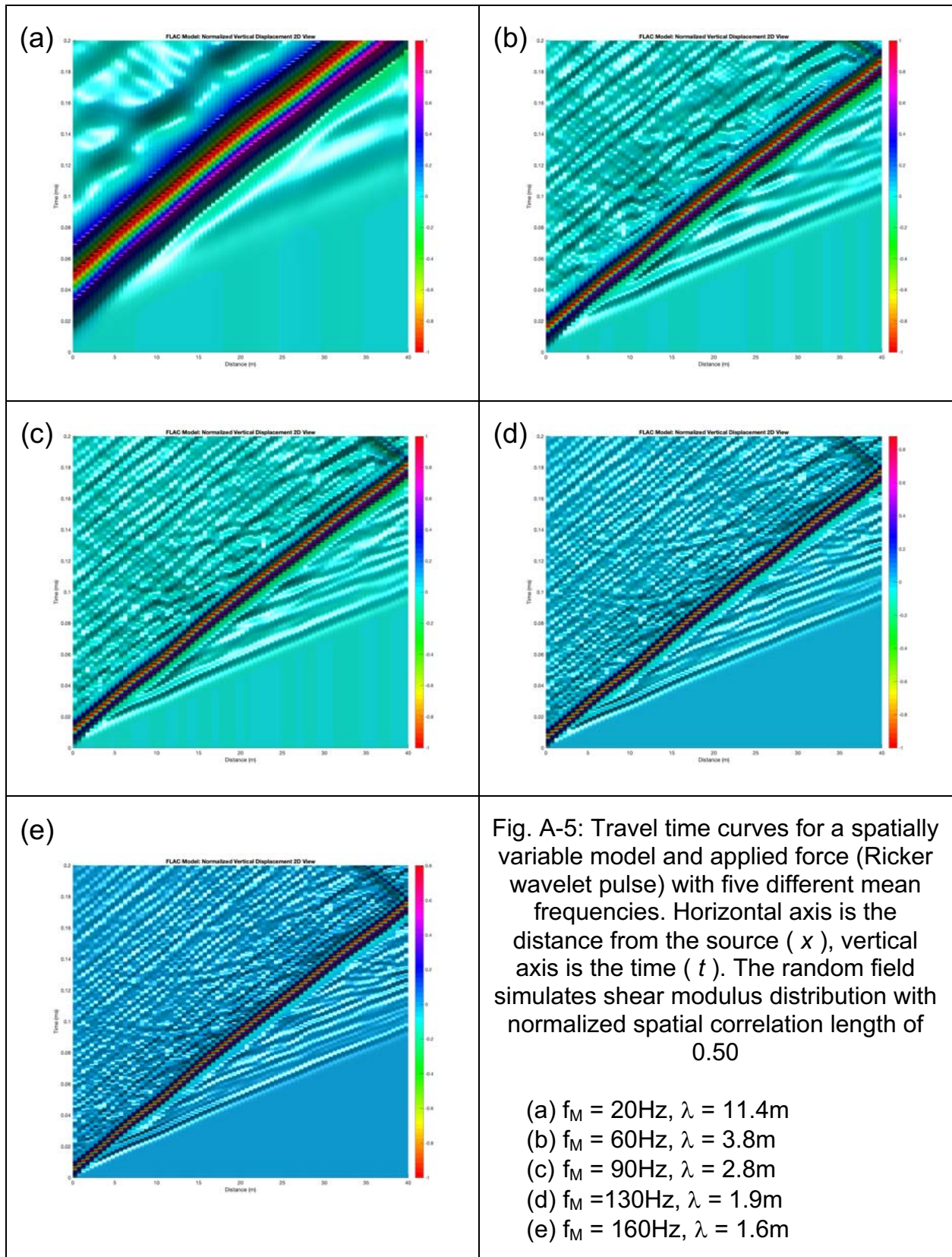


Fig. A-5: Travel time curves for a spatially variable model and applied force (Ricker wavelet pulse) with five different mean frequencies. Horizontal axis is the distance from the source (x), vertical axis is the time (t). The random field simulates shear modulus distribution with normalized spatial correlation length of 0.50

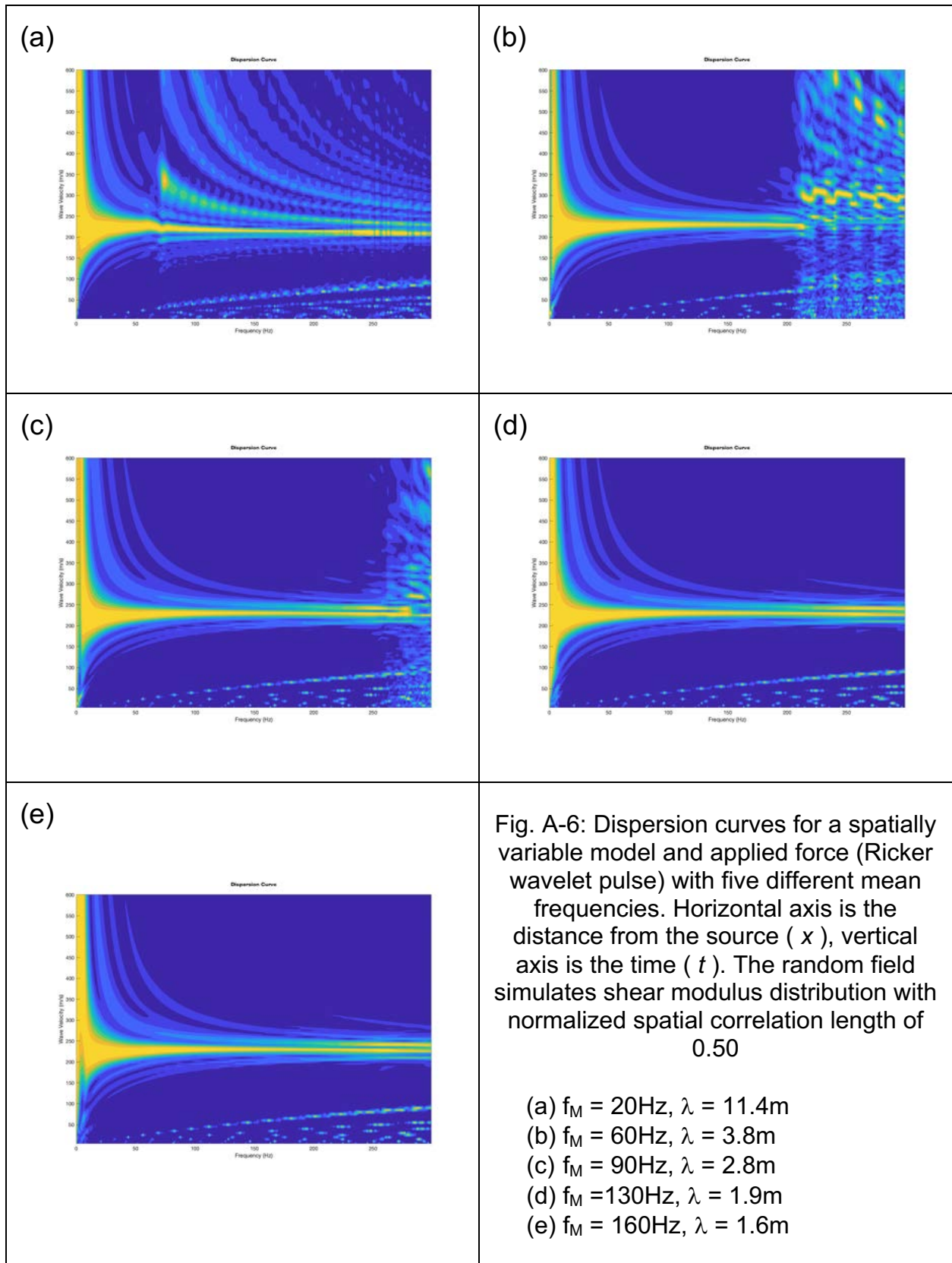
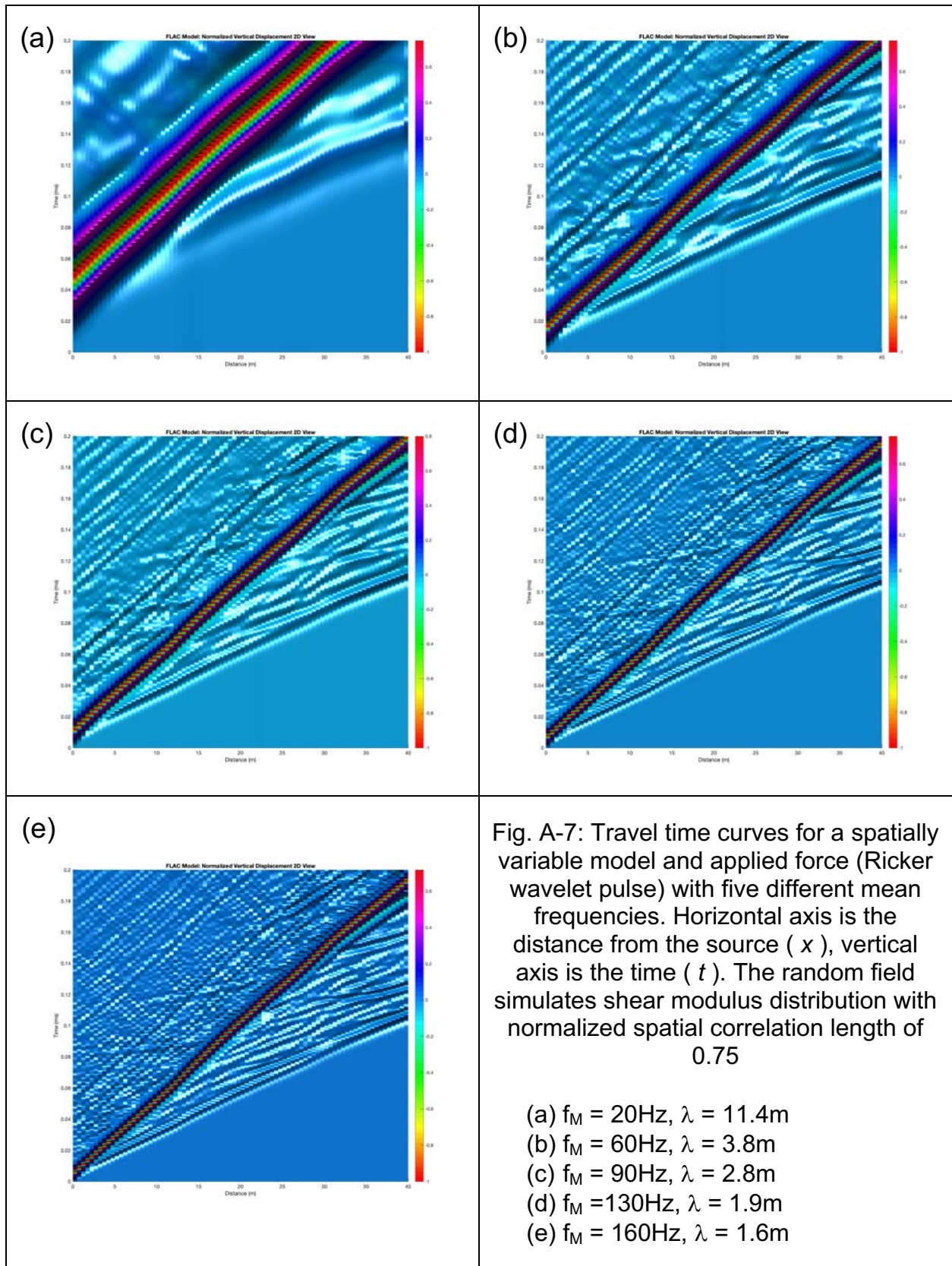


Fig. A-6: Dispersion curves for a spatially variable model and applied force (Ricker wavelet pulse) with five different mean frequencies. Horizontal axis is the distance from the source (x), vertical axis is the time (t). The random field simulates shear modulus distribution with normalized spatial correlation length of 0.50



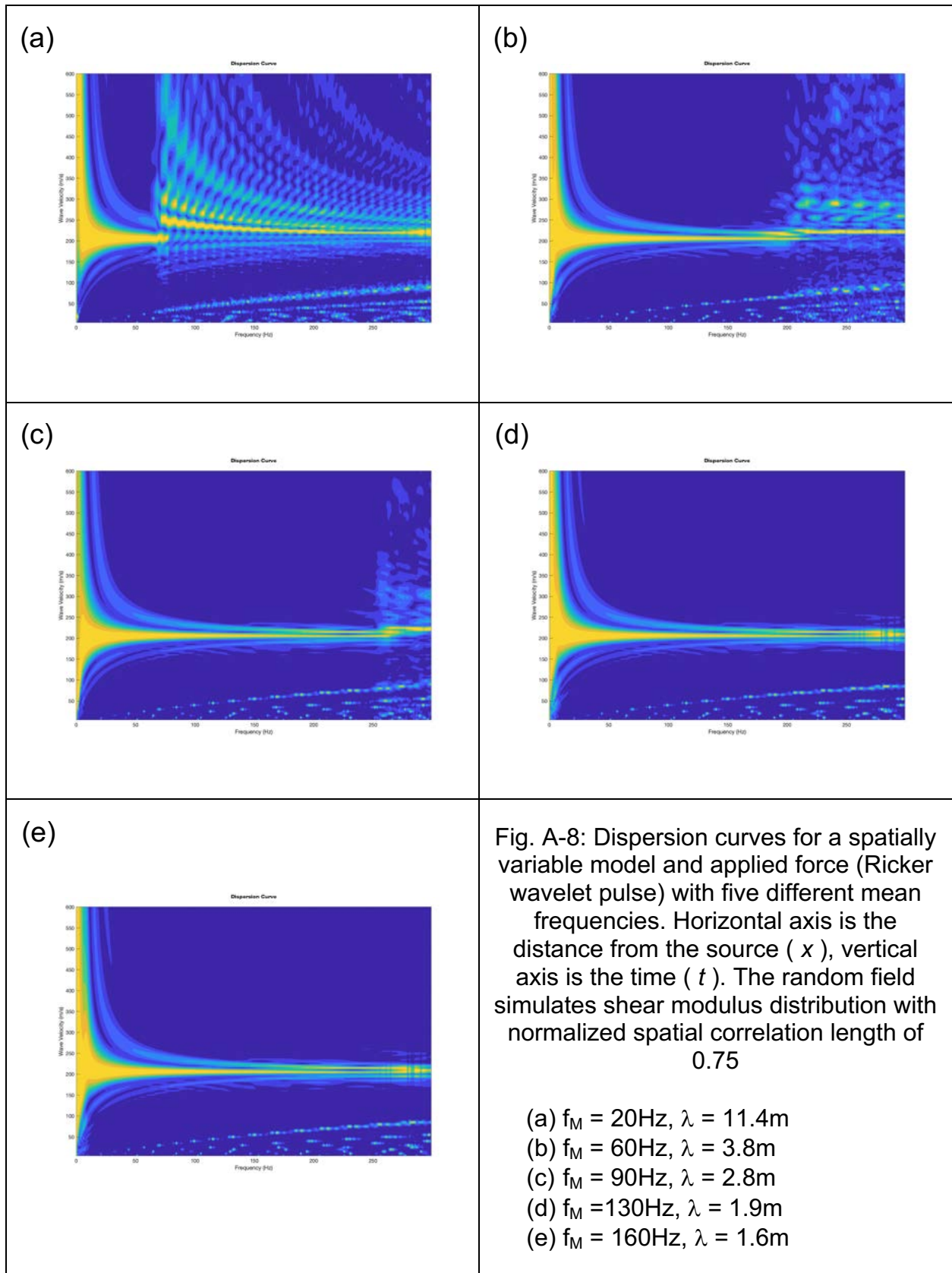
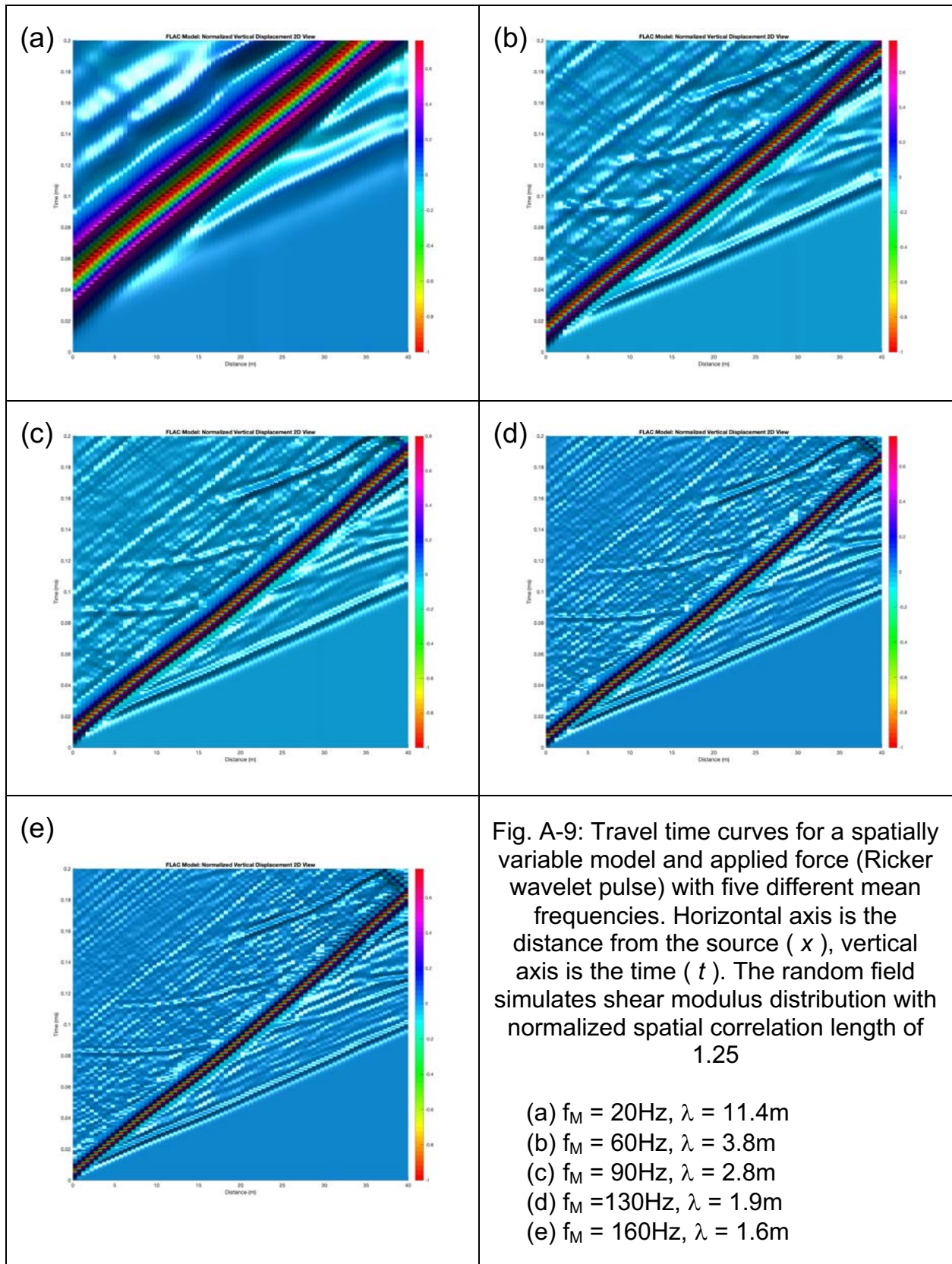


Fig. A-8: Dispersion curves for a spatially variable model and applied force (Ricker wavelet pulse) with five different mean frequencies. Horizontal axis is the distance from the source (x), vertical axis is the time (t). The random field simulates shear modulus distribution with normalized spatial correlation length of 0.75

- (a) $f_M = 20\text{Hz}$, $\lambda = 11.4\text{m}$
- (b) $f_M = 60\text{Hz}$, $\lambda = 3.8\text{m}$
- (c) $f_M = 90\text{Hz}$, $\lambda = 2.8\text{m}$
- (d) $f_M = 130\text{Hz}$, $\lambda = 1.9\text{m}$
- (e) $f_M = 160\text{Hz}$, $\lambda = 1.6\text{m}$



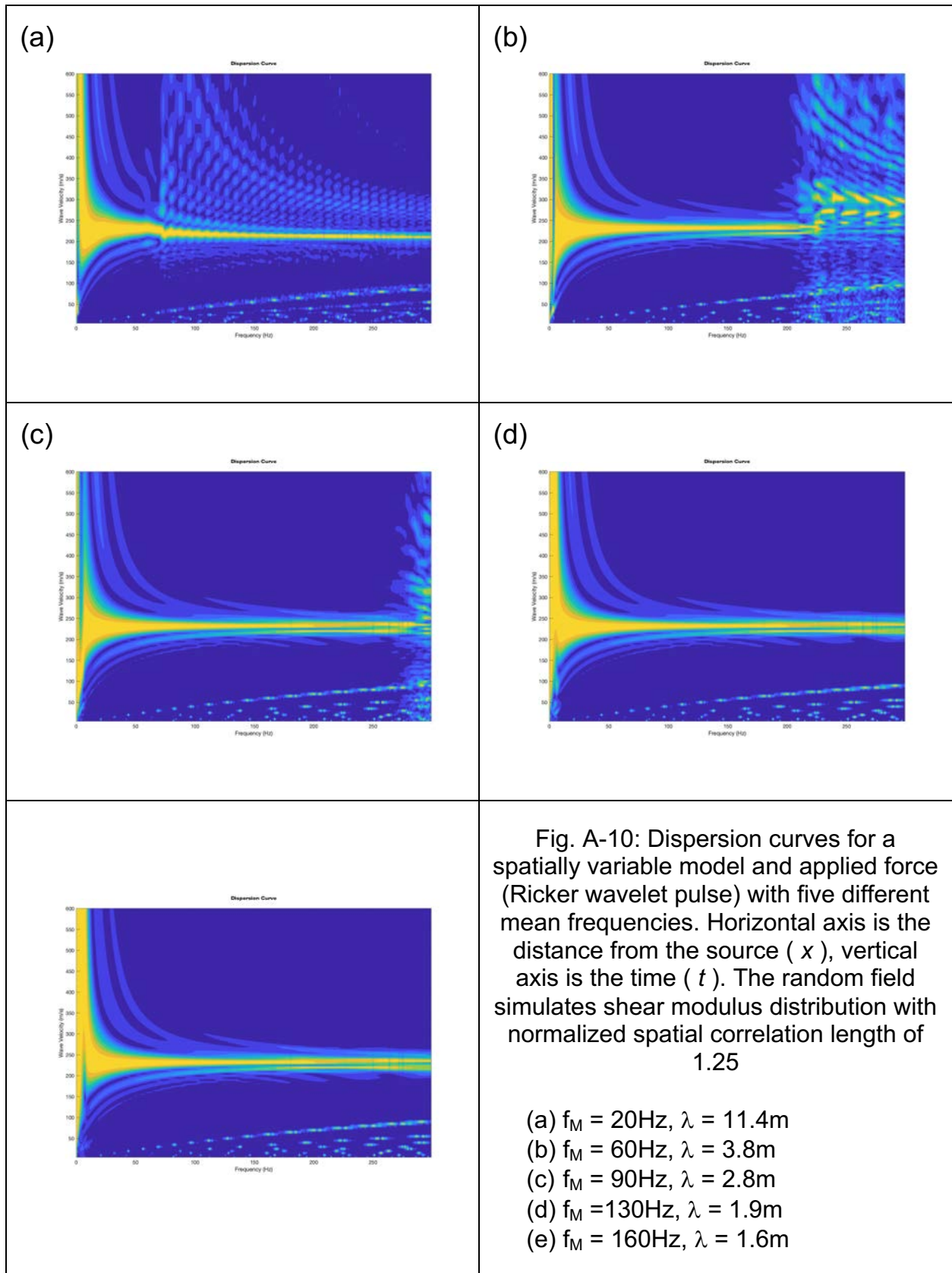


Fig. A-10: Dispersion curves for a spatially variable model and applied force (Ricker wavelet pulse) with five different mean frequencies. Horizontal axis is the distance from the source (x), vertical axis is the time (t). The random field simulates shear modulus distribution with normalized spatial correlation length of 1.25

Appendix B: Computation of Fast Fourier Transform (FFT)

A time signal is defined as the variation of any variable with time, for example, the displacement with time. A signal can also represent a variation with space; however, signals with variation in space are out of the scope of this study.

Signal processing techniques are used to extract important information from time signals. Several techniques have been developed over the years. For this study, the technique to extract frequency domain information is most relevant. This technique is called 'Fourier Transform' named after the mathematician Joseph Fourier (1768-1830).

Fourier transform (FT)

FT is a process of decomposing a time signal into weighted sums of sines and cosines of increasing frequencies. The objective is to match sines and cosines of different frequencies and determine the level of presence of those frequencies. Different types of FT can be used in theory depending on if the time signal is discrete or continuous and periodic or non-periodic (Haykin and Van Veen, 2007). However, the FT used in digital computers is the Discrete Fourier Transform (DFT). DFT is performed on signals which are discrete and (assumed) periodic.

DFT of a discrete signal $x[n]$ is given by the equation

$$X[i] = \sum_{n=0}^{N-1} x[n] e^{-j\left(\frac{2\pi}{N}in\right)} \quad (10-1)$$

where n = sample no. of the signal, N = total no. of samples of $x[n]$ and i is the sample no. representing the frequency. Eq. 10-1 shows that both the time signal (x) and frequency function (X) are discrete. If both time and frequency are continuous functions, then the equivalent of Eq. 10-1 would be

$$X(\omega) = \int_{-\infty}^{\infty} x(t) e^{-j(\omega t)} dt \quad (10-2)$$

Eq. 10-2 shows that the summation becomes integral in continuous domain; this represents another type of FT.

The exponential in Eq. 10-2 is related to the complex sinusoids through the Euler's identity

$$e^{\pm jx} = \cos(x) \pm j \sin(x) \quad (10-3)$$

DFT computes the inner product of signal $x[n]$ and the complex sinusoids to determine the level of presence of these complex sinusoids in the signal $x[n]$. The resulting values of $X[i]$ are complex numbers as a function of frequencies ranging from $i = 0$ to $i = (N-1)$ ($2\pi / N$). The magnitude of the complex number at a particular frequency i ($2\pi / N$) indicates the level of presence of the sinusoid of that frequency; phase angle of that complex number represents the phase of the sinusoid. An example using the programming language MATLAB™ is presented below to explain this concept. The 'fft' command of MATLAB™ computes the magnitude and phase information of any given time signal. Note that MATLAB™ uses the Fast Fourier Transform (FFT) algorithm to compute the DFT of the signal.

Fast Fourier Transform (FFT): executing the DFT formula on a time signal can be extremely slow. Several algorithms have been developed to increase the computing speed to calculate the frequency spectrum of a signal; these are called the Fast Fourier Transform (FFT) algorithms. The most commonly used FFT algorithm is the Cooley–Tukey algorithm where Cooley and Tukey showed that the summation in Eq. 10-3 can be split in two terms; one for the odd numbered values ($n = 2m$) and one for the even numbered values ($n = 2m+1$) as shown in Eq. 10-4 below

$$\begin{aligned} X[i] &= \sum_{n=0}^{N-1} x[n] e^{-j\left(i\frac{2\pi}{N}n\right)} \\ X[i] &= \sum_{m=0}^{N/2-1} x[2m] e^{-j\left(i\frac{2\pi}{N}2m\right)} + \sum_{m=0}^{N/2-1} x[2m+1] e^{-j\left(i\frac{2\pi}{N}2m+1\right)} \\ X[i] &= \sum_{m=0}^{N/2-1} x[2m] e^{-j\left(i\frac{2\pi m}{N/2}\right)} + e^{-j\left(i\frac{2\pi}{N}\right)} \sum_{m=0}^{N/2-1} x[2m+1] e^{-j\left(i\frac{2\pi m}{N/2}\right)} \end{aligned} \quad (10-4)$$

Eq. 10-4 shows that the summation in Eq. 10-1 is simply split into smaller DFTs. Since the range of i is $0 \leq i < N$ and of m is $0 \leq m < N/2$, the symmetric properties of the summation allow the computations to be reduced by half for each sub-summation in Eq. 10-4. Therefore, the computations reduced from the order of N^2 to the order of M^2 where $M = N/2$. This process can continue as long as the sub-DFT has an even valued M ; this process continues until the computation reduced to the asymptotic limit of the order of $N \log N$.

For a signal which does not have the required samples for the Cooley-Tukey algorithm to be executed, MATLABTM adds the samples of zeros to prolong the signal to a length of a power of 2 (zero-padding, see below).

Consider a time signal $x[n]$ given as

$$x[n] = 3 \cos(2\pi f_1 n \Delta t + 0.2) + \cos(2\pi f_2 n \Delta t - 0.3) + 2 \cos(2\pi f_3 n \Delta t - 2.4) \quad (10-5)$$

where f_1 , f_2 , and f_3 are 20 Hz, 30 Hz, and 40 Hz respectively and Δt is the time step.

Note that the above signal is composed of three sinusoids with the three frequencies f_1 , f_2 and f_3 , each with a magnitude and a phase. The amplitudes of these sinusoids are $a_1 = 3$, $a_2 = 1$, and $a_3 = 2$ respectively, while the phase angles are $\varphi_1 = 0.2$, $\varphi_2 = -0.3$ and $\varphi_3 = -2.4$ respectively. The DFT computed for the above signal should show the information about the magnitudes and phase angles of the sinusoids in the time signal $x[n]$.

Appendix C: Linear time-invariant (LTI) system

The concepts of laboratory methods used in this study for measuring the dynamic properties of soils are based on the assumption that the system of soil specimen and the equipment are LTI because the strain levels in these techniques are in very small to small range.

Analysis of systems which are linear and time-invariant is significantly simpler than that of other systems. The assumption of LTI system facilitates the *system identification* problems (explained below). A time-invariant system is the one which does not change its characteristics over time; a linear system is the one in which the superposition principle can be applied i.e. sum of time-shifted input is directly related to the sum of time shifted output. Details of LTI systems such as their properties can be reviewed from Santamarina and Fratta (2005).

System identification in time domain

The mass-dashpot system is a single-degree-of-freedom (SDOF) LTI system which is represented by the equation of motion

$$m\ddot{y} + c\dot{y} + ky = f \quad (10-6)$$

where (f) is the input force, (y) is the response, and (m), (c), and (k) represent the SDOF system properties; these properties characterize the LTI system. The problem of identifying these system properties is termed as the 'inverse problem' where an impulse response can be used to determine these properties. An impulse response is the response of the system (for example the mass-dashpot system) when an impulse is applied to that system (f in Eq. 10-6 is impulse)

The underdamped impulse response of a SDOF system is given by

$$h(t) = \frac{e^{-\xi\omega_0 t}}{m\omega_0\sqrt{1-\xi^2}} \sin(\omega_0\sqrt{1-\xi^2} t) \quad (10-7)$$

where (ω_0) is the radial resonance frequency, (ξ) is the damping ratio, and (m) is the mass of the SDOF system.

The advantage of assuming an LTI system is that the impulse response contains all the information about the system. Obtaining impulse response in practice is not possible because the impulse function and its response are mathematical ideologies. The system characteristics are obtained by processing the input and output results in frequency domain (next section). However, if an appropriate analytical model of the system is available, the measured impulse response can be curve-fitted to obtain approximations of the system characteristics.

System identification in frequency domain

Consider again the SDOF system represented by Eq. 10-6. In time domain, an impulse is used as the input force to determine the impulse response. If the input force is replaced by a complex exponential, Eq. 10-6 can be written as:

$$m\ddot{y} + c\dot{y} + ky = F_o e^{j(\omega t)} \quad (10-8)$$

where F_o is the amplitude of the input force. The response of the system then becomes

$$y(t) = H(\omega) F_o e^{j(\omega t)} \quad (10-9)$$

Substituting $y(t)$ in Eq. 10-9 will yield the expression for the transfer function $H(\omega)$ as

$$H(\omega) = \frac{1}{k} \left[\frac{\omega_n^2}{\omega_n^2 + j2\xi\omega\omega_n - \omega^2} \right] \quad (10-10)$$

Eq. 10-10 is a complex function which represents the frequency response function or the transfer function of the SDOF system based on the displacement response (y). Similar transfer functions can be obtained for velocity (\dot{y}) and acceleration (\ddot{y}) responses. They are expressed as:

$$H(\omega) = \frac{1}{k} \left[\frac{j\omega\omega_n^2}{\omega_n^2 + j2\xi\omega\omega_n - \omega^2} \right] \quad \text{for velocity} \quad (10-11)$$

$$H(\omega) = \frac{1}{k} \left[\frac{-\omega^2\omega_n^2}{\omega_n^2 + j2\xi\omega\omega_n - \omega^2} \right] \quad \text{for acceleration} \quad (10-12)$$

The frequency response functions presented above also completely characterize the system in frequency domain. Although the displacement impulse (Eq. 10-9) and displacement frequency (Eq. 10-10) responses are in different domains, they provide the same system information; therefore, they must be related. Indeed, the frequency response is the Fourier transform of the impulse response expressed as

$$H(\omega) = \int_{-\infty}^{\infty} h(t) e^{-j(\omega t)} dt \quad (10-13)$$

Similar conclusion can be made for the velocity and acceleration transfer functions.

$$\delta = \ln \frac{a_n}{a_{n+1}} = \frac{2\pi\xi}{\sqrt{1-\xi^2}} \quad (10-14)$$

where a_n and a_{n+1} are obtained from the time domain response.

Appendix D: Guideline for the selection of the near-surface techniques intended to be used in soft grounds

This guideline is intended to give direction to practitioner when dealing in the field with soft grounds such that they could lead to a very low value of impedance ratio between the top two layers in the soil profile.

Planning Underground Investigation in Soft Soils

Every soft-ground study should be initiated with a desktop study, often starting with a review of the relevant geological and geomorphological information, possible types of soils, land use and surface conditions, followed by an assessment of aerial photographic and satellite images for different periods of time, looking for some evidence of previous ground disturbance, either natural or man-made.

Once this information is available, the potential for geophysical survey should be assessed and the preliminary selection of geophysical techniques to be used could be made. It is particularly important to establish a secure and agreed timetable in which the fieldwork stages are correctly integrated. The timetable should be sufficiently flexible to accommodate additional contingency survey, when the geophysical technique has to be changed due to local conditions, and costing should allow for this.

Beyond the project

It is strongly recommended that field evaluation, and any geophysical survey that it includes, should be part of an integrated programme of research. English Heritage (2008) identify two sets of instances where assessment of the potential of the geophysical survey data may be required as part of the execution stage of the larger programme:

- Where such data indicates that further survey would be of significant advantage to the realisation of specified research objectives.
- Where the geophysical survey data, in its own right, has significant potential for advancing research into geophysical prospecting techniques, or the interpretation of geophysical data.

By following the above recommendations this guideline is not just going to be updated, but also it is going to include every new advance in planning, choosing and surveying near-surface geophysical methods, as well as interpreting results.

First Selection of Possible Near-Surface Geophysical Methods

The purpose of the following section is to make a preliminary decision about the geophysical techniques more feasible to be used in wetlands for determining the depth of hard strata. This is based on literature review, guidelines, manuals and standard recommendations.

The user of this document must be aware that the choice of survey method(s) will vary with the site conditions, logistics and time constraints particular to each separate evaluation project. Jones (2008) recommends that adequate time should be allowed for the geophysical survey to be undertaken and reported on once this has been identified as a preferred evaluation technique.

Seismic refraction and reflection techniques, electrical resistivity and ground penetrating radar (GPR) were selected as the most appropriate technique, given the evidence of use reported in the literature for determining depth to firm bottom, as well as the ASTM standard recommendations.

- ***Ground Penetrating Radar***

Jones (2008) recognizes the potential of GRP to be used in wetlands. Actually they stated this about GPR technique: *“The only technique that at present seems to offer any potential is GPR over low mineral content peat. At low frequencies (e.g. 100MHz) the peat/mineral interface of peat basins is detectable at depths up to about 10m (Theimer et al 1994; Utsi 2001), and reflections have also been recorded from substantial objects such as bog oaks (Glover 1987). [...] Although such accounts are promising, there is a need for further experimentation, and reference to ground-truth, before GPR can be recommended as a routine approach in these circumstances. In other types of wetland, in clay or saline situations, GPR and other techniques are ineffective at locating organic structures.” [sic]*

Summary of expected GPR response over various types of site and features.

site stratigraphy: (moderate)

Providing adequate physical contrast between adjacent layers and features exists, stratigraphy can be resolved within the limits of spatial resolution for the antenna

Wetlands: (moderate/good)

Response may be highly site-dependent and influenced by the presence of high-conductivity clays. Success has been reported for imaging targets in peat and below fresh water.

Geomorphology (moderate/good)

Lower-frequency antenna may be required in the presence of alluvial clays, but palaeochannels and other large scale features can still be located. The depth of overburden can also be mapped.

- **Seismic techniques**

Specific site conditions and the aims of the survey will define the sampling methodology to be adopted. According with documentation reviewed so far the most suitable techniques are: seismic refraction, seismic reflection, and multichannel analysis of surface waves.

- **Electrical Resistivity**

The maximum acceptable sampling interval for area surveys is 1m along traverses separated by a maximum of 1m.

Area surveys, using the twin probe (or twin electrode) probe configuration, are the preferred method of ground coverage. The square array (often employed on cart-based systems) is also acceptable for area surveys. Other methods require special justification.

For twin probe systems the mobile probe spacing should usually be 0.5m; wider separations and/or multiplexed arrays require explanation. The equivalent spacing for a square array would typically be 0.75m.

Table D.1. Main characteristics of geophysical techniques preliminary selected.

	Seismic Refraction	Seismic Reflection	DC Electrical Resistivity	GPR
Depth	Typically, less than 30 m.	From about 15 to 300 m deep.	Related to electrode spacing and electrical subsurface properties.	Can be more than a 30 m in materials having conductivity of a few milliSiemens/meter.
Source for Shallow	Sledgehammer or a shotgun.	Sledgehammer, shotgun, or rifle as seismic sources.	Sledgehammer, shotgun, or rifle as seismic sources.	Antennas may be pulled by hand or with a vehicle at speeds from 0.8 to 8 kph, or more, that can produce considerable data/unit time.
Ease of Use	Labour intensive. Transducers coupling needed.	Relatively difficult to make and are labour intensive. Transducers coupling needed. Source must be in contact with the ground.	Relatively slow and labour intensive. Measurements are made on a station by station basis.	Relatively easy to make. Penetration in mineralogical clays and in materials having conductive pore fluids may be limited to less than 1 m. Measurements also can be made in lakes and rivers with low conductivity (fresh) water.
Interpretation Methods	Time intercept Delay time Ray tracing Generalized reciprocal method	Two different approaches to data acquisition: common offset method and the common depth point (CDP) method.	It allows obtaining depth, thickness, and resistivity of layers. Processing can be done by curve matching or by using forward and inverse modeling.	Data can often be interpreted without data processing. Highest lateral and vertical resolution of any surface geophysical method. Variety of frequency antennas (10 to 3000 mHz).
Resolution	<u>Vertical</u> : layer thickness \ll depth to upper surface. It resolves three to four layers. <u>Horizontal</u> : function of transducers spacing (2 - 6m)	<u>Vertical</u> : proportional to the frequency of the source. (e.g. 1 m with 500 Hz) Optimum conditions are saturated fine-grained soils. <u>Horizontal</u> : function of transducers spacing (0.3 - 3m)	Lateral resolution is a function of electrode spacing, as well as, the spacing between station measurements. Resistivity soundings typically can resolve three to four layers.	<u>Vertical</u> : ranges from a few centimeters to a meter (inches to more than a foot). <u>Horizontal</u> : determined by the distance between station measurements, or the sample rate, or both, and with the towing velocity of the antenna.
Limitations	Sensitivity to acoustic noise and vibrations. Velocity increasing with depth. It does not detect thin layers. Source - geophone distance 3 to 5 times the desired depth of investigation is needed	Sensitivity to acoustic noise and vibrations. Distance source to farthest geophone is usually 1 to 2 times the desired depth of investigation.	Measurements are susceptible, to interference from nearby metal pipes, cables, or fences. The spacing between electrodes must extend three to five times the depth of interest.	The major limitation of radar is its site specific performance. Often, the depth of penetration is limited by the presence of mineralogical clays or high conductivity pore fluids.

Second Selection of Possible Near-Surface Geophysical Methods

The process to guide the second selection of possible near-surface geophysical methods includes three steps. First, the drawing of some initial conceptual models based on the preliminary definition of specific conditions for the target area to be surveyed; second, numerical forward modeling and laboratory simulations; third, field work that allows the calibration of some specific geophysical technique array and at the same time that allows getting preliminary results that confirm or discard the use of some specific geophysical technique.

Preliminary Definition of Specific Conditions for the Site to Survey

Geophysical techniques can, as yet, have little part to play in wetland evaluation. Structural remains (such as pile dwellings, trackways, etc.) in organic sediments, in particular, are often undetectable. Traditional dry land geophysical techniques are best attempted in areas of relative dryness and shallow overburden ('islands' or wetland margins) and features so detected may then have some indirect bearing on the likely location of significant sites elsewhere obscured. Aerial photography, LIDAR and remote sensing (Cox, 1992; Donoghue and Shennan, 1988), linked with augering and test trenching can offer the best overall evaluation, geophysics being drafted in for the examination of specific shallow or marginal sites. (Jones, 2008)

Initial Conceptual Models: Forward Modeling

One important concept, in planning near-surface geophysical surveys on wetlands, is the development of simple forward models of the geophysical properties of the targets of interest and the geophysical technique that is proposed to map the area. Abraham and Cannia (2011) stated that forward models, when an appropriate level of system noise is added, can be priceless in determining the usefulness of some specific geophysical techniques in mapping the target of interest.

There are several modeling programs that can provide informative forward models to the potential user, either for seismic wave propagation, for electrical resistivity or for electromagnetic induction. However, Abraham and Cannia (2011) also remarked that it is very important to be aware that forward models only provide information as good as the

input. Good input data is basically a good understanding of the geophysical properties of the materials of interest.

The lessons learned are that if a shortcut is taken at any step in the process, the end product usually suffers (Abraham and Cannia, 2011). The success of near-surface geophysical surveys is dramatically impacted by everything from careful calibration and acquisition to how the information is displayed in final reports.

Field Work: preliminary field tests

All fieldwork for near-surface geophysical surveys on wetlands must be conducted under the principle of repeatability, meaning that the data obtained should be capable of independent duplication.

The following stages of geophysical survey fieldwork should be considered and planned for, where appropriate:

Pilot (test or trial) survey: it may occasionally be necessary for a preliminary assessment to be made of a site's response to geophysical survey, particularly where large areas (>20ha) are concerned. This procedure should indicate whether local conditions are suitable for useful results to be obtained and what techniques and sampling methodology may be most appropriate. Such preliminary information, based on expert assessment, can forestall the wasteful deployment of resources on inappropriate techniques and on sites where the use of geophysics is unlikely to be helpful. A brief site visit may be all that is required. Any pilot survey should not usually take more than a day to achieve, and the results should be made available immediately for incorporation into the project design. Project managers should ensure that they are made aware of the geophysical potential, or lack of it, of their site(s) at the outset; the justification for survey must be clear.

Full survey: once this justification is assured an agreed survey strategy can proceed. This may be full or partial coverage of the site at high or low levels of detail, using one or more techniques, depending on the strategy adopted.

Extended coverage: in some circumstances it may be necessary to accommodate additional survey if earlier results (or subsequent excavation) indicate that this would be

profitable. Where appropriate, allowance for such contingencies should be made in briefs and specifications.

This section is intended to present the field test results conducted at the geophysical test site at University of Waterloo. The objective of the test is to evaluate the reliability of geophysical methods for the detection of competent strata in soil profiles with high water content and also understand the frequency effects in the estimation of shear wave velocity from two different geophysical field tests. The results of the tests are compared with the numerical simulations.

- ***Field test: general site description***

An example of the expected general site description is this:

“The University of Waterloo’s Columbia Lake Test Site (UW-CLTS) is a geophysical test site for the calibration and testing of Electromagnetic and Ground Penetrating Radar instruments. The site is also used by University of Waterloo’s Earth Science students for instruction purposes. The UW-CLTS is located north of Columbia Lake on the North Campus of the University of Waterloo, in Waterloo, Ontario Canada. The site is 50 m by 50 m in size and consists of mainly silty clay till soil. For instructional and calibration purposes, following targets are buried at various locations on the site: vertical steel drums, sheet steel, and steel and plastic pipes, respectively (Phillips 2001). The site was chosen for the current testing due to its vicinity to the University of Waterloo, the low ambient noise level, the open field and the relatively flat ground surface, and availability of test results from previous studies.”